Versatile Applications of Metal-Organic Frameworks (MOFs) and Derived Materials
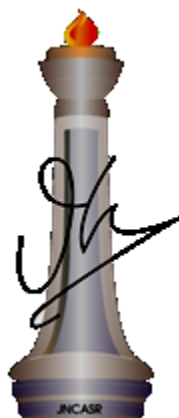
A THESIS SUBMITTED FOR DEGREE OF

Doctor of Philosophy

By

JAYA RAMULU KOLLEBOYINA

**Chemistry and Physics of Materials Unit
Jawaharlal Nehru Centre for Advanced
Scientific Research
(A Deemed University)
Bangalore-560 064
October 2013**

Versatile Applications of Metal-Organic Frameworks (MOFs) and Derived Materials

Dedicated to Amma, Nana, Sri, Rakhi
Teachers/Friends Shirisha, Maji, Subi and Eswar

Declaration

I hereby declare that the matter embodied in the thesis entitled "***Versatile Applications of Metal-Organic Frameworks (MOFs) and Derived Materials***" is an authentic record of research work carried out by me under supervision of Prof. Tapas Kumar Maji, at the Chemistry and Physics of Materials Unit, Jawaharlal Nehru Centre for Advanced Scientific Research, Bangalore, India and that it has not been submitted elsewhere for the award of any degree or diploma.

In keeping with the general practice in reporting the scientific observations, due acknowledgement has been made whenever the work described is based on the findings of other investigators. Any omission that might have occurred due to oversight or error in judgement is regretted.

Kolleboyina Jayaramulu

Acknowledgments

First and foremost, I would like to thank my research supervisor Prof. Tapas Kumar Maji, without whom none of this would be been possible. I am indebted to him for taking me in his research group, and teaching me how to appreciate science to perform research, to communicate ideas, and to have a vision for the future. Not only has he been an excellent teacher and mentor, but also a valuable moral support one the personal front. I am fortunate to know him as a great scientist and above all a very kind human being, who has taught me always, look at the bright side. The strong scientific foundation that he has given me will continue to guide and inspire me in my future career.

I thank Prof. C. N. R Rao, FRS who has been a constant source of inspiration for me. I am grateful to him for the interest that he had shown in my research work in the form of many valuable suggestions. I consider it an honour to have worked with him on various research problems.

It has been a great pleasure working with prof. M. Eswaramoorthy and Prof. Subi J George. I am extremely grateful to them for teaching me various aspects of personal and experimental guidance.

I would like thank to thank Prof. M. Eswaramoorthy, Prof. Subi J. George, Prof Balasubramanian, Prof. Chandrabhas Naryanan, Prof. Satyen Saha, Dr. KKR Datta, Mrs. Lakshmi Sirisha, Praveen (ONGC), Ramesh, Nagaraj and Mrs. Maji for their encouraging words and hospitality.

I am thankful all collaborators Prof. C.N.R. Rao, Prof. Kitagawa (Kyoto university, Japan), Prof Balasubramanian, Prof. Chandrabhas Naryanan, Prof. M. Eswaramoorthy, Prof. Subi J. George, Prof. Ranjan Datta, Prof. T. Govindraju, Prof. Umesh Waghmare, Prof. Aninda Bhattacharya (IISC) and Prof. Peter Sebastian for guiding me in various research problems.

I am thankful to the past and present chairman of CPMU for allowing me to utilize the various facilities in the center. I am thankful to the faculty members of JNCASR and Indian Institute of Science (IISC) for the course that have been extremely beneficial to this study. In particular, I would like to thank Prof. T. N. Guru Row, Prof. T. G. Raju, Dr. Subi J George, Prof. G.U. Kulkarni, Prof. Chandrabhas Naryanan, Dr. Vidyadiraja, Prof. M. Eswaramoorthy, and Prof. Balasubramanian for their courses and hospitality.

Certificate

I hereby certify that the work described in this thesis entitled "***Versatile Applications of Metal-Organic Frameworks (MOFs) and Derived Materials***" has been carried out by Mr. Jaya Ramulu Kolleboyina under my supervision at the Chemistry and Physics of Materials Unit, Jawaharlal Nehru Centre for Advanced Scientific Research, Bangalore, India and that it has not been submitted elsewhere for the award of any degree or diploma.

Prof. Tapas Kumar Maji

(Research Supervisor)

Preface

The thesis is organized in eight chapters that cover recent developments of MOFs, nano porous carbon materials in terms of synthesis, characterization, classification and advance applications.

Chapter 1 deals with basic concepts and current developments of all porous materials. This chapter gives a brief overview of functional metal-organic frameworks (MOFs) at bulk and nanoscale and porous carbon materials, discusses their importance, properties and applications.

Chapter 2 deals with a luminescent MOF and its application in metal ion sensing. A three dimensional porous framework $\{Mg(DHT)(DMF)_2\}_n$ (DHT: 2,5-dihydroxyterephthalate) has been synthesized solvothermally and structurally characterized. The MOF composed of excited state intramolecular proton transfer (ESIPT) responsive linker DHT shows tunable multicolour emission in different solvent systems based on polarity. The desolvated framework exhibits large stoke shifted green emission in solid state and has been exploited for metal ion sensing through binding with the pendent –OH groups aligned on the pore surface. The framework shows reversible highly selective sensing for Cu(II) up to nano-molar concentration among the number of metal ions based on emission quenching. The immobilized Cu(II) can be selectively removed from the framework by chelating agents like EDTA without any structural disintegration.

Chapter 3 is related to functional nanoscale MOFs and consists of two subchapters. The first part deals with a simple and straightforward method for fabricating shape assisted micronic cages of $[M(C_4O_4)(H_2O)_2]_n$ (where M = Co^{II} (**1**), Zn^{II} (**2**), and Cd^{II} (**3**), $C_4O_4^{2-}$ = squarate dianion) from micron size cubes where polyvinylpyrrolidine (PVP) acts as a structure directing agent. The cubes/cages are post-synthetically functionalized with organic chromophore OPV to obtain green luminescent cubes or cages. 2nd part of this chapter deals with a porous magnetic nanotape $\{[Co_2(\mu\text{-}OH)_2(C_4O_4)](H_2O)\}_n$. The nanotape is further coated with SiO_2 and then attached with fumaric acid to link with the Tb(III) metal ions. The resulting multifunctional nanocomposite $\{NMOF@SiO_2@Fu@Tb\}$ exploited for sensing of adenosine triphosphate (ATP) nucleotide.

Chapter 4 depicts two different strategies to obtain mesoporous MOFs. A mesoporous MOF $\{[Zn_6(L)_2(H_2O)_6].5DMF\}$ based on a hexacarboxylate linker L = 5,5',5"-[1,3,5-phenyltri-(methoxy)]triisophthalate) has been prepared solvothermally and consist of three different cages with different window dimensions. The framework has been exploited for gas storage and dye separation based on the window dimensions. The inherent blue luminescent of the mesoporous has been further utilized for efficient light harvesting based on a suitable acceptor dye fluorescein. This chapter also describes an easy and facile fabrication of MMIL-110 (Al) hierarchical porous MOF based on a

cooperative self-assembly of a surfactant CTAB which acts as a template, capping and structure directing agent. Based on the hierarchical micro and meso porosity, meso-MOF unveils size-selective encapsulation of both donor (Acridine orange) and acceptor (Rhodamine B) concomitantly and the resulting composite exhibits efficient excitation energy transfer from donor Acridine orange to an acceptor Rhodamine B dye.

Chapter 5 reports synthesis and structural characterization of a three dimensional pillared-layer metal-organic framework, $[Cd(bipy)_{0.5}(Himdc)](DMF)]_n$ (bipy = 4,4′-bipyridine and Himdc = 4,5-imidazoledicarboxylate) and their H_2 and CO_2 storage properties. The high heat isosteric heat of H_2 (9.0 kJ/mol) and CO_2 (35.4 kJ/mol) adsorption has been correlated to the highly polar pore surfaces decorated with the pendent oxygen atoms of the Himdc linkers.

Chapter 6 reports synthesis and structural characterization of a three dimensional antiferromagnetic bio-MOF of Fe(III) $\{[Fe(\mu\text{-}OH)(1,4\text{-}napdc)](H_2O)\}$, (1,4-napdc = 1,4-naphthalenedicarboxylate). The framework shows guest responsive reversible crystal dynamics associating with the mobile rotational properties of naphthalene moiety of 1,4-napdc linker. The framework exhibits selective CO_2 uptake properties. This Bio-MOF has been used as a matrix for loading and in vitro drug delivery of dopamine under physiological conditions.

Chapter 7 deals with the stabilization of Au, Pd, Pt, and Cu_2O nanoparticles on a 2D MOF $\{[Zn(Himdc)(4,4'\text{-}bipy)](H_2O)\}_n$ composed of mixed linkers system. The functional polar porous environment of MOF helps to stabilize of various nano particles. **Pd@MOF** has been used for catalytic three component coupling reaction for the synthesis propargylamines whereas **Cu₂O@MOF** hybrid shows efficient and selective catalytic activities for 1, 3- dipolar cycloaddition reaction based on different terminal alkynes and aliphatic/aromatic azides.

The final **Chapter 8** deals with MOF derived carbon based materials. The first part reports synthesis, characterization and gas storage properties of hierarchical porous carbons based on IRMOF-3. The porosity of the3 carbons has been modulated by the external carbonizing agent sucrose. 2nd part of this chapter contains synthesis of borocarbonitride (BC_4N) from a boron based MOF $\{Zn_4(1,4\text{-}ndc)_3(bim)_2]\cdot 2H_2O\}$ (bim =tetrakis(1-imidazolyl)borate)) and application in gas storage and in-situ stabilization of various metal nanoparticles.

Contents

Chapter 1   Brief Overview and Recent Developments of Metal-Organic   Frameworks (MOFs) and Derived Materials

Chapter 2   Tunable Emission from a Porous Metal-Organic Framework by Employing and Excited-State Intramolecular Proton Transfer (ESIPT) Responsive Ligand: Specific Sensing and Removal of Metal Ions

Chapter 3   Nanoscale Metal-Organic Frameworks (NMOFs)

Chapter 3.1   Shape Assisted Fabrication of Fluorescent Cages of Squarate based Metal–Organic Frameworks

Chapter 3.2   Facile   Synthesis   of   Multifunctional   Porous-Magnetic-Luminescent Nanotape Metal-Organic Framework: Highly Selective Sensing for Adenosine Triphosphate (ATP)

Chapter 4   Mesoporous Metal-Organic Frameworks (MMOFs)

Chapter 4.1 A Luminescent Mesoporous Metal-Organic Framework for Selective CO2 Uptake, Selective Dye Inclusion and Light Harvesting Properties

Chapter 4.2 Supramolecular template based hierarchical porous metal-organic framework MMIL-110 (Al): dye scavenging and efficient scaffold for light harvesting application

Chapter 5 Three-Dimensional Metal-Organic Framework with Highly Polar Pore Surface: H_2 and CO_2 Storage Characteristics.

Chapter 6 A 3D Bio-MOF of Fe(III): Guest-Responsive Structural Transformation, Selective CO$_2$ Uptake and Controlled Drug Delivery

Chapter 7 Honeycomb Porous Framework of Zn(II): Effective Host for Pd and Cu$_2$O Nanoparticles and Catalytic Activities

Chapter 8 Metal-Organic Framework (MOF) derived Materials for Energy and Environmental Applications

Chapter 8.1 Nanoporous Carbons Derived from MOF with Tunable Porosity based On External Carbonizing Agent: Excellent Candidates for Gas Storage And Electrochemical Storage

Chapter 8.2 A Nanoporous Borocarbonitride (BC$_4$N) with Novel Properties Derived from a Boron Imidazolate based Metal-Organic Framework.

List of Acronyms

0D – Zero Dimensional

1D- One Dimensional

2D- Two Dimensional

3D- Three Dimensional

AC- Alternating Current

ADP-Adenosine Diphosphate

AFM- Atomic Force Microscopy

AMP Adenosine Monophosphate

AO- Acridine Orange

ATP Adenosine Triphosphate

BCN- Borocarbonitride

BET- Brunauer-Emmett-Teller

BTC-1,3,5-benzenetricarboxylate

CE- Conventional electric heating

CLSM-Confocal Laser Scanning Microscopy

CN- Carbonitride

CNT- Carbon Nanotube

COF- Covelent Organic Frameworks

CTAB- Cetyltrimethylammonium Bromide

CTAB- Cetyltrimethylammonium Bromide

CV- Cyclic Voltammetry

CVD-Chemical Vapour Deposition

DFT-Density Functional Theory

DHT-2,5- Dihydroxyterephthalate

DSC- Differential Scanning Calormetry

EC- Electrochemistry

ED- Electron Diffractions

EDAX- Energy Dispersive- X-ray Analysis

EDLC- Electrochemical Double-Layer Capacitor

EELS-Electron Energy Loss Spectroscopy

ESIPT- Excited State Intramolecular Proton Transfer

FC- Field-cooled

FE-SEM- Field Emission Scanning Electron Microscopy

FL-Fluorescein

FRET- Förster resonance Energy Transfer

FT-IR   Fourier Transform Infrared Spectroscopy

GC- Gas Chromatography

GCMC- Grand Canonical Monte Carlo

GTH-Goedecker-Teter-Hutter

HKSUT- Hongkong Univeristy of science and Technology

HRTEM High Resolution Transmission Electron Microscopy

ICP-MS- Inductively Coupled Plasma Mass Spectroscopy

ICP-OES-Inductively Coupled Plasma-Optical Emission Spectroscopy

IMDC-4,5-Imidazoledicarboxylate

IRMOF- Iso Reticular Metal-Organic Framework

I-V – Current Voltage

JCPDS- Joint Committee on Powder Diffraction Standards

KIT- Korean Institute of Technology

LCD- Liquid Crystal Display

LED- Light Emitting Diode

LMCT- Ligand to Metal Charger Transfer

MCM- Mobil Crystalline Material

MIL-Material of Institut Lavoisier

MLCT- Metal to Ligand Charge Transfer

MOC- Metal-Organic Cube

MOCF- Metal-Organic Coordination Framework

MOCVD-Metal Organic Chemical Vapour Deposition

MOF- Metal-Organic Framework

MOP- Metal-Organic Polyhedra

MRI- Magnetic Resonance Imaging

MW- Microwave

NCP- Nano Coordination Polymer

NDC-1,4-napthalenedicarboxylate

NHE- Normal Hydrogen Electrode

NLDFT- Non-Local Density Functional Theory

NMOF- Nano Metal-Organic Framework

NMR- Nuclear Magnetic Resonance

NOTT- University of Nottingham

NPC- Nano porous Carbon

NU- North-western University

OHML- Ordered Hierarchical Micro/Meso porous Framework

OLEDs-Organic Light Emitting Devices

OPV-Oligo(phenylenevinylene)

PBS-Phosphate Buffered Saline

PC- Porous Carbon

PCP- Porous Coordination Polymer

PL- Photoluminescence

PVP- Polyvinylpyrrolidine

PXRD-Powder X-ray Diffraction

Rh 6G- Rhodamine 6G

SBA- Santha Barbara Amorphous

SBU-Secondary Building Unit

SERS- Surface Enhanced Raman Spectroscopy

STP- Standard Temperature and Pressure

SXRD- Single Crystal X-ray Diffraction

TEM- Transmission Electron Microscopy

TEOS- Tetraethylorthosilicate

TFA- Trifluoroacetic acid

TGA- Thermo Gravimetric Analysis

UMCM-Unsaturated Metal Sites

USM- Ultrasonic method

UV-Vis Ultraviolet-Visible

XPS- X-ray Photoelectron Spectroscopy

ZFC-Zero field-cooled

Chapter 1

Brief Overview and Recent Developments of Functional Metal-Organic Frameworks (MOFs) and Derived Materials

Brief Overview and Recent Developments of Metal-Organic Frameworks (MOFs) and Derived Materials

1.1   Introduction to Porous Materials

Porous materials are the solids of great technological importance, due to their ability to interact with gases and liquids, not only at the surface, but throughout their bulk.[1] Indeed, a "porous materials mania" is sweeping through essentially all the fields of science and engineering.[2] These porous solids constitute a rich and active research field, owing to the fact that they are at the heart of several   important applications namely heterogeneous catalysis, gas storage/separation, water purification, adsorption of pollutants, drug delivery, chromatography, earth science (the soil porosity confirms exchange between the soil and the atmosphere), energy (porous materials are envisaged for hydrogen storage and lithium ion batteries) owing to their high surface area, large pore volumes, chemical inertness, mechanical and good thermal stability.[3]

According to the definition of the International Union of Pure and Applied Chemistry (IUPAC), porous materials are classified into three classes based on their pore diameter (d): microporous (<2.0 nm), mesoporous (2-50 nm) and macroporous (>50nm).[4] The pore architectures (size, shape, connectivity), the nature of the pore size distribution and the chemical characteristics of the pore walls determine the properties of such materials. In recent times, hierarchical porous structures have been explored with pore sizes spanning various length scales.[5] However, there are a number of other potential applications in which presence of micropores or even meso pores would be preferable, for instance, adsorption of biomolecules. Therefore the development of micro porous as well as meso porous, materials is of the great importance not only from a fundamental research point of view, but also from its practical application point of view.[6]

The porosity or pore system of a porous sorbent material can be characterized using several methods as shown in Figure 1, which essentially describes the most important physical methods and their ranges of diameter of cylindrical pores or width of slit like pores.[7] Modern techniques enable the adsorption experiments with gases *viz.* nitrogen, argon or carbon dioxide, which can be used to characterize the pore system of a porous sorbent material.[8]
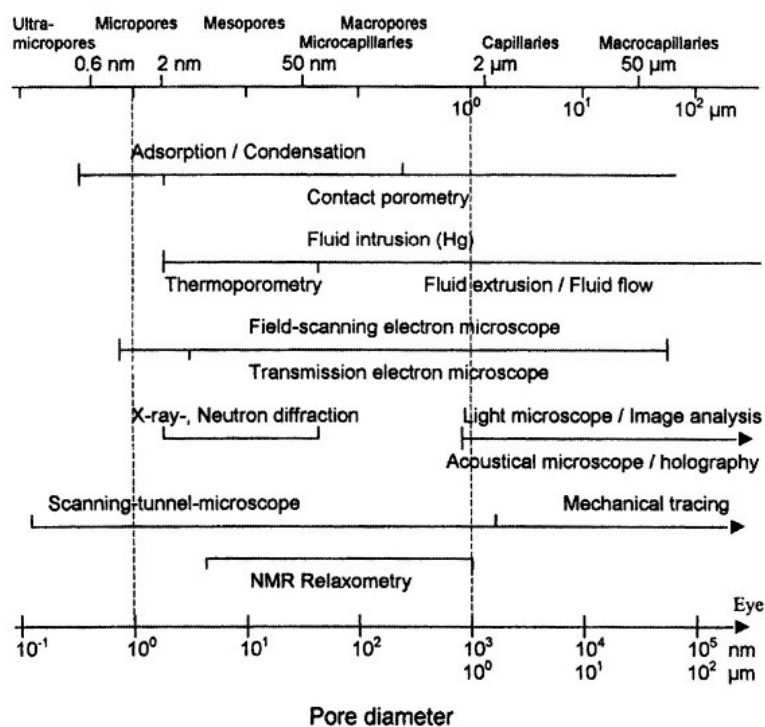
Figure 1 Physical methods for characterization of porous sorbent materials (reproduced with permission from ref 7).

Decreasing the pore size
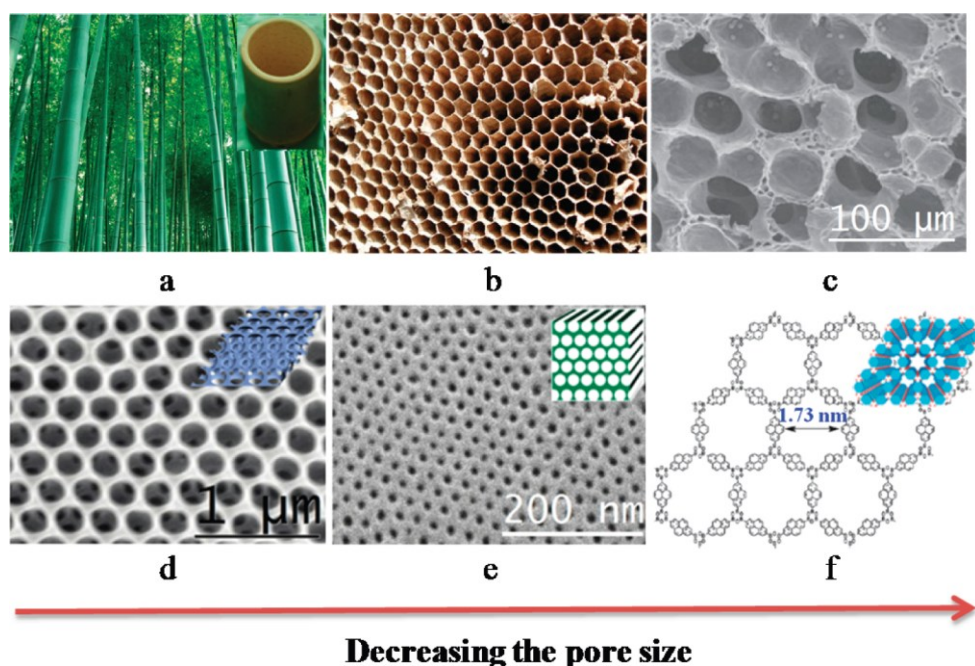
Figure 2 Illustration of porosity existing in nature and in synthesized materials with a decreasing pore size: (a) bamboo; (b) honeycomb; (c) SEM image of alveolar tissue in mouse lung (d) SEM image of an ordered macroporous polymer from direct templating (e) SEM image of an ordered mesoporous polymer from self-assembly of block copolymers (f) structural representation of an ordered microporous polymer (reproduced with permission from ref 9).

However, these materials, both naturally occurring and chemically synthesized have been investigated for potential applications that arise from their openings equivalent to the sizes of innumerable molecules (Figure 2).[9]

1.2 Classification of Porous Materials

The porous materials are characterized by nitrogen adsorption isotherms. Adsorption of guest molecules onto the internal pore surface shows an important role in determining the properties of porous materials.[10] Typically, an adsorption isotherm is a relation between the pressure and adsorbed amount at a constant temperature. The horizontal axis is the relative pressure (P/P_0), which is the equilibrium pressure divided by the saturation pressure. The relative pressure can be from 0 to 1 and $P/P_0 = 1.0$ means that the condensation of adsorptive occurs in the sample cell. The adsorption isotherm is the measurement of adsorptive density which becomes greater bulk (gas) phase density due to the interaction between the adsorptive and solid surface atoms below its condensation pressure.[11] The amount of adsorption on the vertical axis is commonly represented as V/ml (STP)g^{-1} which is expressed by the standard gas volume (at 0 ^{o}C and 1 atm).
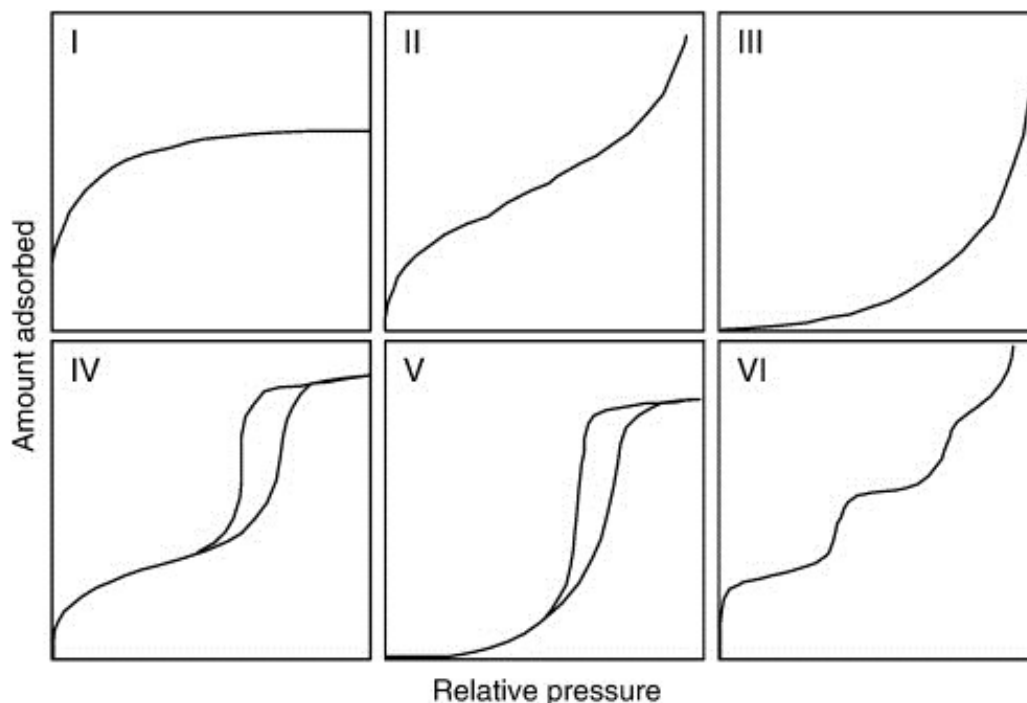
Figure 3 IUPAC classifications of adsorption isotherms (reproduced with permission from ref 11).

According to IUPAC system, adsorption isotherms are classified into six types as shown in Figure 3. The Type I adsorption isotherm is for microporous materials, while type II for nonporous materials, Type III are for non-porous materials and materials which have the weak interaction between the adsorbate and adsorbent, Type IV and V are for mesoporous and Type VI are for homogeneous surface materials. Moreover, the type of adsorption isotherm is unwavering by the pore size and surface character of the porous compounds.

However, several significant structural characteristics of porous solids should also be designated which majorly includes pore geometry, pore surface functionality, pore size and a polymeric framework structure with the topology and functionality is depicted in Figure 4. Based on the difference in their composition, these porous materials can be classified into two major classes: either pure organic or wholesome inorganic materials.[11]
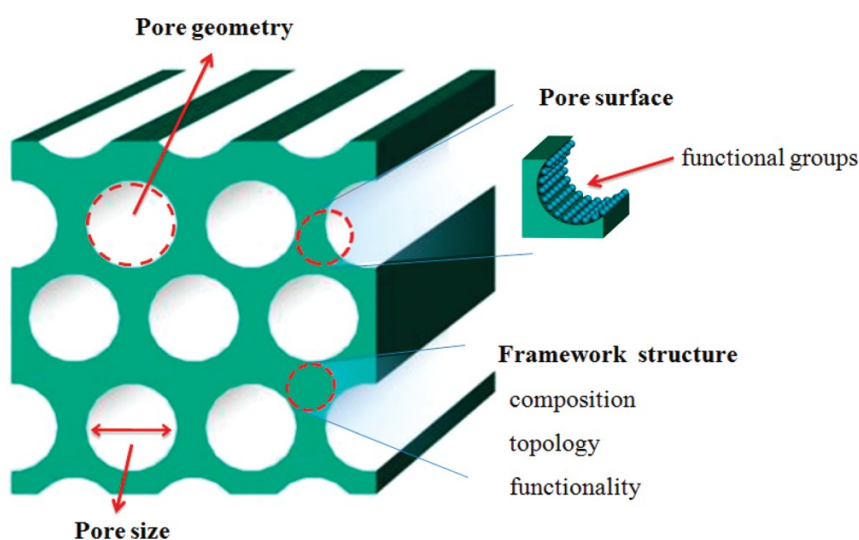
Figure 4 Illustration of pore geometry, pore surface, pore size, and framework structure of porous polymers (reproduced with permission from ref 9).

1.3 Inorganic Porous Materials

Inorganic porous materials cover a range of solids, both oxides and monoxides, crystalline and amorphous, that have a pore size extending from about 1-50 nm.[12-14] Traditionally, the largest subclass of porous inorganic materials are aluminosilicate and aluminophosphate zeolitic materials formed through TO_4 tetrahedral linkages (T=Al, Si, or P). Structured porous inorganic materials e.g. zeolites (Figure 5) or MCM-41**,** MCM-48 (Mobil Composition of Matter), SBA-15 (Santa Barbara Amorphous), KIT-6

(Korean Institut of Technology) and metal oxides (Figure 6) show high chemical and mechanical stability and has generated an increasing interest in different scientific disciplines such as physics, chemistry and biology.[15]Due to the nature of their framework and the porosity, these materials are potential candidates for heterogeneous catalysis, adsorption, ion-exchange, sensor devices, medical therapy, and biomedical applications.[16]
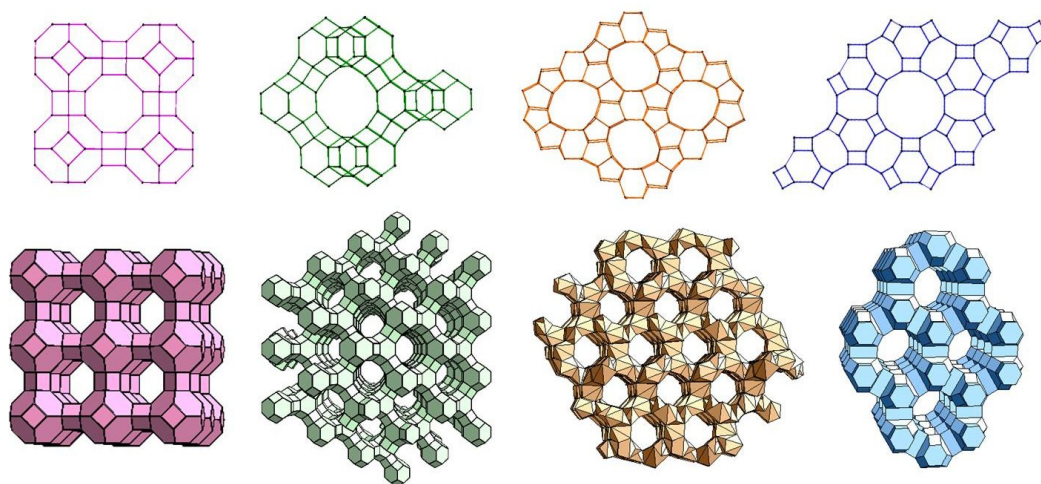
Figure 5 A representation of the zeolite A structure (LTA) as an assembly of framework's cages (reproduced with permission from ref 21).

Indeed this organized porosity has been used to achieve a sustained, controlled, or pulsed release in drug delivery applications. Moreover, most of the research interest has been focused on new synthetic approaches, such as 'supramolecular templating', that have empowered precise engineering of pore shape, size, and connectivity on the nanoscopic scale.[17-20]
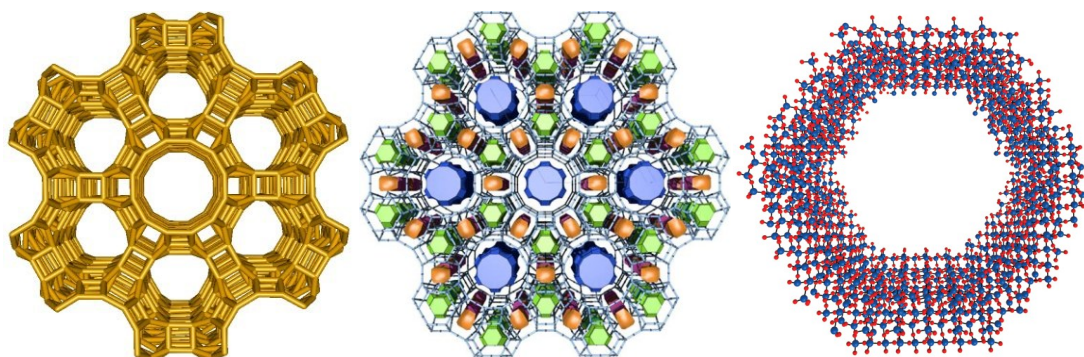
Figure 6 various inorganic porous materials like zeolites and porous silica (reproduced with permission from ref 21).

1.4 Organic Porous Materials

Porous organic materials are a fascinating class of nanoporous material with high surface area and diverse pore dimensions, topologies and chemical functionalities.[22-23] These materials have attracted an ever-increasing attention from scientists of different fields owing to their potential applications in gas storage, adsorptive separation and photovoltaic devices due to their inherent tunable pore size and high specific surface area. Building blocks with extensive π-conjugation would show luminescence and can be used as light harvesting and conducting materials.[24-26] The versatile networks are constructed from covalent bonds (B–O, C–C, C–H, C–N, etc.) between the organic linkers by homo- or hetero-polymerizations Boronic acid, amino, alkynyl, bromine and cyan group-based coupling reactions have been exploited for the synthesis of various types novel porous covalent organic frameworks (Figure 7).[27-33]

COF-108

TPP
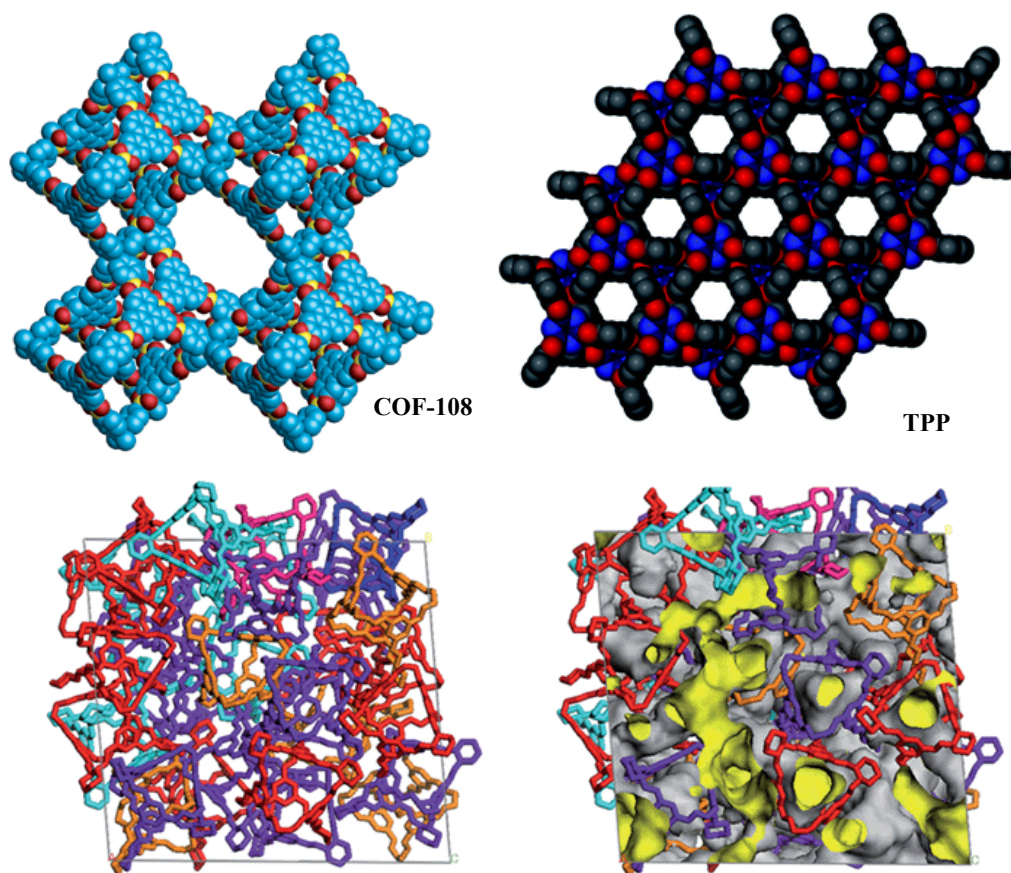
Figure 7 porous organic molecules as COF-108, TPP-1, organic cages (reproduced with permission from ref 27)

In contrast, organic–inorganic hybrid materials such as periodic mesoporous organo-silica may not only combine the respective beneficial characters of organic and inorganic components but also often exhibit exceptional properties that exceed what would be excepted for a simple mixture of the components.[28] The term hybrid material is used for many different systems spanning a wide area of chemical components such as highly ordered, crystalline coordination polymers or metal-organic frameworks (MOFs) or porous coordination polymers (PCPs), amorphous sol-gel compounds, layered silicate (clay) hybrids, colloids, nanoporous materials (Figure 8).[29]

Development of hybrid materials with extraordinary properties has attracted a lot of interest in recent years. Current challenges in this rapidly growing field include designing novel hybrid materials for applications in the fields of energy and environment, biology etc.[30] For these porous solids, the structure can usually be determined using X-ray or neutron diffraction.[31] In contrast to regular porous solids, there is no direct and simple way to determine the structural properties of disordered porous materials, due to the complexity of their pore network and their amorphous nature.[32-43]
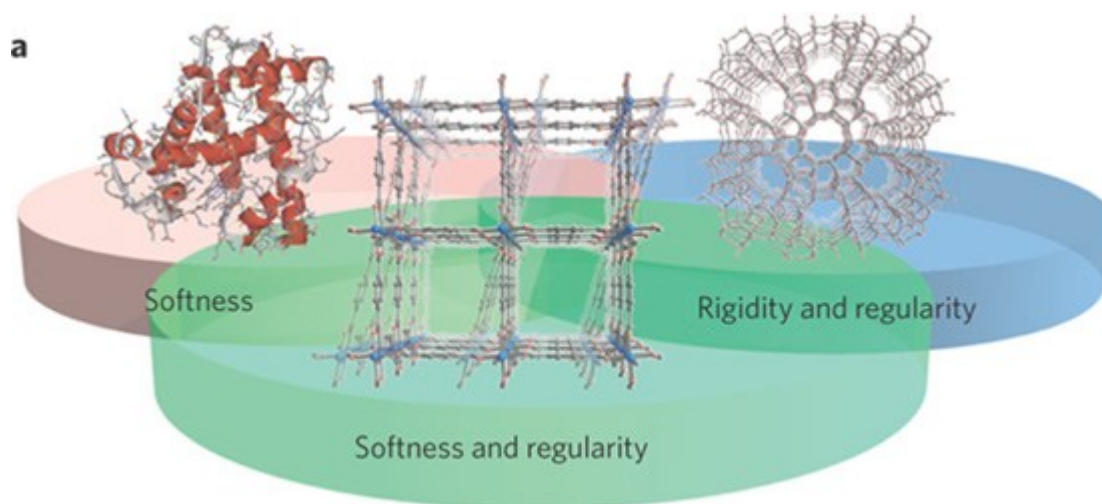
Figure 8 Three classes of host materials categorized according to attributes of softness, hardness (rigidity) and regularity. Materials at the left (bio-molecules) and right (zeolites) sides have softness and hardness, respectively. Materials at the centre (porous coordination polymers) possess both attributes with regularity. The overlapping zone of the two stages indicates materials belonging to either of the ends (reproduced with permission from ref 44).

1.5 Metal-Organic Frameworks (MOFs)

The synthesis, structure, and reactivity of novel complexes and materials from simple metal−ligand complexes have been an area of intense research over the past 120 years.[45] Specifically, the porous nature of many of these materials makes them attractive for numerous applications. Over the past two decades, novel hybrid micro porous metal−organic frameworks (MOFs) have been developed as a new class of tunable hybrid organic inorganic materials comprised of ordered networks formed from organic linkers and metal cations.[45-51]

They are typically synthesized under mild conditions via coordination-directed self-assembly processes, and are also called coordination polymers or coordination networks. By virtue of their high surface areas (~ 7200 m^2/g) with large porosity, tunable pore sizes and functionalities, MOFs show potential applications in various fields ranging from gas storage to biology. In particular, one of the first MOFs, MOF-5 which contains Zn(II) cation and 1,4-benzenedicarboxylate (1,4-BDC) residues as linkers has been extensively studied which was synthesized by Yaghi and coworkers (Figure 9).[45]
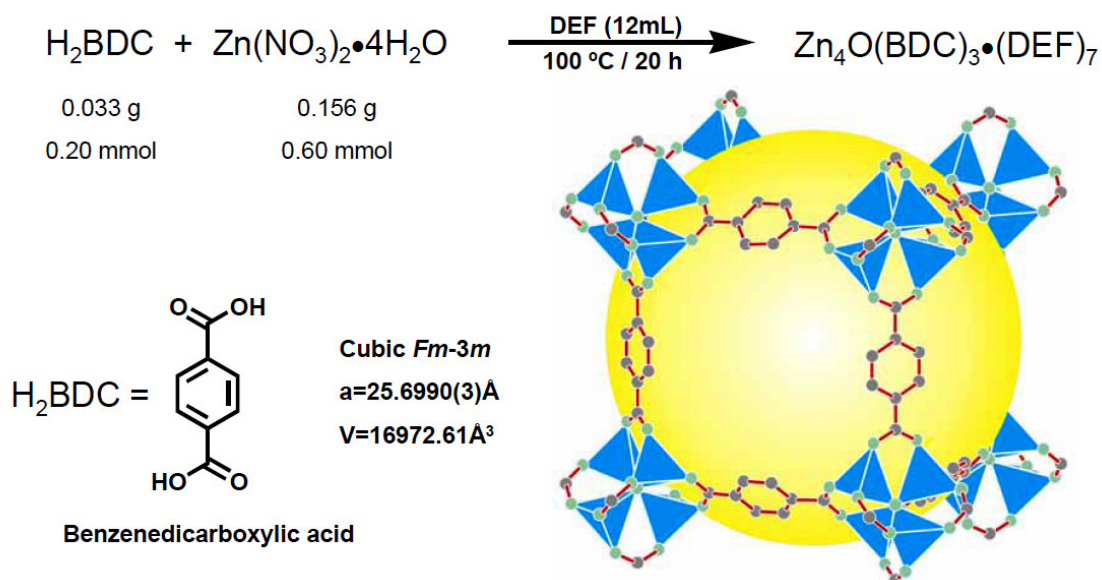
Figure 9 MOF-5. Chemists use rigid organic struts (top left) to link clusters of metal atoms (in this case four zinc atoms, bottom left) to build open framework-like materials (right) (reproduced with permission from ref 45).

The synthesis of metal– organic frameworks with desirable structures and properties is still arduous. A possible reason may be that crystallization is a very complicated self-assembling process, in which subtle changes, such as assistant ligands, pH value, solvent system and reaction temperature, could have unpredictable effects on the final compositions and structure.[56] Literature suggests that the above factors also play a key role in determining dimensionalities as 1D (chain), 2D (network) and 3D (framework). It has been previously demonstrated that the coordinating nature of the metal centre and sensible choice of organic ligands are very crucial factors for targeted-design of MOFs (Figure 10).[52]
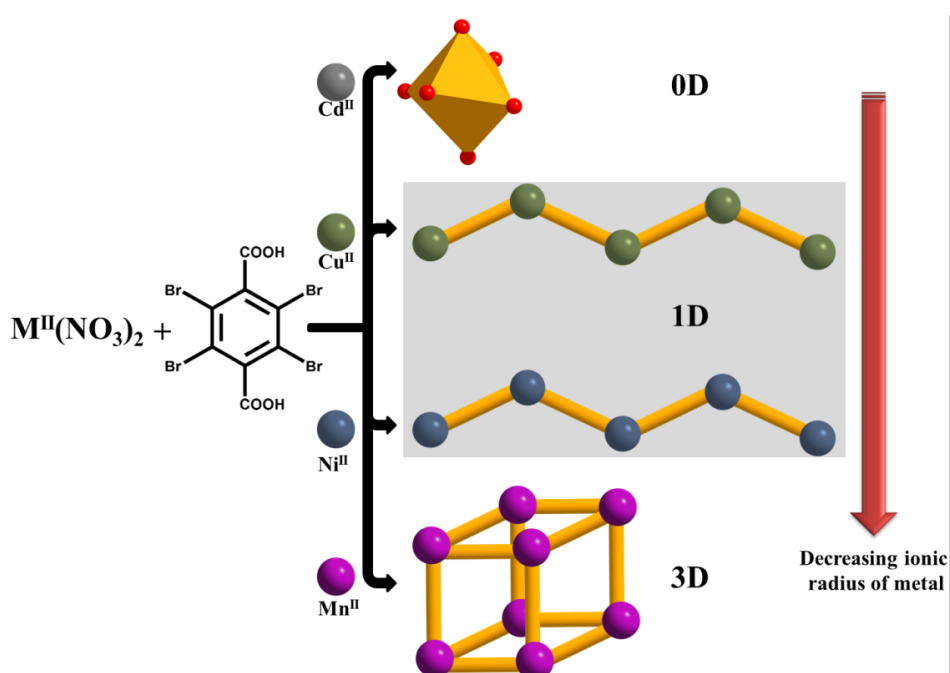
Figure 10 Changes in dimensionality in coordination compounds with varying the metal ion size (reproduced with permission from ref 52).

Among the many synthetic methods that have been applied are room temperature synthesis, conventional electric (CE) heating, microwave (MW) heating, electrochemistry (EC), mechanochemistry (MC), and ultrasonic (US) methods (Figure 11). The main goal in MOF synthesis is to establish the synthesis conditions that lead to defined inorganic building blocks without decomposition of the organic linker. At the same time, the kinetics of crystallization must be appropriate to allow nucleation and growth of the desired phase to take place. However, Figure 11 summarizes different synthetic methods that have been applied in the last 20 years.[53]
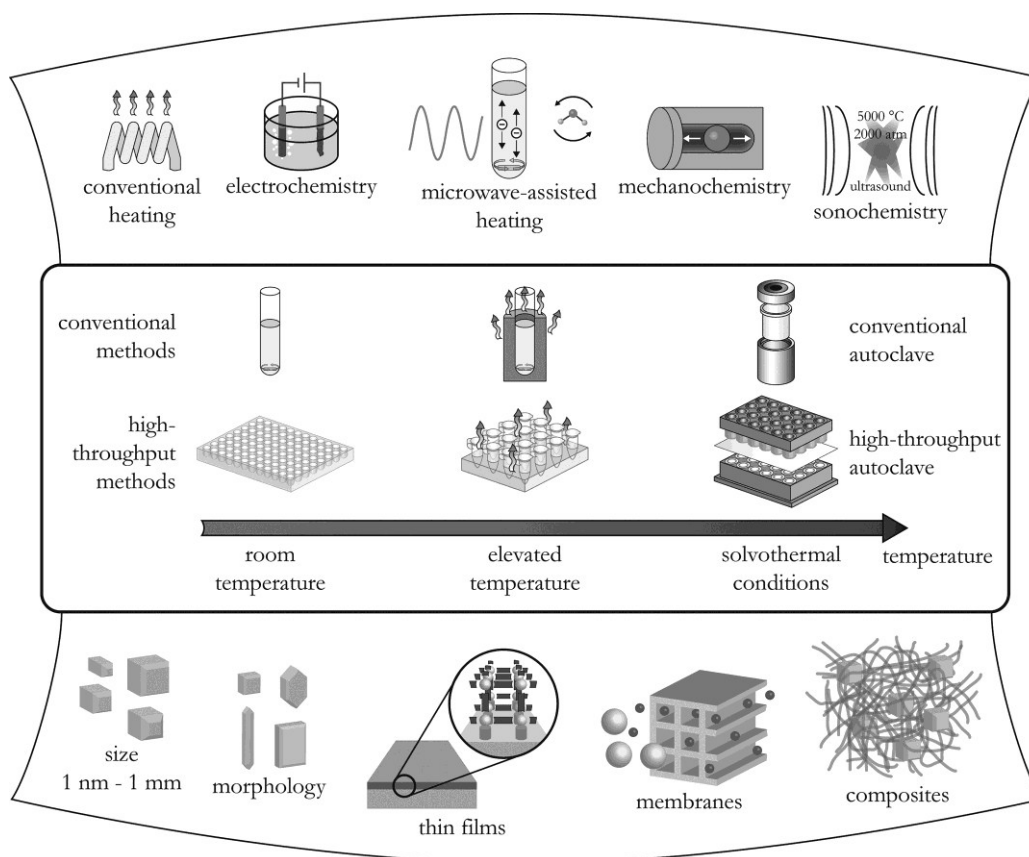
Figure 11 Overview of synthesis methods, possible reaction temperatures, and final reaction products in MOF synthesis (reproduced with permission from ref 51).

1.6 Classifications of MOFs/PCPs

MOFs/PCPs were classified into three categories: first, second and third generations (Figure 12). The first-generation materials are unstable, whose porosity collapses irreversibly after the removal of the guests. Whereas second generation MOFs have stable and robust frameworks, which maintain the original porous structures before and after guest sorption. Indeed these compounds can be used as an adsorbent and are regarded as analogous to zeolites. The third generation has flexible or dynamic porous frameworks also called as soft porous crystals; which reversibly respond to external stimuli, not only chemical but also physical and it clearly shows the importance of MOF in field hybrid porous materials. Moreover the representative dynamics of MOFs exhibiting their flexibility depends on various parameters as temperature, pressure, solvent molecules etc.
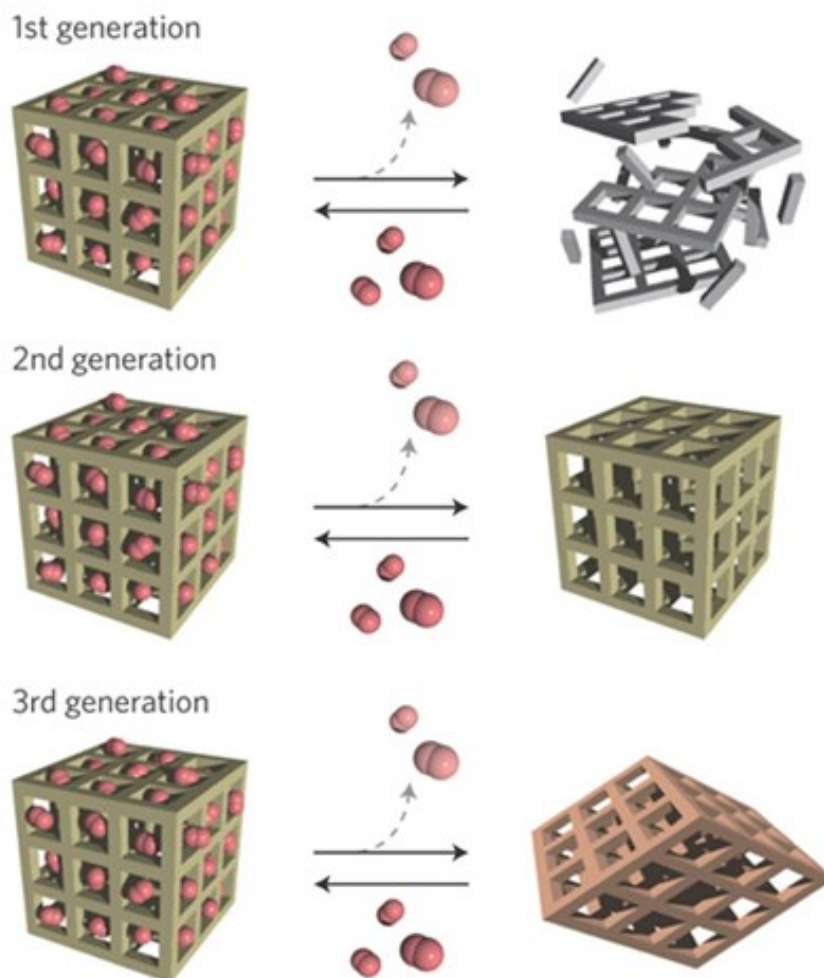
Figure 12 The Schematic of the classification of porous coordination polymers into three categories. The first-generation materials collapse on guest removal. The second-generation materials have robust and rigid frameworks, and retain their crystallinity when the guests are not present in the pores. The third-generation materials are transformable accompanied by structural transformation. A combination of metal ion and organic ligand gives freedom to both structural and physical properties (such as spin, charge or photonic) and the various softness factors represents a synergistic effect in the porous structure. This effect can also be observed when the specific guests access the channels (reproduced with permission ref 44).

Some notable examples of metal-organic frameworks are given in Figure 13.HKUST is a microporous material and has been extensively studied due to its high thermal and hydrolytic stability. MILs are also very stable porous materials where some of them show interesting structural breathing reactions (the MIL-53 series).[53-54] A very high surface area (~7000 m^2/g) has been reported by Hupp et.al. as shown in Figure 14
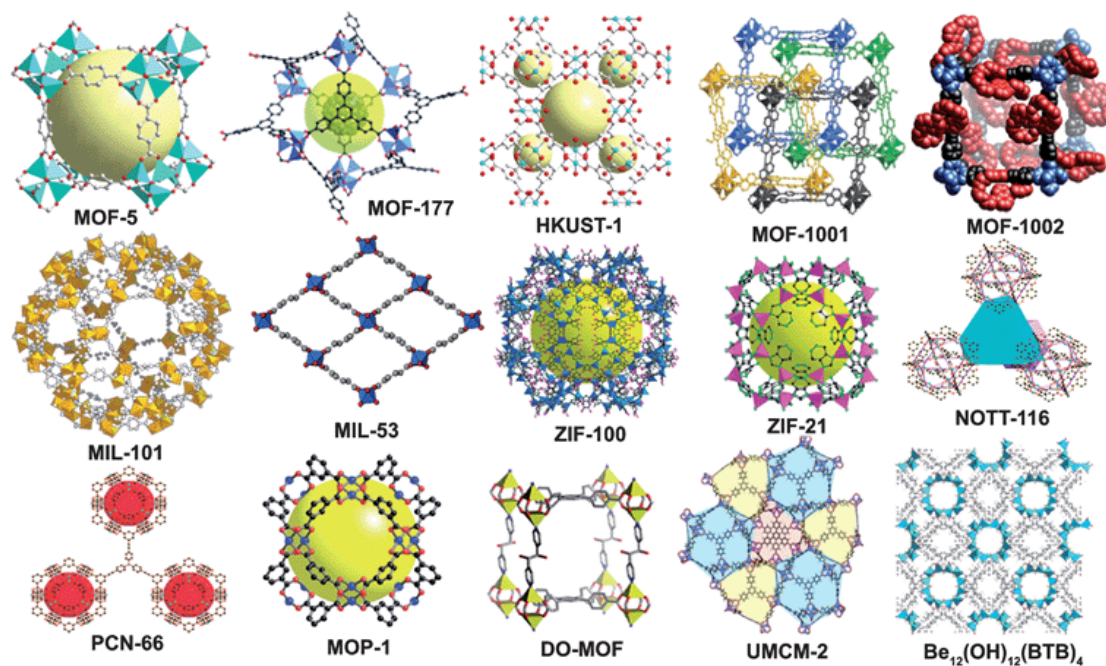
Figure 13 The 3D structures of representative MOFs (MOF-5; MOF-177; MIL-101; MIL-53; HKUST-1MOF-1001, 1002; ZIF-100; ZIF-21; NOTT-116; PCN-66; MOP-1; DO-MOF; UMCM-2; $Be_{12}(OH)_{12}(BTB)$) (reproduced with permission from ref 53).
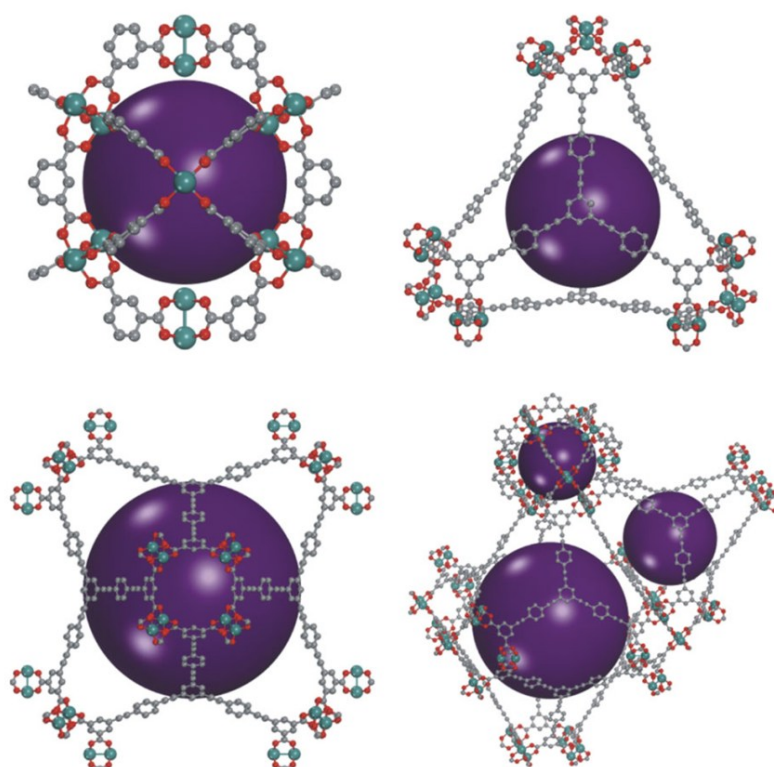
Figure 14 Representations of the single-crystal X-ray structure of **NU-100** and its different cages (reproduced with permission from ref 54).

1.7 Applications of MOFs

 Indeed, MOFs became an intense research area in scientific communities around the world, with more than hundreds of peer-reviewed articles being published every year because of their potential to be used in applications in various fields such as fluorescence, catalysis, gas storage and separation, magnetism, thin films, sensing or recognition, proton conduction and drug delivery (Figure 15).[55-71] Although still in their infancy, the currently available results have explicitly confirmed that a bright future is predicted for the development of MOFs in these aspects.

Figure 15 Versatile applications of metal-organic framework for society in industry, environment, life and space (reproduced with permission from ref 44).

In our attempt to explore the functional behaviour of MOFs, my thesis has focused solely on recent developments in various fields as (i) luminescent MOFs as sensors, (ii) shape assisted fluorescent nanoscale MOFs, (iii) meso porous MOFs exploited for light harvesting applications; (iv) MOF and MOF composites like silica, graphene and aminoclay for gas storage, (v) Flexible Bio-MOF for controlled drug delivery systems, (vi) heterogeneous catalysis through supports/host matrices for small metal nanoparticles, (vi) MOF derived carbon and metal oxides with important applications in energy storage and conversion (supercapacitors, batteries).

1.8 Nanoscale Metal-Organic Frameworks (NMOFs)

Engineering of controlled nanoscale hybrid material systems constitutes one of the most active and exciting pursuit of the field with respect to their technological and biomedical applications *viz.* catalysis, drug-delivery, diagnostics and solar cells.[72] During the past decades, the creativity of chemists and materials scientists provided a means for developing a wide variety of traditional MOFs. Moreover, MOFs in the form of traditional bulk crystalline materials do not always achieve all specific needs for these applications.[73] Indeed, nanoregime materials have the capability for their internalization into cells, and this limits the applications of MOF's as delivery vehicles, diagnostics. However, these nanoscale MOFs are classified into two types based on the crystallinity, as nanoscale metal-organic frameworks (NMOFs) or nanoscale coordination polymers (NCPs). Nanoscale MOFs (NMOFs) have well-defined, non-spherical morphologies, suggesting the predominance of crystal lattice energy over particle/solvent interactions.[74] The crystalline nature of NMOFs provide information that allows an exact understanding of their compositions and structures, and greatly facilitates the delineation of composition, structure, and property interrelationships in this class of nanostructures.[75] Whereas nano coordination polymers (NCPs) are amorphous in nature and it adopts a spherical morphology to minimize the interfacial free energy between the particles and solvent. In general NMOFs are synthesized by different ways; (i) formation and precipitation of particles triggered by the introduction of a solvent into a solution of ligands and metal cations, which causes precipitation of the particles as they form (ii) the use of micro- emulsion techniques (iii) solvothermal/hydro synthesis.[76] Recently, a spray-drying technique that can be exploited as a general, low-cost, rapid and scalable method for the synthesis and self-assembly of nano MOFs was employed (Figure 16).[77] Moreover, enormous amount of research is focused on various morphologies ranging from 0-D amorphous ICPs and crystalline NMOFs (with multiple shapes) to 1-D rod-like crystals, fibres and tubes due to their fascinating applications in biology and optoelectronics (Figure 17). Their use can allow the fabrication of electronic or optoelectronic thin films, membranes with catalysis, gas separation capabilities, new surface sensors, magnetic platforms, drug delivery, bio sensing and multimodal imaging. Moreover, thin films/membranes of NMOFs have shown potential application in gas separation.[78] Recently, Oh *et.al* reported a simple technique for the synthesis of NMOF.[79]
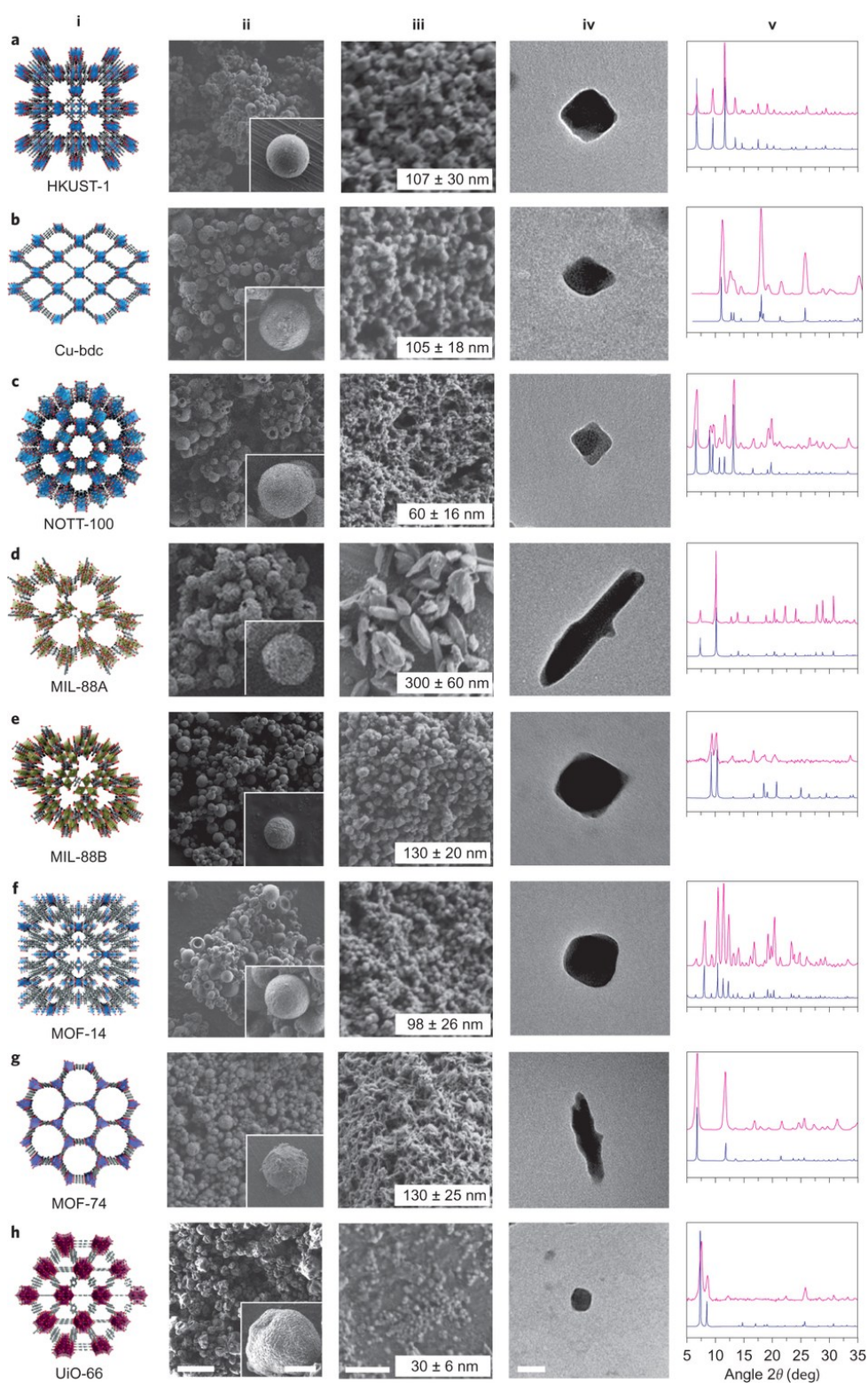
Figure 16 Synthesized nanoscale MOFs: **a**, HKUST-1 . **b**, Cu-bdc. **c**, NOTT-100. **d**, MIL-88A. **e**, MIL-88B. **f**, MOF-14. **g**, Zn-MOF-74. **h**, UiO-66. FESEM (**ii**, **ii** inset, **iii**) and TEM (**iv**) images of the synthesized MOF superstructures and discrete nanoMOF crystals, and the corresponding experimental (pink) and simulated (blue) XRPD patterns (**v**, for comparison), are shown for each MOF. Scale bars: 10 μm (**ii**), 2 μm (inset to **ii**), 500 nm (**iii**), 50 nm (**iv**) (reproduced with permission from ref 83).
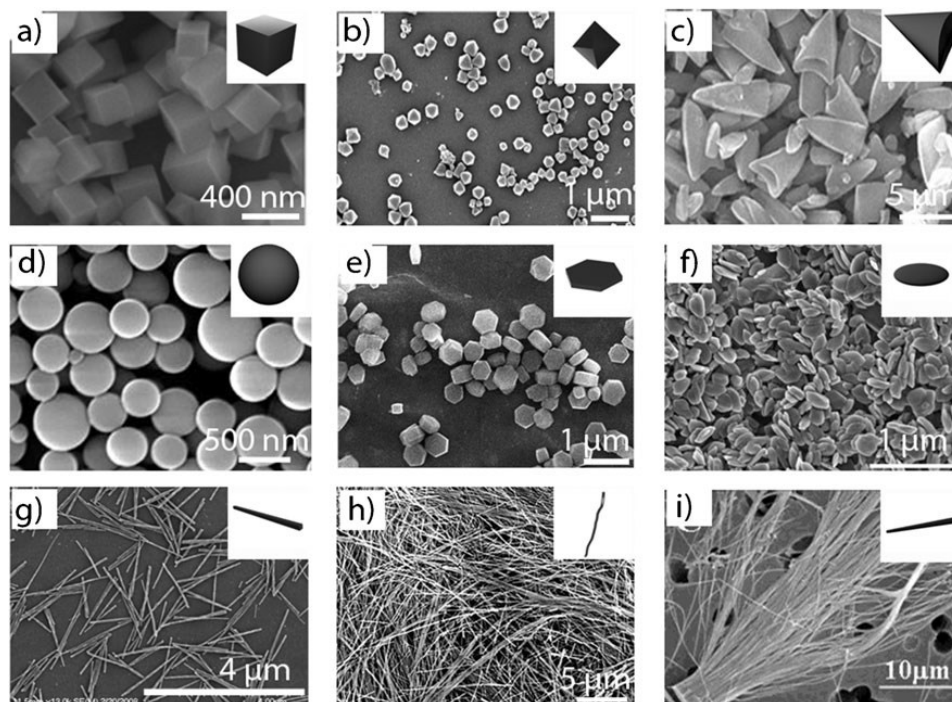
Figure 17 Diverse nanoscale morphologies of different MOFs: (a) cubic particles, (b) octahedral particles, (c) arrow-like particles, (d) spheres, (e) hexagonal lumps,(f) plate-like particles, (g) rods, (h) fibers, and (i) tubes (reproduced with permission from ref 81).
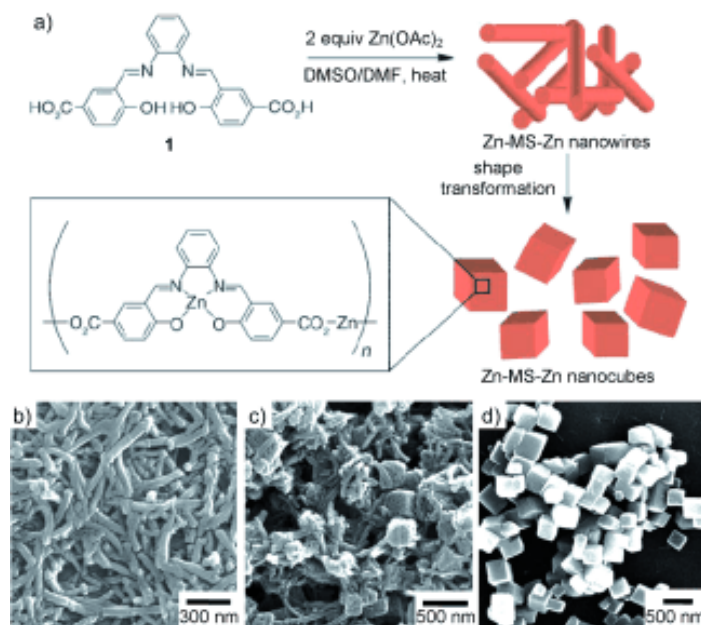
Figure 18 a) Scheme for the synthesis of Zn–MS–Zn nanowires and their subsequent transformation into nanocubes (MS=metalated salen). b)–d) SEM micrographs illustrating the transformation of nanowires into nanocubes during the synthesis (reproduced with permission from ref 79).

Interestingly, by closely monitoring the particle growth, morphological transformation during the synthesis was observed. Solution of N,N'-phenylene bis (salicylideneimine) dicarboxylic acid in DMSO was added to a DMF solution containing two equivalents of $Zn(OAc)_2$ in solvothermal conditions.[80] Each Zn (II) chelates with salen linker, while the other connects the resulting metallo-ligands. Moreover, when the resultant solution was heated to 120 ^{o}C for 60 min, nanowires transformed into nanocubes by aggregation and intra-structural fusion (Figure 18). Indeed, the size of nanocubes can be controlled by various reaction conditions such as temperature and solvent concentration.[79]

1.9 Metal Nanoparticles@MOF

Metals at the nano-size regime often show fascinating optical, chemical and electronic properties that are distinctly diverse from those of bulk. Indeed, metal nanoparticles have received a great interest in the field nanomaterials owing to their extraordinary properties and thus finds applications in fields like sensors, catalysis, optical, electronics and biology.[82] However, significant context of nanostructured materials in chemistry is mainly dependent on size, structure and shape. Various synthetic strategies (bottom-up) are reported in the literature to obtain noble-metal nanostructures using chemical reduction of metal precursor in presence of a capping agent with thiols, polymers, surfactants, amine-borane complexes and dendrimers. However, for catalytic applications, these nanoparticles are preferably dispersed on templates like silica, alumina, carbon, clay and zeolites.[83] The size and shape of the nanoparticles can be well defined by the right template.[84]

Recently, MOFs have been shown to be suitable for embedding and supporting functional nanoparticles (NPs) similar to microporous zeolites or mesoporous siliceous materials and related matrices due to their extraordinarily high surface area and well defined pore structure.[85] It also has been shown that the embedding of functional nanoparticles inside the cavities of MOFs is relevant for a number of applications, including heterogeneous catalysis and hydrogen storage. Indeed, the incorporation of range of metals like Cu, Ru, Pd, Au, Ag and Pt into MOF cavities have been reported by various methods such as chemical vapour deposition (CVD), solid grinding, microwave irradiation, solution impregnation and surface grafting. The stabilization of metal nanoparticles are classified as three types.[87]
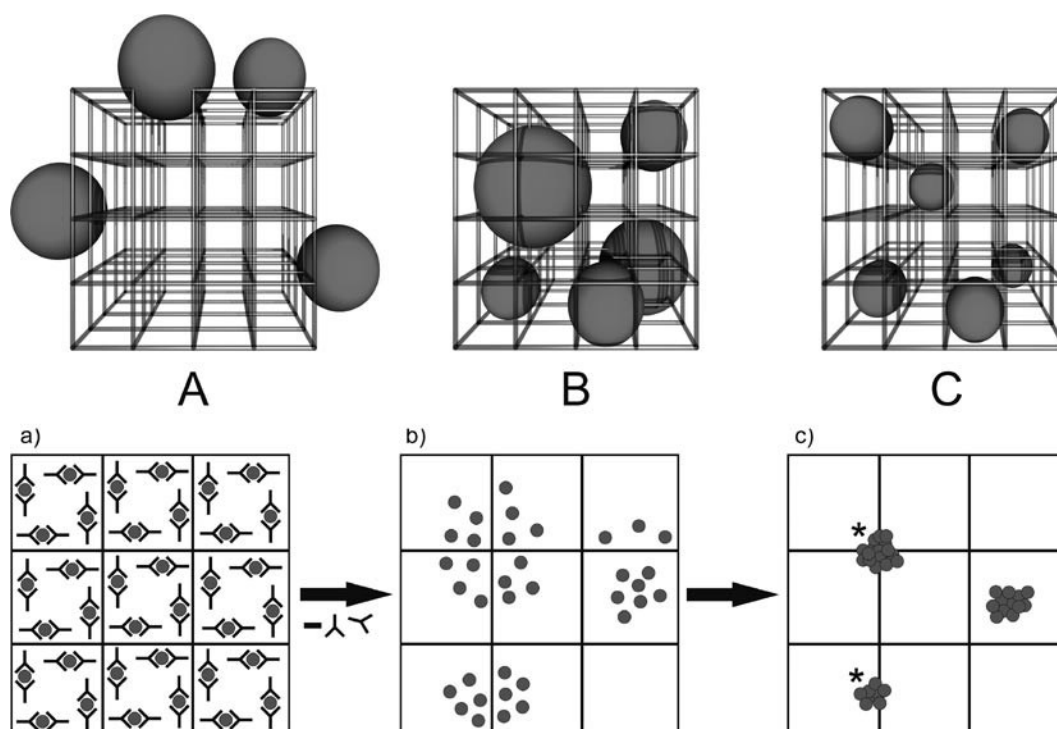
Figure 19 Top: The limiting cases A, B and C of metal nanoparticles supported by MOFs addressed as metals/MOFs (A) and as metals@ MOFs (B, C). Bottom: The concept of particle formation inside MOF cavities: (a) The MOF matrix is loaded with a metal precursor. The balls represent the metal centre, and Y-shaped sticks represent the organic ligands or counter ions. (b) After the decomposition of the precursor the agglomeration process starts. (c) Stars indicate the partial degradation of the framework and the formed metal nanoparticles. Note that processes like (b) and (c) may also take place during thermal annealing and/or TEM imaging of the as-synthesized sample (reproduced with permission from ref 87).

In Figure 19, class A shows the metal nanoparticles were deposited at the outer surface of a MOF crystal or close to pore size of MOF. Class B shows particle size characteristically larger than the dimensions of the pores.[87] Whereas Class C shows pore size absolutely matching with nano particles size. Indeed, these hybrids can be successfully characterized through various TEM techniques like bright-field TEM (BF-TEM), high-angle annular dark field scanning TEM (HAADF-STEM) and ICP, IR, NMR, EPR spectroscopy, elemental analysis, EXAFS, XPS, TEM, electron tomography, and PXRD. The advantages of using MOFs as supports for M-NPs are the following: (1) the confinement effect of MOFs provide limited growth of M-NPs and generates rather uniform and small sized NPs, (2) the structural diversity of MOFs having different pore sizes and channel systems offers the choice of appropriate MOFs for NPs generation, (3) the organic parts of a MOF can interact with NPs and stabilize

them without an extra stabilizing agent even though NPs bigger than the pore sizes are generally formed. Recently, Fischer et. *al* reported, high metal loading up to 30–40 wt% in a single loading step using metal–organic chemical vapour deposition (MOCVD) of [Ru(cod)(cot)] (cod = 1,5-cyclooctadiene and cot = 1,3,5-cyclooctatriene) method in MOF-5 (Figure 20).[87]

[Ru(cod)(cot)]@MOF-5   Ru-NP@MOF-5
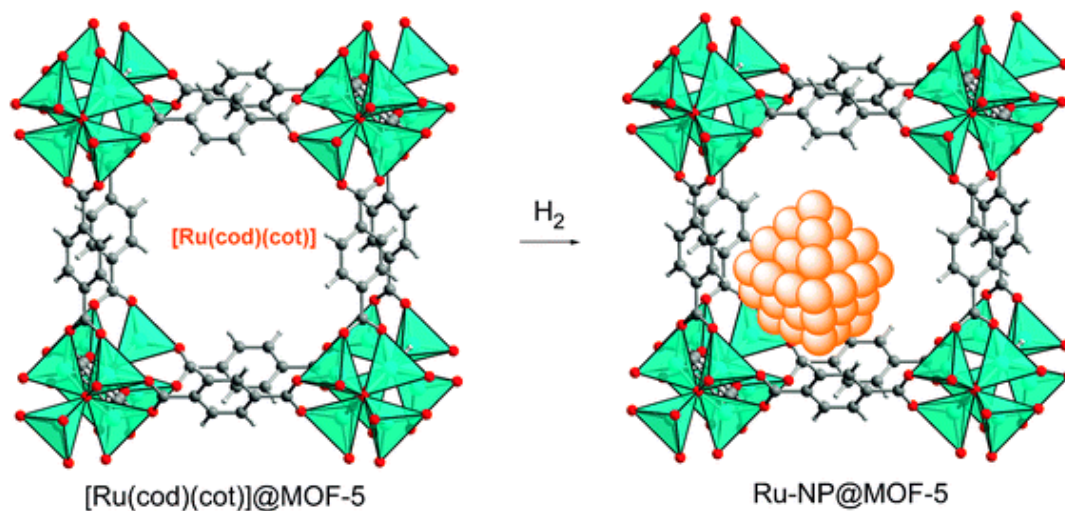
Figure 20 Schematic presentation of the formation of Ru-nanoparticles (Ru-NP) from [Ru(cod)(cot)] by dihydrogen reduction inside MOF-5 (reproduced with permission from ref 87).

In particular, MOFs embedded with Pd NPs have been proven to have improved H_2 uptake at room temperature. The phenomena have been explained by the spill over effect of Pd NPs that split H_2 molecules into hydrogen atoms before they are adsorbed in the MOF, although controversy still exists over the real mechanism. Recently Pd@MIL-100 (Al) reveals the hydrogen storage capacity (1.3 wt% percent at 4 MPa) at low temperatures is lower than values reported for MOF materials without metal nanoparticles incorporated inside the matrix.[87] Surprisingly, at room temperature Pd@MIL-100 (Al) shows almost double (0.35 wt.%) amount of hydrogen uptake relative to the bare MOF. However, it is well-known that bulk Pd absorbs hydrogen at room temperature and forms a β palladium hydride phase at low pressures and it is proven through temperature dependent powder XRD.[106] Indeed, a lot of research interest is focused on the fabrication of various metal nano particles with different catalytic applications (Figure 21).[86] However, the confinement and the amount of loading are two important factors for catalytic reactions.[87]
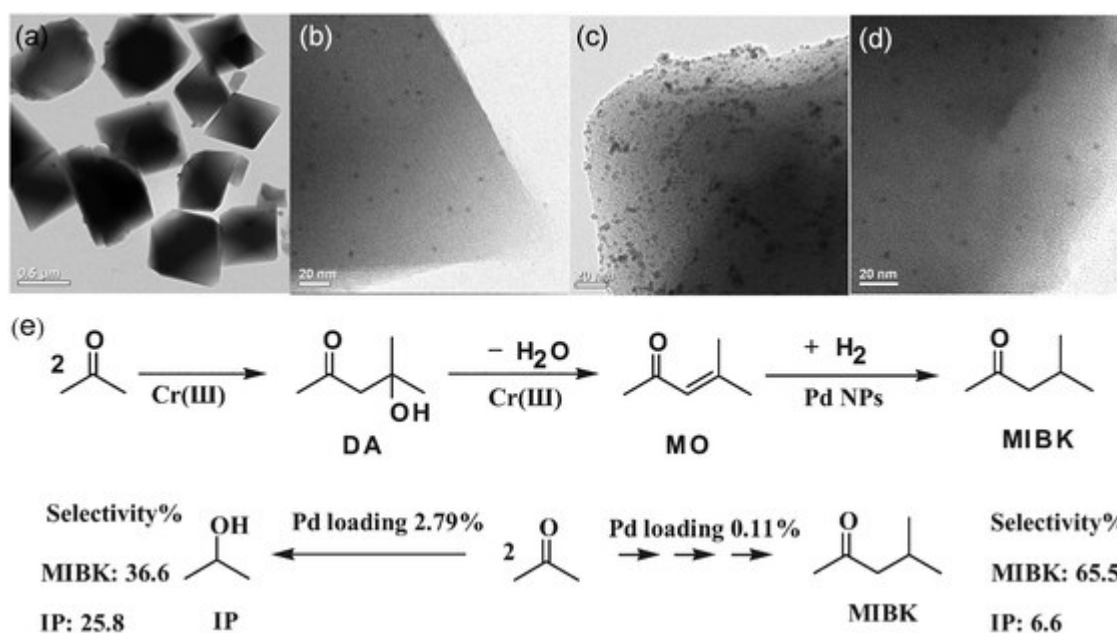
Figure 21 TEM images of 0.11 wt% (a, b and d) and 0.87 wt% (c) Pd@MIL-101(Cr) before (a–c) and after (d) reaction, and schematic illustration of synthesis of MIBK promoted by Pd@MIL-101(Cr) and the effect of Pd loading on the MIBK selectivity (e) (reproduced with permission from ref 87).

1.10 Mesoporous Metal-Organic Frameworks

Emerging from some key pioneering publications, the past two decades have experienced an extraordinary development of a wide range of ordered mesoporous materials, mostly obtained by template routes. Actually, the term ''mesoporous materials'' refers to solids based on either ordered or disordered networks with broad or narrow distribution of pores in the range between 2 and 50 nm.[5] Indeed mesoporous materials have emerged as an important class of catalytic materials, which has significant number of advantages with respect to both zeolites and their microporous materials.[88] Although metal–organic frameworks (MOFs) have greatly expanded the scope of porous materials, especially in terms of chirality, materials design, and very high surface areas, they are largely restricted to the microporous regime.[89] Furthermore, micropores are seldom accessible for anchoring molecular catalysts or for impregnation of catalyst precursors or voluminous drug molecules, which limits their applications.[90] Additionally, the potential advantages offered by mesoporous MOFs can be appreciated by the following considerations, (i) as mentioned in the foregoing discussion, unlike traditional mesoporous materials, mesoporous MOFs are completely ordered crystalline materials whose structures can usually be solved by single-crystal X-ray diffraction, (ii)

the structure and porosity of the mesoporous MOFs are tunable. The desired extended network can be easily obtained by the choice of organic linkers, metal clusterbased on secondary building units (SBUs), and post-synthetic modifications; (iii) these mesoporous MOFs may have very large surface areas (6000m^2/g), which will give rise to a number of potential applications in gas storage and separation, although new models need to be developed to calculate the effective surface area of a mesoporous MOF.[91] Meso porous MOFs can enlarge their use as hosts to accommodate larger bulky molecules, allowing their free reaction or transformation without diffusion limitations in a confined space. However, the major challenge was often centred on monitoring and controlling their pore size and framework stability.[92]

The pores of the assynthesized MOFs are usually occupied by solvent molecules that must be removed to induce a permanent porosity without inducing its structural collapse. Therefore, it is a great challenge to synthesize robust mesoporous MOFs, especially those with pore sizes greater than 2 nm in diameter. Meso porous MOF's is an emerging field, which is relatively not much developed compared to traditional MOFs. Yaghi and coworkers reported the first meso porous MOF: IRMOF-16 using organic linker tetraphenyl dicarboxylic acid. According to IUPAC system, traditional meso porous materials show 2-50 nm pore size.[93] It is worth noting that mesoporous MOFs show a type IV isotherm. While the type I curve indicates traditional micro porous system.[110] However, these meso MOFs have micro porous windows to open meso porous cages. These meso porous MOFs are classified in to four types as :

1.10.1 Mesoporous MOFs with 3-D Channels

In this class, ligand extension is an apparent strategy, while open MOFs built from large ligands tend to disintegrate after the removal of guest molecules. Moreover, the ligand extension causes interpenetration or decomposition of framework upon removal of guest molecules. Moreover, the nature of isotherm will be both type-I and type-IV. In 2002, IRMOF-16, that was synthesized by Yaghi *et.al.* and obtained from Zn^{2+} and p-terphenyl-4,4″-dicarboxylic acid (H$_2$TPDC) in DEF at 100 °C for 4 days. This MOF has the expected topology of CaB$_6$ adapted by the prototype IRMOF-1 (also named as MOF-5) in which an oxide-centered Zn$_4$O tetrahedron is edge-bridged by six carboxylate groups to give the octahedron-shaped SBU that reticulates into a 3-D cubic

porous network. In the structure of IRMOF-16, the free- and fixed-diameter values are 19.1 Å and 28.8 Å, respectively (Figure 22). [94]
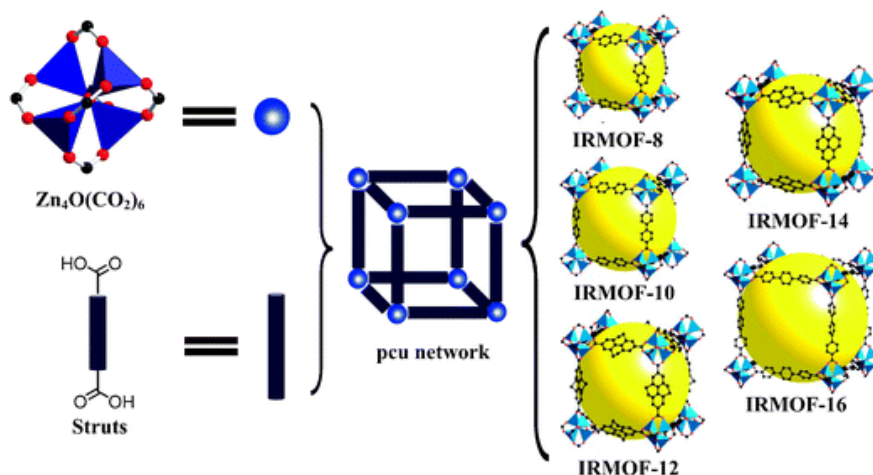
Figure 22 The "expansion" of IRMOFs-n based on ligand extension strategy (reproduced with permission from ref 94).

1.10.2 Mesoporous MOFs with 1-D Channels

In this class, two synthetic strategies have been employed to build up porous MOFs with large 1-D channels: the construction of infinite rod-shaped SBUs and the mixture of two different organic ligands. [94] By constructing infinite rod-shaped SBUs, the framework of the compound will form an impenetrable wall, which inhibits additional ligands from filling in between adjacent linkers and the interpenetrated structure.
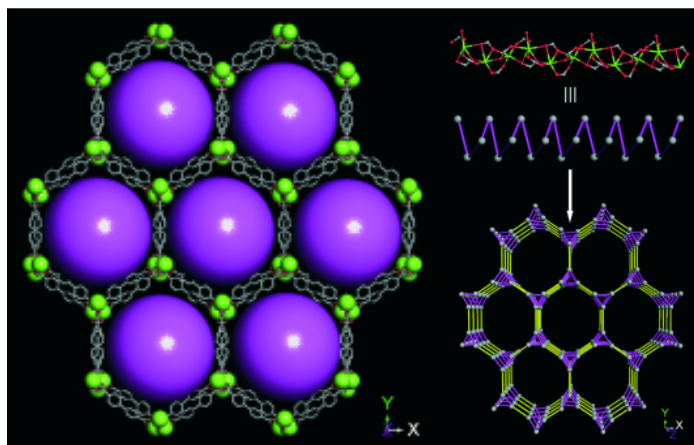
Figure 23 Development of the structure of JUC-48: top, the Cd[II] ions are linked together by carboxylate groups of bpdc to construct 1D Cd-O-C chains as rod-shaped SBUs (the terminal DMF molecules except for their oxygen atoms are omitted for clarity); middle, the carboxylate carbon atoms of the chain can be connected to construct a pseudo 3_1 or 3_2 helix; bottom, the helices are linked by biphenyl groups (yellow lines) of bpdc to generate bnn parallel rod packing with etb topology (reproduced with permission from ref 94).

JUC-48 is synthesized from a rigid and linear organic O-donor ligand, bpdc (bpdc= 4,4-biphenyldicarboxylate) where the Cd centers are linked together by carboxylate groups of BPDC to generate 1D metal chains that are interconnected through BPDC to form a 3D non-interpenetrating extended network with etb topology. The framework has 1D hexagonal channels of 24.5×27.9 Å^2 viewed along the c-axis direction (Figure 23). The tubular channel has an impenetrable wall based on the rod-shaped SBUs, which prohibits additional ligands from filling in between adjacent linkers. JUC-48 exhibits a typical Type I N$_2$ adsorption isotherm, with a Langmuir surface area of 880 m^2 g^{-1}.[94]

1.10.3 Mesoporous MOFs with Large Cavities

These compounds have mesoporous cavities surrounded by microporous windows.[87] A series of mesoporous MOFs with large cages have been prepared by changing organic linkers, utilizing rare-earth metal ions or mixing different ligands. A new computational strategy to solve the crystal structures of mesoporous MOFs has been developed and utilized for the synthesis of compounds MIL-100 and 101(Figure 24).
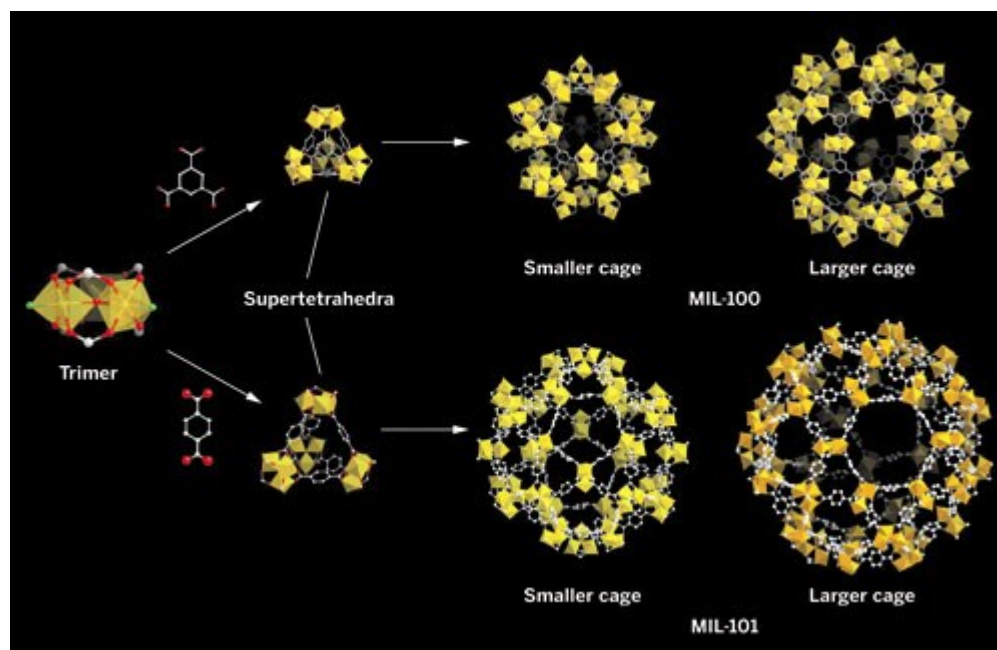
Figure 24 Structural representations of MIL-100 with larger cavities of 29 Å, MIL-101 with larger cavities of 34 Å (reproduced with permission from ref 94).

1.10.4 Mesoporous MOFs Based on Supramolecular Templates

In this method supramolecular template strategy has been successfully applied to design mesostructured MOFs with tunable pore size, pore volume and surface area.[95] Zhang *et.al.* used the surfactant cetyltrimethylammoniumbromide (CTAB) as a structure-directing agent, and chose Cu(II) and benzene-1,3,5-tricarboxylate ions as framework-building blocks to illustrate the supramolecular template strategy for designing and preparing mesostructured MOFs with tailored porosity (Figure 25).

= metal ion or metal cluster
= multifunctional organic ligand
= micelles (template)
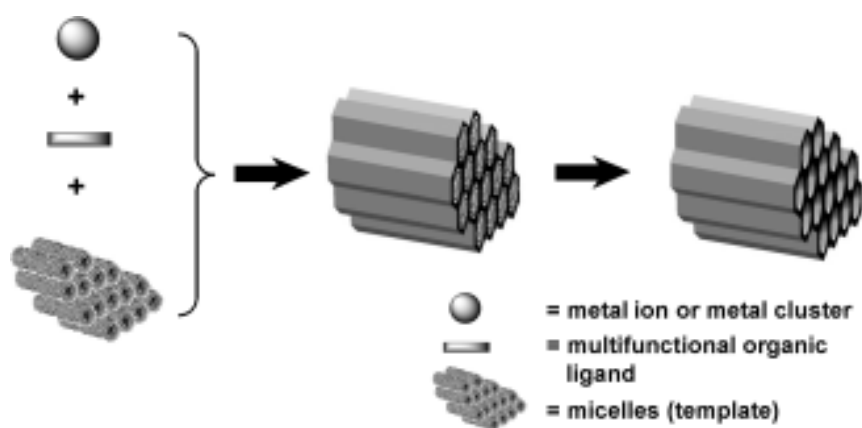
Figure 25 Mesostructured MOFs self-assembled from metal ions and multifunctional organic ligands in the presence of surfactant micelles as supramolecular templates (reproduced with permission from ref 95).

Meso MOFs facilitate the uptake of gases at high pressure; while the hierarchical arrangement of micro/mesopores optimizes the adsorption and separation capacity.[96] Meso MOFs have the ability to selectively adsorb large amounts of substrate molecules such as organic dyes and drugs from the liquid phase. Functionalized meso MOFs have been demonstrated to have high efficiency and/or selectivity in some catalytic processes and has shown excellent recyclability and reusability. Encapsulation of nanoparticles inside meso MOF cavities has greatly extended their applications in catalysis and hydrogen storage by catalytic spillover.[97] One prominent merit for meso MOFs lies in their possibility to exert homo-chirality for enantio selective processes. Additionally, meso MOFs provide a platform for controlled drug delivery and imaging owing to well defined pore shapes and sizes as well as limited aperture sizes.[97]

1.11 MOF Derived Materials for Energy Applications

Exploration of the use of MOFs in removing toxic or environmentally hazardous gases has been confined primarily to CO_2 capture and separation from flue gas in the environment.[96] MOFs as (i) electrode materials for batteries, (ii) electro catalysts for important reactions taking place in fuel cells or electrolysers, (iii) electrode materials for supercapacitors, (iv) Li^+ or H^+ conductive materials for batteries or fuel cells, and (v) as surface films for corrosion inhibition have been utilized.[97] MOF derived materials show potential applications in the fields of hydrogen energy (hydrogen sorption, nano-confinement of chemical hydrides, hydrogen generation), fuel cells, Li-ion rechargeable batteries, super capacitors and solar cells according to MOF's roles (Figure 26).[98]
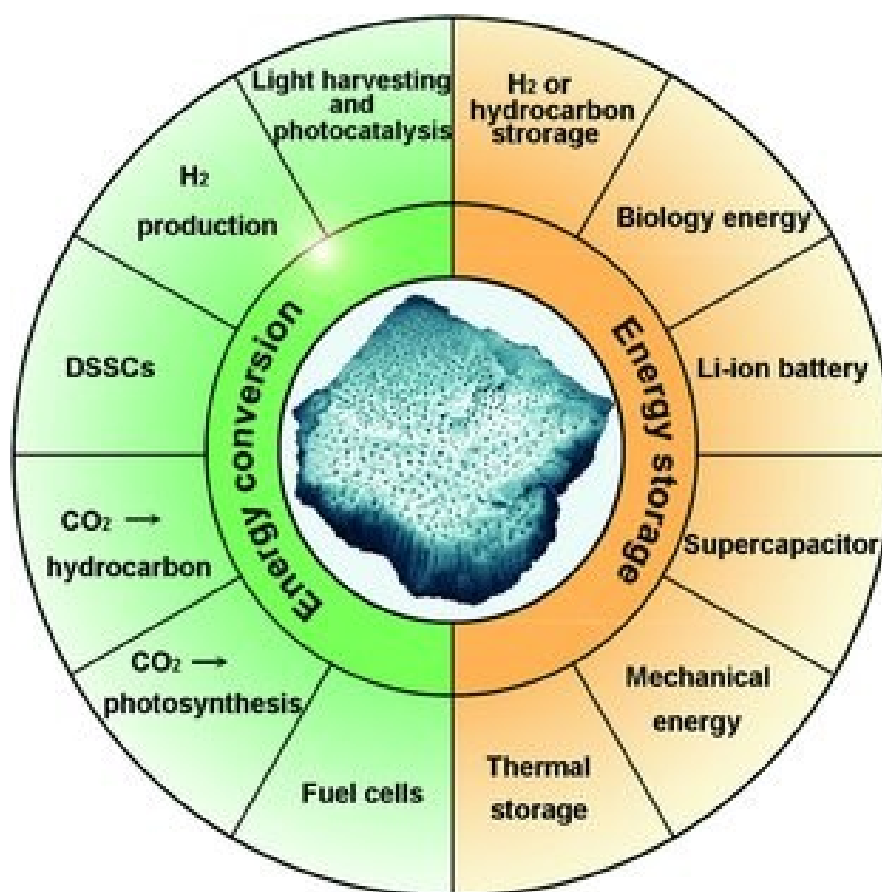
Figure 26 Illustration of the potential applications of carbon based materials (reproduced with permission from ref 98).

1.11.1. MOF derived Nanoporous Carbon Materials

Nanoporous carbons, another class of non-oxide porous materials, are of great scientific and technological importance due to the applications in areas of water and air purification, templates, separation, gas storage, electrochemistry, biology and catalysis.[99] The widespread use of porous carbon results from their remarkable properties like high surface area, chemical inertness, thermal stability, good mechanical stability, biocompatibility, etc. Synthesis of hierarchical carbon structures with designed porosity are often based on the hard and soft-templating approaches.[99a] Nanoporous carbons prepared by the latter method have diverse structures and morphologies; however, they can be obtained only from a few suitable combinations of thermally stable carbon gels and less stable organic templates that can be thermally decomposed before completion of the carbonization process. In contrast, the former nanocasting approach offers nanoporous carbons with ordered micro-, meso-, and macrospores depending on the original hard-templates (i.e., zeolites, mesoporous silica's, and colloidal crystals, respectively), although it is slightly complex and unfavourable for large-scale production.[99b]
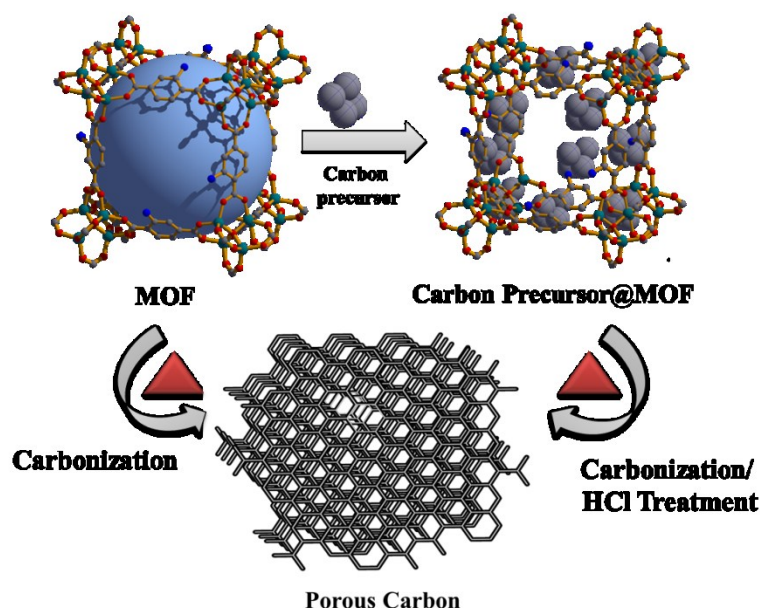
Figure 27 Schematic representation of construction of nanoporous carbons from MOFs with furfuryl alcohol as a carbon source.

MOFs have been of immense interest in recent years as a novel class of nanoporous materials mainly because of their designable framework structures modularly built from transition-metal clusters as nodes and organic ligands as struts.[99d]

Inspired by their assorted structures, high surface area, and large pore volume, MOFs have been considered as an alternative precursor to construct nanoporous carbons, as they may broaden the library of nanoporous carbons with novel structures and properties as shown in schematic representation (Figure 27).[99e] Therefore several MOF's such as MOF-5, Al-PCP and ZIF-8 have been used as promising templates using external carbon precursor, yielding nanoporous carbons and showing excellent properties in gas adsorption, electrochemical capacitance, sensing, and catalysis.[99f]

1.11.2 MOF Derived Metal Oxides

Metal oxide nanoparticles represent a field of materials chemistry which attracts considerable interest due to the potential technological applications of these compounds. The implications of these materials on fields such as medicine, information technology, catalysis, energy storage and sensing has driven much research in developing synthetic pathways to such nanostructures.[100a] Indeed compared with other transition metal oxides such as Co_3O_4, Mn_3O_4, SnO_2, iron oxide nanocrystals (Fe_3O_4, Fe_2O_3), TiO_2 are favourable due to low cost, high electronic conductivity and environmental benignity.[100b] However, controlled synthesis of metal oxide nanoparticles is essential for successful application, and solution-phase methods provide a large degree of control over the synthesis products.[100c] However, in most of these attempts, the main research target was the use of MOFs as a template for the synthesis of porous carbon and the metal oxide was removed from the metal/metal oxide nanoparticle–carbon hybrid to afford the pure form of carbon.[100d] Currently, no attempt has been made to systematically study the properties of the resulting metal/metal oxide nanoparticles dispersed inside the carbon matrix, although its importance for future applications, such as magnetically separable materials, highly activated catalyst, lithium battery has been acknowledged.

1.12 Conclusions

This chapter demonstrates the properties of MOFs that opens the door to an incredible range of important applications with their potential in fields ranging from analytical chemistry to drug delivery. The uniquely ordered, tunable functional porous environment is the key feature for development of MOFs. Here, MOFs as platforms for various recent developments *viz.* gas separation, heterogeneous catalysis, meso porous MOFs for light harvesting applications, as supports/host matrices for small metal

nanoparticles, and as templates or metal oxide for other new hetero dopant nano porous carbon syntheses. There is still plenty of scope to improve and invent new properties of the MOF materials. Further efforts in this field will certainly contribute to the development and practical applications of clean and renewable energy. Especially, the applications of MOFs in solar cells will be one of the research focuses in the future. It is believed that MOFs will provide extraordinary advantages over porous inorganic and organic materials, which we anticipate will have an important and permanent impact on the future of porous compounds.

At present, the research effort is aimed at development of functional porous materials into appropriate scales that will advance the development of important technologies. The work in this thesis contains the design and synthesis of several novel materials with potential applications in various fields that are summarized below: For the first time we have reported tunable emission from microporous MOF based Excited State Intramolecular proton Transfer (ESIPT) responsive linker with selective sensing and removal of metal ions. More interestingly, fabrication of nanoscale MOFs with various fascinating nano morphologies (cage, cube, octahedron, tape, and coral) have also been exploited for potential applications in biology, energy and environment. Hierarchical (micro/meso) ordered porous MOFs have also been developed for gas storage and light harvesting applications. Furthermore, a controlled drug delivery system has been synthesized using soft porous materials based on a biocompatible Fe(III) MOF. Nanoporous carbon, borocarbonitrides (BCNs) materials have been exploited for energy applications (supercapacitor, lithium battery and oxygen evolution catalyst) and environment (H_2, CO_2 gas storages). Lastly, nanomaterials like different metals and metal oxides have been stabilized in MOF templates and resulting hybrid metal/metal oxide@MOF have been exploited for several catalytic reactions.

1.13 References

1) a) C. Perego, R. Millini, *Chem. Soc. Rev.* **2013**, *42*, 3956; b) A. B. Murcia, *ISRN Nanotechnol.* **2013**, 257047; c) A.-H. Lu, G.-P. Hao, Q. Sun, *Angew. Chem. Int. Ed.* **2013**, *52*, 7930-7932.

2) a) B. Yu, *Vol. 1*, American Society of Mechanical Engineers, **2010**, 781; b) M. Weclas, *J. Thermodyn.* **2010**, 789262; c) R. J. White, V. Budarin, R. Luque, J. H. Clark, D. J. Macquarrie, *Chem. Soc. Rev.* **2009**, *38*, 3401; d) J. T. Hupp, K.

R. Poeppelmeier, *Science* **2005**, *309*, 2008; e) S. B. Bhaduri, *Adv. Perform. Mater.* **1994**, *1*, 205.

3) a) M. Vallet-Regi, M. Manzano, Wiley-VCH Verlag GmbH & Co. KGaA, **2012**, 601; b) M. Nasef, John Wiley & Sons, Inc. **2009**, 233; c) M. A. Mujeebu, M. Z. Abdullah, M. Z. A. Bakar, A. A. Mohamad, M. K. Abdullah, *Appl. Energy.* **2009**, *86*, 1365:   d) Y. L. He, Q. Li, Y. Wang, G. H. Tang, *Chin. Sci. Bull.* **2009**, *54*, 4117; e) H. Wang, K. Zhang, Y. Liu, *Zhongguo Zuzhi Gongcheng Yanjiu Yu Linchuang Kangfu* **2008**, *12*, 8189; f) L. Yao, C. Chen, D. Wang, Q. Bao, J. Ma, B. Qi, *Surf. Rev. Lett.* **2006**, *13*, 103; g) Z. Rogulski, W. Lewdorowicz, W. Tokarz, A. Czerwinski, *Pol. J. Chem.* **2004**, *78*, 1357.

4) E. A. Boucher, *J. Mater. Sci.* **1976**, *11*, 1734.

5) a) K. Hadjiivanov, K. Chakarova, N. Drenchev, M. Mihaylov, *Curr. Phys. Chem.* **2012**, *2*, 151; b) K. S. W. Sing, *Colloids Surf., A* **2004**, *241*, 3; c) J. C. Dore, J. B. W. Webber, J. H. Strange, *Colloids Surf. A* **2004**, *241*, 191; d) P. J. Barrie, *Annu. Rep. NMR Spectrosc.* **2000**, *41*, 265

6) L. M. Berger, *Adv. Powder Metall. Part. Mater.* **1992**, 235.

7) a) J. P. Olivier, *Stud. Surf. Sci. Catal.* **2004**, *149*, 1; b) J. P. Olivier, *Prepr. - Am. Chem. Soc. Div. Pet. Chem.* **2003**, *48*, 179; c) J. A. Lercher, *Stud. Surf. Sci. Catal.* **1999**, *123*, 543.

8) E. F. Vansant*, Vol. 7*, Elsevier, **1996**, 485.

9) D. Wu, F. Xu, B. Sun, R. Fu, H. He, K. Matyjaszewski, *Chem. Rev.* **2012**, *112*, 3959.

10) S. L. Brantley, A. F. White, M. E. Hodson, *Kluwer Academic Publishers*, **1999**, 291.

11) A. J. Salkind, *Tech. Electrochem.* **1972**, *1*, 293.

12) D. I. Fried, F. J. Brieler, M. Froeba, *ChemCatChem* **2013**, *5*, 862.

13) D. V. P. Van, E. F. Vansant, P. Cool, Taylor & Francis, **2012**, 6162.

14) J. P. de, Wiley-VCH Verlag GmbH & Co. KGaA, **2012**, pp. 431.

15) M. Arruebo, *Wiley Interdiscip Rev Nanomed Nanobiotechnol* **2012**, *4*, 16.

16) M. E. Medina, A. E. Platero-Prats, N. Snejko, A. Rojas, A. Monge, F. Gandara, E. Gutierrez-Puebla, M. A. Camblor, *Adv. Mater.* **2011**, *23*, 5283.

17) Y. Liu, W. Xuan, Y. Cui, *Adv. Mater.* **2010**, *22*, 411.

18) M. Takahashi, M. Fuji, *Kona.* **2002**, *20*, 84.

19) P. Kumar, Y. Oumi, K. Yamana, T. Sano, *Materiaru Raifu Gakkaishi* **2002**, *14*, 7.

20) E. F. Vansant, *Proc. Technol. Proc.* **1994**, *11*, 229.

21) Zeolites for Cleaner Technologies. *Imperial College Press*, London, **2002**.

22) Y. Jin, Y. Zhu, W. Zhang, *CrystEngComm* **2013**, *15*, 1484.

23) N. Perez-Hernandez, E. H. L. Falcao, C. Perez, D. Fort, J. D. Martin, J. Eckert, *J. Phys. Chem. B* **2010**, *114*, 5694.

24) M. Antonietti, A. Thomas, P. Kuhn, Max-Planck-Gesellschaft zur Foerderung der Wissenschaften e.V., Germany. **2008.**

25) Y. Zhao, D. Li, W. Sang, D. Yang, M. Jiang, *Appl. Surf. Sci.* **2007**, *253*, 4566.

26) T. Tozawa, J. T. A. Jones, S. I. Swamy, S. Jiang, D. J. Adams, S. Shakespeare, R. Clowes, D. Bradshaw, T. Hasell, S. Y. Chong, C. Tang, S. Thompson, J. Parker, A. Trewin, J. Bacsa, A. M. Z. Slawin, A. Steiner, A. I. Cooper, *Nat. Mater.* **2009**, *8*, 973-978.

27) J. Tian, P. K. Thallapally, B. P. McGrail, *CrystEngComm* **2012**, *14*, 1909.

28) H. Kim, Y. Kim, M. Yoon, S. Lim, S. M. Park, G. Seo, K. Kim, *J. Am. Chem. Soc.* **2010**, 132, 12200.

29) M. Mastalerz, M. W. Schneider, I. M. Oppel, O. Presly, *Angew. Chem., Int. Ed.* **2011**, *50*, 1047

30) J. Tian, P. K. Thallapally, S. J. Dalgarno, P. B. McGrail and J. L. Atwood, *Angew. Chem., Int. Ed*. **2009**, *48*, 5492.

31) Y. Jin, B. A. Voss, R. D. Noble and W. Zhang, *Angew. Chem. Int. Ed.* **2010**, *49*, 6348 .

32) J. H. Chong, S. J. Ardakani, K. J. Smith and M. J. MacLachlan, *Chem.–Eur. J.* **2009**, *15*, 11824.

33) S. Jiang, J. T. A. Jones, T. Hasell, C. E. Blythe, D. J. Adams, A. Trewin and A. I. Cooper, *Nat. Commun.* **2011,** *2*, 207

34) U. Schubert, *Chem. Soc. Rev.* **2011**, *40*, 575.

35) M. Rawolle, M. A. Niedermeier, G. Kaune, J. Perlich, P. Lellig, M. Memesa, Y.-J. Cheng, J. S. Gutmann, P. Mueller-Buschbaum, *Chem. Soc. Rev.* **2012**, *41*, 5131.

36) C. Coelho, T. Stimpfling, F. Leroux, V. Verney, *Eur. J. Inorg. Chem.* **2012**, *2012,*

37) M. Yamazaki, T. Takewaki, R. Yamauchi, Y. Katou, A. Takaki, *Nippon Kasei*

Chemical Company Limited, Japan . **2011**, 73.

38) J. Lopez-Sanz, E. Perez-Mayoral, E. Soriano, M. Sturm, R. M. Martin-Aranda, A. J. Lopez-Peinado, J. Cejka, *Catal. Today* **2012**, *187*, 97.

39) S. Liu, M. Sun, F. Gao, Y. Xiao, K. Liu, *Zhongnan Daxue Xuebao, Ziran Kexueban* **2013**, *44*, 345.

40) H.-Y. Liu, L. Bo, J. Yang, Y.-Y. Liu, J.-F. Ma, H. Wu, *Dalton Trans.* **2011**, *40*, 9782.

41) D. Bousquet, F.-X. Coudert, A. G. J. Fossati, A. V. Neimark, A. H. Fuchs, A. Boutin, *J. Chem. Phys.* **2013**, *138*, 174706.

42) A. U. Ortiz, A. Boutin, A. H. Fuchs, F.-X. Coudert, *Phys. Rev. Lett.* **2012**, *109*, 195502.

43) M. Pera-Titus, D. Farrusseng, *J. Phys. Chem. C* **2012**, *116*, 1638.

44) S. Horike, S. Shimomura, S. Kitagawa, *Nat. Chem.* **2009**, *1*, 695.

45) H.-C. Zhou, J. R. Long, O. M. Yaghi, *Chem.Rev.* **2012**, *112*, 673.

46) Y.-m. Xu, T.-p. Hu, X.-q. Hu, *Guangzhou Huagong* **2011**, *39*, 8, 56.

47) J. J. I. V. Perry, J. A. Perman, M. J. Zaworotko, *Chem. Soc. Rev.* **2009**, *38*, 1400.

48) X.-q. Hu, T.-p. Hu, Y.-m. Xu, *Guangzhou Huagong* **2011**, *39*, 13.

49) M. Zhong, D. Wang, P. Wang, G. Li, W. Yuan, *Guangdong Huagong* **2011**, *38*, 318.

50) J. Klinowski, P. F. A. Almeida, P. Silva, J. Rocha, *Dalton Trans.* **2011**, *40*, 321.

51) N. Stock, S. Biswas, *Chem. Rev.* **2012**, *112*, 933.

52) K. Jayaramulu, R. Haldar, T. K. Maji, *Polyhedron* **2013**, *52*, 553.

53) Z. Xiang, D. Cao, J. Lan, W. Wang, D. P. Broom, *Energy Environ. Sci.* **2010**, *3*, 1469.

54) O. K. Farha, A. Özgür Yazaydın, I. Eryazici, C. D. Malliakas, B. G. Hauser, M. G. Kanatzidis, S. T. Nguyen, R. Q. Snurr, J. T. Hupp, *Nat Chem* **2010**, *2*, 944.

55) Y. I. Aristov, *Appl. Therm. Eng.* **2013**, *50*, 1610.

56) W. Chaikittisilp, K. Ariga, Y. Yamauchi, *J. Mater. Chem. A* **2013**, *1*, 14.

57) E. Coronado, E. G. Minguez, *Chem. Soc. Rev.* **2013**, *42*, 1525.

58) C. Janiak, *Chem. Commun. Cambridge, U. K.)* **2013**, *49*, 6933.

59) J. H. Jung, J. H. Lee, J. R. Silverman, G. John, *Chem. Soc. Rev.* **2013**, *42*, 924.

60) N. A. Khan, Z. Hasan, S. H. Jhung, *J. Hazard. Mater.* **2013**, *244-245*, 444.

61) Y. Liu, Z.-T. Li, *Aust. J. Chem.* **2013**, *66*, 9.

62) H. Miyasaka, *Acc. Chem. Res.* **2013**, *46*, 248.

63) Y. Yu, Y. Ren, W. Shen, H. Deng, Z. Gao, *TrAC, Trends Anal. Chem.* **2013**, *50*, 33.

64) Anon, *IP.com J.* **2012**, *12*, 48.

65) M. P. Attfield, P. Cubillas, *Dalton Trans.* **2012**, *41*, 3869.

66) A. Dhakshinamoorthy, H. Garcia, *Chem. Soc. Rev.* **2012**, *41*, 5262.

67) I. Erucar, G. Yilmaz, S. Keskin, *Chem. - Asian J.* **2013**, *8*, 1692.

68) C. H. Hendon, D. Tiana, A. Walsh, *Phys. Chem. Chem. Phys.* **2012**, *14*, 13120.

69) A. Jankowska, P. Florczak, S. Kowalak, *Microporous Mesoporous Mater.* **2013**, *171*, 78.

70) S. H. Jhung, N. A. Khan, Z. Hasan, *CrystEngComm* **2012**, *14*, 7099.

71) M. Lalonde, W. Bury, O. Karagiaridi, Z. Brown, J. T. Hupp, O. K. Farha, *J. Mater. Chem. A* **2013**, *1*, 5453.

72) R. J. Della, W. Lin, *Eur. J. Inorg. Chem.* **2010**, 3725.

73) R. C. Huxford, R. J. Della, W. Lin, *Curr. Opin. Chem. Biol.* **2010**, *14*, 262.

74) W. J. Rieter, K. M. L. Taylor, W. Lin, *J. Am. Chem. Soc.* **2007**, *129*, 9852.

75) Y. Cui, H. L. Ngo, W. Lin, *Inorg. Chem.* **2002**, *41*, 1033.

76) K. E. deKrafft, Z. Xie, G. Cao, S. Tran, L. Ma, O. Z. Zhou, W. Lin, *Angew. Chem. Int. Ed.* **2009**, *48*, 9901.

77) R. C. Huxford, K. K. E. de, W. S. Boyle, D. Liu, W. Lin, *Chem. Sci.* **2012**, *3*, 198.

78) R. C. Huxford-Phillips, S. R. Russell, D. Liu, W. Lin, *RSC Adv.* **2013**, *3*, 14438.

79) W. Lin, J. W. Rieter, K. M. L. Taylor, *Angew. Chem., Int. Ed.* **2009**, *48*, 650.

80) W. J. Rieter, K. M. Pott, K. M. L. Taylor, W. Lin, *J. Am. Chem. Soc.* **2008**, *130*, 11584.

81) A. Carne, C. Carbonell, I. Imaz, D. Maspoch, *Chem. Soc. Rev.* **2011**, *40*, 291.

82) R. J. Della, D. Liu, W. Lin, *Nanomedicine* **2012**, *7*, 303.

83) A. Carné-Sánchez, I. Imaz, M. Cano-Sarabia, D. Maspoch, *Nat. Chem.* **2013**, *5*, 203.

84) H. R. Moon, D.-W. Lim, M. P. Suh, *Chem. Soc. Rev.* **2013**, *42*, 1807.

85) A. Cao, R. Lu, G. Veser, *Phys.Chem.Chem.Phys.* **2010**, *12*, 13499.

86) A. Dhakshinamoorthy, H. Garcia, *Chem. Soc. Rev.* **2012**, *41*, 5262.

87) M. Meilikhov, K. Yusenko, D. Esken, S. Turner, G. Van Tendeloo, R. A. Fischer, *Eur.J. Inorg. Chem.* **2010**, *2010*, 3701.

88) S. Wang, L. Li, J. Zhang, X. Yuan, C.-Y. Su, *J. Mater. Chem.* **2011**, *21*, 7098.

89) L. Ma, W. Lin, *J. Am. Chem. Soc.* **2008**, *130*, 13834-13835.

90) J. Park, J.-R. Li, S. E. Carolina, D. Yuan, H.-C. Zhou, *Chem. Commun.* **2012**, *48*, 883.

91) R. Krishna, B. J. M. van, *Chem. Eng. Sci.* **2009**, *64*, 3159

92) W. Xuan, C. Zhu, Y. Liu and Y. Cui, *Chem. Soc. Rev.* **2012,** 41, 1677.

93) C. M. A. Parlett, K. Wilson and A. F. Lee, *Chem. Soc. Rev.* **2013,** 42, 3876.

94) Q.-R. Fang, T. A. Makal, M. D. Young, H.-C. Zhou, *Comment. Inorg. Chem.* **2010**, *31*, 165

95) L.-G. Qiu, T. Xu, Z.-Q. Li, W. Wang, Y. Wu, X. Jiang, X.-Y. Tian, L.-D. Zhang, *Angew. Chem. Int. Ed.* **2008**, *47*, 9487.

96) Y.Q. Lan, H.L. Jiang, S.L. Li and Q. Xu, *Adv. Mater.* **2011,** 23, 5015.

97) L. Song, J. Zhang, L. Sun, F. Xu, F. Li, H. Zhang, X. Si, C. Jiao, Z. Li, S. Liu, Y. Liu, H. Zhou, D. Sun, Y. Du, Z. Cao and Z. Gabelica, *Energy Environ. Sci.* **2012**, 5**,** 7508.

98) a)Y. Li, Z.-Y. Fu, B.-L. Su, *Adv. Fun. Mat.* **2012**, *22*, 4634; b) A. Almasoudi, R. Mokaya, *J.Mater.Chem.* **2012**, *22*, 146.

99) a)W. Chaikittisilp, K. Ariga, Y. Yamauchi, *J.Mater.Chem. A* **2013**, *1*, 14; b) Y. I. Aristov, *Appl. Therm. Eng.* **2013**, *50*, 1610; c).N. F. Attia, S. M. Lee, H. J. Kim, K. E. Geckeler, *Micropor. Mesopor. Mater.* **2013**, *173*, 139: d)A. Banerjee, R. Gokhale, S. Bhatnagar, J. Jog, M. Bhardwaj, B. Lefez, B. Hannoyer, S. Ogale, *J. Mater. Chem.* **2012**, *22*, 19694.

100)   a)Y. Liu, Y. Cao, Y. Shen, *Taoci Xuebao* **2011**, *32*, 135; b) Y. Shin, G. J. Exarhos, John Wiley & Sons Ltd., **2009**, 315; c) M. Tiemann, *Chem. - Eur. J.* **2007**, *13*, 8376; d) D. N. Srivastava, N. Perkas, A. Zaban, A. Gedanken, *Pure Appl. Chem.* **2002**, *74*, 1509; e)D. Brunel, N. Bellocq, P. Sutra, A. Cauvel, M. Lasperas, P. Moreau, R. F. Di, A. Galarneau, F. Fajula, *Coord. Chem. Rev.* **1998**, *178*, 1085.

Summary

This chapter deals with a novel molecular design concept to control the emission of a metal–organic framework, $\{Mg(DHT)(DMF)_2\}_n$ based on excited state intramolecular proton transfer (ESIPT) responsive organic linker (DHT) (DHT: 2,5-dihydroxyterephthalate), organic linker. The framework unveils permanent porosity and exhibits ligand-based multicolor emission that can be tuned and well controlled by the solvent molecules in solution as well as in the solid state. Furthemore the desolvated microporous framework with pendent –OH groups on the pore surface was exploited for binding and specific sensing of metal ions via Lewis acid –base interactions. The luminescence intensity significantly quenches with Cu^{II} among various *s*- and *d*-block metal ions and highly selective sensing of Cu^{II} ions has been realized in both solid and solution states (up to nano molar concentration). The immobilized Cu^{II} metal ions can be selectively removed by chelating agent like EDTA without any structural disintegration, as revealed by the luminescence and gas adsorption studies.

2.1 Introduction

Metal–organic frameworks (MOFs) or porous coordination polymers (PCPs) are a novel class of crystalline materials and have shown wide range of potential applications in various fields as gas storage, separation, catalysis, magnetism, ion exchange and drug delivery owing to their high surface area, large pore volume, significant thermal and chemical stabilities with additional unique ordered flexible tunable functional porous environment.[1-3] In addition to the inherent porous properties of MOFs, the current research of porous materials widely expanding towards new technological challenges in which the functional electronic properties of the frameworks are pivotal.[4] Among a plethora of porous MOFs investigated, multi-functional luminescent MOFs, exhibiting the combined properties of stable porosity and intense fluorescence, have attracted enormous interest recently in the field of sensors and light-emitting diodes.[5] Several metal and ligand centred approaches (MLCT, LMCT, LLCT, MMCT) have been made to design luminescent MOFs.[6] However, pure ligand-based emission due to various photo physical processes of the linking chromophores in the framework is relatively unexplored for the design of luminescent MOFs. Recently, guest-responsive fluorescent frameworks were shown to exhibit tunable emission due to excited-state intermolecular complex (exciplex) formation.[7] On the other hand, the excited state intramolecular proton transfer (ESIPT) process has been used extensively to design certain molecules and polymers with tunable emission and has found application in optoelectronic devices such as solid state lasers and organic light emitting devices (OLEDs).[8] Despite a larger number of luminescent MOFs reported in the literature, tunable emission of frameworks based on a ligand cantered ESIPT process are yet to be explored. Moreover, immense interest in luminescent MOFs stems from their potential applications in molecular sensors, as probes in biomedical assays, and in cell biology.[9] Alternatively, the detection of a trace amount of metal ion is of paramount importance with regard to environmental and biomedical applications.[10] In this respect, luminescent porous framework-based sensors would be very attractive because they can also capture metal ions, anions, or organic molecules and, hence, can be used for their removal unlike their molecular chemosensor counterparts.[11] Moreover, we envisage that enhanced sensitivity can be expected through signal amplification in MOF based sensors.[12] Although various luminescent MOFs based on chromophoric linkers and metal centers (lanthanide ions)

have already been reported, the design of corresponding analogues for the selective capture and sensing of metal ions remains challenging because this requires specific Lewis basic sites that can post synthetically interact with the metal ions.[13] In particular, real-time and easy detection of trace amounts of Cu^{II} is very important for the treatment of copper metabolism disorders such as Wilsons' disease and neurodegenerative disorders like Alzheimer's disease.[14] Therefore, the use of highly sensitive optical fluorescent technology to probe the presence of Cu^{II} at a nanomolar concentration level is very promising in real diagnostic query.[15] The luminescent (metal- or ligand-cantered) porous frameworks with free Lewis acidic/basic sites can act as anion/cation receptors and, hence, are attractive candidates as novel sensor materials.[16] The immobilization of free sites within the porous frameworks is difficult because they tend to coordinate with other metal ions to form higher dimensional structures. MOFs functionalized with free pyridyl, carboxylate, and amide groups aligned in the pore structure have been elegantly employed for the sensing of metal ions and catalytic activities.[17] This chapter reports a novel molecular design concept to control the emission of a MOF, $\{Mg(DHT)(DMF)_2\}_n$ (**1**), (DHT: 2,5-dihydroxyterephthalate) based on excited state proton transfer of the organic linker, DHT is an exciting multifunctional organic linker that has constitutional stiffness, with four pH dependent abstractable protons that can be used for generating stable and rigid higher dimensional MOFs. The choice of the DHT molecule, which is a bifunctional salicylic acid derivative, as ligand was also in line with the well-known ESIPT properties of the structurally similar salicylic acid derivatives. The DHT incorporated framework **1** exhibits ligand-based multicolor emission in solution as well as in the solid state that can be tuned and well controlled by the solvent molecules. Moreover, **1** exhibits a permanent porosity with high selectivity to CO_2. Furthermore, The most characteristic feature of **1** is the presence of free Lewis basic −OH groups within the pores, which can, in turn, be used for the binding of different metal ions and thus for sensing functions. Herein, we report for the first time a ligand-based luminescent MOF (**1**) for the selective sensing and removal of metal ions, by exploiting the functional OH groups on their pore surface. The desolvated framework $\{Mg(DHT)\}_n$ (**1a**) exhibits highly selective sensing of Cu^{II} ions in a dimethyl sulfoxide (DMSO) solution as well as in the solid state among a number of transition-metal and *s*-block metal ions. Moreover, the

captured Cu^{II} ions can be removed from pores using chelating agents like EDTA without any structural change, demonstrating the reusability of the MOFs.

2.2 Experimental Section

2.2.1 Materials

All reagents were obtained from commercial sources and used without further purification. High purity $Mg(NO_3)_2 \cdot 6H_2O$, $Ca(NO_3)_2 \cdot 6H_2O$, $Cd(NO_3)_2.4H_2O$, $Co(NO_3)_2 \cdot 6H_2O$ $Cu(NO_3)_2 \cdot 2.5H_2O$, $Li(NO_3).6H_2O$, $Mn(NO_3)_2 \cdot 4H_2O$, $NaNO_3$, $Ni(NO_3)_2 \cdot 6H_2O$, $Zn(NO_3)_2 \cdot 6H_2O$, and 2,5-dihydroxyterephthalic acid (DHT) were purchased from Aldrich Chemical Co. and used as received.

2.2.2 Synthesis of $[Mg(DHT)(DMF)_2]_n$ (1)

A mixture of $Mg(NO_3)_2.6H_2O$ (0.128 g, 0.5 mmol), 2,5-dihydroxyterephthalic acid (0.099 g, 0.5 mmol) and 15 μL of Triethylamine and 8 mN,N-dimethylformamide (DMF) was placed in a 23 mL teflon bomb and the whole reaction mixture was stirred for 1 h. Then Teflon bomb was subsequently placed in a steel autoclave and heated at 120 ºC under autogenous pressure for 72 h and then cooled to ambient temperature. Light yellow colored block shaped crystals were isolated by decanting the supernatant liquid and washed thoroughly several times with DMF. (Yield 80 %). IR (KBr cm^{-1}); v(O-H), 3468; v_{as}(OCO), 1609; v_s(OCO), 1455. Anal. Calcd. for $C_{14}H_{18}MgN_2O_8$: C, 45.82; H, 4.90; N, 7.63. Found: C, 45.21; H, 5.01; N, 7.49%.

2.3 Characterization Techniques

2.3.1 Physical Measurements

The elemental analyses were carried out using a Perkin Elmer 2400 CHN analyzer. IR spectra of the compounds were recorded on a Bruker IFS 66v/S spectrophotometer using the KBr pellets in the region 4000–400 cm^{-1}. Thermogravimetric analyses (TGA) were carried out on METTLER TOLEDO TGA850 instrument in the temperature range of 25–650 °C under nitrogen/oxygen atmosphere (flow rate of 50 mL min^{-1}) at a heating rate of 5 °C min^{-1}. Powder X-ray diffraction (PXRD) pattern in different state of the samples were recorded on a Bruker D8 Discover instrument using Cu Kα radiation. XPS spectra were recorded on a OMICRON nanotechnology spectrometer. Energy-dispersive analyses of X-rays (EDAX) were obtained by means of FEI (Nova-

Nano SEM-600 Netherlands). Fluorescence quantum yields were measured by the C9920-02 Absolute PL Quantum Yield Measurement System.

2.3.2 Adsorption Measurements

N_2 (77 K), CO_2 (195 K) and H_2 (77 K) adsorption study of the dehydrated sample of **1** was carried out using QUANTACHROME AUTOSORB-1C analyzer. In the sample chamber maintained at $T \pm 0.03$ K was placed the adsorbent sample (100-150 mg), which had been prepared at 493 K under a high vacuum (10^{-1} Pa) for 18 hours prior to measurement of the isotherms. The adsorbate was charged into the sample tube and then the change of the pressure was monitored and the degree of adsorption was determined by decrease of the pressure at the equilibrium state. All operations were computer-controlled and automatic.

2.3.3 Single-crystal X-ray Diffraction

A suitable single crystal for **1** was carefully selected under a polarizing microscope and fixed to a separate thin glass fiber by commercially available glue. X-ray single crystal structural data was collected by a Bruker Smart –CCD diffractometer equipped with a normal focus, 2.4 kW sealed tube X-ray source (Mo K$_\alpha$ radiation, 0.71073 Å) operating at 50 kV and 30 mA. The programme SAINT[18] was used for integration of diffraction profiles and an empirical absorption correction based on symmetry equivalent reflections was applied using the SADABS program.[19] The structure was solved by direct method using SIR92 programme[20] and refined by full matrix least square method using SHELXL 97.[21] Potential solvent accessible area or void space was calculated using the PLATON 99[22] multipurpose crystallographic software. Final refinement included atomic positions for all the atoms, anisotropic thermal parameters for all the non-hydrogen atoms. All calculations were carried out using WinGX system, Ver 1.70.01.[23] Bond lengths and angles are given in Table 1.

2.3.4 Crystal Data of [Mg(DHT)(DMF)₂]*n* (1)

Formula $C_{14}H_{18}MgN_2O_8$, *Mr*= 366.61, Monoclinic, Space group *C*2/*c* (no. 15), *a* = 16.1344(16) Å, *b* = 11.9074(11) Å, *c* = 9.5856(9) Å, *β* = 114.296(3)°, *V* = 1678.5(3) Å^3, *Z* = 4, ρ_{calc} =1.451 g cm-3, μ (Mo-K$_\alpha$) = 0.152 mm^{-1}, T = 150 K, λ (Mo-Kα) = 0.71073 Å, θmax = 20.5°, Total data = 5363, Unique data = 846, (R$_{int}$ = 0.048), Observed data [I > 2σ(I)] = 713, R = 0.0692, R$_w$ = 0.1950, GOF = 1.04.

2.4 Results and Discussion

2.4.1 Structural Description of [Mg(DHT)(DMF)$_2$]$_n$ (1)

Light yellow colored, square block shaped single crystals of 1 were synthesized under solvothermal conditions using Mg(NO$_3$)$_2$ and DHT in DMF at 120 ^{o}C. Compound **1** crystallizes in a monoclinic *C*2/*c* space group and the X-ray structure determination revealed a three dimensional coordination framework of Mg(II) bridged by DHT linkers. The asymmetric unit is comprised of one Mg(II) atom, one DHT and two DMF molecules. Each octahedral Mg(II) center is connected to four DHT linkers in the equatorial position through carboxylate oxygen atoms (O1, O1b, O2b and O2c) whereas the axial positions are occupied by two oxygen atoms (O4, O4b) from two DMF molecules (Figure 1a). The Mg1–O bond distances are in the range of 2.049(4)– 2.085(4) Å and the slight distortion from the ideal octahedral geometry of Mg(II) is reflected in the *cisoid a*ngles of 83.86(16)–96.14(16)^o. Each DHT acts as a tetradentate linker where each carboxylate group connects two Mg(II) centers through a *syn-anti* bridging mode forming a 1D {Mg(CO$_2$)}$_n$ chain. The 1D chains are interlinked by DHT linkers in an alternative manner, thus forming a 3D coordination framework (Figure 1b).
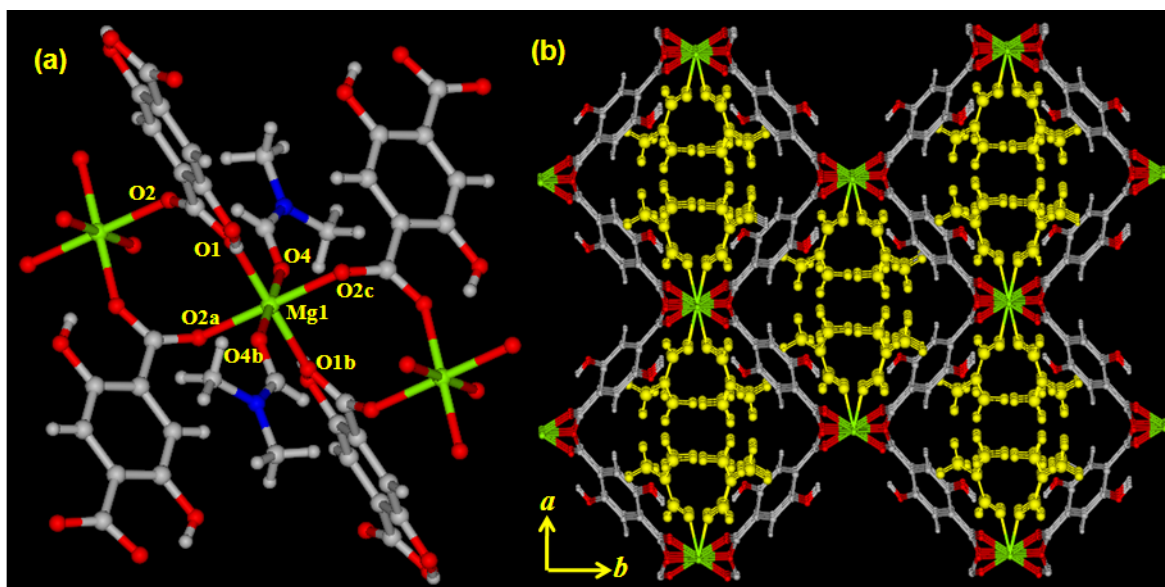
Figure 1 (a) View of the coordination environment around Mg(II); (b) 3D framework of **1** bridged by DHT along the c-axis (coordinated DMF molecules are shown in yellow color; a = 2-x,y,3/2-z; b = 2-x,-y,1-z; c = x,-y,-1/2+z).

Topological analysis shows that 1 consists of a 4-connected uninodal net and can be described by the Schläfli symbol of $4^2 8^4$ (Figure 2).[24]
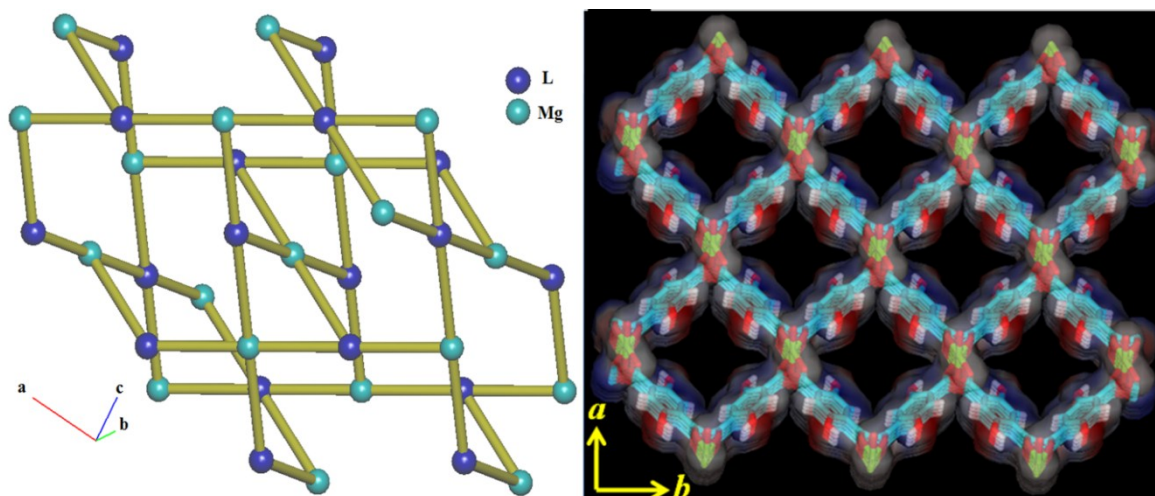
Figure 2 (left) 4-connected uninodal network topology of **1** analysis by the TOPOS (from ref 24); (Right) View of the 3D framework of 1, after the removal of DMF molecules showing square shaped channels along c-axis.

In the 3D framework, the Mg--Mg separation along the *syn-anti* carboxylate bridges and along the DHT linker are about 3.3 and 8.9 Å, respectively. Upon removal of the coordinated DMF molecules, the 3D framework shows 1D square shaped channels along the crystallographic *c*-axis (Figure 2) without any additional opening along the *a* and *b*-axes (Figure 3).
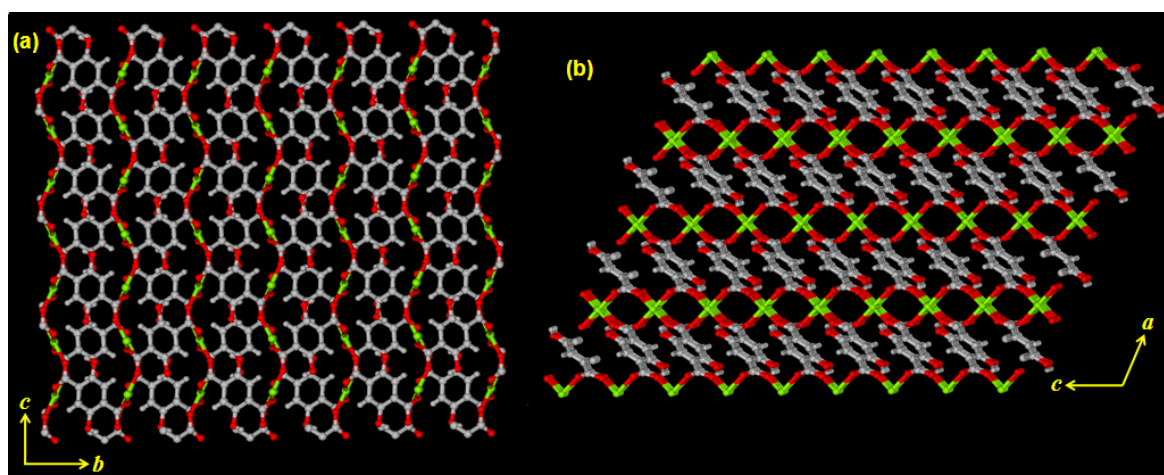
Figure 3 View of the 3D framework (a) along crystallographic *a*-axis; and (b) along crystallographic *b*-axis.

The dimension of the channels is about 5.3×5.3 Å^2 which are occupied by the four pendent –OH groups of the DHT linkers. The desolvated framework shows 55.7% void space to the total crystal volume as calculated by the PLATON.

[Mg(DHT)(DMF)$_2$]$_n$ (1)			
Mg1-O1	2.072(5)	Mg1-O4	2.085(4)
Mg1-O2_a	2.049(4)	Mg1-O1_b	2.072(5)
Mg1-O4_b	2.085(4)	Mg1-O2_c	2.049(4)
O1-Mg1-O4	89.25(17)	O1-Mg1-O2_a	91.89(17)
O1-Mg1-O1_b	180.00	O1-Mg1-O4_b	90.75(17)
O1_b-Mg1-O4	90.75(17)	O4-Mg1-O4_b	180.00
O2_a-Mg1-O4_b	89.47(7)	O1_b-Mg1-O2_a	93.09(7)
O1_b-Mg1-O4_b	96.14(16)	O1_b-Mg1-O2_a	180.00
O2_c-Mg1-O4_b	89.25(17)	O1_b-Mg1-O2_c	91.89(17)
Symmetry code: a = 2-x,y,3/2-z; b = 2-x,-y,1-z; c = x,-y,-1/2+z			

Table 1 Selected Bond Distances [Å] and Angles [deg] for **1**.

2.4.2 Framework Stability

TGA study suggests step-wise release of two Mg (II) bound DMF molecules in the temperature range of 175–295 ºC and the resultant desolvated solid is stable up to ~400 ºC without further weight loss (Figure 4).
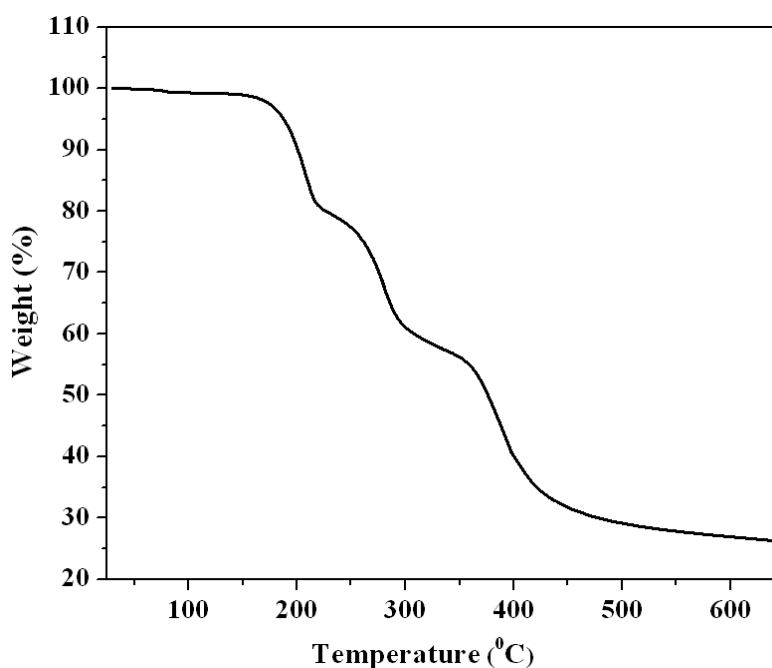
Figure 4 TGA analysis of **1** under N$_2$ atmosphere.

The PXRD pattern of the desolvated solid shows sharp lines with shifting of some Bragg peak positions in comparison to the as-synthesized framework 1, suggesting retention of the framework upon desolvation (Figure 5).
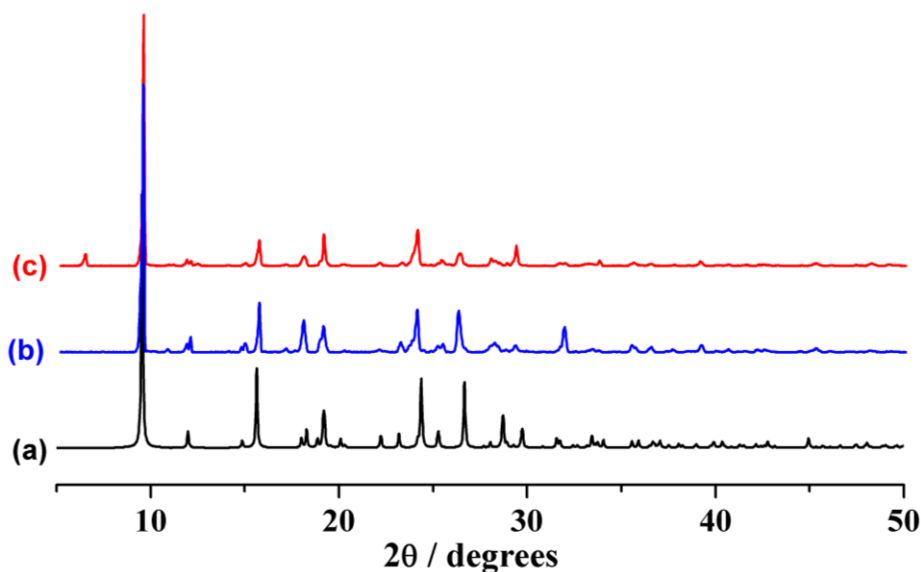
Figure 5 PXRD pattern of **1** in different states; (a) simulated from X-ray single crystal data, (b) as-synthesized and (c) desolvated at 220 °C under high vacuum (10^{-1} Pa).

2.4.3 Adsorption Study

In order to study the permanent porosity of the desolvated framework, CO_2 (195 K), H_2 and N_2 (77 K) sorption measurements were carried out in Quanta chrome Autosorb-1C analyzer. The framework exhibits a typical type-II isotherm for N_2 (kinetic diameter, 3.6 Å) (Figure 6a) and type-I profile for CO_2 (3.3 Å) (Figure 6b). The surface area calculated from CO_2 sorption using the Langmuir equation is 308 m^2 g^{-1}, suggesting the microporosity of the framework. The hysteretic sorption and large isosteric heat of adsorption, (Qst, ϕ) value of 32 kJ mole^{-1} (*calculated using the Dubinin-Radushkevich equation*) suggests strong interaction of the CO_2 molecules with the desolvated framework. This could be due to the quadrupole moment of CO_2 (-1.4 X10^{-39} C m^2) that is interacting with unsaturated Mg(II) sites in the framework more effectively compared to N_2.[25] Hydrogen sorption at 77 K and up to 1 atm is found to be 0.3 wt% (Figure 6c). The selectivity in sorption can be correlated with the smaller aperture in the desolavted framework compared to the kinetic diameter of N_2 or due to the 1D channel systems in the framework.
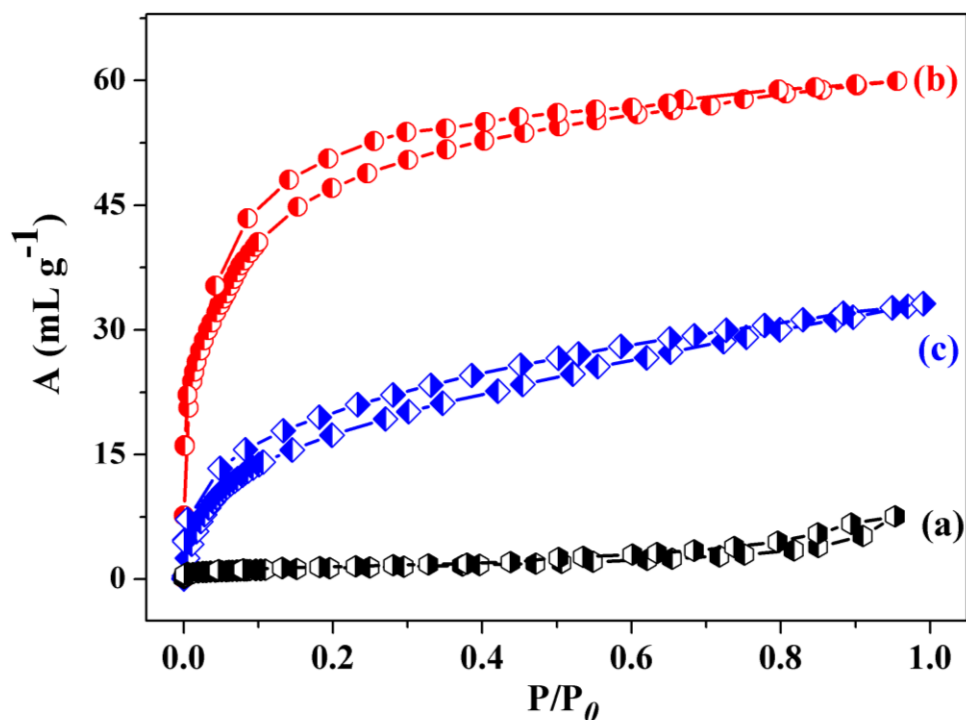
Figure 6 Adsorption Isotherms (a) N_2 sorption at 77 K (black line) ; b) CO_2 sorption at 195 K (red line) ; c) H_2 adsorption at 77 K for the desolvated framework **1**.

2.4.4 Photoluminescence Study

We have done detailed fluorescence spectroscopic studies to investigate the effect of the ESIPT sensitive DHT linker on the MOF fluorescence. As expected, the solid of **1** showed a strongly Stokes shifted bright green emission, which can presumably be attributed to the ESIPT process (Figure 7).
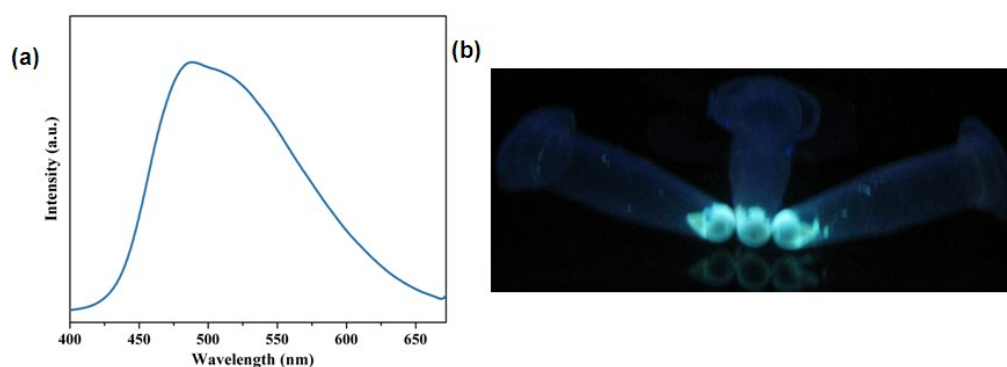
Figure 7 (a) Solid state emission spectra of **1**; and (b) corresponding photographs of the as-synthesized MOF under UV irradiation.

In order to get a deeper insight into the excited state luminescence properties, we first carried out spectroscopic studies of the free DHT linker and MOF dispersed in different solvents. The MOF **1** was found to be partially soluble in polar solvents which could be due to the high ionic character of Mg(II) that facilitates the effective solvation by polar molecules. The significant emission changes observed in the case of the free DHT linker with different solvents, similar to that of well-characterized salicylic acid derivatives, provided definitive proof for the ESIPT induced green emission. For example, in polar solvents like DMSO and DMF, free DHT showed a green emission with maxima at 510 nm (Figure 8). At the same time, DHT exhibits absorption bands only in the UV region (~360 nm) in different solvents. The absence of absorption bands in the visible region and the large Stokes shift observed in the spectra clearly suggests additional photophysical processes in the excited state, such as ESIPT. This is further confirmed by the appearance of a high-energy blue emission around 440 nm in protic solvents like ethanol suggesting that the blue and green emissions are attributable to that from the enol and keto isomers, respectively, of the free DHT ligand.
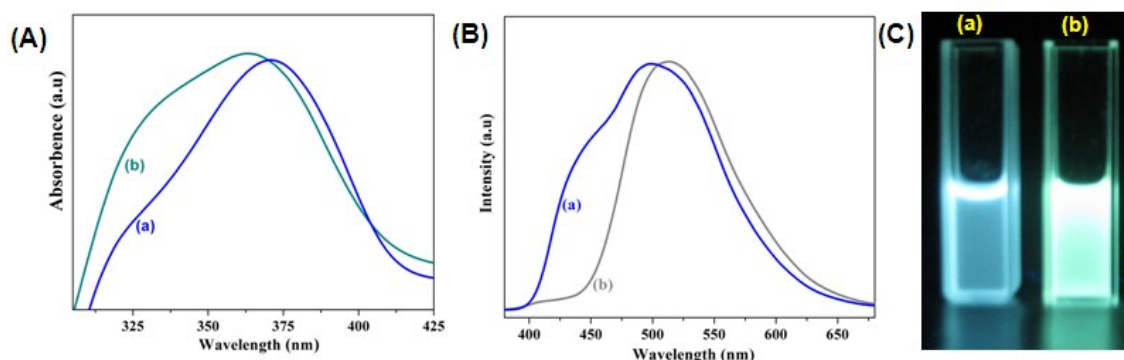
Figure 8 (A) Normalized absorption spectra of DHT linker in different solvents (a) Ethanol, (b) DMF; (B) Corresponding normalized emission spectra of DHT linker (a) Ethanol, (b) DMF; (C) Corresponding photographs of the solution under UV irradiation (a) Ethanol, (b) DMF.

Remarkably, ESIPT induced fluorescence changes of the ligand were also observed in MOF **1**, which showed a multi-color emission, ranging from blue to yellow, depending on the solvents. In an ethanol solution, **1** shows a blue emission with maxima at 404 and 429 nm, whereas a significantly red-shifted green emission at 508 nm was observed in a DMSO solution, characteristic of ESIPT induced changes (Figure 9 and 10(top)).
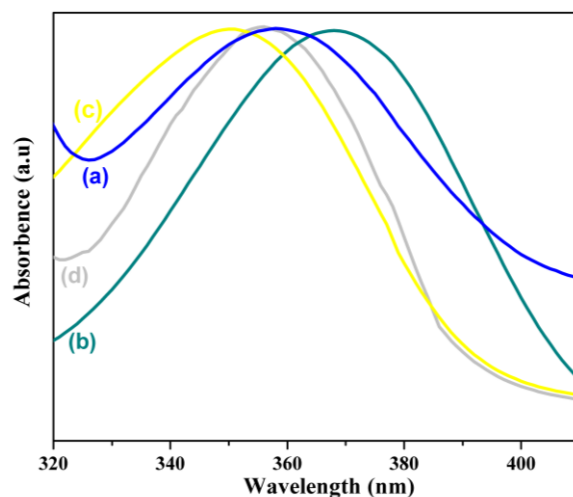
Figure 9 Normalized absorption spectra of **1** in different solvents, (a) Ethanol; (b) DMSO, (c) H_2O and (d) DMF.
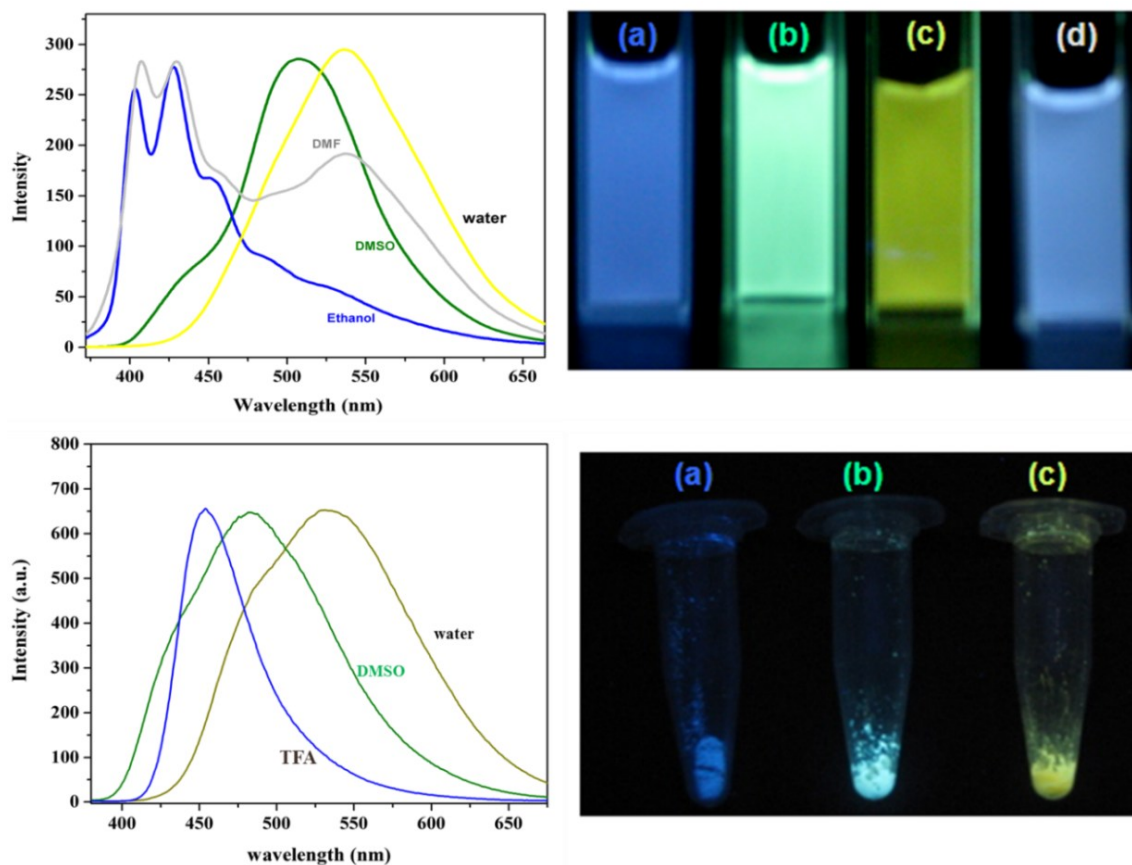
Figure 10 (Top) Normalized emission spectra of 1 in different solvents and corresponding photographs of the solutions under UV irradiation; (a) ethanol, (b) DMSO, (c) water and (d) DMF. (Bottom) Normalized emission spectra of solid framework of 1 after grinding with the different solvent and the corresponding photographs under U irradiation; (a) TFA, (b) DMSO and (c) water.
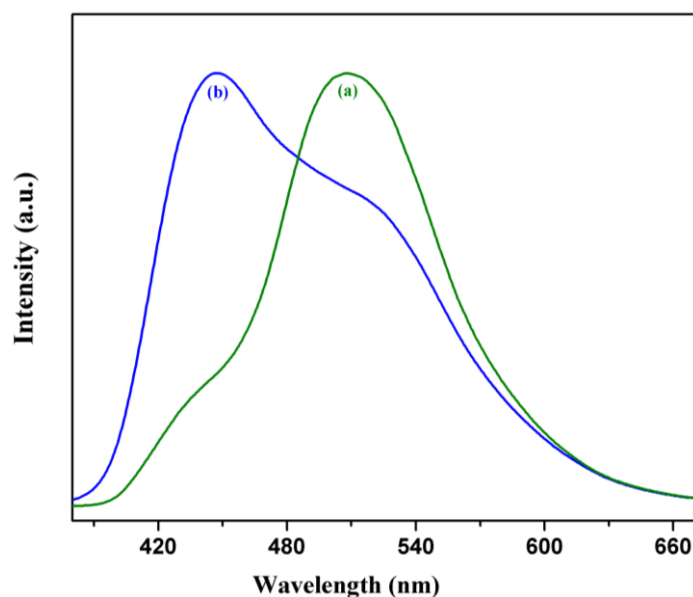
Figure 11 Normalized emission spectra of **1**; (a) in DMSO; (b) in DMSO containing trifluoroacetic acid (TFA).

This is further confirmed by the appearance of blue-shifted emission on the addition of trifluoroacetic acid (TFA) to the green fluorescent DMSO solution of **1**, which would prevent the ESIPT process by forming intermolecular H-bonds with the ligand (Figure 11). Surprisingly, in water, a highly polar protic solvent, intense yellow emission was observed with a further red-shifted emission maximum at 532 nm, which could be due to an intermolecular proton transfer with the solvent. Also, in a solvent like DMF, a broad emission ranging from blue to yellow with different spectral features was observed suggesting interplay between the various excited state processes discussed above, which can be exploited further for the generation of white light emission (Figure 10). Since the tuning of fluorescence in the solid state is a prerequisite for luminescent MOF based applications, we have grinded the as-synthesized framework solid with solvents (TFA, DMSO and water) of different polarity. The PXRD patterns and the CO_2 gas adsorption data of the solvent grinded samples also showed the intact of 3D porous framework (Figure 12 and 13). As expected, the solid powders of **1** showed blue (λ_{max} = 454 nm), green (λ_{max} = 483 nm) and yellow (λ_{max}=535 nm) emission with TFA, DMSO and water solvents, respectively (Figure 10 (bottom)). This clearly suggests that the ESIPT based fluorescence observed in solution can also be extended to the solid state upon the binding of appropriate solvent molecules with different polarities. In summary, we have successfully demonstrated for the first time, the use of

ESIPT sensitive salicylic acid derivative as a ligand for the design of a porous luminescent MOF with tunable emission properties in solution as well in the solid state.
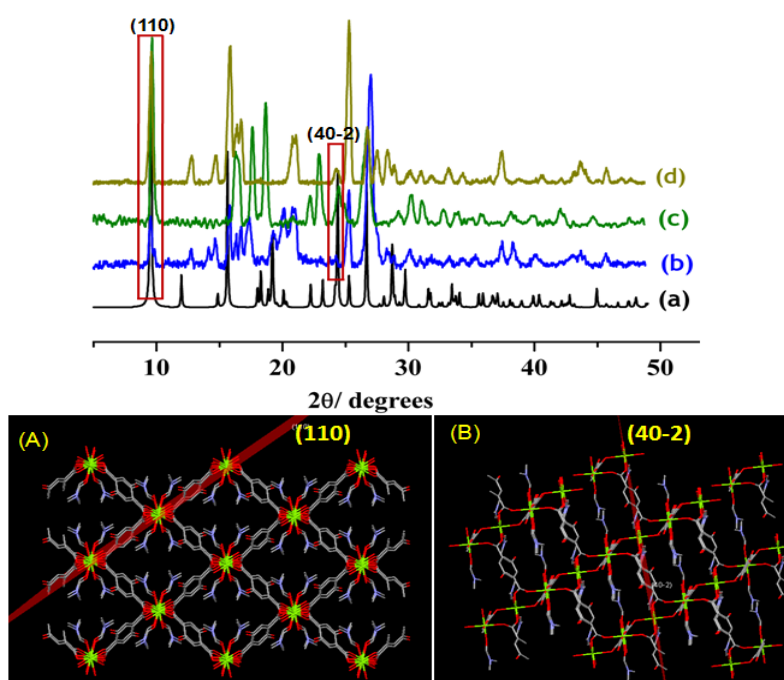
Figure 12 (Top) PXRD pattern of **1** in different states, (a) assynthesized **1**; (b) **1** grinded with trifluoroacetic acid (TFA); (b) **1** grinded with DMSO; (c) **1** grinded with water. (Bottom) Extended structure of **1** with different crystallographic planes; (A) (110) and (B) (40-2) plane.
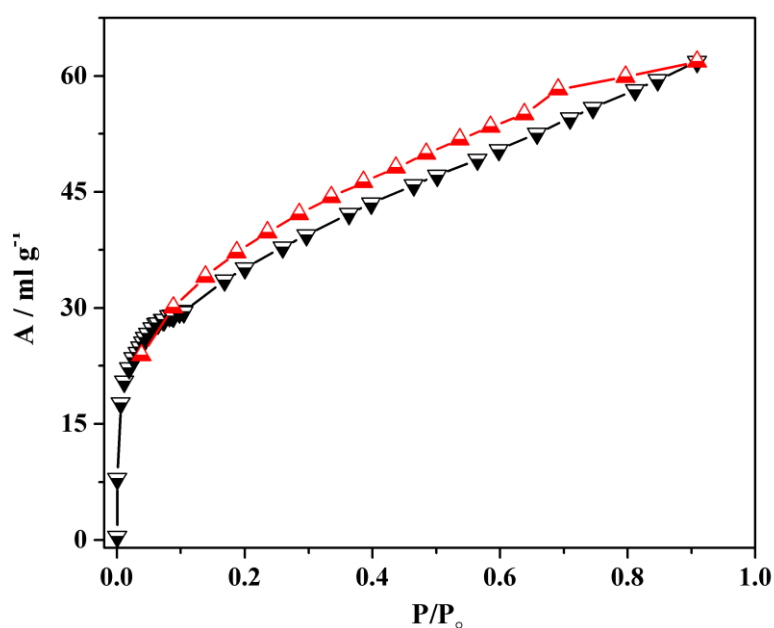
Figure 13 CO_2 sorption isotherm for DMSO grinded sample of **1** at 195 K.

2.4.5 Specific Sensing and Removal of Metal ions

MOF **1** features a three dimensional framework with 1D channels along the crystallographic *c*-axis, which are occupied by coordinated DMF molecules. Upon removal of the coordinated DMF molecules, the 3D framework **{Mg(DHT)}**$_n$ (**1a**) shows 1D square shaped channels along the crystallographic *c*-axis without any additional opening along *a* and *b*-axis. The desolvated framework **1a** contains 55.7% void space and the dimensions of the channels are about 5.3 × 5.3 Å^2 which are occupied by the pendent –OH groups of DHT linkers (Figure 14). The framework **1a** is stable up to ~400 ºC and permanent porosity of the framework has been confirmed by the type I CO_2 adsorption profile typical for microporous materials. Compound **[Mg(DHT)]**$_n$**(1a)** is partially soluble in organic solvents like DMSO and recovered solid from DMSO solution or DMSO grinded sample of **1a** shows the composition **{[Mg(DHT)]·2DMSO}**$_n$ (**1b**). The PXRD patterns and the CO_2 adsorption studies of the DMSO grinded samples exhibit, 3D porous structure which rules out the possibility of the disintegration of the compound into free ligand or metal salts in presence of DMSO. The DMSO grinded solid sample of **1a** and DMSO solution of **1a** show large Stokes shifted green emission (λ_{max} = 508 nm) when excited at 370 nm due to excited state intramolecular proton transfer (ESIPT) state of the DHT linker in polar solvents.
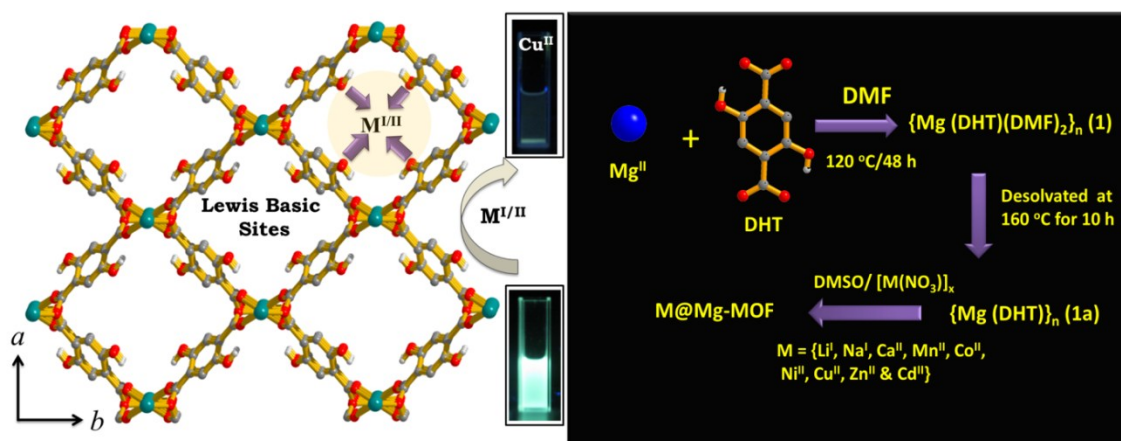
Figure 14 (left) View of the 3D framework of {Mg(DHT)}$_n$ along crystallographic c-axis showing Lewis basic pendant –OH groups and photograph under UV-light corresponding {Mg(DHT)}$_n$ and after immobilized Cu^{II} in DMSO; (Right) Immobilization of metal ions (M = Li^I, Na^I, Ca^{II}, Mn^{II}, Co^{II}, Ni^{II}, Cu^{II}, Zn^{II} and Cd^{II}) in to pores contains pendant –OH groups of {Mg(DHT).2DMSO}$_n$ activated in 10^{-3} M.

Therefore we have studied the sensing properties of different metal ions with **1a** in DMSO. The compound **1a** was immersed in DMSO solutions containing different metal ions (10^{-3} M) (M = Li^I, Na^I, Ca^{II}, Mn^{II}, Co^{II}, Ni^{II}, Cu^{II}, Zn^{II}and Cd^{II}) and resulting solution in each case was continuously stirred to prepare metal ion incorporated product {**M@Mg-MOF**} (Figure 14). The solid products were filtered, washed with DMSO, and characterized by IR, PXRD, and energy-dispersive X-ray absorption studies. The PXRD patterns of the {M@MOF} sample after the incorporation of different metal ions shows sharp lines with slight shifting of the Bragg's peaks in comparison to 1b, suggesting that the framework structure remains intact even after metal immobilization in a DMSO solution (Figure 15a and b).
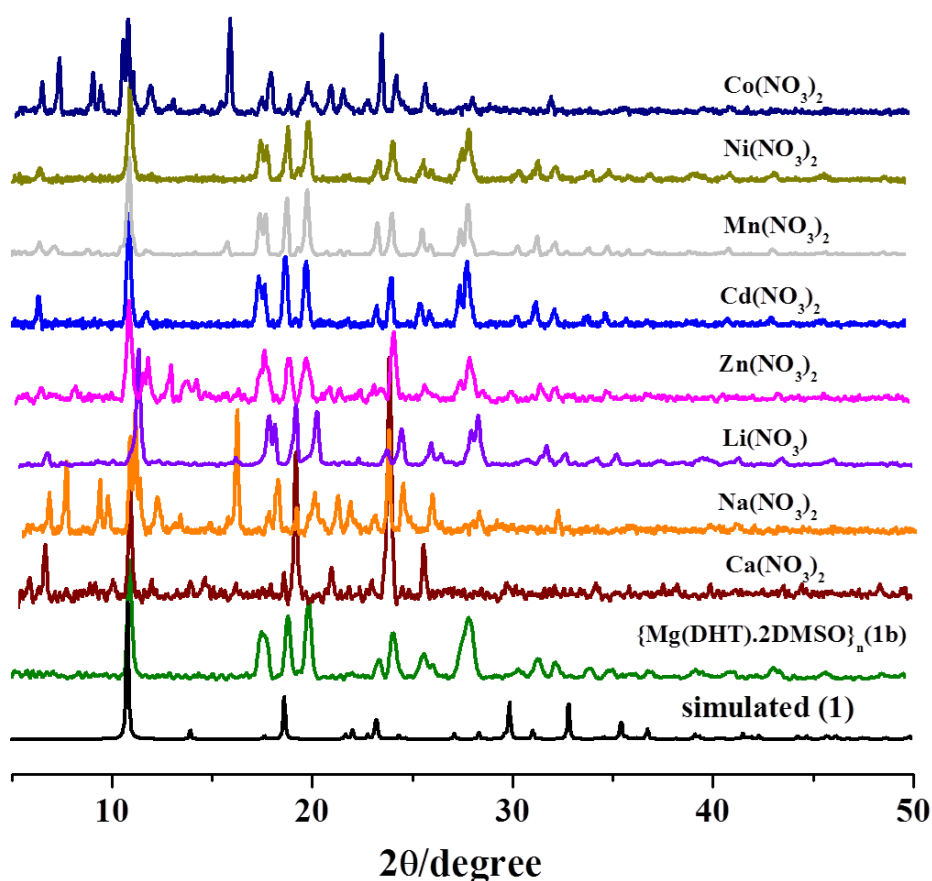
Figure 15a Powder XRD pattern of the compounds obtained after treating **1a** with different metal ions (10^{-3} M) in DMSO solution.
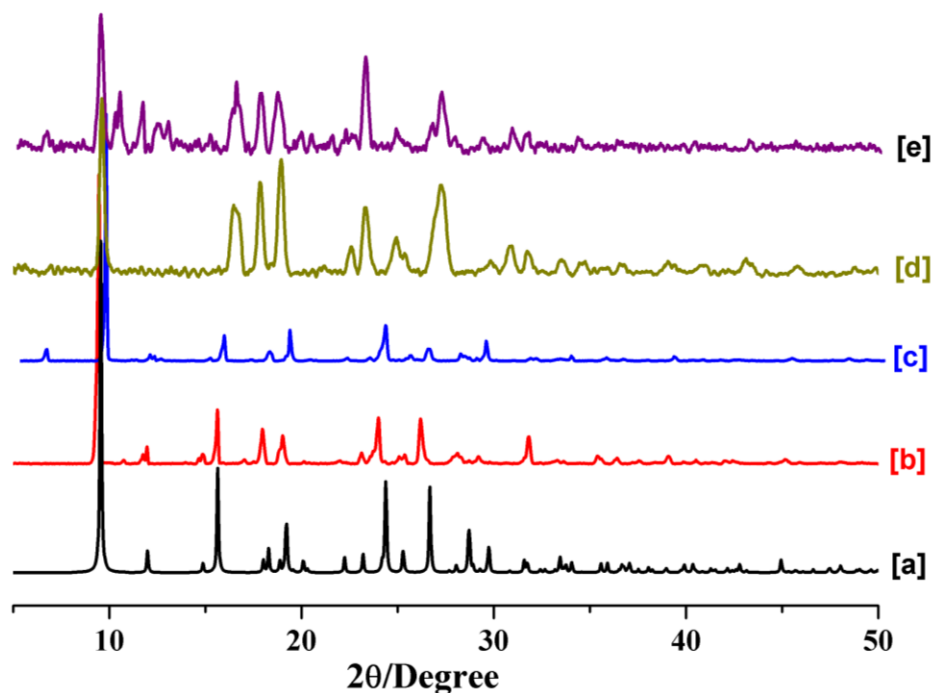
Figure **15b** Powdered XRD pattern of compound 1 [a]-simulated [b] assynthesized [c] MOF 1a [d] {Mg(DHT).2DMSO}$_n$(**1b**) [e] Cu@Mg-MOF
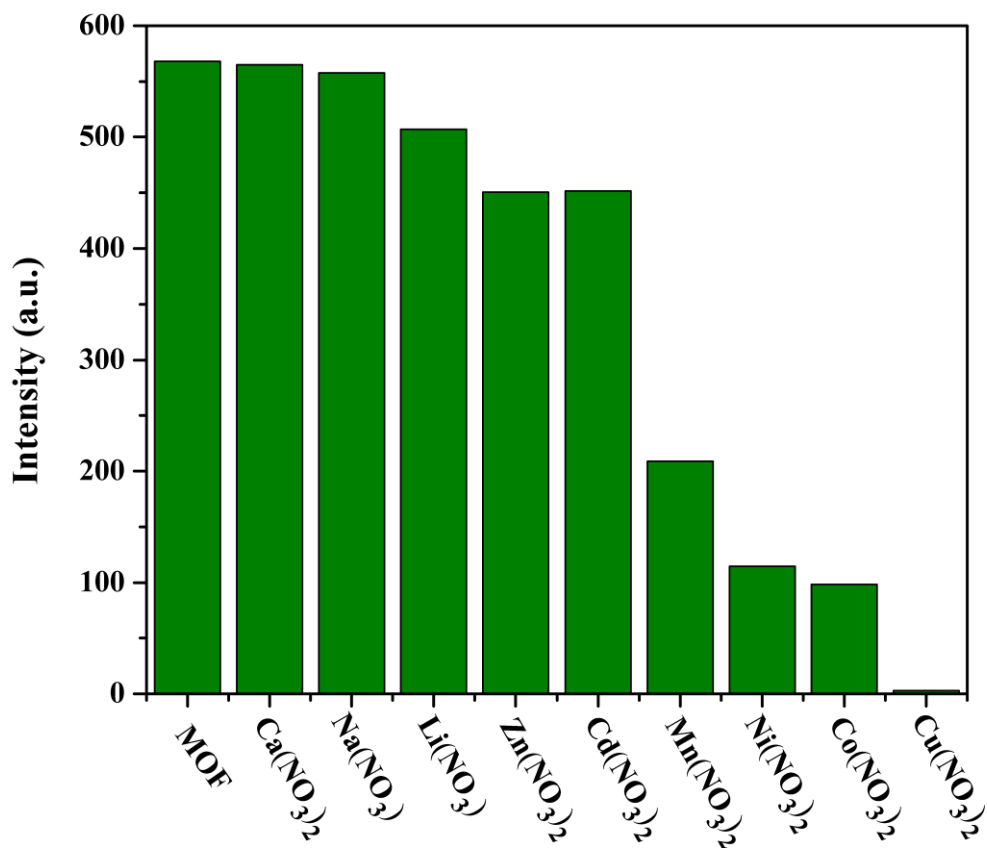
Figure 16 Comparison of the luminescence intensities of solid **1a** after immobilization with different metal ions (10^{-3} M) in DMSO.

Fluorescence spectroscopic studies of the samples **{M@Mg-MOF}** obtained with different metal ions showed green emission when excited at 370 nm. Interestingly, the luminescence intensity of **{M@Mg-MOF}** is dependent on the nature of metal ions, providing room for selective sensing. For example, alkali, alkaline-earth, and transition metal ions with filled d shells (Zn^{II} and Cd^{II}) have no effect on the luminescent intensity after incorporation into the pores (Figures 16). Interestingly quenching in emission is observed with the transition metal ions like Ni^{II}, Co^{II} and Cu^{II}, in particular the quenching effect with Cu^{II} ions is most significant. The luminescent intensity of the Cu^{II} incorporated **{Cu@Mg-MOF}** form obtained from 10^{-3} M $Cu(NO_3)_2$ solution six times less intense than the 1a suggesting high sensitivity towards Cu^{II} for **1a** (Figure 17).
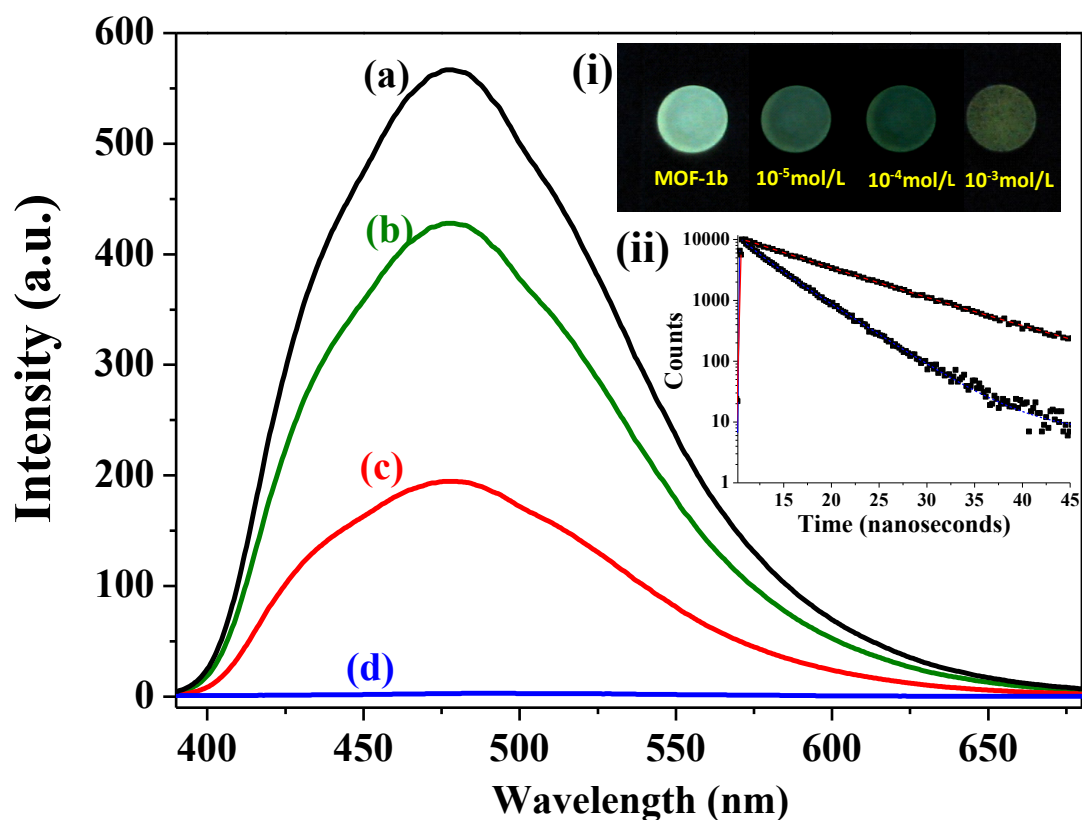
Figure 17 Luminescence spectra of solid {Cu@Mg-MOF} obtained after the incorporation of different concentrations of Cu^{II} in 1a in DMSO: (a) 1a; (b) 10^{-5} M; (c) 10^{-4} M; (d) 10^{-3} M. Insets: (i) Photographs of the corresponding samples under UV light; (ii) lifetime data for 1a and {Cu@Mg-MOF} (10^{-3} M).

The luminescent quenching effect of MOF 1a by Cu^{II} has been further examined by time resolved fluorescence studies. The fluorescence life time of 10.3 ns for **1a** is significantly reduced to 3.6 ns in the presence of 10^{-3} M $Cu(NO_3)_2$ (inset, Figure 17). The significant luminescent quenching with high sensitivity by **1a** further allowed visual detection of the existence of Cu^{II} under when viewed under UV light (Figure 14). Furthermore, the absolute quantum yield has been decreased to 0.059 % in **{Cu@Mg-MOF}**(10^{-3} M Cu(II)) from 1.5436 % of native framework, **{[Mg(DHT)]·2DMSO}**$_n$. The pore surfaces of the dehydrated MOF 1a is occupied by the pendent –OH groups and the nearest neighbour distances between the –OH groups in the pores are 5.44, 7.11 and 7.17 Å (Figure 18). Therefore, the immobilized metal ions on the pore surface can bind effectively with the free −OH groups.
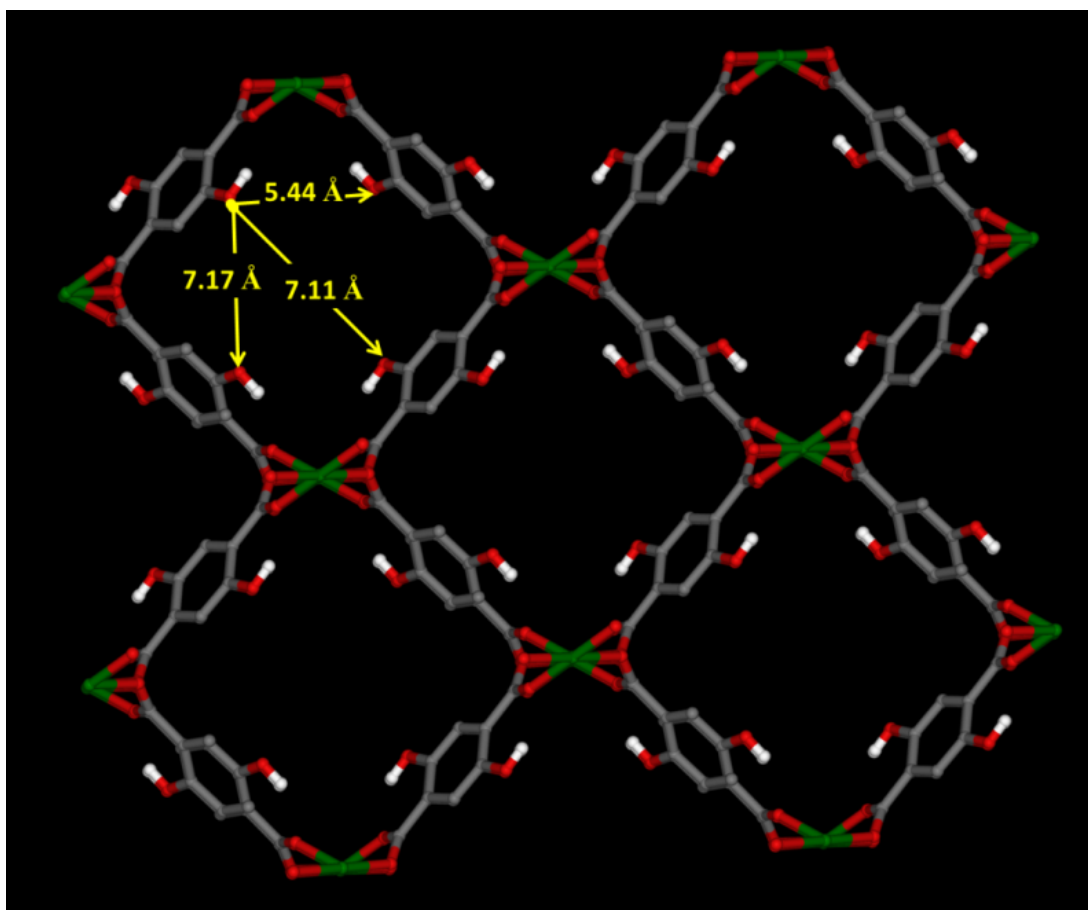
Figure 18 View of the 1D channel system of the framework {Mg(DHT)(DMF)2}n (**1**) (coordinated DMF molecules have been removed for clarity). The distances between the pendent -OH groups are shown which can bind with the encapsulated metal ions on the pore surface.

IR and X-ray photoelectron spectroscopy (XPS) spectra of the **{Cu@Mg- MOF}** sample clearly indicate that the Cu^{II} ion has been immobilized into the MOF structure (Figures 19). The broad peak corresponding to the core-level XPS transition of Cu $2p^{3/2}$ appears at 931.9 eV, which is an agreement with the value of $Cu(OH)_2$, suggesting the binding of Cu^{II} ions through pendent −OH groups of 1a. Energy dispersive X-ray spectra and elemental analysis further indicated that 0.5 atom of CuII has been incorporated per formula unit of 1b (Figure 20).
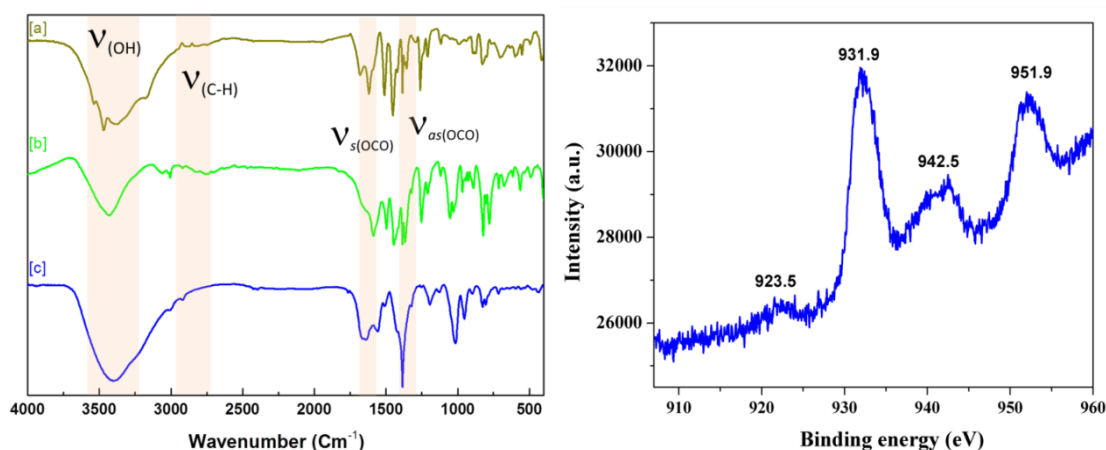
Figure 19 (left) FT-IR spectra for (a) {Mg(DHT).(DMF)$_2$}$_n$ (**1**); (b) {Mg(DHT). 2DMSO}$_n$ (**1b**) and (c) {**Cu@Mg-MOF**}; (Right)   XPS spectra (Cu 2p3/2) for {**Cu@Mg-MOF**}.
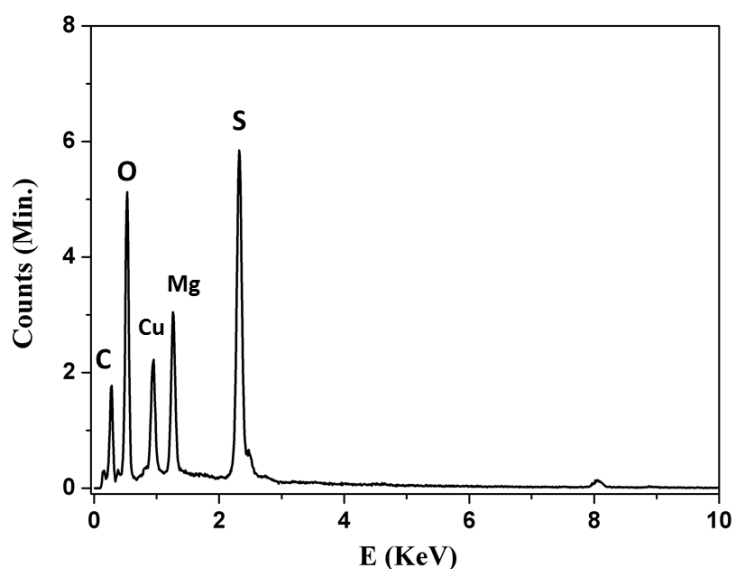
Figure 20 EDX analysis for {**Cu@Mg-MOF**} based on (10^{-3} M) Cu^{II} concentration

Furthermore, CO_2 adsorption study with the {**Cu@Mg-MOF**} compound shows negligible uptake with a type II profile, which unequivocally suggests the presence of Cu^{II} on the pore surfaces (Figure 21).
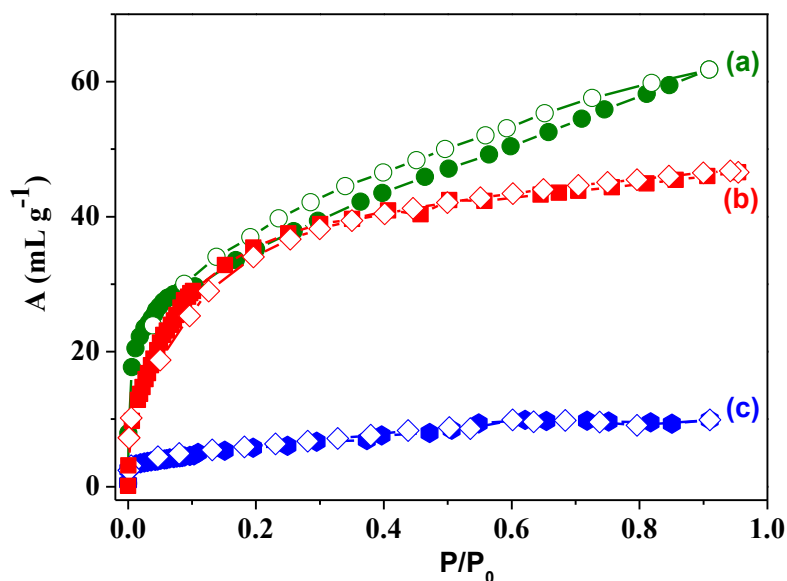
Figure 21 CO_2 adsorption (closed) and desorption (open symbol) isotherms at 195 K for (a) desolvated 1b, (b) {**Cu@Mg-MOF**} and (c) a compound obtained from {**Cu@Mg-MOF**} after treatment with EDTA.

The quenching of the ligand-based emission in 1a upon complexation with the paramagnetic transition-metal ions (Co^{II}, Ni^{II}, and Cu^{II}) could be due to the energy/charge transfer processes through the partially filled d orbitals based on ligand-field transitions (d−d) or due to reabsorption of the emission energy for the d−d transition. Moreover, quenching is not observed with the Cd^{II}, Zn^{II}, alkali, and alkaline-earth metal ions with no unpaired electrons (filled d^{10} or p^6 configurations). The quenching effect can also be quantitatively determined by the Stern−Volmer equation. The Stern−Volmer quenching coefficient K_{sv} for Cu^{II} is calculated to be 170.2 M^{-1} suggesting the highly selective and sensitive sensing of Cu^{II} in this framework. To show the feasibility of the sensing effect even in solution, we have done titration of MOF 1a in a DMSO solution with increasing concentrations of $Cu(NO_3)_2$, and probing of the corresponding emission spectra (Figure 22) suggests that quenching is pronounced even with a nanomolar concentration of $Cu(NO_3)_2$. Interestingly, a similar quenching effect is not observed with a free DHT ligand solution in DMSO with Cu^{II} (Figure 22). Hence, it is evident that the confined small pores in MOF **1a** enhance the binding of Cu^{II} with the free −OH groups on pore surfaces.
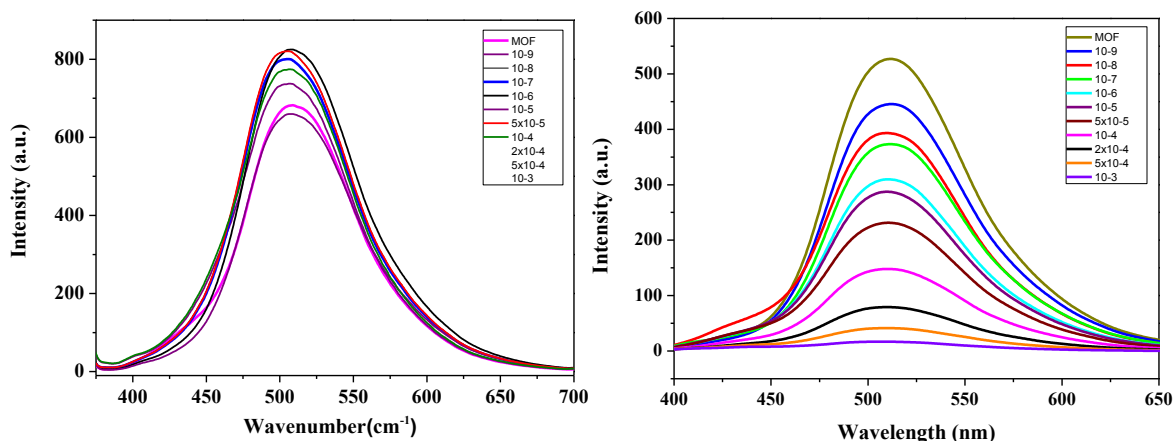
Figure 22 Comparison of luminescence intensities of copper metal ion in solution state as incorporated in to (left) Ligand DHT ; (Right) {Mg(DHT)}*n* **1a** in DMSO after incorporation of different concentration of copper ion (10^{-3} -10^{-9} M).

It is worth mentioning that the quenched fluorescence emission of {**Cu@Mg-MOF**} can be restored by removal of the metal ion using EDTA through complexation. More importantly, the recovered MOF after removal of Cu^{II} showed porous nature, which is evident from a CO_2 uptake profile similar to that of MOF 1a (Figure 21).Furthermore, the similarity in the PXRD pattern of the Cu^{II}-removed solid with that of 1a indicates the reversal of encapsulation of metal ions into the MOF structure and the reusability of MOF for sensory applications (Figure 23).
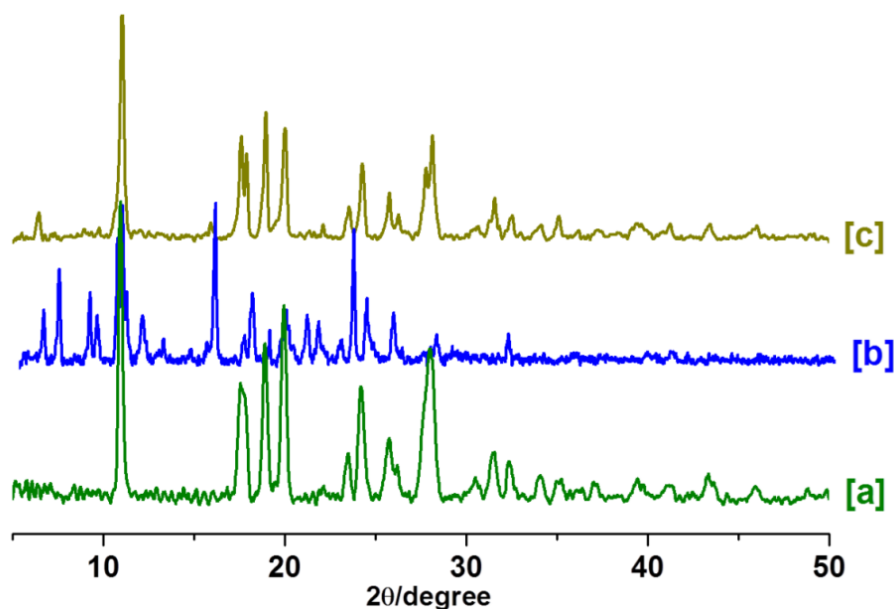
Figure 23 Comparison of powder XRD patterns, (a) {Mg(DHT).2DMSO} (**1b),** (b) {**Cu@Mg-MOF}**; (c) {**Cu@Mg-MOF}** after treating with EDTA solution.

2.5 Conclusions

In summary, we have successfully demonstrated for the first time, the use of ESIPT sensitive salicylic acid derivative as a ligand for the design of a porous luminescent MOF with tunable emission properties in solution as well in the solid state. This work is expected to open up a new dimension in the design of luminescent MOFs, where various photophysical

processes based on ligand chromophores are exploited. In addition, broad emission exhibited by the MOF in the presence of solvent molecules like DMF could be further exploited for white light emission and the experiments in this direction are underway. Additionally, luminescent microporous MOF exhibiting remarkable selective quenching of the Cu^{II} ion in solution as well as in the solid state has been reported based on confined coordination space within the MOF structure having Lewis basic sites (pendent $-OH$ groups). The foregoing results demonstrate that the novelty of the MOF system for specific sensing of metal ions relies on its porous structure to direct specific recognition, selectivity, and quantitative separation. Moreover, the reversal in the system allows one to reuse such MOF materials for further sensing functions.

2.6 References

1) A. M. Breul, M. D. Hager, U. S. Schubert, *Chem. Soc. Rev.* **2013**, *42*, 5366.

2) J. Rocha, L. D. Carlos, F. A. A. Paz, D. Ananias, *Chem. Soc. Rev.* **2011**, *40*, 926.

3) a) G. Ferey, *Dalton Trans* **2009**, 4400; b) P. Horcajada, C. Serre, G. Maurin, N. A. Ramsahye, F. Balas, M. V. Regi, M. Sebban, F. Taulelle, G. Fere´y, *J. Am. Chem. Soc.* **2008**, *130*, 6774; c) S. Kitagawa, R. Kitaura, S. Noro, *Angew. Chem., Int. Ed.,* **2004**, *43*, 2334; d) J. Lee, O. K. Farha, J. Roberts, K. A. Scheidt, S. T. Nguyen, J. T. Hupp, *Chem. Soc. Rev.* **2009**, 38, 1450; e) J.-R. Li, R. J. Kuppler , H.C. Zhou, *Chem. Soc. Rev.* **2009**, *38*, 1477; f) T. K. Maji, R. Matsuda , S. Kitagawa*, Nat. Mater.* **2007,** *6*, 142;

4) a) C. Janiak, *Dalton Trans* **2003**, 2781; b) D. Maspoch, D. Ruiz-Molina , J. Veciana, *Chem. Soc. Rev.* **2007**, *36*, 770; c) M. P. Suh, Y. E. Cheon , E. Y. Lee, *Coord. Chem. Rev.* **2008**, *252*, 1007; d) C. L. Cahill, D. T. de Lilla , M. Frisch, *Cryst Eng Comm* **2007**, *9*, 15.

5) a) W. S. Liu, T. Q. Jiao, Y. Z. Li, Q. Z. Liu, M. Y. Tan, H. Wang , L. F. Wang,

J. Am. Chem. Soc., **2004**, *126*, 2280; b) K. L. Wong, G. L. Law, Y. Y. Yang , W. T. Wong, *Adv. Mater.* **2006**, *18*, 1051; c) M. S. Wang, S. P. Guo, Y. Li, L. Z. Cai, J. P. Zou, G. Xu, W. W. Zhou, F. K. Zheng , G. C. Guo, *J. Am. Chem. Soc.* **2009**, *131,* 13572.

6) a)M. D. Allendorf, C. A. Bauer, R. K. Bhakta , R. J. T. Houk, *Chem. Soc. Rev.* **2009,** *38*, 1330; b) B. L. Chen, Y. Yang, F. Zapata, G. N. Lin, G. D. Qian , E. B. Lobkovsky, *Adv. Mater.* 2007, 19, 1693; c) K. C. Stylianou, R. Heck, S. Y. Chong, J. Bacsa, J. T. A. Jones, Y. Z. Khimyak, D. Bradshaw , M. J. Rosseinsky, *J. Am. Chem. Soc*. **2010**, *132*, 4119; d) C. A. Bauer, T. V. Timofeeva, T. B. Settersten, B. D. Patterson, V. H. Liu, B. A. Simmons , M. D. Allendorf, *J. Am. Chem. Soc.* **2007**, *129*, 7136.

7) a) B. D. Wagner, G. J. McManus, B. Moultan , M. J. Zaworotko, *Chem. Commun.* **2002**, 2176;   b) D. Tanaka, S. Horike, S. Kitagawa, M. Ohba, M. Hasegawa, Y. Ozawa , K. Toriumi, *Chem. Commun.* **2007**, 3142.

8) a) P. T. Chou, W. S. Yu, Y. M. Cheng, S. C. Pu, Y. C. Yu, Y. C. Lin, C. H. Huang , C. T. Chen, *J. Phys. Chem. A* **2004**, *108*, 6487; b) W. S. Yu, C. C. Cheng, Y. M. Cheng, P. C. Wu,Y. H. Song, Y. Chi , P. T. Chou, *J. Am. Chem. Soc.* **2003**, *125*, 10800;   c) S. Kim, S. Y. Park, I. Yoshida, H. Kawai , T. Nagamura, *J.   Chem. B* **2002**, *106*, 9291; d) W. H. Sun, S. Y. Li, R. Hu, Y. Qian, S. Q. Wang , G. Q. Yang,   *J. Phys. Chem. A* **2009**, 113, 5888; e) K. Sakai, T. Tsuzuki, Y. Itoh, M. Ichikawa , Y. Taniguchi, *App. Phy. Lett,* **2005**, 86, 0811031; f) S. M. Chang, Y. J. Tzeng, S. Y. Wu, K. Y. Li , K. L. Hsueh, *Thin Solid Films* **2005**, *477*, 38.

9) a) J.C. G. Bünzli , C. Piguet, *Chem. Soc. Rev.* **2005**, *34,* 1048;   b) L. D. Carlos, R. A. Sá Ferreira, V. de Zea Bermudez , S. J. L. Ribeiro, *Adv. Mater.* **2009**, *21*, 509;   c) K. Binnemans, *Chem. Rev.* **2009**, *109*, 4283.

10) a) H. Kozlowski, A. Janicka-Klos, J. Brasun, E. Gaggelli, D. Valensin, , G. Valensin, *Coord. Chem. Rev.* **2009**, *253*, 2665.

11) a) C. A. Bauer, T. V. Timofeeva, T. B. Settersten, B. D. Patterson, V. H. Liu, B. A. Simmons , M. D. Allendorf, *J. Am. Chem. Soc.* **2007**, 129, 7136; b) Y. Bai, G. J. He, Y. G. Zhao, C. Y. Duan, D. B. Dang , Q. J. Meng, *Chem. Commun.* **2006**, 1530;   c) K.-L. Wong, G.-L. Law, Y.-Y. Yang , W.-T. Wong, *Adv. Mater.* **2006**, *18*, 1051.

12) B. Zhao, X.-Y. Chen, P. Cheng, D.-Z. Liao, S.-P. Yan , Z.-H. Jiang, *J. Am. Chem. Soc.* **2004**, *126*, 15394.

13) M. D. Allendorf, C. A. Bauer, R. K. Bhakta , R. J. T. Houk, *Chem. Soc. Rev.* **2009**, *38*, 1330.

14) H. Tapiero, D.M. Townsend , K.D. Tew, *Biomed. Pharmacother.* **2003**, *57*, 386.

15) E. L. Que, D.W. Domaille , C.J. Chang, *Chem. Rev.* **2008**, *108*, 1517.

16) Y. Cui, Y. Yue, G. Qian , B. Chen, *Chem. Rev.* **2011**, *112*, 1126.

17) J. Rocha, L. D. Carlos, F. A. A. Paz , D. Ananias, *Chem. Soc. Rev.* **2011**, *40*, 926.

18) SMART (V 5.628), SAINT (V 6.45a), XPREP, SHELXTL; Bruker AXS Inc. Madison, Wisconsin, USA, **2004**.

19) G. M. Sheldrick, *Siemens Area Detector Absorption Correction Program*, University of Göttingen, Göttingen, Germany, **1994**.

20) A. Altomare, G. Cascarano, C. Giacovazzo A. Gualaradi, *J. Appl. Cryst.* 1993, 26, 343.

21) G.M. Sheldrick, SHELXL-97, *Program for Crystal Structure Solution , Refinement*; University of Göttingen, Göttingen, Germany, **1997**.

22) A.L. Spek, *J. Appl. Cryst.* **2003**, *36*, 7.

23) L.J. Farrugia, *WinGX - A Windows Program for Crystal Structure Analysis. J. Appl. Crystallogr.* **1999**, *32*, 837.

24) a) V.A. Blatov, A.P. Shevchenko, V. N. Serezhkin, *J. Appl. Crystallogr.* **2000**, *33*, 1193; b) V.A. Blatov, L. Carlucci, G. Ciani, D. M. Proserpio, *Cryst. Eng. Comm.* **2004**, *6,* 377.

25) M. M. Dubinin, *Chem. Rev.* **1960**, *60,* 235.

Chapter 2

Tunable Emission from a Porous Metal–Organic Framework by Employing an Excited-State Intramolecular Proton Transfer (ESIPT) Responsive Ligand: Specific Sensing and Removal of Metal Ions
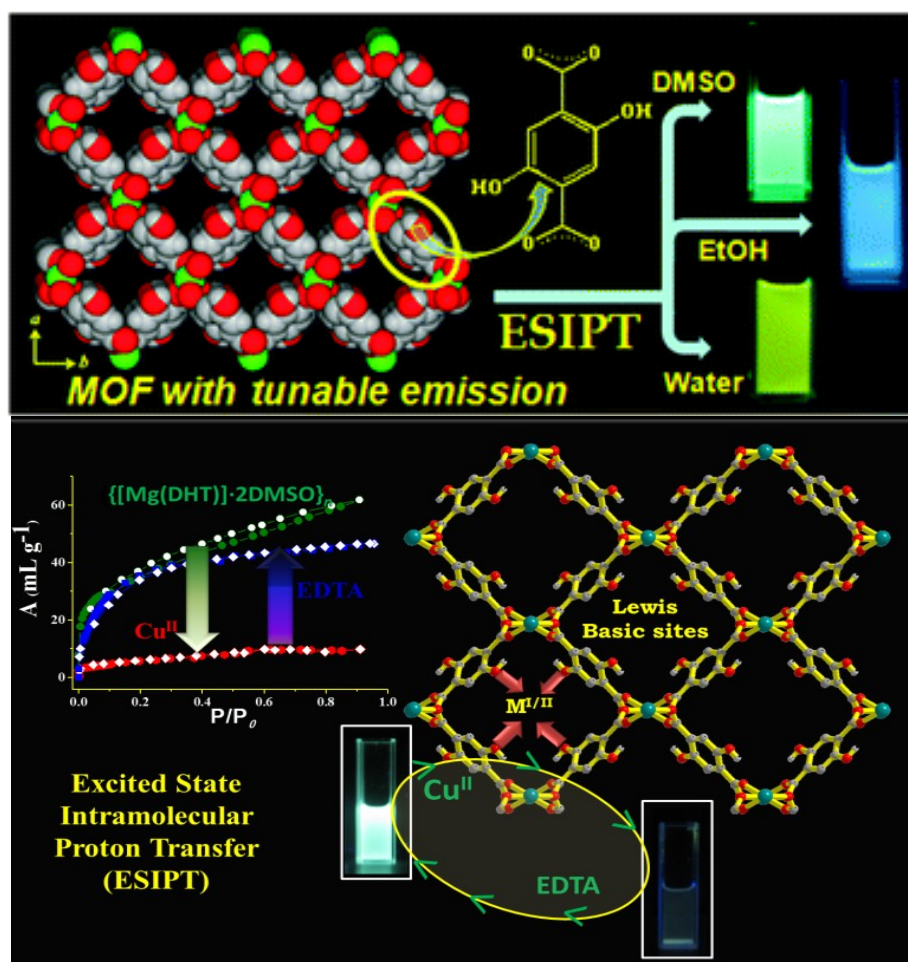
Chapter 3

Nanoscale Metal-Organic Frameworks (NMOFs)
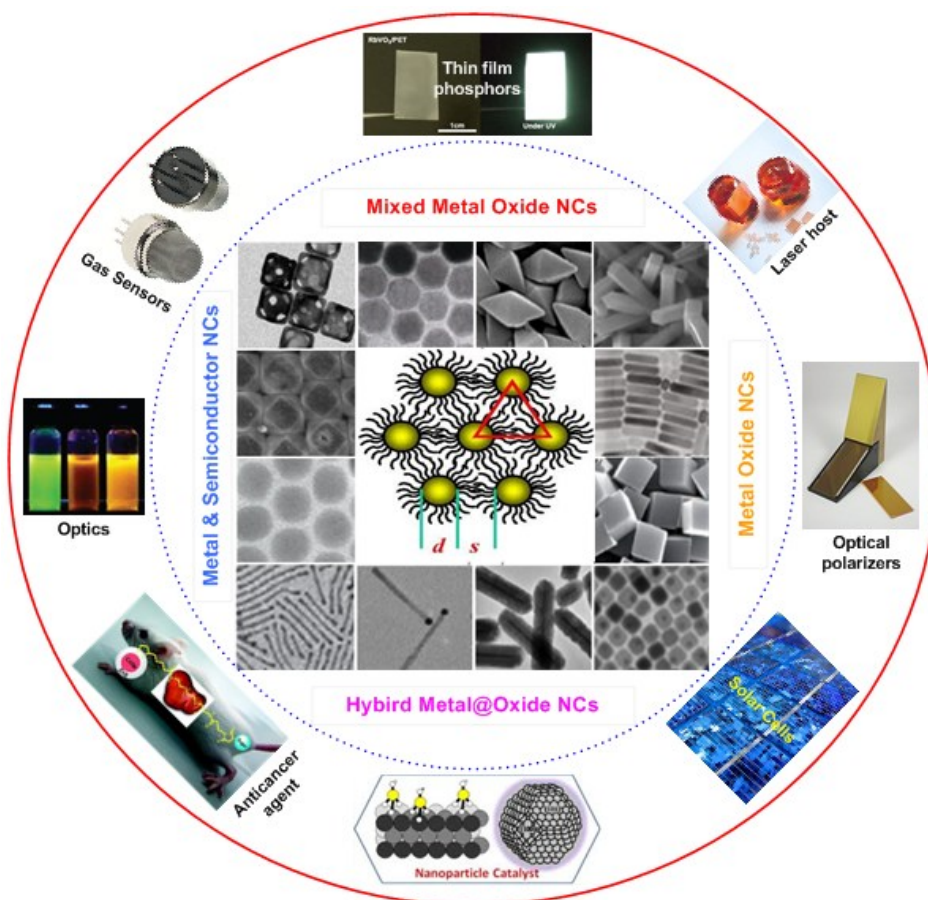
Chapter 3.1

Shape Assisted Fabrication of Fluorescent Cage of Squarate based Metal-Organic Frameworks
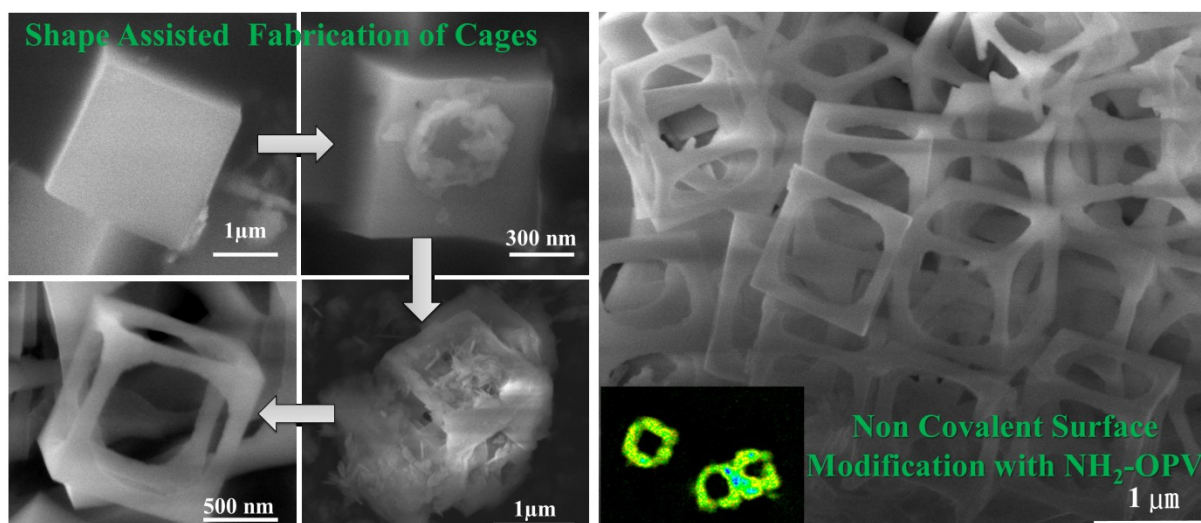
ChemComm
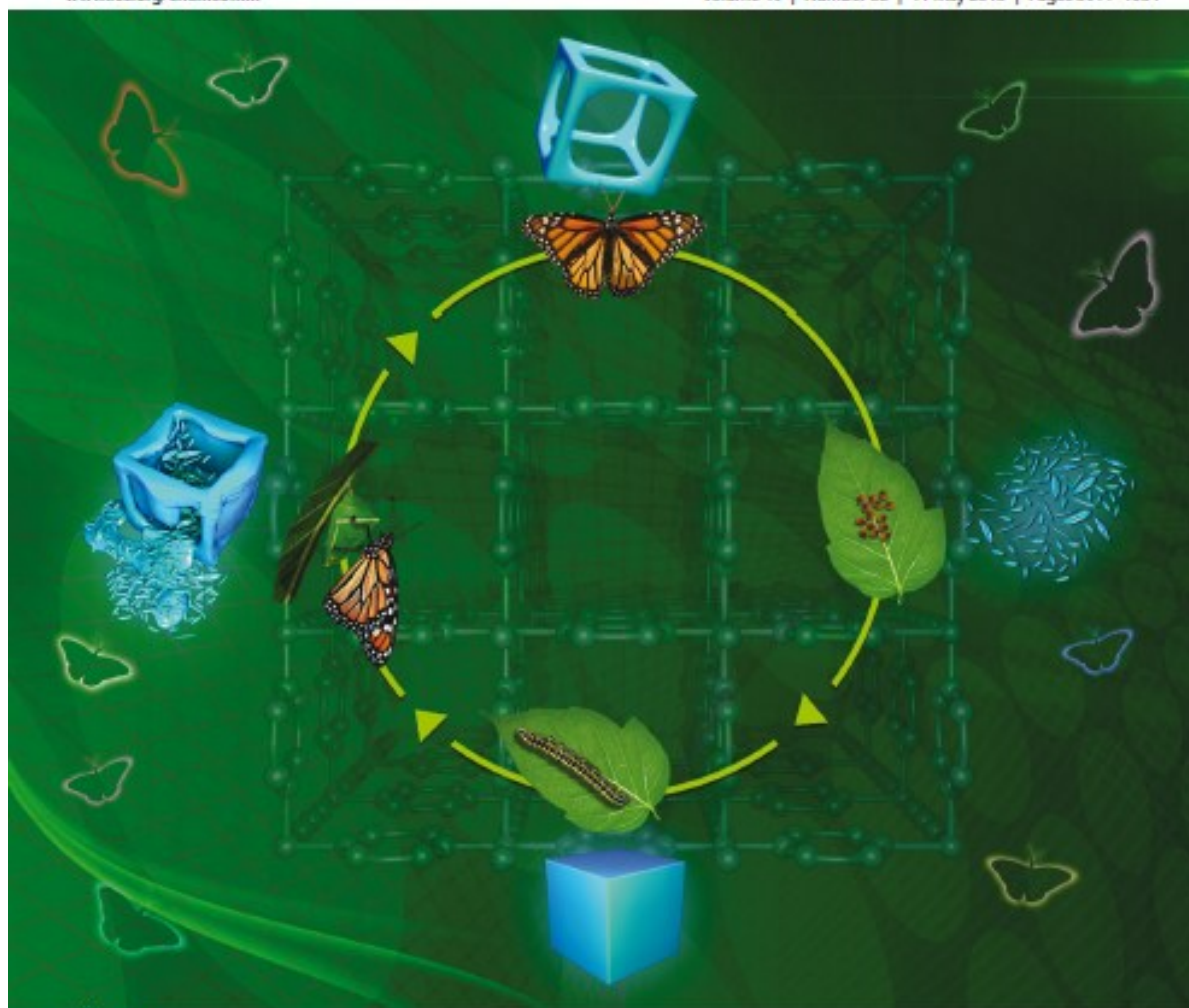
Summary

This chapter deals with cage structures of squarate based isomorphous metal-organic frameworks (MOFs) $[M(C_4O_4)(H_2O)_2]_n$ (where M = Co^{II} (1), Zn^{II} (2), and Cd^{II} (3)), which have been fabricated for the first time by specific anion selective etching of cubes. Time and stoichiometry dependent synthesis and their corresponding microscopic studies have provided a mechanistic insight into the cage formation. Furthermore, a non-covalent post-synthetic strategy has been adopted to functionalize the nano cubes or cages with chromophores rendering the resulting hybrids green fluorescent.

3.1.1 Introduction

Synthesis of inorganic nanomaterials with complex shapes and structures evoked a great deal of interest among the researchers ever since some of the underlying principles in the development of exquisite morphologies in biominerals have been unravelled.[1] In particular, nanostructures with cube, or cage-like morphologies with hollow interiors are emerging as a new class of materials in recent years, complementing their size-dependent electronic, magnetic and optical properties with the shape dependent attributes.[1b] Although, cages and nano frames of a variety of metals and metal oxides have been reported[2], the extension of these nanoscale morphologies to metal–organic frameworks (MOFs), a new class of functional organic–inorganic hybrid materials,[3] is rarely explored. Novel hybrid nano structures of MOFs would enrich their applicability in many areas as already shown in drug delivery, magnetic resonance imaging, luminescence sensing, spin-crossover and gas storage characteristics.[4]

For the synthesis of nano MOF or coordination polymer nanoparticles several approaches like coordination modulation by various reagents, microwave, ultra-sound, solvent induced precipitation and reverse micro-emulsion techniques have been developed.[5] The challenge of this field is to prepare materials with different shapes and morphologies tailored for specific purposes. Recently, there are few reports of shape assisted synthesis of uniform thin film, hollow spheres, nanocubes of nanoscale coordination polymer (NCP) or Infinite coordination polymer (ICP) for applications like catalysis or selective permeation of guest molecule or gas storage.[6]

The current investigation demonstrates a simple and straightforward method for fabricating shape assisted cage-like structures of squarate based metal-organic coordination frameworks $[M(C_4O_4)(H_2O)_2]_n$ (where M = Co^{II} (**1**), Zn^{II} (**2**), and Cd^{II} (**3**)) hitherto, known only in case of few metals and metal oxides. Detailed microscopic studies of different intermediates have provided a mechanism for the formation of cages. To the best of our knowledge, there are no accounts on the formation of cage-like morphology. In addition, we have also constructed fluorescent cages by the post-synthetic, non-covalent functionalization with green fluorescent organic chromophores.

3.1.2 Experimental Section

3.1.2.1 Materials

All the reagents and solvents employed were commercially available and used as supplied without further purification. $Co(OH)_2$, Squaric acid and polyvinylpyrrolidine (PVP) were obtained from Aldrich chemical company.

3.1.2.2 Synthetic Procedure for $[M(C_4O_4)(H_2O)_2]_n$ Cages

In a typical synthesis $M(OH)_2$ (0.75 mmol) (where M = Co, Zn and Cd) is dissolved in water (8 ml) and mixed with polyvinylpyrrolidine (0.122 g, M_w = 25,000). To this solution, squaric acid (0.5 mmol) dissolved in deionized water (5 ml) is added in a quick succession. The mixture is then transferred to a teflon container (23 ml capacity) and stirred for 30 min. The container is then put inside a steel autoclave and heated at 180°C for 96 h in a temperature-controlled oven (Additionally, the reaction time is varied to 1 h, 5h, 24 h, 48 h, and 72 h for arresting the intermediate structures during formation). After 96 h of reaction time, the solid obtained is washed thoroughly with water and ethanol and dried at room temperature for further analysis.

3.1.3 Characterization Techniques

3.1.3.1 Physical Measurements

The elemental analyses were carried out using a Perkin Elmer 2400 CHN analyzer. IR spectra of the compounds were recorded on a Bruker IFS 66v/S spectrophotometer using the KBr pellets in the region 4000–400 cm^{-1}. Thermogravimetric analyses (TGA) were carried out on METTLER TOLEDO TGA850 instrument in the temperature range of 25–650 °C under nitrogen/oxygen atmosphere (flow rate of 50 mL min^{-1}) at a heating rate of 5 °C min^{-1}. Powder X-ray diffraction (PXRD) pattern in different state of the samples were recorded on a Bruker D8 Discover instrument using Cu Kα radiation. Energy-dispersive analyses of X-rays (EDAX) were obtained by means of FEI (Nova-Nano SEM-600 Netherlands). The morphologies of the samples obtained in all the experiments were examined with field emission scanning electron microscope (FESEM, FEI Nova-Nano SEM-600, and Netherlands) and TEM (JEOL JEM-3010 with an accelerating voltage at 300 KV). Confocal Microscopy imaging was taken at room temperature using a Zeiss LSM 510META laser scanning confocal

microscope. The microscope objective of 40X (NA 0.75) and 100X (NA 1.3) were employed. To excite CSP, a 514 nm line (Argon laser) with a band pass filter of 525-670 nm was used and emission spectra were recorded using a META PMT detector array.

3.1.3.2 Adsorption Measurements

N_2 (77 K) adsorption study of the dehydrated sample of $[Co(C_4O_4)(H_2O)_2]_n$ cages was carried out using QUANTACHROME AUTOSORB-1C analyzer. The adsorption isotherms of water at 298 K were measured in the vapour state by using BELSORP-aqua-3 volumetric adsorption instrument from BEL, Japan. In the sample chamber maintained at $T \pm 0.03$ K was placed the adsorbent sample (100-150 mg), which had been prepared at 493 K under a high vacuum (10^{-1} Pa) for 18 hours prior to measurement of the isotherms. The adsorbate was charged into the sample tube and then the change of the pressure was monitored and the degree of adsorption was determined by decrease of the pressure at the equilibrium state. All operations were computer-controlled and automatic.

3.1.4 Results and Discussion

3.1.4.1 Synthesis, Structural and Morphological Characterization

In our approach, polyvinylpyrrolidone (PVP) is employed as an effective capping agent to restrict the growth of the metal squarate (M^{II}-C_4O_4) coordination polymer. The reaction of metal hydroxide, $M(OH)_2$ (where $M = Co^{II}$, Zn^{II}, and Cd^{II}) with $H_2C_4O_4$ and PVP ($M_w = 25,000$) in a hydrothermal synthesis at 180 °C for 96 h produces pink powder for Co^{II} and white powder for Zn^{II} and Cd^{II}. The powder samples have been characterized by the elemental analysis, FT-IR spectroscopy, thermogravimetric analysis (TGA) and powder X-ray diffraction (PXRD) studies. The FT-IR spectroscopy analysis of **1** clearly shows the carbonyl stretching frequency at 1523 cm^{-1} corresponding to the squarate di-anion and the peak at ~3400 cm^{-1} suggest the presence H_2O molecule (Figure 1). The TGA of the compounds (**1** and **2**) shows weight loss at around 250 °C (15% weight loss) corresponding to the removal of two water molecules (Figure 2). The dehydrated phase is stable up to 350 °C. The IR spectroscopy, TGA and elemental analyses (Table 1) unequivocally suggest the composition of the powder samples is $[M(C_4O_4)(H_2O)_2]$ [$M = Co^{II}$ (**1**), Zn^{II} (**2**), and Cd^{II} (**3**)].
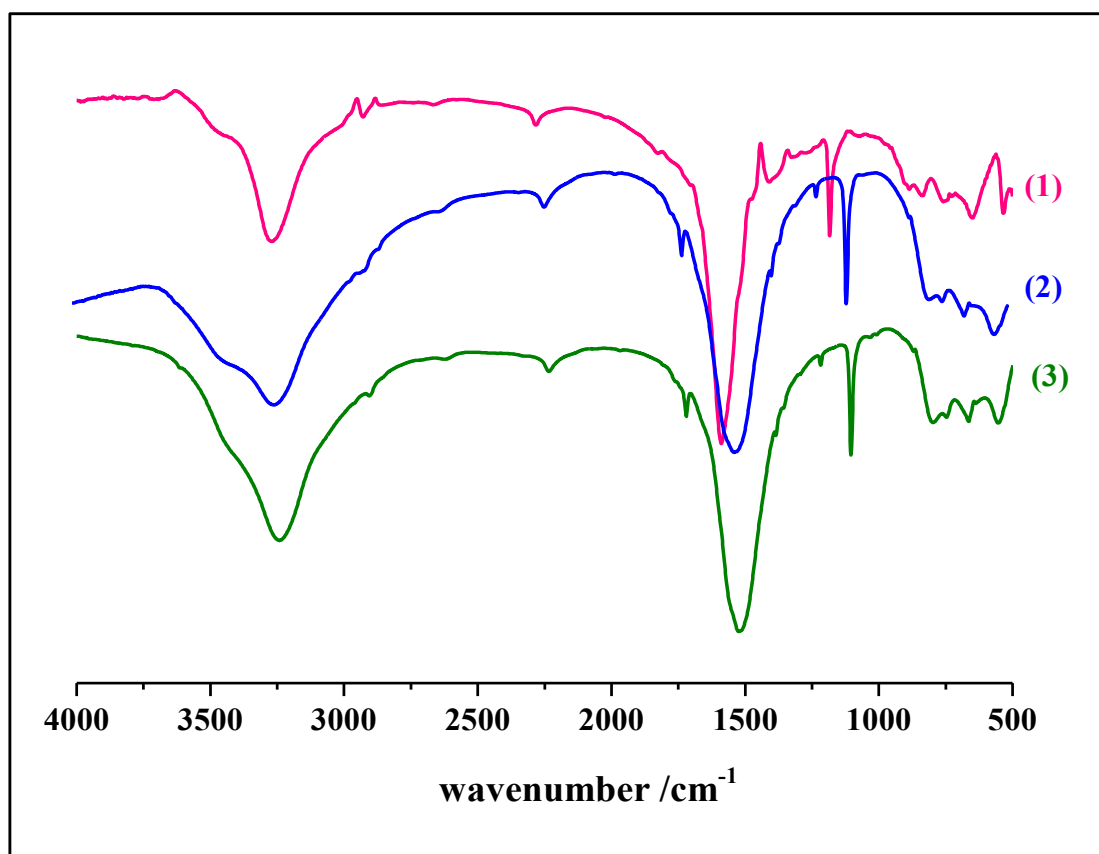
Figure 1 FT-IR spectra of [M(C$_4$O$_4$)(H$_2$O)$_2$] cages where M= Co(**1**), Zn(**2**) and Cd(**3**).
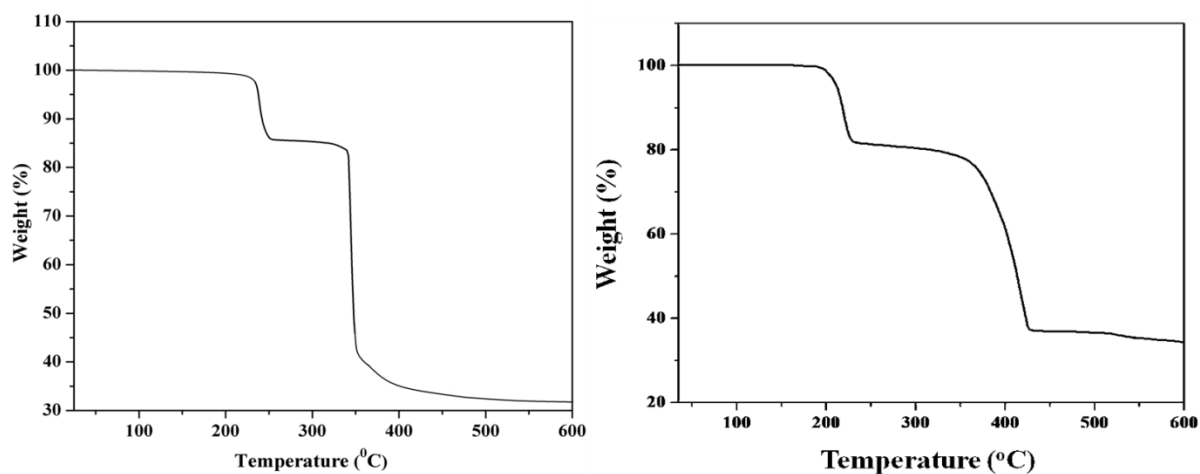
Figure 2 TGA plots for cages Co(**1**) (left); Zn(**2**) (right).

Table 1 Elemental analyses data for the cages

S.No.	Co(C$_4$O$_4$).2H$_2$O (1)		Zn(C$_4$O$_4$).2H$_2$O (2)		Cd(C$_4$O$_4$).2H$_2$O (3)	
	Carbon (%)	Hydrogen (%)	Carbon (%)	Hydrogen (%)	Carbon (%)	Hydrogen (%)
Experimental	23.17	1.89	22.36	1.91	18.54	1.62
Calucalated	23.12	1.93	22.49	1.87	18.43	1.53

The morphologies of the metal squarates prepared in presence of PVP were analysed using FESEM and TEM. Figure 3a shows FESEM image of the as formed [Co(C$_4$O$_4$)(H$_2$O)$_2$]$_n$ (**1**) exhibiting micronic cage like morphology obtained in good yield. The sizes of the cages are in the range of 1 to 4 μm having rim thickness of 300 - 500 nm. Fig. 1b shows the TEM image of a [Co(C$_4$O$_4$)(H$_2$O)$_2$] cage of ~3 μm with a rim thickness of ~500 nm. Similarly, Figures 1c and 1d show the TEM images of Zn^{II} (**2**), and Cd^{II} (**3**), respectively. Close observation shows that these cages are of single entities and not an aggregated structure of particles reported earlier for cobalt cages and further supports that these cages are derived from a single solid cube structures (Figure 3(b-d)).
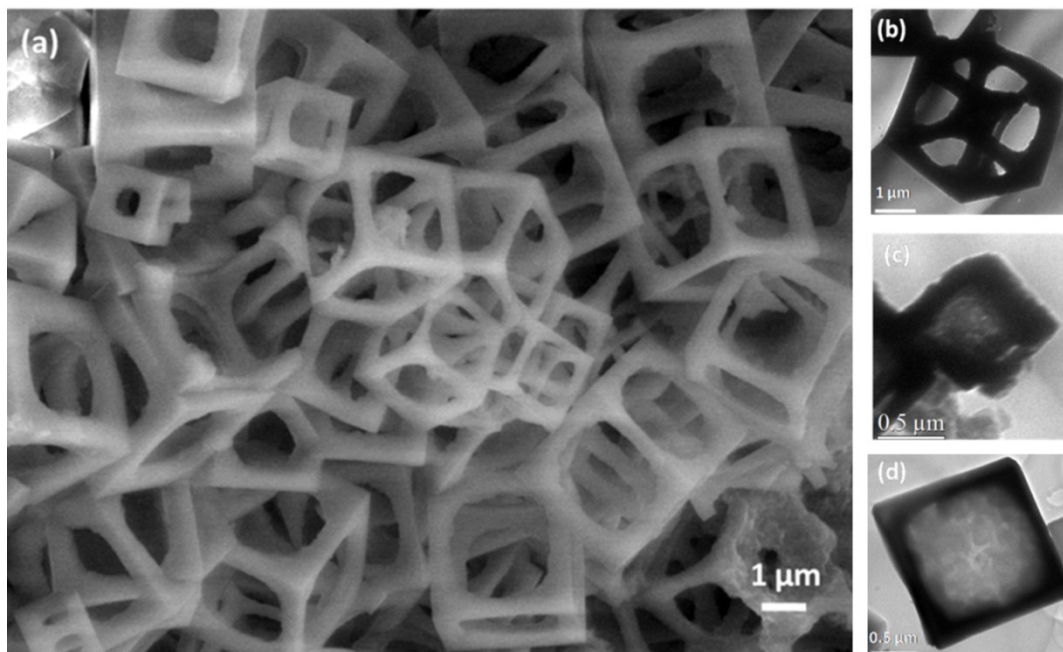
Figure 3 (a) FESEM (field emission scanning electron microscope) image showing cages of [Co(C$_4$O$_4$)(H$_2$O)$_2$]$_n$ (**1**) coordination framework; TEM (transmission electron microscope) image of cages (b) [Co(C$_4$O$_4$)(H$_2$O)$_2$]$_n$ (**1**), (c) [Zn(C$_4$O$_4$)(H$_2$O)$_2$]$_n$ (**2**), (d) [Cd(C$_4$O$_4$)(H$_2$O)$_2$]$_n$ (**3**).
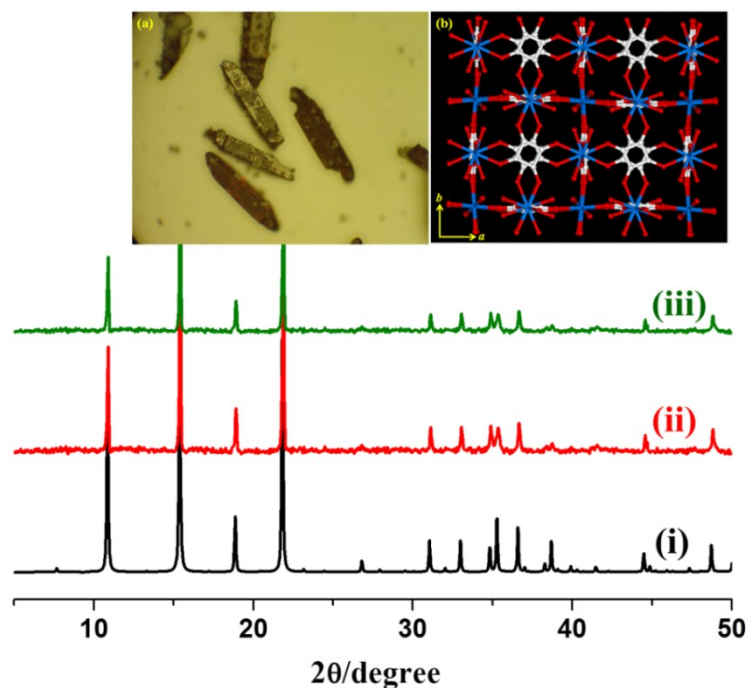
Figure 4   PXRD pattern of $[Co(C_4O_4)(H_2O)_2]$ (i) simulated pattern (ii) without PVP and (iii) with PVP. Inset shows (a) Optical image of the crystals obtained without using PVP, (b) View of the 3D MOF of $[Co(C_4O_4)(H_2O)_2]$ (**1**).
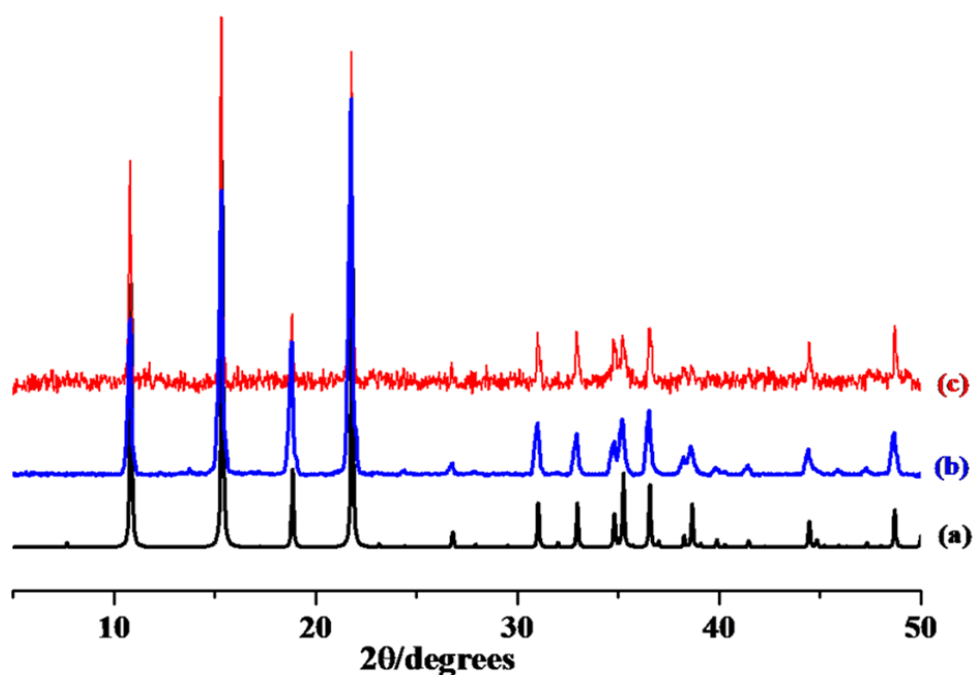
Figure 5 Powder X-ray diffraction (PXRD) patterns of the cages. (a) simulated pattern of $[Co(C_4O_4)(H_2O)_2]_n$; (b) assynthesized cage of $[Zn(C_4O_4)(H_2O)_2]_n$; (c) assynthesized cage of $[Cd(C_4O_4)(H_2O)_2]_n$.

We have done X-ray diffraction (XRD) studies to find out the molecular structure of the cages where PXRD patterns of the powder samples of **1-3** show resemblance with the simulated pattern of the reported coordination polymer $[M(C_4O_4)(H_2O)_2]_n$ where (M = Co^{II} and Zn^{II}) (Figure 4 and Figure 5).[8] Indexing of the powder data of **1** suggests a similar cell parameters as of reported single crystals. (Table 2) However, in the absence of PVP the experiment yielded millimetre-sized crystals (Inset Figure 4a)

Table 2 Indexing result from the powder data of cage $[Co(C_4O_4)(H_2O)_2]_n$ (**1**).

From TREOR programme
$a = 16.248(1)$ $b = 16.248(1)$ $c = 16.248(1)$Å, $\alpha = \beta = \gamma = 90.00°$
UNIT CELL VOLUME = 4290.12 Å^3

H	K	L	SST-OBS	SST-CALC	DELTA	2TH-OBS	2TH-CALC	D-OBS
2	0	0	.008997	.008989	.000007	10.886	10.881	8.1211
2	2	0	.017987	.017979	.000008	15.415	15.411	5.7435
2	2	2	.026998	.026968	.000030	18.914	18.904	4.6881
6	2	0	.089959	.089895	.000064	34.907	34.894	2.5683
5	4	0	.092151	.092142	.000009	35.343	35.342	2.5375
6	2	2	.098908	.098884	.000024	36.661	36.656	2.4493
7	0	0	.110030	.110121	-.000091	38.745	38.762	2.3222

NUMBER OF OBS. LINES = 7
NUMBER OF CALC. LINES = 7

The crystal structure of $[M(C_4O_4)(H_2O)_2]_n$ (M = Co^{II} and Zn^{II}) shows each $C_4O_4^{2-}$ is connected to four different Co^{II}/Zn^{II} centers to form a 3D framework (Inset Figure 4). Therefore, each Co^{II} is connected to twelve different Co^{II} centers via tetradentate $C_4O_4^{2-}$ and the octahedral geometry is fulfilled by two coordinated water molecules (Figure 6). The six sides, *i.e.* [100] plane, contain a 2D sheet of $[Co(C_4O_4)_{0.5}(H_2O)_2]$ which further linked through $C_4O_4^{2-}$ to form a 3D coordination framework.
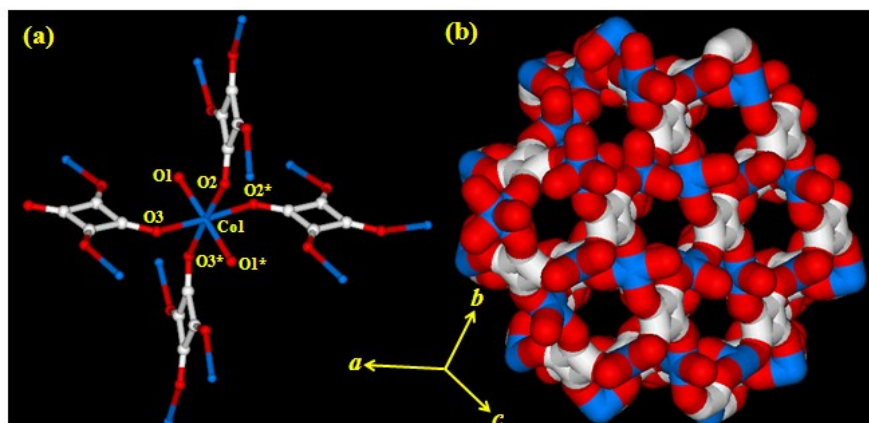
Figure 6 (a) View of the coordination environment of Co(II) and binding of the squarate dianion in $[Co(C_4O_4)(H_2O)_2]_n$ (**1**); (b) View of the hexagonal channels along [110] direction.

3.1.4.2 Mechanistic Study for Cage Formation

To get insight into the remarkable observation of cage formation of **1**, the intermediates obtained at different time intervals were analysed with FESEM.After 1 h reaction time, random flaky solid particles were obtained in the reaction medium whereas, after 24 h time cube-shaped structures of **1** were isolated (Figure 7a and 8a). Extension of the aging time to 48 h, shows the signs of holes sprouted out from the faces of the cubes (Figure 7b). On further continuation of the reaction to 72 h, flaky particles were falling out from the core of the cube through the opened-up holes on the sides (Figure 7c). When similar conditions are maintained up to 96 h, perfectly symmetric shape assisted cube to cages were obtained in good yield (Figure 7d, Figure 8a and for Cd^{II} (**2**) and Zn^{II} (**3**) as shown in Figure 9). However, the cages were broken down when the reaction time is extended to 120 h.
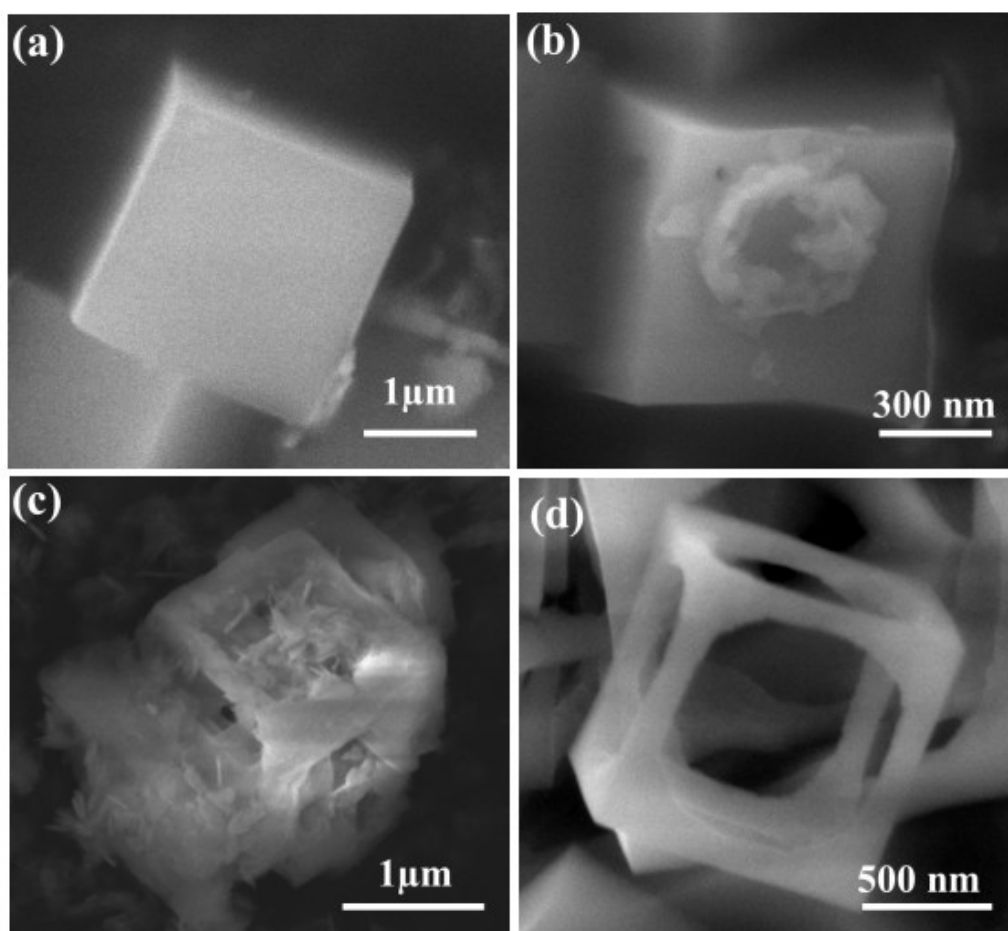
Figure 7 Formation of $[Co(C_4O_4)(H_2O)_2]$ (**1**) cage structure; FESEM images of intermediate structures obtained at various time intervals (a) cube obtained after 24 h,

(b) cube with a hole in its face formed after 48 h, (c) flaky solid coming out of the holes formed after 72 h leads to cage formation and (d) perfectly formed cage after 96 h.
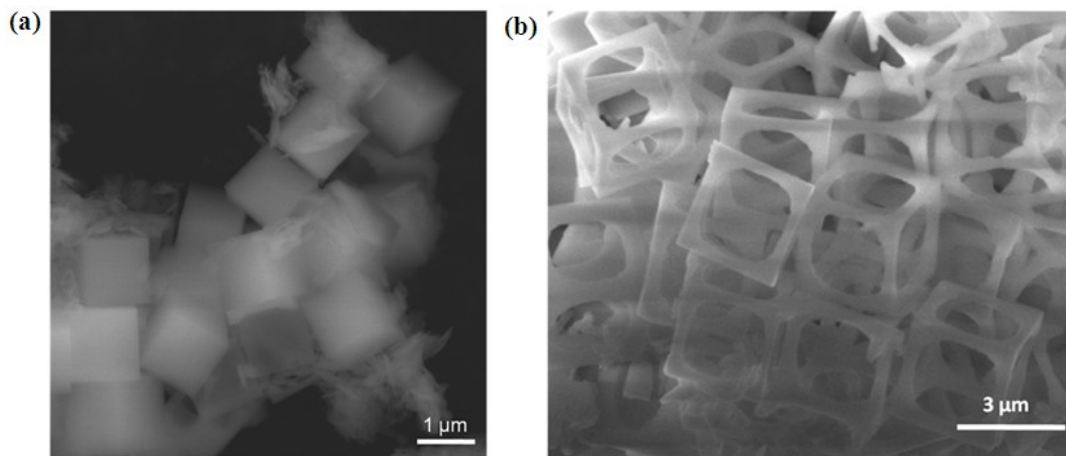
Figure 8 (a) Cubes of $[Co(C_4O_4)(H_2O)_2]$ (**1**) obtained in good yield after 24 h of reaction time. (b) Cages of $[Co(C_4O_4)(H_2O)_2]$ (**1**) obtained in good yield after 96 h of reaction time.
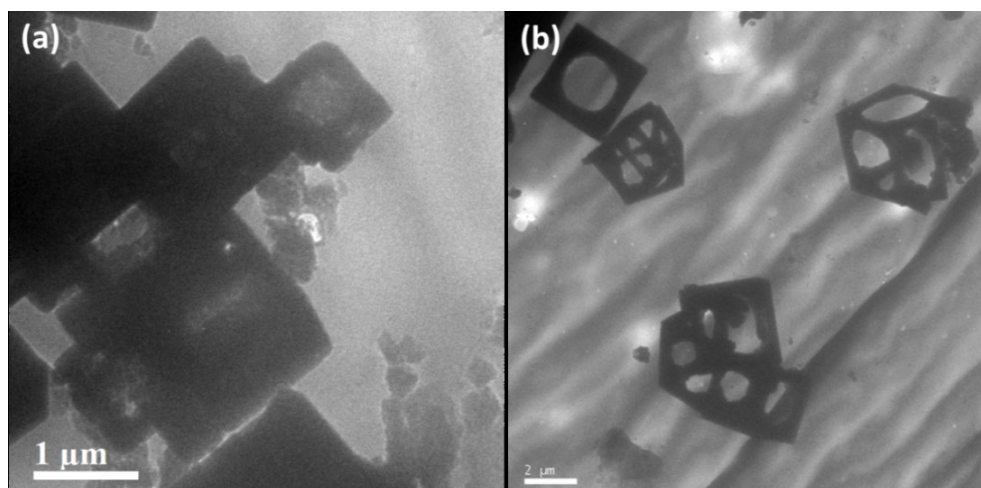
Figure 9 TEM image of (a) Zn^{II} (**2**) ; (b) Cd^{II} (**3**) showing presence cage structures throughout the sample.

The importance of the concentration of PVP as the structure directing agent is established through the synthesis of **1** with varying PVP concentrations (Table 3). Similarly, when PVP with different molecular weights (M_w = 13,00,000 & 10,000) used for synthesis, the reaction did not yield cubes suggesting the crucial role of PVP in cube formation. In addition further aspects of cage formation were investigated with varying temperatures, different anions and metal-anion to PVP ratio (Table 3 and Figure 10) and the best condition for the perfect cage formation is 180 °C for 96 h reaction time with PVP (Mw = 25,000) under hydrothermal condition.

Table 3. Details of the different experiments performed

Change of Morphology with PVP

Template	PVP (M. Wt. 25000)	PVP (M. Wt. One lakh)	PVA (M. Wt. 5000)
Morphology	Cubes/cages	Flaky particles	Flaky particles

Conditions: [Temperature =180 °C, Time = 72 h, PVP =(polyvinylpyrrolidine, PVA= poly vinyl alcohol), $Co(OH)_2$ = (0.069g, 0.75mmol,) and squaric acid = (0.5 mmol, 0.057g)]

Temperature

Temperature	Room Temp	100 °C	120 °C	180 °C	200 °C
Morphology	Flakes	Flakes	Rods	Cube/cage	flakes

Conditions: Time = 72 h, PVP = (1.09 mmol, 0.122 g, M. Wt. 25000), $Co(OH)_2$ = (0.75 mmol 0.069 g) and squaric acid = (0.5 mmol, 0.057 g)

Metal Anions

Anion (X)	Hydroxyl	Chloride	Acetate	Nitrate	perchlorate
Morphology	Cubes/cages	No cube/cages	No cube/cages	No cube/cages	No cube/cages

Conditions: Time = 72 h, PVP = (1.09 mmol, 0.122 g), Temperature = 180 °C and squaric acid (0.5 mmol, 0.057g)

Metal precursor to PVP ratio:

$M(OH)_2$ (X) PVP (Y)	5 h	24 h	48 h	72 h	96 h	120 h
X: Y/5	Cubes/ partly cages	Dandelion-like / cubes	Flaky particles	Flaky particles	Flaky particles	Broken cages
X: Y	flakes	cubes	Partially etched cubes	Cubes/ cages	Cages	Broken cages
X: 2Y	Cubes/faceted cages	Cubes/faceted cages	Broken cages	Broken cages	Broken cages	Broken cages

Conditions:

X= $M(OH)_2$ [$Co(OH)_2$ (0.75 mmol 0.069 g]Y = PVP [1.09 mmol, 0.122 g], (monomeric unit's molecular weight has been considered as 1 mol) All experiment at temperature = 180 °C; and squaric acid (0.5 mmol, 0.057g)

71
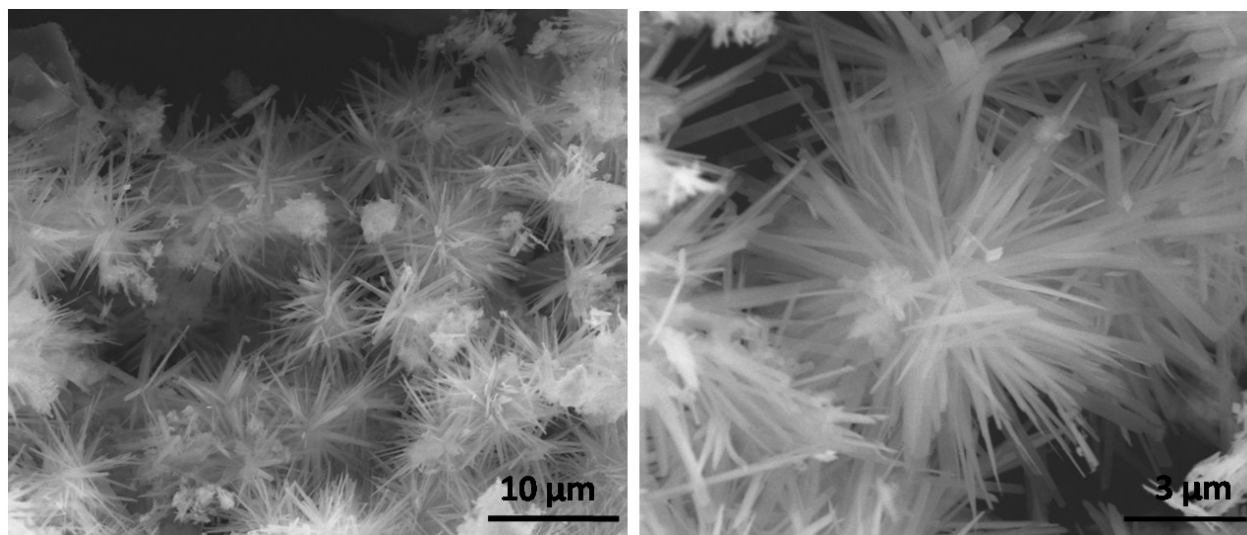
Figure 10 Dandelion-like nanostructures obtained after 24 h reaction time while using lower amount of PVP.

It is important to note that the hydroxide precursors play a vital role in the formation of cage-like morphology of the metal squarates. If the metal precursors used were nitrates, chlorides, or acetates, no cage formation was observed (Table 3).However, KOH addition along with metal chloride precursors, favors the cage formation. These experiments unambiguously suggest that OH^- ions present in the reaction medium play a crucial role in etching the faces of the growing cubes leading to the formation of cages. The OH^- ions selectively etch the growing [100] faces of the cubes, leaving its edges unaffected. The local concentration OH^- is higher in the central part of each faces of the cube compared to edges resulting in a higher etching rate in the central part thereby forming hollow cages. A time-based extraction and analysis of the intermediate structures provides proof to such mechanism (Figure 7). Recently similar mechanism has been proposed by Yamauchi *et al.* for synthesis of Prussian blue nanoparticles with a hollow interior. [9] Anion based etching method in which anion acting as a coordinating liagnd to obtain Co and Pd cages has been reported.[2b2d] Here PVP acts as a structure directing agent for the syntheis of micronic cubes of the metal squarates.

3.1.4.3 Adsorption Study

To study the permanent porosity of **1**, we have performed N_2 adsorption for the desolvated **1** at 77 K showing typical type-II isotherm suggesting only surface adsorption due to the smaller pore size compared to the kinetic diameter of N_2 (Figure 11). Interestingly water (at 298 K) shows a hysteretic sorption profile with steep uptake

at low pressure region corroborating strong interaction of the adsorbate with the pore surface decorated with unsaturated Co^{II} sites (Figure 12)
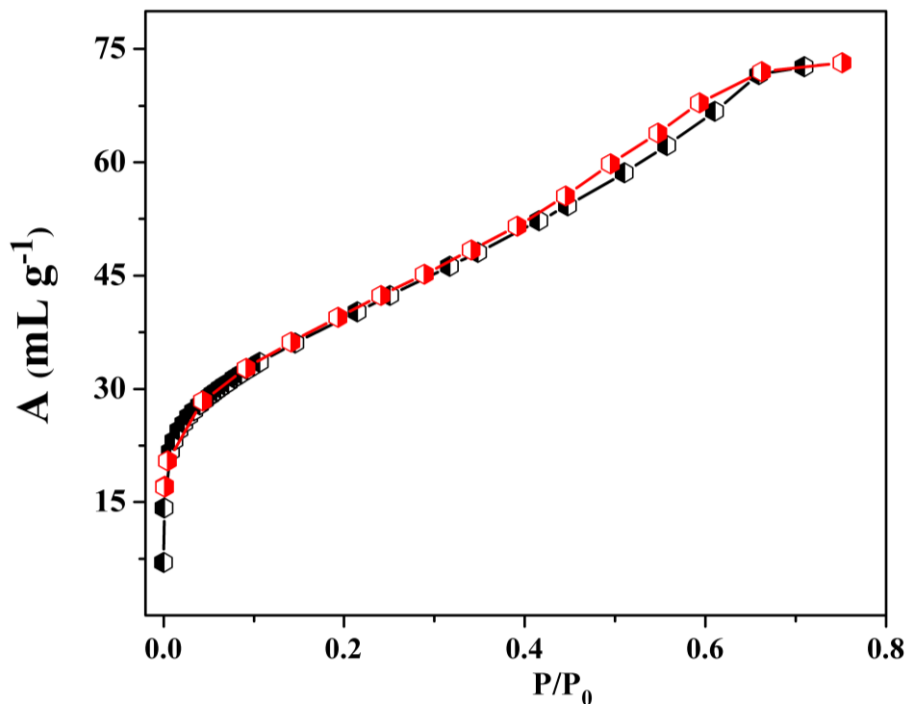
Figure 11 Nitrogen adsorption isotherm for the dehydrated cage structure of $[Co(C_4O_4)(H_2O)_2]_n$ at 77 K.
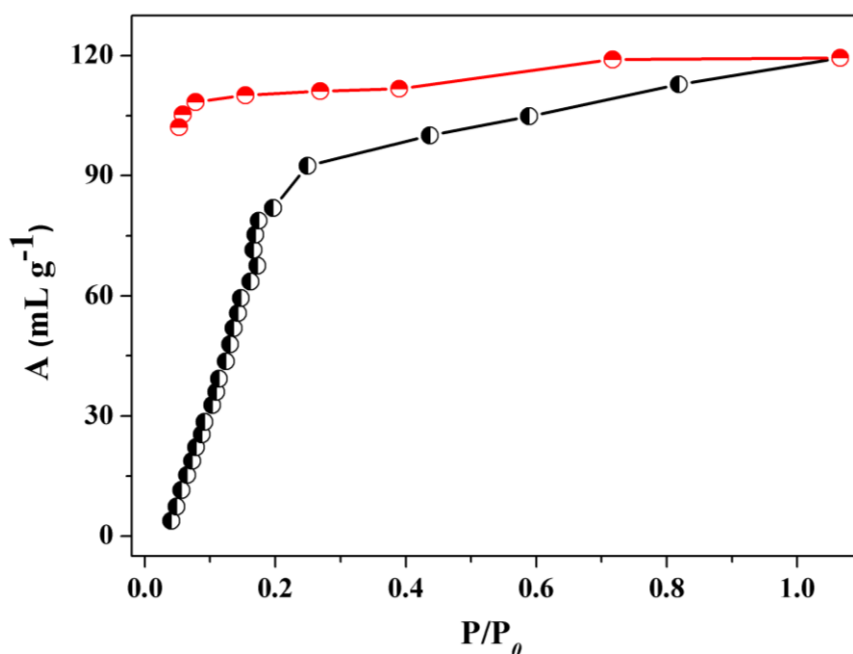
Figure 12 Water sorption isotherms of dehydrated cage $[Co(C_4O_4)(H_2O)_2]$ (**1**) H_2O at 298 K **$(P_o$ is the saturated vapor pressure of the adsorbates at the corresponding temperature, blue curve for adsorption and red curve for desorption).

3.1.4.4 Photoluminescent Study: Post-Synthetic Modification of Cubes/Cages

The cages are blue fluorescent; they have been further characterized by confocal laser scanning microscopy (CLSM) (Figure 13 a-b). The blue emission from the cages of **2** showed a maximum at 429 nm, which could be due to the squarate based ligand emission (Figure 13c). The ligand emission in the coordination framework is enhanced, when compared to the corresponding squarate emission in the solid-state, which could be either due to the spatial positioning of the ligands or due to the metal-to-ligand-charge transfer (MLCT) in the coordination framework (Figure 14). In our strategy, we envisage a non-covalent approach by exploiting H-bonding groups on the coordinated water and squarate ligands on the surface of the framework with an aptly functionalized fluorophore.
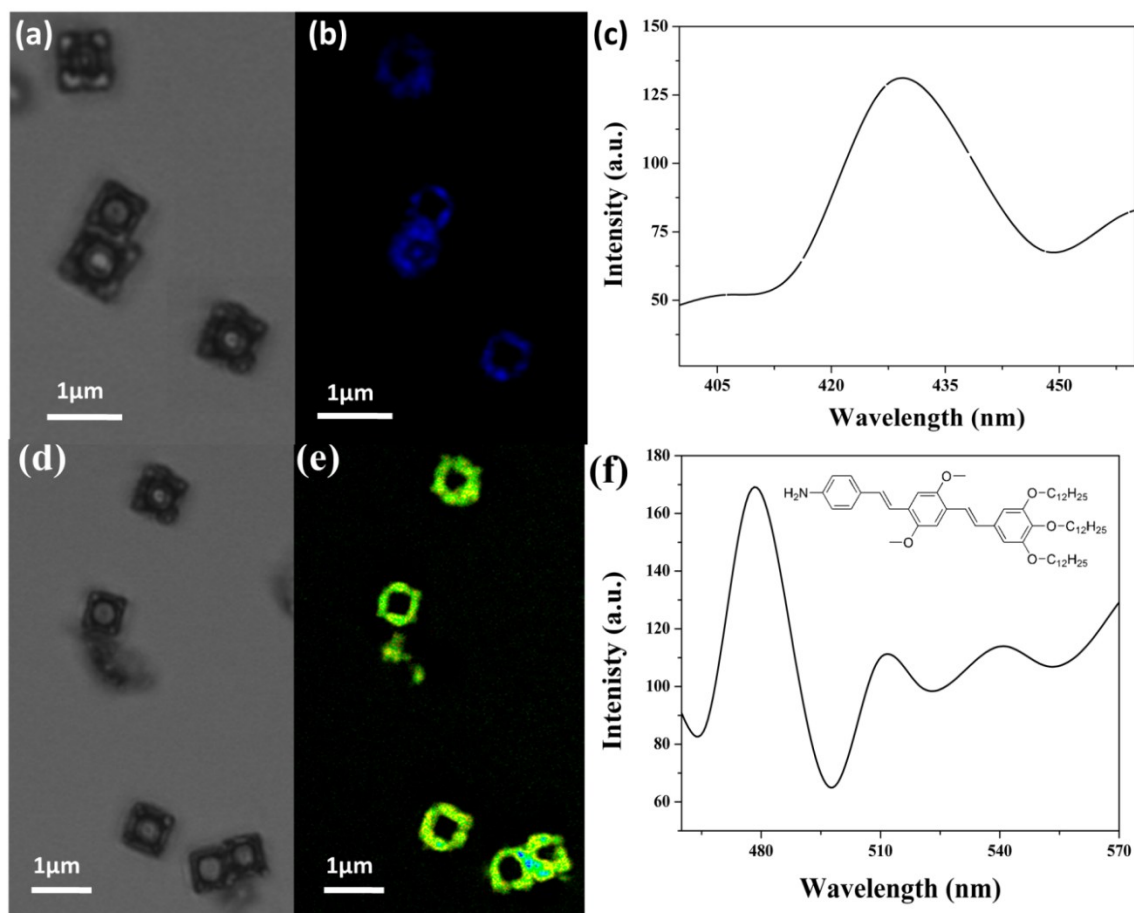
Figure 13 Confocal laser scanning microscopic images of pristine and surface modified (with OPV-NH$_2$) [Zn(C$_4$O$_4$)(H$_2$O)$_2$] cages; (a) and (d) without excitation; (b) and (d) with excitation at 321 nm and 421 nm: Corresponding emission spectrum showing (c) squarate based blue and (e) surface modified green emission.
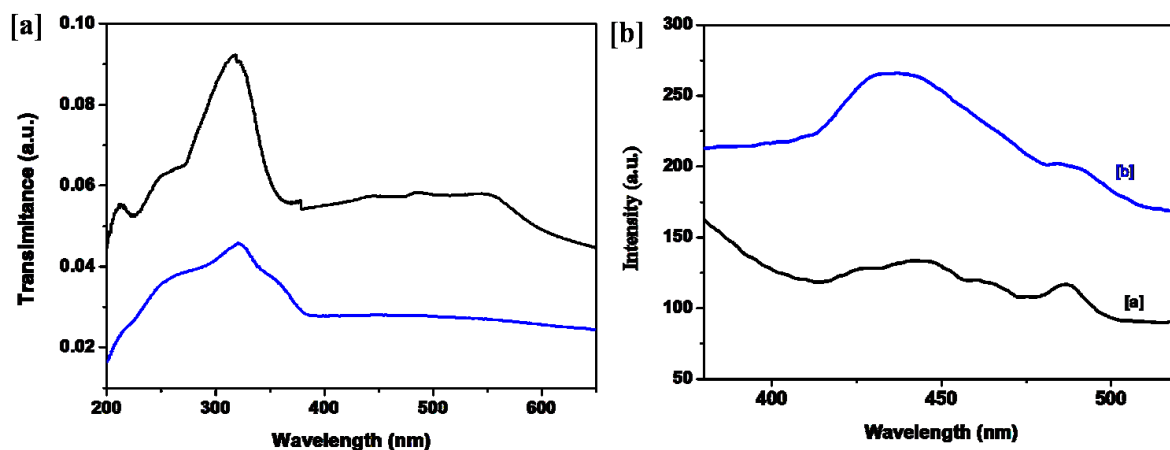
Figure 14 [a] UV-vis spectra and [b] emission spectra of squaric acid and $[Zn(C_4O_4)(H_2O)_2]_n$ (**2**) cages. [black line for squaric acid and blue line for $[Zn(C_4O_4)(H_2O)_2]_n$ cages)

An oligo(phenylenevinylene) derivative functionalized with amine groups and other end three dodecyl groups (OPV-NH$_2$) exhibiting a strong green emission was chosen as the functional organic molecule for the surface functionalization of the nano cubes and cages of Zn^{II} (**2**) (Figure 13d-f & Figure 15) .
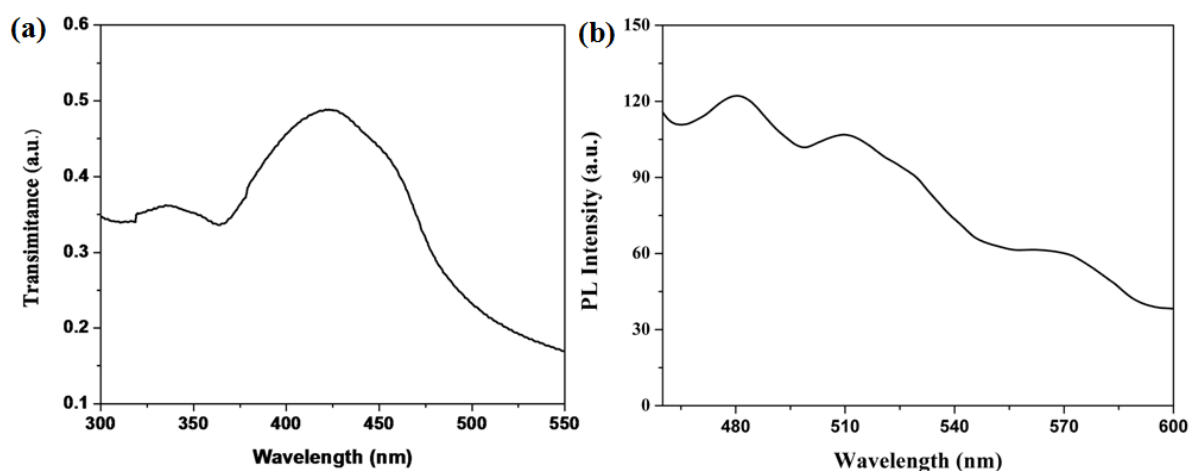
Figure 15 (a) UV-vis and (b) emission spectra of OPV-NH$_2$ in solid state.

In a typical procedure, the micronic cubes or cages were immersed in an ethanol of OPV-NH$_2$ with the care of non-surface adsorption. The CLSM images of the surface-modified cubes and cages (Figure 13 and 16) showed green emission only at the cage surfaces, suggesting the successful decoration of the cages. The fluorescence spectrum of the cubes or cages obtained from CLSM corresponds to that of the molecularly dissolved spectrum of OPV-NH$_2$ (λ_{max} = 479 nm) in ethanol, which clearly indicates that the green fluorescence under the microscope is indeed due to the cage-surface

decorated with OPV-NH$_2$.We envisage that the OPV-NH$_2$ molecules are non-covalently attached to the cubes or cages by means of O---H-N H-bonding interactions between -NH$_2$ group of OPV and H$_2$O and C$_4$O$_4$$^{2-}$ linker of the cube or cages. However, the emission spectrum of the cages also showed shoulders with maxima at 512 and 541 nm, suggesting that there is a small amount of aggregation on the surface due to π-π interactions
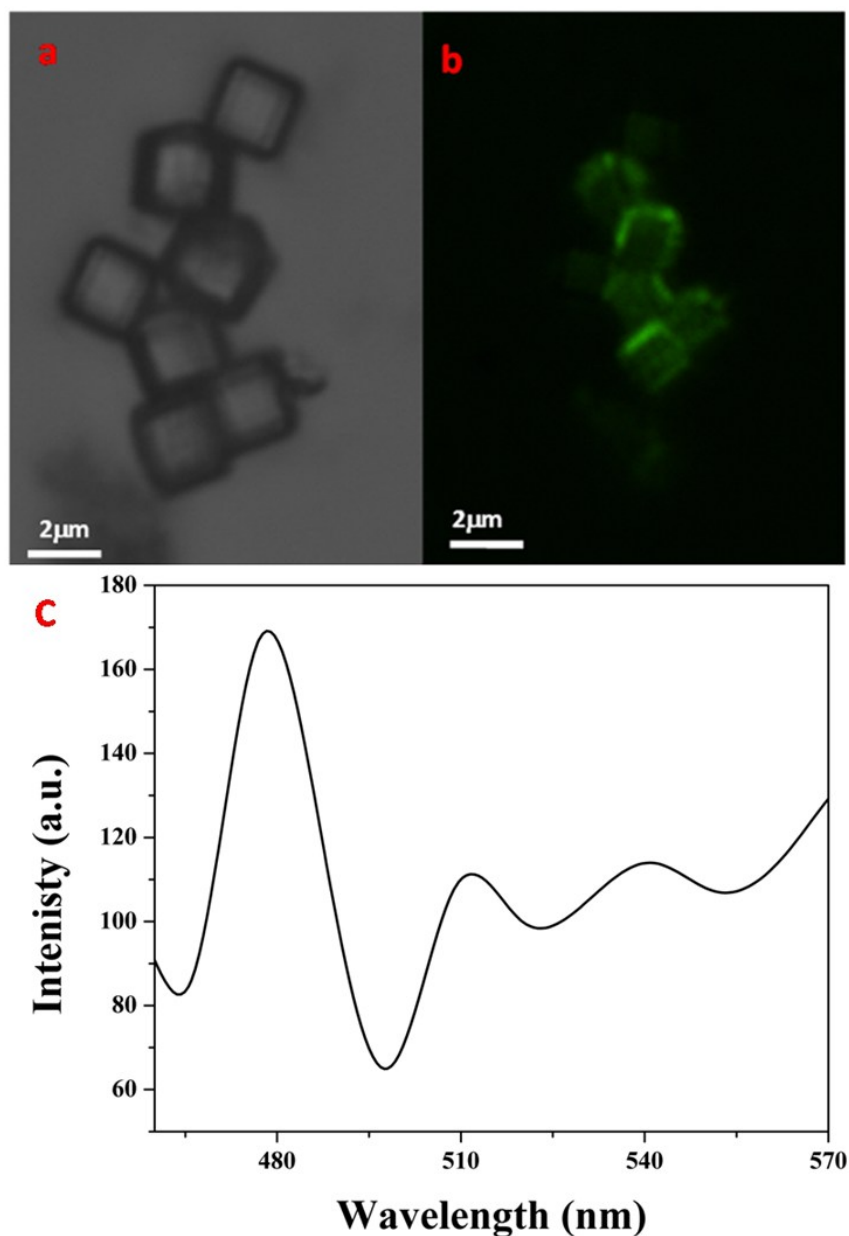
Figure 16 Confocal laser scanning microscopic images (CLSM) of [Zn(C$_4$O$_4$)(H$_2$O)$_2$] cubes after functionalization with OPV-NH$_2$. cubes (a) without excitation (b) with excitation at 421 nm showing green fluorescent cubes and (c) corresponding emission spectra of the cubes obtained under the confocal microscope.

3.1.5 Conclusions

In summary, we demonstrated a very unique and elegant method to synthesize cage structures of metal-squarate coordination framework using PVP and it acts capping as well as structure directing agent, where shape assisted micronic cubes transform to cages by selective OH⁻ anion driven etching process. The morphology evolution and the mechanism of formation were studied in detail by elucidating the intermediate structures formed during the synthesis. The blue luminescent cubes or cages are further surface functionalized by OPV-NH$_2$ luminophore based on noncovalent interactions. This work would open up the way for fabricating very complex morphologies by the simple anion dissolution method of MOF for the different advanced applications.

3.1.6 References

1) a) S. Mann, G. A. Ozin, *Nature* **1996**, *382*, 313; b) S. E. Skrabalak, J. Chen, Y. Sun, X. Lu, L. Au, X. Cobley, Y. Xia, *Acc. Chem. Res*. **2008**, *1*, 1587.

2) a) G. D. Moon, S. Ko, Y. Min, J. Zeng, Y. Xia, U. Jeong, *Nano Today* **2011**, *6*, 186; b) X. Wang, X. Fu, A. Peng, T. Zhai, Y. Ma, F. Yuan , Z. Yao*, Adv. Mater.* **2009**, *21*, 1636; c) C. J. Jia, L. D. Sun, Z. G. Yan, L. P. You, F. Luo, X. D. Han, Y. C. Pang, Z. Zhang , C.H Yan, *Angew. Chem. Int. Ed.* **2005**, *44*, 4328.

3) a) S. Kitagawa, R. Kitaura, S. I. Noro, *Angew. Chem. Int. Ed*. **2004**, *43*, 2334; b) P. Kanoo, R. Haldar, S. T. Cyriac , T. K. Maji, *Chem. Commun.* **2011,** *47***,** 11038; c) Y. Cui, Y. Yue, G. Qian , B. Chen, *Chem. Rev.* **2011**, *112*, 1126; d) M. K. Sharma, P. K. Bharadwaj, *Inorg. Chem.* **2011,** *50*, 1889; e) K. Jayaramulu, P. Kanoo, S. J. George , T. K. Maji, *Chem. Commun.* **2010**, *46*, 7906; f) J. Liu, P. K. Thallapally, B. P. McGrail, D. R. Brown , J. Liu, *Chem. Soc. Rev*. **2012**, *41*, 2308.

4) a) A. C. McKinlay, R. E. Morris, P. Horcajada, G. Férey, R. Gref, P. Couvreur , C. Serre, *Angew. Chem. Int. Ed.* **2010**, *49*, 6260; b) I. Boldog, A. B. Gaspar, V. Martínez, P. Pardo-Ibñnez, V. Ksenofontov, A. Bhattacharjee, P. Gütlich. J. A. Real, *Angew. Chem. Int. Ed*. **2008**, *47*, 6433 c) J. Della Rocca, D. Liu , W. Lin, *Acc. Chem. Res.* **2011**, *44*, 957.

5) a) W. Lin, W. J. Rieter , K. M. L. Taylor, *Angew. Chem. Int. Ed.* **2009**, *48*, 650; b) M. Spokoyny, D. Kim, A. Sumrein , C. A. Mirkin, *Chem. Soc. Rev.*

2009, *38*, 1218; c) A. Carné, C. Carbonell, I. Imaz, D. Maspoch, *Chem. Soc. Rev.* **2011**, *40*, 291.

6) a) R. Ameloot, F. Vermoortele, W. Vanhove, M. B. J. Roeffaers, B. F. Sels , D. E. De Vos, *Nat. Chem.* **2011**, *3*, 382; b) S. Aguado, J. Canivet , D. Farrusseng, *Chem. Commun.* **2010***, 46*, 7999; c) S. Jung , M. Oh, *Angew.Chem. Int. Ed.* 2008**, 47**, 2049; d) N. Stock , S. Biswas *Chem. Rev.* **2011**, *112*, 933; e) M. Pang, A. J. Cairns, Y. Liu, Y. Belmabkhout, H. C. Zeng , M. Eddaoudi, *J. Am. Chem. Soc.* **2012**, *134*, 13176; f) Y. Pan, D. Heryadi, F. Zhou, L. Zhao, G. Lestari, H. Su, Z. Lai *CrystEngComm* **2011**, *13*, 6937.

7) a) Z. Wang , S.M. Cohen, *Chem. Soc. Rev.* **2009**, *38*, 1315; b) S. J. George, S. J.; T. F. A. de Greef, R. Bovee, J. L. Van Dongen, A. P. H. Schenning , E.W. Meijer, *Chem. Asian. J.* **2009**, *4*, 910.

8) S. Neeraj, M. L. Noy, C. N. R. Rao , A.K. Cheetham, *Solid State Sci.* **2002**, *4*, 1231.

9) a) Q. Zhang, T. Zhang, J. Ge , Y. Yin, *Nano Lett.,* **2008,** *8,* 2867; b) M. Hu, S. Furukawa, R. Ohtani, H. Sukegawa, Y. Nemoto, J. Reboul, S. Kitagawa , Y. Yamauchi, *Angew. Chem. Int. Ed.* **2012**, *51*, 984; c) H. C. Zeng *Curr. Nanosci.* **2007,** 3, 177**.**

Chapter 3.2

Facile Synthesis of Multifunctional Porous-Magnetic-Luminescent Nanotape Metal-Organic Framework: Highly Selective Sensing for Adenosine Triphosphate (ATP)
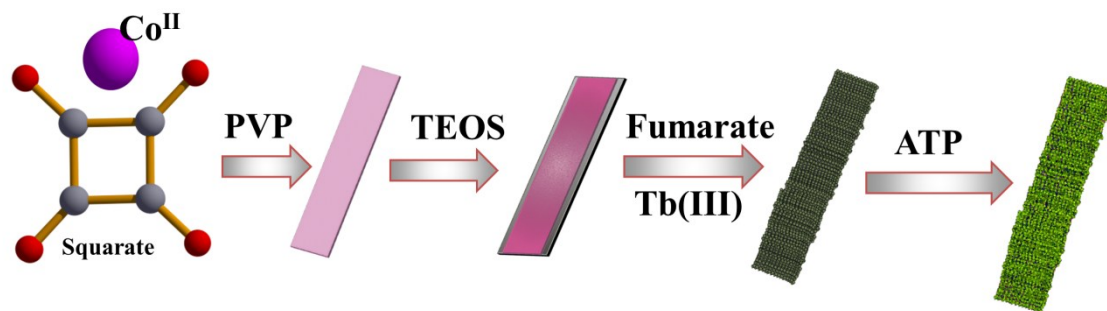
Summary

This chapter deals with a novel synthetic strategy for synthesizing multifunctional porous-magneto-luminescent nanocomposite based on a MOF $\{[Co_2(\mu\text{-}OH)_2(C_4O_4)].3H_2O\}_n(1)$ or **NMOF 1** ($C_4O_4^{2-}$ = squarate dianion). The structural organization, porosity, magnetism of the **NMOF 1** was thoroughly characterized by various techniques. **NMOF 1** shows permanent porosity as realized by type-I CO_2 uptake profile and it also exhibits canted antiferromagnetism with T_c= 11K. FESEM and TEM analysis revealed **NMOF 1** has tape-like morphology with $\sim$ 25 nm thicknesses. **NMOF 1** has been coated with silica for further functionalization to enhance in solution processibility. Silica coated $\{$**NMOF1@SiO$_2$**$\}$ has been further covalently attached with fumaric acid and then connected with Tb(III) ions resulting porous-magneto-luminescent nanocomposite **{NMOF1@SiO$_2$@fum@Tb}**. Multi-functional nanocomposite was exploited for sensing of biological important nucleotides. Among, adenosine monophosphate (AMP), adenosine diphosphate (ADP) and adenosine triphosphate (ATP), the luminescence significantly enhanced with ATP in pure water at pH $\sim$7. This selective sensing of ATP has been realized even up to 10^{-5} molar concentration.

3.2.1. Introduction

Metal-organic frameworks (MOFs) are a crystalline inorganic-organic hybrid materials which showed potential applications is several fields including catalysis,[1] gas storage/separation,[2] sensors[3] and optoelectronics.[4] To date such applications of MOFs have been mainly centered on the bulk crystalline powder and tried to correlate their physical and chemical properties with respect to the crystal structure. Recently a paramount effort has been directed for preparing nanoscale MOFs (NMOFs) keeping the same periodic structure as of the bulk state with aiming advanced applications in material and biological sciences.[5] Several elegant approaches such as sol-gel process, reverse micelles, hydro/solvo thermal, precipitation, coordination modulation and microwave assisted methods have been demonstrated.[6] In the nanoscale, surface area to volume (S/V) ratio increases, therefore NMOFs reveal a higher surface area with enhanced sorption kinetics and show high solution processibility. Based on these characteristics several important functionalities such as bio-sensing, biolabeling, drug delivery, multimodal imaging, gas separation and catalysis would be realized which are yet be properly accounted.[6] Lin *et al.* prepared several NMOFs with potential application in MRI contrast agent and as drug delivery vehicles.[6e] Horcajada *et al.* reported nanoscale bioactive Fe(III) based MOF for imaging and in vitro drug delivery applications.[7] Kitagawa *et al.* showed higher uptake of CO_2 gases in NMOFs with high sorption kinetics.[8]

The successful applications of NMOFs are critically depend upon the stability and biocompatibility.[9a] Coating of NMOFs with silica would enable enhanced biocompatibility, high solution dispersibility and the ability to further functionalize with condensation of organic molecules (siloxy derivative) to fabricate multifunctional composite through post synthetic modification.[9] Among the various biomolecules, Adenosinetriphosphate (ATP) is one of most important biologically active molecules that stores and transports chemical energy within the cells for metabolism. ATP is involved DNA replication, transcription and other essential activities like as substrate in signal transduction pathways by kinases that phosphorylate proteins and lipids.[10] The ATP concentration in inside the cell is typically 1-10 mM and varieties of calorimetric and fluorescent probes based on organic chromophores or transition metal based complexes for detection and quantification of ATP have been developed.[11] Lanthanide based luminescent probe yet to be explored properly. Sharp line likes emission bands,

large Stokes shift and long life time are advantageous for biological studies as they typically remove the background fluorescence of other organic substances.[11e] Therefore real time detection and monitoring trace amount of ATP level is essential for the study of multiple cellular mechanisms, enzyme activity and other activities involving the production of and consumption of ATP.[10-11] This chapter reports the design and synthesis of multifunctional nanocomposite based on a porous magnetic MOF nanotape $\{[Co_2(\mu\text{-}OH)_2(C_4O_4)].3H_2O\}_n$ (**NMOF1**) ($C_4O_4^{2-}$ = squarate dianion) and the luminescent lanthanide probe using silica coating and further condensing with fumaric acid to **NMOF 1**. The green luminescent probe {**NMOF1@SiO$_2$@fum@Tb**} after immobilizing with Tb(III) was exploited for highly sensitive and selective probe for ATP, and can discriminate from ADP and AMP in pure water at pH ~7.

3.2.2 Experimental Section

3.2.2.1 Materials

All the reagents and solvents employed were commercially available and used as supplied without further purification. $Co(OH)_2$, Squaric acid and polyvinylpyrrolidine (PVP) were obtained from Aldrich chemical company.

3.2.2.2 Synthetic procedure for $\{[Co_2(\mu\text{-}OH)_2(C_4O_4)].3H_2O\}_n$ (1)

In a typical synthesis $Co(OH)_2$ (0.75 mmol) is dissolved in water (8 ml) and mixed with polyvinylpyrrolidine (0.122 g, M_w = 25,000). To this solution, squaric acid (0.5 mmol) dissolved in deionized water (5 ml) is added in a quick succession. The mixture is then transferred to a teflon container (23 ml capacity) and stirred for 30 min. The container is then put inside a steel autoclave and heated at 120°C for 48 h in a temperature-controlled oven. After 48 h of reaction time, the solid obtained is washed thoroughly with water and ethanol for several times and dried at room temperature for further analysis. (Yield 70 %). Anal. Calcd. for $C_4H_8Co_2O_9$: C, 15.25; H, 2.36; Found: C, 15.93; H, 2.41 %. IR (KBr cm^{-1}); v(CO), 1523; v(μ-OH), 950.

3.2.3 Characterization Techniques

3.2.3.1 Physical Measurements

The morphologies of the **NMOF 1** obtained in all the experiments were examined with field emission scanning electron microscope (FESEM, FEI Nova-Nano SEM-600, The

Netherlands) and Transmission electron microscopy (TEM) (JEOL JEM-3010 with an accelerating voltage at 300 KV). Powder X-ray diffraction (XRD) patterns were measured by using BRUKER Discover D8 diffractometer employing Cu-K$_\alpha$ radiation. Thermogravimetric analysis (TGA) was performed using Mettler Toledo TGA 850 instrument. The IR spectra were recorded using Fourier-transform infrared instrument (FT-IR, Bruker, IFS 66 V/s) in the range of 400 - 4000 cm^{-1}.Confocal Microscopy imaging was taken at room temperature using a Zeiss LSM 510META laser scanning confocal microscope. The microscope objective of 40X (NA 0.75) and 100X (NA 1.3) were employed. Magnetic measurements were carried out with a vibrating sample magnetometer in Physical Properties Measurement Systems (PPMS, Quantum Design, and USA)

3.2.3.2 Adsorption measurements

N$_2$ adsorption (77 K) and CO$_2$ (195 K) study of dehydrated **NMOF 1** sample was carried out using QUANTACHROME AUTOSORB-1C analyzer. In the sample chamber maintained at $T \pm 0.03$ K was placed the adsorbent sample (100-150 mg), which had been prepared at 413 K under a high vacuum (10^{-1} Pa) for 18 hours prior to measurement of the isotherms. The adsorbate was charged into the sample tube and then the change of the pressure was monitored and the degree of adsorption was determined by decrease of the pressure at the equilibrium state. All operations were computer-controlled and automatic.

3.2.4 Results and Discussion

3.2.4.1 Synthesis, Structural and Morphological Characterization

The hybrid nanocomposite was fabricated in four stages as shown in Scheme 1; (a) first synthesis of a nanotape metal organic framework $\{[Co_2(\mu-OH)_2(C_4O_4)].3H_2O\}_n$ (**NMOF1**) using a homo-polymer polyvinylpyrrolidine (PVP) (b) coating of the **NMOF1** with silica to fabricate **NMOF1@SiO_2**, and finally (c) immobilizing the organic linker fumaric acid on the silica surface to obtain {**NMOF1@SiO_2@fum**} (d) covalently attach Tb(III) ions with carboxylate of fumarate and surface –OH groups of silica resulting in a multifunctional porous, magnetic and luminescent hybrid nanocompsite, {**NMOF1@SiO_2@fum@Tb(III)**}.
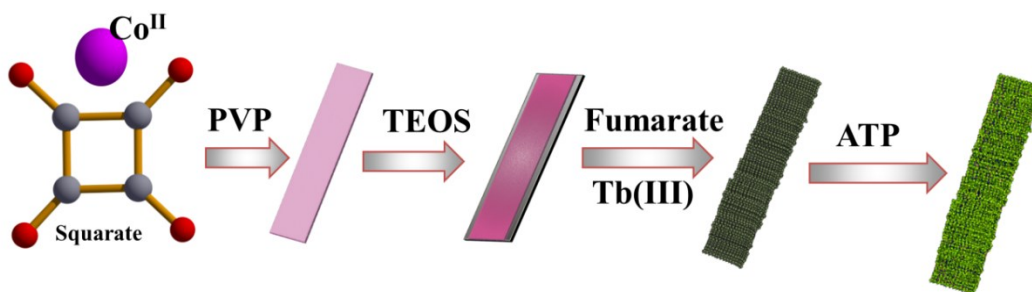
Scheme 1 Scheme illustrating the preparation of multifunctional porous-magneto and luminescent hybrid nanocomposite (i) **NMOF**; (ii) {**NMOF@SiO_2**}; (iii) {**NMOF1@ SiO_2@fum@Tb(III)**} (e) **NMOF@SiO_2@fum@Tb(III)@ATP**.

The MOF **1** has been synthesized under hydrothermal conditions using polyvinylpyrrolidine (PVP). However, PVP acts as both capping as well as structure directing agent to control the size and morphology of 1. The powder sample of **1** has been characterized by elemental analysis, FT-IR spectroscopy and powder XRD (PXRD) studies (Figure 1). The IR spectrum shows a strong band at 1523 cm^{-1} attributing C=O stretching frequency of squarate dianion ($C_4O_4^{2-}$) and the shifting to lower frequency indicating all the –C=O groups are involved in bonding with Co(II) centers. The broad peak at 3450 cm^{-1} indicates the presence of water molecules. The peaks at 950 cm^{-1} indicate the presence of μ-OH group (Figure 1). TGA shows a weight loss in the region 120-150 °C and the desolvated framework is stable up to 350 °C. The elemental analysis, IR spectroscopy and TGA suggest that the probable formula of the compound is $\{[Co_2(\mu-OH)_2(C_2O_4)]\cdot 3H_2O)\}$ (**1).**
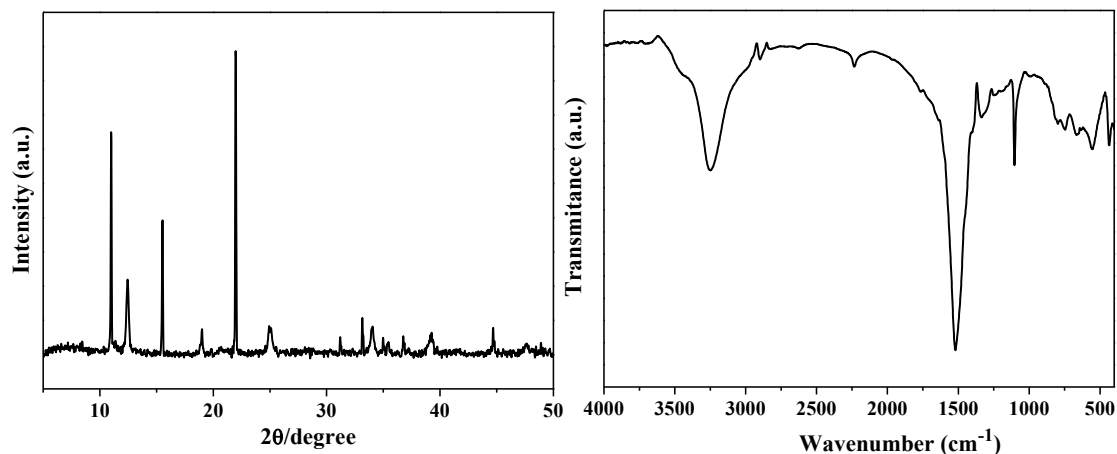
Figure 1 (Left) Powder XRD pattern (Right) FT-IR spectrum of **1**.

PXRD pattern shows high crystalline nature as realized by intense Bragg's reflections. The PXRD pattern indexed by DICVOL-91 program[12] suggests that the compound crystallizes in monoclinic system with the following cell parameters (Table 1).

Table 1 Indexing result from the powder data of desolvated **(NMOF 1)**
From DICVOL-91[12]

a=17.81 (1) b=5.71 (4) c=8.81 (7) $\alpha = \gamma = 90.00°$, $\beta = 114.36(7)°$
UNIT CELL VOLUME =   747.03 Å^3

H	K	L	DOBS	DCAL	DOBS-DCAL	QOBS	QCAL	2TH.OBS	2TH.CAL	DIF.2TH.
1	0	-1	8.03928	8.07164	-.03236	.01547	.01535	10.997	10.952	.044
2	0	-1	7.10000	7.09850	.00150	.01984	.01985	12.457	12.460	-.003
0	1	0	5.70010	5.70193	-.00183	.03078	.03076	15.533	15.528	.005
2	1	0	4.66743	4.66395	.00348	.04590	.04597	18.999	19.013	-.014
2	0	-2	4.03755	4.03582	.00173	.06134	.06140	21.997	22.007	-.010
2	1	1	3.56908	3.57466	-.00559	.07850	.07826	24.928	24.888	.040
4	0	-2	3.54740	3.54925	-.00185	.07947	.07938	25.083	25.070	.013
1	1	2	2.86385	2.86036	.00349	.12193	.12222	31.206	31.245	-.039
6	0	0	2.69999	2.70244	-.00246	.13718	.13693	33.153	33.122	.031
6	1	-1	2.62953	2.62920	.00032	.14463	.14466	34.068	34.073	-.004
1	2	1	2.56281	2.56320	-.00039	.15225	.15221	34.984	34.978	.005
7	0	-1	2.53009	2.52832	.00177	.15622	.15644	35.451	35.476	-.026
6	1	0	2.44324	2.44205	.00119	.16752	.16768	36.755	36.774	-.019
3	2	-2	2.29825	2.29647	.00178	.18932	.18962	39.166	39.197	-.032
8	0	0	2.02658	2.02683	-.00025	.24348	.24342	44.680	44.674	.006

NUMBER OF OBSERVED LINES =15

NUMBER OFCALCULATED LINES =15

Further, we have performed energy dispersive X-ray spectroscopy (EDS) and elemental analysis measurements which suggests presence of Cobalt (Co), carbon and oxygen elements in the **NMOF 1** (Figure 2). We did not observe any nitrogen impurity corresponding to PVP, because PVP has been completely removed by the several washing with 1:1 water: ethanol mixture.
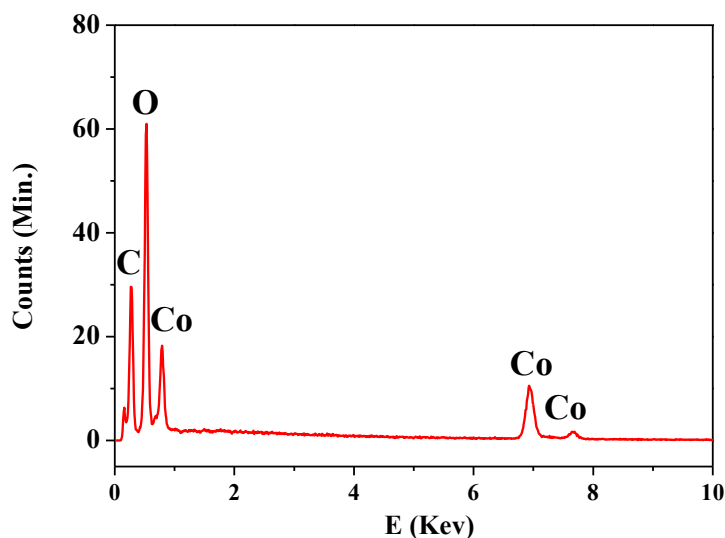
Figure 2 EDX analysis for $\{[Co_2(\mu-OH)_2(C_2O_4)].3H_2O)\}$ **(1)**

The compound **1** has also been characterized by the several microscopic techniques to understand the size and morphology. Field emission scanning electron microscope (FESEM) images shown in Figure 3 reveals bundles of transparent nanoparticles homogeneously distributed throughout the sample. High resolution FESEM images show that tape-like morphology with length of few microns and diameter in the range of 50-60 mm.
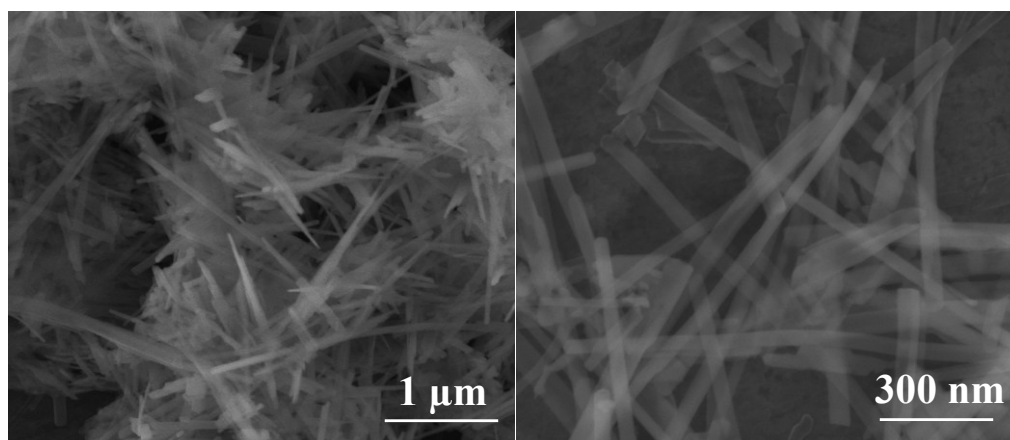
Figure 3 FESEM image of $\{[Co_2(\mu-OH)_2(C_2O_4)].3H_2O)\}$ **(1)** showing nanotape-like morphology.

TEM image also shows similar tape-like morphology (Figure 4) and electron diffraction (ED) reveals single-crystalline nature of the particles (Inset Figure 4). Atomic force microscopy (AFM) study further supports the tape like morphology of **NMOF 1** particles with rectangular cross- section and average thickness of 25 nm.
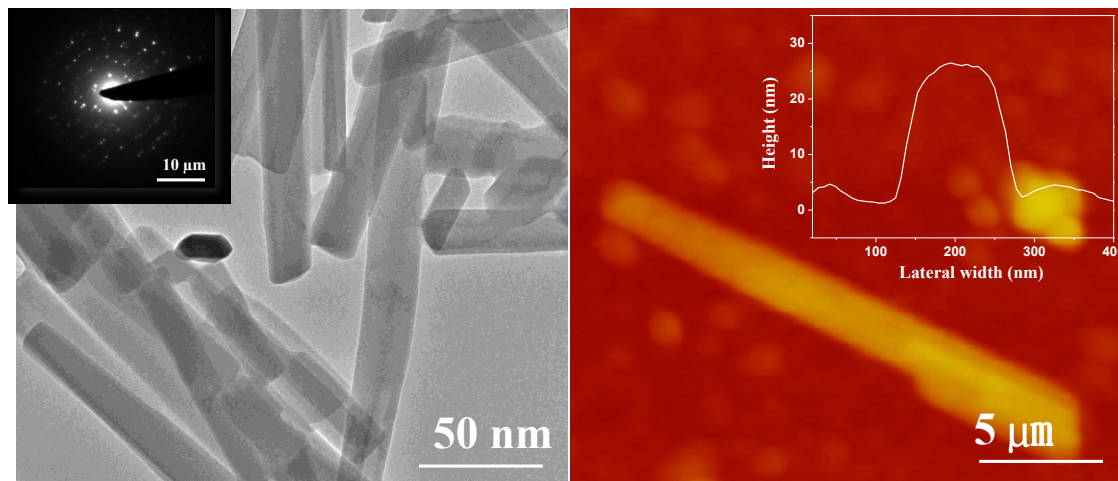
Figure 4 (Left) TEM image of **1**, inset shows ED pattern, (Right) AFM image of **1** showing nanotape morphology with thickness of each tape of about 25 nm.

3.2.4.2 Adsorption Study of NMOF1

In order to study the permanent porosity of **NMOF 1**, we have measured N_2 at 77 K after activating the sample at around 413 K for 12 hour. **NMOF 1** shows typical type-II profile for N_2 (kinetic diameter, 3.6 Å) (Figure 5a) indicating only surface adsorption. However CO_2 adsorption at 195 K exhibits typical type-I profile with steep uptake at low pressure region suggesting microporous nature (Figure 5b) of the **NMOF 1**. The final uptake volume is 53 ml/g corresponding to 1 molecule per formula of the compound. This corresponds to BET surface area of about ~162 m^2/g, and pore volume of 0.098 cm^3/g. The sorption profile also revealed small hysteresis which can be attributed to the polar pore surface of the compound consisting of (μ–OH) group and squarate dianion.
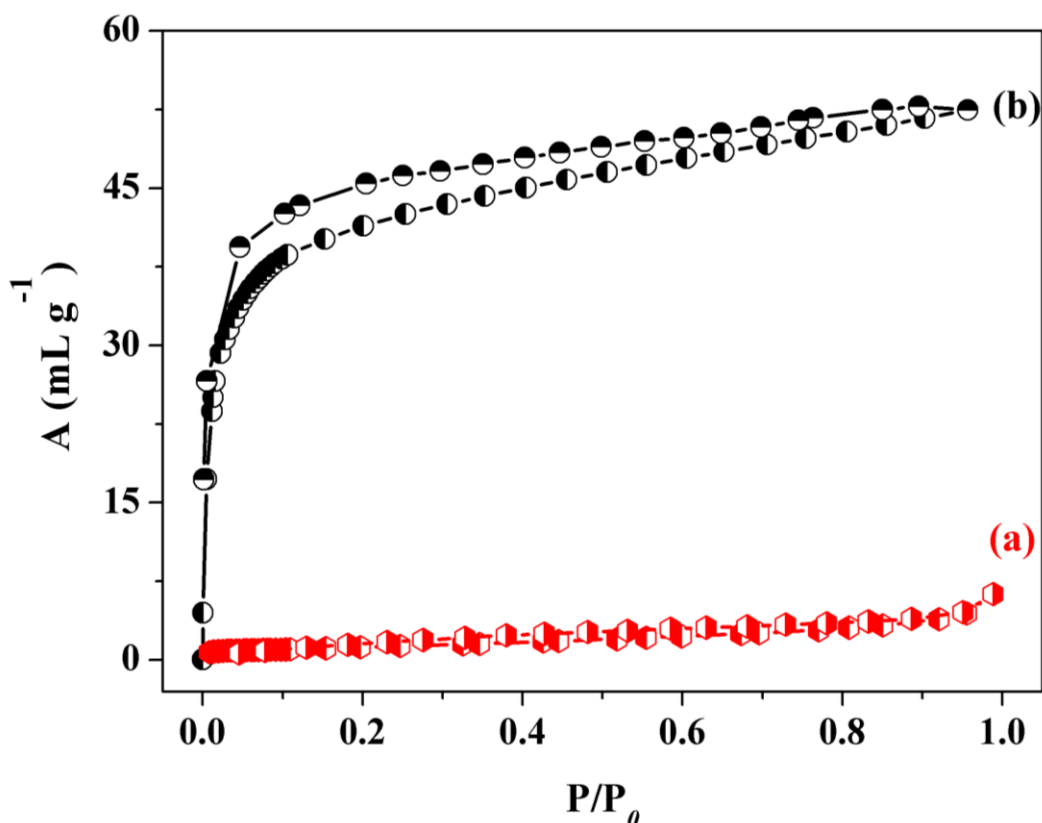
Figure 5 (a) N_2 sorption at 77 K; **(b)** CO_2 sorption at 195 K for **NMOF 1**.

3.2.4.3 Magnetic Property of NMOF1

Figure 6a shows the $\chi_M T$ *vs. T* plot of **NMOF 1** measured at 500 Oe. At 300 K, the $\chi_M T$ value is 5.09 cm^3 mol^{-1}K, typical for two high spin Co(II) ions, with orbital contribution of the Co(II) centres. The temperature dependence of the reciprocal susceptibility above 106 K (Figure 7a inset) follows the Curie–Weiss law with a Weiss constant θ of −55.6 K, which can be a result of spin-orbit coupling effect of Co(II) ions in octahedral field or due to antiferromagnetic coupling between Co(II) ions. The product $\chi_M T$ first decreases up to 33 K and then increases rapidly and finally decreases on further cooling (Figure 6b). The spontaneous increase in $\chi_M T$ at low temperature indicates a possibility of long range ordering. The field-cooled (FC) and zero field-cooled (ZFC) magnetization measured at 500 Oe show a bifurcation at 11 K, suggesting a phase transition at that temperature and indicating a magnetized state exists below this temperature (Figure 6b).
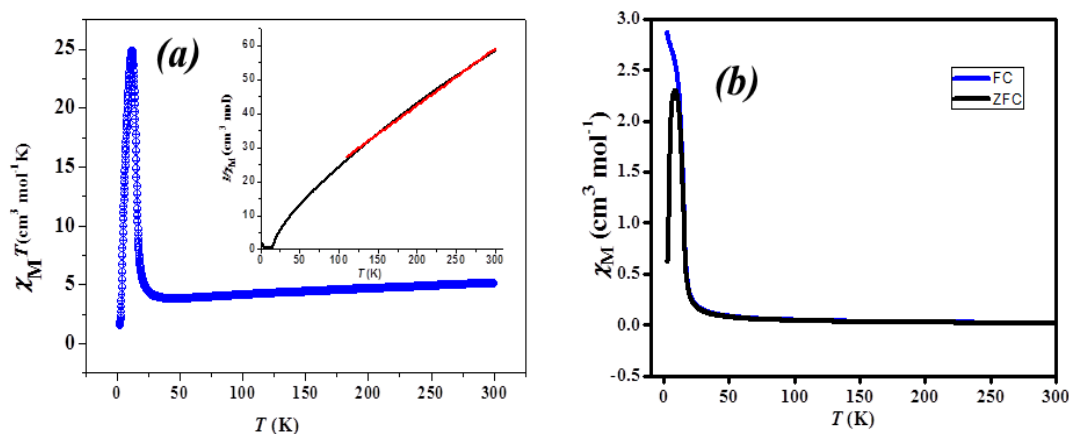
Figure 6 (a) The plots of $\chi_M T$ *vs.* *T* for **1**. The inset shows Curie–Weiss fitting above 105 K. The red line indicates the best fit obtained. Weiss constant θ is −55.6 K. (b) The temperature dependence of the magnetic susceptibility at 500 Oe under field-cooled (FC) and zero-field-cooled (ZFC) conditions.
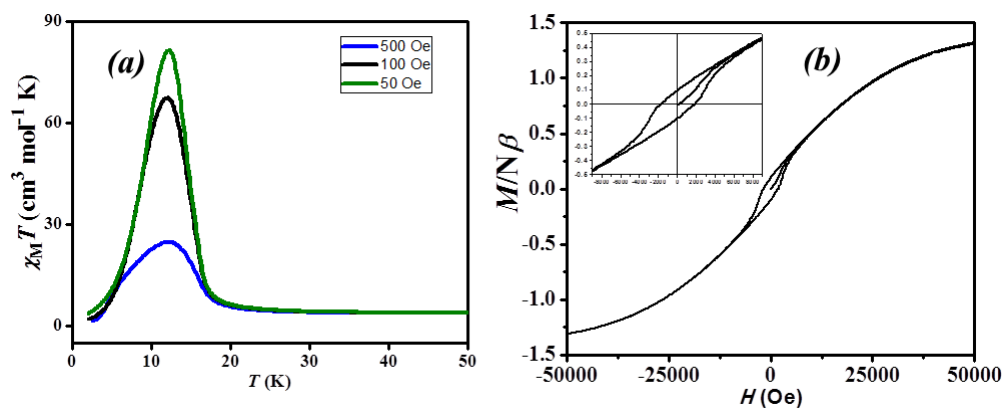
Figure 7 (a) Temperature dependence of the magnetic susceptibility of **1** at 50, 100, and 500 Oe (b) Isothermal magnetization of **1** measured by cycling the field between 50 and -50 KOe at 2 K (inset shows the hysteresis loop)

A plot of FC susceptibility *vs.* *T* at different dc field strengths shows a field-dependent behaviour below 16 K (Figure 7a) and the spontaneous increase of $\chi_M T$ product is more pronounced at lower field strength, suggesting spin-canting in this system. The plot of the reduced magnetization(*M*) *vs.* *H* at 2 K (Figure 7b) is clearly indicative of a hysteresis loop corresponding to a very soft ferromagnet (small coercive field) with a remnant magnetization (M_r) of 0.097 Nβ and a coercive field (H_c) of 1770 Oe. The magnetization value at 5 T is 1.33 Nβ for below saturation magnetization for a two Co(II) centres, further suggesting canting antiferromagnetism exists in the system. Assuming the saturation magnetization value of 6 Nβ (expected value for two spin only Co(II) ion), the estimated canting angle for **1** [$\sin^{-1}(0.097/6)$] is 0.92°.

3.2.4.4 Coating and Functionalization of NMOF 1 with SiO₂ and Fumarate

The **NMOF 1** was subsequently coated with silica shells by Stobber's process using tetraethyl orthosilicate (TEOS) in ammonical solution of propyl alcohol.[9d] The resulting core-shell {**NMOF1@SiO₂**} has been characterized by IR spectroscopy, PXRD and TEM. Furthermore, FT-IR shows an additional band at 1046 cm^{-1} corresponds to γ(Si-O) of silica. The presence of bands at 3400-3450 cm^{-1} suggests that surface has free OH groups upon silica coating {**NMOF@SiO₂**} particles (Figure 8). In addition, PXRD of {**NMOF@SiO₂**} shows all the peaks related to **NMOF1** with reduced intensity compared to pristine MOF, suggests retention of structural integrity after silica coating (Figure 9).
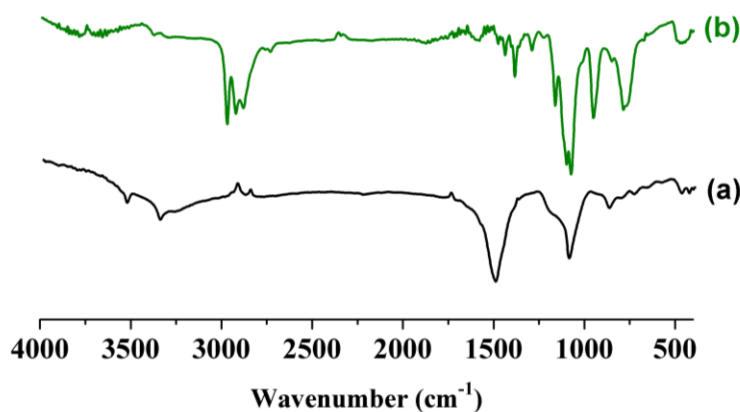
Figure 8 FT-IR spectra (a) {**NMOF@SiO₂**} (b) {**NMOF1@SiO₂@fum**}
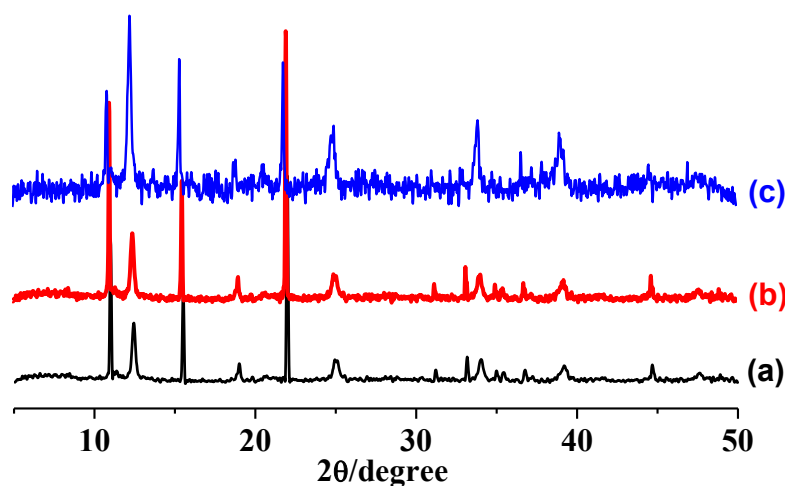
Figure 9 Powder XRD patterns of (a) **NMOF 1** (b) **NMOF 1a** (c) {**NMOF1@SiO₂**}.
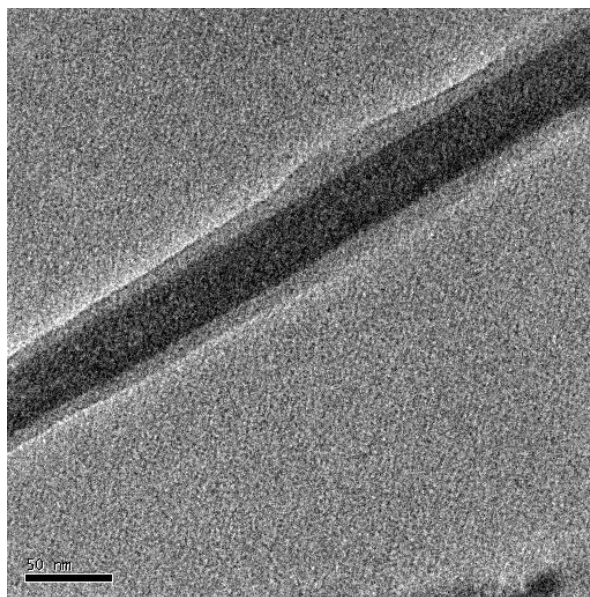
Figure 10 TEM image of **{NMOF@SiO₂}** showing nanotape **coated** with silica shell thickness ~ 5nm.

TEM image shows NMOF is uniformly coated with silica shell of thickness of 5 nm (Figure 10). It is worth mentioning that the thickness of silica coating could be controlled by the amount of silica and pH of the medium and prolonging the reaction time.[6a] The silica coated NMOF, hybridized with organic linker and luminescent Tb(III) ions. We have employed fumaric acid (**fum**) as a linker where one side can covalently link with the silica surface and other end carboxylic group would remain free for coordinating with Tb(III) ions. The presence of C=O stretching band at 1736 cm^{-1} for fumaric acid modified composite **{NMOF@SiO₂}** indicates condensation via ester formation. The IR band near 1438 cm^{-1} indicates the presence of C-O-H in plane bending vibration of carboxylic acid (Figure 8b). Free Tb(III) ions show very weak characteristic emission band in aqueous solution but reveal intense green emission when connected with carboxylate organic linker like fumarate, BTC etc as revealed by several Tb-based coordination polymer.[11] Tb(III) shows enhanced emission band at 489 nm, 544.5 nm and 584.5 nm corresponding to $^5D_4$ to ^7F_J (J= 6,5, 4), transitions (Figure 11 left). This is due to efficient binding with the hard donor oxygen atoms of fumarate linker which provides efficient energy transfer. Finally, the luminescent Tb(III) ions were immobilized on the surface of **{NMOF1@SiO₂@fum}** through the coordination with carboxylate groups of the fumarate, results a **{NMOF@SiO₂@fum@Tb}**.The

nanocomposite enhanced emission bands compared to free Tb(III) due to the antenna effect after binding with fumaric acid.
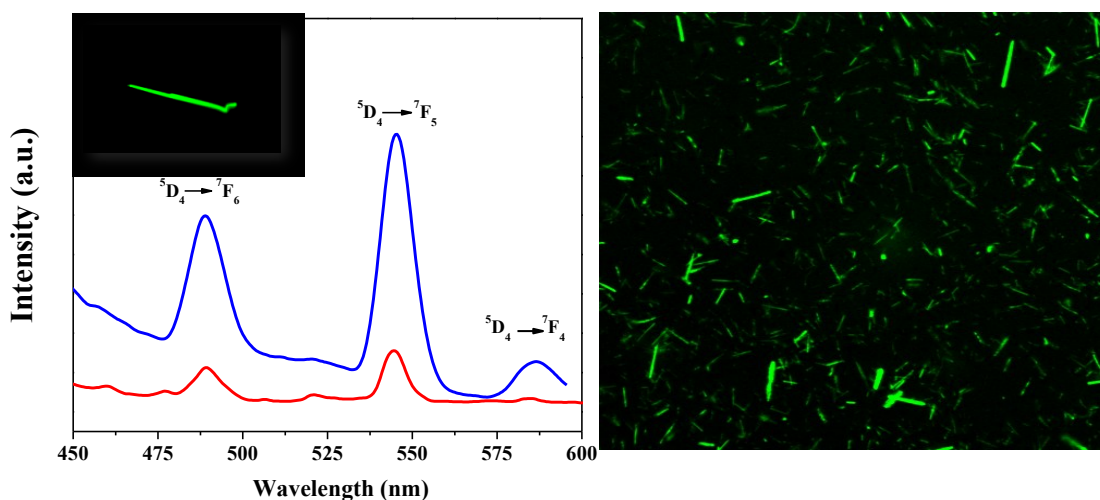
Figure 11 Emission spectra Tb(III) (redline) and **{NMOF1@SiO$_2$@fum@Tb}** (blue line) (left); (right) CLSM image for **{NMOF1@SiO$_2$@fum@Tb}** showing green fluorescent nanotapes.
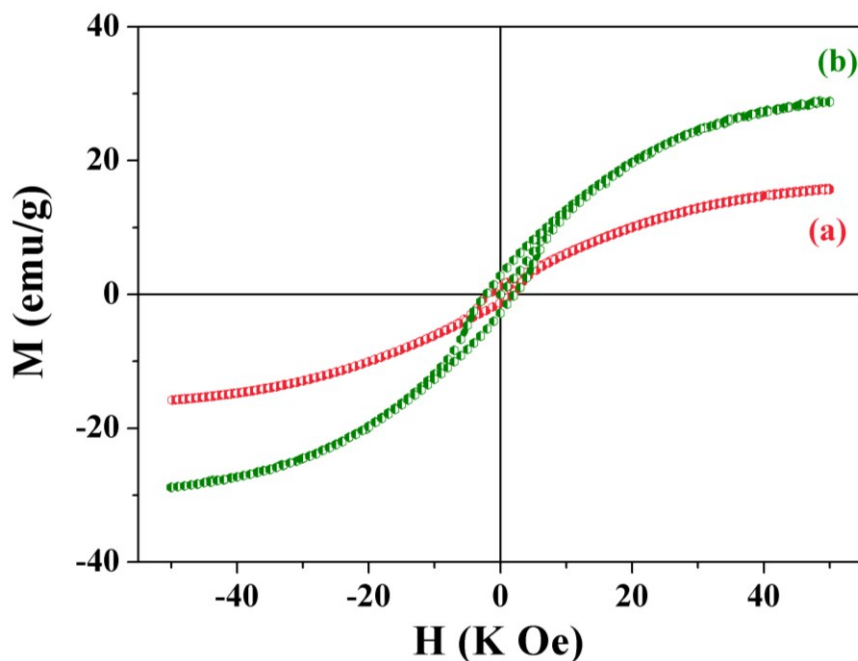
Figure 12 Field dependent magnetization curves measured at 2.5 K: (a) **NMOF 1** and (b) {**NMOF 1@SiO2@fum@Tb(III)**}

The tagging of Tb(III) ions to the surface was confirmed by EDX analysis which shows peaks of Tb(III). The **{NMOF1@SiO$_2$@fum@Tb}** nanotapes are green fluorescent; they have been further characterized through by confocal laser scanning microscopy

(CLSM) (Figure 11 right). Furthermore, we have measured the field dependent magnetization of **NMOF 1** and {**NMOF 1@SiO2@fum@Tb(III)**} multifunctional nanocomposite up to 5T (Figure 12). The magnetization value in case of {**NMOF 1@SiO2@fum@Tb(III)**} is increased significantly compared to **NMOF 1**, which is due to presence of paramagnetic Tb(III) with S=3.

3.2.4.5 Nucleotide sensing of {NMOF1@SiO$_2$@fum@Tb}

The nucleotides like adenosine monophosphate (AMP), adenosine diphosphate (ADP) and adenosine triphosphate (ATP) contains phosphate anions and these are biologically important molecules (Figure 13). Recognition of such nucleosides is thus very important in this regard. We exploited our multifunctional nanocomposite {**NMOF1 @SiO2@fum@Tb**} for such purpose as the phosphate anions are prone to coordinate to Tb(III) metal ions. In aqueous solution of AMP, ADP and ATP (10^{-3} M) 0.01 g of {**NMOF1@SiO2@fum@Tb**} was immersed and stirred overnight. The solid products were filtered, washed with water and characterized by XPS and powder XRD analysis. The powder XRD patterns after incorporation of various nucleotides show similar patterns that of **NMOF1@SiO$_2$@fum@Tb,** suggesting that the MOF structure remains intact even after nucleotide immobilization in water solution (Figure 14).
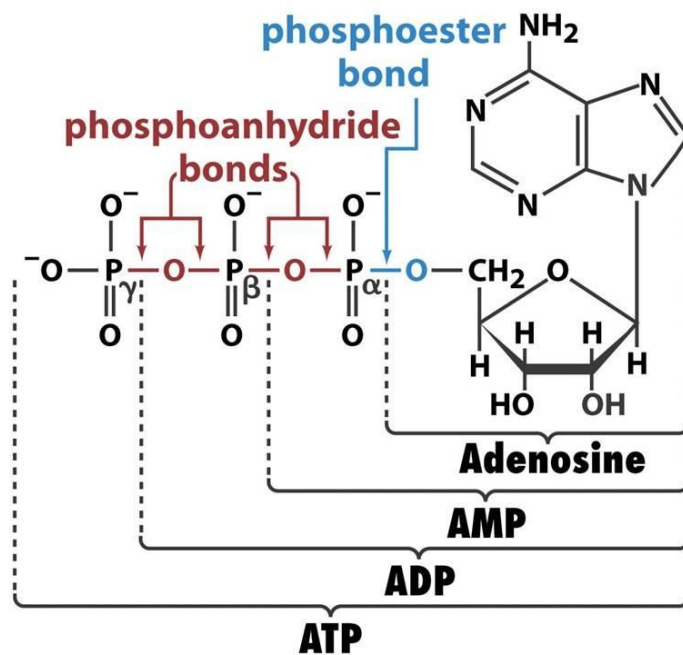
Figure 13 Structures of three nucleotides AMP, ADP and ATP
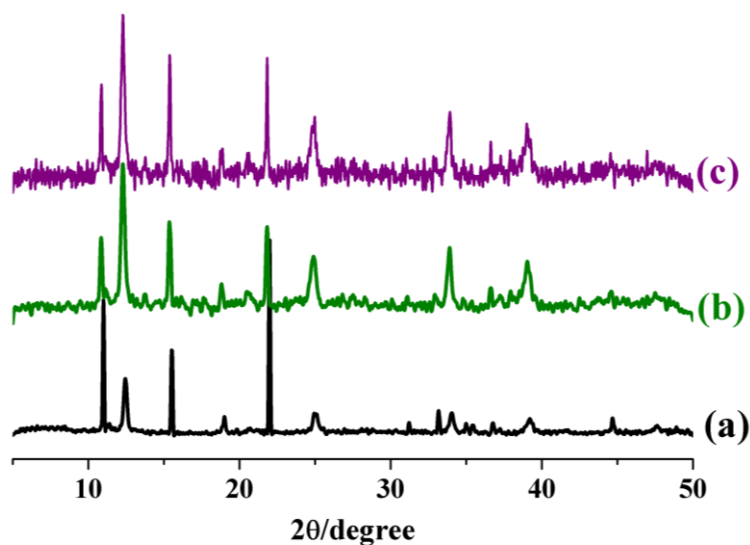
Figure 14 Powder XRD patterns (a) **NMOF** (b) **{NMOF1@SiO₂@fum@Tb}** (c) **{NMOF1@SiO₂@fum@Tb@ATP}**

Evidence of binding to the metal center came from XPS studies. Though the present solvent water molecules also can bind to the metal center but phosphate binding strength is higher than that and binds to the metal center efficiently. XPS spectrum of **{NMOF1@SiO₂@fum@Tb@ATP}** sample clearly indicates that phosphate –oxygen bond (P-O) as clearly observed XPS transition of O 1S appears at 532.85 eV, suggesting the binding of ATP through phosphate ions with Tb metal ions (Figure 15).
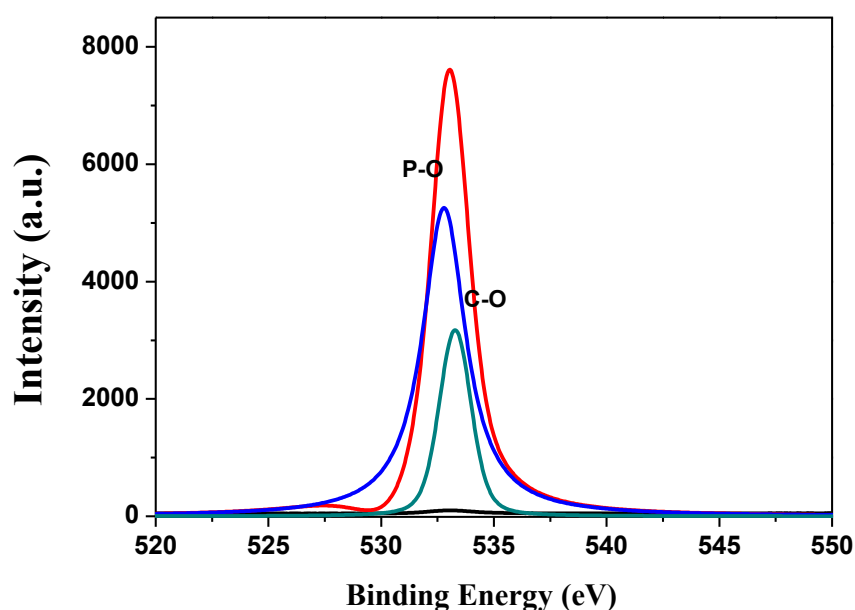
Figure 15 XPS spectra of O1S of **{NMOF1@SiO₂@fum@Tb@ATP}**.

Fluorescence spectra of all three composites show interesting changes compared to that of **NMOF1@SiO$_2$@fum@Tb**. In all three cases green emission (λ_{ex}= 250 nm) from Tb(III) were observed but we noticed a sharp enhancement in the intensity. When we have attached AMP, ADP and ATP nucleotides with the multifunctional composite, the emission intensity of the $^5D_4$-$^7F_5$ peak significantly increases from AMP to ADP (Enhancement ratio of 1: 1.5 for AMP and 1:1.8 for ADP with respect to the composite). The increase is most pronounced in the case of ATP with the ratio of enhancement of 1:3 (Figure 16). Therefore, **NMOF1@SiO$_2$@fum@Tb** is a highly sensitive and selective sensor of ATP. A study of concentration dependent study reveals that even very low concentration (10^{-5} M) also Tb(III) emission enhances significantly and almost saturates at (10^{-1} M) concentration (Figure 17). Such enhancement is clearly due to binding of the adenosine moieties to the metal center through the phosphate anions. The adenosine part acts as an antenna molecule and through binding it provides sufficient energy for bright emission of Tb(III). As the number of phosphate anions increases from AMP to ATP, binding strength also increases which results in highest enhancement for ATP making the composite selective towards ATP.
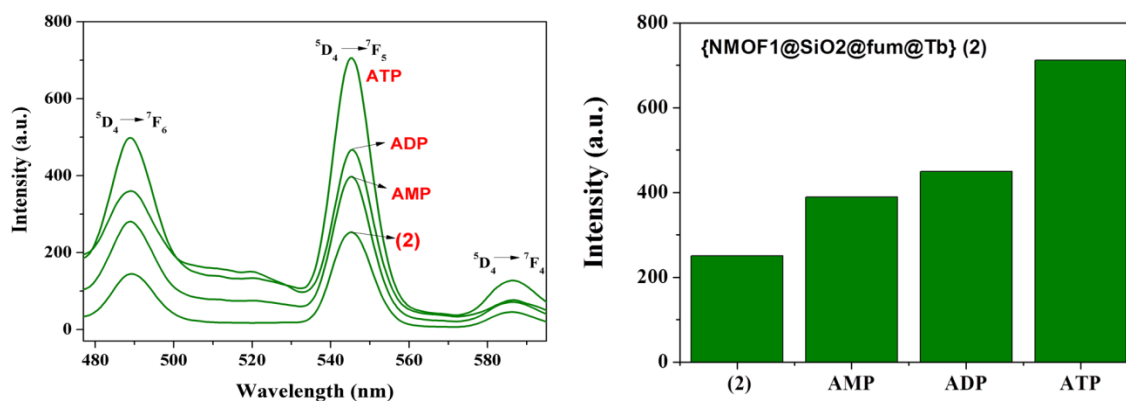
Figure 16 Comparison of the luminescence intensities of **NMOF1@SiO$_2$@fum@Tb** after immobilization with different nucleotides (10^{-3} M) in water (comparing intensity of transition 5D4$\rightarrow$7F5)
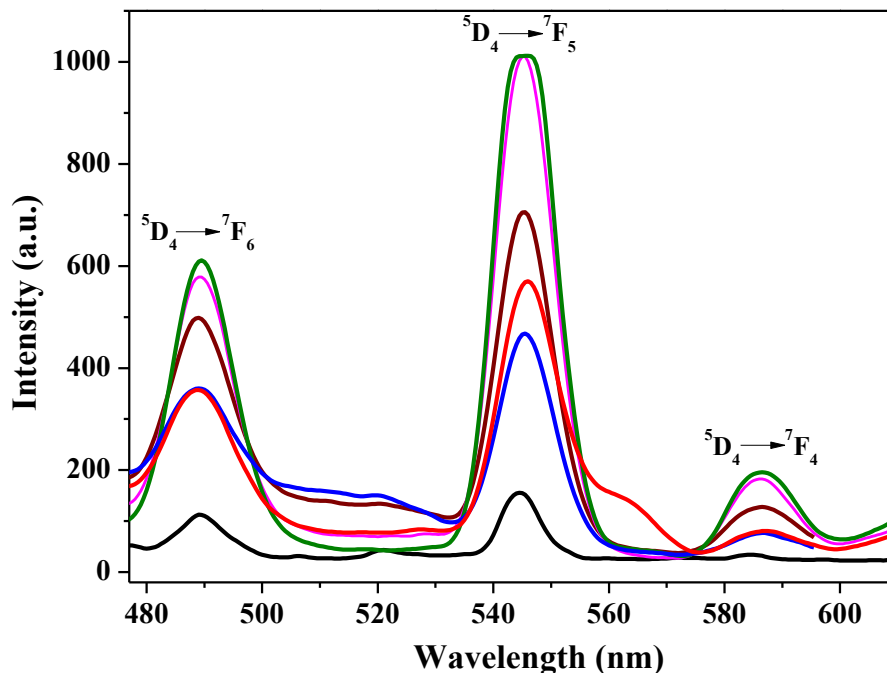
Figure 17 Comparison of fluoroscence intensities of {**NMOF1@SiO$_2$@fum@Tb**} in water after incorporation of different concentration of ATP ion (green 10^{-1}, pink 10^{-2}, violet 10^{-3}; red 10^{-4}; blue 10^{-5} M, respectively).

3.2.5 Conclusions

In conclusion, we demonstrated a facile and simple strategy to multifunctional nanocomposite based cobalt metal, squarate ion in presence of structure directing agent PVP. The NMOF 1 shows permanent porosity and canted antiferromagnetism characterized through adsorption and magnetic measurements. The microscopic techniques reveals that obtain NMOF has nanotape morphology with a thickness ~25 nm. The addiotnal luminescence property obtained through successful surface medication of NMOF with silica, fumaric acid with Tb(III) ions. Multifunctional {**NMOF1@SiO$_2$@fum**@Tb} exhibits significant sensitive and selective behaviour towards ATP among other nucleotides AMP and ADP in pure water at pH ~7.

3.2.6 References

1) a) H. Jodai, *CSJ Curr. Rev.* **2010**, *3*, 53; b) H. R. Moon, D.-W. Lim, M. P. Suh, *Chem. Soc. Rev.* **2013**, *42*, 1807; c) P. Valvekens, F. Vermoortele, V. D. De, *Catal. Sci. Technol.* **2013**, *3*, 1435; d) J.-L. Wang, C. Wang, W. Lin, *ACS Catal.* **2012**, *2*, 2630; e)M. Yoon, R. Srirambalaji, K. Kim, *Chem. Rev.* **2012**,

112, 1196.

2) a) R. J. Kuppler, D. J. Timmons, Q.-R. Fang, J.-R. Li, T. A. Makal, M. D. Young, D. Yuan, D. Zhao, W. Zhuang, H.-C. Zhou, *Coord. Chem. Rev.* **2009**, *253*, 3042; b) J. An, O. K. Farha, J. T. Hupp, E. Pohl, J. I. Yeh and N. L. Rosi, *Nat. Commun.* **2012**, *3*, 604; c) K. Jayaramulu, S. K. Reddy, A. Hazra, S. Balasubramanian and T. K. Maji, *Inorg. Chem.* **2012**, *51*, 7103.

3) a) M. D. Allendorf, C. A. Bauer, R. K. Bhakta and R. J. T. Houk, *Chem.Soc. Rev.* **2009**, *38*, 1330; b) Y. Cui, Y. Yue, G. Qian and B. Chen, *Chem.Rev.* **2011**, *112*, 1126; c) K. Jayaramulu, R. P. Narayanan, S. J. George and T. K. Maji, *Inorg. Chem.* **2012**, *51*, 10089.

4) a) J. C. Tan and A. K. Cheetham, *Chem. Soc. Rev.* **2011**, *40*, 1059; b) M. D. Allendorf, A. Schwartzberg, V. Stavila and A. A. Talin, *Chem.Eur. J.* **2011**, *17*, 11372.

5) a) R. C. Huxford, K. K. E. de, W. S. Boyle, D. Liu and W. Lin, *Chem. Sci.* **2012**, *3*, 198; b) K. Jayaramulu, K. S. Krishna, S. J. George, M. Eswaramoorthy and T. K. Maji, *Chem. Commun.* **2013**, *49*, 3937.

6) a)W. Lin, J. W. Rieter and K. M. L. Taylor, *Angew. Chem., Int. Ed.* **2009**, *48*, 650; b) D. Liu, R. C. Huxford and W. Lin, *Angew. Chem., Int. Ed.* **2011**, *50*, 3696; c) A. Kondo, S. Takanashi and K. Maeda, *J. Colloid Interface Sci.* **2012**, *384*, 110; d) D. Bradshaw, A. Garai and J. Huo, *Chem. Soc. Rev.* **2012**, *41*, 2344; e) R. J. Della, D. Liu and W. Lin, *Acc. Chem. Res.* **2011**, *44*, 957.

7) P. Horcajada, T. Chalati, C. Serre, B. Gillet, C. Sebrie, T. Baati, J. F. Eubank, D. Heurtaux, P. Clayette, C. Kreuz, J.-S. Chang, Y. K. Hwang, V. Marsaud, P.-N. Bories, L. Cynober, S. Gil, G. Ferey, P. Couvreur and R. Gref, *Nat. Mater.* **2010**, *9*, 172.

8) D. Tanaka, A. Henke, K. Albrecht, M. Moeller, K. Nakagawa, S. Kitagawa and J. Groll, *Nat Chem* **2010**, *2*, 410-416.

9) a) W. J. Rieter, K. M. L. Taylor, W. Lin, *J. Am. Chem. Soc.* 2007, *129, 9852;* b) S. Pal, D. Jagadeesan, K. L. Gurunatha, M. Eswaramoorthy and T. K. Maji, *J. Mater. Chem.* **2008**, 18, 5448.

10) a) E. A. Amiott, J. A. Jaehning, *Mol. Cell* **2006**, *22*, 329; b) B. Bennetts, G. Y. Rychkov, H.-L. Ng, C. J. Morton, D. Stapleton, M. W. Parker, B. A. Cromer, *J. Biol. Chem.* **2005**, *280*, 32452; c) N. Inagaki, T. Gonoi, S. Seino, *Saishin Igaku*

1996, *51*, 1581; d) E.-J. Lee, E. A. Groisman, *Nature* **2012**, *486*, 271; e) D. C. Liemburg-Apers, H. Imamura, M. Forkink, M. Nooteboom, H. G. Swarts, R. Brock, J. A. M. Smeitink, P. H. G. M. Willems, W. J. H. Koopman, *Pharm. Res.* **2011**, *28*, 2745; f) S. Takeda, S. Mizuguchi, H. Funahashi, H. Shiigi, T. Nagaoka, *Chem. Sens.* **2008**, *24*, 70; g) K. Tanaka, I. Shitanda, Y. Hoshi, M. Itagaki, *Chem. Sens.* **2013**, *29*, 120: e) W. Tedsana, T. Tuntulani, W. Ngeontae, *Anal. Chim. Acta* **2013**, *783*, 65; f) P. Y. Watson, M. J. Fedor, *Nat. Chem. Biol.* **2012**, *8*, 963; g) Z. Xu, N. J. Singh, J. Lim, J. Pan, H. N. Kim, S. Park, K. S. Kim, J. Yoon, *J. Am. Chem. Soc.* **2009**, *131*, 15528-15533.

11) a) C. Bazzicalupi, S. Biagini, A. Bencini, E. Faggi, C. Giorgi, I. Matera , B. Valtancoli, *Chem. Commun.* **2006**, 4087; b) A. B. Descalzo, M. D. Marcos, R. Martinez-Manez, J. Soto, D. Beltran , P. Amoros, *J. Mater.Chem.* **2005**, *15*, 2721; c) Z. Kejik, K. Zaruba, D. Michalik, J. Sebek, J. Dian, S. Pataridis, K. Volka , V. Kral, *Chem. Commun.* **2006**, 1533; d) N. Shao, J. Jin, G. Wang, Y. Zhang, R. Yang , J. Yuan, *Chem. Commun.* **2008**, 1127; e) H. Wang , W.-H. Chan, *Org.Bio. Chem.* 2008, *6*, 162; (f) C. Yin, F. Gao, F. Huo , P. Yang, *Chem. Commn.* **2004**, 934; g) L. Basabe-Desmonts, D. N. Reinhoudt , M. Crego-Calama, *Chem. Soc. Rev.* **2007**, *36*, 993; h) D. Kalia, G. Merey, S. Nakayama, Y. Zheng, J. Zhou, Y. Luo, M. Guo, B. T. Roembke , H. O. Sintim, *Chem. Soc. Rev.* **2013**, *42*, 305; i) K. Lee, L. K. Povlich , J. Kim, *Analyst* 2010, *135*, 2179; j)Y. Zhou, Z. Xu , J. Yoon, *Chem. Soc. Rev.* **2011**, *40*, 2222.

12) A. Boultif, *Powder Diffr.* **2005**, *20*, 284.

Chapter 4.1

Luminescent Mesoporous Metal-Organic Framework for CO$_2$ Uptake, Dye Separation and Light Harvesting Applications
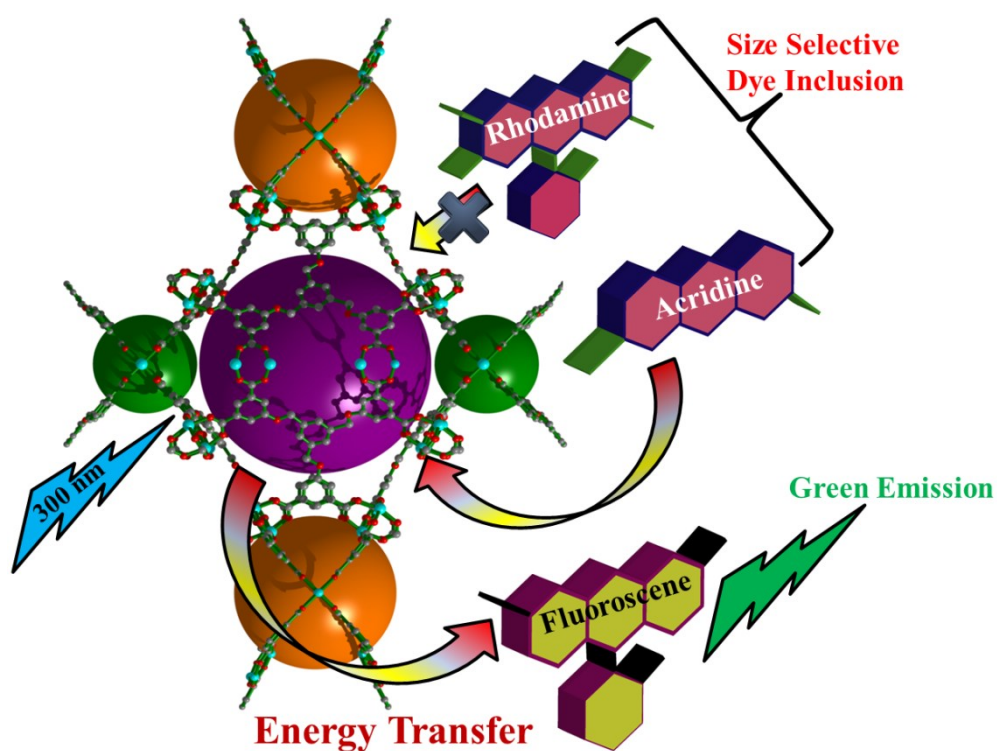
Summary

This chapter deals with, a synthesis, structural characterization of a novel luminescent mesoporous metal-organic framework (MOF) $\{[Zn_6(L)_2(H_2O)_6]\cdot 5DMF\}_n$ obtained from the self-assembly of Zn(II) and a hexacarboxylate linker (H_6L) 5,5′,5″- [1,3,5-phenyl-tri(methoxy)]-tris-isopthalic acid under solvothermal condition. The paddle-wheel type $\{Zn_2(COO)_4\}$ secondary building unit (SBU) is linked by the linker L to form a 3D framework structure. The framework is built of three different interconnected cages of dimensions 26.4×26.4 (cage A), 15.7×13.6 (cage B) and 14.6×7.8 $Å^2$ (cage C). The three cages have different window dimensions. N_2 adsorption at 77 K shows a combination of type I and type IV adsorption profile. The steep uptake at the low pressure and large hysteresis at $P/P_0 > 0.6$ suggest the framework contains bimodal hierarchical micro as well as mesopores which are consistent with the 3D framework structure. The t-plot suggests high degree of mesoporosity and has been exploited for dye separation based on their sizes. The framework shows efficient encapsulation of Acridine orange(AO) whereas completely excludes Rhodamine 6G (Rh6G). The framework shows ligand based blue emission with a maxima centered at 420 nm. Furthermore, inclusion of fluorescein dye (2 wt% and 5wt %) whose absorbance overlaps with the emission of the framework shows efficient Förster resonance energy transfer (FRET) from donor framework to acceptor guest fluorescein dye (FL).

4.1.1 Introduction

The recent upsurge on design and synthesis of new metal-organic frameworks (MOFs) is stem from their tunable pore structure based on versatile organic linkers and metal ions with different geometry.[1] These materials have shown great potential in gas storage,[2] catalysis,[3] separation,[4] and drug delivery.[5] The mentioned applications have been exploited based on permanent porosity in MOFs particularly in microporous regions. In the context of mass transfer, encapsulation and separation of large molecules, microporous MOFs have significant limitations that are attributed to the small pore size (< 2 nm). Therefore, design and synthesis of mesoporous MOFs with tunable structure posed a great importance and in this regard only handful examples are reported in the literature.[6] These hierarchically porous framework materials may find potential application in industry for catalysis, adsorption of bulky molecules and sensing.[6,7] Recently based on tri/tetra or hexa carboxylate linkers several cage like mesoporous frameworks have been reported and mostly these reports describe the large pore window size or cage size which is important for separation of large molecules or gas storage purposes.[7] One of the advantages of cage type mesoporous structure is large number of functionality or unsaturated metal sites (UMSs) can be incorporated in one single cage and this could lead to improved adsorption properties.[8] The high density of such UMSs is not easily achievable in a microporous framework. On the other hand excitation energy transfer place crucial role in natural photosynthesis process. Thus mimicking a natural light harvesting antenna which can efficiently funnel the excitation energy to an acceptor center is of interest of intense research.[9] As the spatial organization and ratio of donor and acceptor is very crucial for an efficient light harvesting process and in this respect some elegant approaches based on mesoporous silica, zeolites, clay hybrids have recently been documented.[10] We envisaged that MOFs with long range structural order and organized nano coordination spaces composed of a chromophoric linker would encapsulate specific acceptor molecule in a periodic manner without giving room for aggregation and also can facilitate anisotropic absorption of light.[11] Such light harvesting system based on MOFs is yet to be properly explored. In case of mesoporous structure, taking advantages of the large cage size, large dye molecules can be included in the framework based on less diffusion barrier. Choice of a proper acceptor dye molecule whose absorbance overlaps with the framework emission that acts as a donor can lead to an efficient energy transfer antenna

and this could be tuned easily by varying the dye doping amount. In MOFs a strut-to-strut energy transfer process based on two different donor and acceptor linkers has been reported earlier[12b] but by introducing different doping amount of dye in framework as an acceptor which could lead to highly efficient light harvesting phenomenon has not been properly explored.[13] This chapter reports a synthesis of a mesoporous framework from a C3 symmetric hexacarboxylate organic linker 5,5′,5″- [1,3,5-phenyl-tri(methoxy)]-tris-isopthalic acid (H_6L). The linker contains flexible aliphatic part (-O-CH_2-) as well as aromatic core and self-assembly with Zn(II), resulting a luminescent mesoporous framework, $\{[Zn_6(L)_2(H_2O)_6]\cdot 5DMF\}_n$ (**1**) that contains three different cages of different sizes interconnected by several windows. Adsorption measurements show presence of larger proportion of mesopores in the framework. Framework **1** was also found to be effective for selective (size) uptake of large dye molecules. Such property was further exploited for light harvesting application. Inclusion of fluorescein (FL) dye showed an efficient energy transfer from host framework to the guest dye molecule and such property in mesoporous MOFs is yet to be explored.

4.1.2 Experimental Section

4.1.2.1 Materials

All reagents were obtained from commercial sources and used without further purification. High purity $Zn(NO_3)_2\cdot 6H_2O$, Tribromomethylbenzene, Dimethyl-5-hydroxyiso phthalate and Na_2CO_3 were purchased from Aldrich Chemical Co. and used as received.

4.1.2.2 Synthesis of 5,5′,5″- [1,3,5-phenyl-tri(methoxy)]-tris-isopthalic acid (H_6L)

3.783 g of dimethyl-5-hydroxyisophthalate (18 mmol) was dissolved in 80 mL of dry THF. To this solution 2.414 g of tribromomesytiline (6 mmol), 2.21 g of K_2CO_3 (16 mmol) and 0.1 g of dibenzo-18-crown-6 (0.277 mmol) were added. The solution mixture was stirred at 85 °C for 48 hours. 40 mL of 1% Na_2CO_3(aq) was added into the above solution at 0 °C and filtered it off. The precipitate was washed with distilled water 2 to 3 times and then with diethyl ether. The resultant product (ester) was dissolved in 100 mL MeOH and aqeous KOH solution (40 mmol of KOH in 100 mL

water) was added and refluxed for 48 hours. The resultant mixture was filtered and 1N HCl was added drop wise to the concentrated filtrate which gives white color precipitate. The precipitate was filtered of and thoroughly washed with water in order to remove the excess acid. The final compound was characterized with ^{1}H-NMR (shown in below), IR and elemental analysis.
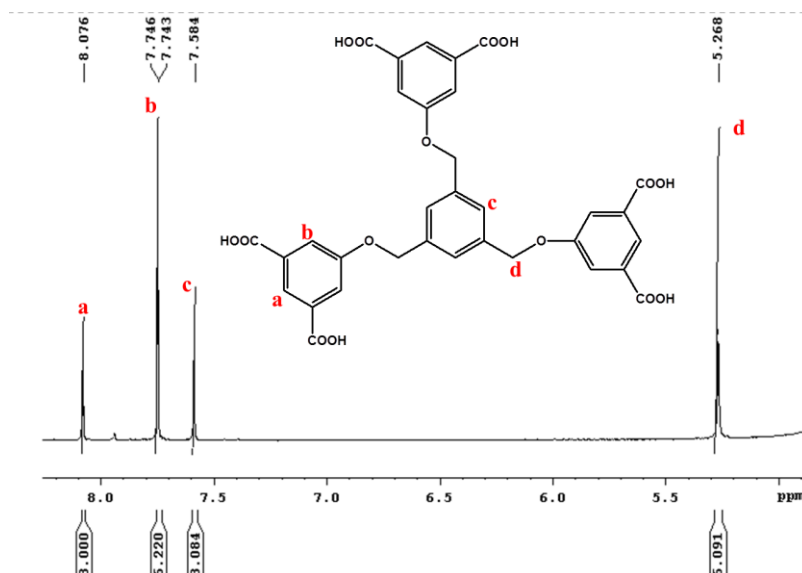
Figure 1 ^{1}H NMR spectra of 5,5′,5″- [1,3,5-phenyl-tri(methoxy)]-tris-isopthalic acid

4.1.2.3 Synthesis of {[Zn$_6$(L)$_2$(H$_2$O)$_6$]·5DMF}$_n$ (1)

A mixture of Zn(NO$_3$)$_2$·6H$_2$O (0.015 g, 0.05 mmol) and 5,5′,5″- [1,3,5-phenyl-tri(methoxy)]-tris-isopthalic acid (0.032 g, 0.05 mmol) in 8 mL N,N-dimethylformamide (DMF) was placed in a 23 mL Teflon lined container and the whole reaction mixture was stirred for 1 h. The Teflon lined container was subsequently placed in a steel autoclave and heated at 120 ºC under autogenous pressure for 72 h and then cooled to ambient temperature. Colorless block shaped crystals were isolated by decanting the supernatant liquid and washed thoroughly several times with DMF. FT-IR (cm^{-1}): 3530, 3087, 3052, 1623, 1529, 1460. Anal. Calculated for Zn$_6$C$_{48}$O$_{26}$N$_5$H$_{65}$: calculated; C 32.23 %; N 0.15 %; H 0.14 %. Experimental; C 31.98 %; N 0.11 %; H 0.17 %

4.1.3 Characterization Techniques

4.1.3.1 Physical Measurements

Elemental analysis was carried out using a Thermo Scientific Flash 2000 CHN

analyzer. IR spectrum was recorded using KBr pellets in the range 4000 - 400 cm^{-1} on Bruker IFS-66v spectrophotometer. Thermogravimetric analyses (TGA) were carried out under nitrogen (flow rate of 50 mL/min) with Metler Toledo TGA-850 TG analyzer in the temperature range between 25 – 650 ºC at a heating rate of 3 ºC/min. Powder X-ray diffraction (PXRD) patterns were recorded on a Bruker D8 Discover instrument using Cu-Kα radiation. Fluorescence studies were accomplished using Perkin Elmer Ls-55 Luminescence spectrometer.

4.1.3.2 Adsorption measurements

N$_2$ (77 K) and CO$_2$ (195 K) adsorption studies of the dehydrated sample of **1** were carried out using QUANTACHROME AUTOSORB-1C analyzer. To activate the sample supercritical activation method was employed. The adsorbate was charged into the sample tube and then the change of the pressure was monitored and the degree of adsorption was determined by decrease of the pressure at the equilibrium state. All operations were computer-controlled and automatic.

4.1.3.3 Single Crystal X-ray Diffraction

A suitable single crystal of **1** was carefully selected under a polarizing microscope and fixed to a separate thin glass fiber using commercially available glue. X-ray single crystal structure data was collected by a Bruker Smart –CCD diffractometer equipped with a normal focus, 2.4 kW sealed tube X-ray source (Mo K$_\alpha$ radiation, 0.71073 Å) operating at 50 kV and 30 mA. The programme SAINT[14] was used for integration of diffraction profiles and an empirical absorption correction based on symmetry equivalent reflections was applied using the SADABS program.[15] The structure was solved by direct method using SIR92 programme[16] and refined by full matrix least square method using SHELXL 97.[17] The hydrogen atoms were fixed by HFIX and placed in ideal positions. Potential solvent accessible area or void space was calculated using the PLATON[18] multipurpose crystallographic software. Final refinement included atomic positions for all the atoms, anisotropic thermal parameters for all the non-hydrogen atoms. All calculations were carried out using WinGX system, Ver 1.70.01.[19] Bond lengths and angles are given in Table 1.

4.1.3.4 Crystallographic data of {[Zn$_6$(L)$_2$(H$_2$O)$_6$]·5DMF}$_n$ (1)

Formula C$_{81}$H$_{83}$ZnN$_5$O$_{41}$, M_r = 2165.62, Tetragonal, Space group $I4/m$ (no. 87), a = 29.470(5) Å, b = 29.470(5) Å, c = 41.6871(10) Å, V = 36204(9) Å^3, Z = 8, ρ_{calc} =0.665 g cm^{-3}, μ(Mo-K$_\alpha$) = 0.820 mm^{-1}, F(000) = 7320, T = 150 K, λ (Mo-K$_\alpha$) = 0.71073 Å, θ_{max} = 29.4°, GOF = 0.87. A total of 184383 reflections were collected, of which 23222 were unique (R_{int} =0.106). R_1= 0.0690for 7848 independent reflections with I>2σ(I), w_{R2} = 0.1680 for all data.

4.1.4 Results and Discussion

4.1.4.1 Structural description {[Zn$_6$(L)$_2$(H$_2$O)$_6$]·5DMF}$_n$ (1)

Single crystal of compound **1** was synthesized from a solvothermal reaction of Zn(II) and H$_6$L at 120 °C. Single crystal X-ray diffraction analysis suggested that compound **1** crystallizes in the tetragonal space group, $I4/m$ and has a 3D extended structure based on {Zn$_2$(CO$_2$)$_4$} paddle-wheel secondary building unit (SBU). Each ligand, L is ligated to six different paddle-wheel units; to be precise, symmetrically four of one type (S1) and two of another type (S2) (Figure 2a). The C3-symmetric geometry of the linker plays important role for the construction the framework. Linker directs the framework in all three directions and it remains almost in a planar conformation (Figure 2b).
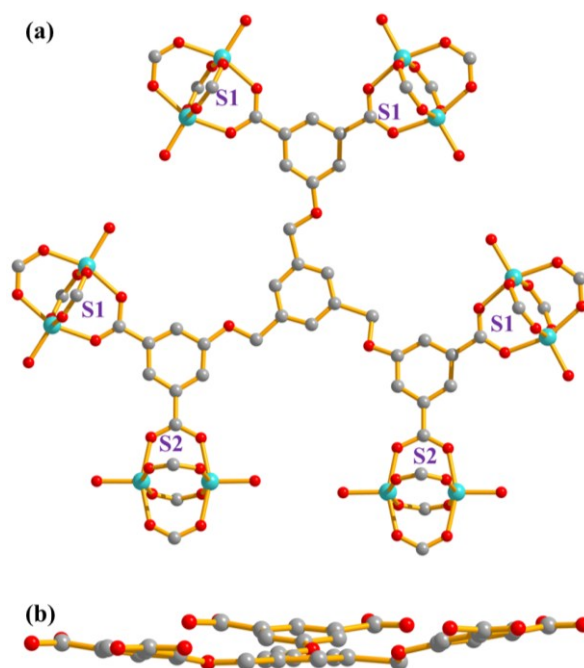
Figure 2 (a) Ligand 5,5′,5″- [1,3,5-phenyl-tri(methoxy)]-tris-isopthalic acid is attached to 6 (4 S1 and 4 S2) paddle-wheel SBUs.

There are three Zn(II) metal center and one L ligand in the asymmetric unit. The Zn(II) metal centers are penta-coordinated; four from oxygen atoms of carboxylates and one oxygen atom from water molecule. The framework houses three different types of interconnected cages shown in Figure 3 as A, B and C, which renders a highly porous structure. The largest square shaped cage, A comprises of eight (8) L ligands and twenty four (24) paddle wheels while two other smaller cages, B and C comprise of twelve (12) and two (2) paddle-wheel units, respectively.
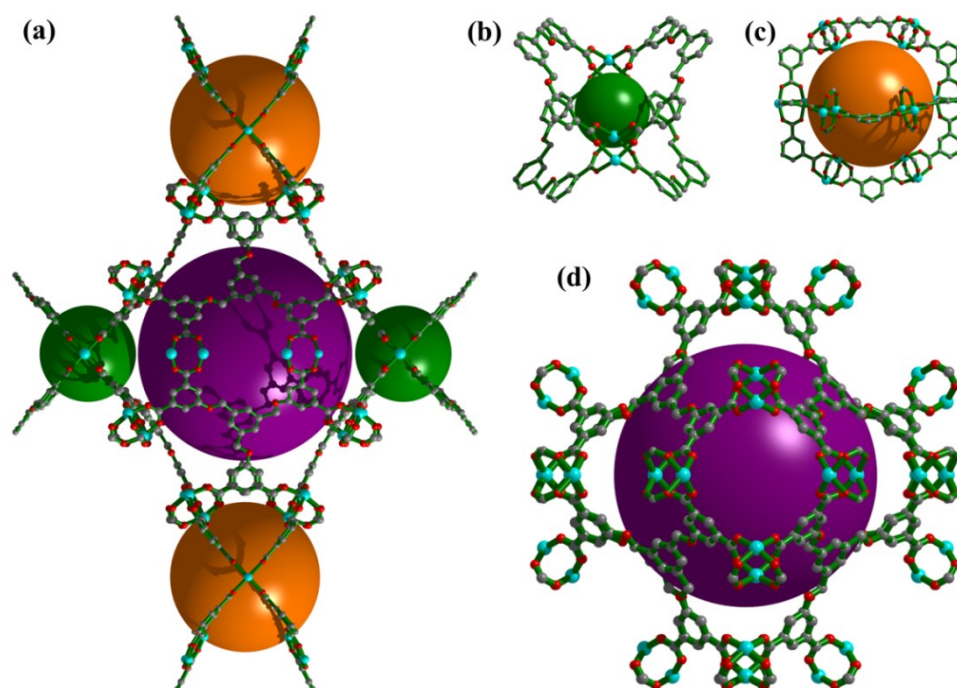
Figure 3 (a) Showing the connectivity of all the three types of cages, (b) cage C, (c) cage B, and (d) cage A.
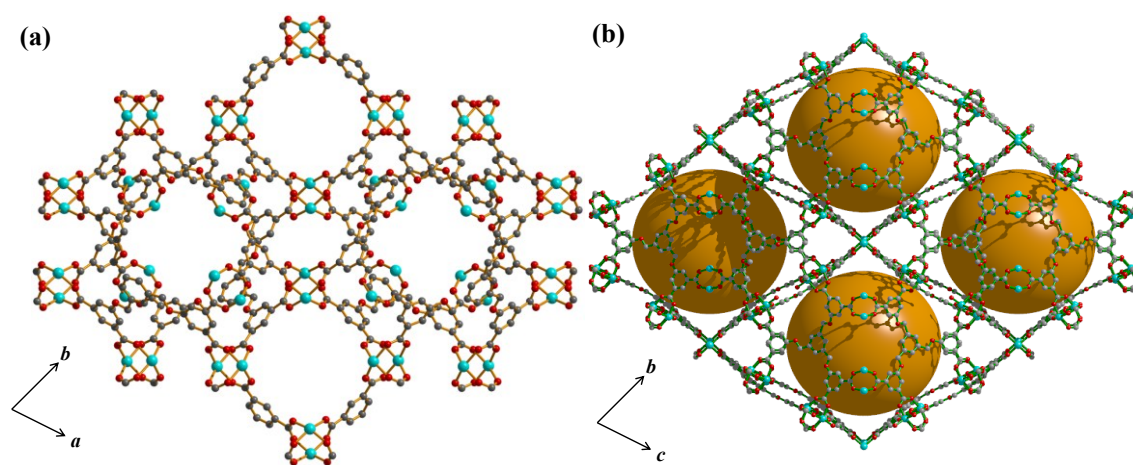
Figure 4 Three dimensional view of **1**; (a) along *c*-direction; (b) along *a*-direction

The dimension of the A cage is 26.4×26.4 Å^2 while the smaller cages, B and C have dimensions of 15.7×13.6 and 14.6×7.8 Å^2, respectively. Each A-type cage is surrounded by two B-type cages along the *c*-direction while four C-type cages along the *a*-direction (Figure 4). The window dimensions are comparatively smaller than the cage inner dimensions; along *a* and *b* axis the dimensions are 6.5×6.5 Å^2 and 0.5×0.5 Å^2 respectively, whereas along *c*-axis it is 8.5×8.5 Å^2 and 7.5×8.5 Å^2..

Table 1 Selected bond distances (Å) and angles (°) of **1.**

	Bond distance		Bond distance
Zn1 -O4	2.034(3)	Zn3 -O9_d	2.021(3)
Zn1-O11_a	2.019(4)	Zn3 -O6_f	2.000(3)
Zn1-O15_l	2.039(4)	Zn4 -O7	2.017(3)
Zn1-O12_m	2.005(3)	Zn4 -O8_b	2.001(3)
Zn2-O5	2.011(4)	Zn4-O8_d	2.001(3)
Zn2-O10_a	2.009(4)	Zn4 -O7_f	2.017(3)
Zn2-O14_l	2.007(4)	Zn2-O13_m	2.016(3)
	Bond Angle		**Bond Angle**
Zn3 -O6	2.000(3)	Zn3 -O9_b	2.021 (3)
O6_f -Zn3 -O9_b	157.29(15)	O4-Zn1-O11_a	89.24(14)
O6_f -Zn3 -O9_d	86.34(14)	O4 -Zn1 -O12_m	88.45(13)
O4 -Zn1 -O15_l	157.76(14)	O7 -Zn4 -O8_b	86.47(14)
O11_a -Zn-O15_l	86.25(14)	O7-Zn4 -O8_d	157.13(15)
O11_a -Zn1 -O12_m	157.77(14)	O7-Zn4 -O7_f	89.48(14)
O12_m -Zn1-O15_l	87.57(14)	O8_b -Zn4 -O8_d	88.58(14)
O7_f -Zn4 -O8_b	157.13(15)	O7_f -Zn4 -O8_d	86.47(14)
O5 -Zn2-O10_a	88.35(14)	O5 -Zn2 -O14_l	158.22(15)
O5-Zn2-O13_m	88.75(13)	O10_a -Zn2-O14_l	86.77(14)
O10_a-Zn2-O13_m	158.12(13)	O6 -Zn3-O9_b	86.34(14)
Symmetry code a = 1-y,x,z; b = 2-x,1-y,z; d = 2-x,1-y,-z; f = x,y,-z; l = 3/2-x,3/2-y,1/2-z; m = 1/2+y,3/2-x,1/2-z			

Topological analysis by TOPOS suggests the framework **1** is a 2-nodal 4,6-connected EBUCOT net with point Schläfli symbol $\{4^3.6^{12}\}2\{4^6\}3$ (Figure 5). Total calculated void space using PLATON is found to be 71% of total cell volume.
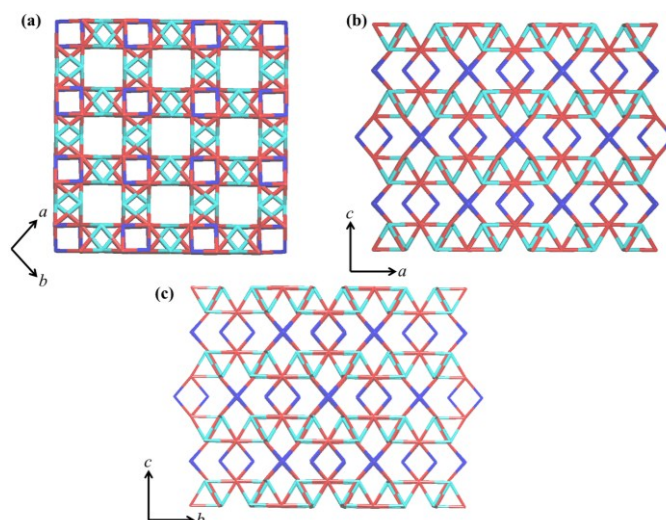
Figure 5   View of the net topology of **1** in three directions.

4.1.4.2 Stability and Adsorption Properties

To measure the permanent porosity of **1** we have carried out N_2 adsorption measurement at 77 K. Prior to measurement the framework was activated based on supercritical drying which is cheaper and effective method for activation of highly porous and low thermal stability MOFs. Hupp *et al.* revealed that supercritical activation is advantageous compared to the conventional activation.[20] To evaluate the stability of **1**, powder X-ray diffraction (PXRD) studies were performed after supercritical activation. Sharp and similar diffraction profiles after activation suggest that framework is stable (Figure 6).
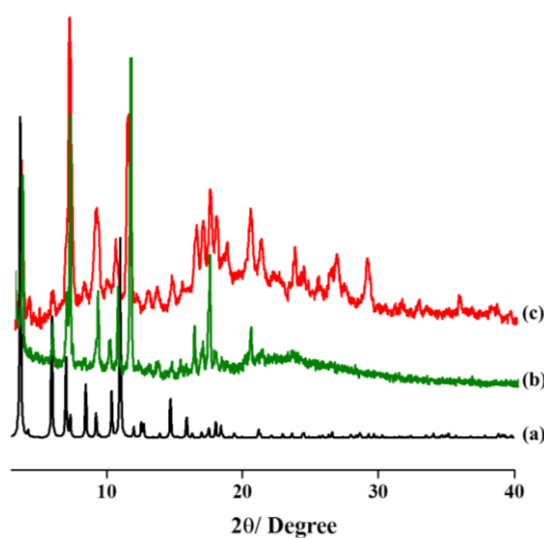
Figure 6 Powder X-ray diffraction of **1** at different states; (a) simulated (b) as-synthesized (c) activated using supercritical CO_2.

It is worth mentioning that normal activation at high temperature shows significant change in the PXRD pattern with disappearance of low angle peak indicating loss of periodic structure. N_2 adsorption at 77 K shows a combination of type-I and type-IV adsorption profile indicating presence of micro as well as mesopore in the framework. Curiously, the pore size distribution curve (Figure 7a) calculated using nonlocal density functional theory (NLDFT) method shows two maxima centered at 1 nm and 2.5 nm (Figure 7b). The distribution at 2.5 nm is higher than micropore suggesting dominance of mesopores in the framework. The calculated micropore volume using t-plot was found to be 0.0329 cc/g while the total pore volume is 0.293 cc/g, suggesting higher proportion of mesopore distribution in the framework. This observation is consistent with the structural features of the framework. At 195 K we also carried out CO_2 gas adsorption measurement and a type-I uptake was observed. The final uptake amount at $P/P_0 \sim 0.97$ is 63 mL/g ($\sim$12.5 wt%) (Figure 7a Inset). The desorption process is not identical to the adsorption path creating a distinct hysteresis. Such hysteresis can be related to the stronger affinity of CO_2 (Lewis base) molecules to bind to the unsaturated metal (Lewis acid) sites, aligned in different cages.
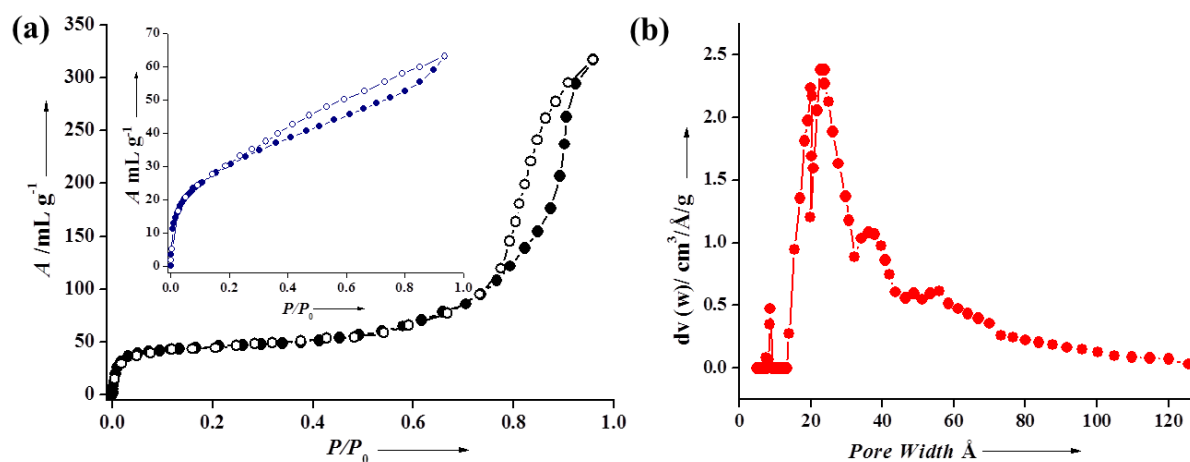
Figure 7 (a) N_2 adsorption isotherm at 77K; inset figure showing CO_2 adsorption isotherm at 195 K (filled circles represent adsorption and empty circles represent desorption); P_0 is the saturated pressure of the gas at measurement temperature (b) Pore size distribution curve calculated using NLDFT method.

4.1.4.3 Size Selective Dye Separation

Based on high degree of mesoporosity and mesopore volume of the framework, we anticipated that the framework will show size selective dye uptake which is of paramount importance in waste water treatment. We opted for two dyes of different molecular dimensions; Rhodamine 6G (Rh6G) (estimated ~ 1.6×0.9 Å^2) and Acridine orange (AO) (estimated ~ 1.3×0.65 Å^2). The crystals of **1** were first exchanged with a low boiling solvent methanol and then evacuated at 60 °C under reduced pressure (10^{-1} Pa) for overnight to get activated **1**. Activated crystals were then immersed into the dye solutions (100 mM) for 48 hrs. The dye uptake was studied using UV-vis spectroscopy which confirmed that the framework selectively absorbs Acridine orange (Figure 8a). A time dependent study shows that within 24 h almost most of the AO is adsorbed by the framework while even after 6 days Rh6G is not adsorbed (Figure 8b). Though the cage inner dimensions are larger than the dye molecules, the windows are comparatively smaller (0.85×0.85 nm along *c* and 0.65×0.5 nm along *a* and *b* axis). Clearly the window dimensions are optimum for AO but Rh6G is larger compared to the window dimension. Hence the selectivity is based on size of dyes and the window dimension plays the crucial role.
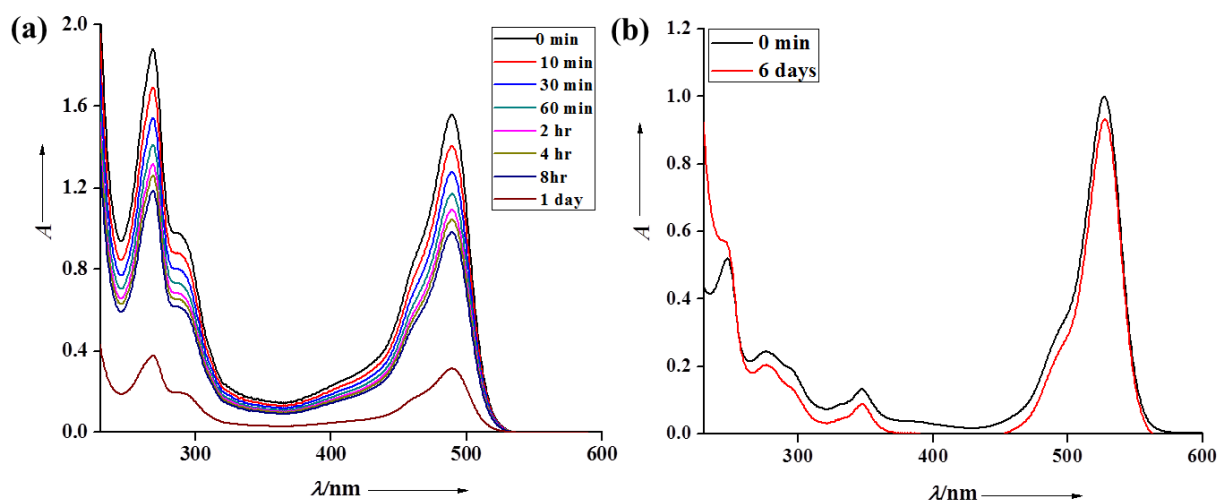
Figure 8 Dye encapsulation study of **1**; (a) Time dependent plot of AO dye in methanol; (b) Time dependent plot of Rh6G dye in methanol.

4.1.4.4 Light Harvesting by Inclusion of Fluorescein Dye

The ligand constitute of several aromatic rings and exhibits emission with maxima centered at 400 nm upon excitation at 300 nm. The framework exhibits emission at 420 nm, slightly shifted compared to the only ligand emission upon 300 nm excitation (Figure 9). Slight red shift compared to that of free ligand emission can be attributed to the metal coordination of ligand. We anticipated that this luminescent framework can act as a light harvesting antenna to a suitable acceptor dye through Förster resonant energy transfer.
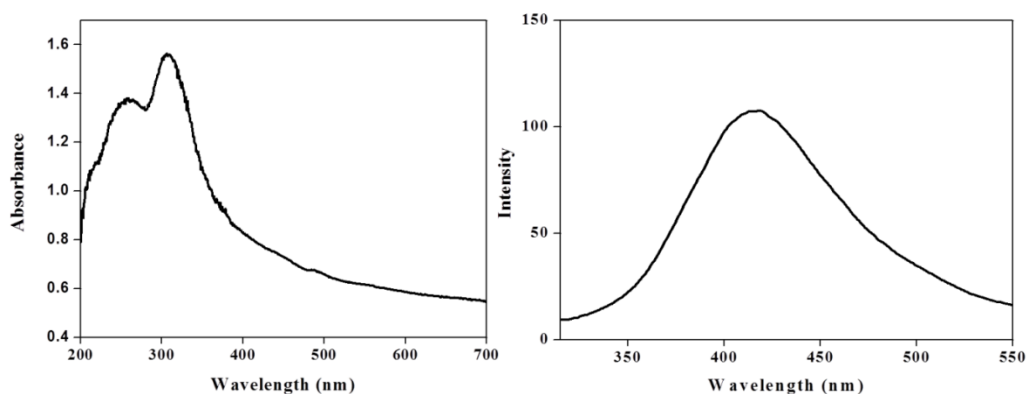
Figure 9 (left) UV-vis and (Right) emission spectrum of **1** (λ_{ex}= 300 nm).

We have chosen fluorescein dye (FL) based on following reasons: (a) the size matches well with the window dimension of the cages, (b) it has well separated emission and absorbance band and also there is a significant overlap of dye (acceptor) absorption with framework (donor) emission (Figure 10), (c) presence of large organic linker with several aromatic rings would help to organize the FL dye through non-covalent interactions.
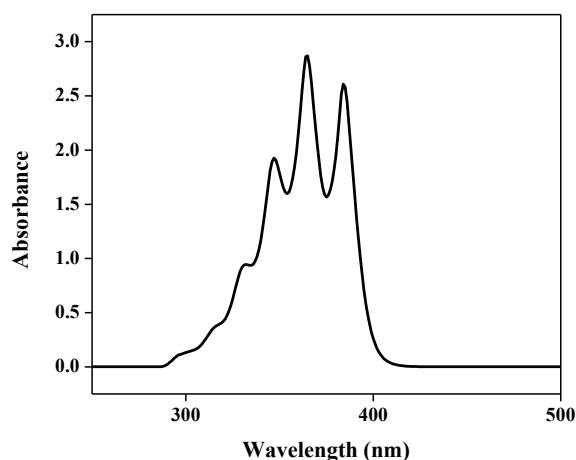
Figure 10 UV-vis spectrum of fluorescein dye (FL).

We have prepared two different dye doped framework **1a** (2 wt %) and **1b** (5 wt %) and the inclusion is confirmed from ^{1}H-NMR, elemental analysis and UV-visible spectra. The UV-visible spectra of **1a-b** show the broad absorbance band centered at ~ 450 nm which corresponds to FL dye molecule (Figure 11).
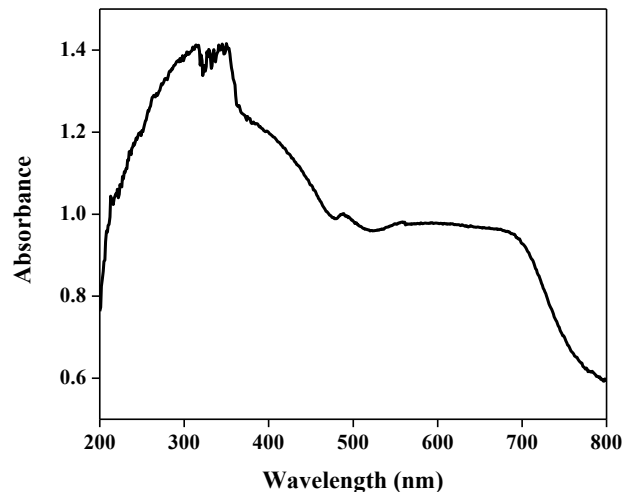
Figure 11 UV-vis spectrum of FL dye@ MOF (**1a**).

Upon excitation at 300 nm **1a** shows a strong emission at 540 nm corresponding to dye emission and a comparatively weak emission is observed at 420 nm related to framework (Figure 12). Clearly the framework emission is absorbed by the dye molecule due to significant overlap between donor framework emission and acceptor (dye) absorbance which causes Förster resonance energy transfer (FRET) process. Increase in the dye concentration in **1b** almost quenches the framework emission at 420 nm and only dye emission is observed indicating efficient energy transfer process from framework to the FL dye (Figure 12).
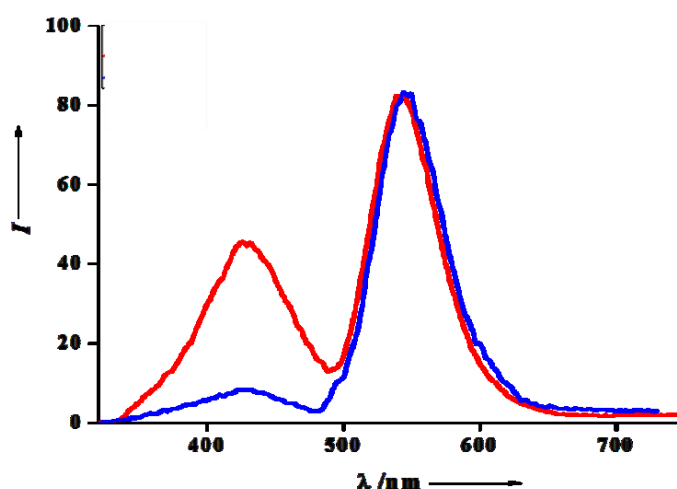
Figure 12 Emission spectra of **1a** and **1b** excited at 300 nm.

The direct excitation of **1b** at 400 nm shows lesser intensity emission at 540 nm compared to the 300 nm excitation suggesting presence of FRET process (Figure 13).
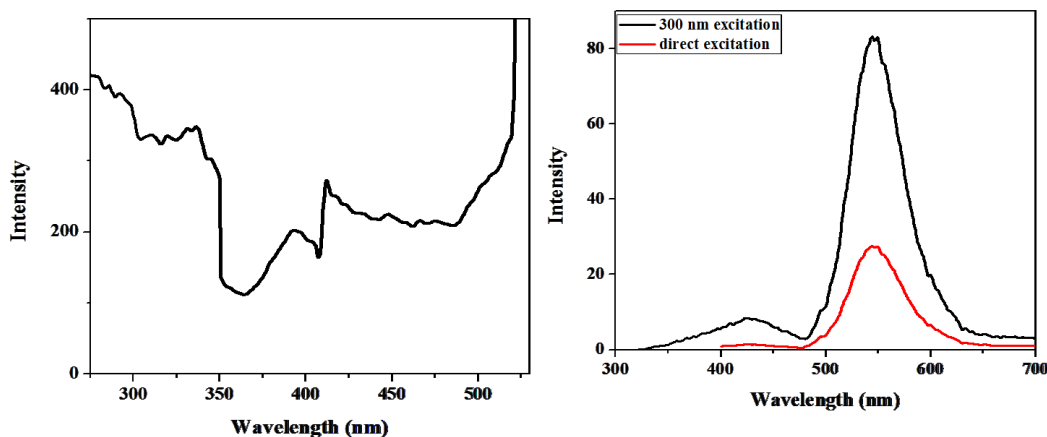
Figure 12 (left) Excitation spectra of **1b** observed at 550 nm; (Right) Emissin spectra of **1b** excitation at 400 nm (red line) and at 300 nm (black line).

Excitation spectrum (Figure 12) monitored at 550 nm shows a band with maximum intensity at 330 nm, which is related to linker absorption, which is futher supporting for light harvesting antenna of **1**. The FL dye decay profile of the composite **1b** was monitored at donor and acceptor emission wavelength (Figure 14). FL dye lifetime observed at 420 nm was found to be significantly less (0.85 ns) compared to the only framework life time (2.4 ns). This predicts that the emission energy from the donor framework is transferred by the acceptor (FL) and we see a bright emission from dye at 540 nm with high FL dye life time of ~ 5.4 ns which is even higher compared to that of only dye (FL).
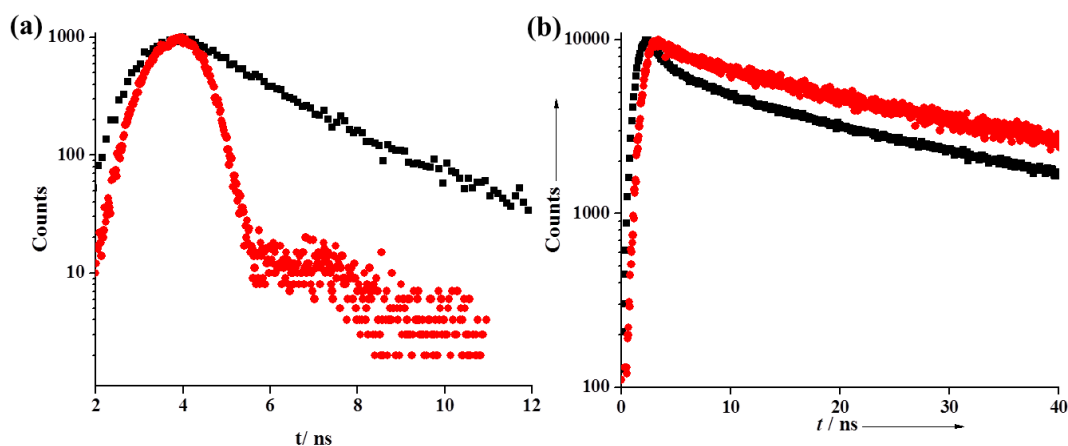
Figure 13 (a) Fluorescence decay profile of **1** (black) and **1b** (red) excited at 405 nm and monitored at 420 nm; (b) Fluorescence decay profile of FL (black) and **1b** (red) excited at 405 nm and observed at 550 nm.

The FL dye included framework showed the emission maxima at 540 nm upon excitation at 300 nm (Figure 13). The framework emission at 421 nm slowly diminishes with increasing dye concentration and dye emission at 540 nm becomes significant. Clearly the framework emission is absorbed by the dye molecule due to significant overlap between donor framework emission and acceptor (dye) absorbance. This Förster resonance energy transfer (FRET) phenomenon is maximum at 5 wt % inclusion of dye in the framework cages.

4.1.5 Conclusions

In conclusion, we have synthesized a novel luminescent mesoporous framework having cage like structures and the pore size distribution suggests very dominant mesopore character in the bulk sample. The structure contains three different types of cages. We exploited the different cage window dimensions for size selective dye inclusion. **1** selectively absorbs AO over Rh6G due to smaller size and preferable shape of AO. When FL dye was doped in the pores of **1**, we observed efficient light harvesting property of the composite **1a**. **1** acts as a donor and the FL dye acts as an acceptor. This is for the first time a mesoporous framework has been utilized for light harvesting applications and this could open a new route to exotic photophysical properties of mesoporous metal-organic frameworks.

4.1.6 References

1) a) Y. Cui, Y. Yue, G. Qian, B. Chen, *Chem. Rev.* **2011**, *112*, 1126; b) M. P. Suh, H. J. Park, T. K. Prasad , D. W. Lim, *Chem. Rev.* **2011**, *112*, 782; c) R. J. Kuppler, D. J. Timmons, Q. R. Fang, J. R. Li, T. A. Makal, M. D. Young, D. Yuan, D. Zhao, W. Zhuang, H.-C. Zhou*, Coord. Chem. Rev.* **2009**, *253*, 3042; d) R. Banerjee, A. Phan, B. Wang, C. Knobler, H. Furukawa, M. O'Keeffe, O. M. Yaghi, *Science* **2008**, *319*, 939.

2) a) O. K. Farha, I. Eryazici, N. C. Jeong, B. G. Hauser, C. E. Wilmer, A. A. Sarjeant, R. Q. Snurr, S. T. Nguyen, A. Ö. Yazaydın , J. T. Hupp, *J. Am. Chem. Soc.* **2012**, *134*, 15016; b) J. Sculley, D. Yuan , H.-C. Zhou, *Energy Environ. Sci.* **2011**, *4*, 2721; c) Y. He, W. Zhou, R. Krishna, B. Chen, *Chem. Commun*. **2012**, *48*, 11813.

3) a) J. Y. Lee, O. K. Farha, J. Roberts, K. A. Scheidt, S. T. Nguyen, J. T. Hupp, *Chem. Soc. Rev*. **2009**, 38, 1450; b) R. K. Das, A. Aijaz, M. K. Sharma, P. Lama, P. K. Bharadwaj, *Chem. Eur. J*. **2012**, 18, 6866.

4) a) L. J. Murray, M. Dinca, J. R. Long, *Chem. Soc. Rev*. **2009**, *38*, 1294; b) J. R. Li, R. J. Kuppler, H. C. Zhou, *Chem. Soc. Rev*. **2009**, *38*, 1477.

5) a) P. Horcazada, C. Serre, M. Sebban, F. Taulelle and G. Férey, *Angew. Chem. Int. Ed.* **2006**, *45*, 5974; b) P. Horcazada, C. Serre, G. Maurin, N.A. Ramsahye, F. Balas, M. Vallet-Regi, M. Sebban, F. Taulelle and G. Férey, *J. Am. Chem. Soc.* **2008, 130**, 6774.

6) a) W. Xuan, C. Zhu, Y. Liu , Y. Cui, *Chem. Soc. Rev.* **2012**, *41*, 1677; b) C. M. A. Parlett, K. Wilson , A. F. Lee, *Chem. Soc. Rev.* **2013**, *42*, 3876; c) Y.Q. Lan, H.L. Jiang, S.L. Li , Q. Xu, *Adv. Mater.* **2011**, *23*, 5015; d) L. Song, J. Zhang, L. Sun, F. Xu, F. Li, H. Zhang, X. Si, C. Jiao, Z. Li, S. Liu, Y. Liu, H. Zhou, D. Sun, Y. Du, Z. Cao , Z. Gabelica, *Energy Environ. Sci.* **2012**, *5*, 7508; e) L. B. Sun, J. R. Li, J. Park , H.-C. Zhou, *J. Am. Chem. Soc.* **2011**, *134*, 126; f) D. Yuan, R. B. Getman, Z. Wei, R. Q. Snurr , H.-C. Zhou, *Chem. Commun,* **2012**, *48*, 3297.

7) a) W. Xuan, C. Zhu, Y. Liu, Y. Cui, *Chem. Soc. Rev*. **2012**, *41*, 1677; (b) Q.-R. Fang, T. A. Makal, M. D. Young, H.-C. Zhou, *Comments Inorg. Chem.* **2010**, *31*, 165

8) O. K. Farha, A. Özgür Yazaydın, I. Eryazici, C. D. Malliakas, B. G. Hauser, M. G. Kanatzidis, S. T. Nguyen, R. Q. Snurr, J. T. Hupp, *Nat. Chem.* **2010**, *2*, 944.

9) a) P. D. Frischmann, K. Mahata, F. Wuerthner, *Chem. Soc. Rev.* **2013**, *42*, 1847; b) J. Yang, M.-C. Yoon, H. Yoo, P. Kim, D. Kim, *Chem. Soc. Rev.* **2012**, *41*, 4808; c) K.-H. Tang, R. E. Blankenship, *Photosynth. Res.* **2012**, *111*, 205; d) M. K. Panda, K. Ladomenou, A. G. Coutsolelos, *Coord. Chem. Rev.* **2012**, *256*, 2601; e) N. Aratani, D. Kim, A. Osuka, *Acc. Chem. Res.* **2009**, *42*, 1922

10) a) K. V. Rao, K. K. R. Datta, M. Eswaramoorthy, S. J. George, *Angew. Chem. Int. Ed.* **2011**, *50*, 1179. b) T. Q. Nguyen, J. J. Wu, V. Doan, B. J. Schwartz, S. H. Tolbert, *Science* **2000**, *288*, 652; c) N. Mizoshita, Y. Goto, T. Tani, S. Inagaki, *Adv. Mater.* **2009**, *21*, 4798. d) G. Calzaferri, S. Huber, H. Maas, C. Minkowski, *Angew. Chem. Int. Ed.* **2003**, *42*, 3732.

11) a) J.-L. Wang, C. Wang, W. Lin, *ACS Catal.* **2012, 2**, 2630; b) S. Jin, H.-J. Son, O. K. Farha, G. P. Wiederrecht , J. T. Hupp, *J. Am. Chem. Soc.* **2013**, *135*, 955;

12) a) C. Y. Lee, O. K. Farha, B. J. Hong, A. A. Sarjeant, S. T. Nguyen , J. T. Hupp, *J. Am. Chem. Soc.* **2011**, *133*, 15858; b) H. J. Son, S. Jin, S. Patwardhan, S. J. Wezenberg, N. C. Jeong, M. So, C. E. Wilmer, A. A. Sarjeant, G. C. Schatz, R. Q. Snurr, O. K. Farha, G. P. Wiederrecht , J. T. Hupp, *J. Am. Chem. Soc.* **2012**, *135*, 862.

13) a) X. Zhang, M. A. Ballem, P. Bergman , K. Uvdal, *Angew. Chem. Int . Ed.* **2011**,*50*, 5729; b) V. M. Suresh, S. J. George, T. K. Maji, *DOI: 10.1002 /adfm.201301178*.

14) SMART (V 5.628), SAINT (V6.45a), XPREP, SHELXTL; Bruker AXS Inc. Madison, Wisconsin, USA, **2004.**

15) Sheldrick, G. M. *Siemens Area Detector Absorption Correction Program*, University of Göttingen, Göttingen, Germany, **1994**.

16) A. Altomare, G. Cascarano, C. Giacovazzo, A.J. Gualaradi, *Appl. Cryst.* **1993**, *26*, 343.

17) G.M. Sheldrick, SHELXL-97, *Program for Crystal Structure Solution, Refinement*; University of Göttingen, Göttingen, Germany, **1997**.

18) A.L. Spek, *J. Appl. Cryst.* **2003**, *36*, 7.

19) L.J. Farrugia, *WinGX- A Windows Program for Crystal Structure Analysis. J. Appl. Crystallogr.* **1999**, *32*, 837.

20) A. P. Nelson, O. K. Farha, K. L. Mulfort, J. T. Hupp, *J. Am. Chem. Soc*. **2009**, *131*, 458.

Chapter 4

Mesoporous Metal-Organic Frameworks
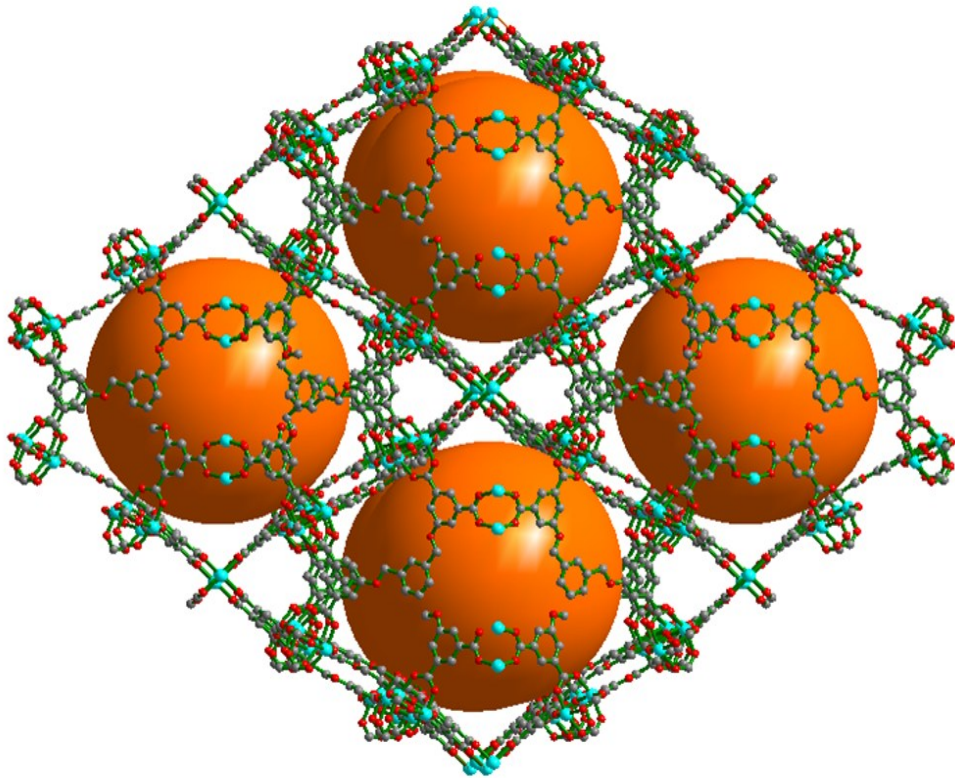
Chapter 4.2

Supramolecular Template based Hierarchical Metal-Organic Framework MIL-110 (Al): Dye Scavenging and Scaffold for Light Harvesting Applications
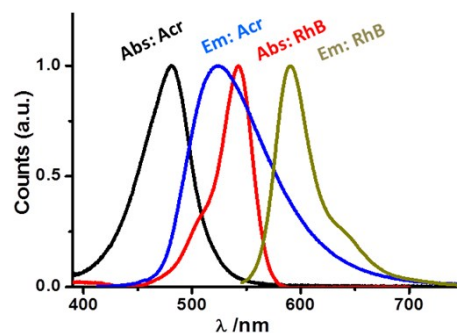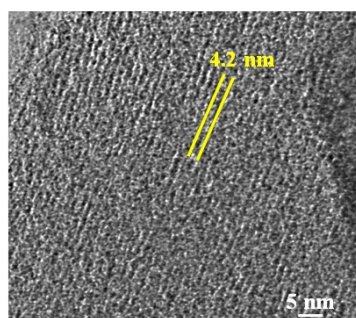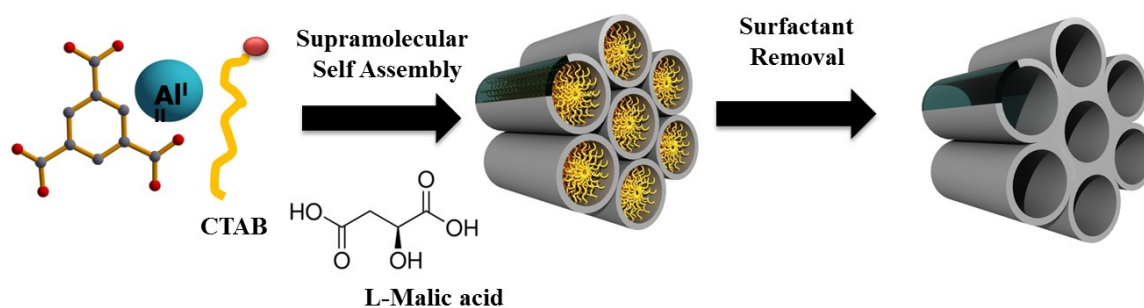
Summary

The design and fabrication of hierarchical mesoporous metal-organic frameworks (MOFs) remain a significant challenge. This chapter reports the design and synthesis of nanoscale hierarchical porous metal-organic framework of aluminium trimesate (MIL-110) $Al_8(OH)_8\{(OH)_3(H_2O)_3\}[btc]_3 \cdot nH_2O$ of octahedron morphology where mesopores are interconnected with the inherent micropores of the MOFs. The mesoporosity in the framework is introduced by a cooperative template method comprising of cationic surfactant, cetyltrimethylammoniumbromide (CTAB) and a chelating agent L-malic acid. These mesostructured MOFs based on MIL-110 (MMIL-110 a, b, c, d) obtained by controlling the chelating agent and L-malic acid and shows tunable pore diameters. Mesoporous MIL-110c was further exploited for dye scavenging. It acts as a good host for two different dyes based on their size. Therefore we have further exploited the meso-MIL110c as a good platform for light harvesting based on Förster resonance energy transfer (FRET) process by immobilizing suitable donor dye acridine orange (AO) in the micropores whose excitation energy transfer to a suitable acceptor dye Rhodamine B (RhB) encapsulated in the mesopores.

4.2.1. Introduction

Inorganic-organic hybrid materials or metal organic frameworks (MOFs) are a class of porous crystalline materials formed by the coordination driven self-assembly of metal ions and bridging organic ligands.[1] The presence of nanoscale periodicity, inherent functionalities along the channels and the structural diversity in MOFs opened up wide range of applications in gas storage, separation, catalysis, drug delivery and sensing.[2-6] Despite the ease of synthesis, porosity in MOFs is so far restricted to micropore regime and very few attempts to attain mesoporous MOFs were successful.[7] The easiest approach to synthesize mesoporous MOFs is to use long organic linkers but such frameworks often suffers from low thermal stability and self-catenation.[8] So the development of rational methods for the fabrication of robust mesoporous MOFs with tailored structure and tunable surface area is of immense importance. Recently, Zhang *et al* and Zhou *et al.* have reported template assisted synthesis of ordered hierarchically micro/mesoporous MOFs using supramolecular aggregates of surfactants or ionic liquid/ surfactant system.[9] Such an elegant approach based on micelles has been successfully demonstrated in the synthesis of mesoporous silica and metal oxides earlier.[10] The hybrid design involves the co-assembly of framework building blocks that form microporous walls and micelles which form supramolecular template to introduce mesoporosity in the ordered mesoporous MOF. The presence of uniform micro/meso channels and unprecedented intrinsic structural features of these supramolecular MOFs would be useful for wide range of applications such as catalysis, encapsulation of large molecules like enzymes and proteins based on high mass transfer/diffusion.[11] Water pollution is a very alarming environmental hazard which if not properly addressed can lead to disastrous consequences for the living species. Industrial wastes comprising a large number of dye molecules which are non-biodegradable need to be separated from the polluted water molecules in order to purify it.[12] Metal-organic frameworks with large pore size would provide low diffusion barriers offer an excellent solution for the scavenging of such dye molecules from waste water due to the inherent porosity present within them. Furthermore, miniaturization of MOFs to nanoscale has been given great interest compared to bulk crystalline MOFs due to their easy immobilization and high solution processibiilty.[13] Various morphologies like cubes, spheres, rods, vesicle and rings have been reported for wide range of applications.[14] Also, nanoscale MOFs would prove to be an added

advantage in this regard because it would provide an even lesser diffusion barrier for the dye molecules. This would lead to their facile and enhanced encapsulation. However, as discussed previously, Metal-organic frameworks have till now been mainly confined to the microporous regime and hence scavenging of dyes of different molecular dimensions have been restricted. Furthermore, fluorescent nanoscale metal organic frameworks (NMOFs) have been attractive candidates as transparent luminescent materials and are potential for solid state light emitting devices like LEDs,[15] sensors[16] and light harvesting materials.[17] Spatial organization of donor and acceptor molecules is a critical feature to be addressed for efficient Förster resonance energy transfer (FRET) process.[18] It is worth mentioning that organic assemblies[19] suffers from limited degree of macroscale organization and reduced energy transfer efficiency due to self-quenching based on molecular aggregates/excimers formation in self-assembled state. Inorganic-organic hybrid materials with nanoscale periodicity and well-defined hierarchical porosity would help in self-organization of chromophores in well-separated state.[20]

Here in, we envisioned that a nanoscale hierarchical bimodal micro-mesoporous MOFs would act as a platform for organization of two different donor-acceptor chromophores in two interconnected pores based on their sizes. Such organization of donor and acceptor assembly would show efficient light harvesting FRET process. With this objective, we have elegantly designed a hierarchically ordered meso porous MOF, $Al_8(OH)_8\{(OH)_3(H_2O)_3\}[btc]_3 \cdot nH_2O$ of Aluminium trimesate (MIL-110) with octahedron morphologies using template directed synthesis where microporous MOF constituting the pore walls of the mesopores (3.6- 4 nm) derived from the supramolecular micelle template. This ordered porous MOF exhibits dye scavenging abilities and also a selective encapsulation of dye molecules micro/meso channels based on the size of the dye molecules. Furthermore, we have successfully explored this hierarchically ordered MOF for efficient light harvesting applications where the donor molecules present in the micropores funnel the excitation energy to the acceptor molecules aligned in the meso channels via Förster resonance energy transfer (FRET) process.

4.2.2 Experimental Section

4.2.2.1 Materials

All the reagents and solvents employed were commercially available and used as supplied without further purification. $Al(NO_3)_3.9H_2O$, 1,3,5-benzenetricarboxylate acid, Cetyltrimethylammonium bromide, L-Malic acid obtained from Aldrich Chemical Co.

4.2.2.2 Synthesis of $\{Al_8(OH)_{12}\{(OH)_3(H_2O)_3\}[btc]_3\}\cdot 4H_2O$ or MIL-110 (Al)

MIL-110 (Al) was prepared according to the literature reported by Ferey *et al.* [21h] A mixture of $Al(NO_3)_3.9H_2O$ (3 mmol), 1,3,5-benzenetricarboxylic acid (1 mmol), 5 μL HF and 10 ml of water was placed in a 23 mL teflon bomb and the whole reaction mixture was stirred for 1 h. Then Teflon bomb was subsequently placed in a steel autoclave and heated at 220 ºC under autogenous pressure for 72 h and then cooled to ambient temperature. Orange colored powder was isolated by decanting the supernatant liquid and washed thoroughly several times with ethanol. IR (KBr cm^{-1}); v(O-H), 3465; v_{as}(OCO), 1629; v_s(OCO), 1468. Anal. Calcd. for $C_{27}H_{38}Al_8O_{40}$: C, 26.16; H, 3.14; Found: C, 27.19; H, 3.05 %.

4.2.2.3 Preparation of Hierarchical Porous MIL-110 (Al) or MMIL-110

In a typical synthesis, (3 mmol) of $Al(NO_3)_3.9H_2O$ were dissolved in 15 ml of de-ionized water and mixed with (1 mmol) of H_3BTC dissolved in 15 ml of ethanol. Then, the supramolecular templating agent (CTAB or CTAB/L-Malic acid) was added while stirring. The mixture was heated at 220 °C for 12 h in a 23 ml Teflon autoclave liner. The resulting powder was filtered off, washed with water and ethanol. Finally, the as-synthesized sample was extracted twice with an ethanol and HCl solution to remove the template (CTAB or CTAB/L-Malic acid) from the framework. In this similar synthetic method we have isolated five different MOFs based on MIL-110.[9b] MMIL-110 stands for mesoporous MOF obtained using only CTAB and MMILa-d obtained using different content of L-malic acid along with CTAB.

4.2.2.4 Synthetic Procedure for Dye Encapsulation

Activated MMIL-110c is stirred with Rhodamine B (RhB) solution (10^{-6}M) for 6hrs. It is centrifuged, washed with ethanol and THF several times and dried at room temperature under vacuum to give RhB@MMIL-110c. This is stirred with Acridine orange (AO) (10^{-6}M) solution for 24 h to result in AO-RhB@MMIL-110c. It is washed with ethanol and dried at room temperature under vacuum.

4.2.3 Characterization Techniques

4.2.3.1 Physcial Measuremnts

The resultant mesostructured MMILs-110 (Al) samples were characterized through different techniques. Powder X-ray diffraction (PXRD) pattern were recorded on a Bruker D8 Discover instrument using Cu-Kα radiation. The morphology and porous nature of NPCs examined with field emission scanning electron microscope (FESEM, FEI Nova-Nano SEM-600, Netherlands) and transmission electron microscope (TEM) (JEOL JEM-3010 with an accelerating voltage at 300 kV). Elemental analyses were carried out using a Thermo Scientific Flash 2000 CHN analyzer. FT- IR spectra were recorded using KBr pellets in the range 4000 - 400 cm^{-1} on a Bruker IFS-66v spectrophotometer. Thermogravimetric analyses (TGA) were carried out under nitrogen (flow rate of 50 mL/min) with Metler Toledo TGA-850 TG analyzer in the temperature range between 25 - 600°C at a heating rate 3°C / min. Fluorescence studies were accomplished using Perkin Elmer Ls-55 Luminescence spectro-meter.

4.2.3.2 Adsorption Measurements

N_2 adsorption (at 77 K) study of dehydrated mesostructured MMILs-110 (Al) samples were carried out using QUANTACHROME AUTOSORB-1C analyzer. In the sample chamber maintained at $T \pm 0.03$ K was placed the adsorbent sample (100-150 mg), which had been prepared at 433 K under a high vacuum (10^{-1} Pa) for 18 hours prior to measurement of the isotherms. The adsorbate was charged into the sample tube and then the change of the pressure was monitored and the degree of adsorption was determined by decrease of the pressure at the equilibrium state. All operations were computer-controlled and automatic.

4.2.4 Results and Discussion

4.2.4.1 Synthesis and Characterization of MMIL-110 (Al)

We have exploited a template based methodology for synthesis of hierarchically micro and mesoporous metal-organic frameworks based on MIL-110 with tunable porosity. The supramolecular template method has been extensively employed to prepare the ordered mesoporous materials like mesoporous silica and metal oxides. The synthesis can be achieved through either an electrostatic pathway based on a supramolecular assembly of charged surfactants with charged inorganic precursors or a neutral pathway where hydrogen bonding is responsible for the cohesiveness between the surfactant and the inorganic precursor. In this work, we have used the surfactant cetyltrimethylammonium bromide (CTAB) as a structure directing agent, L-malic acid as a chelating agent, along with Al(III) and benzene 1,3,5-tricarboxylate (BTC) as framework building blocks (Scheme 1). The hydrothermal reaction of $Al(NO_3)_2.9H_2O$, BTC and HF at 220 °C resulted as-synthesized MIL-110, $Al_8(OH)_2\{(OH)_3(H_2O)_3\}$ $[BTC]_3 \cdot nH_2O$ which is reported by Ferey et al.[21h] The honeycomb like network of MIL-110 with hexagonal channels of dimension 16 Å, built up by the connection of octahedrally coordinated aluminium octameric motifs with the BTC linker (Figure 1).
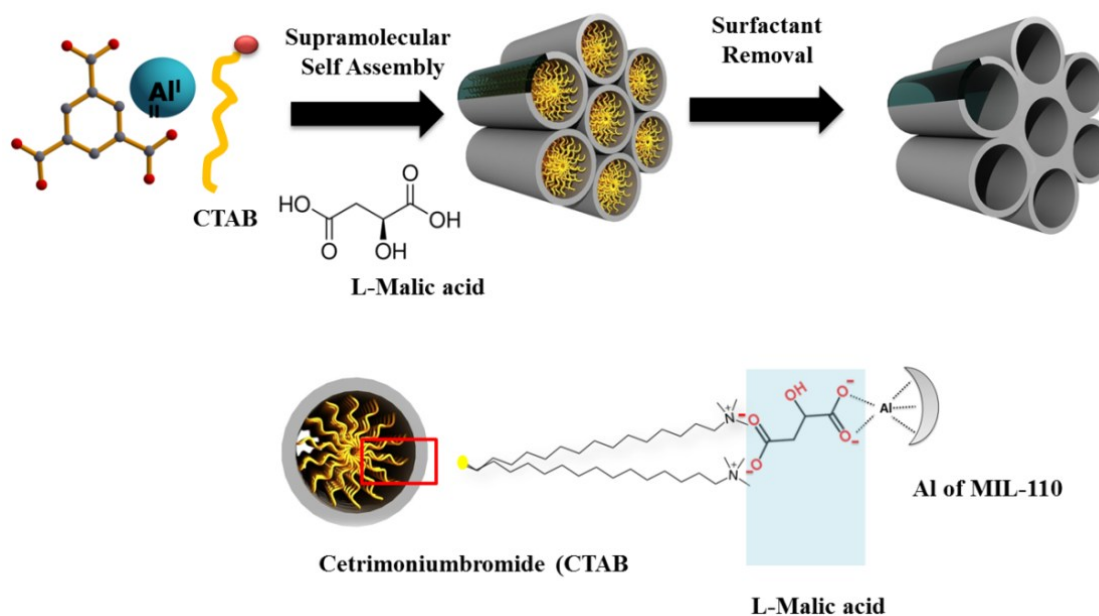
Scheme1 Schematic showing, synthesis of ordered (hierarchically micro/meso) porous MMIL-110 (Al) based on supramolecular template method.
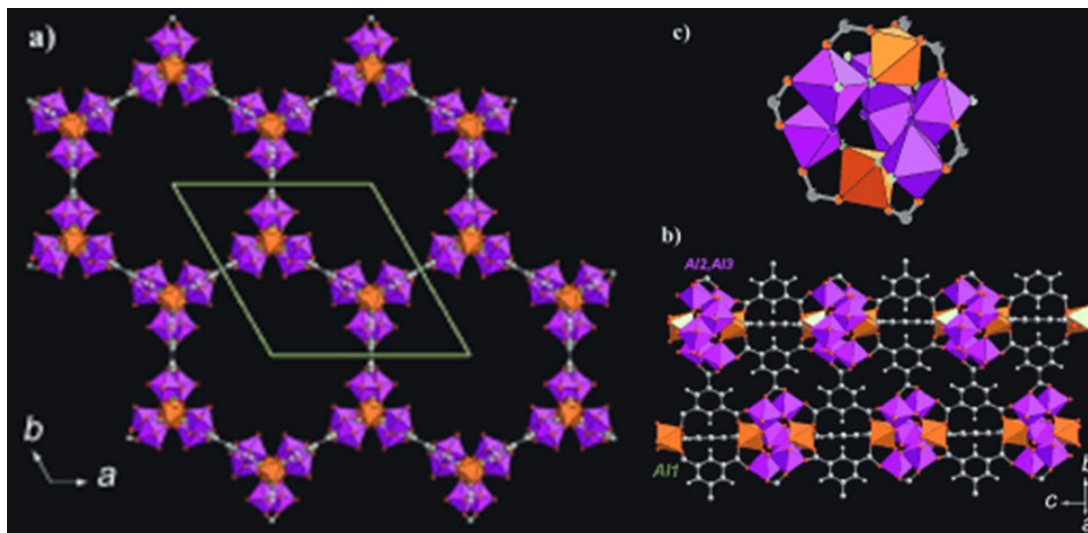
Figure 1 View of a) the structure of MIL-110 along *c*, showing the hexagonal channels and b) along *a*, showing the channel wall of connected aluminium clusters, c) linked through the trimesate ligand (btc). c) The inorganic cluster consists of 8 octahedral aluminium, 2 Al(1) (orange) and 6 Al(2,3) (purple). The Al(1) is connected to Al(2,3) through corner-bridging μ_2-OH (green), while Al(2,3) is bonded to edge-bridging μ_2-OH (blue) and terminal η_1-H$_2$O or η_1-OH (yellow) (reproduced from ref 21f).

Nine carboxylate groups cap the octamers linking the aluminium octahedral, which can be formulated as Al$_3$(OH)$_3$ and AlO$_2$(OH)$_3$(H$_2$O)$_2$ or AlO$_2$(OH)$_4$ (Figure 1). The structure is microporous as revealed by the N$_2$ adsorption isotherms at 77K; BET surface area is around 1400 m^2/g. First we have prepared mesoporous MMIL-110 by the reaction of Al(NO$_3$)$_3$, BTC in presence of cationic surfactant CTAB adopting the similar reaction conditions as of assynthesized MIL-110 mentioned in the experimental part. The isolated product has been characterized by IR, elemental analysis and XRD that are corroborating the similar structure as of as-synthesized MIL-110. Field emission scanning electron microscope (FESEM) and transmission electron microscope (TEM) studies were provided insights of the morphology and detailed structural characteristics of the MMIL-110. FESEM images as shown in Figure 2(a-b) show nanoscale perfect octahedron architecture of MMIL-110 of size in the range of 50-100 nm. TEM images also indicate octahedron morphology and high resolution images clearly reveal the existence of ordering with the spacing between the layers is about 2.5 nm and the wall thickness of around 1.5 nm (Figure 2c). This suggests clear mesoporous ordering in the framework. Here CTAB is playing a dual role; (a) supramolecular template for generating mesoporous structure and (b) capping agent for nanoscale growth of MMIL-110.
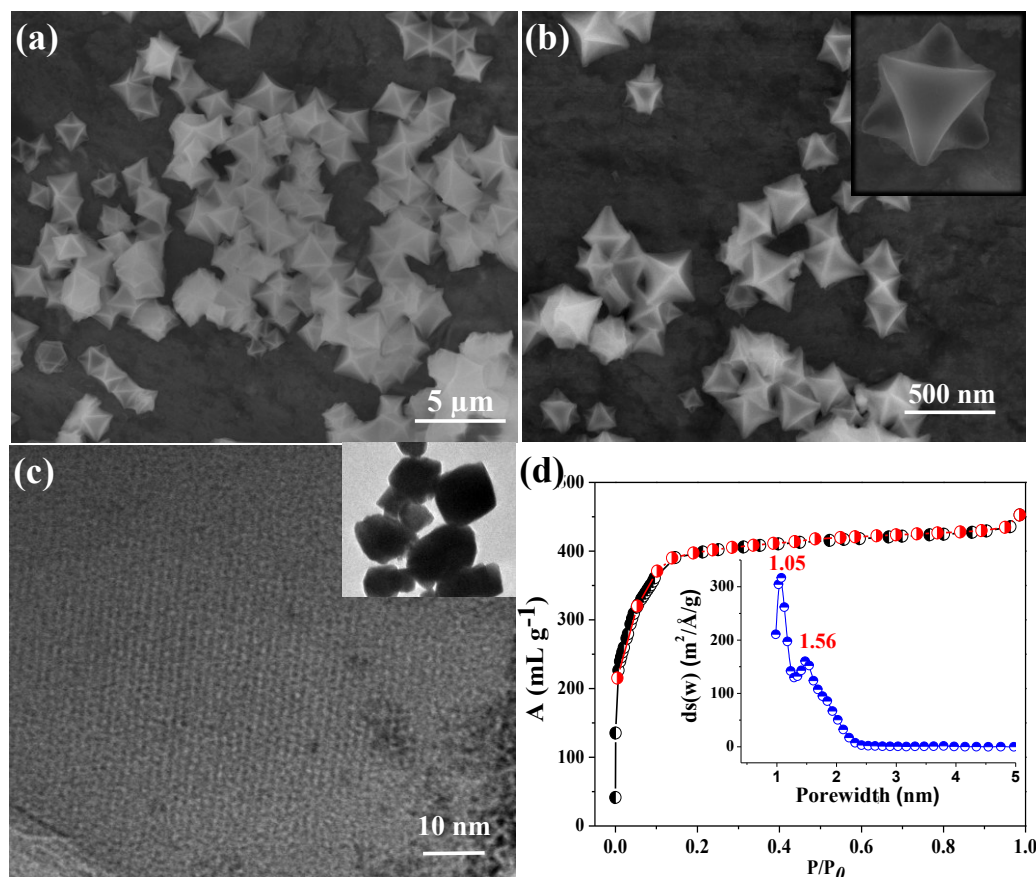
Figure 2 (a-b) FESEM images of MMIL-110 showing octahedron morphology in nanoscale; (c) HRTEM image showing ordered meso porous nature, Inset TEM image showing a octahedron morphology; (d) N_2 adsorption (black)-desorption (red) at 77 K and inset pore size obtained using NLDFT method.

Surprisingly, the N_2 adsorption-desorption isotherm for MMIL-110 at 77K shows a typical type-I profile without any hysteresis (Figure 2d). The specific surface area calculated by Brunauer-Emmet-Teller (BET) is about 1020 m^2/g and the pore volume is 0.95 cm^3/g. Pore size calculated from the Non-local density functional theory (NLDFT) method, reveals two types of pores centered at 1.07 and 1.55 nm corresponding to micropore region, similar to assynthesized MIL-110. These results suggest that surfactant CTAB alone cannot produce a stable mesoporous framework. This is probably due to weak interaction of cationic surfactant CTAB with the MOF precursor in particular with Al(III). Activation at high temperature mesoporous order of the structure is lost. Similar observation was reported by Zhou *et al.*[9b] and then we modified our synthetic approach to obtain mesoporous MMILs-110 with tunable porosity. Here we have used L-malic acid, which acts as a mediator and bridges between the surfactant and metal ions Al(III) through columbic attraction and

coordination interaction respectively (Scheme 1). Therefore, L-malic acid will act as a contemplate and an external chelating agent for the formation of a stable mesoporous framework through considerable interaction between the surfactant template and framework building blocks. By varying L-malic acid content, we have isolated four different MMILs, which we have designated as MMIL-110a, MMIL-110b, MMIL-110c and MMIL-110d. Figure 3 show N_2 adsorption-desorption isotherms for all four samples that exhibit combination of typical type-I and type-IV isotherms.
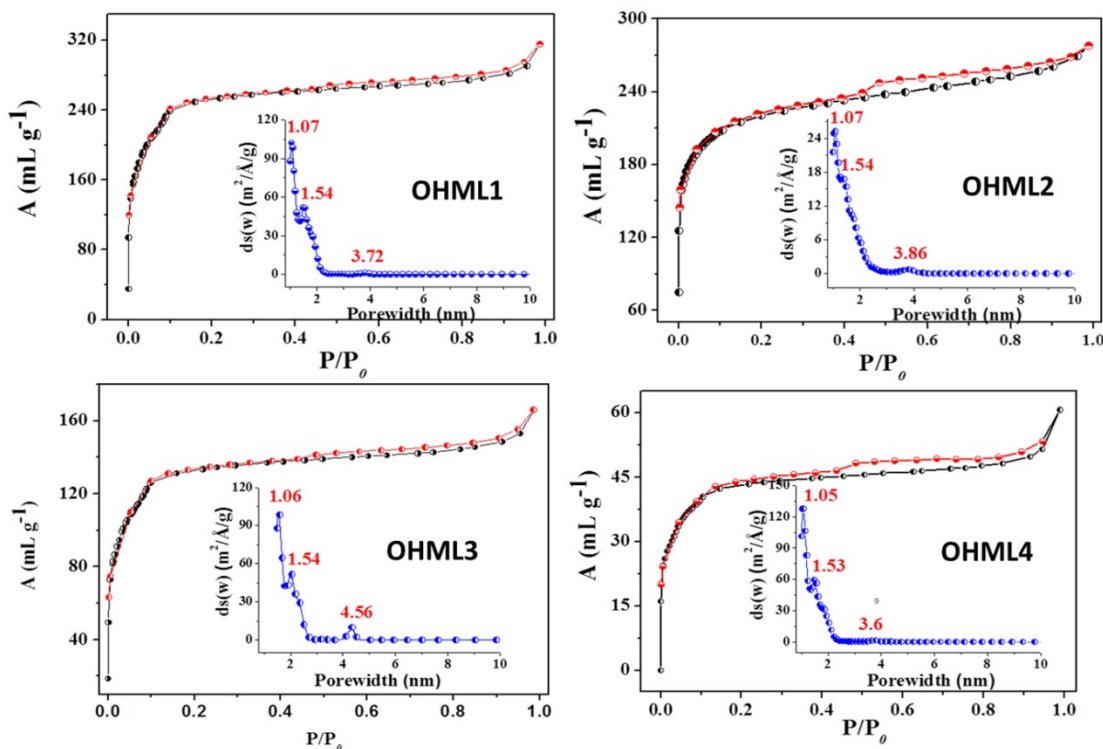
Figure 3 N_2 adsorption (black)-desorption (red) isotherms for MMIL-110a-d; (a) MMIL-110a; (b) MMIL-110b; (c) MMIL-110c: (d) MMIL-110d, Inset showing corresponding pore size distribution obtained from NLDFT method.

The H1 type broad hysteresis loop at higher relative pressure (P/Po >4) indicates capillary condensation of N_2 within the uniform mesopores in the MMILa-d. The textural parameters for all the compounds are compiled in Table1. The BET surface areas for MMIL a-d are 829, 716, 438 and 190 m^2/g respectively. The steep uptake at low pressure regions in all the compounds suggests high degree of microporosity in all the samples. The pore size distribution obtained from NLDFT method are given in the insets of Figure 3 reveal that mesopore diameter increases with increasing content of L-malic acid and for MMIL-110c the mesopore diameter is 4.31 nm and then decreases to 3.6 nm in MMIL-110d with increasing the L-malic acid. It is

worth to note that in all cases micropore diameter remains same as of MMIL-110. These results suggest that by using a cooperative template mesoporous MOFs with different pore sizes have been successfully fabricated in which mesopore walls consists of micropores of MIL-110. It is noteworthy that the similar mesoporous MIL-110 can also be obtained with other chelating agents like citric acid or mucic acid.

Table 1 Different synthesis and textural parameters for MMILs-110.

Sample	Amount of L-Malic Acid (mg)[a]	Lower angle/d space (nm) from PXRD[b]	S_{BET}[c] (m²/g)	S_{Lang}[d] (m²/g)	V_t[e] (cm³/g)	Micropore Diameter[f] (nm)	Mesopore diameter[f] (nm)
MMIL-110a	10	3.6	829	1128	0.86	1.07,1.57	3.72
MMIL-110b	30	3.8	716	945	0.75	1.07,1.54	3.86
MMIL-110c	60	4.4	438	675	0.72	1.06,1.54	4.31
MMIL-110d	100	3.3	190	289	0.65	10.6,1.53	3.6

(a) amount of chelating agent, L-malic acid in mg
(b) Mesoscale ordering calculated from lower angle powder XRD
(c) S_{BET} is the BET specific surface area.
(d) S_{Lang} is the Langmuir specific surface area calculated from the N_2 adsorption isotherm
(e) V_t is the total specific pore volume determined by using the adsorption branch of the N_2 isotherm at P/P_0=0.99.
(f) The pore diameter is determined from the local maximum of the NLDFT distribution of pore diameters obtained in the adsorption branch of the N_2 isotherm

FESEM images of the MMIL-110a-d samples show similar octahedron morphology of size in the range of 50-100 nm (Figure 4a). TEM images further confirm the existence of octahedron morphology. The high resolution TEM image of MMIL-110c sample shows ordered meso channels of size 4.4 nm with the wall thickness of 1.5 nm (Figure 4b-d). This mesopore size for MMIL-110c is consistent with mesopore size obtained from N_2 adsorption profile. In general MOFs are sensitive to the high energy electron beam, the clear image suggest this MMOFs are quite stable.
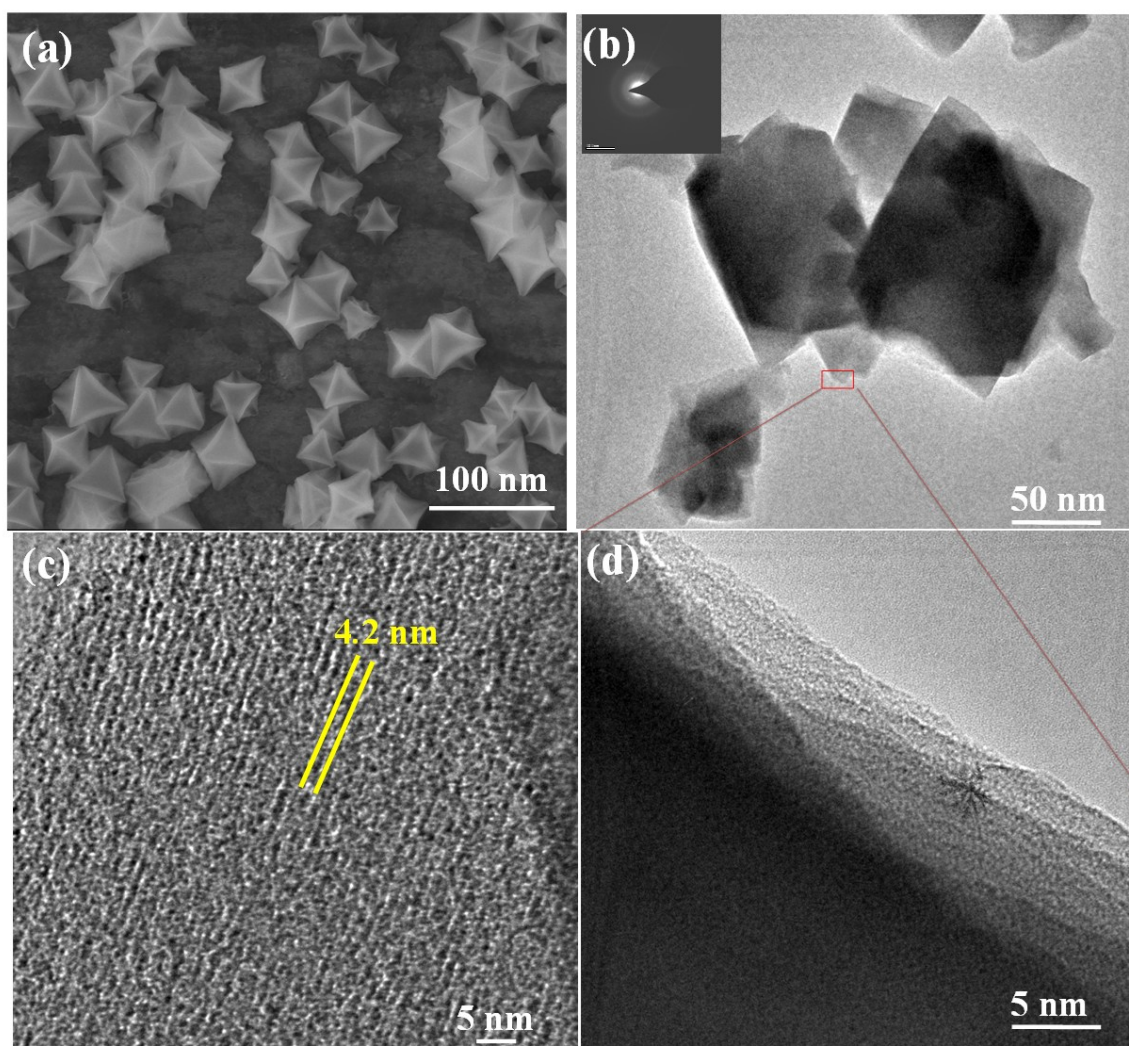
Figure 4 (a) FESEM and (b) TEM images of MMIL-110c. (c), (d) HRTEM images showing ordered meso porous nature with edges layered nature for MMIL-110c.

PXRD patterns of all the MMILs show strong diffraction and corroborates well with the simulated pattern of MIL-110 (Figure 5). Although, difference of intensities of some of the peaks can be attributed to presence of chelating agent L-malic acid. All the samples exhibit low angle diffraction peak, indicating meso-structure ordering in the systems (Figure 5 Inset). The low angle peaks indexed with Debye-Scherrer formula for MMIL-110a, MMIL-110b, MMIL-110c and MMIL-110d which corresponds to 3.3, 3.6, 4.4 and 3.8 nm respectively consistent with the pore size distribution obtained from N_2 adsorption profiles and also from the TEM analysis (Table 1).
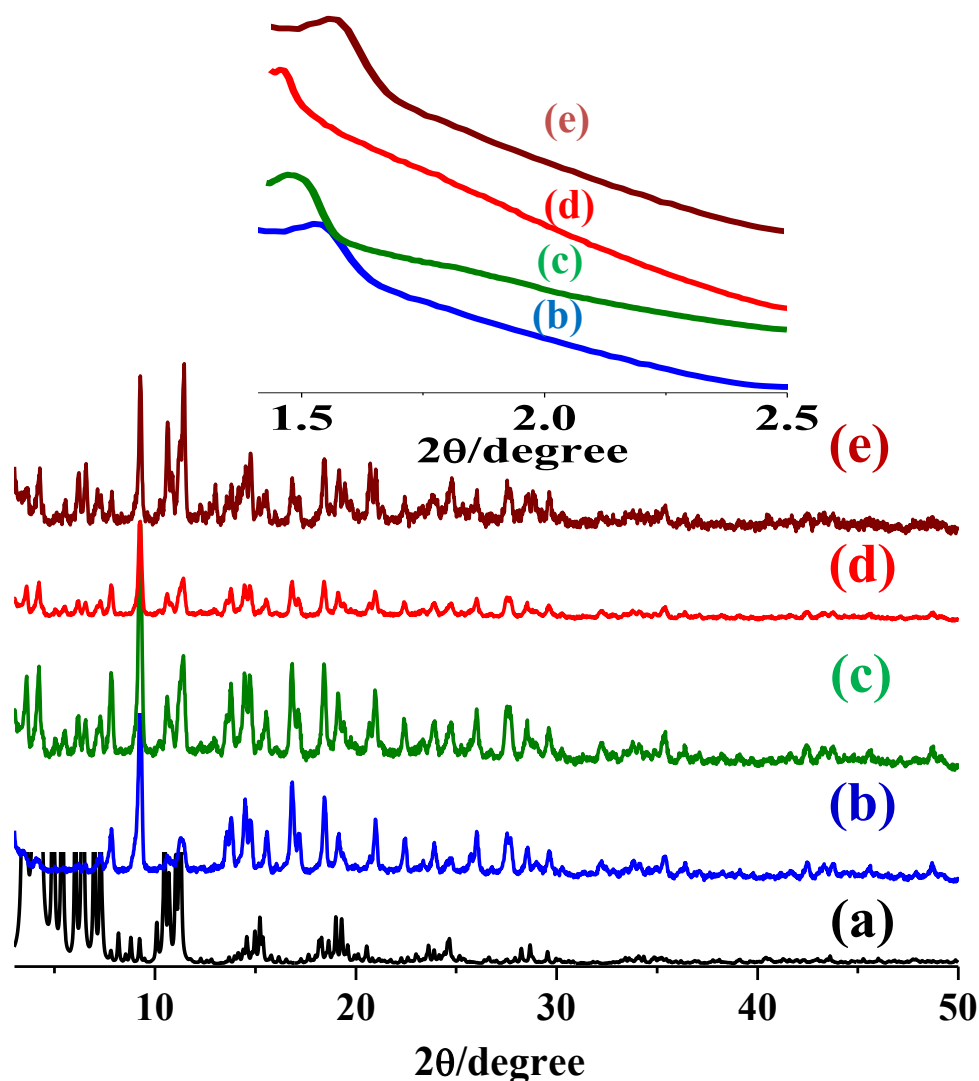
Figure 5 Powder XRD patterns of MMIL-110s (a) MMIL-110; (b) (b) MMIL-110a; (c) MMIL-110b; (d) MMIL-110c: (d) MMIL-110d, Inset showing lower angle XRD patterns of corresponding MMIL-110s

Above discussion clearly suggest that surfactant CTAB alone cannot produce a stable mesoporous MOF as the interaction between the MOF precursor and surfactants is much weaker. However, CTAB in combination with L-malic acid generate a cooperative template that exhibited excellent structure directing effect for producing a stable mesoporous MOFs. L-malic acid though chelation with Al^{III} and interaction with CTAB produce a strong template. It is noteworthy that surfactant to chelating agent ratio has a substantial effect on the mesopore formation as the amount of L-malic acid increases the mesoporosity increases and then decreases and optimum ratio is 0.77. It is noteworthy that with further increasing this ration it produces another phase as observed from the powder pattern.

4.2.4.2. Dye Scavenging Experiments

We anticipated that the hierarchical porous nature of our MMIL-110c would also provide a good mix of micro and mesopores to scavenge dyes of different molecular dimensions. In a typical dye scavenging experiment, 10 mg of MMIL-110c was added to a 10^{-6} molar dye solution in water and stirred for 12 hours at room temperature. The solution was filtered and the filtrate was collected for UV-visible absorption experiments. The UV-visible absorption profile of the respective dye solutions in water (10^{-6} M) was monitored and gave characteristic absorption peaks at 269 and 492 nm for Acridine orange (AO), 555nm for Rhodamine B (RhB) and 664nm for Methylene blue dye (MB) (Figure 6 a, b, c).
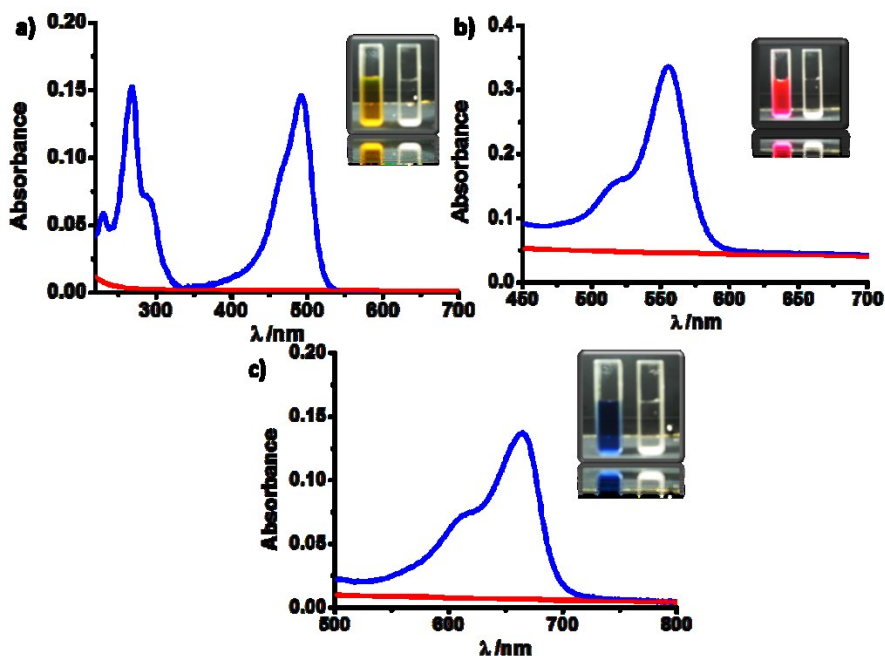
Figure 6 UV absorption spectra of a) Acridine orange dye before MMIL-110c addition (blue) and after MOF addition (red) b) Rhodamine B dye before MMIL-110c addition (blue) and after MMIL-110c addition (red) c)) Methylene blue dye before MMIL-110c addition (blue) and after MMIL-110c addition (red) Inset: Colour of the respective dye solutions before and after scavenging.

Interestingly the dye scavenged solution by the MMIL-110c showed no visible absorption peaks at the corresponding areas of the dye absorption. This observation was uniform for all the three dye scavenged solutions. This proves that our hierarchical MMIL-110c is capable of scavenging dye molecules completely from its aqueous solution confirmed by the total absence of dye absorption peaks in the scavenged

solution (Figure 6a, b, c). The comparison of the solution colour of dye molecules before and after scavenging further asserts our claim where the colour of the aqueous solution containing the individual dye molecule becomes completely colourless after scavenging by the MMIL-110c. The time dependence of scavenging was also studied and it revealed that the time required for a static system consisting of 10 mg MMIL-110c in 10^{-6}M aqueous dye solution to be scavenged takes around 24 hours (Figure 7).
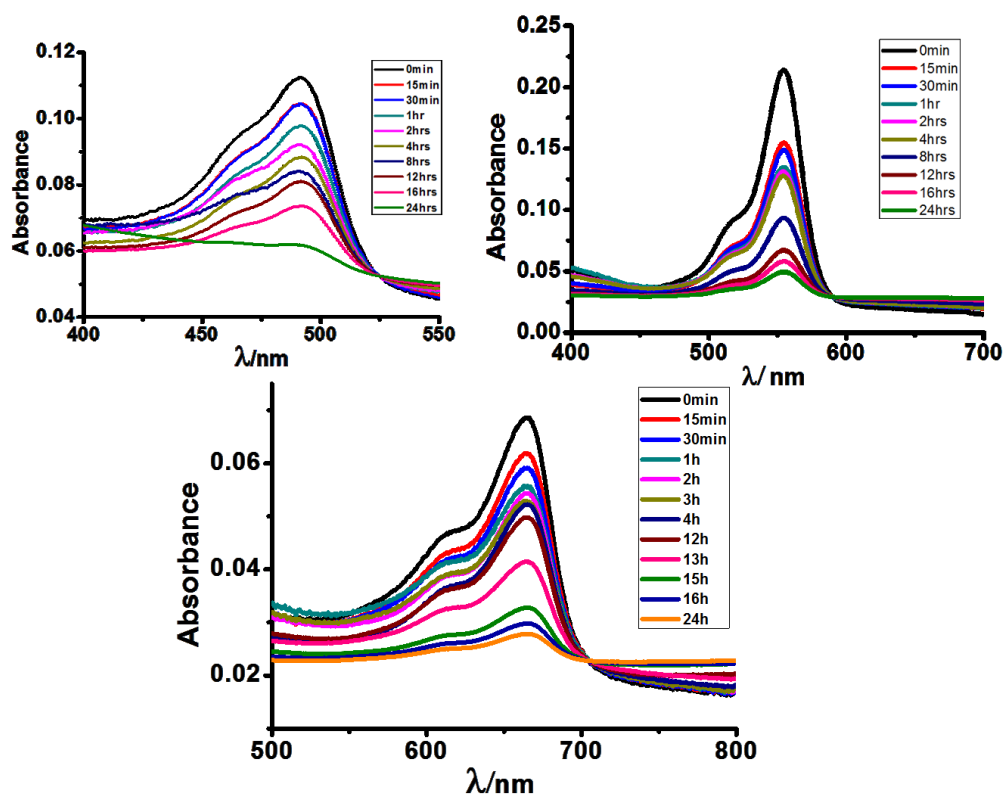
Figure 7 Time dependant dye scavenging study: UV spectra of (a) Acridine Orange Dye (b) Rhodamine B dye and (c) Methylene Blue dye

4.2.4.3 Dye encapsulation: Effect on porosity

We then envisioned that blocking the pores of MMIL-110c framework with these dyes of different molecular dimensions would help in the characterization of the hierarchical nature of the pores. The framework structure doped with RhB dye molecule (molecular dimensions= $1.59 \times 1.18 \times 0.56$ nm) revealed microporous nature as realized from N_2 adsorption isotherm measured at 77K, 1 atm pressure. This is because the RhB dye molecules can only selectively enter the mesopores in system leaving inherent

micropores MMIL-110c vacant which gives rise to the type I nature of the curve with a reduced uptake of 126ml/g (Figure 8b).
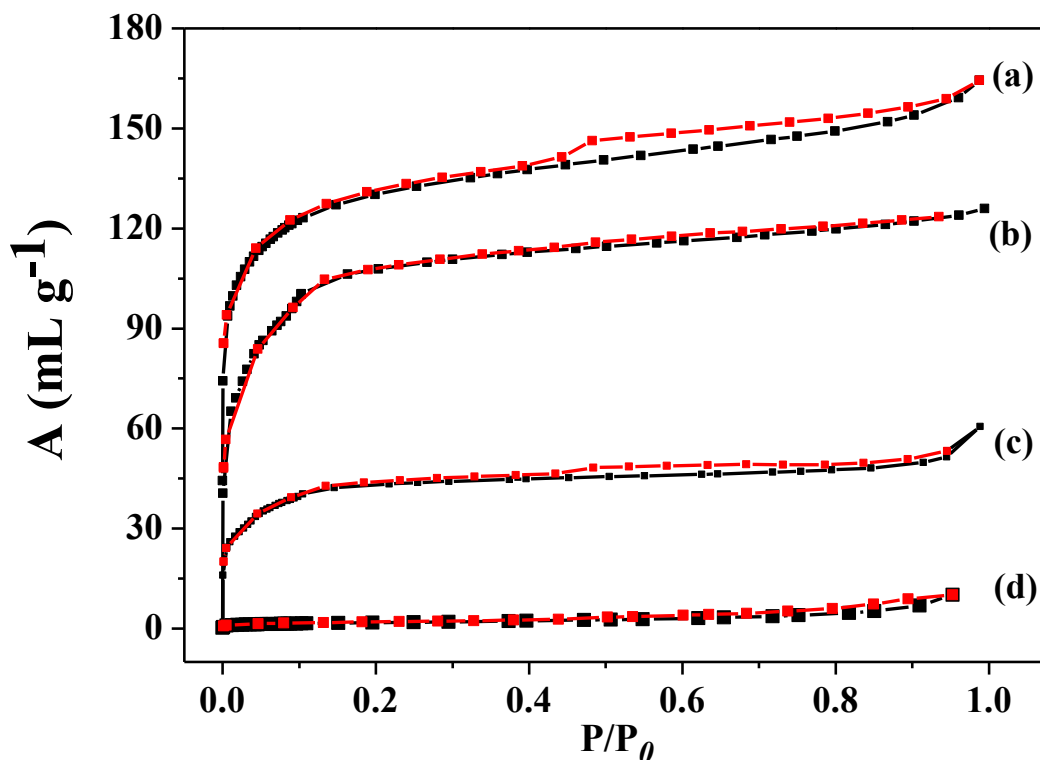
Figure 8 N_2 adsorption (black)-desorption (red) isotherms of MMIL-110c : (a) pure MMIL-110c; (b) RhB@ MMIL-110c; (c) AO@ MMIL-110c; (d) RhB@AO@ MMIL-110c

On doping the framework with a dye of smaller molecular dimension such as AO, the N_2 adsorption isotherm at the same temperature and pressure revealed a Type IV curve with a reduced uptake of 56ml/g at 77K. This reduced uptake at the low pressure region indicating that the AO dye molecules are filling up the micropores (Figure 8c). However it is inconclusive whether the AO dye molecules are also entering the mesopores after the filling up of the micropores. It was now expected that on doping the framework with both dyes at the same time would reduce the N_2 gas uptake due to the blocking of both the micro and mesopores. In subsequent experiments, the MOF was first doped with RhB dye molecules so that the mesopores are blocked and the resultant composite was further doped with AO dye molecules to block the micropores. N_2 adsorption experiments were carried out at 77K and 1 atm pressure to reveal a type II profile with a much reduced uptake of 29mL/g (Figure 8d). This was conclusive evidence that there exists a hierarchical nature of micro and mesopores MMIL-110c. The N_2 adsorption data are given in Table 2.

Table 2 Dye encapsulation and textural parameters based on nitrogen adsorption of MMIL-110c.

Sample	Nature of N_2 Isotherm	Amount of N_2 Uptake (mL/g)
MMIL-110c	IV	164
RhB @MMIL-110c	I	126
AO@ MMIL-110c	IV	56
AO-RhB@ MMIL 110c	II	29

4.2.4.4 Light Harvesting Application of AO-RhB@MMIL-110c

These interesting results of selective dye encapsulation in micro and mesopores based on their size prompted us to study the possibility of Förster resonance energy transfer (FRET) process from acridine to Rhodamine B molecules present in MOF. AO@MMIL-110c shows absorption and emission maxima at 490 nm and 530 nm respectively, whereas RhB@MMIL-110c exhibits absorption and emission maxima at 550 nm and 590 nm respectively.   Figure 9a shows sufficient spectral overlap (emission of AO and absorption of RhB) suggesting that AO and RhB can act as donor and acceptor respectively for FRET process, where MMIL-110c nano-octahedron would act as a platform to encapsulate different dyes in two different pores based on confinement and required geometry and distance for efficient exciton migration from donor to acceptor.
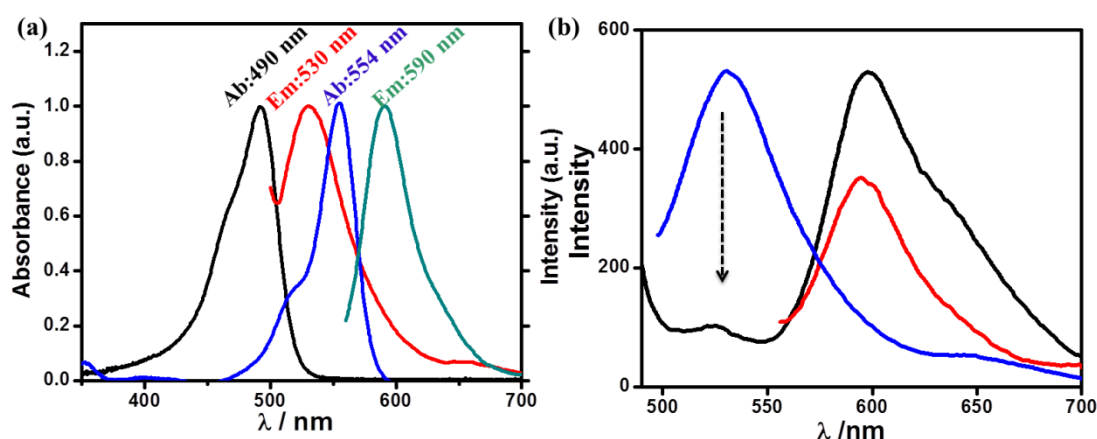
Figure 9 (a) Overlap spectra of AO and RhB; Absorbance of AO (black), RhB (blue) and emission of AO (red), RhB(cyan). (b) Emission spectra of AO@MMIL-110c (blue) and FRET plot of AO-RhB@MMIL-110c excited at 470 nm (black) and direct excitation at 540 nm.

Initially, activated MOF is stirred with aq. RhB for 6hrs so that all the meso channels are filled up to form RhB@MMIL-110c, leaving micro channels unaffected. Sample is centrifuged and washed with ethanol and THF several times to remove any dye molecules from the surface of MOF. Selective filling of mesopores is supported by N_2 adsorption isotherms, where the mesoporous nature of the MOF is intact but with reduced contribution from mesopores compared to assynthesized MOF. Now the RhB@MMIL-110c is stirred with AO solution that can selectively fill the micro channels left over. Sample is centrifuged and washed with THF several times and dried under vacuum so the resulting sample designated as AO-RhB@MMIL-110c. In order to validate the proposal of FRET process between AO and Rhb encapsulated in MOF, AO-RhB@MMIL-110c is excited at 470 nm, surprisingly, rise in the emission at 590 nm is observed with concomitant quenching of the emission from AO at 540 nm (Figure 9b) suggesting the funneling of excitation energy from AO present in micropores to RhB in mesopores.
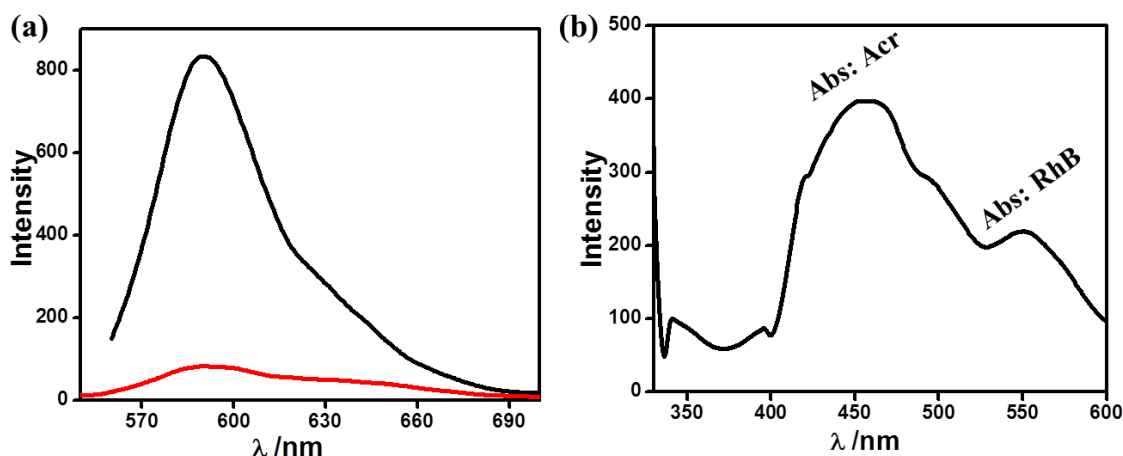
Figure 10 (a) Emission spectra of RhB@MMIL-110c different excitations; black (Ex: 550 nm and red (Ex: 480 nm). (b) Excitation spectra of AO-RhB@MMIL-110c collected at 590 nm.

Also, direct excitation of AO-RhB@MMIL-110c at 550 nm shows lower intensity compared to the excitation at 470 nm further supports the energy transfer process from AO to RhB. Excitation of RhB@MMIL-110c at 470 nm shows no emission (Figure 10a) in contrast to 550 nm excitation. Energy transfer is further confirmed from excitation spectra of composite collected at 590 nm shows peaks correspond to AO and RhB in the composite and maxima is observed to be at 470 nm which is clearly

indicating the long wavelength emission of composite is through excitation energy transfer rather than direct excitation (Figure 10b).

FRET process is further confirmed by time resolved fluorescence spectroscopy studies. Life time of AO-RhB@MMIL-110c detected at 530 nm is observed to be shorter (τ_{avg} = 3.38 ns) than AO@MMIL-110c (τ_{avg} = 4.57 ns) (Figure 11). Also, the life time of Rhodamine B in composite, AO-RhB@MMIL-110c observed at 590 nm is longer (τ_{avg} = 3.48 ns) than Rhb@MOF (τ_{avg} = 2.73 ns). These results clearly indicate the process of excitation energy transfer from acridine orange to Rhodamine B in the composite, AO-RhB@MMIL-110c.
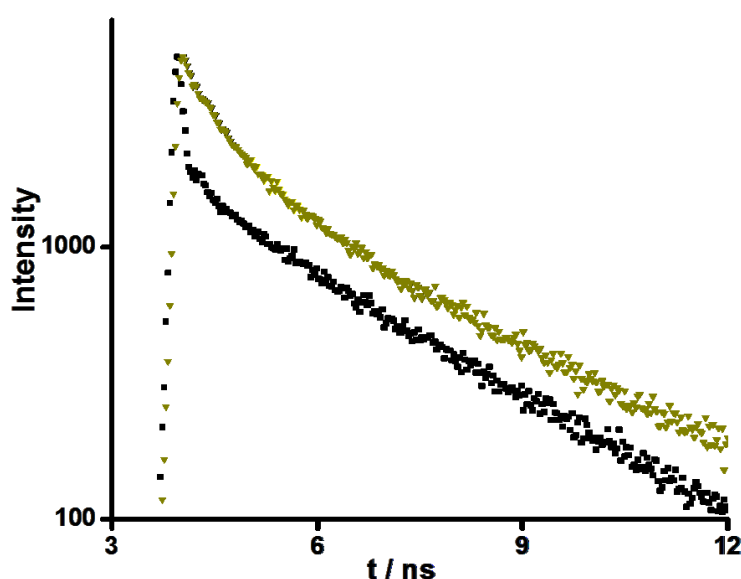
Figure 12 Life time plot of RhB@MMIL-110c and AO-RhB@MMIL-110c detected at 590 nm.

4.2.5 Conclusions

In conclusion, we have successfully demonstrated a novel approach for synthesis of hierarchically ordered MMOFs by the co-assembly of MOF building units and surfactant molecules. The rational design involving additional chelating agent provides higher stability of the co-assembly through strong electrostatic interactions of MOF framework with mesoporous walls. Further, we showed fine-tuning of mesopore size by varying the amounts of chelating agent. The elegant design can be extended to a range of MOFs with pore size throughout the micropore regime by selection of appropriate organic linkers and metal ions. Careful selection of organic linker allows size selective encapsulation of different photoactive dyes along micro/meso channels. Further,

encapsulation of chromophoric donor and acceptor molecules along periodic micro/meso channels extended the applicability of MMOF for funneling excitation energy and efficient light harvesting applications. Moreover, choice of fluorescent organic linkers would further extend MMOFs for color tuning applications through subsequent funneling of excitation energy via Försters resonance energy transfer process. Superior processibility, robust framework structure and encapsulation of wide range of photoactive dyes in these MMOFs would pave the way for fabrication of novel advanced photoactive materials for optoelectronics and solar cells.

4.2.6 References

1) a) S. L. James, *Chem. Soc. Rev.* **2003**, *32*, 276; b) J. J. I. V. Perry, J. A. Perman, M. J. Zaworotko, *Chem. Soc. Rev.* **2009**, *38*, 1400; c) D. J. Tranchemontagne, J. L. Mendoza-Cortes, M. O' Keeffe, O.M. Yaghi, O. M. *Chem. Soc. Rev.* **2009**, *38*, 1257. d) H. C. Zhou, J.R. Long, O.M. Yaghi, O. M. *Chem. Rev.* **2012**, *112*, 673; e) R. A. Smaldone, R. S. Forgan, H. Furukawa, , J. J. Gassensmith, A. M. Z. Slawin, O. M. Yaghi, J. F. Stoddart, *Angew. Chem. Int. Ed.* **2010**, *49*, 8630; f) S. Kitagawa, R. Kitaura, S. Noro, *Angew. Chem. Int. Ed.* **2004**, *43*, 233.

2) a) H. Furukawa, K. E. Cordova, M. O' Keeffe, O. M. Yaghi, *Science* **2013**, *341*, 974; b) K. Konstas, T. Osl, Y. Yang, M. Batten, N. Burke, A. J. Hill, M. R. Hill, *J. Mater. Chem.* **2012**, *22*, 16698; c) R. Banerjee, *J. Indian Chem. Soc.* **2012**, *89*, 1197; d) S. Ma, H.-C. Zhou, *Chem. Commun.* **2010**, *46*, 44.

3) a) Z. Zhang, Y. Zhao, Q. Gong, Z. Li, J. Li, *Chem. Commun.* **2013**, *49*, 653; b) I. Erucar, G. Yilmaz, S. Keskin, *Chem. - Asian J.* **2013**, *8*, 1692; c) J. Jiang, *Curr. Opin. Chem. Eng.* **2012**, *1*, 138; d) Z.-Y. Gu, C.-X. Yang, N. Chang, X.-P. Yan, *Acc. Chem. Res.* **2012**, *45*, 734; (e) Y. Liu, W. Xuan, Y. Cui, *Adv. Mater.* **2010**, *22*, 4112; f) J.-R. Li, R. J. Kuppler, H. C. Zhou, *Chem. Soc. Rev.* **2009**, *38*, 1477; f) T. K. Maji, R. Matsuda, S. Kitagawa, *Nat. Mater.* **2007**, *6*, 142.

4) a) P. Valvekens, F. Vermoortele, V. D. De, *Catal. Sci. Technol.* **2013**, *3*, 1435; b) H. R. Moon, D.-W. Lim, M. P. Suh, *Chem. Soc. Rev.* **2013**, *42*, 1807; c) H.-L. Jiang, T. A. Makal, H.-C. Zhou, *Coord. Chem. Rev.* **2013**, *257*, 2232.

5) a) C.-Y. Sun, C. Qin, X.-L. Wang, Z.-M. Su, *Expert. Opin. Drug. Deliv.* **2013**, *10,* 89; b)R. J. Della, D. Liu, W. Lin, *Acc. Chem. Res.* **2011**, *44*, 957; c) M. Vallet-Regi, F. Balas, D. Arcos, *Angew. Chem. Int. Ed.* **2007**, *46*, 7548; d) P.

Horcajada, R. Gref, T. Baati, P. K. Allan, G. Maurin, P. Couvreur, G. Férey, R. E. Morris, C. Serre, *Chem. Rev.* **2011**, *112*, 1232.

6) a) L. E. Kreno, K. Leong, O. K. Farha, M. Allendorf, D. R. P. Van, J. T. Hupp, *Chem. Rev.* **2012**, *112*, 1105; b) Y. Cui, Y. Yue, G. Qian, B. Chen, *Chem. Rev.* **2012**, *112*, 1126; c) J. Rocha, L. D. Carlos, F. A. A. Paz, D. Ananias, *Chem. Soc. Rev.* **2011**, *40*, 926; d) M. D. Allendorf, C. A. Bauer, R. K. Bhakta, R. J. T. Houk, *Chem. Soc. Rev.* **2009**, *38*, 1330; e) K. Jayaramulu, P. Kanoo, S. J. George, T. K. Maji, *Chem. Commun.* **2010**, *46*, 7906.

7) a) W. Xuan, C. Zhu, Y. Liu and Y. Cui, *Chem. Soc. Rev.* **2012,** 41, 1677; b) C. M. A. Parlett, K. Wilson and A. F. Lee, *Chem. Soc. Rev.* **2013,** 42, 3876; c) Q.-R. Fang, T. A. Makal, M. D. Young, H.-C. Zhou, *Comment. Inorg. Chem.* **2010**, *31*, 165.

8) a)Y.Q. Lan, H.L. Jiang, S.L. Li and Q. Xu, *Adv. Mater.* **2011,** 23, 5015; b) L. Song, J. Zhang, L. Sun, F. Xu, F. Li, H. Zhang, X. Si, C. Jiao, Z. Li, S. Liu, Y. Liu, H. Zhou, D. Sun, Y. Du, Z. Cao and Z. Gabelica, *Energy Environ. Sci.* **2012**, *5***,** 7508.

9) a) L.-G. Qiu, T. Xu, Z.-Q. Li, W. Wang, Y. Wu, X. Jiang, X.-Y. Tian, L.-D. Zhang, *Angew. Chem.* **2008**, *120*, 9629; b) L.-B. Sun, J.-R. Li, J. Park, H.-C. Zhou, *J. Am. Chem. Soc.* **2012**, *134*, 126; c) L. Peng, J. Zhang, J. Li, B. Han, Z. Xue, G. Yang, *Chem. Commun.* **2012**, *48*, 8688; d)Y. Zhao, J. Zhang, B. Han, J. Song, J. Li, Q. Wang, *Angew. Chem. Int. Ed.* **2011**, *50*, 636.

10) a) Y. J. Sa, K. Kwon, J. Y. Cheon, F. Kleitz, S. H. Joo, *J. Mater. Chem. A* **2013**, *1*, 9992; b) D. Petkovich, A. Stein, *Chem. Soc. Rev.* **2013**, *42*, 3721; c) A. Inayat, B. Reinhardt, H. Uhlig, W.-D. Einicke, D. Enke, *Chem. Soc. Rev.* **2013**, *42*, 3753; d)S. S. Park, S.-W. Chu, C. Xue, D. Zhao, C.-S. Ha, *J. Mater. Chem.* **2011**, *21*, 10801; e) S. R. Gajjela, K. Ananthanarayanan, C. Yap, M. Gratzel, P. Balaya, *Energy Environ. Sci.* **2010**, *3*, 838; f) Z.-Y. Yuan, B.-L. Su, *J. Mater. Chem.* **2006**, *16*, 663.

11) a) C. M. A. Parlett, K. Wilson, A. F. Lee, *Chem. Soc. Rev.* **2013**, *42*, 3876; b)A. B. Murcia, *ISRN Nanotechnol.* **2013**, 257047; c) W. Ou, Y. Yan, *Huagong Jinzhan* **2009**, *28*, 1766-1770, 1776; d) J. R. Jones, P. D. Lee, L. L. Hench, *Philos. Trans. R. Soc. London, Ser. A* **2006**, *364*, 263; e) M. W. Anderson, S. M. Holmes, R. Mann, P. Foran, C. S. Cundy, *J. Nanosci. Nanotechnol.* **2005**, *5*, 92.

12) S. Sandhya, K. Sarayu, K. Swaminathan, *Bioresour. Tech.* **2008**, *99*, 5793.

13) a) W. J. Rieter, K. M. Pott, K. M. L. Taylor, W. Lin, *J. Am. Chem. Soc.* **2008**, *130*, 11584; (b) A. Carne, C. Carbonell, I. Imaz, D. Maspoch, *Chem. Soc. Rev.* **2011**, *40*, 291; (c) K. Otsubo, T. Haraguchi, O. Sakata, A. Fujiwara, H. Kitagawa, *J. Am. Chem. Soc.* **2012**, *134*, 9605.

14) E. A. Fluegel, A. Ranft, F. Haase, B. V. Lotsch, *J. Mater. Chem.* **2012**, *22*, 10119.

15) a) B. D. Chandler, D. T. Cramb, G. K. H. Shimizu, *J. Am. Chem. Soc.* **2006**, *128*, 10403; b) X. Rao, Q. Huang, Y. Yang, Y. Cui, Y. Yang, C. Wu, B.Chen, G.J. Qian, *Mater. Chem.* **2012**, *22*, 3210.

16) H. Xu, F. Liu, Y. Cui, B. Chen, G. Qian, *Chem. Commun.* **2011**, *47*, 3153.

17) a) X. Zhang, Z. K. Chen, K. P. Loh, *J. Am. Chem. Soc.* **2009**, *131*, 7210; b)X. Zhang, M. A. Ballem, M. Ahren, A. Suska, P. Bergman, K. J. Uvdal, *J. Am. Chem. Soc.* **2010**, *132*, 10391; c) C. A. Kent, D. Liu, L. Ma, J. M. Papanikolas, T. J. Meyer, W. Lin, *J. Am. Chem. Soc.* **2011**, *133*, 12940; d) X. Zhang, M. A. Ballem, Z. J. Hu, P. Bergman, K. Uvdal, *Angew. Chem. Int. Ed.* **2011**, *50*, 5728; e) V. M. Suresh, S. J. George, T. K. Maji, *DOI: 10.1002/adfm.201301178.*

18) a) A. Ajayaghosh, V. K. Praveen, C. Vijayakumar, *Chem. Soc. Rev.* **2008**, *37*, 109; b) M. R. Wasielewski, *Acc. Chem. Res.* **2009**, *42*, 1910; c) B. K. An, J. Gierschner, S.Y. Park, *Acc. Chem. Res.* **2012**, *45*, 544.

19) a) A. Ajayaghosh, S. J. George, V.K. Praveen, *Angew. Chem. Int. Ed.* **2003**, *42*, 332; b) C. Devadoss, P. Bharathi, J. S. Moore, *J. Am. Chem. Soc.* **1996**, *118*, 9635; c)Y. Ishida, T. Shimada, D. Masui, H. Tachibana, H. Inoue, S. Takagi, *J. Am. Chem. Soc.* **2011**, *133*, 14280; d) M. S. Choi, T. Yamazaki, I. Yamazaki, T. Aida, *Angew. Chem. Int. Ed.* **2004**, *43*, 150.

20) a) K. V. Rao, K. K. R. Datta, M. Eswaramoorthy, S. J. George, *Angew. Chem. Int. Ed.* **2011**, *50*, 1179; b)T. Q. Nguyen, J. J. Wu, V. Doan, B. J. Schwartz, S. H. Tolbert, *Science* **2000**, *288*, 652; c) N. Mizoshita, Y. Goto, T. Tani, S. Inagaki, *Adv. Mater.* **2009**, *21*, 4798; d) G. Calzaferri, S. Huber, H. Maas, C. Minkowski, *Angew. Chem. Int. Ed.* **2003**, *42*, 3732.

21) a)Y. Mao, W. Cao, J. Li, L. Sun, X. Peng, *Chem. - Eur. J.* **2013**, *19*, 11883; b) Y. Lin, C. Kong, L. Chen, *Chem. Asian J.* **2013**, *8*, 1873; c) M. Haouas, C. Volkringer, T. Loiseau, G. Ferey, F. Taulelle, *Chem. Mater.* **2012**, *24*, 2462; d)

M. Gaab, N. Trukhan, S. Maurer, R. Gummaraju, U. Mueller, *Micropor. Mesopor. Mater.* **2012**, *157*, 131; e) M. S. Y. Parast, A. Morsali, *Inorg. Chem.Commun.* **2011**, *14*, 645; f) M. Haouas, C. Volkringer, T. Loiseau, G. Ferey, F. Taulelle, *Chem.Eur. J.* **2009**, *15*, 3139; g) C. Volkringer, M. Meddouri, T. Loiseau, N. Guillou, J. Marrot, G. Ferey, M. Haouas, F. Taulelle, N. Audebrand, M. Latroche, *Inorg. Chem.* **2008**, *47*, 11892; h) C. Volkringer, D. Popov, T. Loiseau, N. Guillou, G. Ferey, M. Haouas, F. Taulelle, C. Mellot-Draznieks, M. Burghammer, C. Riekel, *Nat. Mater.* **2007**, *6*, 760.

Chapter 5

Three-Dimensional Metal-Organic Framework with Highly Polar Pore Surface for H₂ and CO₂ Storage Characteristics
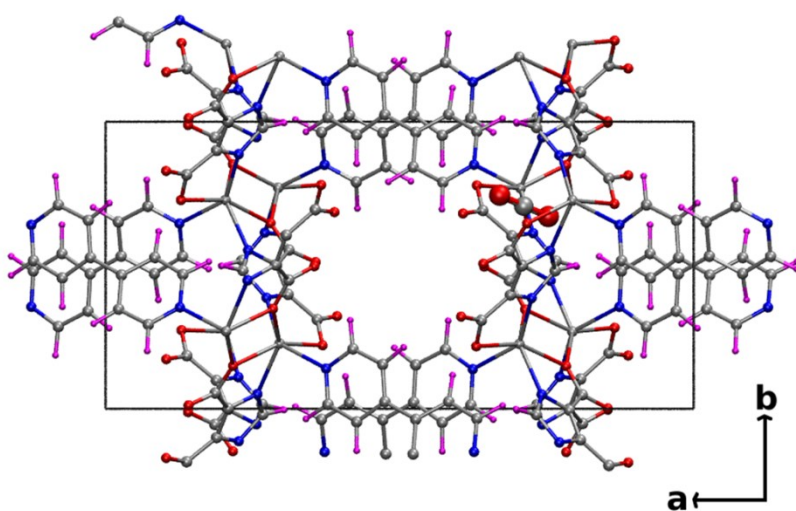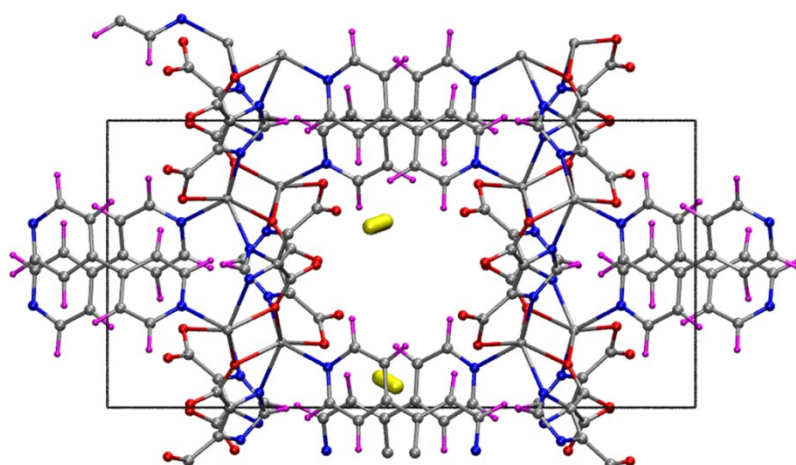
Summary

This chapter deals with synthesis, structural characterization and adsorption properties of a 3D pillared-layer metal-organic framework, $[Cd(bipy)_{0.5}(Himdc)](DMF)]_n$ (**1**), (bipy = 4,4′-bipyridine and Himdc = 4,5-imidazoledicarboxylate). The highly rigid and stable framework contains a 3D channel structure with highly polar pore surfaces decorated with the pendent oxygen atoms of the Himdc linkers. The desolvated framework $[Cd(bipy)_{0.5}(Himdc)]_n$ (**1′**) is found to exhibit permanent porosity with high H_2 and CO_2 storage capacities. Two H_2 molecules occluded per unit formula of **1′** and the corresponding heat of H_2 adsorption (ΔH_{H2}) is about ~13.3 kJ/mol, among the highest reported value in a MOF system. The high value of ΔH_{H2} stems from the preferential electrostatic interaction of H_2 with the pendent oxygen atoms of Himdc and aromatic bipy linkers as determined from first-principles density functional theory (DFT) based calculations. Similarly, DFT studies indicate CO_2 to preferentially interact electrostatically ($C^{\delta}\cdots O^{\delta-}$) with uncoordinated pendent oxygen of Himdc and also with bipy through $C\cdots O$ bonding thus rationalizing the high heat (ΔH_{CO2} ~ 35.4 kJ/mol) of CO_2 uptake. Our work unveiled that better H_2 or CO_2 storage materials can be developed through the immobilization of reactive hetero atoms (O, N) at the pore surfaces in a metal-organic framework.

5.1 Introduction

Porous coordination polymers (PCPs) or metal-organic frameworks (MOFs) are widely regarded as a promising functional materials for many applications such as gas storage,[1] catalysis,[2] separation,[3] luminescent sensing,[4] magnetic materials,[5] ion-exchange,[6] and even as delivery vehicles for controlled medicine.[7] In recent years, the synthesis and characterization of MOFs based on mixed ligand systems attracted considerable interest due to its control over: (i) structural dimensionality, (ii) interpenetration, (iii) pore size, (iv) chemical environment and the polarity of the pore in the resulting MOF structure.[8] Many groups including ours have reported the porous properties particularly H_2 storage characteristics of the modified and tunable pore surfaces in MOF composed of mixed ligand systems.[8d-i] Recent research suggest that an energy of interaction of about 22-25 kJ/mol would be enough to maintain high capacity H_2 adsorption in porous materials at 298 K in the pressure range of 1.5 – 30 bar.[9] The immobilization of unsaturated metal sites (UMCMs) in the coordination framework has been one of the successful method for the increase of heat of H_2 adsorption[10] and we have previously shown that an unsaturated alkali metal cation (K^I) has pronounced effect in the enhancement of heat of H_2 adsorption which was also supported by first principle calculations.[10a] MOFs with heterogeneous surface structure with local dipoles may enhance H_2 and CO_2 uptake capacity as they can interact more strongly than only through weak dispersion forces. Therefore, the inclusion of heteroatom or highly electronegative atom like F, O or N in the aromatic backbone or in the pore surface is another effective way to increase adsorption energies for H_2 and CO_2.[11] Recently we and other groups have showed that MOFs with fluorinated linkers have profound impact on the heat of H_2 adsorption and which has been correlated with the dipole induced dipole interactions.[11a-c] Similarly, the potential of fluorine or amine groups to interact with CO_2 is now reasonably well understood as chemisorption by amines is an effective technology for removal of CO_2 from power plant flue gases. Recent results suggest that modifying the pore surface by incorporating Lewis basic sites (-amino, -pyrimidine, -hydroxo) or organic cations enhances low pressure CO_2 uptake and isosteric heat of adsorption.[11d-l] In this context 4,5-imidazoledicarboxylic acid (H_3imdc) is a versatile linker having three pH dependent abstractable protons and may provide diverse binding mode based on two imidazole nitrogen and four carboxylate oxygen atoms.[12] Therefore, a MOF composed of H_3imdc and aromatic linkers can afford several adsorption sites for electrostatic

interactions with H_2 or CO_2 and can increase adsorption enthalpy. This chapter reports, synthesis and structural characterization of a 3D rigid metal-organic framework $[Cd(bipy)_{0.5}(Himdc)](DMF)]_n$ (1), (bipy = 4,4′-bipyridine and Himdc = 4,5-imidazoledicarboxylate) composed of mixed ligand system. It possesses high thermal stability and exhibits permanent porosity with moderate surface area. The framework shows 1.23 wt% uptake for H_2 at 77 K under high pressure with high heat of adsorption, ΔH_{ads} = 13.3 kJ/mol. Similarly, the framework exhibits 23.5 wt% and 9.0 wt% CO_2 storage capacity at 195 K and 298 K, respectively, with heat of adsorption of about ~35.4 kJ/mol. The high heat adsorption can be attributed to the favourable interactions of H_2 or CO_2 with the pore surface. Using first principles calculations, we substantiate this energy quantitatively and unearth the nature of H_2/CO_2−MOF interactions from the detailed structures determined for various sites of interactions and we demonstrate that hetero atoms (e.g. N, O) or aromatic sites on the pore surface are the favourable adsorption sites.

5.2 Experimental Section

5.2.1 Materials

All the reagents and solvents employed were commercially available and used as supplied without further purification. $Cd(NO_3)_2 \cdot 4H_2O$, 4,5-imidazoledicarboxylic acid and 4,4′-bipyridine were obtained from Aldrich Chemical Co.

5.2.2 Synthesis of [Cd(bipy)$_{0.5}$(Himdc)](DMF)]$_n$ (1)

$Cd(NO_3)_2 \cdot 4H_2O$ (0.25 mmol, 0.077 g) was dissolved in 12.5 mL acetonitrile with constant stirring. 4,5-imidazoledicarboxylic acid (H_3imdc) (0.25 mmol, 0.039 g) and 4,4′-bipyridine (bipy) (0.125 mmol, 0.0195 g) was dissolved in 12.5 mL N,N-dimethylformamide (DMF) solution and stirred well for 30 min to make a homogeneous solution. Acetonitrile solution (2 mL) of $Cd(NO_3)_2$ was slowly and carefully layered on top of the ligand solution of DMF (2 mL) using the 2 mL buffer solution of acetonitrile and DMF (1:1). After two weeks, colorless block type single crystals were grown at the junction of the two different solvents. The crystals were separated and washed with acetonitrile, which was subjected to X-ray diffraction. Yield: 80%. Anal. Calcd. for $C_{13}H_{13}N_4O_5Cd$: C, 37.44; H, 2.88; N, 13.44. Found: C,

37.35; H, 2.98; N, 13.24 %. IR (KBr, cm^{-1}): ν(N-H), 3244; ν(C-H), 2928; ν_{as}(OCO), 1602; ν_s(OCO), 1368 and ν_s(Ar$_{C=C}$)1557.

5.3 Characterization Techniques

5.3.1 Physical Measurements

The elemental analyses were carried out using a Thermo Scientific Flash 2000 CHN analyzer. IR spectrum of the compound was recorded on a Bruker IFS 66v/S spectrophotometer using KBr pellet in the region 4000-400 cm^{-1}. Thermogravimetric analysis (TGA) was carried out on METTLER TOLEDO TGA850 instrument in the temperature range of 25 - 600 °C under nitrogen atmosphere (flow rate of 50 mL/min) at a heating rate of 3°C/min. Powder X-ray diffraction (PXRD) studies in different state of the samples were recorded on a Bruker D8 Discover instrument using Cu-K_α radiation.

5.3.2 Adsorption Measurements

Adsorption studies of N_2 (77 K), CO_2 (195 and 298 K) and H_2 (77 K and 87 K) on the dehydrated samples prepared at 473 K under high vacuum, were carried out using QUANTACHROME AUTOSORB-1C analyzer. The adsorption isotherm of different solvents (like CH_3CN, EtOH and C_6H_6, at 298 K and MeOH at 293 K) were measured in the vapour state by using BELSORP-aqua volumetric adsorption instrument from BEL, Japan. In the sample chamber (~12 mL) maintained at T ± 0.03 K was placed the adsorbent sample (100-150 mg), which had been prepared at 473 K at 10^{-1} Pa for 18 hours prior to measurement of the isotherms. The adsorbate was charged into the sample tube, and then the change of the pressure was monitored and the degree of adsorption was determined by the decrease of the pressure at the equilibrium state. All operations were computer-controlled and automatic. High-pressure H_2 (77 K) and CO_2, CH_4 (298 K) sorption measurements were carried out on a fully computer controlled volumetric BELSORP-HP, BEL JAPAN high pressure instrument. All the gases used for the high pressure measurements are scientific/research grade with 99.999% purity. For the measurements, approximately 300 mg sample was taken in a stainless-steel sample holder and degassed at 493 K for a period of 18 hours under 0.1 Pa vacuum. Dead volume of the sample cell was measured with helium gas of 99.999% purity. Non-ideal correction for H_2 and CO_2 gases were made by applying virial coefficients at the respective measurement temperature.

5.3.3 Single-crystal X-ray Diffraction

A suitable single crystal of compound **1** was mounted on a thin glass fiber with commercially available super glue. X-ray single crystal structural data were collected on a Bruker Smart–CCD diffractometer equipped with a normal focus, 2.4 kW sealed tube X-ray source with graphite monochromated Mo-K_α radiation (λ = 0.71073 Å) operating at 50 kV and 30 mA, with ω scan mode. The programme SAINT[13] was used for integration of diffraction profiles and absorption correction were made with SADABS programme.[14] The structure was solved by direct method using SIR-92[15] and followed by successive Fourier and difference Fourier syntheses. All the non-hydrogen atoms were refined anisotropically. Potential solvent accessible area or void space was calculated using the PLATON[16] multipurpose crystallographic software. All calculations were carried out using SHELXL 97,[17] SHELXS 97,[18] PLATON 99[16] and WinGX system, ver. 1.70.01.[19] All crystallographic and structure refinement data of **1** are summarized below. Selected bond distances and angles are given in Table 1.

5.3.4 Crystal Data of [Cd(bipy)$_{0.5}$(Himdc)](DMF)]$_n$ (1)

Formula $C_{13}H_{13}CdN_4O_5$, M_r = 417.62, Monoclinic, Space group $C2/c$ (no. 15), a = 22.382(3) Å, b = 10.7731(15) Å, c = 13.5325(18) Å, β = 100.108(6)°, V = 3212.4(8) Å^3, Z = 8, ρ_{calc} =1.694 g cm^{-3}, μ(Mo-K_α) = 1.388 mm^{-1}, F(000) = 1592, T = 293 K, λ (Mo-K_α) = 0.71073 Å, θ_{max} = 26.3°, GOF = 1.14. A total of 17917 reflections were collected, of which 3237 were unique (R_{int} = 0.056). R_1= 0.0444 for 2771 independent reflections with I>2σ(I), w_{R2} = 0.1345 for all data.

5.3.5 Computational Details

Bulk periodic density functional theory (DFT) calculations were carried out using the plane wave code CPMD.[20] The super cell consisted of one unit cell of the metal-organic framework (MOF) and/or gas molecules (H_2 or CO_2). Solvent molecules were not included in modelling of these systems. Valence electrons were represented using a plane wave basis set with an energy cutoff of 80 Ry. The interaction of valence electrons with the core electrons and the nuclei were represented by a norm-conserving pseudopotential of Troullier and Martins type.[21] The gradient-corrected Becke, Lee, Yang and Parr functional (BLYP) functional was employed[22] to treat the exchange and correlation interactions.

Initial calculations consisted of iterative optimization of the cell parameters and atomic positions until a minimum energy configuration was found. Further, to identify the preferred locations of H_2 or CO_2 molecules in the MOF, molecular dynamics (MD) simulations using the Car-Parrinello method (CPMD)[23] were carried out at a temperature of 50 K. These were performed by constraining the MOF and allowing the gas molecules (H_2 or CO_2) to explore various regions within the framework as a function of time. Temperature was maintained through a Nose-Hoover chain thermostat [24] using a coupling constant of 3250 cm^{-1}. In these runs, the H_2 atoms were replaced by deuterium atoms so as to enable the use of a larger time step of 5 a.u. The trajectory was generated for 3 ps and an animation demonstrated that the gas molecules explored all the regions of the pore(s). Locations of the gas molecules possessing low energies were identified from this trajectory. Direct optimization of the geometry (i.e., of the MOF and of the gas molecule) was initiated from such favoured locations. Optimization of geometry was pursued until the maximum force on any atom was less than 10^{-4}a.u. Gas molecules are known to interact with MOF through van der Waals (vdW) forces in addition to other interactions.[25] While many methods to treat vdW interactions within the DFT formalism exist, an easier route is to add it as an empirical potential. In the present study, we have employed the vdW parameters of Grimme as derived for the BLYP functional.[26] The binding energy of the gas molecule (H_2 or CO_2) with MOF is calculated using the following formula,

$$\Delta E = E(MOF + gas) - E(MOF) - n*E(gas)$$

Where E (MOF + gas), E (MOF) and E(gas) represent the energies calculated for MOF with H_2 or CO_2, MOF and isolated gas molecule. Here, E(gas) was calculated in the same simulation box as that of the MOF and 'n' gives the number of gas molecules present in the MOF. Thermal contributions to the binding energy were not considered. This contribution is expected to be less than 1 kJ/mol and would not change the results much. All the structures were visualized using Jmol[27] and VMD.[28]

5.4 Results and Discussion

5.4.1 Structural Description of [Cd(bipy)$_{0.5}$(Himdc)](DMF)]$_n$ (1)

Compound **1** crystallizes in the monoclinic *C*2/*c* space group (details in experimental part) and structure determination reveals a 3D pillared layer coordination framework of Cd(II) bridged by the Himdc and bipy linkers. The asymmetric unit of **1** consists of one octahedral Cd(II) atom, one Himdc, half bipy and one guest DMF molecule (Figure 1a and 1b). Each Himdc chelates to two Cd(II) centers through (N2, O1) and (N3, O4) atoms and connects to another Cd(II) through oxo(μ_2-O4) bridge and thus forming a 2D {Cd(Himdc)$_2$} corrugated layer in the crystallographic *bc* plane (Figure 2a). The dimeric fragments Cd$_2$(μ_2-O4)$_2$ in the layer (<Cd-O4-Cd = 114.85(18)°, Cd···Cd = 4.047 Å) are connected in the axial coordination with bipy forming a 3D pillared-layer framework (Figure 2b). Structural analysis with TOPOS software[29] suggests 2D layer is a 3-c uninodal net considering Cd1 and Himdc as a single node and the corresponding Schläfli symbol is {4.8^2} (Figure 3a).
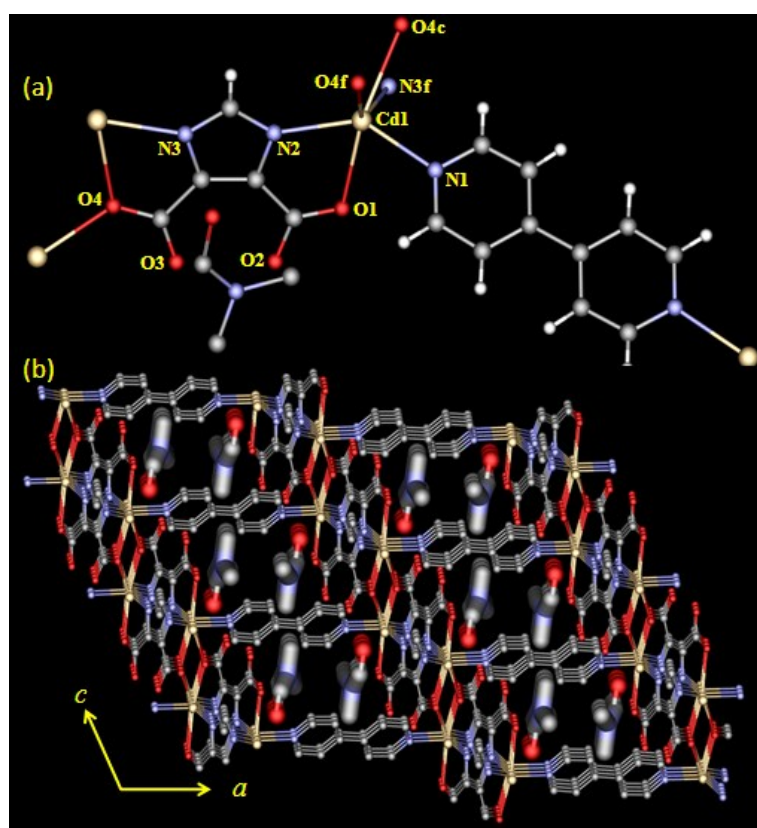
Figure 1 (a) View of the coordination environment around Cd(II) centre; (b) View of the 3D pillared-layer framework showing rectangular shaped channels along *b*-axis occupied by the DMF molecules.

Table 1 Selected bond distances (Å) and angles (°) for **1**.

Cd1-O1	2.489(6)	Cd1-N1	2.271(5)
Cd1-N2	2.223(4)	Cd1-O4_c	2.319(4)
Cd1-O4_f	2.483(4)	Cd1-N3_f	2.257(4)
O1-Cd1-N1	81.8(2)	O1-Cd1-N2	71.29(17)
O1-Cd1-O4_c	141.20(17)	O1-Cd1-O4_f	153.23(16)
O1-Cd1-N3_f	84.67(17)	N1-Cd1-N2	137.94(18)
O4_c-Cd1-N1	89.36(17)	O4_f-Cd1-N1	96.81(17)
N1-Cd1-N3_f	99.68(18)	O4_c-Cd1-N2	91.89(15)
O4_f-Cd1-N2	121.61(15)	N2-Cd1-N3_f	109.05(16)
O4_c-Cd1-O4_f	65.15(15)	O4_c-Cd1-N3_f	134.13(15)
O4_f-Cd1-N3_f	69.14(14)	Cd1_d-O4-Cd1_g	114.85(18)

Symmetry code: c = x,1-y,-1/2+z; d = x,1-y,1/2+z; f = 1/2-x,-1/2+y,1/2-z;

g = 1/2-x, 1/2+y, 1/2-z.
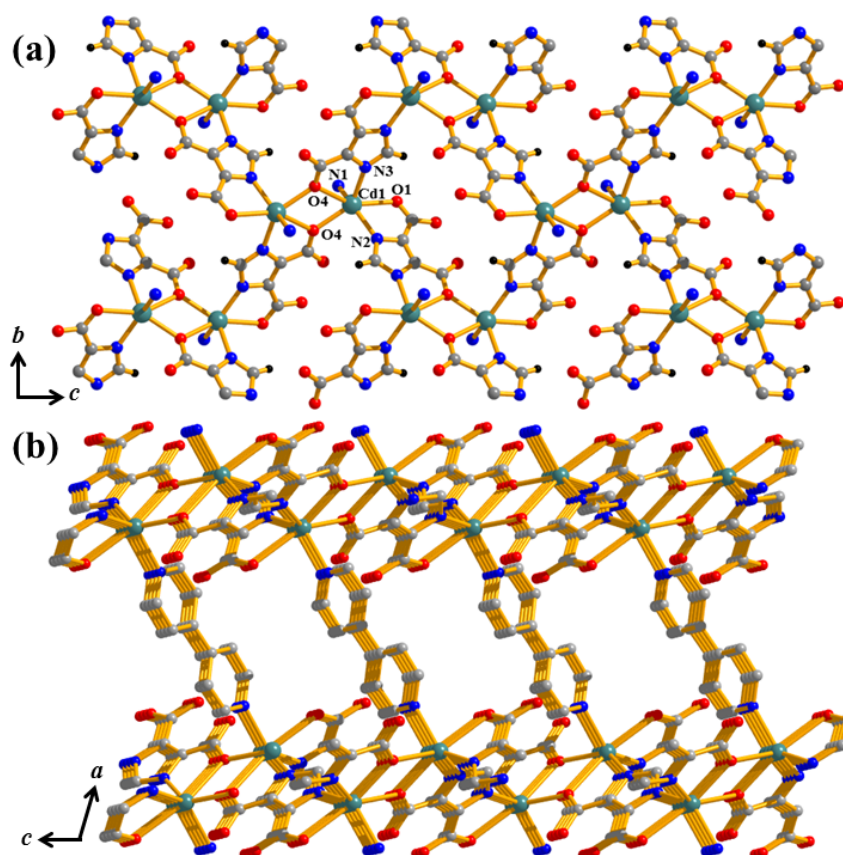
Figure 2 (a) View of the 2D corrugated sheet of [Cd(Himdc)]$_n$. (b) View of the 3D pillared-layer structure where parallelly aligned bipy linkers connect the layers to form rectangular channels along the *b*-direction.

The overall 3D framework reveals a 3-nodal 2,3,4-c net (Figure 3b) with stoichiometry (2-c)(3-c)2(4-c)2 and the corresponding Schläfli symbol for the net is $\{12\}\{4.8^2.12^3\}2\{4.8^2\}2$. In **1**, Cd1-O and Cd1-N bond distances are in the range of 2.319(4) – 2.489(6) Å and 2.223(4) – 2.271(5) Å, respectively (Table 1).
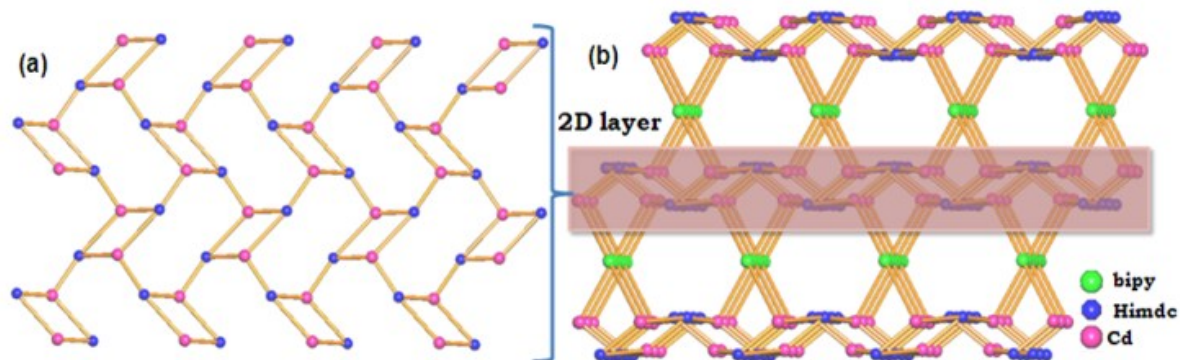
Figure 3 Network topology of compound **1** analyze by TOPOS. (a) 3-connected uninodal 2D net; (b) 2,3,4-connected 3D framework formed by pillaring the 2D layer by bipy linker (simplifying Cd, Himdc and bipy as a single node).

The degree of distortion from the ideal octahedral geometry is reflected in *cisoid* angles (range: 69.14(14) – 134.13(15)°) and *transoid* angles (range: 137.94(18) – 153.23(16)°) around Cd(II) (Table 1). The bipy pillars are aligned parallelly along the crystallographic *b*-axis and connecting diagonally the {Cd(Himdc)$_2$} corrugated layers, to form rectangular channels with the dimensions of 3.84 × 1.06 Å^2 (Figure 2b and 1b). Moreover, along the *c*-axis bipy pillars are in a criss-cross and canted fashion supported by π-π interactions which results in oval-shaped channels with dimension of 4.68 × 3.84 Å^2 (Figure 4a). It is worth mentioning that viewing along the perpendicular to *b*-axis framework also shows rectangular channels of dimension of 3.2 × 2.1 Å^2 (Figure 4b). The 3D channels are occupied by the guest DMF molecules and each pore is decorated by the uncoordinated pendent oxygen atoms (O2, O3) from the Himdc and panels of bipy pillars, resulting in a highly polar pore surface (Figure 2 and 4). The calculation using PLATON [16] suggest that the 3D framework contains 42.2% void space to the total crystal volume after removal of the guest DMF molecules. The Cd…Cd separation along the Himdc and bipy pillar is 8.894 and 11.596 Å, respectively.
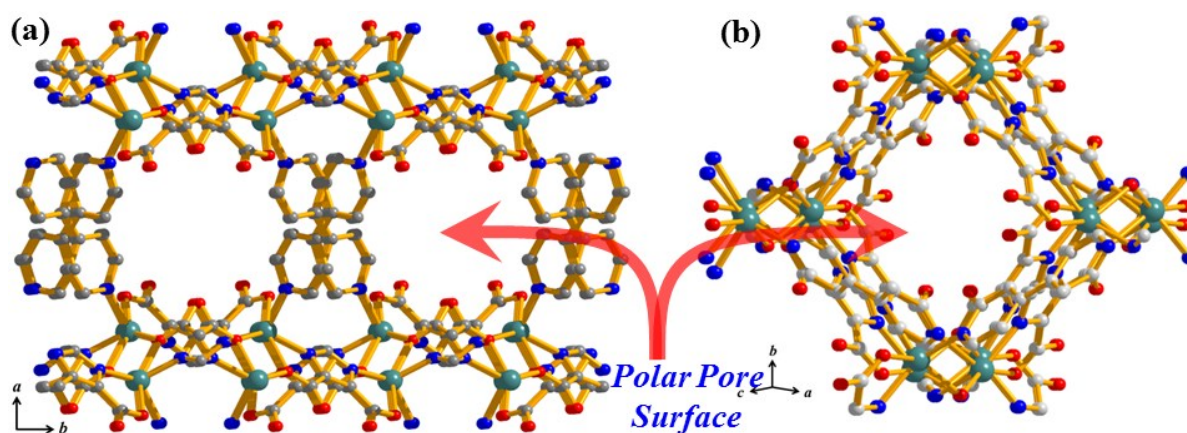
Figure 4 View of the 3D framework (a) along the *c*-axis showing oval shaped channels decorated with pendent carboxylate oxygen atoms and pyridyl moieties; (b) square shaped channels along perpendicular to *b*-axis decorated with pendent carboxylate oxygen atoms.

5.4.2 Framework Stability

To study the framework stability of **1**, we performed thermogravimetric analysis (TGA) and powder X-ray diffraction (PXRD) studies after removal of the guest DMF molecules. TGA shows the loss of one DMF molecule in the temperature range of 30 – 200 °C (obs. wt. loss ~ 17.11% and calc. wt. loss ~ 17.45%) and the desolvated framework $[Cd(bipy)_{0.5}(Himdc)]_n$ (**1′**) is stable up to 250 °C (Figure 5). Upon further heating, another weight loss (~ 16 %) was observed in the temperature range of 250 – 290 °C which corresponds to half of bipy molecule (obs. wt. loss ~ 35.39 % and calc. wt. loss ~ 36.45%) and later, the framework decomposes to an unidentified product.
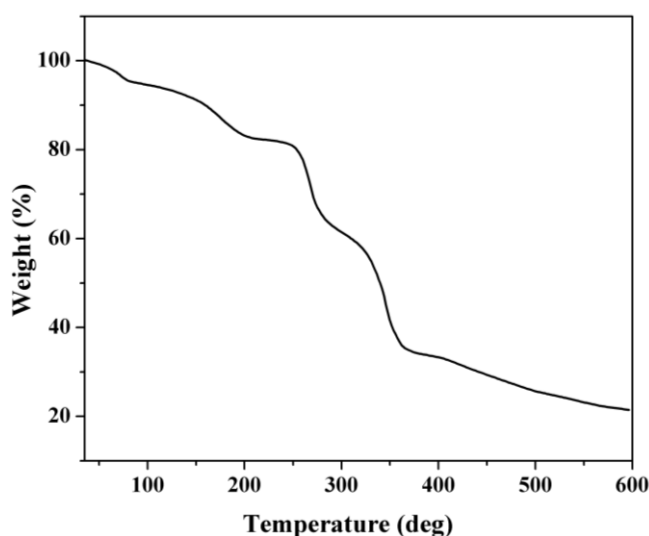
Figure 5 TGA plot of compound **1** measured under nitrogen atmosphere.

The PXRD pattern of **1′** exhibits sharp lines without shifting the peak positions and intensities, suggesting that framework is highly rigid and robust (Figure 6).
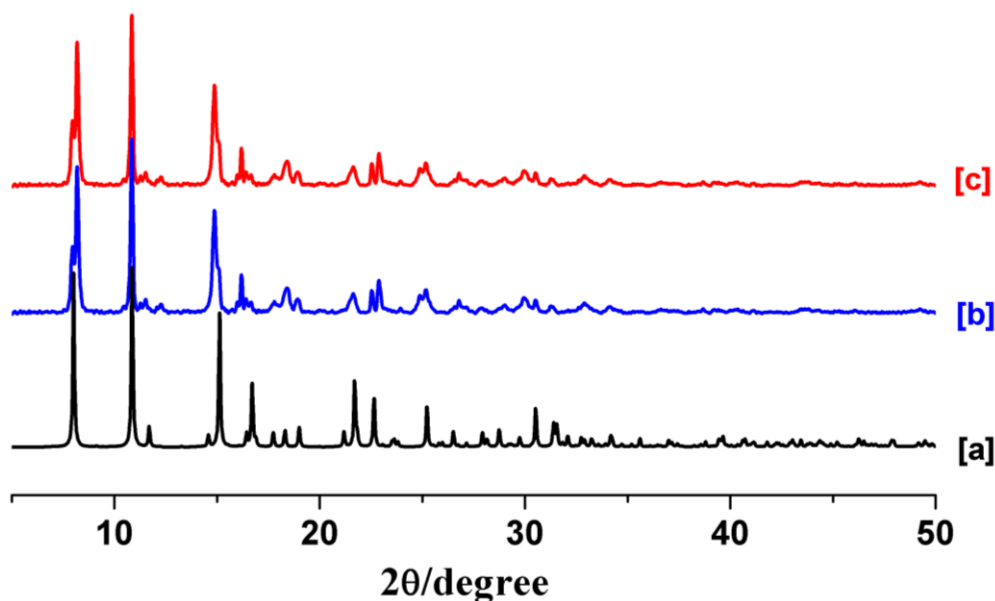
Figure 6 PXRD pattern of **1** in different states: (a) simulated from X-ray single crystal data, (b) as-synthesized and (c) desolvated at 190 °C under high vacuum (10^{-1} Pa).

5.4.3 Permanent Porosity and Gas Storage Properties

Encouraged by the 3D channel structure, and the high thermal stability and structural rigidity, the permanent porosity of the desolvated framework (**1′**) was determined. The N_2 (kinetic diameter = 3.6 Å)[30] adsorption isotherm shows typical type I profile, suggesting a microporous nature of the framework (Figure 7). The surface area calculated from the Langmuir equation is about 648.8 m^2/g and the corresponding BET surface area is 498.12 m^2/g. The slight discrepancy between the measured pore volume (0.22 cm^3/g), from the N_2 adsorption isotherm and the value calculated from the single-crystal X-ray structure (0.29 cm^3/g) using PLATON is possibly due to the inability of N_2 molecules effectively enter into the small pores at 77 K. This happens owing to some energy barrier or blocking of pores by strongly adsorbed N_2 molecules. The inset to Figure 7 shows the differential pore volume distributions as function of pore width calculated by the Saito-Foley (S-F)[31] method which suggests that the pore size is about 4.6 Å. This agrees well with the pore size obtained from single crystal structure.
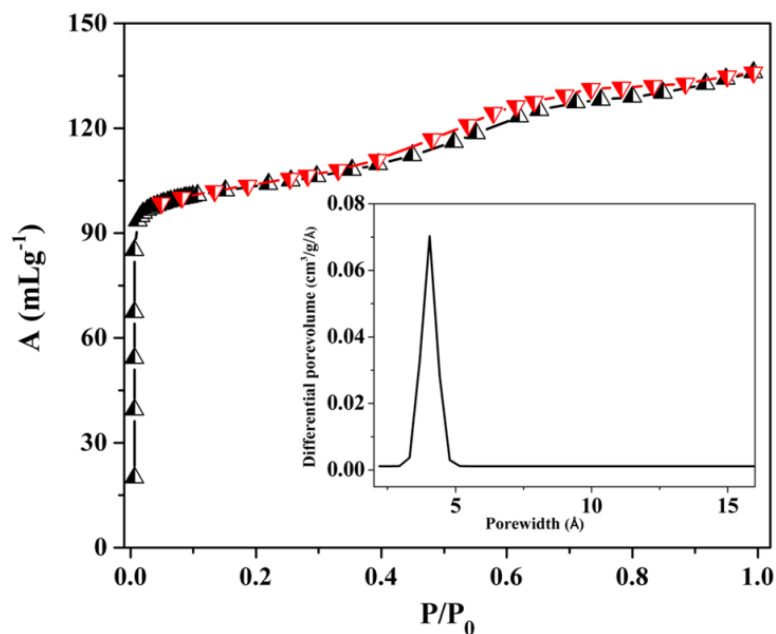
Figure 7 N_2 sorption isotherm for **1′** at 77 K. (Inverted red triangles are for adsorption and black triangles are for desorption). Inset: Pore volume *versus* pore size distribution by S-F method.

We have measured H_2 storage capacity of **1′** at 77 and 87 K up to 1 atm ($P/P_0 = 1$) and the profile shows steep uptake at low pressure region which was ended without saturation (inset to Figure 8).
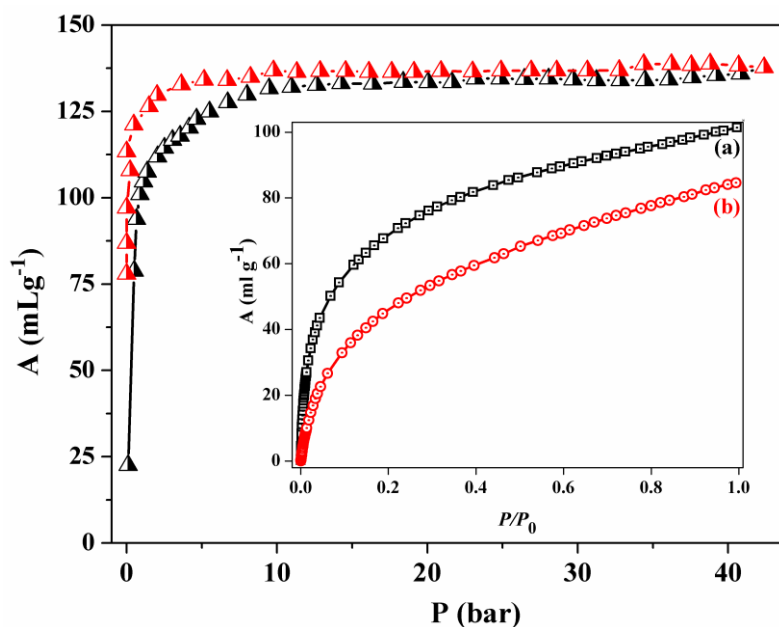
Figure 8 High-pressure H_2 sorption isotherms for **1′** at 77 K; inset: H_2 sorption profile at 77 K (a) and 87 K (b) up to 1 atm.

The final uptake amounts are 101 and 84 mL/g which match up about of 0.9 and 0.75 wt% storage capacity. Excess high pressure H_2 adsorption capacity of **1′** was measured with BELSORP HP apparatus at the 77 K and the corresponding storage capacity was found to be 1.23 wt% (Figure 8). The steep uptake at low pressure regions (up to 3 bar) suggests strong interaction of H_2 with the pore surface of **1′** decorated with the pendent oxygen atoms (O2 and O3) from the Himdc linker and aromatic π-cloud. The framework saturated with respect to H_2 at 77 K at about 10 bar and the saturated amount indicates about two H_2 molecules inclusion per formula unit of **1′**. The heat of H_2 adsorption (ΔH_{ads}) was derived from the Clausius –Clapeyron equation[32a,11b] and the value is ΔH_{ads} = 13.3 kJ/mol at low coverage regions (see details in Figure 9-11). This value is well compatible to the highest reported value of ΔH_{ads} in MOF systems.[32b]

5.4.4 Analysis of Gas Adsorption Isotherms

Hydrogen adsorption isotherms (77 K and 87 K) were fitted to the Langmuir-Freundlich[1] equation instead of the more commonly used Langmuir equation.[2] An accurate fit was obtained (Figure 9 and 10) by using this equation which results a precise prediction over the quantity of hydrogen adsorbed at saturation. A variant of the Clausius-Clapeuron equation was used to calculate enthalpy of adsorption.

$$ln \left(\frac{P_1}{P_2}\right) = \Delta H_{ads} \times \left(\frac{T_2 - T_1}{R \times T_2 T_1}\right)$$

Where, P_n is = Pressure for isotherm n

T_n = Temperature for isotherm n

R = Universal Gas constant = 8.314 J mol^{-1} K^{-1}

Pressure as a function of amount of adsorption was determined by using the Langmuir-Freundlich fit for each isotherm.

$$\frac{Q}{Q_m} = \frac{B \times P^{(\frac{1}{t})}}{1 + (B \times P^{(\frac{1}{t})})}$$

Where, Q = moles adsorbed

Q_m = moles adsorbed at saturation

P = Pressure

B and t = constant

By rearranging this equation we get $\quad P = \left(\dfrac{\frac{Q}{Q_m}}{B - \left(B \times \frac{Q}{Q_m}\right)}\right)^t$

Substituting this into Clausius-Clapeuron equation we get

$$\Delta H_{ads} = \frac{R \times T_1 \times T_2}{T_2 - T_1} \ln \frac{\left(\dfrac{\frac{Q}{Q_{m1}}}{B_1 - \left(B_1 \times \frac{Q}{Q_{m1}}\right)}\right)^{t_1}}{\left(\dfrac{\frac{Q}{Q_{m2}}}{B_2 - \left(B_2 \times \frac{Q}{Q_{m2}}\right)}\right)^{t_2}}$$

Where, the subscript 1 and 2 are representing the data corresponding to 77 and 87 K respectively.
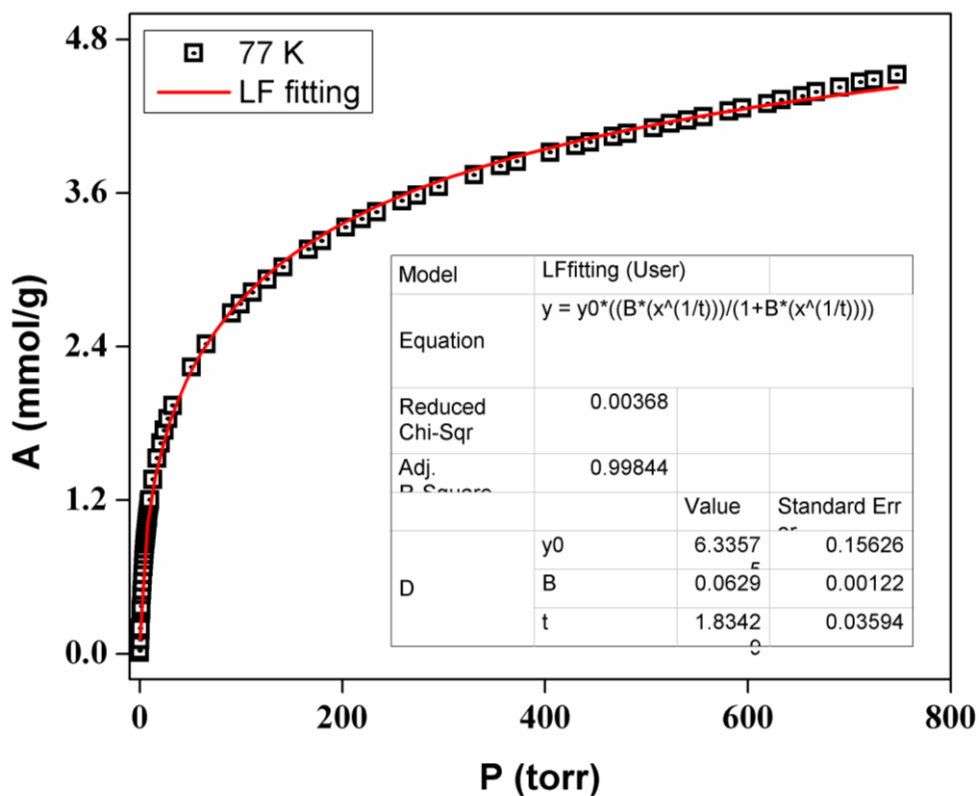
Figure 9 H_2 adsorption isotherm for **1´** at 77 K. The solid line represents the best fit to the data using the Langmuir-Freundlich equation, as described above

Model	LFfitting (User)		
Equation	$y = y0*((B*(x^{(1/t)}))/(1+B*(x^{(1/t)})))$		
Reduced Chi-Sqr	0.00177		
Adj. R-Square	0.99904		
		Value	Standard Error
	y0	6.54518	0.21443
D	B	0.016	3.96965E-4
	t	1.50393	0.02494
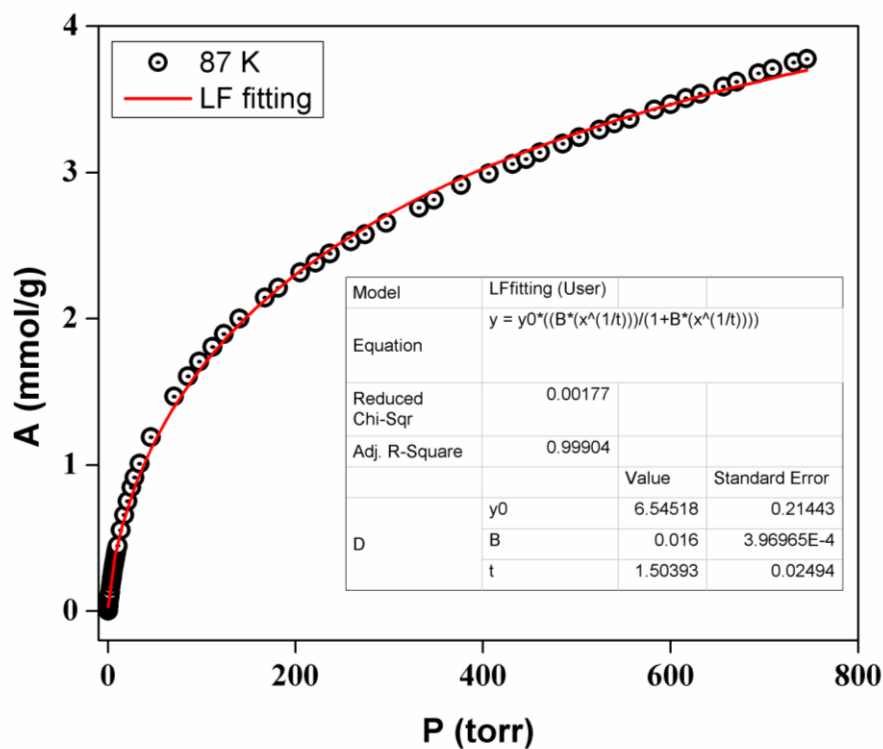
Figure 10 H_2 adsorption isotherm for **1′** at 87 K. The solid line represents the best fit to the data using the Langmuir-Freundlich equation, as described above
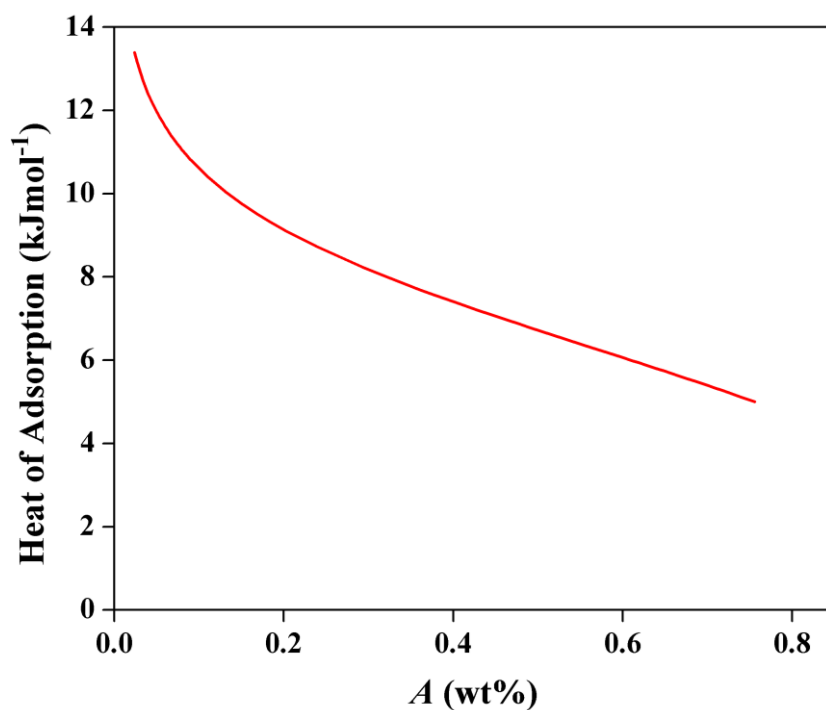
Figure 11 Enthalpy of H_2 adsorption for **1′** calculated using Clasius-Clapeyron equation.

However, the value calculated using the Clausius–Clapeyron approach exhibits a sudden rising behaviour at low coverage. We have thus used an alternate virial method which reduces to Henry's law from which the isosteric heat of adsorption is calculated to be ~9.0 kJ/mol (Figures 12 and 13)
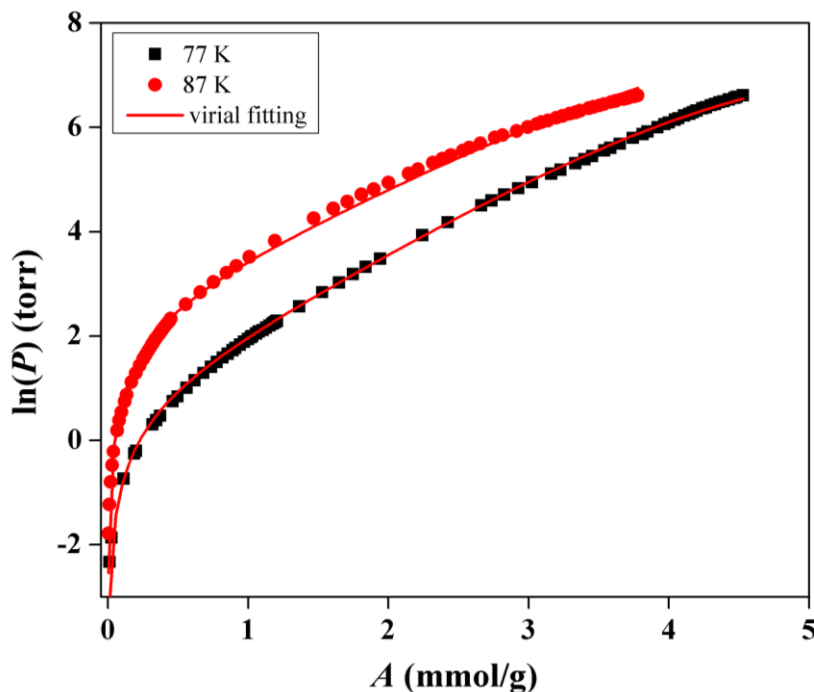
Figure 12 Virial fittings of H$_2$ adsorption curves measured at 77 (black) and 87 K (red).
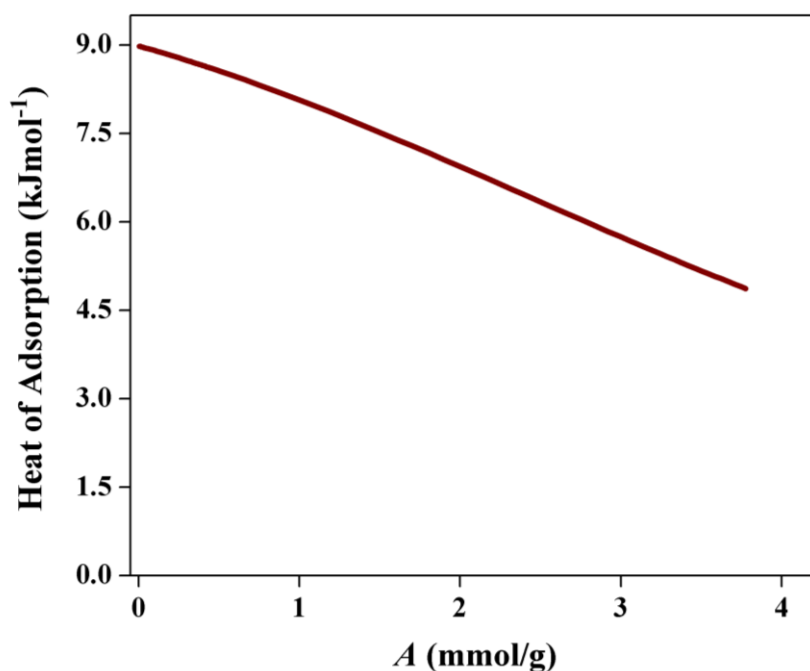
Figure 13 Plot of heat of adsorption (Q_{st}) vs loading calculated applying virial method.

The CO_2 gas sorption isotherm of **1′** measured at 195 K and 298 K are shown in Figure 14. The adsorption isotherm at 195 K shows a two steps process with a small hysteresis (Figure 14a). The two step adsorption process is clearly evident from the plot of log (P/P_0) *vs* uptake profile (inset Figure 14). In the initial step, it uptakes 64 mL/g (12.15 wt% at STP), in the range of *P/P_0* ~ 0.001 − 0.055. In the next step, the framework adsorbs about 36 mL (7.07 wt %) up to P/P_0 ~1.
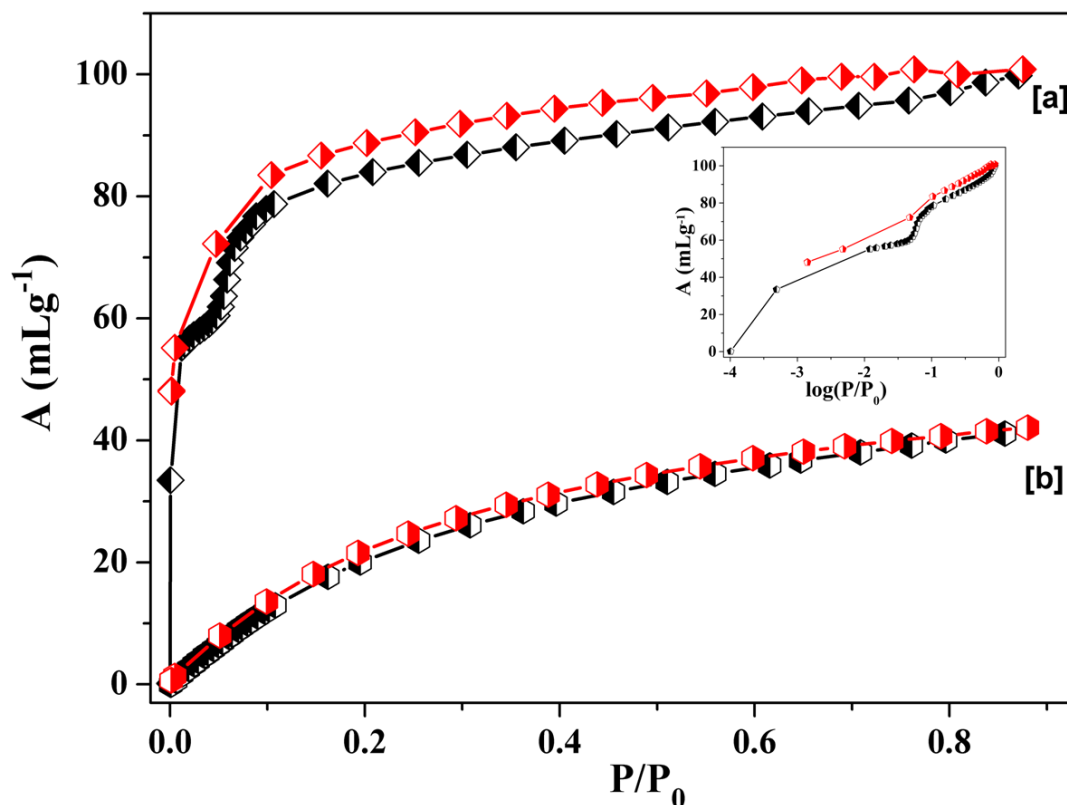
Figure 14 CO_2 sorption profile for **1′** (a) at 195 K and (b) 273 K. Inset: log profile showing the double step adsorption.

Such stepwise, hysteretic pressure dependent adsorption of CO_2 uptake has been observed in several flexible and dynamic porous MOFs, which respond to specific adsorbate molecules by means of a breathing or gate opening process related to structural expansion or close-open pore system.[8f,33]However, stepwise adsorption in a rigid framework is extremely rare and could stem from different adsorption sites. The small hysteresis and steep uptake at low pressure region is indicating of strong interaction of the CO_2 molecules with the pore surface. The isosteric heat of adsorption ($q_{st,\phi}$), calculated using the Dubin-Radushkevich (DR) equation[34] is about 35.4 kJ/mol. The CO_2 storage capacity at 298 K up to 1 atm is ~ 9 wt% (Figure 14b) which is

significantly increases to ~11.4 wt% at high pressure (Figure 15a). It is worth mentioning that the saturation amount at high pressure measurement shows commensurate adsorption with about one molecule of CO_2 inclusion per formula unit of **1′** and no double-step profile was observed. Moreover, the corresponding methane storage capacity of **1′** suggests about 6.5 wt% at 298 K up to 48 bar (Figure 15b). The pore surface are decorated with the pendent oxygen atoms (O2 and O4) from the Himdc linker and π-cloud of pyridyl ring of bipy which gives rise to an electric field in the host framework, can interact with the quadrupole moment of CO_2 (-1.4 × 10^{-39} C m^2) providing additional energy for adsorption.
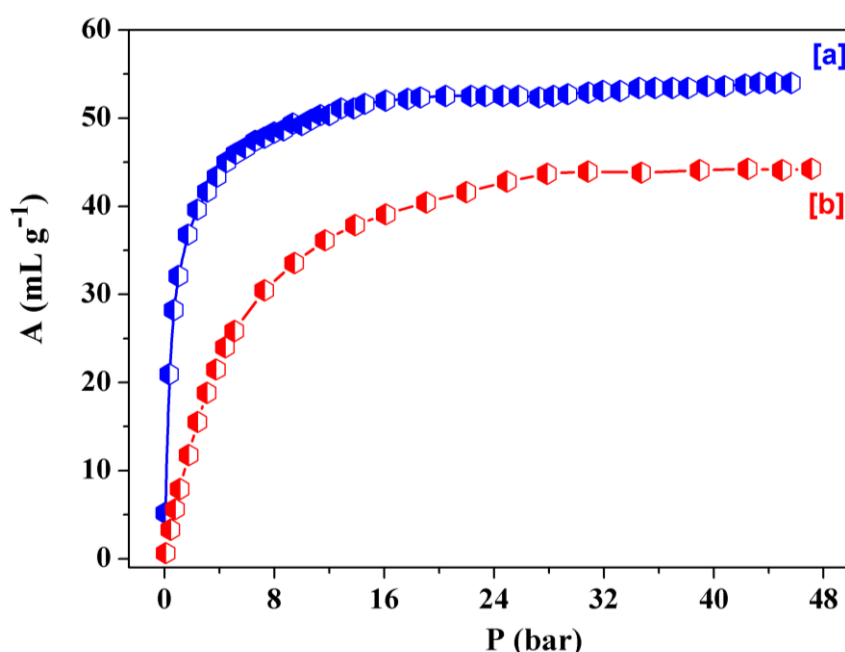
Figure 15 (a) CO_2 and (b) methane sorption profile for **1′** measured at 298 K.

5.4.5 Solvent Adsorption Study

Inspired by the highly active pore surface in **1′**, we anticipated interesting sorption behaviour with solvent molecules depending upon the polarity (Lewis basicity) of guest molecules. To analyse the effect of small molecules on the pore surfaces, we have carried out a vapour sorption study with different solvent molecules (methanol (MeOH), ethanol (EtOH), acetonitrile (CH_3CN) and benzene (C_6H_6)) of varying size and polarity. The sorption profiles of MeOH (3.8 Å), CH_3CN (4.0 Å), and EtOH (4.3 Å) reveal a type I curve with small hysteresis and sorption amount increases with increasing pressure (Figure 16).
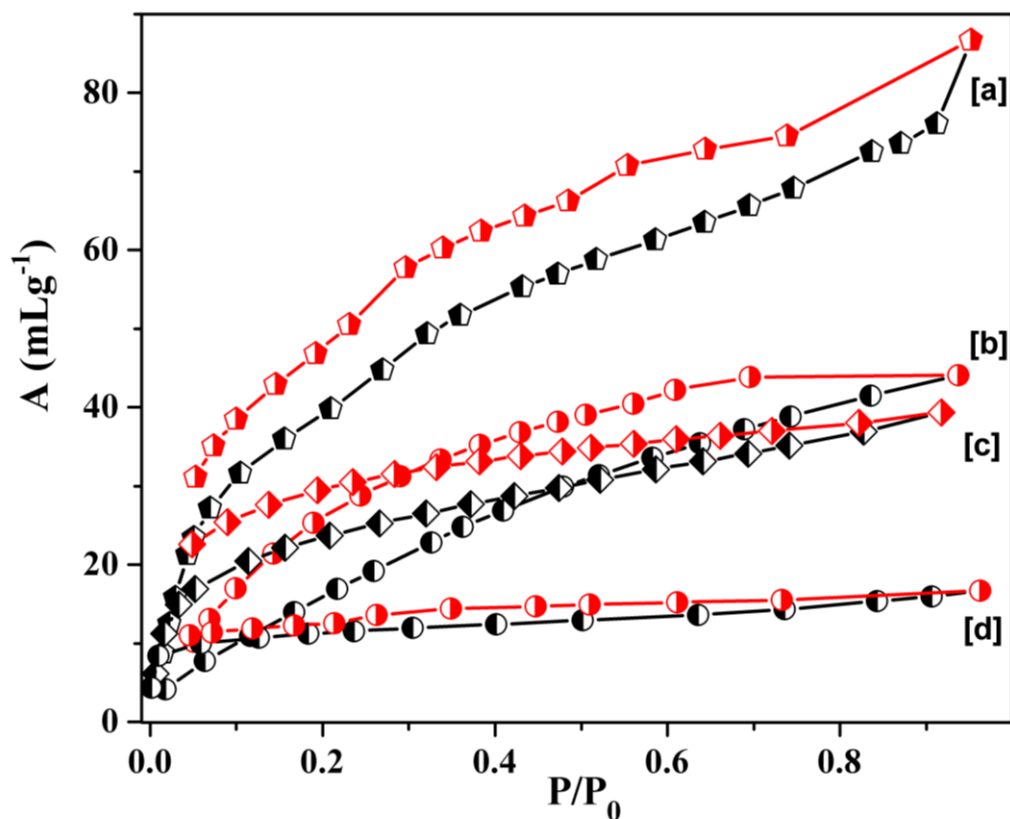
Figure 16 Vapor sorption isotherm for **1′** (a) MeOH (293 K); (b) EtOH (298 K); (c) CH$_3$CN (298 K); and (d) C$_6$H$_6$ (298 K). (P$_0$ is the saturated vapor pressure of the adsorbates at the respective temperatures.

Moreover, consistent with the smaller pore size and polarity of **1′**, no significant uptake of C$_6$H$_6$ (5.8 Å) is observed (Figure 16d). The calculations using the final sorption amount of MeOH, EtOH and CH$_3$CN suggest an uptake of 1.3, 0.72, and 0.58 molecules, respectively per formula unit of **1′**. All the profiles were analyzed by the DR equation and the values of *βE$_0$*, which reflect adsorbate-adsorbent affinity, are 7.59 kJ/mol for MeOH, 4.36 kJ/mol for EtOH and 3.56 kJ/mol for CH$_3$CN. This also reflects the high polarity of the pore surfaces as among all the guest solvent molecules MeOH is the most polar and can interact effectively through different hydrogen-bonding (O-H….O/N) interactions between pendant and coordinated oxygen and nitrogen atoms from Himdc or bipy linker compared to EtOH and CH$_3$CN molecules.

5.4.6 Theoretical Study

To better understand the ability of the framework to store H_2 and CO_2 and the origin of high heat of H_2 and CO_2 adsorption in different experiments, we have carried out density functional theory (DFT) calculations augmented by empirical van der Waals correction terms as described in detail in the experimental part later. Favourable adsorption sites for H_2 and CO_2 within the MOF and their energies have been determined. Many people have explained successfully the adsorption of gas molecules in MOF using computational methods. [35]
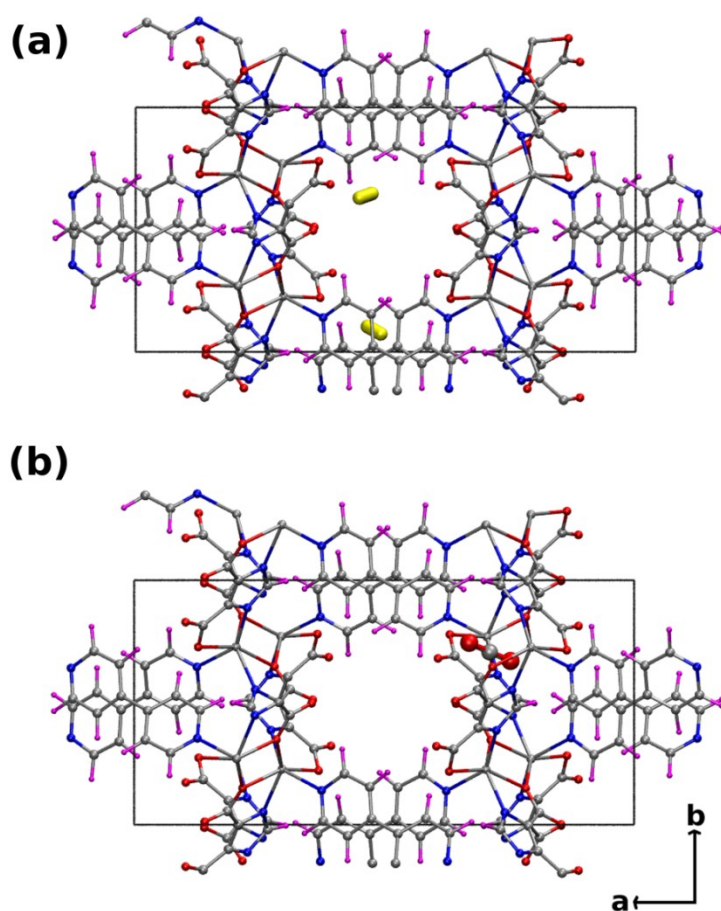
Figure 17 Locations of the (a) two H_2 molecules (shown as yellow tube) (top panel) and (b) one CO_2 molecule (bottom panel) are shown in the oval shaped channels of the crystal viewed along the *c*-axis.

In this chapter, geometry optimization runs were initiated from many configurations in each of which the gas molecule was positioned in a different location inside the MOF pore. In addition, CPMD simulations at 50 K were also carried out, to identify low

energy positions for the H_2 and CO_2 molecules. The optimal positions of the H_2 and CO_2 molecule in the MOF channel are shown in Figure 17. For H_2, the experimental heat of adsorption (-13.3 kJ/mol) is reproduced when two H_2 molecules interact with the MOF and the calculated value is -12.88 kJ/mol. Figure 18a shows the positions of the two molecules, named as H_2-I and H_2-II, yielding this value. The contribution of the individual H_2 molecules to the total adsorption energy was also calculated and the values are -5.74 and -8.00 kJ/mol for H_2-I and H_2-II molecules, respectively.The sum of these two values is not equal to the calculated total heat of adsorption mentioned earlier (-12.88 kJ/mol) due to minor variations in the optimized MOF coordinates between each of these three runs. Table 2 shows the binding energies of H_2 and CO_2 molecules with the MOF. van der Waals (vdW) corrections to the DFT energies are seen to be crucial to obtain a good comparison to experimental heats of adsorption, for both the gases. To identify the atoms of MOF interacting with adsorbate and thus to understand the nature of interactions, we have studied differences of electron densities. Figure 18b and 18c show the difference plot of electron density. It is calculated as: $\rho_{(MOF+H2)} - \rho_{(MOF)} - \rho_{(H2)}$ where ρ is the electron density and the latter two terms are calculated for the pure MOF and for a H_2 molecule in the gas phase respectively.
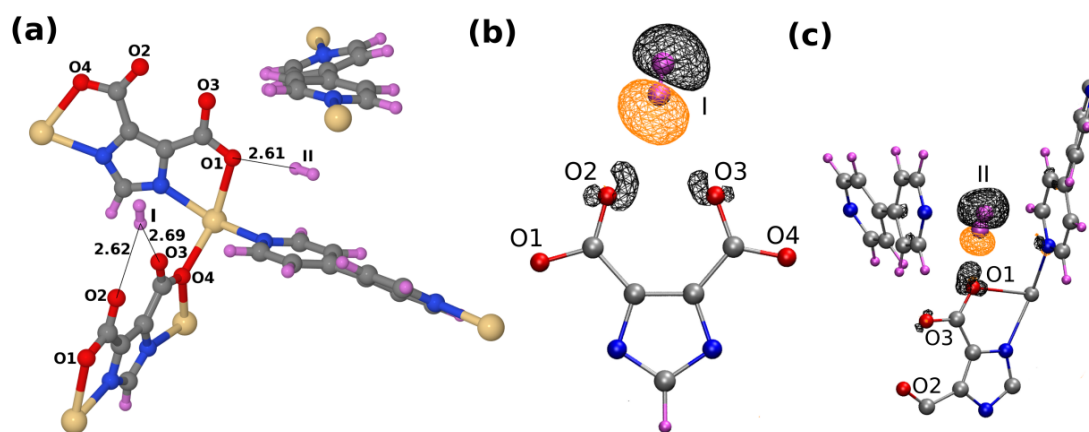
Figure 18 (a) Environment around the two adsorbed H_2 molecules at two different sites I and II as obtained from density functional theory calculations. [Distances are in Å]. (b) and (c) Isosurface of the difference in the electron density of the system due to the adsorption of the H_2 molecules at I and II sites, respectively. Negative and positive values of electron density difference are shown in orange and black respectively. Isosurface value is 0.0003 a. u. [Color code: C, grey; H, magenta; N, blue; O, red. Other atoms of MOF are not shown for clarity].

A change in electron density of MOF atoms surrounding the H_2 molecules can be clearly seen. H_2-I molecule lies nearly in the plane of the imidazolium ring with one of its atom slightly positively charged. The latter interacts electrostatically with the two free oxygens (O2 and O3) of the carboxylate groups of the Himdc linker (Figure 18a). The distances of this H_2 atom from these two free oxygen atoms are 2.62 and 2.69 Å. H_2-II molecule interacts in two ways: one is the electrostatic interaction between H_2 and the oxygen (O1) (which is bonded to metal atom) atoms, and other is the interaction of the π-electron cloud over the pyridine ring with the H_2 molecule. This H_2 molecule is at a distance of 2.61 Å from the oxygen atom (O1) and lies between two pyridine rings at almost equal distance from both, with its molecular axis parallel to the plane of each ring (Figure 18a).
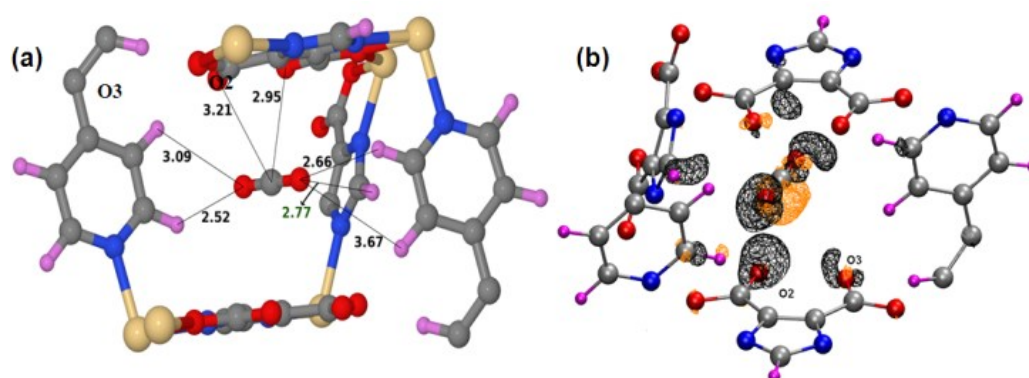
Figure 19 (a) View of the environment around the adsorbed CO_2 molecule. [Measured distances are in Å]. Other atoms of the MOF are not shown for the sake of clarity. (b) Isosurface of the difference in the electron density of the system due to the adsorption of CO_2 molecule. Negative and positive electron density differences are shown in orange and black respectively. The Isosurface value is 0.0006 a. u. [Color code: C, grey; H, magenta; N, blue; O, red. Other atoms of MOF are not shown for clarity].

	H_2	CO_2
BLYP	-6.14	-6.44
BLYP + vdW	-12.88	-39.14
Experiment	-13.3[a]	-35.4[b]

Table 2 Binding energies of H_2 and CO_2 molecules in the MOF calculated using BLYP/85 Ry level of theory with[26(b)] and without empirical van der Waals corrections compared against experimental values of the heat of adsorption. The energies are in kJ/mol.[a] adsorption enthalpy value at 77 K. [b] adsorption enthalpy value at 195 K.

The distances of this H_2 atom from these two free oxygen atoms are 2.62 and 2.69 Å. H_2-II molecule interacts in two ways: one is the electrostatic interaction between H_2 and the oxygen (O1) (which is bonded to metal atom) atoms, and other is the interaction of the π-electron cloud over the pyridine ring with the H_2 molecule. This H_2 molecule is at a distance of 2.61 Å from the oxygen atom (O1) and is lies between two pyridine rings at almost equal distance from both, with its molecular axis parallel to the plane of each ring (Figure 19a). The binding energy for CO_2 adsorption is calculated to be -39.14 kJ/mol which is slightly higher than the experimental estimate of -35.4 kJ/mol. This overestimate could be possibly due to with the vdW parameters employed here. These were originally developed to describe systems in the gas phase. It has been recently shown that these parameters could overestimate the vdW contribution to the total energy in the condensed state.[36] One needs a good qualitative description of these long range interactions in periodic systems to be able to accurately reproduce the experimental heats of adsorption. The environment around the CO_2 molecule present within the MOF is shown in Figure 19a. We identify three possible kinds of interaction between CO_2 and MOF, based purely on its location. The primary contribution to the binding energy is likely to come from the interaction of the electron deficient carbon atom of CO_2 with the lone pairs of the two free oxygen atoms (O2 and O3) of carboxylate groups as shown in Figure 19a. This molecule is at a distance of 2.95 and 3.21 Å from the two oxygens with its molecular axis parallel to the plane of imidazolium ring. A slight deviation of the backbone angle of CO_2 to a value of 178.1° is seen, with the carbon of the CO_2 bending towards the two free oxygen atoms.[37] The observed asymmetry in the measured distances from the carbon atom to the two carboxylate (free) oxygens is due to the existence of very weak hydrogen-bonding between one of the oxygen atoms of the CO_2 molecule and the acidic hydrogen of imidazolium ring as shown in Figure 19a. The hydrogen bond distance is 2.79 Å and angle is 105.8°. This system is possibly further stabilized by a coulombic interaction between the two oxygen atoms of CO_2 and the hydrogens of pyridine ring. All these interactions are clearly captured in a plot of the difference in the electron density brought upon the system due to the adsorption of CO_2, shown in Figure 19b.

5.5 Conclusions

In summary, a pillared-layer framework of Cd(II), [Cd(bipy)$_{0.5}$(Himdc)](DMF)]$_n$ (**1**), (bipy = 4,4′-bipyridine and Himdc = 4,5-imidazoledicarboxylate) with 3D channel structure composed of mixed ligand system has been successfully synthesized and characterized. The desolvated framework **1′** shows permanent porosity and high H$_2$ and CO$_2$ uptake characteristics. The high adsorption energy for H$_2$ (~13.3 kJ/mol) and CO$_2$ (~35.4 kJ/mol) in **1′** is realized by the interactions with pendant oxygen atoms and aromatic pyridyl moieties. Density functional theory calculations is quantitatively agrees with the experimental values of heat of adsorption and are also able to uncover the nature of interactions between H$_2$ (or CO$_2$) with the atoms of the MOF. This has been made possible through detailed structure analyses augmented by an analysis of the electron density. The experimental and theoretical investigations unequivocally suggest that the high polarity of the pore surfaces decorated by the oxygen atoms and aromatic rings provide significant contribution for the high heat of adsorption values. Thus, by modulating the pore environment *via* immobilizing the hetero atoms (N, O, F) in the pore surface, the gas adsorption properties of the resulting MOF can be fine-tuned. This affords a methodology for the development of high capacity of H$_2$/CO$_2$ storage materials that may operate at ambient conditions which is significant in the context of global energy and environment issues.

5.6 References

1) a) H. Li, M. Eddaoudi, M. O. Keeffe, O. M. Yaghi, *Nature* **1999**, *402*, 276; b) T. K. Maji, , S. Kitagawa, *Pure. Appl. Chem.* **2007**, *79*, 2155; c) M. Eddaoudi, J. Kim, N. Rosi, D. Vodak, J. Wachter, M. O. Keeffe, O. M. Yaghi, *Science* **2002**, *295*, 469; d) R. Vaidhyanathan, S. S. Iremonger, K. W. Dawson , G. K. H. Shimizu, *Chem. Commun.* **2009***, 35*, 5230.

2) a) D. Farrusseng, S. Aguado , C. Pinel, *Angew. Chem., Int. Ed.* **2009**, *48*, 7502; b) L. Q. Ma, C. Abney, W. B. Lin, *Chem. Soc. Rev.* **2009**, *38*, 1248; c) O. Ohmori, M. Fujita, *Chem. Commun.* **2004**, 1586.

3) a) K. Gedrich, I. Senkovska, N. Klein, U. Stoeck, A. Henschel, M. R. Lohe, I. A. Baburin, U. Mueller , S. Kaskel, *Angew. Chem. Int. Ed.* **2010**, *49*, 8489; b) Z. Y. Gu , X. P. Yan, *Angew. Chem.Int. Ed.* **2010**, *49*, 1477; c) J. R. Li, R. J.

Kuppler   , H. C. Zhou, *Chem. Soc. Rev.* **2009**, *38*, 1477; d) S. Horike, S. Shimomura, S. , Kitagawa *Natur. Chem.* **2009**, *1*, 695.

4) a) Y. Takashima, V. M. Martinez, S. Furukawa, M. Kondo, S. Shimomura, H. Uehara, M. Nakahama, K. Sugimoto, S. Kitagawa, *Nat. Commun.* **2011**, *2*, 168*;* b) K. Jayaramulu, P. Kanoo, S. J. George , T. K. Maji, *Chem.Commun.* **2010**, *46*, 7906; c) M. D. Allendorf, C. A. Bauer, R. K. Bhakta , R. J. T. Houk, *Chem. Soc. Rev.* **2009**, *38*, 1330; d) J. Rocha, L. D. Carlos, F. A. A. Paz, D. Ananias, *Chem. Soc. Rev.* **2011**, *40,* 926.

5) a) M. Kurmoo, *Chem. Soc. Rev.* **2009**, *38*, 1353; b) C. M. Nagaraja, J. N. Behera, T. K. Maji, S. K. Pati , C. N. R. Rao. *Dalton Trans* **2010**, *39*, 6947; b) M. Du , X. H. Bu, *Prog. Chem.,* **2009**, *21*, 2458; c) H. P. Jia, W. Li, Z. F. Ju, J. Zhang, *Eur. J. Org. Chem.* **2006**, *4*, 4264.

6) a) T. K. Maji, R. Matsuda , S. Kitagawa, *Nat. Mater.* **2007**, *6*, 142; b) B. C. Tzeng, T.H. Chiu, B.S. Chen , G. H. Lee, *Chem. Eur. J.* **2008**, *14*, 5237; c) S. Muthu, J. H. K. Yip , J. J. Vittal, Chem. Soc., *Dalton Trans.* **2002**, 4561.

7) a) P. Horcajada, C. Serre, G. Maurin, N. A. Ramsahye, F. Balas, M. Vallet-Regi, M.Sebban, F. Taulelle , G. Ferey, *J. Am. Chem. Soc.* **2008**, *130*, 6774; b) N. J. Hinks, A. C. McKinlay, B. Xiao, P. S. Wheatley , R. E. Morris, *Microporous Mesoporous Materials* **2010**, *129*, 330; c) W. B. Lin, W. J. Rieter, , K. M. L. Taylor, *Angew. Chem. Int. Ed.* **2009**, *48*, 650; d) K. M. L. Taylor-Pashow, J. Della Rocca, R. C. Huxford , W. B. Lin, *Chem. Commun.* **2010**, *46*, 5832.

8) a) M. Higuchi, D. Tanaka, S. Horike, H. Sakamoto, K. Nakamura, Y. Takashima, Y. Hijikata, N. Yanai, J. Kim, K. Kato, Y. Kubota, M. Takata , S. Kitagawa, *J. Am. Chem. Soc.* **2009,** *131*, 10336; b) D. Tanaka, K. Nakagawa, M. Higuchi, S. Horike, Y. Kubota, T. C. Kobayashi, M. Takata , S. Kitagawa, *Angew. Chem. Int. Ed.* **2008**,*47*, 3914; c) T. Fukushima, S. Horike, Y. Inubushi, K. Nakagawa, Y. Kubota, M. Takata , S. Kitagawa, *Angew. Chem. Int. Ed.* **2010**, *49*, 4820; d) A.D. Burrows, *Cryst. Eng. Comm.* **2011**, *13*, 3623; e) B. Q. Ma, K. L. Mulfort , J. T. Hupp, *Inorg. Chem.* **2005**, *44*, 4912. f) P. Kanoo, R. Sambhu , T. K. Maji, *Inorg. Chem.* **2011**, *50*, 400; (g) H. J. Park, M. P. Suh, *Chem. Eur. J.* 2008, 14, 8812; h) P. Kanoo , T. K. Maji, *Eur. J. Inorg.*

Chem. **2010**, 3762 ; i) P. Kanoo, R. Matsuda, M. Higuchi, S. Kitagawa , T. K. Maji, *Chem. Mater.* **2009**, *21*, 5860.

9) E. Garrone, B. Bonelli , C. Otero Area, *Chem. Phys. Lett*. **2008**, *456*, 68.

10) a) J. L. C. Rowsell , O. M. Yaghi, *Angew. Chem. Int. Ed.* **2005**, *44*, 4670; b) M. D.A. Dailly, Y. Liu, C. M. Brown, D. A. Neumann , J. R. Long, *J. Am. Chem. Soc.* **2006***, 128*, 16876; c) S. S. Kaye , J. R. Long, *J. Am. Chem. Soc.* **2008**, *130*, 806.

11) a) Z. Hulvey, D. A. Sava, J. Eckert , A. K. Cheetham, *Inorg. Chem*. **2011**, *50*, 403; b) K. Uemura, A. Maeda, T. K. Maji, P. Kanoo , H. Kita, *Eur. J. Inorg. Chem*. **2009**, 2329; c) G. Feréy, M. Latroche, C. Serre, F. Millange, T. Loiseau , A. P. G. Gan, *Chem. Commun.* **2003**, 2976; d) J. L. C. Rowsell , O. M. Yaghi, *J. Am. Chem. Soc.* **2006**, *128*, 1304; e) M. Dinca, A. Dailly, C. Tsay , J. R. Long, *Inorg. Chem*. **2008**, *47*, 11; f) R. Vaidhyanathan, S. S. Iremonger, K. W. Dawson , G. K. H. Shimizu, *Chem. Commun*. **2009**, 5230; g) R. Vaidhyanathan, S. S. Iremonger, G. K. H. Shimizu, P. G. Boyd, S. Alavi , T. K. Woo, *Science* **2010**, *330*, 650; h) H. Hayashi, A. P. Cote, H. Furukawa, M. O'Keeffe , O. M. Yaghi, *Nat. Mater*. **2007**, 6, 501.

12) a) K. L. Gurunatha, K. Uemura , T. K. Maji, *Inorg. Chem.* **2008**, *47*, 6578; b) T. K. Maji, G. Mostafa, H. C. Chang , S. Kitagawa, *Chem. Commun*. **2005**, 2436; c) J.-Z. Gu, W.-G. Lu, L. Jiang, H. C. Zhou , T.-B. Lu, *Inorg. Chem.* **2007**, *46* , 5837; d) W. G. Lu, C.Y. Su, T.B. Lu , L. Jiang, J.M. Chen, *J. Am. Chem. Soc.* **2006** , *128* , 34; e) Y. L. Liu, V. Kravtsov, R. Larsen , M. Eddaoudi, *Chem. Commun.* **2006**, 1488; f) R. Q. Fang , X. M. Zhang, *Inorg. Chem.* **2006**, *45*, 4801.

13) *SAINT*, 6.02 ed., Bruker AXS, Madison, WI, **1999**.

14) G.M.Sheldrick, *SADABS, Empirical Absorption Correction Program*, University of Göttingen, Göttingen, Germany, **1997**

15) A. Altomare, G. Cascarano, C. Giacovazzo, A. Gualaradi, *J.Appl. Crystallogr.* **1993**, *26*, 343.

16) A. L. Spek, *J. Appl. Crystallogr,* **2003**, *36*, 7.

17) G. M.Sheldrick, *SHELXL 97*, Program for the Solution of Crystal Structure, University of Göttingen, Germany, **1997**.

18) G.M. Sheldrick, *SHELXS 97*, Program for the Solution of Crystal Structure, University of Göttingen, Germany, **1997**.

19) WinGX, A Windows Program for Crystal Structure Analysis: L. J. Farrugia, *J. Appl. Crystallogr*. **1999**, *32*, 837.

20) J. Hutter, J. P. Ballone, M. Bernasconi, P. Focher, E. Fois, S. Goedecker, D. Marx, M. Parrinello , M. E. Tuckerman, *CPMD Version* 3.13.2, *Max Planck Institutfuer Festkoerperforschung,* Stuttgart, IBM Zurich Research Laboratory, **1990**.

21) N. Troullier , J. L. Martins, *Phys. Rev. B* **1991**, 43, 1993.

22) a) A. D. Becke, Phys. *Rev. A*. **1988**, *38*, 3098; b) C. Lee, W. Yang , R. G. Parr, *Phys. Rev. B*. **1988**, *37*, 785.

23) R. Car, M. Parrinello, *Phys. Rev. Lett*. **1985**, 55, 2471.

24) G. J. Martyna, M. L. Klein , M. E. Tuckerman, *J. Chem. Phys*. **1992**, *97*, 2635.

25) K. Sillar, A. Hofmann , J. Sauer, *J. Am. Chem. Soc*. **2009**, *131*, 4143.

26) S.J. Grimme, *Comput. Chem.* **2006**, *27*, 1787.

27) a) Jmol: An open-source Java viewer for chemical structures in 3D. http://www.jmol.org/ ; b) B. McMahon , R. M. Hanson, *J. Appl. Crystallogr.* **2008**, *41*, 811.

28) W. Humphrey, A. Dalke, K. Schulten, *J. Mol. Graphics* **1996**, *14*, 33

29) a) V. A. Blatov, L. Carlucci, G. Ciani , D. M. Proserpio, *Cryst Eng Comm.* **2004**, *6*, 377;   b) V. A. Blatov, A. P. Shevchenko , V. N. Serezhkin, *J. Appl. Crystallogr.* **2000**, *33*, 1193.

30) a) D. W. Beck, *Zeolite Molecular Sieves*, *Wiley & Sons,* New York, **1974**; *b*) C. E. Webster, R. S. Drago , M. C. Zerner, *J. Am. Chem. Soc.* **1998**, *120*, 5509.

31) a) A. Saito , H. C. Foley, *AIChE. J.* **1991**, *37*, 429; b) H. J. Park, Y. E. Cheon, M. P. Suh, *Chem. Eur. J*. **2010**, *16*, 11662.

32) a) S. S. Kaye , J. R. Long, *J. Am. Chem. Soc.* **2005**, *127*, 6506; b) Y. E. Cheon , Myunghyun Paik Suh, *Chem. Commun.* **2009**, 2296.

33) a) G. Feréy , C. Serre, *Chem. Soc. Rev.* **2009**, *38*, 1380; b) F. X. Coudert, C. M. Draznieks, A. H. Fuchs , A. Boutin., *J. Am. Chem. Soc.* **2009**, *131*,11329; c) H. J. Park , M. P. Suh, *Chem. Commun*. **2010**, *46*, 610; d) S. Bourrelly, P. L. Llewellyn, C. Serre, F. Millange, T. Loiseau , G. Feréy, *J. Am. Chem. Soc*. **2005**, *127*, 13519.

34) M. M. Dubinin, *Chem. Rev.* **1960**, *60*, 235.

35) a) A. Kuc, T. Heine, G. Seifert , H. A. Duarte, Theor. *Chem. Acc.* **2008**, 1*20*, 543; b) A. Kuc, T. Heine, G. Seifert , H. A. Duarte, *Chem. Eur. J.* **2008**, *14*, 6597; c) R. B. Perez, E. G. Pérez, J. J. G. Sevillano, P. J. Merkling , S. Calero, *Adsorption Science , Technology* **2010**, *28*, 823; d) F. Salles, H. Jobic, A. Ghoufi, P. L. Llewellyn, C. Serre, S. Bourrelly, G. Ferey , G. Maurin, *Angew. Chem. Int. Ed.* **2009**, *48*, 8335; e) C. O. Areán, S. Chavan, C. P. Cabello, E. Garrone , G. T. Palomino, *Chem. Phys. Chem.* **2010**, *11*, 3237.

36) B. L. Bhargava , S. Balasubramanian, *Chem. Phys. Lett.* **2007**, *444*, 242.

37) T. Bucko, J. Hafner, S. Lebegue , J. G. Angyan, *J. Phys. Chem. A.* **2010**, *114*, 11814.

38) a) O. Talu, *Adv. Colloid Interface Sci.* **1998**, *227*,76 ; b) J Purewal, *Hydrogen adsorption alkali metal graphite intercalation compounds. Ph.D. Dissertation, California Institute of Technology, Pasadena,* CA, **2010**.

Chapter 6

A 3D Bio-MOF of Fe(III): Guest-Responsive Structural Transformation, Selective CO$_2$ Uptake and Controlled Drug Delivery
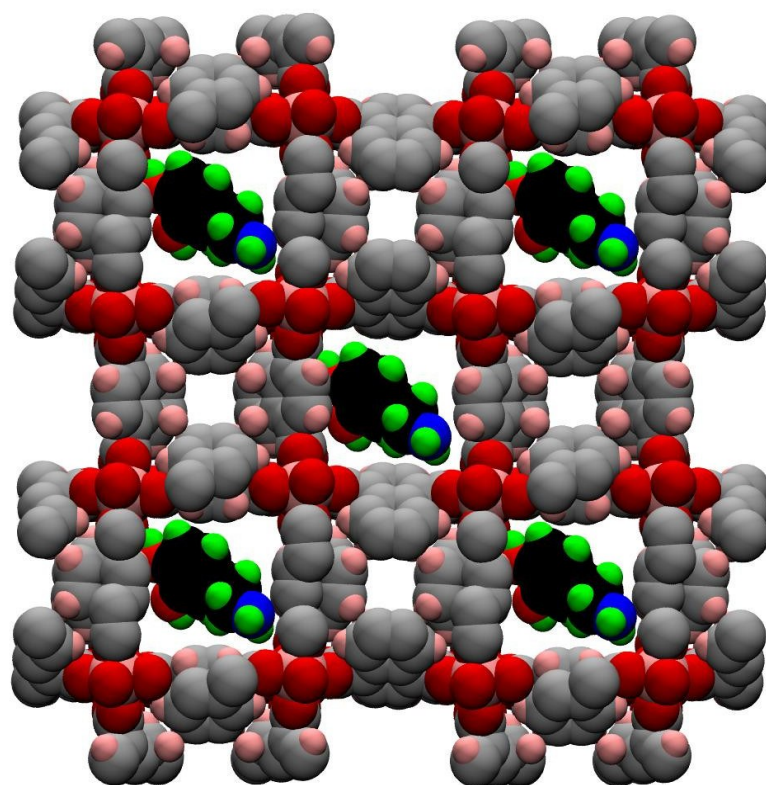
Summary

This chapter describes the synthesis and structural charaterization of a 3D antiferromagnetic metal-organic framework of Fe(III), $\{[Fe(1,4\text{-napdc})(\mu\text{-OH})](H_2O)\}_n$ (**1**) (1,4-napdc = 1,4-naphthalenedicarboxylate). Structure determination reveals that 1D Fe^{III}-OH-Fe^{III} inorganic chains are crosslinked by the 1,4-napdc linkers resulting in a 3D biporous framework. The framework shows guest responsive reversible crystal dynamics, associated with the mobile rotational properties of the naphthalene moiety of 1,4-napdc linker as realized from single-crystal-to-single-crystal structural transformation.   The framework is hydrophobic in nature and exhibits selective CO_2 uptake characteristics at 195 K. Furthermore, the bio-compatible, flexible, thermally and chemically stable framework **1** was exploited as a drug delivery system. Framework **1** exhibits a remarakable loading capacity of dopamine (360 mg of drug per gram of MOF), which is known to inhibit parkinson's disease. In vitro studies reveal that there is a controlled release of the dopamine from the framework over a time period of 15 days under physiological conditions. Furthermore, DFT calculations were performed to understand the microscopic interactions of dopamine in the pore surface of the desolvated framework $\{[Fe(1,4\text{-napdc})(\mu\text{-OH})]\}_n$ (**1a**).

6.1. Introduction

Compared to the conventionally used microporous inorganic materials such as zeolites, metal-organic frameworks (MOFs) provide more flexibility and functionality through the rational design and control of the framework architecture.[1] In particular, these ordered porous materials are capable of selective sorption of certain gases and are also expected to find applications in sensing and separation of these gases from geaseous mixtures.[2] The characteristics of the pore surface, like polarity strongly depends upon the choice of organic linkers and metal ions.[2a] Moreover, the incorporation of a mobile linker having rotatable group(s) could lead to a dynamic guest responsive behavior in MOFs.[1a] Molecular rotation in porous solids in response to the external stimulus such as light, heat, or electric fields is important for the development of nanoscale devices.[1b] In an ever expanding field of MOF research, Fe^{III} based frameworks have been less developed so far, although they are important for material chemistry due to their abundance, safeness and environmental persistence. These play a significant role as active centers in a variety of important biological functions.[3] Furthermore, synthesis of Fe^{III} based MOFs have received particular interest because of their biocompatibility and preliminary in vivo studies suggest that Fe^{III}-carboxylate MOFs are biodegradable, with recycling of Fe^{III} and a comfortable clearance of the carboxylate linker. Recent in vitro and in vivo toxicological studies on Fe^{III}-carboxylate MOFs are extremely promising.[4] Feréy and coworkers first reported a high loading and controlled drug delivery sytems under physiological coditions based on rigid (MIL-100 and MIL-101) and flexible MOFs (MIL-53-Fe) (MIL= Materails of Institut Lavoisiser) with ibuprofen as a model drug.[5] Lin *et al.* showed the release of cis-platin over three days under physiological conditions in PBS with a silica coated Fe^{III}-terephtalate MOF.[6] Recetly Horcajada *et al.* reported a nanoscale Fe^{III}-carboxylate MOF and demonstrated the encapsulation and controlled delivery of a large number of therapeutic molecules such as busulfan, porcidofovir, and azidothymidine with potential antitumor and antiretroviral activities.[3a] In this context, it is worth mentioning that the other porous materails such as zeolites and mesoporous silicas exhibit low drug storage capacity and also a rapid delivery which is known as the 'burst' effect.[7] Also hydroxo, oxo or carboxylate bridged Fe(III) compounds are expected to exhibit unique magnetic behaviors. Therefore with the improved

168

applications in biology, gas storage and magnetic properties, the design and synthesis of a novel flexible and dynamic Fe(III) based MOFs with ordered porous structure is highly sought after.[4] For this purpose, we have utilized a planar 1,4-naphthalene dicarboxylate (1,4-napdc) anion because it has not only a constitutional stiffness and hydrophobic properties but also a rotatable naphthalene ring for fabrication of Fe(III)-MOF. This chapter deals with a synthesis, structural characterization, magnetic and sorption properties of a 3D Fe(III)-MOF, {[Fe(1,4-napdc)(μ-OH)](H_2O)}$_n$ (**1**). The framework shows guest responsive reversible crystal dynamics, associated with the mobile rotational properties of naphthalene moiety of 1,4-napdc linker as realized from single-crystal-to-single-crystal structural transformation. The framework is hydrophobic in nature and exhibits selective CO_2 uptake characteristics at 195 K. Furthermore the dehydrated framework **1a** has been used as matrices for the adsorption and in vitro drug delivery of dopamine under physiological conditions using a phosphate buffered saline (PBS).[8]

6.2 Experimental Section

6.2.1 Materials

$FeCl_2.4H_2O$, 1,4-napthalenedicarboxylate (1,4-napdc), phosphate buffered saline (PBS) and dopamine were purchased at an analytical pure grade and were used without any further purification. Millipore water and ethanol were used wherever essential.

6.2.2 Synthesis of {[Fe(1,4-napdc)(μ-OH)](H_2O)}$_n$ (1)

In a typical synthesis of **1**, $FeCl_2.4H_2O$ (1 mmol, 0.198 g), 1,4-napdcH_2 (1 mmol, 0.216 g) and KOH (2 mmol, 0.112 g) were mixed well in H_2O (8 ml) and the whole reaction mixture was placed in a 23 mL Teflon-lined autoclave. The reaction mixture was subsequently heated to 180°C for 5 days. The autoclave was cooled over a period of 12 hrs at a rate of 10°C /h. The final product was filtered and washed with H_2O. Yellowish-orange needles of compound **1** were present as a minor phase and the major phase in the product was yellow-orange powder. The crystals were separated manually under microscope. IR (KBr cm^{-1}); v(O-H), 3443; v_{as}(OCO), 1615; v_s(OCO), 1443. Elemental analysis (%) calcd. for $C_{12}H_9O_6Fe$: C, 47.21; H, 2.950. Found: C, 46.59; H, 2.84.

6.2.3 Incorporation of Dopamine

The dopamine loading was performed by introducing 10mg of the desolvated framework in different amounts dopamine in a 10 ml ethanol solution. The adsorbed amount of dopamine in the framework **1a** was estimated by various techniques such as UV-Vis spectroscopy, thermogravimetric analysis (TGA), elemental analysis and FT-IR.

6.2.4 Drug Release Experiments

The drug release experiment was performed in a glass apparatus at 37°C under physiological PBS conditions. Framework **1a** containing a known amount of dopamine was suspended in physiological PBS (100 mL). The mixture solution was mechanically stirred and the temperature was maintained at 37 ^{o}C in a water bath. Samples (2 mL) were periodically removed and assayed. The volume of each sample withdrawn was replaced by the same volume of fresh physiological PBS.

6.3 Characterization Techniques

6.3.1 Physical Measurements

Elemental analysis was carried out using a Thermo Scientific Flash 2000 CHN analyzer. IR spectra were recorded using KBr pellets in the range 4000 - 400 cm^{-1} on Bruker IFS-66v spectrophotometer. Thermogravimetric analyses (TGA) were carried out under nitrogen (flow rate of 50 mL/min) with Metler Toledo TGA-850 TG analyzer in the temperature range between 25 - 650°C at a heating rate 3°C / min. Powder X-ray diffraction (PXRD) pattern were recorded on a Bruker D8 Discover instrument using Cu-Kα radiation. XPS spectra were recorded on a OMICRON nanotechnology spectrometer. Energy-dispersive analyses of X-rays (EDAX) were obtained by means of FEI (Nova-Nano SEM-600 Netherlands). IR spectra were recorded using KBr pellets in the range 4000 - 400 cm^{-1} on Bruker IFS-66v spectrophotometer.UV-Vis absorption measurements were carried out at room temperature with a Perkin-Elmer model Lambda 900 UV/Vis/NIR spectrometer. Magnetic measurements were carried out with a vibrating sample magnetometer in Physical Properties Measurement Systems (PPMS, Quantum Design, USA).

6.3.2 Adsorption Measurements

Adsorption studies of N_2 (77 K), CO_2 (195 and 298 K) and H_2 (77 K) on the dehydrated samples prepared at 393 K under high vacuum, were carried out using QUANTACHROME AUTOSORB-1C analyzer. The adsorption isotherm of different solvents (like H_2O, EtOH and C_6H_6, at 298 K and MeOH at 293 K) were measured in the vapour state by using BELSORP-aqua volumetric adsorption instrument from BEL, Japan. In the sample chamber (~12 mL) maintained at T ± 0.03 K was placed the adsorbent sample (100-150 mg), which had been prepared at 393 K at 10^{-1} Pa for 18 hours prior to measurement of the isotherms. The adsorbate was charged into the sample tube, and then the change of the pressure was monitored and the degree of adsorption was determined by the decrease of the pressure at the equilibrium state. All operations were computer-controlled and automatic. High-pressure CO_2 and CH_4 (at 298 K) sorption measurements were carried out on a fully computer controlled volumetric BELSORP-HP, BEL JAPAN high pressure instrument. All the gases used for the high pressure measurements are scientific/research grade with 99.999% purity. For the measurements, approximately 300 mg sample was taken in a stainless-steel sample holder and degassed at 393 K for a period of 18 hours under 0.1 Pa vacuum. Dead volume of the sample cell was measured with helium gas of 99.999% purity. Non-ideal correction for H_2 and CO_2 gases were made by applying virial coefficients at the respective measurement temperature.

6.3.3 Single-Crystal X-ray Diffraction

A suitable single crystal for **1, 1a** (dehydrated) and **2** (rehydrated) was carefully selected under a polarizing microscope and fixed to a separate thin glass fiber by commercially available glue. X-ray single crystal structural data was collected by Rigaku mercury–CCD diffractometer equipped with a normal focus, 2.4 kW sealed tube X-ray source (Mo-K$_\alpha$ radiation, 0.71073 Å) operating at 50 kV and 30 mA. The programme SAINT[9] was used for integration of diffraction profiles and an empirical absorption correction based on symmetry equivalent reflections was applied using the SADABS program.[10] The structure was solved by direct method using SIR92 programme[11] and refined by full matrix least square method using SHELXL 97.[12] The hydrogen atoms were fixed by HFIX and placed in ideal positions. Potential solvent accessible area or void space was calculated using the PLATON 99[13] multipurpose

crystallographic software. Final refinement included atomic positions for all the atoms, anisotropic thermal parameters for all the non-hydrogen atoms. All calculations were carried out using WinGX system, Ver 1.70.01.[14]

6.3.4 Crystal data

(a) Crystal data of 1: $FeC_{12}H_6O_6$, M_w= 302.02, Tetragonal, $P4_2/nmc$ (no. 137), $a = b =$ 21.432(3) Å, c = 6.8745(10) Å, V = 3157.7(8) Å^3, Z = 8, ρ_{calc} = 1.271 g cm^{-3}, μ (Mo-K_α) = 0.970 mm^{-1}, T = 243 K; λ(Mo-K_α) = 0.71069 Å, θ_{max} = 27.5°, Total data =12455, Unique data = 1908, R_{int} = 0.037, Observed data [$I>2\sigma(I)$]= 1633, R = 0.0628, R_w = 0.0954, GOF = 1.32; (b) Crystal data of 1a (dehydrated) : $FeC_{12}H_6O_5$, M_w= 286.02, Tetragonal, $P4_22_12$ (no. 94), $a = b$ = 21.430(3) Å, c = 6.8706(9) Å, V = 3149.4(7) Å^3, Z = 8, ρ_{calc} = 1.207 g cm^{-3}, μ(Mo-K_α) = 0.964 mm^{-1}, T = 373 K; λ(Mo-$K\alpha$) = 0.71069 Å, θ_{max} =27.5°, Total data = 26786, Unique data = 3612, R_{int} = 0.038, Observed data [$I> 2\sigma(I)$]= 3346, R = 0.0625, R_w = 0.1582, GOF = 1.19, Flack x = 0.5; (c) Crystal data of 2 (rehydrated) : $FeC_{12}H_6O_6$, M_w = 302.02, Tetragonal, $P4_2/nmc$ (no.137), $a = b$ = 21.409(3) Å, c = 6.8620(10) Å, V = 3145.2(8) Å^3, Z = 8, ρ_{calc} = 1.276 gcm^{-3}, μ(Mo$_{K\alpha}$) = 0.973 mm^{-1}, T = 293 K; λ(Mo-$K\alpha$) = 0.71069 Å, θ_{max} =27.5°, Total data = 24252, Unique data = 1902, R_{int} = 0.038, Observed data [$I> 2\sigma(I)$] = 1652, R = 0.0566, R_w = 0.1211, GOF = 1.23.

6.3.5 Computational Details

In order to find the position of dopamine drug molecules in **1a**, density functional theory (DFT) studies were carried out using the QUICKSTEP module in CP2K software.[15] All valence electrons were treated in a mixed basis set with an energy cut-off of 280 Ry. The short-range version of double zeta single polarization basis set was used. The effect of core electrons and nuclei were considered by using pseudopotentials of Goedecker-Teter-Hutter (GTH).[16] The exchange and correlation interaction between electrons was treated with the Perdew-Burke-Ernzerhof (PBE) functional.[17] Since van der Waals interactions between the dopamine and **1a** were very important, their effects were accounted by employing empirical corrections developed by Grimme. Three schemes, PBE, PBE-D2 and PBE-D3, were used to calculate the cell volume and binding energy.[18]

6.4 Results and Discussion

6.4.1. Structural Description of {[Fe(1,4-napdc)(μ-OH)](H$_2$O)}$_n$(1)

MOF **1** was synthesized under hydrothermal reaction conditions and yellowish-orange crystals were obtained with the reaction of FeCl$_2$.4H$_2$O and 1,4-napdcH$_2$ in the presence of KOH. Single crystal X-ray crystallographic results revealed a 3D porous framework built up by Fe(III) and 1,4-napdc (Figure 1a). All the Fe atoms were assigned to be high-spin Fe(III) by XPS spectra (Figure 2). The Fe atom, located on an inversion centre, is in an octahedral environment with the four carboxyl and two μ_2-hydroxyl oxygen atoms.
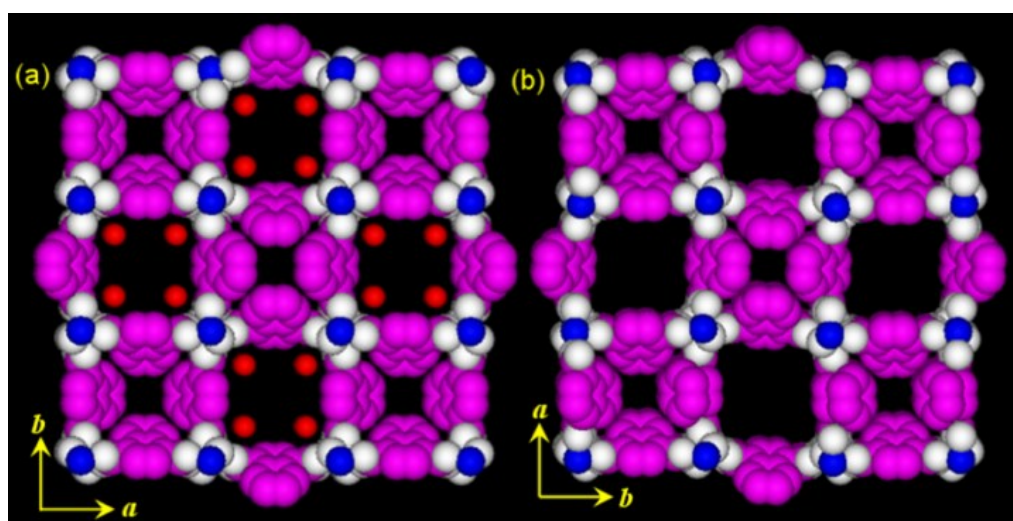
Figure 1 (a) View of the 3D network of **1** with alternating hydrophilic (water filled) and hydrophobic channel along the crystallographic *c*-axis; (b) View of the 3D dehydrated framework (**1a**).
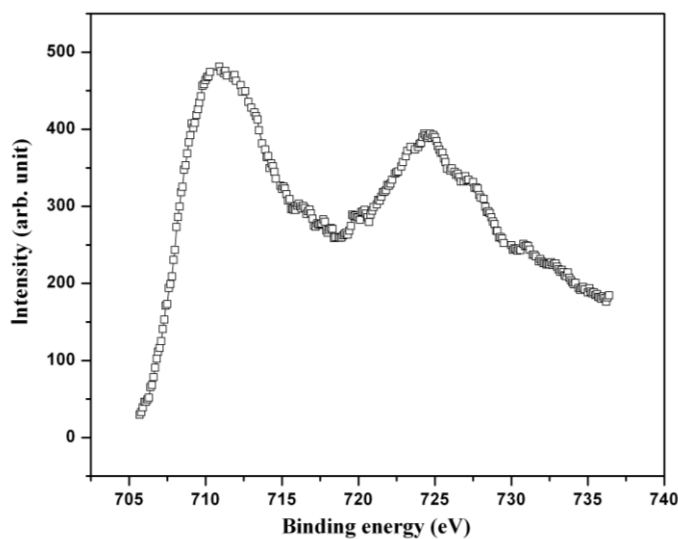
Figure 2 XPS for {[Fe(1,4-napdc)(μ-OH)](H$_2$O)}$_n$ (**1**).

Table 1 Selected Bond Distances [Å] and Angles [deg] for **1, 1a** and **2.**

{[Fe(1,4-napdc)(μ-OH)](H$_2$O)}$_n$ (1)			
Fe1-O1	1.9577(9)	Fe1-O1_h	1.9577(9)
Fe1-O2	2.0208(17)	Fe1-O3_p	2.0265(15)
Fe1-O3_g	2.071(2)	Ni1-N1#1	2.098(2)
O1-Fe1-O2	91.74(6)	O2-Fe1-O2_h	180.00
O1-Fe1-O3_g	90.91(6)	O2-Fe1-O3_p	87.76(7)
O1-Fe1-O1_h	180.00	O1_h-Fe1-O3_g	89.09(6)
O1-Fe1-O2_h	88.26(6)	O2_h-Fe1-O3_g	87.76(7)
O1-Fe1-O3_p	89.09(6)	O3_g-Fe1-O3_p	180.00
O2-Fe1-O3_g	92.24(7)	O1_h-Fe1-O2_h	91.74(6)
O1_h-Fe1-O2	88.26(6)	O1_h-Fe1-O3_p	90.91(6)
O1-Fe1-O2	91.74(6)	O2_h-Fe1-O3_p	92.24(7)
Symmetry Code: g = 1-y,1-x,1/2-z; h = 1-x,1-y,1-z; p = y,x,1/2+z			
{Fe(1,4-napdc)(μ-OH)}$_n$ (1a)			
Fe1-O1	2.064(5)	Fe1-O4_c	2.025(3)
Fe1-O5	2.090(4)	Fe1-O2_f	2.016(3)
Fe1-O6	2.102(5)	Fe1-O3_g	2.006(3)
O1-Fe1-O5	88.40(11)	O2_f -Fe1-O6	90.67(11)
O1-Fe1-O6	91.35(11)	O3_g -Fe1-O6	87.76(11)
O1-Fe1-O4_c	89.11(13)	O2_f -Fe1-O4_c	178.08(14)
O1-Fe1-O2_f	92.66(14)	O3_g-Fe1-O4_c	90.80(14)
O1-Fe1-O3_g	179.10(14)	O2_f -Fe1-O3_g	87.42(15)
O5-Fe1-O6	179.63(9)	Fe1-O5-Fe1_e	123.10(11)
O4_c-Fe1-O5	91.70(11)	Fe1-O6-Fe1_f	123.84(11)
O2_f-Fe1-O5	89.08(11)	O2_f -Fe1-O6	90.67(11)
Symmetry Code: c = -1/2+y,1/2-x,-1/2+z; e = y,x,-1-z; f = y, x,-z; g = 1/2-x,-1/2+y,-1/2-z.			
{[Fe(1,4-napdc)(μ-OH)](H$_2$O)}$_n$ (2)			
Fe1-O1	1.9521(8)	Fe1-O1_h	1.9521(8)
Fe1-O2	2.0174(15)	Fe1-O2_h	2.0174(15)
Fe1-O3_g	2.0185(13)	Fe1-O3_o	2.0185(13)
O1-Fe1-O2	91.81(6)	O2-Fe1-O3_o	88.34(6)
O1-Fe1-O3_g	91.14(6)	O1_h-Fe1-O3_g	88.86(6)
O1-Fe1-O1_h	180.00	O2_h-Fe1-O3_g	88.34(6)
O1-Fe1-O2_h	88.19(6)	O3_g-Fe1-O3_o	180.00
O1-Fe1-O3_o	88.86(6)	O1_h-Fe1-O2_h	91.81(6)
O2-Fe1-O3_g	91.66(6)	O1_h-Fe1-O3_o	91.14(6)
O1_h-Fe1-O2	88.19(6)	O2_h-Fe1-O3_o	91.66(6)
O2-Fe1-O2_h	180.00	O2-Fe1-O3_o	88.34(6)

The FeO$_6$ octahedron is slightly compressed, where axial Fe-O (μ-OH; O1, O1*) bond lengths are 1.9577(9) Å, equatorial Fe-O (O2, O2*, O3 and O3*) bond lengths are in the range of 2.0208(17) – 2.0265(15) Å, and the *cisoid* angles are 87.76(7)-92.24(7)° (Figure 3 and Table 1).
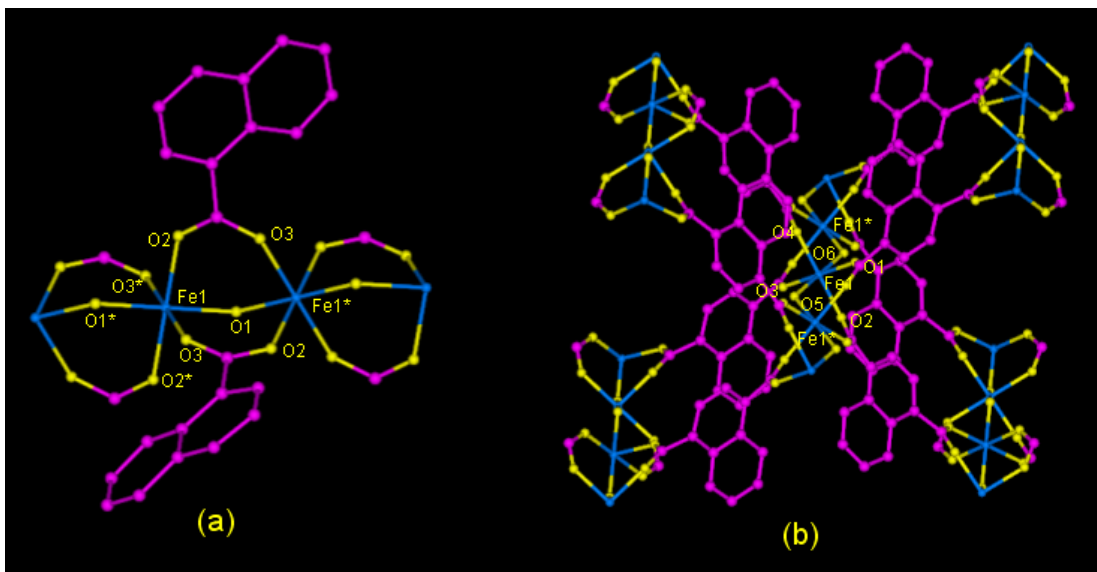
Figure 3 Views of the coordination environment around Fe(III): (**a**) in as-synthesized framework (**1**) and (b) dehydrated framework (**1a**).

The axial hydroxyl oxygen atoms are shared by the neighbouring octahedron, resulting in a zigzag -Fe-OH-Fe-OH- backbone along the *c*-axis with the Fe-OH–Fe angle of 122.78(9)°. The 1D chains are cross-linked by the 1,4-napdc ligands on the *ab* plane to form a 3D framework with 1D channels along the *c*-axis. The Fe….Fe separation along the Fe-OH-Fe backbone and 1,4-napdc bridge is 3.437(1) Å (= *c*/2) and 10.716(1) Å (= *a*/2 = *b*/2), respectively. On the mirror symmetric 1,4-napdc bridge, the dihedral angle between the naphthalene ring and the mean plane defined by O2, O3, O2*, O3* (*:1-x, 1-y, 1-z) is 41.37°. The 1D channels encompass two kinds of square shaped channels, one is hydrophilic filled with the four water molecules and other is hydrophobic where the naphthalene rings protrude into the groove making the channel narrower than the other (Figure 1a). The dimensions of hydrophilic and hydrophobic channels are 9.1 x 9.1 Å^2 and 3.5 x 3.5 Å^2, respectively[19 a],and the void space is estimated to be 38.7% to the total crystal volume (Figure 1a).[19b] Férey *et. al.*, recently reported a similar framework, [M(1,4-bdc)(μ-OH)], [M = V(III) (MIL-47) and Cr(III) (MIL-43)] with 1,4-benzene dicarboxylate linker having a single 1D hydrophilic channel structure.[4] In case of framework **1**, an alternate arrangement of the two channels with different polarity is provided by the kink of the 1,4-napdc linker with the pendent hydrophobic benzene ring.

6.4.2 Framework Stability

The TGA curve (Figure 4) of **1** indicates that the release of the guest water molecules occurred at ~ 348 K to give the dehydrated form, $[Fe(1,4\text{-napdc})(\mu\text{-OH})]_n$ (**1a**), which is stable up to ~538 K.
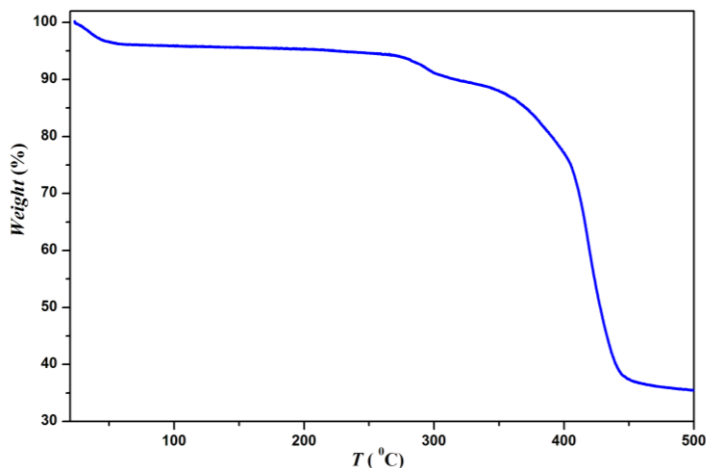
Figure 4 TG analysis of $\{[Fe(1,4\text{-napdc})(\mu\text{-OH})](H_2O)\}_n$(**1**) over the temperature range from 25-500°C at heating rate of 5°C/min under the N_2 atmosphere.

Figure 5 shows XRPD patterns simulated from the X–ray single crystal data of **1**, as–synthesized framework (**1**) and dehydrated framework (**1a**). The XRPD pattern of **1a** is similar to **1** but with a new peak around $2\theta = 9.02^0$, indicating that the framework undergoes a structural distortion upon dehydration and the structural integrity is maintained even without any guest water molecules.
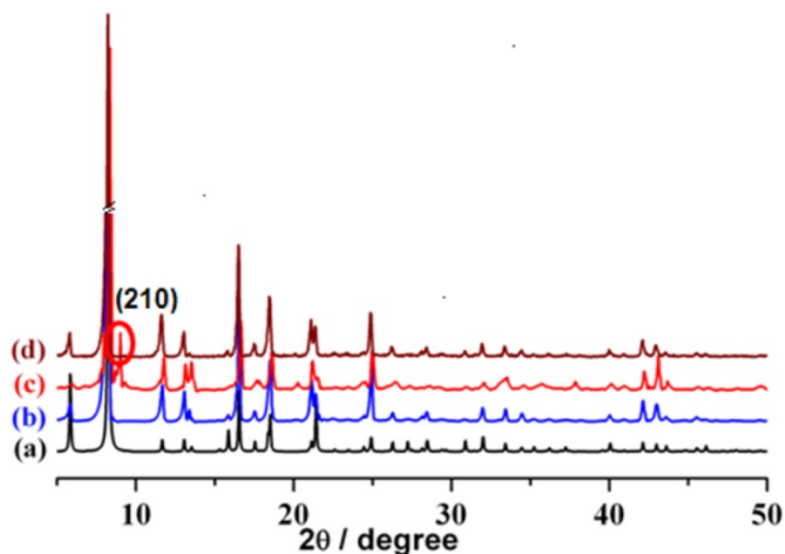
Figure 5 Powder XRD patterns: (a) simulated from X-ray single crystal data of **1**; (b) as-synthesized (**1**); (c) dehydrated (**1a**) and (d) Exposed to MeOH vapor.

6.4.3 Magnetic Property

The χ_M and $\chi_M T$ *vs.* T plots of **1** were shown in Figure 6. The $\chi_M T$ value gradually decreased with decreasing temperature, and reached a minimum value of 0.034 cm^3 K mol^{-1} at 2 K, which suggest a strong antiferromagnetic interaction between Fe(III) through the hydroxyl bridge. The Neel temperature, T_N, was determined to be 6.2 K from the weak field magnetization (Figure 6a(inset)) and ac magnetic responses (Figure 7). The low T_N stems from a very weak interaction between the antiferromagnetically coupled 1D Fe(III) chains through the 1,4-napdc bridges. The *M vs. H* plot of **1** at 2 K, showed a pronounced sigmodial shape with an inflection point at around 8 kOe and a small magnetization of 0.13 $N\beta$ at 50 kOe (Figure 6b (inset)). The metamagnet-like behavior is attributed to its structural anisotropy based on the 1D chain. The dehydrated and rehydrated compounds also showed essentially the same magnetic behavior as **1** (Figure 8).
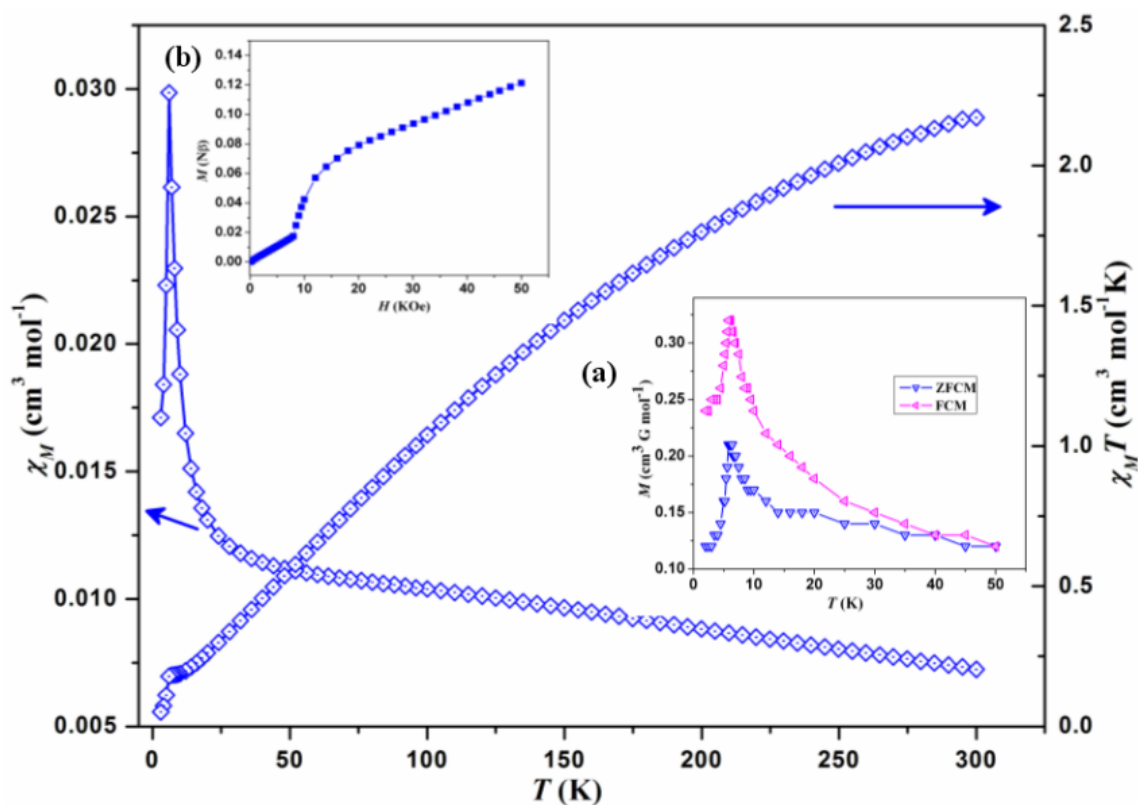
Figure 6 χ_M *vs. T* and $\chi_M T$ *vs. T* plots of **1** at 500 Oe. (Inset (a): ZFC and FC at 5 Oe; (b) magnetization *vs.* applied field at 2K).
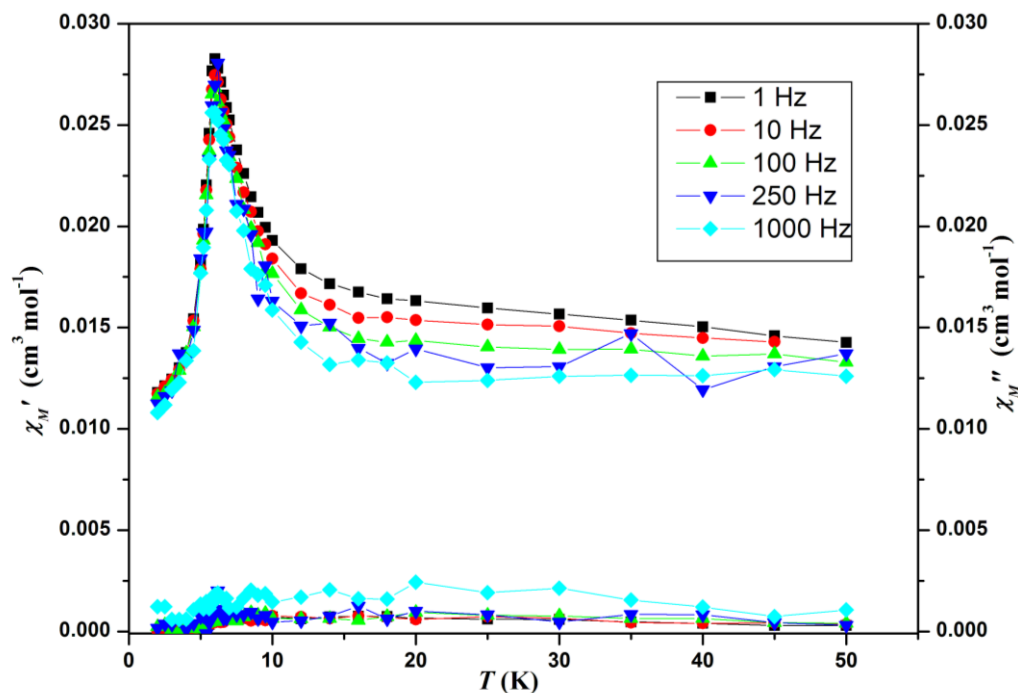
Figure 7 Temperature dependence ac magnetic susceptibility for **1**.
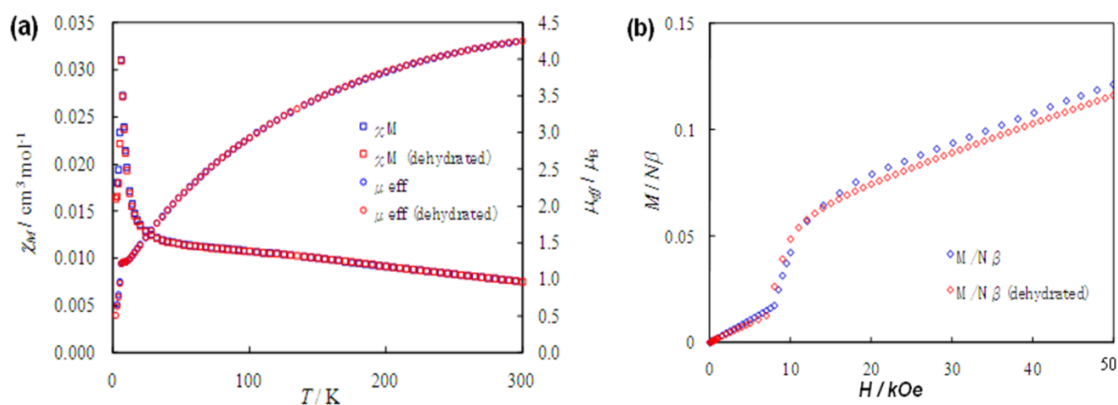
Figure 8 (a) Temperature dependencies of χ_M and μ_{eff} before/after dehydration (blue and red, respectively). The sample was dehydrated by heating in the SQUID at 400 K for 3 h with He substitution of the sample room; (b) Field dependencies of Magnetization before/after dehydration (blue and red, respectively).

6.4.4 Single –Crystal-Single-Crystal Structural Transformation

To confirm the structural change upon dehydration, single crystal data was collected at 393 K. After dehydration, the space group changed from achiral ($P4_2/nmc$ for **1**) to chiral ($P4_22_12$ for **1a**) with similar unit cell parameters. Based on the space group, the new peak in XRPD of **1a** is indexed (210) which is never observed in **1** due to the extinction rule. However, the Flack parameter was estimated to be 0.5, suggesting a racemic twinned crystal. In the racemic twinning case, enantiomeric

sublattice randomly coexists in the crystal and a chiral structure is determined for each sublattice. Therefore, it can be described that structural chirality was induced in the framework by dehydration. In the asymmetric unit of **1a**, each carboxylate group coordinates to the Fe atoms, now located in a general position, with the different Fe-O-C bridging angles and Fe-O-C-C torsion angles. The structural change induces the channel asymmetry and decreases the pore size (hydrophilic = 7.65 x 7.65 Å^2, hydrophobic = 3.06 x 3.06 Å^2) and also the void space (37.9%) compared to the initial framework **1**. Fe-O bond distances are in the range of 1.9466(11)-2.025(3) Å, similar to the as-synthesized framework. The dihedral angle between the naphthalene ring and the mean plane defined by two carboxylate groups (O1, O2, O3, O4) is reduced to 38.44°compared to **1** keeping with the twist of 1,4-napdc.
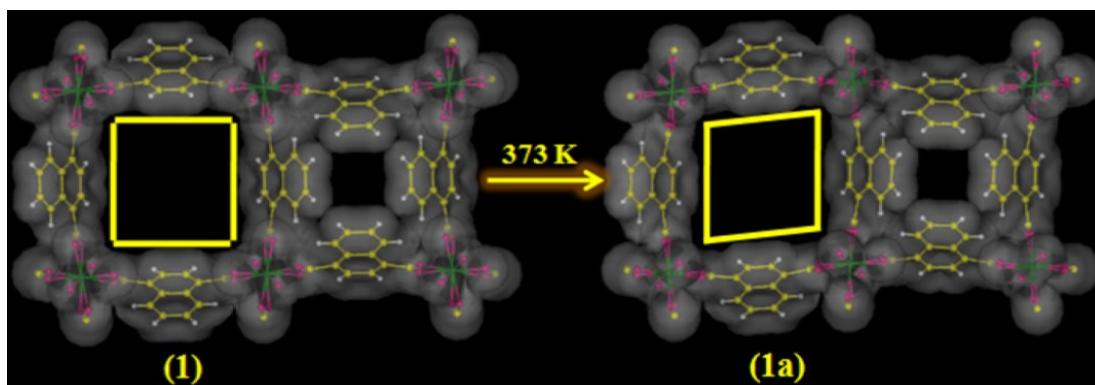
Figure 9 View of the asymmetry in pore surface after dehydration showing square shaped channel transformed to the rectangular shaped channel due to the ligand rotation after dehydration.

The Fe…Fe spacing lost $c/2$ relation as in **1** and spread over two unequal Fe…Fe distances. The Fe…Fe* (y, x, -z) and Fe…Fe* (y, x, -1-z) distances along Fe-OH-Fe backbone are 3.448(1) Å (d1) and 3.423(1) Å (d2), respectively and the sum of two distances equal the length of c-axis (d1 + d2 = c). The Fe….Fe separation along 1,4-napdc bridge is 10.711(1) Å. The of Fe$_2$(1,4-napdc)$_4$ of **1** and **1a** reveal the rotational motion of the framework components in the MOF after dehydration (Figure 9). Figure 9 shows that the structural transformation is induced by the reorientation of the mobile 1,4-napdc and a mild shift of Fe atoms after the release of solvent molecules. The *trans* 1,4-napdc ligands rotates in opposite directions with unequal amount about carboxylate C-C axis by 4.09^0, 4.06^0 and 56.01^0, 56.06^0, respectively.
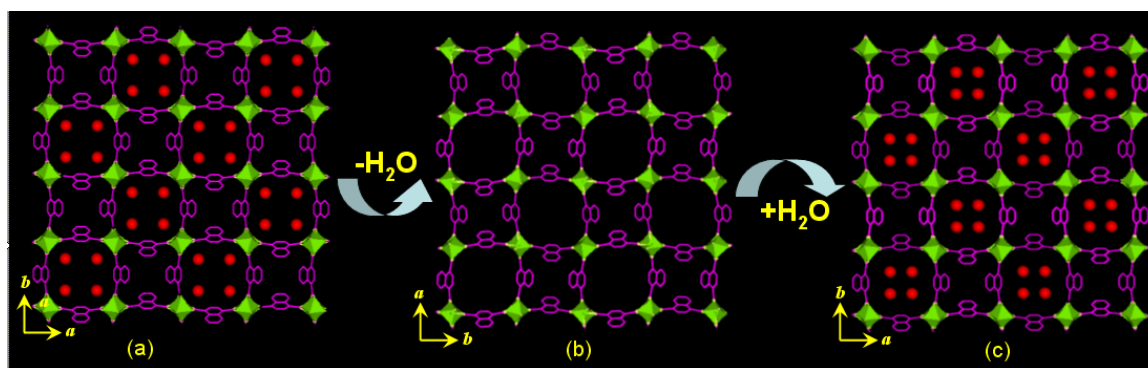
Figure 10 Single crytsal-to-single crystal strcutural transformation: Views of the 3D framework of (**a**) as-synthesized (**1**); dehydrated (**1a**) and rehydrated (**2**) along the crystallographic *c*-axis.

The chirality stems from the shift of Fe atom, which vanishes the centre of symmetry, and the unequal rotation of 1,4-napdc, which removes the mirror symmetry. When the dehydrated single crystal of **1a** was exposed to the ambient atmosphere for a week, it returns to the virgin crystal. X-ray structure determination of the rehydrated crystal (**2**) shows that the initial framework was completely regenerated with the space group of $P4_2/nmc$ (Figure 10).

6.4.5 Adsorption Studies

Sorption experiments with different adsorbates were carried out to confirm the permanent porosity of dehydrated framework (**1a**). The nitrogen adsorption-desorption isotherm obtained for the **1a** at liquid nitrogen temperature 77 K shows a typical type-II profile suggesting surface adsorption. Despite being a stable framework and having an adequate effective pore size, no N_2 (surface area = 16.3 $Å^2$, kinetic diameter = 3.64 Å)[23] diffusion at 77 K into the micropores was observed (Figure 11a). On the other hand, an appreciable amount of CO_2 (17.9 $Å^2$, 3.4 Å) uptake was observed at 195 K, despite the gas having a similar size with with N_2 (Figure 11(i)) The CO_2 adsorption study at 195 K reveals a steep uptake at low pressure region and shows a type-I curve where the amount of uptake was 110 ml/g (22 wt%), which signifies micro porous nature of the framework, Also **1a** shows a significant CO_2 uptake at 273 K of 22 mL/g (4.3 wt%) (Figure 11(i)). The Brunauer–Emmett–Teller (BET) surface area calculated from the CO_2 adsorption profile is 342 m^2g^{-1} and the corresponding pore volume is 0.108 cm^3g^{-1}. The framework **1a** exhibits a remarkbly high CO_2 and CH_4 uptake at room temperature

of 68 ml/g (14 wt%) and 45 ml/g (3.3 wt%) at 20 bar pressure respectively (Figure 11(ii)). The Dubinin–Radushkevich (DR) plot is almost linear in the higher pressure region and suggests a micropore volume of about 190.2 m^2/g, which corresponds to 0.42 molecules of CO_2 per formula unit.[20]
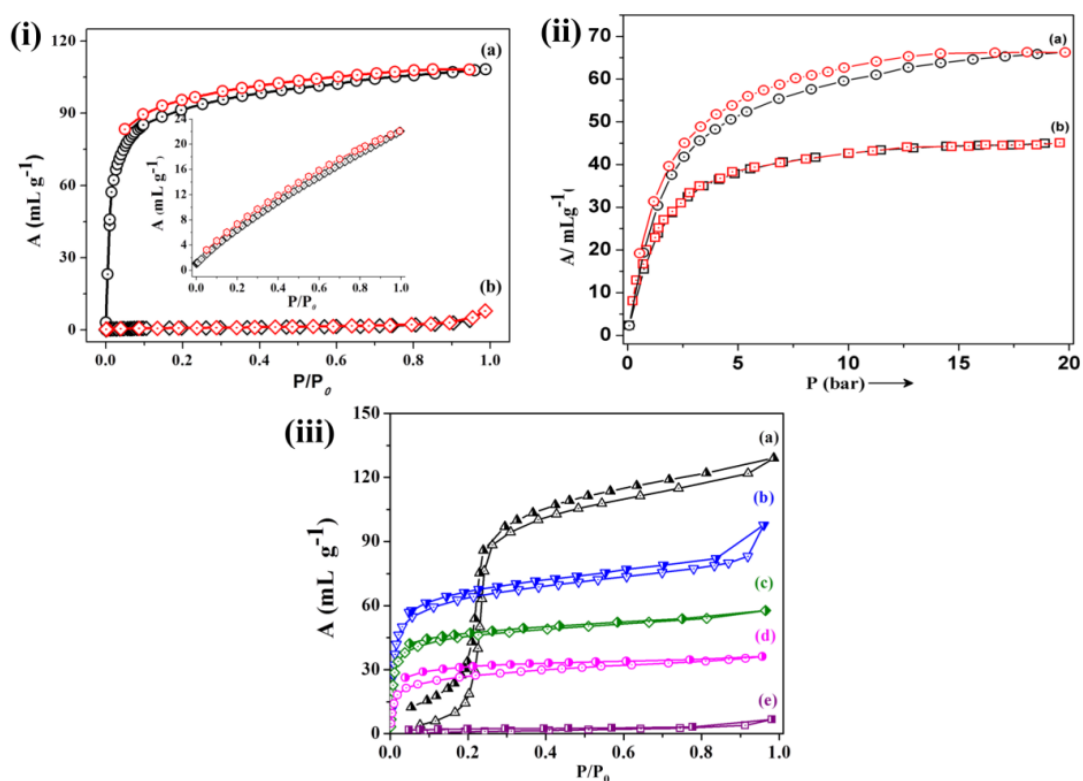
Figure 11 (i) (a) CO_2 at 195 K; (b) N_2 at 77K; Inset showing CO_2 at RT (1atm); (ii) (a) CO_2 and CH_4 atRT at 20 bar pressure; (iii) Sorption isotherm for different solvent vapors in **1a**: (a) H_2O, (b) MeOH, (c) EtOH, (d) C_6H_6, and (e) cyclohexane (C_6H_{12}) at 298 K, where P_0 is the saturated vapour pressure of the adsorabtes at 298 K.

In **1a**, the 1D channel along *c*-axis would be blocked by the condensed N_2 molecules at low temperature (77 K). Whereas, in the case of CO_2 (at 195 K) such condensation would be overcome by the thermal energy and the pore surface surrounded by the naphthalene ring which can provide stronger affinity and contribution to the potential energy for adsorption of CO_2 (dipole induced dipole interactions). Furthermore, to analyze the nature of the pore surface of **1a**, we have carried out a vapour sorption study with different solvent molecules (water (H_2O) methanol (MeOH), ethanol (EtOH), cyclohexane (C_6H_{12}) and benzene (C_6H_6)) of varying size and polarity. Interestingly water adsorption shows an unusual type-V profile with steep uptake at $P/P_0 \sim 0.2$ and saturates over $P/P_0 \sim 1$ with a significant

hystersis loop ((Figure 11(iii)). However, the sorption profiles of MeOH (3.8 Å), C_6H_6 (4.0 Å), EtOH (4.3 Å) and cyclohexane (4.5 Å) reveal a type I curve with small hysteresis and sorption amount increases with increasing pressure suggesting hydrophobic nature of pore and that it can interact with molecules at various polarities.

6.4.6 Flexible Bio-MOF for Controlled Drug Delivery

One of the promising applications of porous materials is controlled drug delivery due to their novel qualites as shown in scheme 1. However, materials with unique ordered functional pores like MOFs are expected to be powerful hosts that can accomodate target drug molecules within their precise nanospace.[21] Nevertheless, flexible MOFs have been successfully exploited as controlled drug delivery capsules. Indeed the flexible Bio-MOFs have an account of various such properties as (i) toxicology (all Fe(III) MOFs are biocompatible) (ii) structure and function and (iii) stablity under physiological conditions. Encouraged by the guest responsive reversible crystal dynamics, associated with the mobile rotational 1,4-ndc linker which provides significant movement of Fe metal ions after release of guest molecules, we have loaded dopamine (neurotransmitter drug used for Parkinson's disease) drug loading and studied its release in **1a** at room temperature under physiological conditions.[8]

Ordered Porous Network
• Control for drug load and release kinetics

High Pore volume
• The required amount of Drugs

High Surface area
• High potential for drug adsorption

Functionality
• Functionality allow a better control over drug loading and release
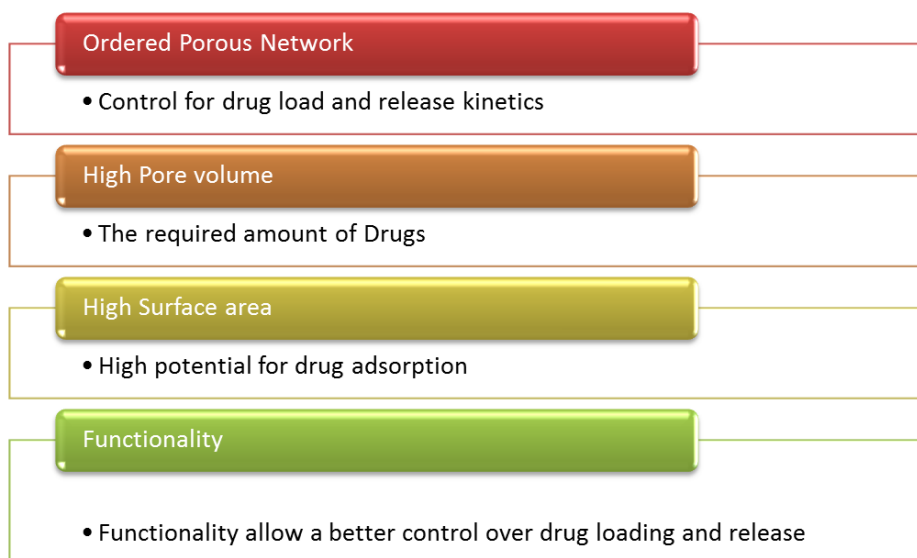
Scheme 1 The required characteristics of MOFs to be used as potential drug delivery systems.

Structural Characterization of dopamine@1a

The incorporation of dopamine was performed by introducing the dehydrated framework **1a** in ethanol containing different amounts of dopamine to reach a maximal amount of drug loading. Increased temperatures or repeated impregnation did not affect the drug loading capacity. The incorporation of dopamine drug molecules in the hydrophilic channels of **1a** has made a significant change in the textural parameters of the materials. Figure 12 shows the CO_2 adsorption-desorption of **1a** before and after incorporation of dopamine drug.
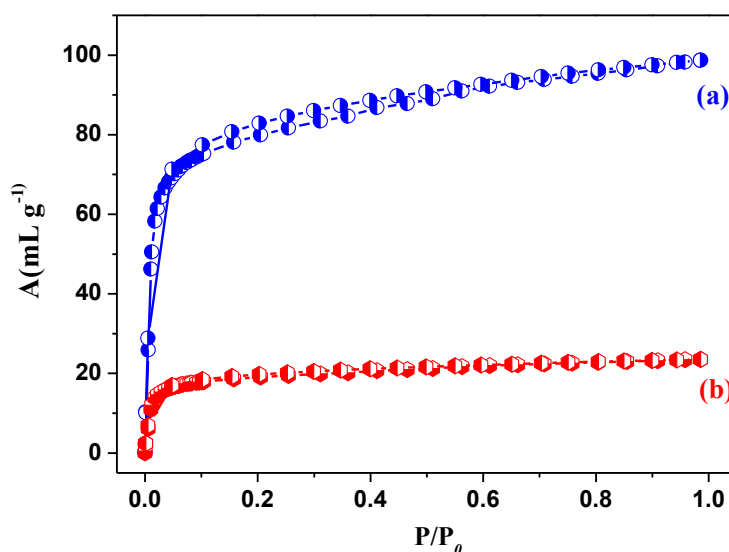
Figure 12 CO_2 adsorption-desorption isotherms at 195K of samples (a) **1a**; (b) **dopamine@1a**.

These results reveal that the uniquely ordered flexible structure is maintained even after the incorporation dopamine drug molecules. A substantial change in the specific surface area and the specific pore volume of the sample **1a** after the dopamine encapsulation was observed. The specific surface area was found to decrease from 342 m^2g^{-1} for pristine **1a** to 64 m^2g^{-1} for **dopamine@1a** whereas, the specific pore volume decreased from 0.108 to 0.035 cm^3 g^{-1} for the same samples. This result could be mainly attributed to the encapsulation of dopamine drug molecules inside the pores. The abrupt change in pore volume and surface area of host **1a** after incorporation of dopamine molecules further reveals that the pores of the host are blocked by the dopamine.Figure 13 shows the energy dispersive X-ray (EDS) pattern of dopamine incorporated **1a.** Peaks for the elements C, N, O and Fe are clearly seen in EDS spectrum. It should be noted that there is a peak of N in the EDS spectrum, indicating the loading of dopamine molecule into pores of framework.
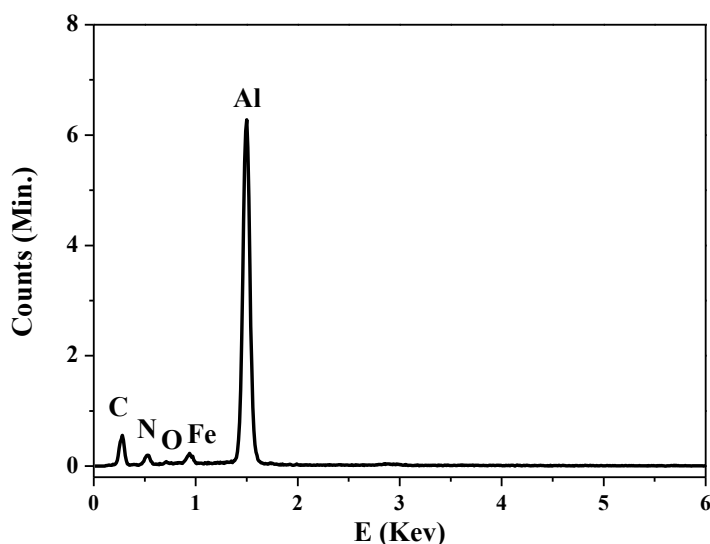
Figure 13 EDS pattern of dopamine molecules incorporated **1a**.

The powder Xray pattern of **dopamine@1a** shows sharp lines with shifting of some Bragg's peak positions. The peak at $2\theta = 6.2^{\circ}$ in **1** disappears in the drug incorporated sample but again reappears after the complete release of dopamine. This suggests that there is a change in the framework due to its mobile rotational organic linker 1,4-napdc and movement of core Fe metal ions after loading with dopamine (Figure 14). TGA of **dopamine@1a** measurment shows that dopamine leaves the pores of **1a** at 250 $^{\circ}$C and the corresponding loading amount being 34 wt% of dopamine in the framework **1a**.
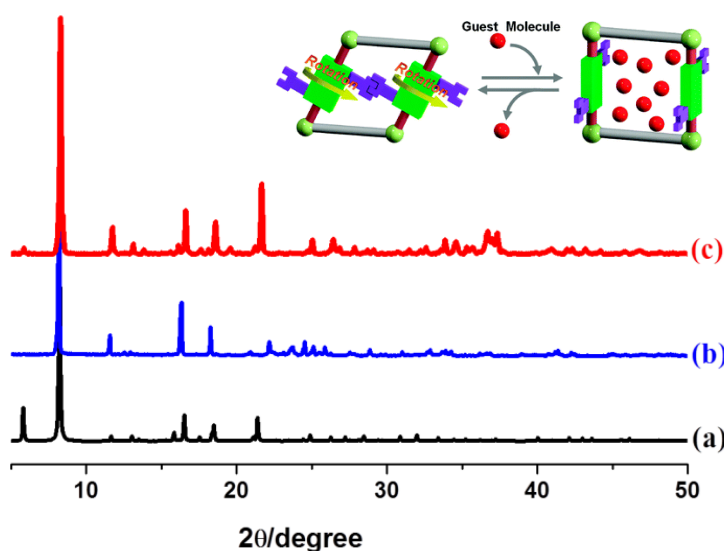
Figure 14 Powder XRD patterns (a) as-synthesized MOF **1**; (b) Dopamine loaded MOF; (c) after complete release of dopamine of MOF

In the Fourier transform infrared (FT-IR) spectrum, the broad peak at 3412 cm^{-1} which corresponds to $\nu_{(O-H)}$ and the appearance of the –NH stretching frequency at 3280 cm^{-1} in **dopamine@1a** compared to pristine dopamine and **1a** further confirmed the incorporation of dopamine in **1a** (Figure 15)**.**
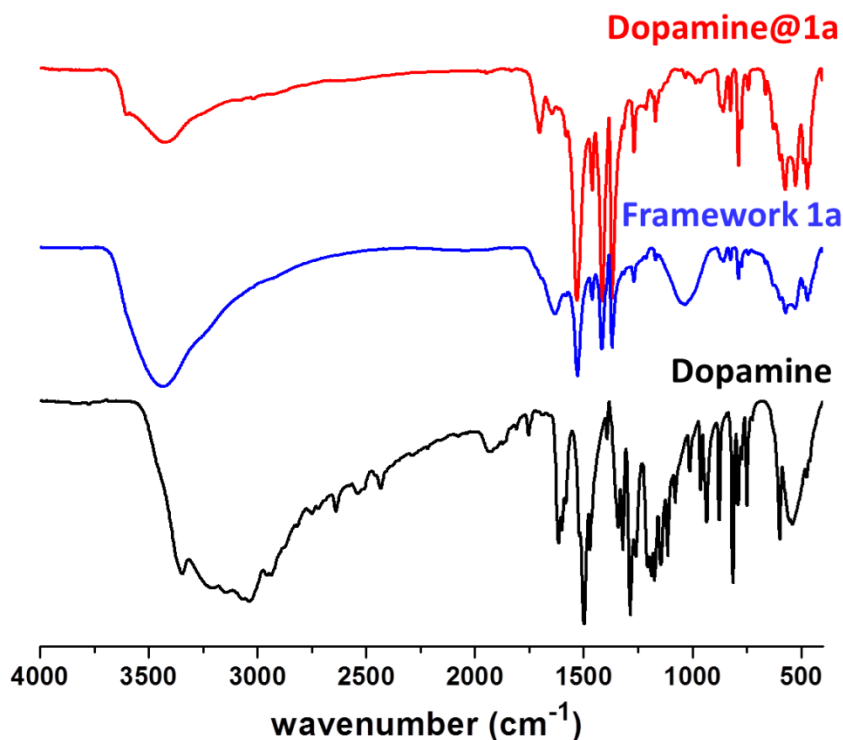
Figure 15 FT-IR spectra of **dopamine@1a**, **1a** and dopamine.

DFT calculations of dopamine@1a

To better understand the position and interaction of dopamine drug molecules with the pore surface of {Fe(1,4-napdc)(μ-OH)}$_n$ (**1a**), we have carried out density functional theory (DFT) calculations using the QUICKSTEP module in CP2K software. Favourable positions and interactions with dopamine drug molecules with in MOF and their energies have been determined. In the current work, geometry optimization runs were initiated for many configurations in each of which the dopamine molecules were positioned in different locations inside the hydrophilic pores of MOF. The optimal positions of dopamine molecules in **1a** are shown in Figure 16. Figure 17 shows the DFT optimized geometry obtained for one dopamine molecules per pore of {Fe(1,4-napdc)(μ-OH)}$_n$ (**1a**), which roughly corresponds to the experimental uptake.
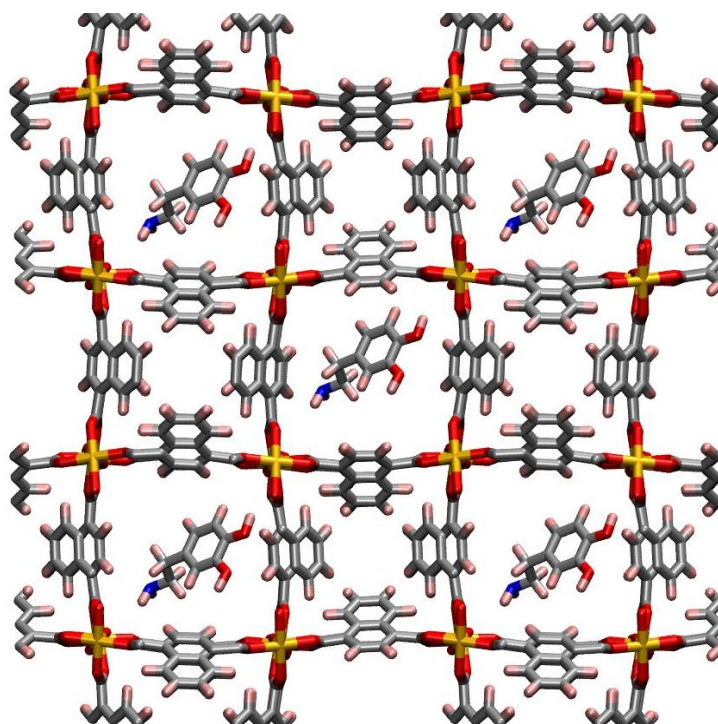
Figure 16 Locations of dopamine molecules in the hydrophilic pores of {Fe(1,4-napdc)(μ-OH)}$_n$ (**1a**) viewed along the *c*-axis.
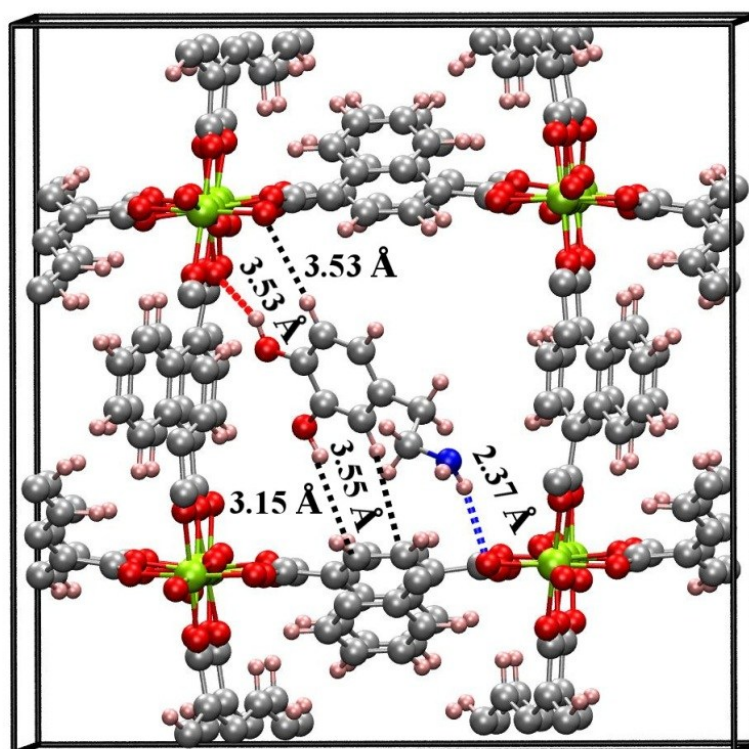
Figure 17 View of environment around the incorporated dopamine molecules. The distances are reported in Å, (Fe in green, oxygen in red, carbon in black, nitrogen in blue and hydrogen in pink).

To identify the atoms of MOF interacting with dopamine and thus to understand the nature of interactions, we have studied differences of electron densities. It shows that the most likely interaction involves strong hydrogen bonding between the OH group of dopamine and bridging hydroxyl oxygen and phenoxy oxygen atom of **1a** with $H_{(OH)}$-$O_{(\mu-OH)}$ and $H_{(OH)}$-$O_{(H-C6H6)}$ distance of 2.12 and 2.69 Å respectively. Additionally, there is strong hydrogen bonding between dopamine $-NH_2$ group and bridging oxygen atom OH of **1a** with $H_{(NH2)}$-$O_{(\mu-OH)}$ distance of 2.37 Å. The optimized geometry of dopamine leads to a high drug-**1a** interaction energy of -107 kJ/mol (Figure 18).
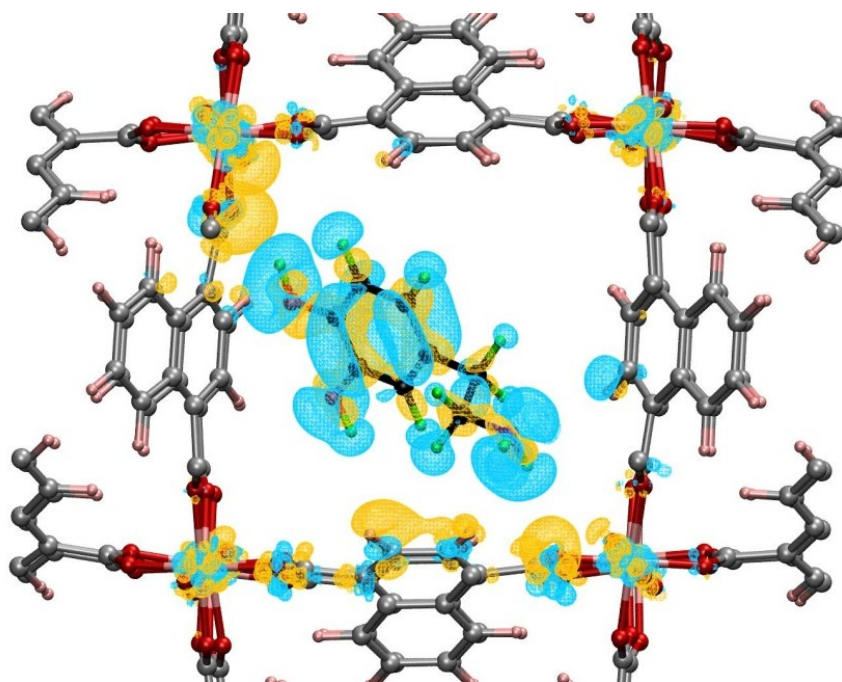
Figure 18 Location of dopamine drug molecules in **1a**. Cyan and Orange indicates the decreased and increased electron densities. An Iso-surface value is 7×10^{-4} a. u.

Drug Release Measurements

Controlled drug release kinetics was monitored using UV-Vis absorption spectroscopy of **dopamine@1a** (Figure 19). Figure 20 shows the release of dopamine in physiological saline at 37 $^{\circ}$C under continuous stirring. The kinetics of dopamine delivery from **dopamine@1a** were empirically adjusted with a regression factor of 0.989 and a value of 10.93 was calculated for the slope (K_H) using a Higuchi model ([dopamine=$K_{H}t_{1/2}$) for the total release process.[20] The complete release of dopamine from **dopamine@1a** was achieved after 15 days as shown in Table 2. The significant and controlled drug release can be due to a favourable hydrogen bonding between dopamine and **1a**.
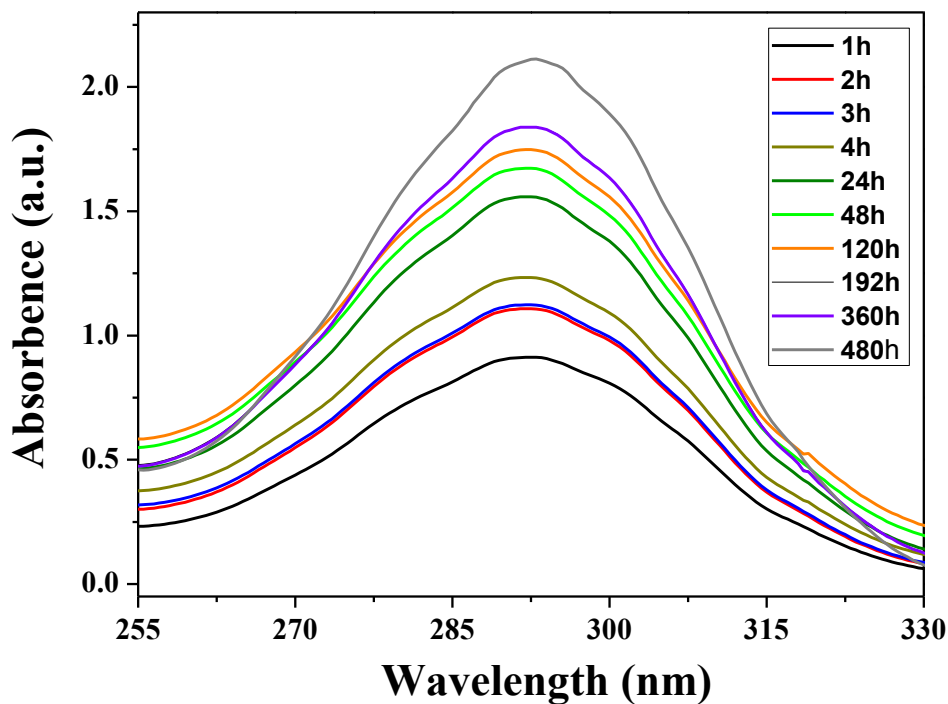
Figure 19 Florescence spectra of dopamine (λ max =290 nm) shows controlled release of dopamine for 15 days at pH~7.4.

Table 2 Drug release kinetic study using Higuchi model.[21]

Time	Absorbance (A)	$\varepsilon*L$	C	Weight/ g of MOF
1h	0.9128	3200	0.00028525	146.0858872
2h	1.1082	3200	0.000346313	181.7405743
3h	1.1236	3200	0.000351125	189.5259534
4h	1.2337	3200	0.000385531	212.5412024
10h	1.5576	3200	0.00048675	270.3019426
19h	1.6725	3200	0.000522656	296.1691312
1d	1.7478	3200	0.000546188	316.2503392
4d	1.84005	3200	0.000575016	339.4057846
15d	1.83768	3200	0.000574275	347.8610175

Where, A= Absorbance, ε= Molar absorptivity, l= Length; C= molar concentration
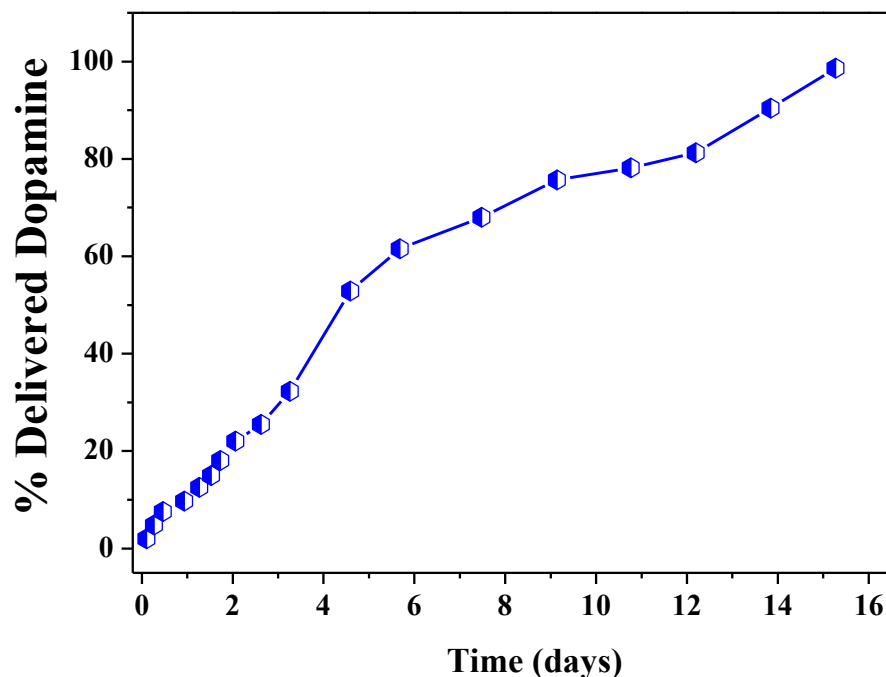
Figure 20 dopamine drug delivery from **dopamine@1a** (% dopamine and time in days)

6.5 Conclusions

In conclusion, a novel 3D microporous coordination polymer of Fe(III) with two types of channels has been prepared using a flexible and rotatable bridging ligand, which exhibits guest responsive reversible structural transformation and selective sorption phenomenon.Our results indicate that (a) the organic linker is capable of rotational motion in response to external stimuli which is realized in single-crystal-to-single crystal structural transformation; (b) rotational energy barier of 1,4-napdc ligand is low and (c) Fe(III) is capable in adopting the flexible geometry. We believe that such moblile ligand-based transformation using guest adsorption/desorption would offer useful tool for selective separation and catalysis. Furthermore, the flexible bio-MOF **1a** shows significant uptake of dopamine drug, and it exhibits controlled drug delivery upto 15 days under physiological conditions.

6.6 References

1) a) S. Horike, S. Shimomura, S. Kitagawa, *Nat. Chem.* **2009**, *1*, 695; b) A. U. Ortiz, A. Boutin, A. H. Fuchs, F.-X. Coudert, *Phys. Rev. Lett.* **2012**, *109*,

195502; c) Z.-J. Lin, T.-F. Liu, Y.-B. Huang, J. Lue, R. Cao, *Chem. Eur. J.* **2012**, *18*, 7896; d) Z.-J. Lin, T.-F. Liu, Y.-B. Huang, J. Lu, R. Cao, *Chemistry* **2012**, *18*, 7896; e) T. Lescouet, E. Kockrick, G. Bergeret, M. Pera-Titus, S. Aguado, D. Farrusseng, *J. Mater. Chem.* **2012**, *22*, 10287; f) E. Coronado, M. Gimenez-Marques, E. G. Minguez, *Inorg. Chem.* **2012**, *51*, 4403 g) F.-X. Coudert, A. Boutin, M. Jeffroy, C. Mellot-Draznieks, A. H. Fuchs, *ChemPhysChem* **2011**, *12*, 247; h)D. V. Soldatov, J. A. Ripmeester, *Stud. Surf. Sci. Catal.* **2002**, *141*, 353.

2) a) T. K. Maji, R. Matsuda, S. Kitagawa, *Nat Mater* **2007**, *6*, 142; b) D. Bousquet, F. X. Coudert, A. Boutin, *J. Chem. Phys.* **2012**, *137*, 044118; c) X.-H. Jin, J.-K. Sun, L.-X. Cai, J. Zhang, *Chem. Commun.* **2011**, *47*, 2667.

3) a) P. Horcajada, T. Chalati, C. Serre, B. Gillet, C. Sebrie, T. Baati, J. F. Eubank, D. Heurtaux, P. Clayette, C. Kreuz, J.-S. Chang, Y. K. Hwang, V. Marsaud, P.-N. Bories, L. Cynober, S. Gil, G. Ferey, P. Couvreur, R. Gref, *Nat. Mater.* **2010**, *9*, 172-178; b) P. Horcajada, C. Serre, G. Maurin, N. A. Ramsahye, F. Balas, M. a. Vallet-Regí, M. Sebban, F. Taulelle, G. r. Férey, *J. Am. Chem. Soc.* **2008**, *130*, 6774.

4) a) C.-Y. Sun, C. Qin, X.-L. Wang, Z.-M. Su, *Expert. Opin. Drug. Deliv.* **2013**, *10*, 89; b) R. J. Della, D. Liu, W. Lin, *Acc. Chem. Res.* **2011**, *44*, 957; c) A. C. McKinlay, R. E. Morris, P. Horcajada, G. Ferey, R. Gref, P. Couvreur, C. Serre, *Angew. Chem. Int. Ed.* **2010**, *49*, 6260; d) R. C. Huxford, R. J. Della, W.-B. Lin, *Curr. Opin. Chem. Biol.* **2010**, *14*, 262; e) P. Horcajada, C. Serre, G. Ferey, P. Couvreur, R. Gref, *Med. Sci.* **2010**, *26*, 761; f) N. J. Hinks, A. C. McKinlay, B. Xiao, P. S. Wheatley, R. E. Morris, *Microporous Mesoporous Mater.* **2009**, *129*, 330; g) M. Vallet-Regi, F. Balas, D. Arcos, *Angew. Chem. Int. Ed.* **2007**, *46*, 7548-7558.

5) a) P. Horcajada, R. Gref, T. Baati, P. K. Allan, G. Maurin, P. Couvreur, G. Ferey, R. E. Morris, C. Serre, *Chem. Rev.* **2012**, *112*, 1232; b) P. Horcajada, C. Serre, M. Vallet-Regi, M. Sebban, F. Taulelle, G. Ferey, *Angew. Chem. Int. Ed.* **2006**, *45*, 5974.

6) a) C. Wang, D. Liu, W. Lin, *J. Am. Chem. Soc.* **2013**, *135*, 13222; b) K. M. L. Taylor-Pashow, R. J. Della, Z. Xie, S. Tran, W. Lin, *J. Am. Chem. Soc.* **2009**,

131, 14261; c) W. J. Rieter, K. M. L. Taylor, W. Lin, *J. Am. Chem. Soc.* **2007**, *129*, 9852.

7) a) M. Vallet-Regí, F. Balas , D. Arcos, *Angew. Chem. Int. Ed.* **2007**, *46*, 7548; b) F. Ke, Y.-P. Yuan, L.-G. Qiu, Y.-H. Shen, A.-J. Xie, J.-F. Zhu, X.-Y. Tian, L. D. Zhang, *J. Mater. Chem.* **2011**, *21*, 3843.

8) a) J. W. Simpkins, N. Bodor, A. Enz, *J. Pharm. Sci.* **1985**, *74*, 1033; b) A. I. Broft, L. A. Berner, D. Martinez, B. T. Walsh, *Physiol. Behav.* **2011**, *104*, 122; c) I. Bokkon, I. Antal, *Curr. Neuropharmacol.* **2011**, *9*, 289; d) R. A. Wise, M. Morales, *Brain Res.* **2010**, *1314*, 38; e) J. A. Staller, S. V. Faraone, *Expert. Rev. Neurother.* **2007**, *7*, 351; f) D. M. P. Lawrence, D. A. Thomas, D.-Y. Wu, *The Scientific World* **2007**, *7*, 86; g) D. Saal, R. C. Malenka, *Cold Spring Harbor Laboratory Press*, **2006**, 361; h) C. G. Di, V. Bassareo, S. Fenu, L. M. A. De, L. Spina, C. Cadoni, E. Acquas, E. Carboni, V. Valentini, D. Lecca, *Neuropharmacology* **2004**, *47*, 227; i) J. Gordon, N. M. Barnes, *Trends Immunol.* **2003**, *24*, 438; j) N. D. Volkow, J. S. Fowler, G. J. Wang, *Behav. Pharmacol.* **2002**, *13*, 355; k)P. W. Kalivas, J. Stewart, *Brain. Res. Rev.* **1991**, *16*, 223.

9) SMART (V 5.628), SAINT (V 6.45a), XPREP, SHELXTL; Bruker AXS Inc. Madison, Wisconsin, USA, **2004**.

10) G. M. Sheldrick, *Siemens Area Detector Absorption Correction Program*, University of Göttingen, Göttingen, Germany, **1994**.

11) A. Altomare, G. Cascarano, C. Giacovazzo A. Gualaradi, *J. Appl. Cryst.* **1993**, *26*, 343.

12) G.M. Sheldrick, SHELXL-97, *Program for Crystal Structure Solution , Refinement*; University of Göttingen, Göttingen, Germany, **1997**.

13) A. L. Spek, *J. Appl. Cryst.* **2003**, *36*, 7.

14) L. J. Farrugia, *WinGX - A Windows Program for Crystal Structure Analysis*. *J. Appl. Crystallogr.* **1999**, *32*, 837

15) J. V,eVondele, M. Krack, F. Mohamed, M. Parrinello, T. Chassaing, X. Hutter , *J. Compt. Phys. Commun.* **2005**, *167*, 103

16) C. Hartwigsen, S. Goedecker , J. Hutter, *Phys. Rev. B*. **1998**, *58*, 3641

17) J. P. Perdew, K. Burke , M. Ernzerhof, *Phys. Rev. Lett.* **1996**, *77*, 3865.

18) a) S.J. Grimme, *Comput. Chem,* **2006**, *27*, 1787; b) S. Grimme, J. Antony, S. Ehrlich, H.J.Krieg, *Chem. Phys*. **2010**, *132*, 154104.

19) (a) The size is measured by considering van der Waals radii for constituting atoms. (b) Spek, A. L. *PLATON*, The University of Utrecht, Utrecht, The Netherlands, **1999**.

20) M. M. Dubinin, *Chem. Rev.* **1960**, *60*, 235.

21) W. R. Zhao, H. R. Chen, Y. S. Li, L. Li, M. D. Lang, J. L. Shi, *Adv. Funct. Mater.* **2008**, *18*, 2780.

Chapter 7

Honeycomb Porous Framework of Zinc (II): Effective Host for Pd and Cu$_2$O Nanoparticles for Catalytic Activity
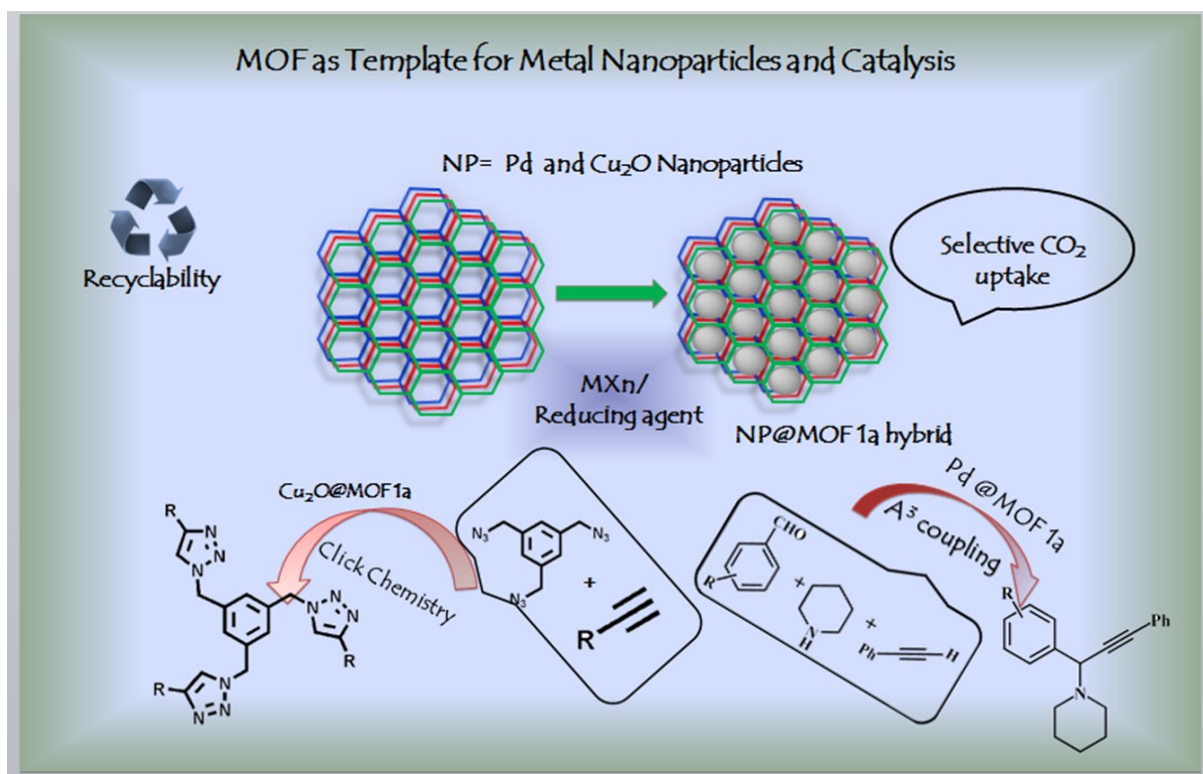
Summary

This chapter demonstrates a simple methodology for stabilization of highly mono dispersed metal and metal oxide nanoparticles with size in the range of 2-4 nm in 2D a metal-organic framework with functional pore surface. A new 2D porous layered type MOF {[Zn(Himdc)(bipy)].DMF} (**1**) (Himdc = 4,5-imidazoledicarboxylate and bipy = 4,4′-bipy) has been synthesized and systematically characterized. The desolvated framework **MOF 1a** shows permanent porosity and highly selective CO_2 uptake properties. The polar pore surface of **MOF 1a** decorated with pendent oxygen atoms from non-coordinated carboxylate of Himdc served as a functional scaffold for the stabilization of Pd and Cu_2O nanoparticles. The **Pd@MOF1a** hybrid shows catalytic activities for the synthesis of propargylamines using A^3 coupling reaction. **Cu_2O@MOF 1a** hybrid acts as a recyclable catalyst for 1, 3- di polar cycloaddition reaction between various terminal alkynes and aliphatic/aromatic azides via click chemistry.

7.1 Introduction

Metal-organic frameworks (MOFs) or porous coordination polymers (PCPs) are a class of highly ordered porous crystalline materials exhibiting a great promise in the areas of gas storage, separation, catalysis, sensing and drug delivery.[1] The propensity for spatial organization of metal ions and organic linkers leads to rationally designed frameworks with nanosized channels and cavities. Furthermore the soft, tunable characteristics of MOFs help them to acquire new properties by filling the cavities with different molecules and clusters.[2] For example, encapsulation of metal nanoparticles in porous MOF matrix is of paramount importance for heterogeneous catalysis and gas storage.[3] Several research groups have reported the stabilization of Cu, Ru, Ag, Pd, Au and Pt nanoparticles within porous MOF matrix[4] by different techniques like chemical vapour deposition (CVD), solid grinding, microwave irradiation, solution impregnation and surface grafting.[5-9] In particular, the stabalization of nanoscale Pd and Cu$_2$O in different porous matrices has attracted tremendous attention due to their catalysis for various organic reactions and hydrogen storage at elevated temperatures.[9d] However, achieving high loading of mono dispersed metal nanoparticles within the nanoscopic voids throughout the MOF matrix is highly demanding and challenging task. This can be realized in a heterogeneous surface MOF structure with polar pendent functional groups on the pore surface which would stabilize metal nanoparticles efficiently through dipole-dipole interactions. This chapter reports, for the first time, the synthesis of a 2D porous layered type MOF, {[Zn(Himdc)(bipy)$_{0.5}$].DMF} (**1**) (Himdc = 4,5-imidazoledicarboxylate and bipy = 4,4′-bipyridine) based on mixed ligand system with pendent carboxylate oxygen atoms decorated on the pore surface. The desolvated MOF **1a** shows hexagonal 1D supramolecular channels which serve as a efficient stabilizer for mono dispersed Pd and Cu$_2$O nanoparticles. The **Pd@MOF1a** hybrid acts as catalytically active species in three component coupling for the synthesis of propargylamines.[10] Propargylamines are versatile synthetic intermediates in organic synthesis and are also important structural elements in natural products and therapeutic drug molecules. On the other hand **Cu$_2$O@MOF 1a** has been exploited for synthesis triazoles based on huisgen 1,3- dipolar cyclo addition reaction (commonly called as click chemistry) between terminal alkynes and aliphatic/aromatic azides via click chemistry. Facile synthesis of these triazole products via click reaction attracted attention in the field of biology and material science, particularly in peptidomietics and

bioconjugations.[12] Furthermore, desolvated framework **1a** exhibits highly selective CO_2 uptake among the number of gases (Ar, O_2, N_2, H_2) at 195 K, suggesting that highly polar pore surface enhances adsorption selectivity based on quadrupole moment of CO_2 molecule.

7.2 Experimental Section

7.2.1 Materials

All reagents were obtained from commercial sources and used without further purification. High purity $Zn(NO_3)_2 \cdot 6H_2O$, 4,5-imdazoledicarboxylic acid (H_3imdc) and ,4′-bipyridyl (bipy) were purchased from Aldrich Chemical Co. and used as received.

7.2.2 Synthesis of $\{[Zn(bipy)_{0.5}(Himdc)](DMF)\}_n$ (1)

$Zn(NO_3)_2 \cdot 4H_2O$ (0.25 mmol, 0.074 g) was dissolved in 12.5 mL acetonitrile with constant stirring. 4,5-imdazoledicarboxylic acid (H_3imdc) (0.25 mmol, 0.039 g) and 4,4′-bipyridyl (bipy) (0.125 mmol, 0.0195 g) was dissolved in 12.5 mL N,N-dimethylformamide (DMF) solution and stirred well for 30 min to obtain a homogeneous solution. Acetonitrile solution (2 mL) of $Zn(NO_3)_2$ is slowly and carefully layered on top of the ligand solution of DMF (2 mL) using the 2 mL buffer solution of acetonitrile and DMF (1:1). Colorless block single crystals grew at the junction of the two different solvents after two weeks. The crystals were separated and washed with acetonitrile, which was subjected to X-ray diffraction. Yield: 80%. Anal. Calcd.for $C_{13}H_{13}N_4O_5Zn$: C, 42.19; H, 4.7; N, 16.9. Found: C, 41.88; H, 4.63; N, 16.64%. IR (KBr cm^{-1}); 1669-1685 $\nu(COO)$; 2265 $\nu_s(CN)$; and 1557 $\nu_s(Ar\ C=C)$.

7.2.3 Preparation of Pd@MOF 1a

The compound **1** was desolvated at 433 K under vacuum (10^{-5} Torr) for 1h, which resulted in removal of DMF molecules. The desolvated **MOF 1a** (0.02 g, 0.01 mmol) was immersed in water (2 mL) by sonication for 2 minutes. To this suspension, $PdCl_2$ (1.5 mL; 2 mmol) was added followed by the addition of $NaBH_4$ (50 μL, 0.04 M). The product was thoroughly washed with water and then dried in an oven at 333k. The resulting hybrid **Pd@MOF 1a** has been characterized by the several techniques like FT-IR, EDAX, Powder XRD and TEM.

7.2.4 Preparation of Cu$_2$O@MOF 1a

The same procedure was adopted as that used for preparation of **Pd@MOF 1a.** Instead of PdCl$_2$, Copper sulphate (1.5 mL; 2 mmol) was added followed by the addition of Hydrazine hydrate (10 µL, 0.02 M). The obtained mixture was washed thoroughly with distilled water and finally dried in an oven at 333 K. The resulting solid has been characterized by IR, PXRD and TEM.

7.3 Characterization Techniques

7.3.1 Physical Measurements

Elemental analysis of **1** was carried out using a Thermo Scientific Flash 2000 CHN analyzer. Thermogravimetric analyses (TGA) was carried out under nitrogen (flow rate of 50 mL/min) with Metler Toledo TGA-850 TG analyzer in the temperature range between 28 - 650°C at a heating rate of 3°C/min. Powder X-ray diffraction (PXRD) patterns of **1**, **1a**, and **NP@MOF1a** were recorded on a Bruker D8 Discover instrument using Cu-Kα radiation. For TEM measurements, the samples were prepared by dispersing the powder products in water by sonication before drop casting on a carbon-coated copper grid. TEM studies were also carried with a FEI TITAN^{3TM} operating at an accelerating voltage of 300 kV and a JEOL JEM 3010 instrument operating at an accelerating voltage of 300 kV. Inductively coupled plasma-optical emission spectral (ICP-OES) analyses of **NP@MOF1a** were carried out using a Perkin Elmer OPTIMA 7000 spectrometer. Raman spectra were recorded with He Ne red laser (632.8 nm) in a custom built Raman spectrometer. The power at the sample was kept low (6 mW) to prevent sample degradation and the graphs have been smoothed with 5 point FFT filter, in which baseline subtraction has been done.

7.3.2 Adsorption Measurements

N$_2$ (77 K& 195 K), CO$_2$, Ar, H$_2$, and O$_2$ (195 K) adsorption studies using the dehydrated sample of **1** (*i.e* **1a**) and CO$_2$ adsorption studies of **NP@MOF1a** hybrid were carried out using QUANTACHROME AUTOSORB-1C analyzer. The adsorbent sample of about 100-150 mg was heated at 493 K under a high vacuum (10^{-1} Pa) for 18 h prior to measurements. The adsorbate was charged into the sample tube and then the change of the pressure was monitored and the degree of adsorption was determined by

the decrease of the pressure at the equilibrium state. All operations were computer-controlled and automatic.

7.3.3 Single-crystal X-ray Diffraction

A suitable single crystal of **1** was carefully selected under a polarizing microscope and fixed to a separate thin glass fiber by commercially available glue. X-ray single crystal structural data was collected by a Bruker Smart-CCD diffractometer equipped with a normal focus, 2.4 kW sealed tube X-ray source (Mo-K$_\alpha$ radiation, 0.71073 Å) operating at 50 kV and 30 mA. The programme SAINT[13] was used for integration of diffraction profiles and an empirical absorption correction based on symmetry equivalent reflections was applied using the SADABS program.[14] The structure was solved by direct method using SIR92 programme[15] and refined by full matrix least square method using SHELXL 97.[16] The hydrogen atoms were fixed by HFIX and placed in ideal positions. Potential solvent accessible area or void space was calculated using the PLATON[17] multipurpose crystallographic software. Final refinement included atomic positions for all the atoms, anisotropic thermal parameters for all the non-hydrogen atoms. All atoms of the DMF solvent molecules was not observed during the structure refinement.[18] Two peaks have been assigned (C7 and O1) of the DMF molecules. The presence of DMF molecule in the structure has been assign on the basis of IR, CHN, TGA and NMR results. All calculations were carried out using WinGX system,Ver 1.70.01.19[22] Selected bond distances and angles of **1** are given in Table 1.

7.3.4 Crystal Data of {[Zn(bipy)$_{0.5}$(Himdc)](DMF)}$_n$ (1)

Formula $C_{13}H_{13}ZnN_4O_5$, *M*r = 370.46, Trigonal, Space group *R*-3m (no. 166), *a* = 23.401(2) Å, *b* = 23.401(2) Å, *c* = 19.195(3) Å, α =90°,β= 90°γ=120°, *V* = 9103.1(18) Å^3, Z = 18, ρ_{calc} =1.066 g cm^{-3}, μ(Mo-K$_\alpha$) = 1.228 mm^{-1}, *F*(000) = 2916, *T* = 293 K, λ(Mo-Kα) = 0.71073 Å, θ_{max} = 17.1°, Total data = 11349, Unique data = 676, (R_{int} = 0.081), Observed data [$I > 2\sigma(I)$] = 533, *R* = 0.0855, *W*R$_2$ = 0.2966, *GOF* = 1.37.

7.4 Results and Discussion

7.4.1 Structural Description of {[Zn(bipy)$_{0.5}$(Himdc)](DMF)}$_n$ (1)

The MOF **1** has been synthesized by the reaction of $Zn(NO_3)_2$ and mixed ligands (Himdc and bipy) at room temperature and crystallizes in trigonal $R3$.m space group. The structure determination reveals a 2D coordination network of Zn^{II} bridged by the Himdc and bipy linkers. The asymmetric unit of **1** comprises of one Zn^{II}, Himdc, half of bipy and a DMF molecule. Each Zn^{II} centre is in a distorted trigonal bipyramidal geometry and connected to two chelated Himdc and one bipy linker (Figure 1). Here each Himdc chelates two Zn^{II} centres through O1 and N2 and acts as a tetradentate bridging ligand and other two carboxylate oxygen atoms (O2 and O2*) remain pendants. The Zn1-O1 bond distance is 2.205(12) and Zn1-N1/2 bond distances are 2.035(17) and 1.983(11) Å, respectively. The most salient characteristic of the structure is that six Himdc chelate to six Zn^{II} centres rendering a hexagonal unit of {Zn$_6$(Himdc)$_6$} which is further connected to another six such units by bipy linkers forming a 2D coordination network lying in the crystallographic ab plane (Figure 2a). The topology of the 2D net is $(6^2,3^2)$. In the 2D periodic net one regular {Zn$_6$(Himdc)$_6$} hexagon with the dimension of 9.0×9.0 Å^2 linked to another six irregular {Zn$_6$(Himdc)$_3$(bipy)$_3$} hexagons of the dimension of 14.6×14.6 Å^2. The 2D sheets stack in a -ABC- manner along the *c*-axis where hexagonal unit {Zn$_6$(Himdc)$_6$} of one net perfectly sits in between irregular {Zn$_6$(Himdc)$_3$(bipy)$_3$} hexagons of other two nets supported by the (bipy)C1-H1…O1(Himdc) interactions resulting in a 3D honeycomb like framework with 1D hexagonal channels occupied by the guest DMF molecules (Figure 2b and Figure 3).
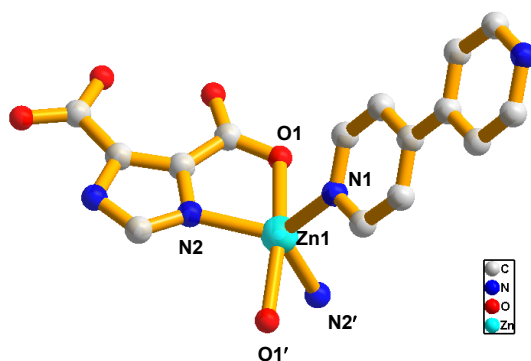
Figure 1 View of the coordination environment around Zn1 in **1**showing two Himdc chelated and fifth coordination is occupied by bipy(hydrogen atoms were removed for clarity).
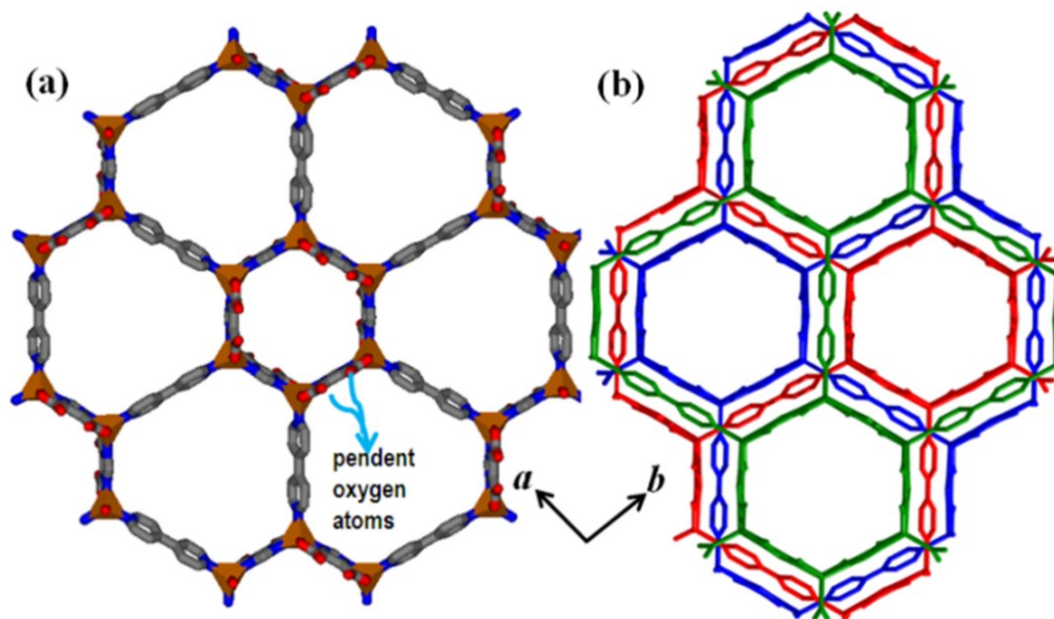
Figure 2 (a) 2D (6,3) net of MOF **1** is formed by the linking {$Zn_6(Himdc)_6$} unit by bipy linkers in the *ab* plane; (b) Stacking of the 2D sheets in −ABC− fashion resulting honeycomb like hexagonal channels along the *c*-axis.
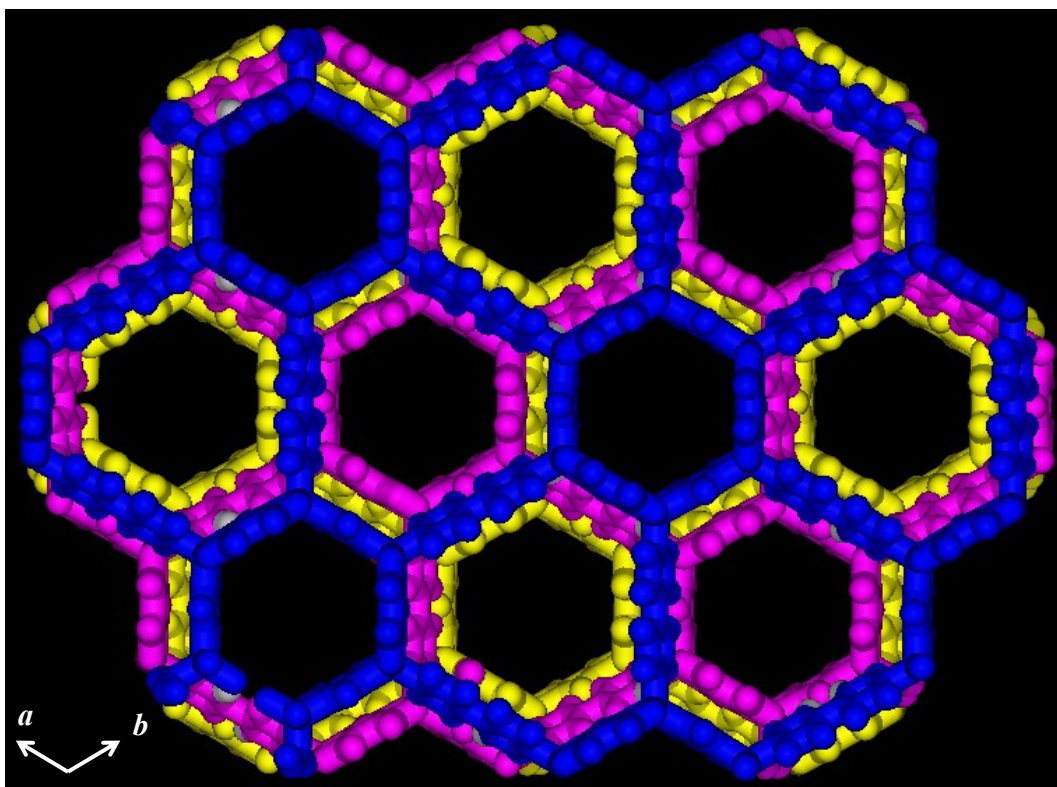
Figure 3 −ABC− Stacking of the 2D sheets of **1** along *c*-axis forming honeycomb like structure with hexagonal 1D channels.

The dimensions of the 1D hexagonal channels are about 9.0×9.0 Å^2 and corresponding void space is about 30% to the total crystal volume. The pores mainly consist of imidazole panels from Himdc where non-coordinated carboxylate oxygen's alternatively positioned in up-down fashion and supported by the bipy linkers (Figure 2b). In the network $Zn^{II}...Zn^{II}$ separation along the Himdc and bipy bridging part are 6.165 Å and 11.070 Å, respectively and nearest neighbour $Zn^{II}...Zn^{II}$ separation between the 2D sheets is 5.16 Å.

Table 1 Selected bond distances (Å), angles (°) for $[Zn(bipy)_{0.5}(Himdc)](DMF)]_n$ (**1**).

Zn1 -O1	2.205(12)	Zn1-O1_e	2.205(12)
Zn1-N1	2.035(17)	Zn1-N2_e	1.983(11)
Zn1-N2	1.983(11)		
O1-Zn1-N1	95.8(3)	O1-Zn1-O1_e	168.4(6)
O1-Zn1 -N2	80.7(4)	O1_e -Zn1-N2	93.8(5)
O1-Zn1-N2_e	93.7(4)	N1-Zn1 -N2	118.5(5)
O1_e -Zn1-N1	95.8(5)	N1 -Zn1-N2_e	118.5(5)
O1_e-Zn1 -N2_e	80.7(5)	N2 -Zn -N2_e	123.1(6)
Symmetry code e =x-y,-y,-z			

7.4.2 Stability of {[Zn(bipy)$_{0.5}$(Himdc)](DMF)}$_n$ (1)

To evaluate the framework stability and structural ordering of **1**, thermogravimetric analysis (TGA) and powder X-ray diffraction (PXRD) studies were performed. TGA shows about 19% weight loss in the temperature range of 100-150 °C which corresponds to the loss of one DMF molecule (cal wt. loss ~19.78%). The desolvated compound **1a** is stable up to 240 °C without further weight loss suggesting high thermal stability of the framework (Figure 4). The PXRD pattern of **1a** shows all the peaks with almost same Bragg intensities as of **1** but appearence of additional new peaks at 2θ = 5.29°, 10.6° and 21.7° suggest the structural reorientation rather than collapse of the framework (Figure 5). Indexing of powder pattern of **1a** by using TREOR programme shows monoclinic crystal system with a = 19.34(3) Å, b = 13.96(1) Å and c = 11.82(1) Å, β =116.14(10)° and V = 2867.43 Å^3 (Table 2)
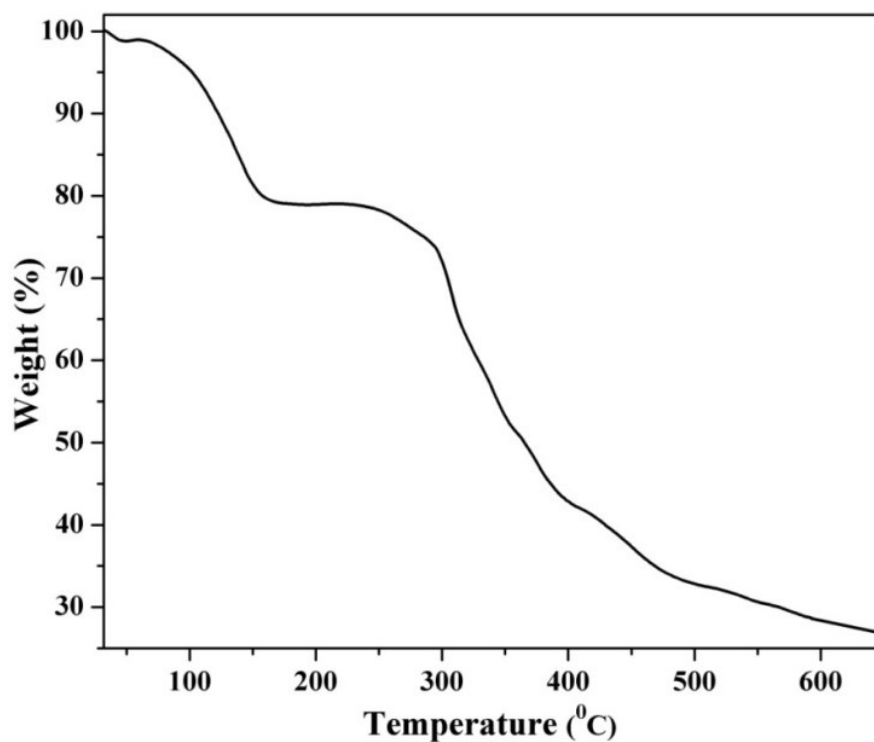
Figure 4 Thermogravimetric analysis of **1** in the temperature range of 25 - 650°C under the flow of N_2 gas (50 mL/min).
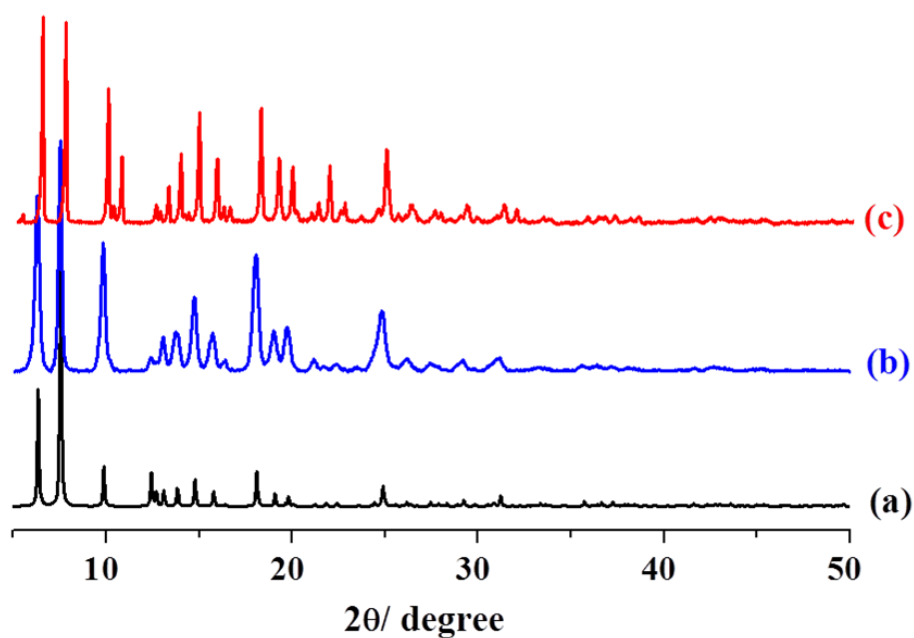
Figure 5 PXRD patterns of (a) simulated from single crystal data, (b) as-synthesized **1** (c) desolvated **1a**

Table 2 Indexing result from the powder data of desolvated MOF 1a (From TREOR)

$a = 19.34(3)$ Å, $b = 13.96(1)$ Å, $c = 11.82(1)$ Å $\alpha = 90.00°$, $\beta = 116.14(10)°$
$\gamma = 90.00°$; UNIT CELL VOLUME = 2867.43 Å^3

H	K	L	SST-OBS	SST-CALC	DELTA	2TH-OBS	2TH-CALC	D-OBS	
1	0	0	.002143	.001967	.000177	5.307	5.084	16.6381	0
0	1	0	.003044	.003044	.000000	6.326	6.326	13.9614	0
-1	0	1	.004402	.004397	.000005	7.609	7.604	11.6100	0
-1	1	1		.007441			9.897		
-2	0	1	.007454	.007461	-.000007	9.906	9.910	8.9222	0
2	0	0	.007868	.007867	.000001	10.178	10.177	8.6839	0
			.011805			12.475		7.0896	0
1	1	1	.013085	.013113	-.000028	13.137	13.151	6.7339	0
-3	0	1	.014431	.014459	-.000028	13.799	13.812	6.4124	0
			.014880			14.013		6.3149	0
			.015283			14.203		6.2309	0
-1	2	1	.016570	.016574	-.000004	14.792	14.793	5.9841	0
2	0	1	.018808	.018806	.000002	15.765	15.764	5.6168	0
-2	2	1	.019648	.019638	.000010	16.115	16.111	5.4955	0
-1	1	2	.020409	.020403	.000006	16.427	16.425	5.3919	0
-3	1	2	.024798	.024793	.000005	18.121	18.119	4.8916	0
0	3	0	.027397	.027398	-.000001	19.055	19.055	4.6538	0
1	3	0		.029364			19.734		
-1	2	2	.029544	.029536	.000008	19.795	19.792	4.4815	0

NUMBER OF OBS. LINES = 17;NUMBER OF CALC. LINES = 16
M(17)= 19 AV.EPS.= .0000201; F 17 = 23.(.019663, 39)
3 LINES ARE UNINDEXED; M-TEST= 19
UNINDEXED IN THE TEST= 3.

7.4.3 Adsorption Properties

To study the permanent porosity, the desolvated framework **1a** was subjected to the gas sorption studies. Despite an adequate effective pore size, to our surprise N_2 adsorption study at 77 K shows type II adsorption profile suggesting only surface adsorption (Figure 6 left). This could be attributed to weak adsorbate-adsorbent interaction or high diffusion barrier for N_2. However, CO_2 sorption study at 195 K reveals a steep uptake at low pressure region and display type I profile typical for microporous materials (Figure 6 Right).The final uptake was found to be ~68 mL/g (12 wt%) which corresponds to two molecules of CO_2 per formula unit of **1a**. The Brunauer-Emmett-Teller (BET) surface area calculated from the CO_2 adsorption profile turns out to be 310 m^2/g and the corresponding pore volume 0.123 cm^3/g. The sorption profile have significant hysteresis which resembles the strong interaction of CO_2 with **1a** and it is also reflected in high value of isosteric heat of adsorption ($q_{st,\phi}$ found to be 32 kJ mol^{-1}) as calculated by Dubinin-Radushkevich (DR) equation.[19] The room temperature uptake of CO_2 was found to be 14 mL/g (Figure 6 inset).
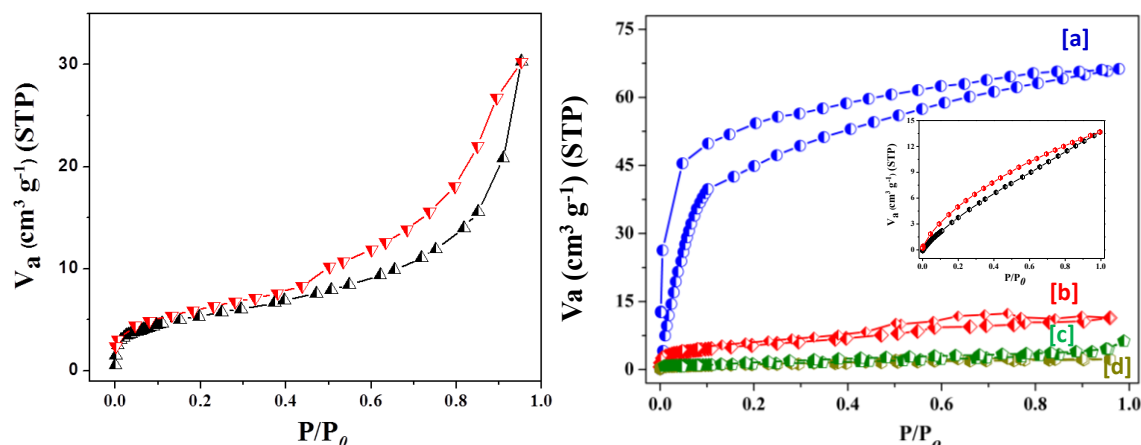
Figure 6   (left) N_2 adsorption isotherm of **1** at 77 K, 1 atm; (right) Adsorption isotherms of **1** for (a) CO_2, (b) Ar, (c) O_2 and (d) H_2 at 195 K, 1atm (Inset showing CO2 adsorption for **1a** at 298 K, 1atm).

Moreover, measurements of adsorption isotherms at 195 K for other gases like N_2, O_2, H_2 and Ar shows negligible uptake suggesting the framework is highly selective towards CO_2 (Figure 6). The hysteretic behaviour and high selectivity could be attributed to the highly polar pore surface uniformly embedded with the carboxylate oxygen from Himdc linker and π-cloud of imidazole and pyridyl ring of bipy which gives rise to an electric field in the host framework, that can interact with the quadrupole moment of CO_2 (-1.4×10^{-39} Cm^2) providing additional energy for adsorption.

7.4.4 Stabilization of Metal Nanoparticles

Uniform and periodic arrangement of hexagonal nanopores possessing polar nature derived from carboxylate groups from the Himdc encouraged us to stabilize Pd and Cu_2O nanoparticles which is yet to be explored in 2D MOF systems. The stabilization of all these metal nanoparticles over the surface of **1a** matrices is shown in Scheme **1**. The periodic arrangement of hexagonal nanopores along with functional groups in the channels helps in stabilizing and controlling the size of nanoparticles.
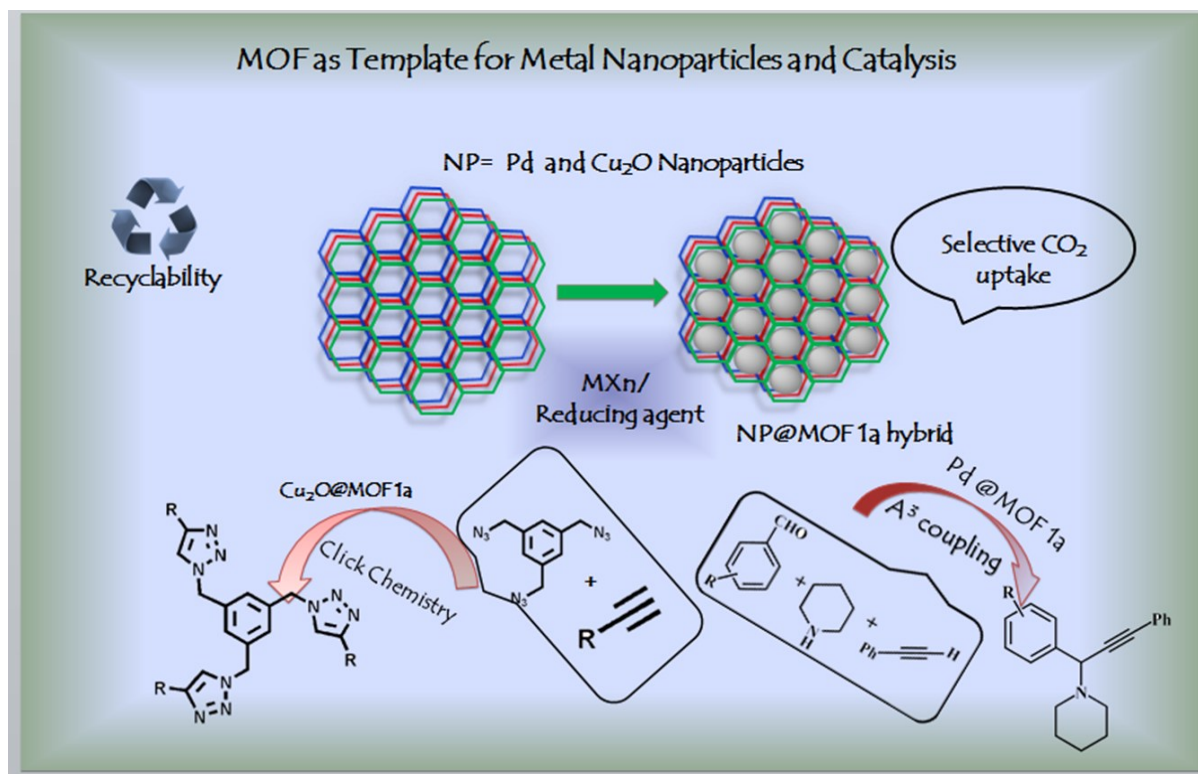
Scheme 1 Schematic showing the stabilization of Pd and Cu_2O nanoparticles in 2D layered MOF **1a** and its varioius catalytic activities.

7.4.5 Stabilization of Pd Nanoparticles in MOF 1a and Catalytic Three-Component Coupling Reaction

The stabilization of Pd nanoparticles over the surface of **1a** matrix is shown in Scheme 1. Pd(II) ions were absorbed over **1a** with the aid of sonication and subsequently reduced to Pd nanoparticles by the addition of $NaBH_4$. The periodic arrangement of hexagonal nanopores along with functional groups in the channels helps in stabilizing and controlling the size of Pd nanoparticles. XRD pattern of **Pd@MOF1a** (Figure 7d) reveals (100) peak becoming highly intense and appearance of some new peaks suggesting the structural reorganization after the loading of the Pd nanoparticles in the framework. Closer examination of the XRD pattern showed (Figure 7 Inset) four additional peaks at $2\theta = 40.2, 46.5, 68.2$ and $81.1°$ corresponding to the (111), (200), (220) and (311) reflections of a face centered cubic structure of crystalline Pd(0). X-ray photoelectron spectrum (XPS) of the **Pd@MOF1a** shows Pd($3d_{5/2}$) and Pd($3d_{3/2}$) peaks centered at 336.3 and 341.6 eV respectively due to the presence of the Pd in zero oxidation state (Figure 8).
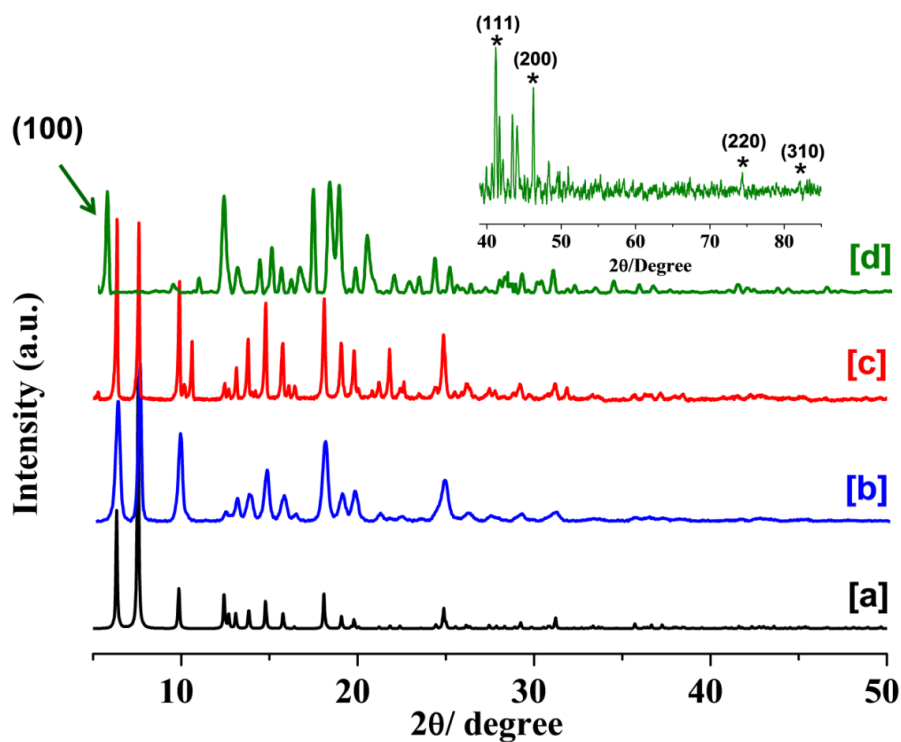
Figure 7 PXRD patterns of (a) simulated from single crystal data, (b) as-synthesized **1** (c) desolvated **1a** (d) **Pd@MOF1a** hybrid (Inset: PXRD pattern of **Pd@MOF1a** showing the diffraction peaks corresponding to Miller indices of Pd fcc crystal structure).
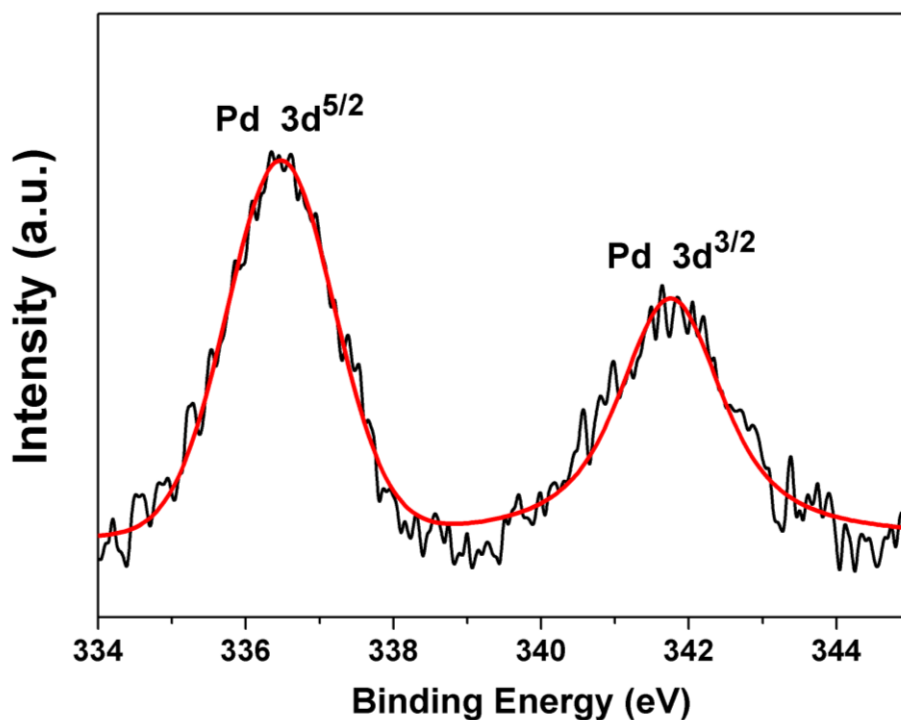
Figure 8 X-ray photoelectron spectrum for **Pd@MOF1a.**
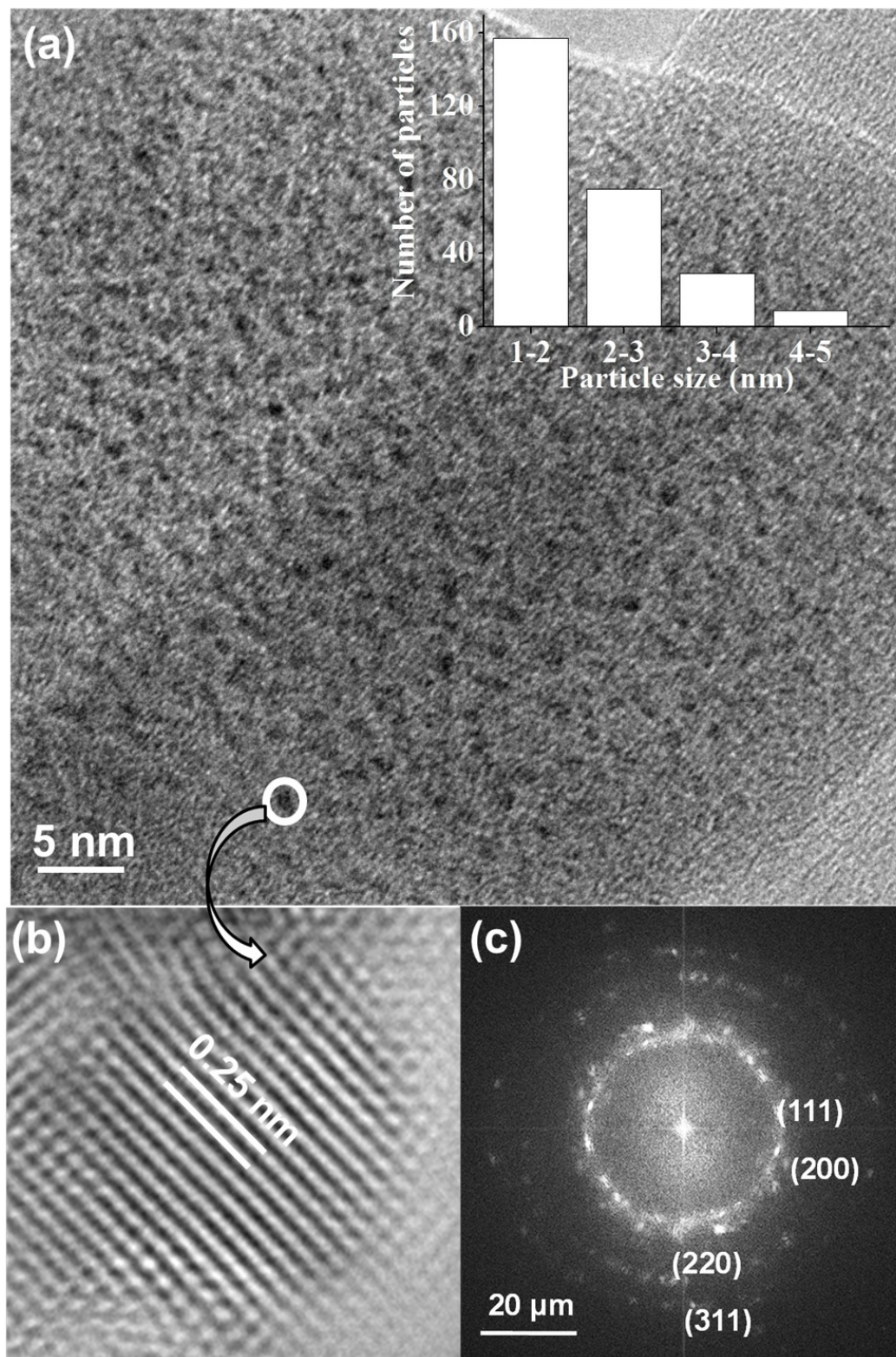
Figure 9 (a) HRTEM image of **Pd@MOF1a** showing Pd nanoparticles encapsulated in **1a**; (inset: corresponding particle size distribution) (b) HRTEM showing lattice planes corresponding to Pd (c) SAED pattern showing the fcc planes of the crystalline Pd nanoparticles.

The high resolution transmission electron microscope (HRTEM) image (Figure 9) shows fine dispersion of Pd nanoparticles over the MOF matrix in the narrow size range of 1-2 nm which is in close agreement with the crystallite size obtained from Scherrer formula by PXRD (~ 2 nm). The loading of Pd in the MOF is about 1.54 wt% obtained from ICP-OES analysis. This honeycomb 2D layer structure of **1** provides ordered pores with free oxygen atoms as stabilizing sites which help in controlling the size and shape of Pd nanoparticles without agglomeration. To investigate the changes in chemical nature and textural properties after the encapsulation of Pd nanoparticles, Raman spectroscopy and gas sorption studies were performed. The Raman spectra of desolvated **1a** and **Pd@MOF1a** are shown in Figure 10 and the corresponding peaks have been summarized in Table 3.
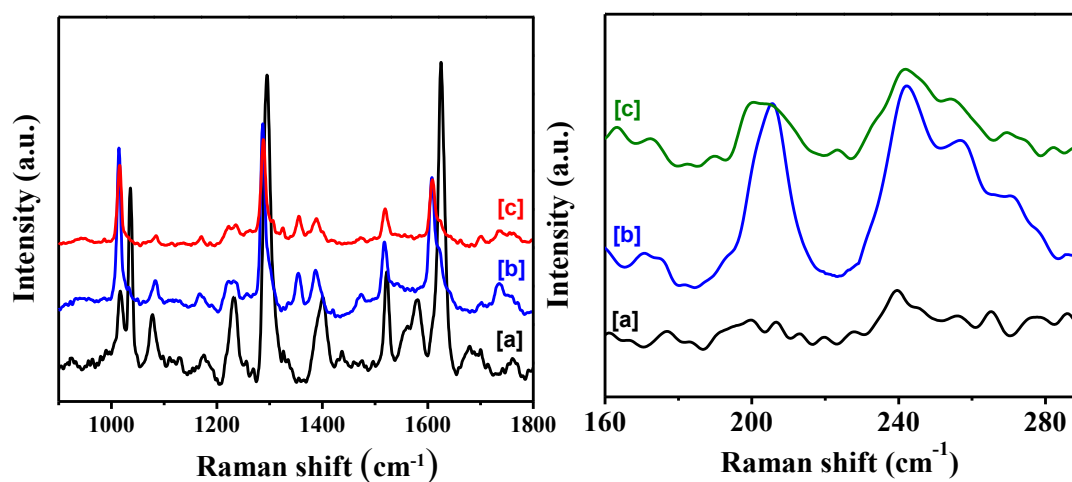
Figure 10 (left) Raman spectra (left) High frequency region (right) low frequency region of (a) **1a,** (b) **Pd@MOF1a** and (c) recovered **Pd@MOF1a** hybrid after four catalytic cycles.

It is observed that there is an overall softening (decrease in frequency) of the modes in **Pd@MOF1a** as compared to **1a**. This is due to the fact that Pd nanoparticles are held in the flexible rings containing bi-pyridyl groups inducing the ring expansion which results in tensile stress. Furthermore, we also observed softening of carbonyl (C=O) and carboxylate (COO) stretching frequencies (Table 3), and a new mode at 1354 cm^{-1}. It is interesting to note that the 1354 cm^{-1} and 1390 cm^{-1} have equal intensities resembling a doublet (Figure 10 left) . Considering that Pd is being coordinated through carboxyl groups of Himdc, it is easy to invoke vibrational coupling due to C=O····Pd····O=C linkage (Figure 11). In addition we also observed Pd-O mode at 205 cm^{-1} confirming the above linkages (Figure 10 right). Based on Raman

investigations we infer that the Pd nanoparticles are present in the hexagonal pores containing bipyridyl linkers held by the pendant carboxylate oxygen moieties of Himdc. Similar observations were also made for Ag nanoclusters formed over MOF-508.[4b]

Table 3 Peak assignments in Raman spectroscopic studies for **1a** and **Pd@MOF1a**.

S. No.	1a	Pd@MOF1a	Peak assignment
1	1017	1015	Ring in plane def (bipy)[a]
2	1037	1035	C-H out pf plane bend (Himdc)
3	1079	1084	ring def
4	1235	1238	δ C-H (bipy)[b]
5	1295	1288	δ(C-H), ν(C-N)
6	-	1354, 1390	ν_{sym}(COO)[c]
7	1400	-	ν_{sym}(COO)
8	1524	1520	N(C-C), ν(C-N) (bipy)
9	1582	-	ring str (bipy), CN str (Himdc)
10	1626	1609	ν(C=O)
11	1626	1623 sh	ν(C-C) (bipy)

ν-stretch, δ-in plane bend, sym-symmetric, asym-asymmetric, def-deformation, bipy-bipyridyl, Himdc-imidazole, s-strong, w-weak, v-very, m-medium
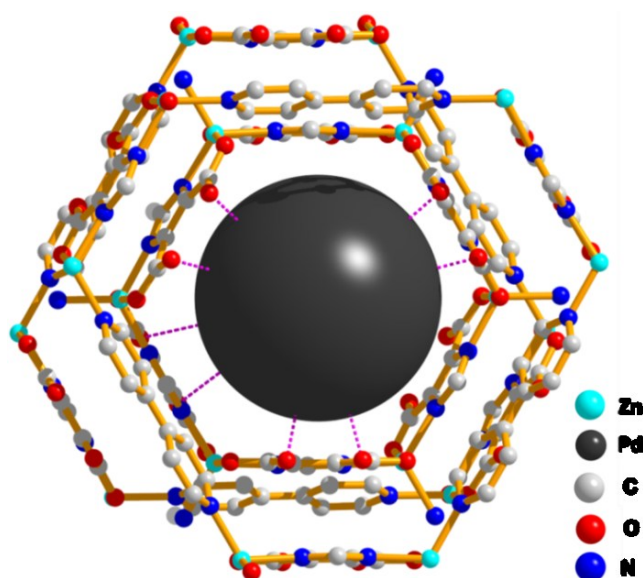
Figure 11 Schematic showing 1D hexagonal channels with pendent oxygen atoms from carboxylate groups of Himdc interactiong with Pd nanoparticles through -C=O····Pd····O=C- linkages

Figure 12 shows decrease in amount of CO_2 uptake after the encapsulation of Pd nanoparticles, with slight change in the nature of isotherm. The BET surface area and pore volume for the **Pd@MOF1a** hybrid is 145 m^2g^{-1} and 0.056 cm^3g^{-1}, respectively which reduce by a factor of two, as compared to **1a**. The appreciable decrease in surface area and pore volume indicates that the cavities of the MOF framework are filled with Pd nanoparticles. It is worth mentioning that CO_2 profile does not show hysteresis suggesting the interaction sites have been obturated by the Pd nanoparticles.
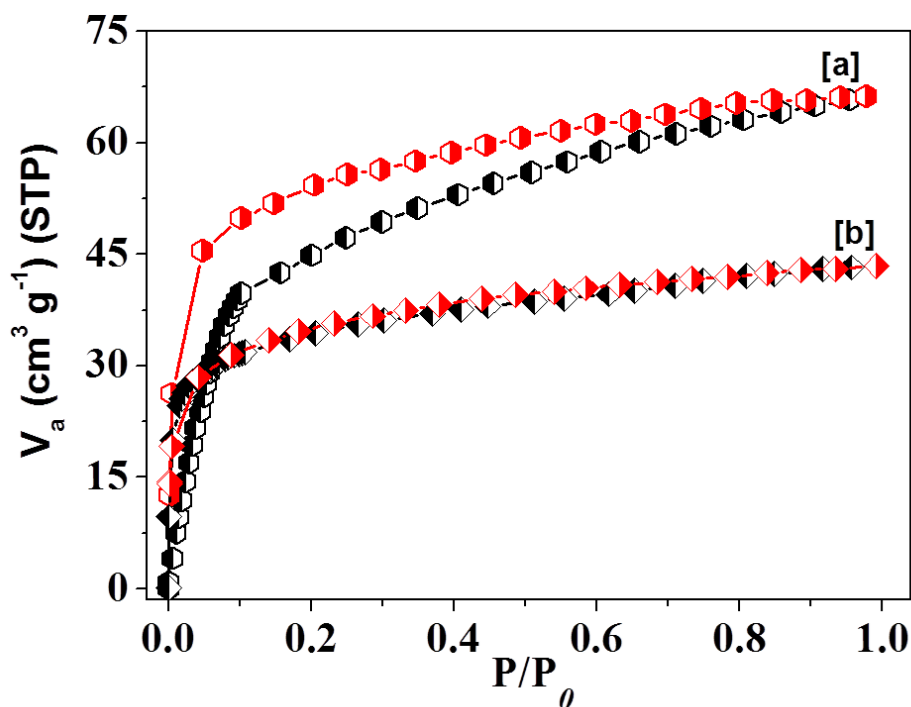
Figure 12 CO_2 sorption profiles for (a) MOF **1a** (b) **Pd@MOF1a** at 195 K.

Furthermore Pd nanoparticles encapsulated MOF has been tested for the catalytic activity of the three component coupling reaction with various aromatic aldehydes, secondary amine (piperidine) and phenyl acetylene. Each reaction was performed at 90°C in toluene (solvent) under nitrogen atmosphere in the presence of catalytic amount of **Pd@MOF1a** (1.54 wt% of Pd). No conversion was found in the absence of catalyst or by using only pure **1a** catalyst under identical conditions. The products were analyzed with Gas Chromatography-Mass Spectrometry (GC-MS) and the conversion was calculated with respect to benzaldehyde. The preliminary reaction has been carried out with benzaldehyde, piperidine and phenylacetylene as substrates and show 20% conversion to propargylamine with respect to benzaldehyde in 6 h which subsequently increases to 39 and 72% in 12 and 24 h, respectively. The reaction with

substituted benzaldehyde such as *p*- and *m*-methylbenzaldehyde produces corresponding propargylamine in 91% and 76% conversion in 24 h. Interestingly, electron deficient aromatic aldehydes such as Cl-benzaldehyde shows reasonable conversion of about 67%, however the conversion significantly reduces to 38% with benzaldehyde with strong electron withdrawing nitro group. This wavering in yields with different substituent on benzaldehyde may be explained on the basis of the electron withdrawing ($-NO_2$, $-Cl$) and donating ($-Me$) effects of the groups and selectivity values are given in (Table 4 and Figure 13).

Table 4. Catalytic activity of **Pd@MOF1a** in A^3 coupling reactions for the synthesis of propargylamines.

Sl. No.	Substrate	Conversion (%)		Selectivity	
		12 h	24 h	12h	24h
1	Benzaldehyde	39	72	69	58
2	p-methyl benzaldehyde	64	91	57	75
3	m-methyl benzaldehyde	48	76	36	56
4	p-chloro benzaldehyde	35	67	42	63
5	p-nitro benzaldehyde	15	38	71	78

 Reagent & Reaction Conditions: benzaldehyde (1 mmol), piperidine (1.2mmol), phenylacetylene (1.3mmol), Cs_2CO_3(0.5 mmol), toluene (2 mL) reaction performed at 90 °C.
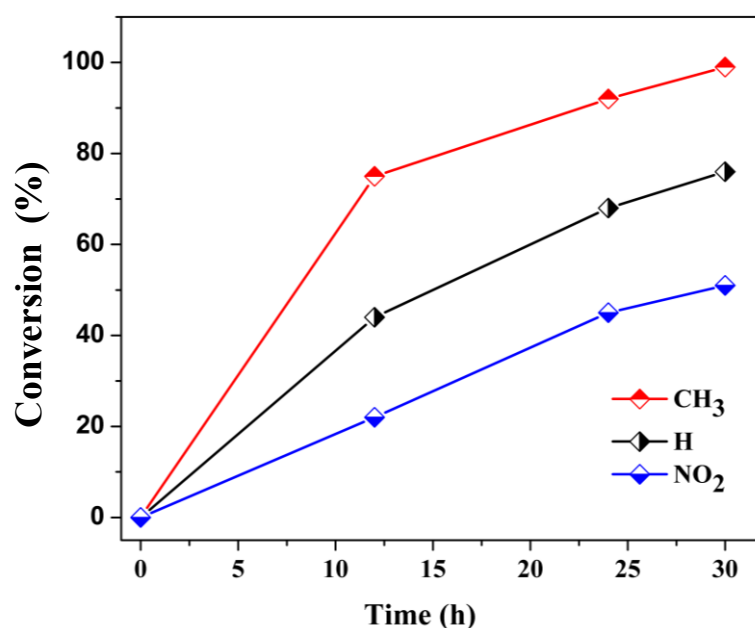
Figure 13 Comparision of catalytic activity of **Pd@MOF1a** hybrid with benzaldehyde and substituted benzaldehyde under identical reaction conditions.

It is worth mentioning that the **Pd@MOF1a** hybrid structure and the particle size almost remains unchanged even after four catalytic reaction cycles as examined from TEM (Figure 14).
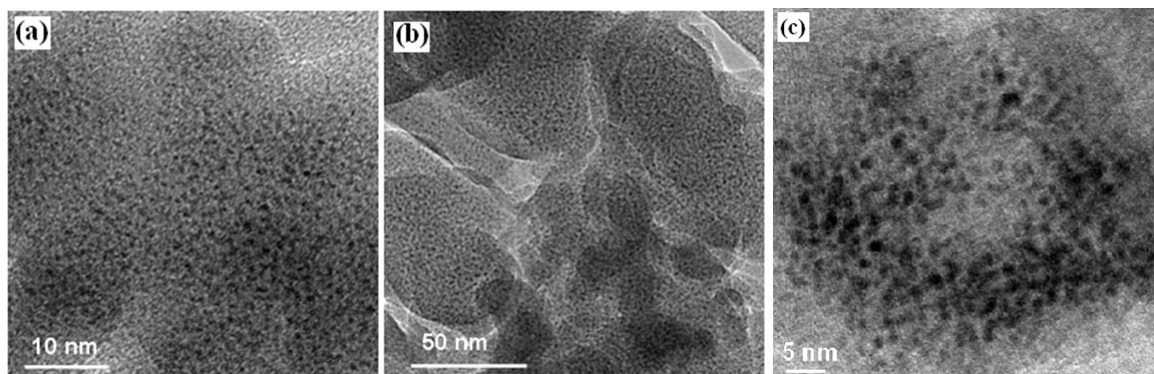
Figure 14 (a) and (b) TEM images at various magnifications showing the stabilization of Pd nanoparticles over MOF**1a**. (c) TEM image of **Pd@MOF1a** after four catalytic cycles.

There is a slight decrease in the conversion after reusing the **Pd@MOF1a** for four catalytic cycles (Figure 15).
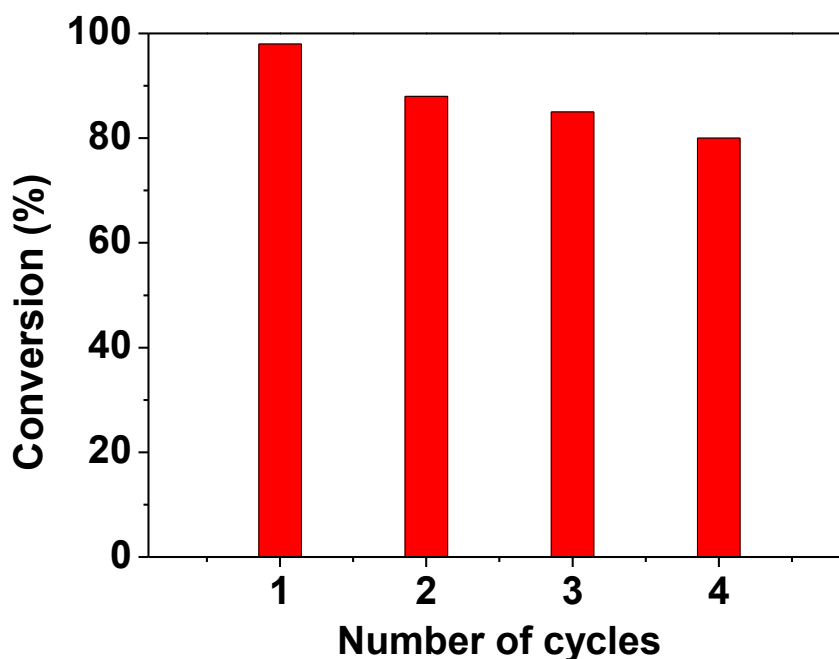
Figure 15 Study or recyclibility (four cycle)of catalytic acitivities of**Pd@MOF1a** in A^3 coupling reaction. Reaction condition: *p*-methyl benzaldehyde (1mmol), piperidine (1.2mmol), phenylacetylene (1.3 mmol), 25 mg of **Pd@MOF1a**, 2 mL toluene, and reaction has been performed at 90$^{\text{o}}$C.

Moreover, Raman spectra and PXRD showed no major changes in the peak positions before and after catalysis (Figure 10c, and Figure 16). The longer lifetime of **Pd@MOF1a** in three component coupling reaction can be explained by the strong binding of Pd nanoparticles with pendant oxygen moieties derived from carboxylate groups which offer steric restriction to stabilize Pd nanoparticles in the pores of MOF thus preventing the agglomeration of Pd nanoparticles.
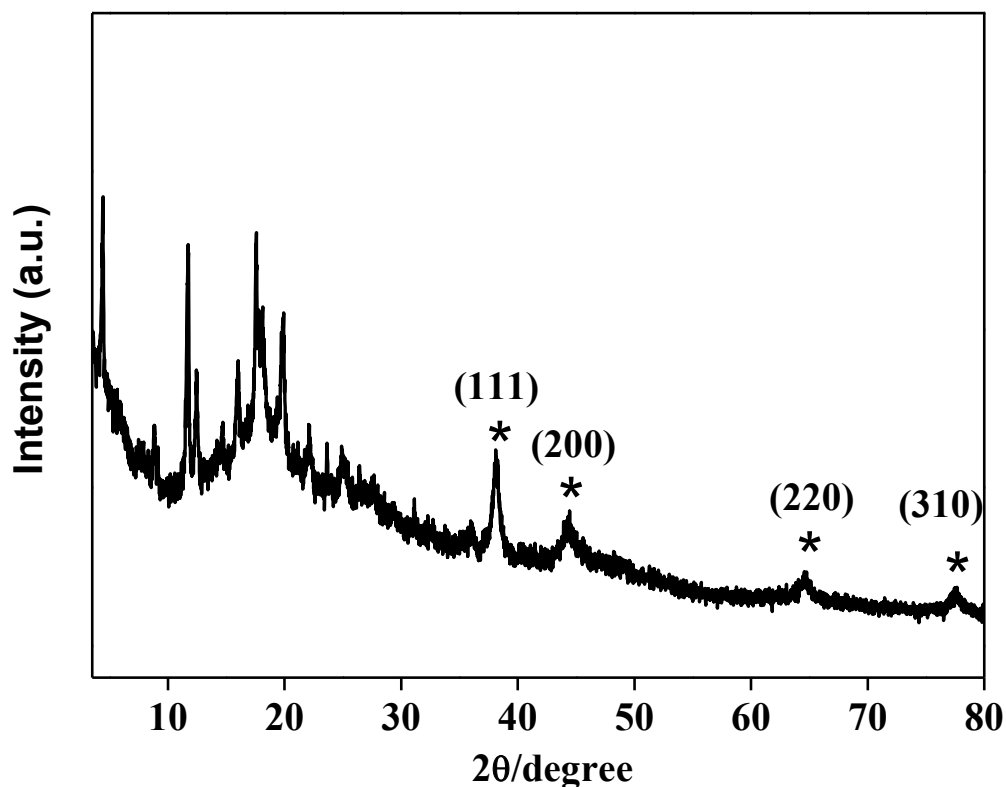
Figure 16 PXRD patterns after catalytic reaction of **Pd@MOF1a** showing the diffraction peaks corresponding to Miller indices of Pd fcc crystal structure.

7.4.6 Stabilization of Cu₂O Nanoparticles and Catalytic 1,3-Dipolar Cycloaddition "click" Reaction

We have used polar pore surface of $\{[Zn\ (Himdc)\ (bipy)_{0.5}]$ (**1a**) decorated with pendent oxygen atoms from non-coordinated carboxylate of Himdc for stabilization of Cu_2O nanoparticles having 2-3 nm size. The cuprous oxide nanoparticles were synthesized over **1a** by reducing $CuSO_4$ with a reducing agent. Figure 17 shows the powder X-ray diffraction pattern of desolvated **MOF 1a** before and after stabilization of cuprous oxide which suggest that there is no significant change in the MOF structure after encapsulation of Cu_2O nanoparticles. The Zoomed version of powdered XRD pattern of **Cu₂O@MOF 1a** showed distinguishable four peaks $2\theta = $ 37.2, 42.2, 61.4, 73.8 which are in good agreement with crystalline Cu_2O with *JCPDS* card no. 05-0667 and it also carries additional impurities for Cu and CuO nanoparticles. The broad and intense peak corresponding to (111) plane signifies the Cu_2O particle size of 3.2 nm according Debye-Scherrer equation.
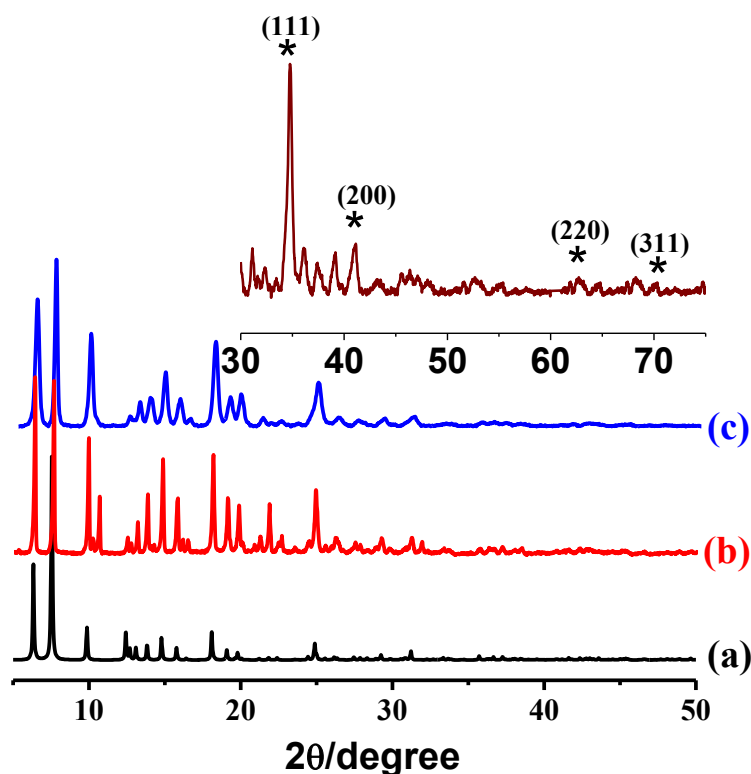
Figure 17 PXRD patterns of (a) simulated from single crystal data, (b) desolvated **1a** (c) **Cu₂O@MOF1a** hybrid. Inset showing PXRD pattern of **Cu₂O@MOF1a** showing the diffraction peaks corresponding to Miller indices of fcc crystal structure of Cu_2O.

Furthermore, XPS spectroscopy performed to understand oxidation of Cu and also the binding with oxygen of Cu. XPS spectra of O1s shows three broad peaks resolved by curve fitting procedure (Figure 18 left). The main peak at lower energy of 529.47 is attributed to Cu-O as consistent with the literature value. And other from oxygen contributions can be attributed to adsorbed oxygen on the surface of the sample and carboxylate oxygen atoms of Himdc linker. In the XPS traces, Cu $2p^{3/2}$ and $2p^{1/2}$ are attributed to 935.0 and 955.0 eV with additional peaks binding energies at 943.6 and 962.9 eV (Figure 17 right). The energy gap between Cu $2p^{3/2}$ and $2p^{1/2}$ is 20.0 eV, which is in good agreement with the literature values for Cu_2O. The additional strong peaks at 943.6 and 962.9 eV corresponding to CuO state, which is indicating the presence of CuO at the surface of the sample due to the oxidation of Cu_2O.
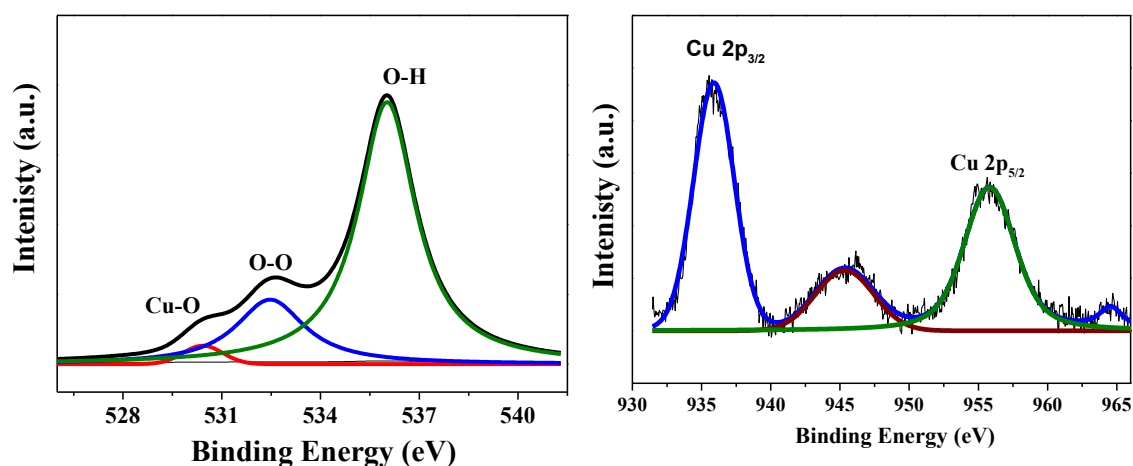
Figure 18 XPS analysis of **Cu₂O@MOF1a** O 1s (left) and Cu 2P (right) .

The size and morphology of Cu_2O nanoparticles inside the pores of **MOF 1a** was examined by transmission electron microscopy (TEM). TEM showed that the homogeneous distribution of dark spherical spots in regular fashion which correspond to Cu_2O nanoparticles with uniform shape and size of 2-3 nm (Figure 19). Energy dispersive X-ray spectroscopy analysis (EDX) and elemental mapping of **Cu₂O@MOF 1a** show peaks corresponding C, N, O, Zn and Cu, and suggests uniform distribution of all elements, which reflects the purity of samples. The amount of loading of cuprous oxide is about **3.46 %** determined through inductively coupled plasma–optical emission spectrometry (ICP-OES) analysis.
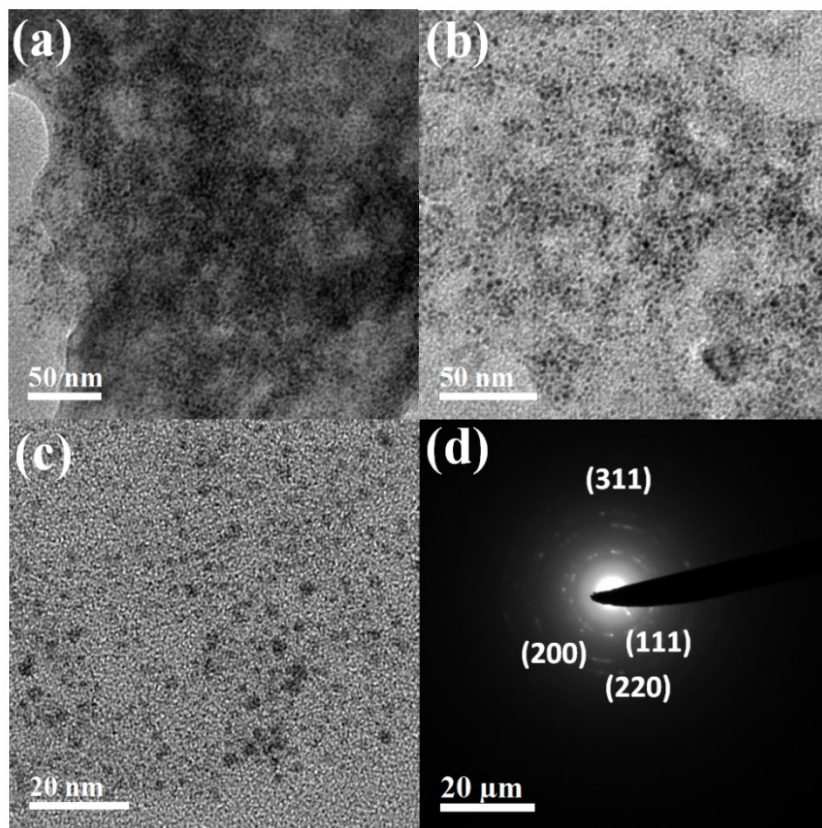
Figure 19 TEM images of **Cu₂O@MOF 1a** showing nanoparticles in the range 2-5 nm.
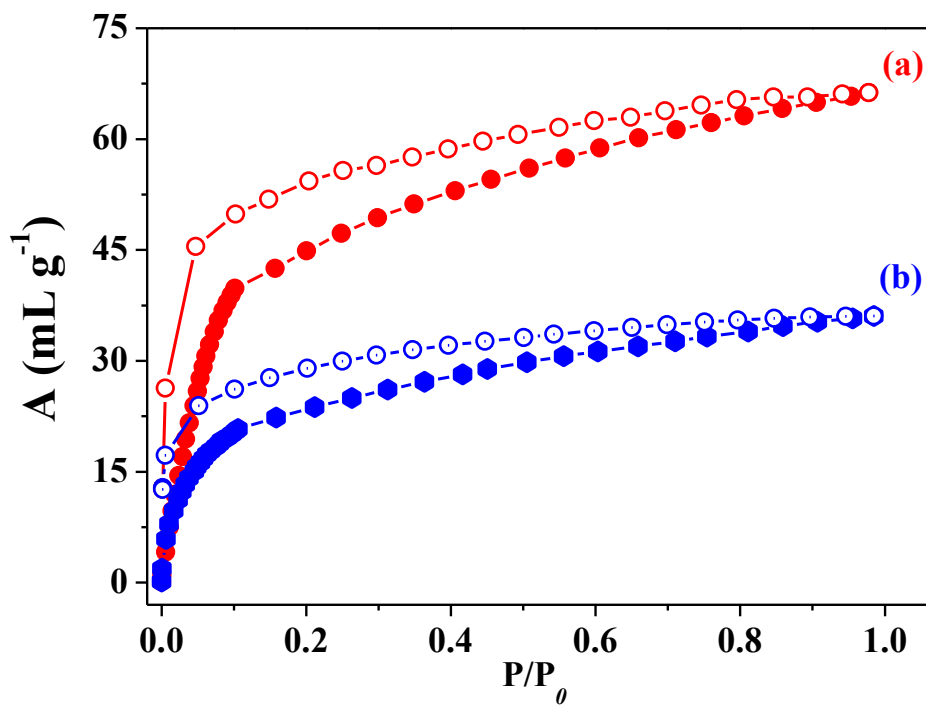
Figure 20 CO_2 adsorption isotherms at 195 K (a) **MOF 1a** (b) **Cu₂O@MOF 1a**.

Figure 20 shows the CO_2 adsorption of **Cu₂O@MOF 1a** and MOF 1a and it exhibits CO2 uptake significantly reduced to half of the amount taken by MOF1a, suggesting Cu_2O nanoparticles are embedded inside the porous matrix. Presence of highly mono-dispersed copper nanoparticles with uniform sizes ranging from 2-3 nm along the MOF matrix prompted us to study the catalytic activity based on Cu₂O@MOF1a hybrids. Initially, we carried out the reaction between 1, 3, 5- methylazido benzene and phenyl acetylene. In a typical reaction, 1mmol of 1, 3, 5- methylazido benzene is treated with 3.5mmol of phenyl acetylene in *t*-BuOH/H₂O (1:2) mixture in presence of catalytic amount of **Cu₂O@MOF** (3.46 % of Cu₂O) at 50 °C. Formation of cyclized products were analysed using GC-MS at regular intervals of time. Reactions were quite clean and went to completion (>98%) within 6hrs.
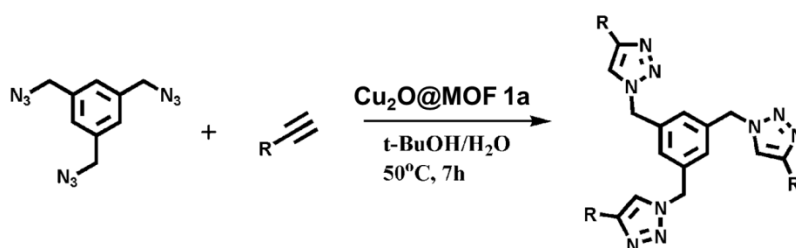
Table 5 Click reactions by using **Cu₂O@MOF 1a** with various organic precursors

S. No.	Compound	R	Time(hrs)	Yield (%)
1		(OEt ester)	7	98
		(phenyl/toluene)	7	>99
		(butyric acid)	7	93
2		(OEt ester)	7	98

Reaction Conditions; Triethyl amine, **Cu₂O@MOF 1a**, t-BuOH/H₂O 5mL water, 50 °C.

Precipitates were successfully collected by filtration and washed with water and *t*-BuOH . The obtained products were characterized qualitatively using ^{1}H NMR

spectroscopy. Encouraged with quantitative yields, we further studied the activity of **Cu₂O@MOF** for electron withdrawing alkynes with similar azide moiety. Interestingly, all reactions proceed to completion within 6h and results are compiled in table (Table 5). On the other hand, blank catalytic reactions in presence of pure MOF shows no conversion suggesting the role of Cu_2O nanoparticles in catalysing click reactions. It is noteworthy to mention that **Cu₂O@MOF 1a** showed no alteration in its catalytic activity even after four catalytic cycles and results in similar yield. These results indicate that the strong interaction of copper nano particles with pendent carboxylate oxygen atoms stabilizes the nanoparticles and resist agglomeration of nano particles.

7.5 Conclusions

In conclusion a 2D layered MOF **1** with pendant carboxylate functional groups was successfully synthesized from mixed Himdc and bipy linkers showing structural flexibility and highly selective CO_2 uptake characteristics among the number of gases. These functional pore channels are utilized as a size controlling scaffold for the stabilization of 2-4 nm sized Pd and Cu_2O nanoparticles. We have exploited hybrid **Pd@MOF 1a** for A^3 coupling reaction of benzaldehyde, piperidine and phenyl acetylene for the preparation of propargylamines. Furthermore, We have also demonstrated the **Cu₂O@MOF** as a highly selective and recyclable catalyst for 1,3 dipolar cycloaddion reaction between terminal alkynes and aliphatic/aromatic azide for synthesis traizole products *via* click chemistry.

7.6 References

1) a) H. Li, M. Eddaoudi, M. O. Keeffe, O. M. Yaghi, *Nature* **1999**, *402,* 276; b) S. Kitagawa, R. Kitaura, S. Noro*, Angew. Chem. Int. Ed.* **2004**, *43*, 2334; c) D. Britt, D. J. Tranchemontagne, O. M. Yaghi, *Proc. Natl. Acad. Sci.* **2008**, *105*, 11623; d) J. Y. Lee, O. J. Farah, J. Roberts, K. A. Scheidt, S. T. Nguyen, J. T. Hupp, *Chem*. *Soc*. *Rev*. **2009**, *38*, 1450; e) M. D. Allendorf, C. A. Bauer, R. K. Bhakta, R. J. T. Houk, *Chem. Soc. Rev.* **2009**, *38*, 1330*;* f) A. C. McKinlay, R. E. Morris, P. Horcajada, G. Férey, R. Gref, P. Couvreur, C. Serre, *Angew. Chem. Int. Ed.* **2010**, *49*, 6260.

2) a) M. Meilikhov, K. Yusenko, D. Esken, S. Turner, G. V Tendeloo, R. A. Fischer, *Eur. J. Inorg. Chem.* **2010,** 3701; b) H. L. Jiang, Q. Xu, *Chem. Commun.* **2011**, *47*, 3351.

3) a) T. Ishida, M. Nagaoka, T. Akita, M. Haruta, *Chem. Eur. J.* **2008**, *14*, 8456; b) Y. Huang, Z. Lin, R. Cao, *Chem. Eur. J.* **2011**, *17*, 12706; c) B. Yuan, Y. Pan, Y. Li, B. Yin, H. Jiang, *Angew. Chem. Int. Ed.* **2010**, *49*, 4054; d)Y. K. Park, S. B. Choi, H. J. Nam, D. Y. Jung, H. C. Ahn, K. Choi, H. Furukawa, J. Kim, *Chem. Commun.* **2010**, *46*, 3086; e) H.L. Jiang, B. Liu, T. Akita, M. Haruta, H. Sakurai, Q. Xu*, J. Am. Chem. Soc.* **2009**, *131*, 11302; f) Y. E. Cheon, M. P. Suh, *Angew. Chem. Int. Ed.* **2009**, *48,* 2899; g) A. Henschel, K. Gedrich, R. Kraehnert, S. Kaskel, *Chem. Commun.* **2008**, 4192; h) C. Zlotea*,* R. Campesi*,* F. Cuevas*,* E. Leroy*,* P. Dibandjo*,* C. Volkringer*,* T. Loiseau*,* G. Férey*,* M. Latroche*, J. Am. Chem. Soc.* **2010***, 132,* 2991; (i) T.H. Park, A. J. Amanda, J. Hickman, K. Koh, S. Martin, A. G. W. Foy, M.S. Sanford, A.J. Matzger, *J. Am. Chem. Soc.* **2011**, *133* , 20138; (j) Y. Huang, S. Gao, T. Liu, J. Lu, X. Lin, H. Li, R. Cao, *ChemPlusChem* **2012***, 77*, 106.

4) R. J. T. Houk, B. W. Jacobs, F. E. Gabaly, N. N. Chang, A. A. Talin, D. D. Graham, S. D. House, I. M. Robertson, M. D. Allendorf, *Nano Lett.* **2009**, *9*, 3413; b) Y. K. Hwang, D.Y. Hong, J. S. Chang, S. H. Jhung, Y.K. Seo, J. Kim, A. Vimont, M. Daturi, C. Serre, G. Ferey, *Angew. Chem., Int. Ed.* **2008**, *47***,** 4144; c) D. Esken, S. Turner, C. Wiktor, S. Kalidindi, G.V. Tendeloo, R. A. Fischer , *J. Am. Chem. Soc*. **2011**, *133*, 16370; d) J.   Hermannsdçrfer, R. Kempe *Chem. Eur. J.* **2011**, 17, 8071; e) H. R. Moon, M. P. Suh, *Eur. J. Inorg. Chem*. **2010**, 3795; f) M. Sabo, A. Henschel, H. Fröde, E. Klemm, S. Kaskel, *J. Mater. Chem.* **2007**, *17*, 3827.

5) a) S. Hermes, M. K. Schröter, R. Schmid, L. Khodeir, M. Muhler, A. Tissler, R. W. Fischer, R. A. Fischer, *Angew. Chem. Int. Ed.* **2005**, *44*, 6237; b) D. Esken, S. Turner, O. I. Lebedev, G. Van Tendeloo, R. A. Fischer, *Chem. Mater.* **2010**, *22*, 6393; c) D. Esken, X. Zhang, O. I. Lebedev, F. Schroder, R. A. Fischer, *J. Mater. Chem.* **2009**, *19*, 1314.

6) a) T. Ishida, N. Kawakita, T. Akita, M. Haruta, *Gold Bull.* **2009**, *42*, 267; b) H.L. Jiang, Q.P. Lin, T. Akita, B. Liu, H. Ohashi, H. Oji, T. Honma, T. Takei, M. Haruta, Q. Xu, *Chem. Eur. J.* **2011**, *17*, 78.

7) M. S. ElShall, V. Abdelsayed, A. E. Rahman S. Khder, H. M. A. Hassan, H. M. ElKaderi, T. E. Reich, *J. Mater. Chem.* **2009**, *19*, 7625.

8) a) H. R. Moon, J. H. Kim, M. P. Suh, *Angew. Chem. Int. Ed.* **2005**, *44*, 1261; b) M. S. AlShall, V. Abdelsayed, A. E. R. S. Khder, H. M. A.Hassan, H. M. E. Kaderi, T. E. Reich*, J. Mater. Chem*. **2009**, *19*, 7625.

9) a) Y. K. Hwang, D. Y. Hong, J. S. Chang, S. H. Jhung, Y. K. Seo, J.Kim, A. Vimont, M. Daturi, C. Serre, G. Férey, *Angew. Chem. Int. Ed.* **2008**, *47*, 4144; b) Y. E. Cheon, M. P. Suh, *Angew. Chem., Int. Ed.* **2009**, *48*, 2899;c) M. Meilikhov, K. Yusenko, R. A. Fischer, *J. Am. Chem. Soc.* **2009**, *131*, 9644; d) Z. Zhang, C. Dong, C. Yang, D. Hu, J. Long, L. Wang, H. Li, Y. Chen, D. Kong, *Adv. Synth. Cat.* **2010**, *352*, 1600.

10) a) C. Wei, C. J. Li, *J. Am.Chem.Soc.* **2002**, *124*, 5638; b) M. K. Patil, M. Keller, B. M. Reddy, P. Pale, J. Sommer, *Eur. J. Org. Chem.* **2008**, 4440; c) L. L. Chng, J. Yang, Y. Wei, J. Y. Ying, *Adv. Synth. Catal.* **2009**, *351*, 2887.

11) a) A. Cao, R. Lu, G. Veser, *PhysChemChemPhys* **2010**, *12*, 13499-13510

12) a) Z. Hulvey, D. A. Sava, J. Eckert, A. K. Cheetham, *Inorg. Chem*. **2011**, *50*, 403; b) A. Hazra, P. Kanoo, T. K. Maji, *Chem. Commun.* **2011**, *47*, 538; c) M. Dinca, A. Dailly, C. Tsay, J. R. Long, *Inorg. Chem*. **2008**, *47*, 11; d) R. Vaidhyanathan, S. S. Iremonger, G. K. H. Shimizu, P. G. Boyd, S. Alavi, T. K. Woo, *Science* **2010**, *330*, 650.

13) SMART (V 5.628), SAINT (V 6.45a), XPREP, SHELXTL; Bruker AXS Inc. Madison, Wisconsin, USA, **2004**.

14) G. M. Sheldrick, *Siemens Area Detector Absorption Correction Program*, University of Göttingen, Göttingen, Germany, **1994**.

15) A. Altomare, G. Cascarano, C. Giacovazzo, A. Gualaradi, *J. Appl. Cryst.* **1993**, *26,* 343.

16) G.M. Sheldrick, SHELXL-97, *Program for Crystal Structure Solution , Refinement*; University of Göttingen, Göttingen, Germany, **1997**.

17) A.L. Spek, *J. Appl. Cryst.* **2003**, *36,* 7.

18) L.J. Farrugia, *WinGX - A Windows Program for Crystal Structure Analysis. J. Appl. Crystallogr.* **1999**, *32*, 837.

19) M.M. Dubinin, *Chem. Rev.* **1960**, *60*, 235.

Chapter 8

Metal-Organic Framework Derived Materials for Energy and Environmental Applications
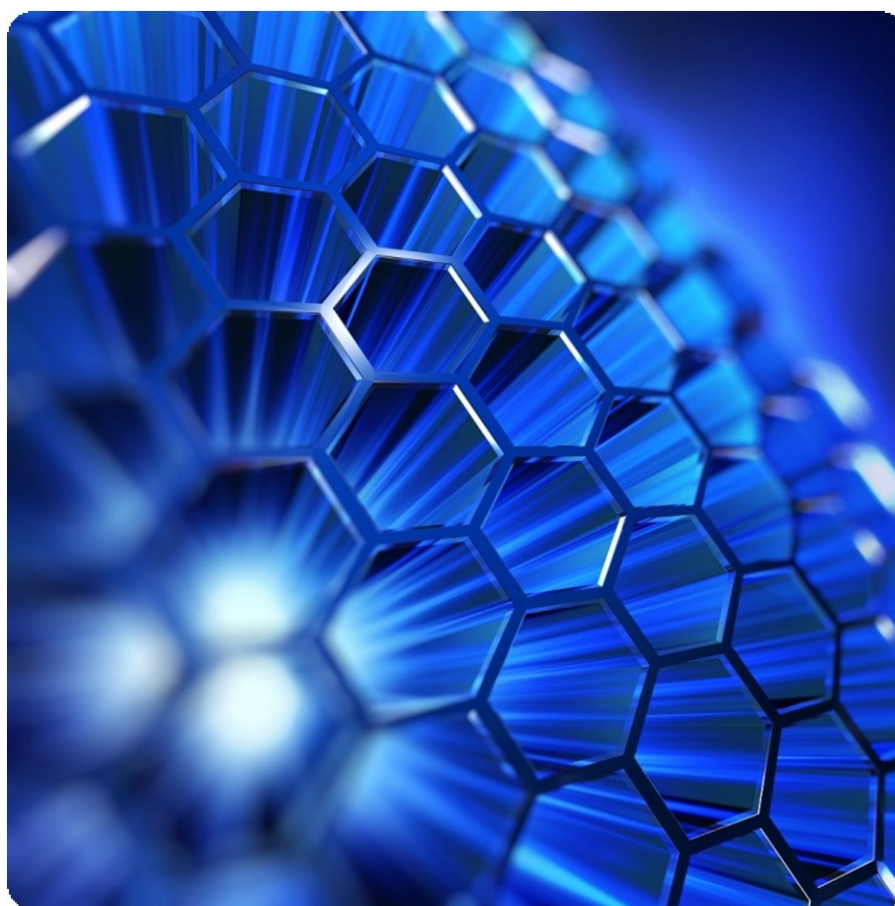
Chapter 8.1

Nanoporous Carbons Derived from MOF with Tunable Porosity: Excellent candidates for Gas (H$_2$ and CO$_2$) and Electrochemical Storage
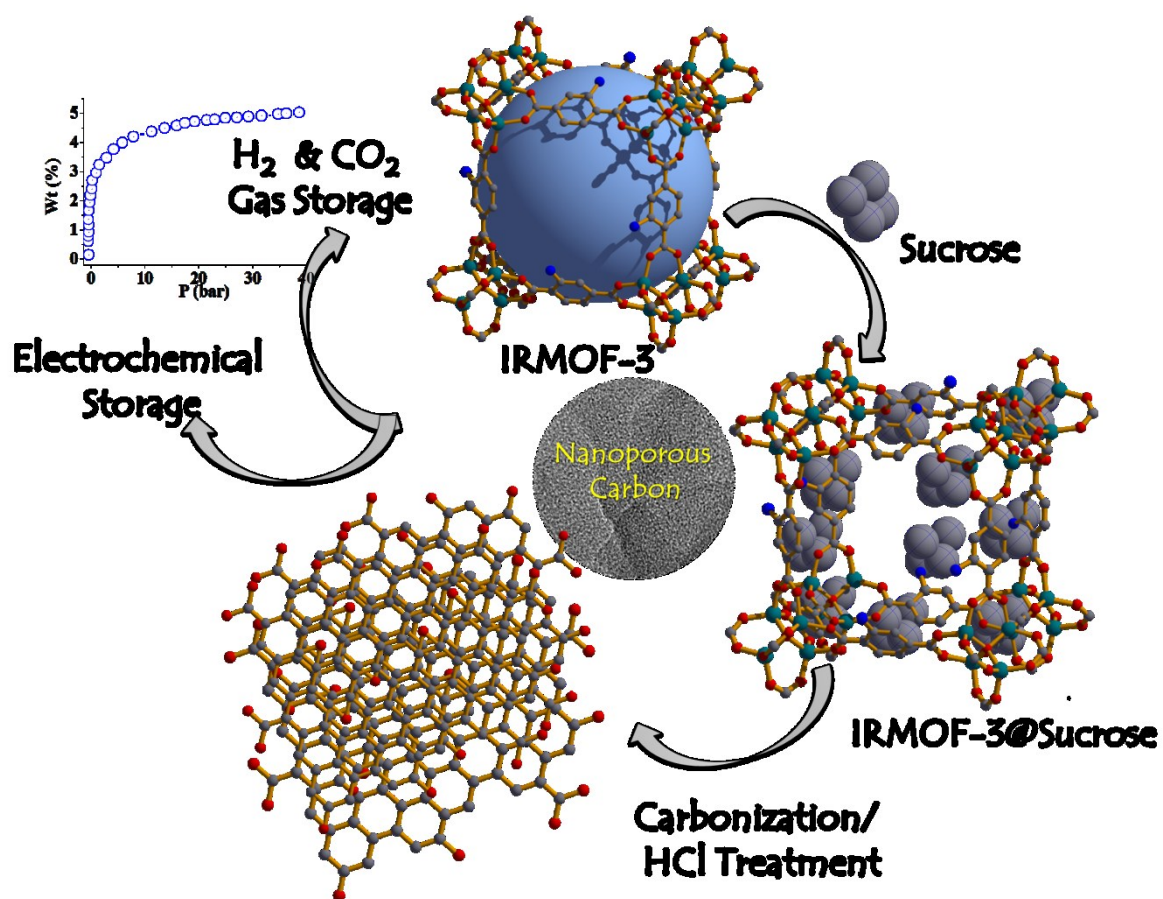
Summary

This chapter deals with a simple and facile strategy for the synthesis of versatile nanoporous carbon (**NPC**) materials with tunable textural parameters using a metal-organic framework (**IRMOF-3**) that acting as a template for external carbon precursor (viz. sucrose) and also a self-sacrificing carbon source. The resultant **NPC** samples (abbreviated as **NPC-0**, **NPC-150**, **NPC-300**, **NPC-500** and **NPC-1000**) have graphitic carbon environment and based on different amounts of sucrose loading exhibit tunable surface area, pore volume and pore sizes. Among these **NPC-300** shows very high surface area (BET$\approx$ 3119 m^2/g, Langmuir $\approx$ 4031 m^2/g) with a large pore volume of 1.93 cm^3/g. High degree of porosity coupled with polar surface functional groups, **NPC-300** exhibits remarkable H$_2$ (2.54 wt% at 1 bar, and 5.1 wt % at 50 bar, 77 K) and CO$_2$ (64 wt% at 1 bar, 195 K and 21 wt % at 50 bar, 298 K) storage capacities. As a working electrode in a supercapacitor cell, **NPC-300** shows excellent reversible charge storage thus, demonstrating multifunctional usage of the carbon materials.

8.1.1 Introduction

Over the past decade, porous carbon materials have attracted a great deal of attention due to their potential applications in the fields of gas storage/separation, catalysis, fuel cell and biology.[1] Nanoporous carbons have received special attention compared to other contemporary porous materials because of its low density, chemical inertness and high thermal stability.[2] Among various techniques (both physical and chemical) to prepare nanostructured carbons, nanocasting approach using sacrificial template is an advantageous method owing to its fine control over pore size, surface area and pore volume.[3] In the past mesostructured silica, zeolites and clays have been utilized as hard templates for synthesizing hierarchical meso- and microporous carbons respectively.[4] Microporous carbon materials possessing high surface area are potential candidates for the adsorption and storage of small molecules such as hydrogen and carbon dioxide.[5] Recent results suggests that for high density hydrogen storage materials need to have appropriate balance between ultra microporosity, pore volume and surface area because of small kinetic diameter and low polarizablity of hydrogen molecule.[6] Therefore the synthesis of nanoporous carbon materials with high surface area and micro pore volume is of paramount importance, although it is not a straightforward. It is even more challenging to obtain features like tunable textural properties in these materials.

Metal-organic frameworks (MOFs) or porous coordination polymers (PCPs), an important class of highly crystalline ordered porous materials, exhibit considerable potential applications in gas storage, separation, catalysis, magnetism and drug delivery based on their structural topology and tunable pore size and environment.[7] MOFs with ordered functional porous environment combined with high crystallinity and thermal stability can also be utilized in the preparation of porous carbon with high surface area.[8] Using MOF as a template, Xu *et al.* first prepared porous carbon materials using furfuryl alcohol as an external carbon precursor.[8] Later, other groups also reported porous carbon materials derived from MOF, with and without external carbon precursor.[7d] Furthermore, porous carbon materials with tunable textural properties have received substantial attention, due to their important industrial applications in catalysis, adsorption, chemical sensing and as a supercapacitor.[9] Therefore, the right choice of carbon precursor and MOF is very critical to fabricate desired tunable nanoporous carbon sample. As MOFs offers ordered and tunable porous environment with various functional groups on organic linker, therefore it is feasible to choice suitable carbon

precursor which can be easily immobilized through intermolecular host-guest interaction. This chapter demonstrates a simple and facile route for the synthesis of nanoporous carbon materials from **IRMOF-3 {[Zn$_4$O(NH$_2$-BDC)$_3$]·xDMF}**, (NH$_2$BDC = 2-amino-1,4-benzenedicarboxylate)[10] which acts a template for external carbon source (sucrose) and as a self-sacrificing carbon precursor. Although the synthesis of porous carbon from MOFs and external carbon precursor are well exploited, their tunable textural property based on the loading of the external carbon precursor is yet to be explored. This work reports for the first time synthesis, characterization, tunable surface area and pore volume (high ratio of micropore to mesopore) of various nanoporous carbon samples (**NPCs)** (**NPC-0**, **NPC-150**, **NPC-300**, **NPC-500** and **NPC-1000**) based on different loadings of sucrose in IRMOF-3. The beneficial influence of external carbon precursor to obtain high surface area **NPC** sample with high micro pore volume has been discussed in the context of gas storage and electrochemical supercapacitors. Among the optimized systems **NPCs**, the sample **NPC-300** shows high BET surface area of (3119 m^2/g) with a large pore volume (1.93 cm^3/g) which has been exploited for hydrogen and carbon dioxide storage and electrochemical double layer super capacitors.[11]

8.1.2 Experimental Section

8.1.2.1 Materials

All the reagents and solvents employed were commercially available and used as supplied without further purification. Zn(NO$_3$)$_2$.6H$_2$O, 2-aminobenzenedicarboxylic acid, sucrose, were obtained from Aldrich Chemical Co.

8.1.2.2 Preparation of Nanoporous carbon using IRMOF-3

IRMOF-3 was prepared according to the literature reported by Yaghi *et al.* [10] using Zn(NO$_3$)$_2$·6H$_2$O (4.8 g, 16 mmol) and of 2-aminoterephthalic (1.32 g, 8 mmol) in 30 ml of dimethylformamide (DMF) at 120 ^{o}C for 6 h. The resultant compound was filtered, thoroughly washed with DMF and then activated by guest exchange with ethanol (20 mL) for 7 days. The sample was then filtered and dried in vacuum at 130 °C. For the synthesis of porous carbon, we took desolvated IRMOF-3, different amounts of sucrose (X =0, 150, 300, 500, 1000 mg), 8 μL of H$_2$SO$_4$ and then all mixed to gether in 2 ml of water to form light yellow colored paste. This mixture

then kept in an oven for successive temperatures 100 ^{o}C for 6 h and 160 ^{o}C for another 6 h. The resulting composites were then pyrolyzed in a nitrogen flow at 900 ^{o}C and kept under these conditions for 6 h to carbonize the composite. The **NPCs** were obtained after removal of ZnO species using 20% hydrochloric acid by filtration, washed several times with water ethanol mixture and dried at 100 ^{o}C. The resultant carbons obtained by variation in sucrose content are denoted by "**NPC-X**", where X indicates that amount of sucrose used. The obtained samples were designated as **NPCs** (**NPC-0**, **NPC-150**, **NPC-300**, **NPC-500** and **NPC-1000**) based on the different amount of sucrose loading. All the resultant **NPCs** were characterized by FT-IR, CHNS analysis, thermogrvitmetric analysis, powder XRD (PXRD), Energy dispersive X-ray analysis (EDS) and different microscopic techniques.

8.1.3 Characterization Techniques

8.1.3.1 Physcial Measuremnts

The resultant **NPC** samples were characterized through different techniques. Powder X-ray diffraction (PXRD) pattern were recorded on a Bruker D8 Discover instrument using Cu-Kα radiation. The morphology and porous nature of **NPCs** examined with field emission scanning electron microscope (FESEM, FEI Nova-Nano SEM-600, Netherlands) and transmission electron microscope (TEM) (JEOL JEM-3010 with an accelerating voltage at 300 kV). The Raman spectra were recorded in backscattering arrangement, using 532 nm laser excitation using 6 mW laser power. Elemental analyses were carried out using a Thermo Scientific Flash 2000 CHN analyzer. FT- IR spectra were recorded using KBr pellets in the range 4000 - 400 cm^{-1} on a Bruker IFS-66v spectrophotometer. Thermogravimetric analyses (TGA) were carried out under nitrogen (flow rate of 50 mL/min) with Metler Toledo TGA-850 TG analyzer in the temperature range between 25 - 600°C at a heating rate 3°C / min.

8.1.3.2 Adsorption Measurements

Adsorption studies of CO_2 (195 K for **NPC-300**), H_2 (77 K for **NPC-300**) and N_2 (77 K) for of **NPC** samples prepared at 423 K under high vacuum, were carried out using QUANTACHROME AUTOSORB-1C analyzer. The adsorption isotherm of different solvents (like H_2O and C_6H_6, at 298 K) for **NPC 300** was measured in the vapor state by using BELSORP-aqua volumetric adsorption instrument from BEL, Japan. In the sample chamber (~12 mL) maintained at T ± 0.03 K was placed the adsorbent sample (100-150 mg), which had been prepared at 423 K in 10^{-1} Pa for 18 hours prior to measurement of the isotherms. The adsorbate was charged into the sample tube, and then the change of the pressure was monitored and the degree of adsorption was determined by the decrease of the pressure on the equilibrium state. All operations were computer-controlled and automatic. High-pressure H_2 (77 K) and CO_2 (298 K) sorption measurements for **NPC 300** was carried out on a fully computer controlled volumetric BELSORP-HP, BEL JAPAN high pressure instrument. All the gases used for higher pressure measurements are scientific/research grade with 99.999% purity. For the measurements, approximately 300 mg sample was taken in a stainless-steel sample holder and degassed at 493 K for a period of 18 hours under 0.1 Pa vacuum. The dead volume of the sample cell was measured with helium gas of 99.999% purity. Non-ideal correction for H_2 and CO_2 gases were made by applying virial coefficients at the respective measurement temperature.

8.1.3.3 Supercapacitor cell measurments

Investigations were carried out using **NPC-300** as a working electrode in a cell containing 1.0 M aqueous H_2SO_4 solution as electrolyte, platinum wire as counter electrode and a saturated calomel electrode (SCE) as a reference electrode. All electrochemical characterizations were performed at room temperature. The composite working electrode was prepared by dispersing a mixture of **NPC-300**, polyvinyldifluoride (PVdF) binder and acetylene black in N-methyl-pyrrolidone (NMP) solvent. The three components were in the ratio 85:05:10 (w/w) in NMP and processed to form homogeneous slurry. The homogeneous mixture is pasted onto stainless steel (SS) current collector (0.5 ×0.5 cm^2) and electrodes were dried at 120 ^{0}C for 12 h under vacuum.

8.1.4 Results and Discussion

8.1.4.1 Synthesis and Characterization of Resultant Nanoporous Carbon Samples (NPCs)

The step-wise synthesis of different nanoporous carbons from sucrose and IRMOF-3 is illustrated in Scheme 1.
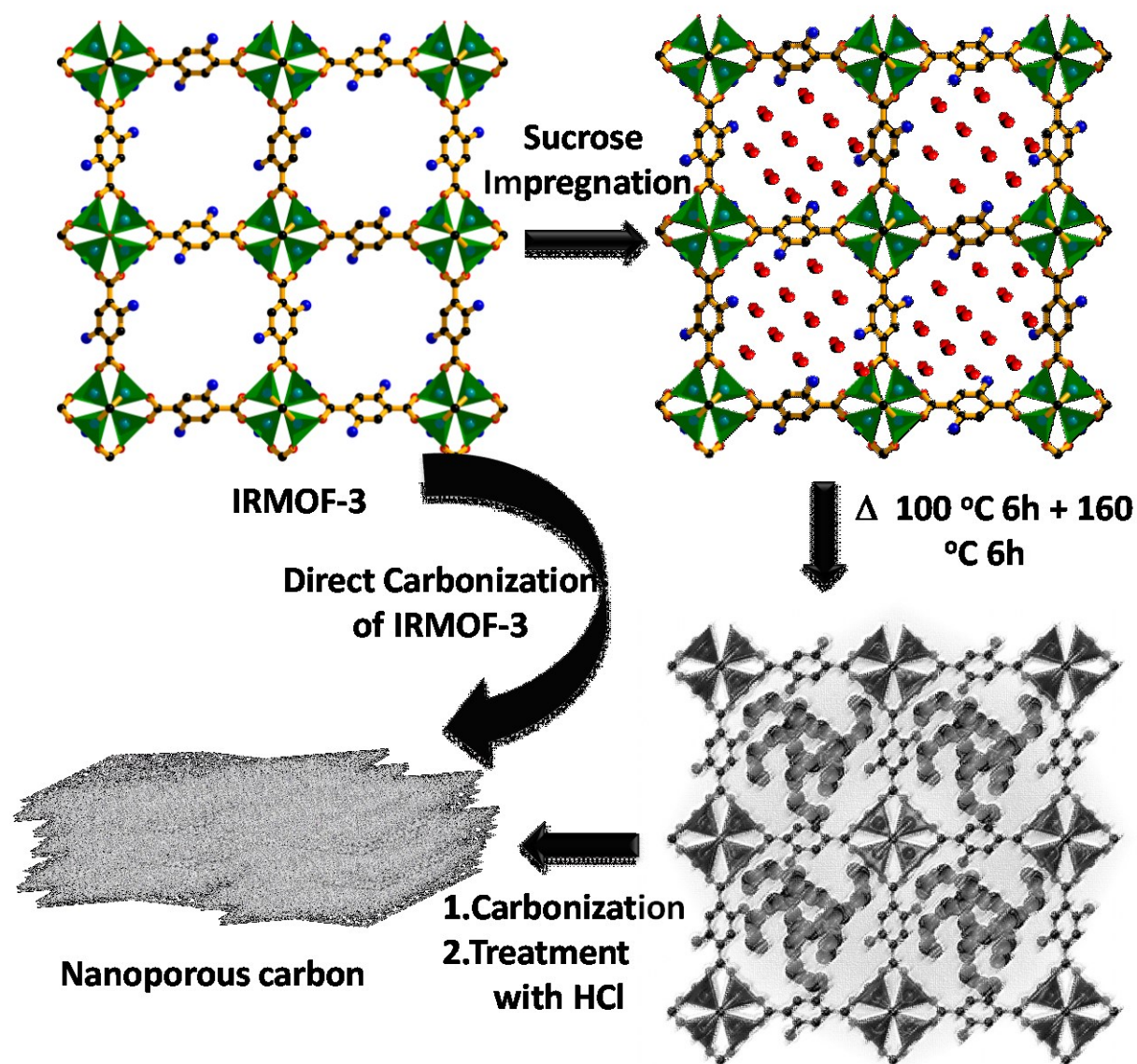
Scheme 1 Flowchart showing detailed synthetic methodology of IRMOF-3 derived nanoporous carbon.

IRMOF-3 $\{Zn_4O(NH_2\text{-}BDC)_3\}$ has three dimensional structure consist of an oxo-centre $\{Zn_4O(CO_2)_6\}$ secondary building units connected by NH_2-BDC linkers. Framework has 3D channels (dimensions of 18 x 18 $Å^2$) decorated with basic functional groups and possessing a surface area of 2371 m^2/g. We conjecture that, the inclusion of sucrose inside the pores is facilitated via its hydrogen bonding interaction with such amine ($-NH_2$) functionalized pore surface in IRMOF-3. Sucrose loaded IRMOF-3 has retained structural intigrity as revealed by powder XRD pattern (Figure 1 left). Sucrose infiltrated IRMOF-3 was heated at 100 and 160 ^{o}C for the polymerization of sucrose and then resulting composite is carbonized under a nitrogen atmosphere at 900 ºC forming a black colored powder. The EDAX analysis and PXRD pattern of this sample suggest the presence ZnO particles in the carbonized sample. Pure porous carbons sample was obtained by treating with HCl solution (20 %) followed by washing with a water / ethanol mixture to remove ZnO particles (Figure 1 right).
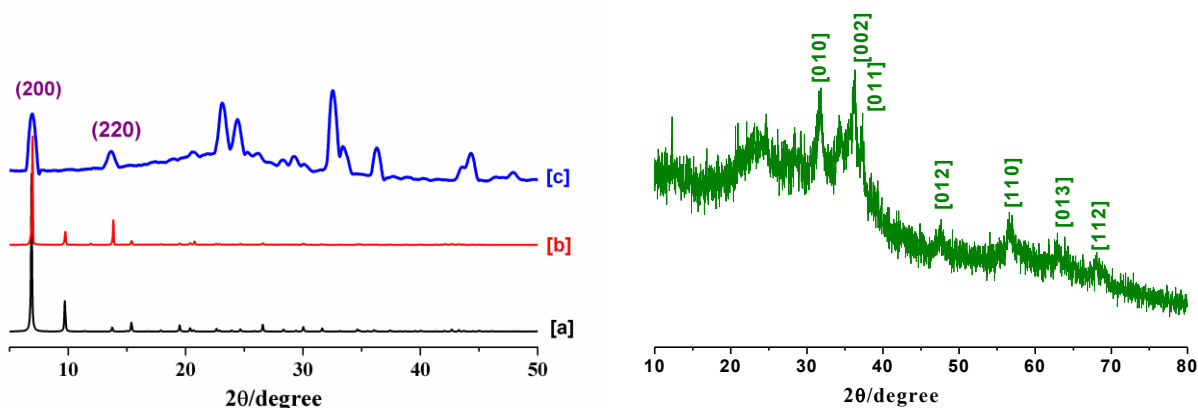
Figure 1 Powder XRD patterns (left) (a) simulated pattern IRMOF-3 (b) assynthesized IRMOF-3(c) mixture of IRMOF-3/Sucrose; (Right) **ZnO@NPC-300** showing hexagonal phase of Wurtzite ZnO.

The same procedure was adopted for various sucrose loadings sample to prepare different **NPCs** (see experimental part). The purity of all resultant **NPC** samples after HCl treatment is confirmed through elemental (CHN) analysis (Table 1) and EDAX measurements. FT-IR spectra of all NPCs show $-C=C-$ vibrational bands along with oxygen containing functional groups like carboxylate (-COOH) and hydroxy (-OH) (Figure 2 for **NPC-300**).

Table 1 CHN elemental analysis of NPC samples.

Sample	Carbon (%)	Hydrogen (%)
Sucrose	73.8	3.9
NPC-0	79.6	4.2
NPC-150	82.0	3.6
NPC-300	91.5	2.5
NPC-500	88.7	4.9
NPC-1000	72.6	5.8
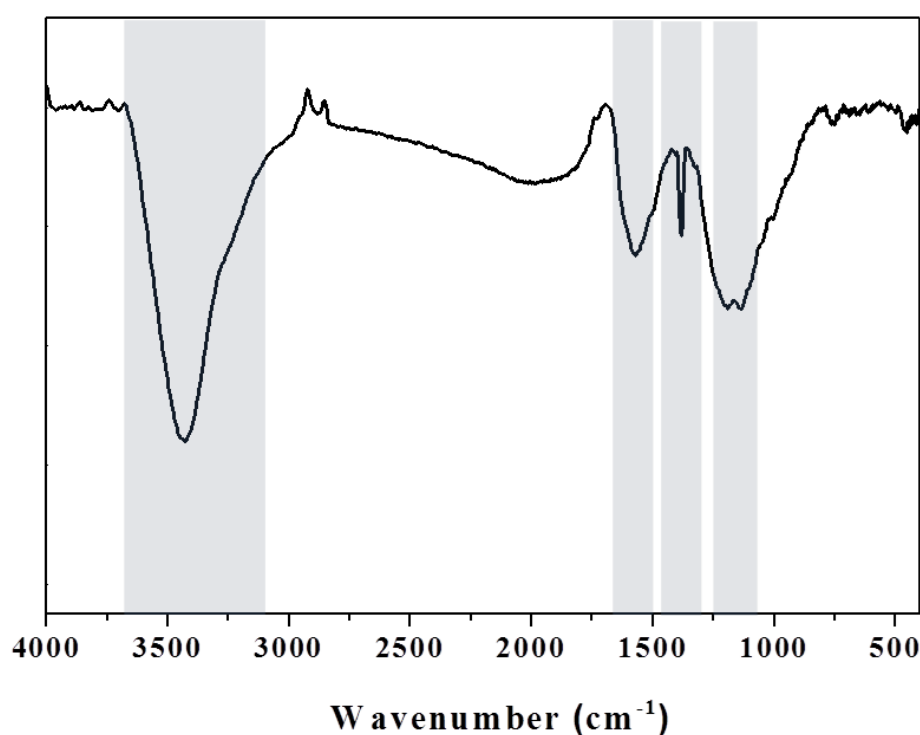
Figure 2 FT-IR spectrum of **NPC-300**.

The PXRD pattern of all the resultant **NPC** samples (**NPC-0**, **NPC-150**, **NPC 300**, **NPC-500** and **NPC-1000)** shown in Figure 3. Interestingly, all **NPC** samples after treating with HCl exhibit two major broad peaks centered at $2\theta = 24.5^\circ$ and 44.3° corresponding to two planes (002) and (101) respectively, which resembles the structural signature of graphitic carbon.
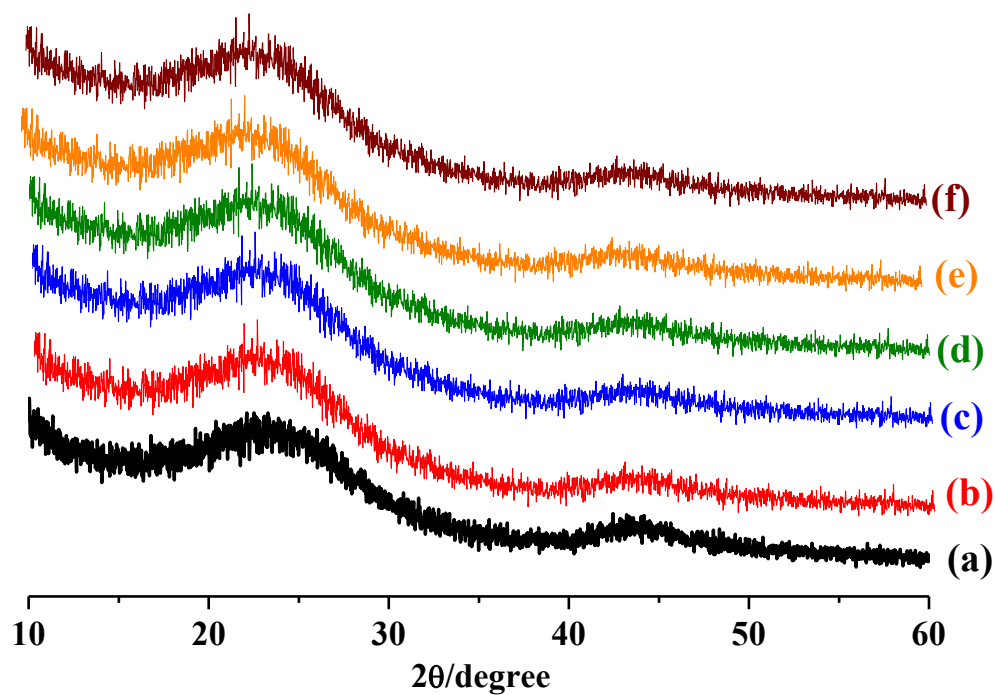
Figure 3 Powder X-ray patterns of all **NPC** samples (a) **NPC-0**,(b) **NPC-150**, (c) **NPC-300**, (d) **NPC-500**, (e) **NPC-1000**, (f) Sucrose derived carbon.
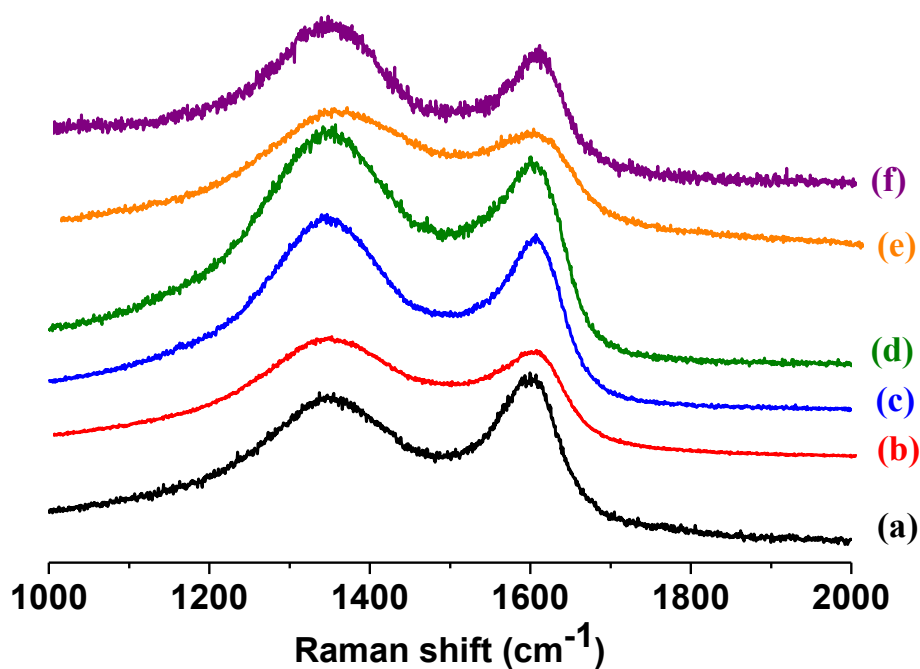
Figure 4 Raman spectra of all NPC samples (a) **NPC-0**,(b) **NPC-150**,(c) **NPC-300**,(d) **NPC-500**,(e) **NPC-1000**,(f) Sucrose derived carbon.

Further Raman spectroscopy measurements were performed to study the local structure of all the **NPC** samples. Raman spectra of all the samples are shown in Figure 4, showing two major broad peaks centered at ~1350 cm^{-1} and ~1629 cm^{-1} and are attributed to D- and G-bands resepctively. The relative ratios of the G band to D band (I_G/I_D) are almost constant ($I_G/I_D \sim 1$) in all the **NPC** samples. The ratio of the intensities of D to G bands signify the degree of crystallization of the graphitic carbon and suggest in all NPC samples that the local crabon structure contains both graphitic and disordered carbon atoms.
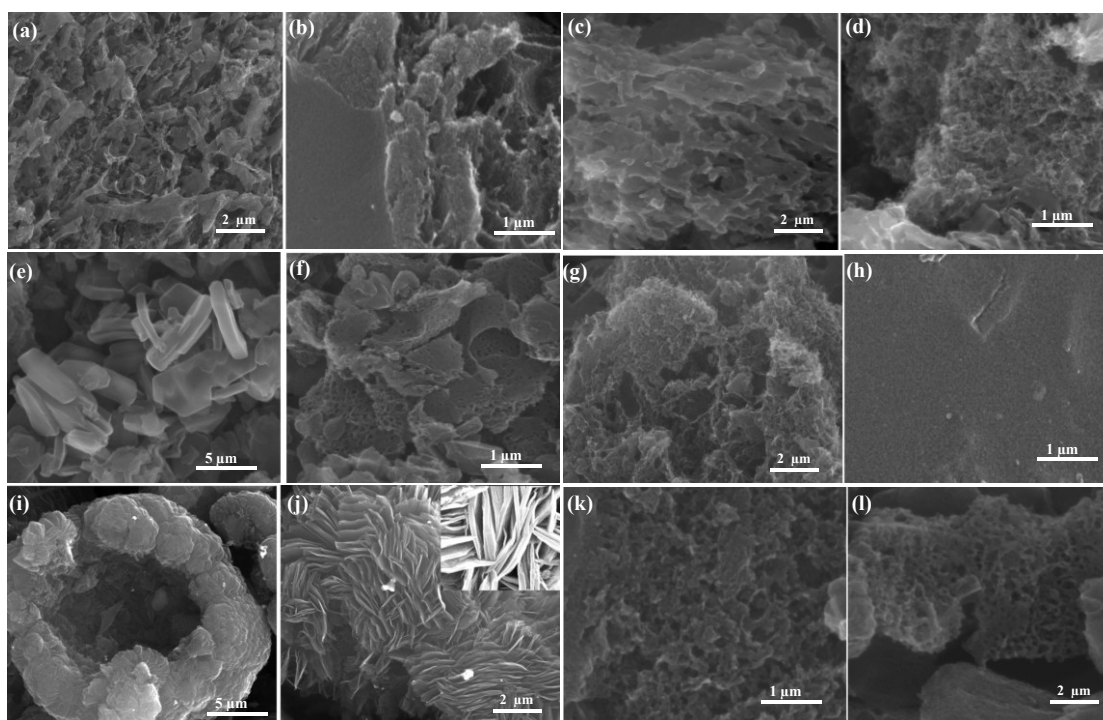
Figure 5 FESEM images of all **NPC** samples; (a-b) **NPC-0**, (c-d) **NPC-150**, (e-f) **NPC-300**, (g-h) **NPC-500**, (i-j) **NPC-1000**, (k-l) Sucrose derived carbon.

Furthermore field-emission scanning electron microscopy (FESEM) analyses were performed to understand the morpholgy of the resulting porous carbons and also the effect of MOF on the resulting morphologies and overall surface terxtural characteristics (Figure 5). FESEM images suggested that the original cubic morphology of the IRMOF-3 was not retained in the **NPC** samples, rather a different morphologies were observed in the different **NPC** samples. In case of **NPC-300** well separated micron size rod or block shaped carbon particles was observed, whereas **NPC-1000** revealed the aggregated sheets of carbon of micron size. Other samples like **NPC-0**, **NPC-150** and **NPC-500** exhibit sponge like

morphologies. However high-magnification images uncovered a wide range of pore sizes from micrometer to nanometer compared to defect free surfaces in IRMOF-3.
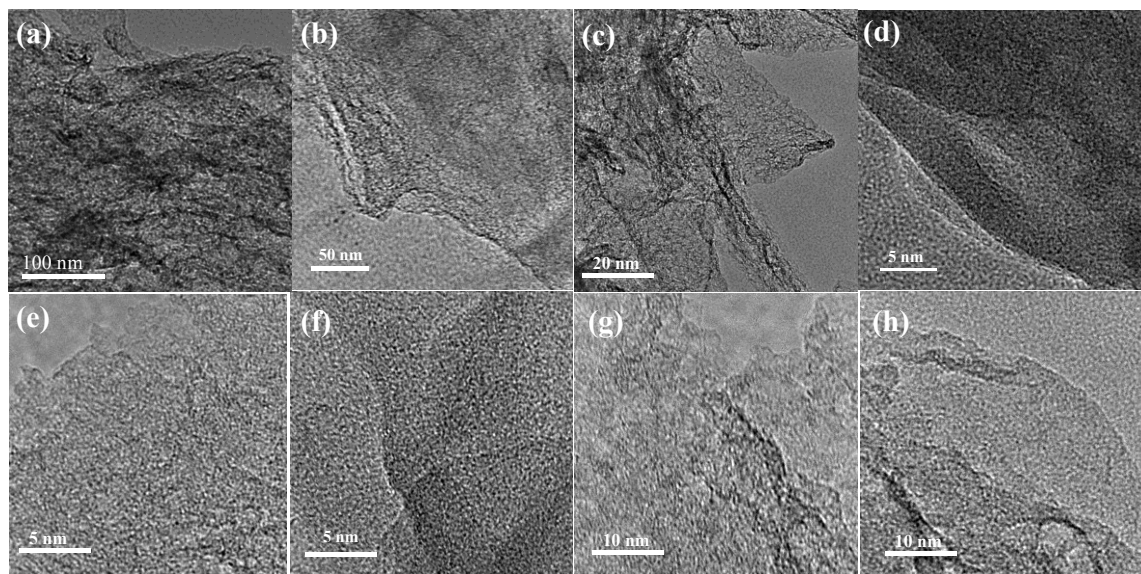
Figure 6 TEM images of all NPC samples; (a) **NPC-0**, (b) **NPC-150**, (c-d) **NPC-300**, (e) **NPC-500**, (f-g) **NPC-1000**, (h) Sucrose derived carbon.

High resolution transmission electron microscope (HRTEM) reveal oriented multilayer domains in all the carbon samples and few indistinguishable parallelly stacked graphene sheets were also observed (Figure 6). Similar structure was observed in previously reported MOF derived carbon materials. In agreemenet with PXRD analysis and Raman spectra mentioned earlier all the samples contain high dgree of disordered graphene layer. The bicontinuous three-dimensional network of nanosized carbon particles with small grain sizes (about 5-10 nm) resulted the hierarchical porosity. The surface texture and charatertistics could be tuned to some extent by changing the content of the carbonizing agents.

8.1.4.2 Textural Parameters of Resultant NPC samples

Nitrogen adsorption experiments (at 77 K) were performed to examine the surface textural characteristics of the **NPC** samples [Figure 7(i) for **NPC-150**, **NPC-300**, **NPC-500**, **NPC-1000** and Figure7(ii)] for **NPC-0** and Sucrose derived carbon). All IRMOF derived samples exhibit combined characteristics of type I and type IV isotherms with a steep uptake at low pressure regions, suggesting the dominant microporous nature in the carbon sample. The hysteresis in desorption curve in $P/P_0 > 0.4$ for all the samples can be accounted for the existence of mesopores as well. The BET surface area for

NPC-150, **NPC-300**, **NPC-500** and **NPC-1000** were found to be 1022, 3119, 1760 and 1077 m^2/g respectively. The corresponding Langmuir surface areas are given in Table 2. The BET surface areas for the **NPC** samples derived exclusively from sucrose and IRMOF-3 were 258 m^2/g and 391 m^2/g, respectively. Among the various **NPC** samples, **NPC-300** shows the highest BET surface sample and Langmuir surface area ($\approx$ 4031 m^2/g) with a micro pore volume of 1.93 cm^3/g. All the samples show wide pore size distribution as obtained from Non-Localized Density Functional Theory (NLDFT) method. The micropore sizes are in the range of 1.2 – 1.8 nm whilst the mesopore sizes fall in the range of 3- 4 nm. Furthermore, the surface areas related to micropore were calculated from the t - plot that suggest that **NPC -300** has a very high micropore surface area (2984 m^2/g) and then decreases with increasing sucrose content, in case of **NPC-1000** the corresponding value is 994 m^2/g. On the other hand mesopore surface area increases with increasing sucrose content after **NPC-300**. The total pore volumes were determined through adsorption profiles up to P/P_0 = 0.99, whereas micro pore volumes were obtained from (NLDFT) method and details are compiled in Table 2. We have clearly shown that hierarchically (micro and meso) nanoporous carbons (**NPCs**) with tunable porosity can be prepared based on loading of different amount of external carbonizing agent. The BET surface area (S_{BET}) measured from N_2 adsorption slowly increases from **NPC-0** to **NPC-300** and then decreases gradually. In addition the mesopore to micropore surface area (S_{meso}/S_{micro}) and mesopore volume to micropore volume (V_{meso}/V_{micro}) can also be varied by the different amount of sucrose loading. This is the first systematic study where textural properties can be systematically tuned in a MOF derived carbon materials by using an external carbon precursor. The BET surface area of **NPC-300** is 2nd highest reported in MOF derived carbon materials using external carbon source and comparable to a carbon material where ZIF-8 is the only carbon precursor.[8j] Upon encapsulation and subsequent polymerization of sucrose resulting in a small pore and concomitant decompose of **IRMOF-3**, that acts as a template and self-sacrificing carbon precursor further contribute towards carbon materials. The high micropore surface area and pore volume in **NPC-300** can be attributed to the optimium condition where maximum loading of the sucrose is possible inside the pores of **IRMOF-3** which resulting in micro pore after carbonization.
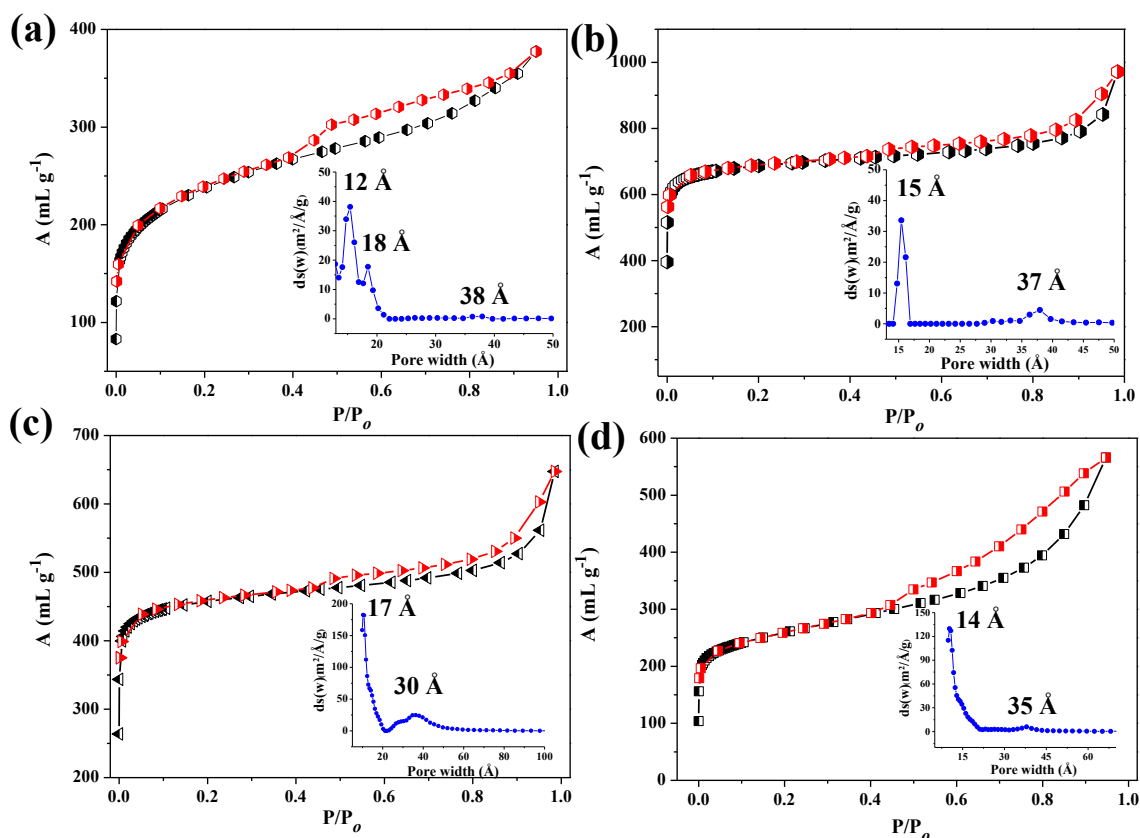
Figure 7(i) Nitrogen adsorption isotherms of (a) **NPC-150**, (b) **NPC-300**, (c) **NPC-500** and (d) **NPC-1000** (Pore size distribution respective samples obtained from NLDFT method).
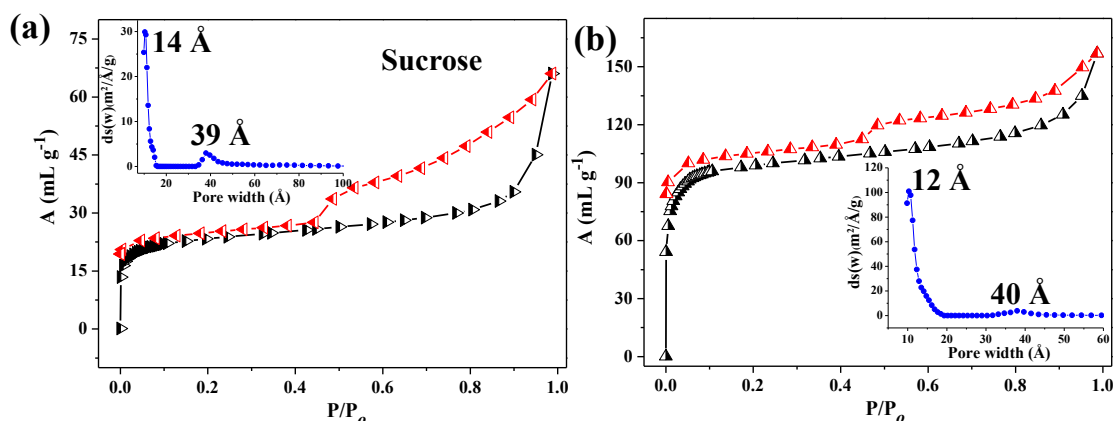
Figure 7(ii) Nitrogen adsorption isotherms of Sucrose, **NPC-0** samples (Pore size distribution respective samples obtained from NLDFT method).

It should be noted that the direct carbonization of sucrose and **IRMOF-3** (**NPC-0**) exhibits major contribution of meso pores with less surface area as clearly observed in Figure 7(ii). The decrease in microporosity and increase in mesoporosity in **NPC-500** to **-1000** probably due to the involvement of the surface adsorbed sucrose.

Table 2 Textural Parameters of the resultant **NPC** samples.

Sample	S_{BET} $[m^2/g]^a$	S_{Lang} $[m^2/g]^b$	S_{micro} $(m^2/g)^c$	S_{meso} $(m^2/g)^d$	S_{Meso}/S_{micro}	V_t $(cm^3/g)^e$	V_{micro} $(cm^3/g)^f$	V_{meso} $(cm^3/g)^g$	$V_{meso/micro}$ (cm^3)
Sucrose	258	391	117	141	1.2	0.17	0.08	0.09	1.125
NPC-0	392	581	299	93	0.31	0.409	0.36	0.049	0.136
NPC-150	1022	1567	898	124	0.13	0.65	0.58	0.07	0.121
NPC-300	3120	4031	2987	133	0.03	1.93	1.89	0.04	0.024
NPC-500	1761	2687	1692	69	0.04	0.74	0.58	0.16	0.103
NPC-1000	1077	1622	994	83	0.08	0.435	0.245	0.19	0.175

[a] S_{BET} is the BET specific surface area; [b] S_{Lang} is the Langmuir specific surface area ; [c] Smicro is the t-plot specific micropore surface area calculated from the N_2 adsorption–desorption isotherm; [d]S_{meso} is the specific mesopore surface area estimated by subtracting S_{micro} from SBET. [e] Vt is the total specific pore volume determined by using the adsorption branch of the N_2 isotherm at P/P_0=0.99; [e] Vmicro is the specific micropore volume calculated by NLDFT; [f] Vmeso is the specific micropore volume calculated by subtracting Vmicro from Vt.

8.1.4.3 H_2 and CO_2 uptake properties

Encouraged by the high surface area and micropore volume, we measured H_2 and CO_2 storage capacity for **NPC-300** at different conditions. As shown in Figure 8a, H_2 uptake capacity is found to be 2.45 wt% at 1 atm, at 77 K, much higher than the IRMOF-3 (1.3 wt% at 77 K, 1 atm). Sorption profile suggests complete reversibility without any hysteresis, indicating H_2 molecule are physisorbed. The storage capacity in this condition is comparable to the highest value reported so far for MOF derived carbon materials (see Table 3) and MOFs of similar surface area.[8] This value is much higher than the activated carbons and zeolites. The H_2 uptake capacity significantly increases at high pressure and it shows about 5.1 wt% at 40 bar, 77 K (Figure 8a). This value is comparable to the best performances MOFs, including IRMOF-77, 176, HKUST, PCN-7.[8f] **NPC-300** has high degree of microporosity which is probably beneficial for hydrogen uptake. To the best of our knowledge this is the highest storage capacity of hydrogen in **NPC** derived from a MOF template.
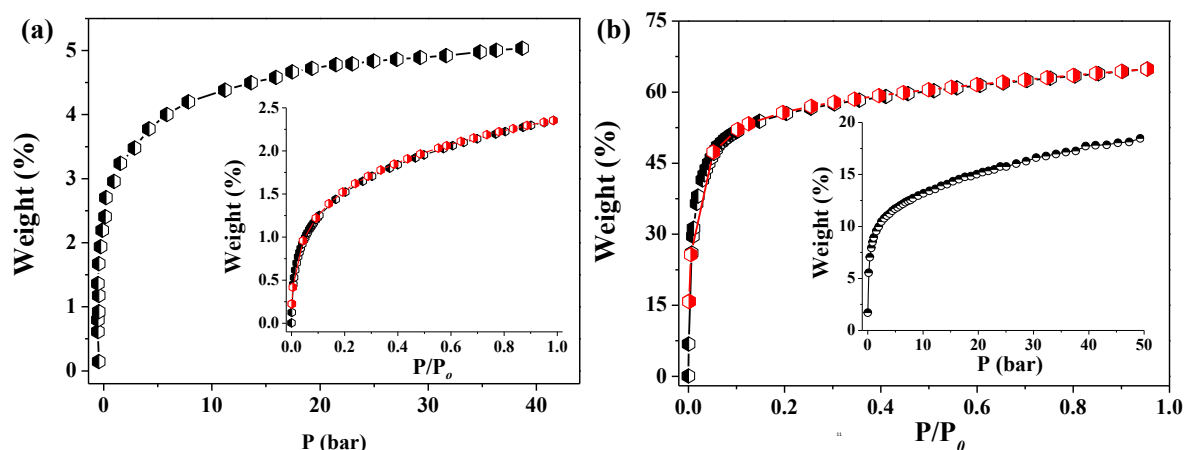
Figure 8 (a) High pressure hydrogen adsorption isotherm for **NPC-300**, upto 40 bar at 77 K, (Inset showing 1 at 77K) (b) CO_2 adsorption isotherm for **NPC-300** 1 atm at 195 K 1atm (Inset CO2 uptake 50 bar at 298 K).

This is attributed to the saturation at large number of adsorption sites at high pressure compared to the lower pressure. Further this material has been tested for CO_2 capture at various conditions and showed exceptionally high capacity of CO_2 uptake. At 195 K and 1 atm, the carbon sample exhibited 64 wt % uptake capacities. Then we have tested at 298 K under high pressure and the uptake amount is 15 wt % (86 ml/g) at 17 bar (Figure 8b).
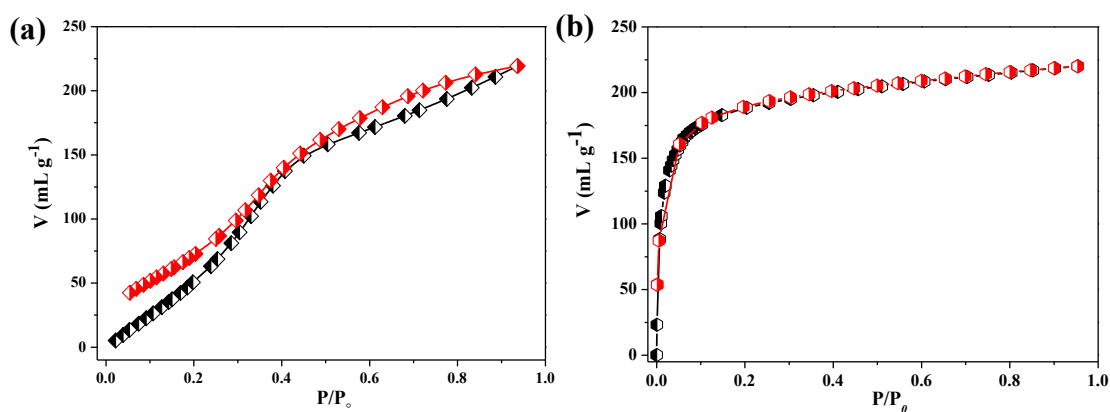
Figure 9 Vapour sorption isotherm for **NPC-300** (a) H_2O (b) C_6H_6 at 298 K (P_0 is the saturated vapour pressure of the adsorbates at the respective temperatures)

The steep uptake at low pressure regions can be attributed to the strong interactions of CO_2 and micropore surface composed with the graphitic carbons as the former having large quadrupole moment which can effectively interact with π cloud of the carbon sample. To understand the polarity of the pore surface in **NPC-300** water and benzene vapour sorption were carried out at 298 K. Benzene adsorption profile

reveals a typical type I profile with steep uptake at low pressure regions whereas water vapour shows unusual type V isotherm with gradual uptake at low pressure regions. The onset steep uptake pressure is about $P/P_0 \sim 0.3$ and final uptake amount is about 220 ml/g at $P/P_0 \sim 1$ with small hysteresis at high pressure region (Figure 9a). The final uptake amount for benzene is 196 m^2g^{-1}. This variation in the adsorption behaviour for benzene and water suggests the graphitic structure of **NPC-300** interact well with nonpolar molecule like benzene. This suggests strong hydrophobic character of the pore surfaces which is also supported by the water adsorption profile. The oxygen containing edges like –hydroxyl, carboxyl groups as observed in the IR spectrum resulting in uptake in water molecules at high pressure regions.

Table 3 Textural parameter, hydrogen and carbon dioxide storage capacities for MOF derived carbon along **NPC-300**.[8]

Sample	S_{BET} (m^2/g)	H_2 uptake (wt %) (1 atm, 77 K)	H_2 uptake (wt %) (30 bar,77 K)	CO_2 uptake (wt %) (1 atm195 K)	Remarks	Source
NC	2872	2.6	-		Gas phase inclusion (furfuryl alcohol)	MOF-5
NC-1000	2524				Gas phase inclusion (furfuryl alcohol)	MOF-5
MAC-A	2222				CCl_4+ Ethylene diamine+KOH	MOF-5
ALPCP-FA2	513				Furfuryl alcohol	Al-PCP
C-1000	3405	2.77	-	-	Furfuryl alcohol	ZIF-8
PCP-800	5500				Direct carbonization/HF	Al-PCP
WMC	2587				Doping with bismuth oxide	MOF-5
HPC	2368				MOCP/Furfuryl alcohol	MOCP
MDC-8	1978	2.41			Direct carbonization	IRMOF-8
C-70	1510	2.37		5.45 (mmol/g)	Furfuryl alcohol	ZIF-70
Z-1000	1110				Direct carbonization	ZIF-8
NPC-0	392				Direct carbonization	IRMOF-3
NPC-300	3120	2.54	5.1	64 wt%	Sucrose (solution phase inclusion)	IRMOF-3

8.1.4.4 Supercapacitor Application

Recently, multi-functional porous carbon materials with hierarchical porous structures have attracted considerable attention in electrochemical energy storage and conversion devices. Supercapacitors are energy storage devices which display very fast charge-discharge rates over several thousands of cycles. Their utility is being realised in various applications including electric vehicles. Electrochemical performance of **NPC-300** based electrode was tested using cyclic voltammetry (CV) and galvanostatic (i.e. at constant current) discharge/charge cycles. Cyclic voltammograms (CVs) of porous carbon supercapacitors obtained in the potential range (-0.5 to 0.5) V at different sweep rates (10-100 mV/s) as shown in Figure 10a.
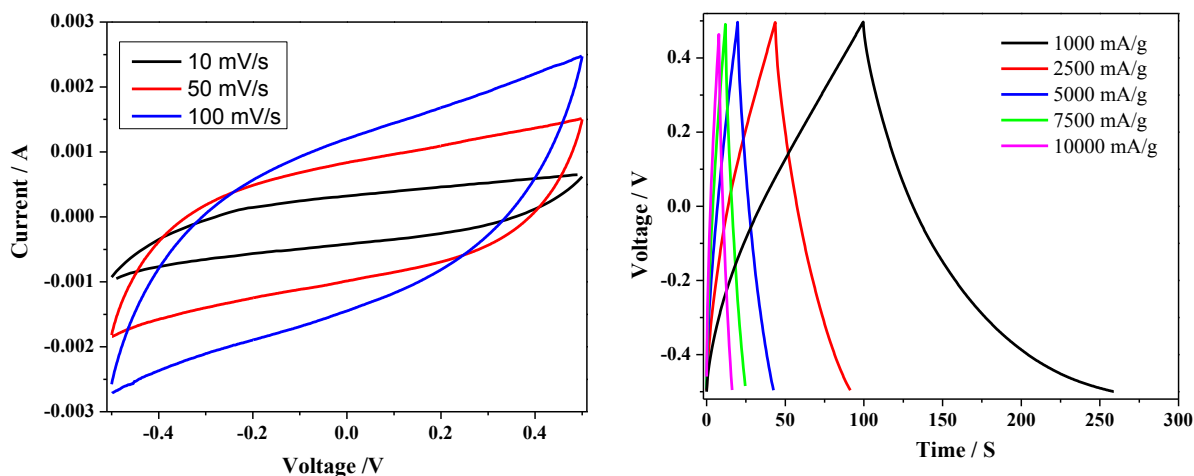
Figure 10 Electrochemistry characteristics of resultant nanoporous carbon **NPC-300**. (a) CV profiles investigated at different scan rates from 5 to 100 mV s^{-1} between -0.5 and 0.5 V in 1.0 M H2SO4 electrolyte using a three electrode capacitor; (b) Galvanostatic charge-discharge curve at different current densities.

The measured CV curves have quasi-rectangular shape ($\approx$ 10 mV/s) without any redox peaks indicating that the **NPC-300** material showing a typical electric double-layer capacitive behaviour. However, the deformation in the CV curves at high scan rate ($\approx$ 100 mV/s) may be attributed to the limited diffusion and migration of electrolyte ions in to the bulk of materials. This is a common disadvantage with carbon materials. The detrimental features can be overcome and better values obtained with additional optimizations in the form of various electrode composition and cell configuration. These are engineering issues and will be taken in the near future. The increase in current with scan rates suggests a good rate capability

for the **NPC-300**. Figure 10b shows the galvanostatic charge/discharge measurements for **NPC-300** electrode material supercapacitor at very high current densities of 1-10 A/g. The specific capacitances calculated from the discharge curves are 159, 118, 111,90 and 78 F/g at 1, 2.5, 5, 7.5 and 10 A/g, respectively. From the high capacity values it is concluded that the **NPC-300** has considerable potential as an electrode in supercapacitors. The decrease in specific capacitance of **NPC-300** electrode is with increasing current densities is due to the increase of iR (voltage) drop and slow ion transfer at high current density. The graphitic environment, hierarchical porosity, high surface area made **NPC-300** as a good supercapacitor materials which is comparable other porous carbons derived from various MOFs.

8.1.5 Conclusions

In summary, for the first time we have demonstrated here a simple and straightforward strategy for the synthesis of MOF derived porous carbon materials with tunable porosity by varying the content of external carbonizing agent sucrose. We have used amine functionalzed **IRMOF-3** for efficient sucrose loading that acts as a template and also a self-sacrificng carbon precursor. **NPC-300** shows remarkable surface area with high micropore volume and good hydrogen and carbon dioxide storage properties. We have also demonstrated **NPC-300** as electrode material for electrochemical double layer capacitor (EDLC). Our results would open up an avenue to syntheze versatile nanoporous carbon materails with tunable textural parameters derived from different porouis MOFs with potential applications in gas storage and electrochemical supercapacitor.

8.1.6 References

1) a) Y. S. Bae , R. Q. Snurr, *Angew. Chem. Int. Ed.* **2011**, *50,* 11586; b) A. Bhatnagar, W. Hogl, M. Marques, M. Sillanpaeae, *Chem. Eng. J.* **2013**, *219,* 499; c) J. Biener, M. Stadermann, M. Suss, M. A. Worsley, M. M. Biener, K. A. Rose , T. F. Baumann, *Energy Environ. Sci.* **2011**, *4*, 656; d) J. L. Figueiredo, *J. Mater. Chem. A* **2013**, *1*, 9351; e) H. Jiang, P. S. Lee , C. Li, *Energy Environ. Sci.* **2013**, *6*, 41.

2) a) A. I. Cooper, *Adv. Mater.* **2003**, *15*, 1049; b) C. Liang, Z. Li, S. Dai, *Angew. Chem. Int. Ed.* **2008**, *47*, 3696; c) A. Stein, Z. Wang, M. A. Fierke,

Adv. Mater. **2009**, *21*, 265.

3) a) B. Sakintuna , Y. Yueruem, *Ind. Eng. Chem. Res.* **2005**, *44*, 2893; b) A. Walcarius, *Trends Anal. Chem.* **2012**, *38*, 79.

4)   Y. Xia, Z. Yang , R. Mokaya, *Nanoscale* **2010**, *2*, 639.

5) a) G. Ferey, C. Serre, T. Devic, G. Maurin, H. Jobic, P. L. Llewellyn, W. G. De, A. Vimont, M. Daturi , J.-S. Chang, *Chem. Soc. Rev.* **2011**, *40*, 550; b) B. McEnaney, E. Alain, Y. F. Yin , T. J. Mays, *NATO Sci. Ser., Ser. E* **2001**, *374*, 295; c)   Z. Xiang, D. Cao, J. Lan, W. Wang , D. P. Broom, *Energy Environ. Sci.* **2010**, *3*, 1469.

6) J. Sculley, D. Yuan , H. C. Zhou, *Energy Environ. Sci.* **2011**, *4*, 2721.

7) a) M. Eddaoudi, J. Kim, N. Rosi, D. Vodak, J. Wachter, M. O'Keeffe , O. M. Yaghi, *Science* **2002**, *295*, 469; b) R. J. Kuppler, D. J. Timmons, Q. R. Fang, J. R. Li, T. A. Makal, M. D. Young, D. Yuan, D. Zhao, W. Zhuang , H. C. Zhou*, Coord. Chem. Rev,* **2009**, *253*, 3042; c) L. J. Murray, M. Dinca , J. R. Long, *Chem. Soc. Rev.* **2009**, *38*, 1294; d) J. Sculley, D. Yuan , H.-C. Zhou, *Energy Environ. Sci.* **2011**, *4*, 2721; e) J. R. Li, R. J. Kuppler , H.-C. Zhou, *Chem. Soc. Rev.* **2009**, *38*, 1477; f) H. B. Tanh Jeazet, C. Staudt , C. Janiak, *Dalton Trans*. **2012**, *41*, 14003; g) W. Lin, *MRS Bull.* **2007**, *32*, 544; h) L. Ma , W. Lin, *Top. Curr. Chem.* **2010**, *293*, 175; i) K. Jayaramulu, K. K. Datta, M. V. Suresh, G. Kumari, R. Datta, C. Narayana, M. Eswaramoorthy , T. K. Maji, *ChemPlusChem* **2012**, *77,* 743 j) P. Horcajada, T. Chalati, C. Serre, B. Gillet, C. Sebrie, T. Baati, J. F. Eubank, D. Heurtaux, P. Clayette, C. Kreuz, J.-S. Chang, Y. K. Hwang, V. Marsaud, P.-N. Bories, L. Cynober, S. Gil, G. Ferey, P. Couvreur , R. Gref, *Nat. Mater.* **2010**, *9*, 172;   k) Y. Cui, Y. Yue, G. Qian , B. Chen, *Chem. Rev.* **2011**, *112*, 1126;   l) K. Jayaramulu, R. P. Narayanan, S. J. George , T. K. Maji, *Inorg. Chem.* **2012**, *51*, 10089.

8) a) B. Liu, H. Shioyama, T. Akita , Q. Xu, *J. Am. Chem. Soc.* **2008**, *130*, 5390; b) B. Liu, H. Shioyama, H. Jiang, X. Zhang , Q. Xu, *Carbon* **2010**, *48*, 456; c) L. Radhakrishnan, J. Reboul, S. Furukawa, P. Srinivasu, S. Kitagawa , Y. Yamauchi, *Chem. Mater.* **2011**, *23*, 1225; d) M. Hu, J. Reboul, S. Furukawa, N. L. Torad, Q. Ji, P. Srinivasu, K. Ariga, S. Kitagawa , Y. Yamauchi, *J. Am. Chem. Soc.* **2012**, *134*, 2864; e) S. Lim, K. Suh, Y. Kim, M. Yoon, H. Park, D. N. Dybtsev , K. Kim, *Chem. Commun.* **2012**, *48*, 7447; f) S. J. Yang, T. Kim, J.

H. Im, Y. S. Kim, K. Lee, H. Jung , C. R. Park, *Chem. Mater.,* 2012, 24, 464; g) W. Chaikittisilp, M. Hu, H. Wang, H.-S. Huang, T. Fujita, K. C. W. Wu, L.-C. Chen, Y. Yamauchi , K. Ariga, *Chem. Commun.* **2012**, *48*, 7259;   h) P. Pachfule, B. P. Biswal , R. Banerjee, *Chem A. Eur. J.* **2012**, *18*, 11399; i) W. Chaikittisilp, K. Ariga , Y. Yamauchi, *J. Mater. Chem. A.* **2013**, *1*, 14; j) S. Ma, G. A. Goenaga, A. V. Call, D.-J. Liu, *Chem. Eur. J.* **2011**, *17*, 2063.

9) a) S.A. Johnson, P.J. Ollivier, T.E. Mallouk, T. E. *Science* 1999, 283, 963; b)A. Vinu, *Adv. Fun. Mater.* **2008**, *18*, 816; c) A. Stein, Z. Wang, M.A. Fierke, M. A. *Adv. Mater.* **2009**, *21*, 265.

10) M. Eddaoudi, J. Kim, N. Rosi, D. Vodak, J. Wachter, M. O'Keeffe , O. M. Yaghi, *Science* **2002**, *295*, 469.

11) a) H. Jiang, P. S. Lee, C. Li, C. *Energy Environ. Sci.* **2013**, *6*, 41; b) D. Pech, M. Brunet, H. Durou, P. Huang, V. Mochalin, Y. Gogotsi, P.L. Taberna, P. Simon, *Nat Nano* **2010**, *5*, 651; c) Z. Fan, Y. Liu, J. Yan, G. Ning, Q. Wang, T.Wei, L. Zhi, F. Wei, F. *Adv. Energy Mater.* **2012**, *2*, 419; d) J. Zhang, C.M. Li, *Chem. Soc. Rev.* **2012**, *41*, 7016; e) X. Zhao, H. Tian, M. Zhu, K. Tian, J.J. Wang, F. Kang, R.A. Outlaw, *J. Power Sources* **2009**, *194*, 1208.

Chapter 8.2

A Nanoporous Borocarbonitride (BC₄N) with Novel Properties Derived from a Boron-Imidazolate-Based Metal–Organic Framework
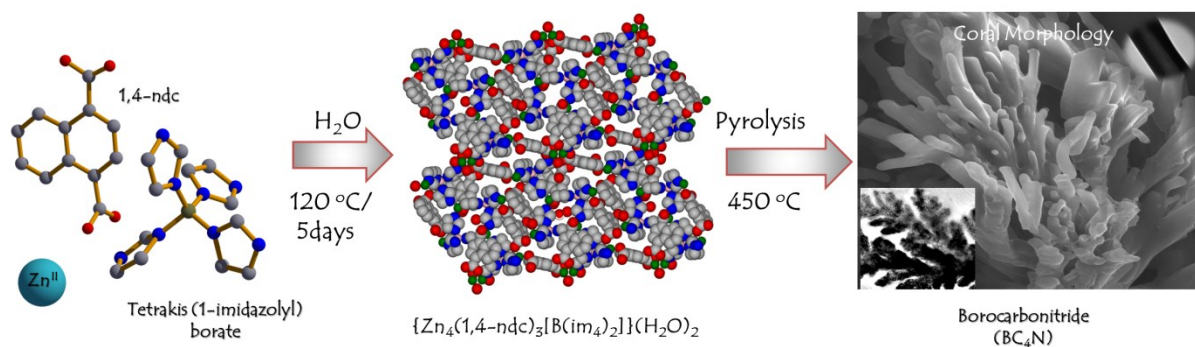
Summary

This chapter deals with a three dimensional boron based metal-organic framework {[Zn$_4$(1,4-ndc)$_3$(bim)$_2$]·2H$_2$O} (**1**) composed of tetrakis (1-imidazolyl)borate (bim), 1,4-naphthalene dicarboxylate and we made use of it as precursor to produce borocarbonitride through pyrolysis at 450 °C. The borocarbonitride has the formula BC$_4$N as estimated by XPS, EELS and elemental analysis. Besides having an unusual coral like morphology, has high surface area 988 m^2/g and exhibits significant carbon dioxide and hydrogen uptake. Nano particles Au and Pd could be stabilized on the surface of the materials without any reducing agent.

8.2.1 Introduction

Carbon materials have emerged as a novel class of porous materials for applications in various fields such as purification and storage of gases, catalysis and double layer capacitors.[1] Doping with boron, sulphur, nitrogen and such heteroatoms in carbon materials bestows novel properties with possible applications.[2] Thus, graphitic borocarbonitrides with high electronegativity differences amongst the component elements (nitrogen ~ 3.5, boron ~ 2.05 and carbon~ 3.0), may have applications as electrical conductors, and gas sensors as well as in optical and electronic devices.[3,4] In addition, good chemical and thermal stability of such materials have implications to areas such as catalysis and gas storage or separation. In spite of the interesting semiconducting and electronic properties bestowed with borocarbonitrides (BCN) materials, synthetic protocols to obtain $B_xC_yN_z$ materials are relatively scarce in the literature.[4] These materials are typically prepared via chemical vapour deposition (CVD), arc discharge, pyrolysis and hard template processes.[3-5] Vinu and coworkers reported the preparation of a mesoporous borocarbonitride through substitution reactions at 1550 °C, using a well-ordered hexagonal mesoporous carbon as the template and boron trioxide as the boron source.[6] Antonietti and co-workers carried out pyrolysis of graphitic carbon nitride with subsequent infiltration with a borane complex to obtain boron carbon nitrides.[2a] Unfortunately, the above protocols are complex and somewhat impractical because of the multistep synthetic procedures. We have recently reported a simple, new kind and inexpensive method for the synthesis of $B_xC_yN_z$ materials by the high temperature reaction of boric acid and urea with high surface area carbon.[7] A few workers have recently reported metal-organic frameworks (MOFs) as precursors for the synthesis of porous carbon and carbon nitride materials.[8] These materials have potential applications in various fields due to their unique porous structure.[9] This chapter demonstrates, for the first time, a simple and facile route for the preparation of a nanoporous borocarbonitride by the direct carbonization of a three-dimensional boron-based MOF,[10] $\{Zn_4(1,4\text{-ndc})_3(bim)_2\}\cdot 2H_2O\}$ (**1**) comprising Zn(II), bim (tetrakis(1-imidazolyl)borate) and 1,4-ndc (ndc = naphthalenedicarboxylate). The borocarbonitride has the composition BC_4N and exhibits a coral-like morphology with a surface area of 988 m^2/g. The material also shows a good storage capacity for hydrogen and carbon dioxide. Furthermore, it acts as a novel support for the stabilization of gold and palladium nanoparticles.

8.2.2 Experimental Section

8.2.2.1 Materials

All the reagents and solvents employed were commercially available and used as supplied without further purification. $Zn(OAc)_2 \cdot 2H_2O$, 1,4-naphthalenedicarboxylic acid, and sodium tetrakis(1-imidazolyl)borate, were obtained from Aldrich Chemical Co.

8.2.2.2 Synthesis of {Zn$_4$(1,4-ndc)$_3$(bim)$_2$]·2H$_2$O} (1)

The compound was synthesized hydrothermally. $Zn(OAC)_2 \cdot 2H_2O$ (0.043 g), 1,4-ndc (0.032 g), $Na[B(im)_4]$ (0.036 g) and imidazole (0.016 g) were mixed together in a telflon-lined container (23 ml) and stirred for 30 min. Then resulting reaction mixture was kept in an autoclave and heated at 120 ^oC for 5 days. After being cooled to room temperature, colorless crystals were separated and washed with water and ethanol which was subjected to X-ray diffraction. Yield: 68%. Anal. Calcd. for $C_{60}H_{46} B_2 N_{16} O_{14}Zn_4$: C, 48.03; H 3.06 ; N 14.99 Found; C, 49.08 ; H 3.21 ; N 14.96. FT-IR (KBr pellet, 4000 - 400 cm^{-1}): 3470 (b), 3124 (m), 1666 (s) 1598 (s), 1426 (s), 1321 (w).

8.2.2.2 Synthesis of Nanoporous Borocarbonitride (BC$_4$N)

The compound **1** of about 300 mg was kept a silica boat and then carbonized for 450 °C under N_2 atmosphere for 6 h with heating rate of 3 °C/min. After the temperature is reached the established settings, it was maintained for 6 h and then the resulting pyrolysed compound was cooled in the furnace with a cooling rate of 1°C /min. The borocarbonitride was obtained after removal of ZnO species using 20% HCl by filtration and subsequently washed several times with water-ethanol mixture and dried at 100 ^oC. The purity of the sample is confirmed through Energy dispersive X-ray spectroscopy (EDAX), FT-IR, EELS, XPS and elemental analysis and characterized through several studies like PXRD and microscopic techniques.

8.2.2.3 In situ synthesis and stabilization of Au and Pd nanoparticles with in NP-BC$_4$N matrices

$HAuCl_4$ and $PdCl_2$ were used as metallic salt precursors for the preparation of Au and Pd nanoparticles. Typically 20 mg of NP-BC$_4$N was dispersed in 2 ml of water by mild sonication for 2 minutes. To this 1.5 ml of 2 mM $HAuCl_4$ solution was added and

stirred for 2 h. The same procedure was adopted for the synthesis of Pd nanoparticles using $PdCl_2$. In both cases obtained reaction mixture was washed thoroughly with distilled water and finally dried in at 60 °C under dynamic vacuum.

8.2.3 Characterization Techniques

8.2.3.1 Physical Measurements

Elemental analysis was carried out using a Thermo Scientific Flash 2000 CHN analyzer. IR spectra were recorded using KBr pellets in the range 4000 - 400 cm^{-1} on Bruker IFS-66v spectrophotometer. Thermogravimetric analyses (TGA) were carried out under nitrogen (flow rate of 50 mL/min) with Metler Toledo TGA-850 TG analyzer in the temperature range between 25 – 650 °C at a heating rate 3 °C / min. Powder X-ray diffraction (PXRD) pattern were recorded on a Bruker D8 Discover instrument using Cu-Kα radiation. The resultant borocarbonitrides morphology and porous nature was examined with field emission scanning electron microscope (FESEM, FEI Nova-Nano SEM-600, and Netherlands) and transmission electron microscope (TEM) (JEOL JEM-3010 with an accelerating voltage at 300 KV). Raman spectrum of the sample was recorded in back scattering arrangement, using 532 nm laser excitation with 6mW laser power.

8.2.3.2 Adsorption Measurements

N_2 (77 K), CO_2 (195 K) and H_2 (77 K) adsorption study of the activated sample of borocarbonitride was carried out using QUANTACHROME AUTOSORB-1C analyser. In the sample chamber maintained at $T \pm 0.03$ K was placed the adsorbent sample (100-150 mg), which had been prepared at 493 K under a high vacuum (10^{-1} Pa) for 18 hours prior to measurement of the isotherms. The adsorbate was charged into the sample tube, and then the change of the pressure was monitored and the degree of adsorption was determined by the decrease of the pressure at the equilibrium state. All operations were computer-controlled and automatic. High-pressure H_2 (77 K) and CO_2 (273 K) sorption measurements were carried out on a fully computer controlled volumetric BELSORP-HP, BEL JAPAN high pressure instrument. All the gases used for higher pressure measurements are scientific/research grade with 99.999% purity. For the measurements, approximately 300 mg sample was taken in a stainless-steel sample holder and degassed at 493 K for a period of 18 hours under 0.1 Pa vacuum. The dead volume of the sample cell was measured with helium gas of 99.99 % purity. Non-ideal

244

correction for H_2 and CO_2 gases were made by applying virial coefficients at the respective measurement temperature.

8.2.3.3 Single-crystal X-ray Diffraction

A suitable single crystal for **1** was carefully selected under a polarizing microscope and fixed to a separate thin glass fiber by commercially available glue. X-ray single crystal structural data was collected by a Bruker Smart –CCD diffractometer equipped with a normal focus, 2.4 kW sealed tube X-ray source (Mo-K_α radiation, 0.71073 Å) operating at 50 kV and 30 mA. The programme SAINT[11] was used for integration of diffraction profiles and an empirical absorption correction based on symmetry equivalent reflections was applied using the SADABS program. [12] The structure was solved by direct methods using SIR92 programme [13] and refined by full matrix least square method using SHELXL 97. [14] The hydrogen atoms were fixed by HFIX and placed in an ideal positions. Potential solvent accessible area or void space was calculated using the PLATON 99 [15] multipurpose crystallographic software. Final refinement included atomic positions for all the atoms, anisotropic thermal parameters for all the non-hydrogen atoms. All calculations were carried out using WinGX system, Ver 1.70.01.[16] Selected bond distances and angles of **1** are given in Table 1.

8.2.3.4 Crystal Data of {Zn₄(1,4-ndc)₃(bim)₂}·2H₂O} (1)

Formula $C_{60}H_{46}B_2N_{16}O_{14}Zn_4$:, Mr = 1494.28, Triclinic, Space group P$\bar{1}$ (no. 2), a = 9.5665(3) Å, b = 16.4803(5) Å, c = 20.9969(7) Å, α = 88.554(2)°, β = 82.025(2)°, γ = 77.759(2)°, V = 3203.77(18) Å3, Z = 2, ρcalc =1.549 g cm-3, μ (Mo-Kα) = 1.557 mm-1, F(000) = 1512, T = 293 K, λ (Mo-Kα) = 0.71073 Å, θmax = 28.0°, GOF = 0.85. A total of 53689 reflections were collected, of which 14449 were unique (Rint = 0.149). R1= 0.0669 for 805 independent reflections with I>2σ(I), wR₂ = 0.2108 for all data.

8.2.4 Results and Discussion

8.2.4.1 Structural Description of {Zn_4(1,4-ndc)$_3$(bim)$_2$]·2H$_2$O} (1)

Colorless block shaped single crystals of the boron based MOF **1**, were obtained under hydrothermal conditions using Zn(II), 1,4-ndc and bim in water at 120 °C.[10] **1** crystallizes in a triclinic crystal system with the space group $P\bar{1}$, the asymmetric unit comprising of four Zn(II) centres, three 1,4-ndc and two bim linkers (Figure 1a). The 3D coordination framework of **1** is built up by the tetrahedral Zn(II) centers connected through 1,4-ndc and bim linkers. Each tetrahedral Zn1 and Zn3 are connected to two different bim (N8, N16 for Zn1 and N6, N9 for Zn3) and two 1,4-ndc (O1, O5 for Zn1 and O2, O3 for Zn3) linkers. Whereas the tetrahedral geometry of Zn2 is furnished by three nitrogen atoms (N2, N3, N12) and one oxygen atom (O10) from three bim and 1,4-ndc linkers respectively (Figure 1b). On the other hand, three different 1,4-ndc (O7, O8, O12) and one bim (N14) form the tetrahedron around Zn4 atom. In the framework, Zn-N and Zn-O bond distances are in the range of 1.940(7) – 2.005(7) Å and 1.910(6) – 1.999(6) Å, respectively. The tetrahedral distortion from the ideal geometry is reflected in the angles around the Zn atoms (Table 1).
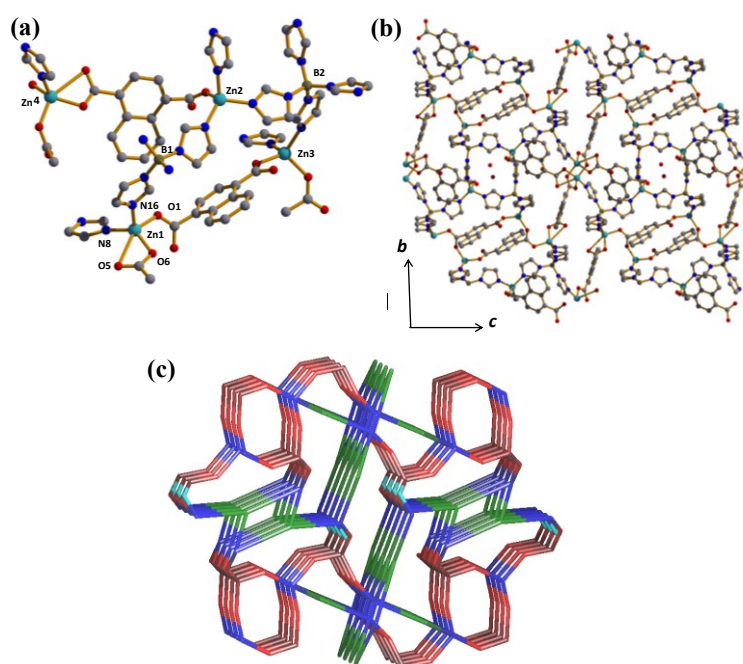
**Figure 1** Crystal structure of {Zn_4(1,4-ndc)$_3$(bim)$_2$]·2H$_2$O} (**1**): (a) View of the coordination environment; (b) View of three dimensional framework along the *a*-axis with 1D water filled channels; (c) Network topology of **1** analyzed with TOPOS.

Table 1 Selected bond distances (Å) and angles (°) {Zn$_4$(1,4-ndc)$_3$ (bim)$_4$]·2H$_2$O} **(1)**.

	Bond Distance		Bond Distance
Zn1 -O1	1.963(6)	Zn1-O5	1.940(7)
Zn1-N8	2.005(7)	Zn1-N16_d	1.961(7)
Zn2 -O10	1.924(9)	Zn2-N2	1.948(8)
Zn2 -N3	1.948(7)	Zn2-N12	1.977(8)
Zn3 -O2	1.963(6)	Zn3-N9	1.997(8)
Zn3-O3_i	1.910(6)	Zn3-N6_i	1.962(8)
Zn4-N14	1.969(9)	Zn4-O8_b	1.994(7)
Zn4-O7_f	1.972(7)	Zn4-O11_h	2.695(11)
Zn4-O12_h	1.968(8)		
	Bond Angle		Bond Angle
O1 -Zn1-O5	103.5(3)	O11_h-Zn4-O12_h	52.9(3)
O1 -Zn1 -N8	98.4(3)	N2-Zn2-N12	119.3(3)
O1-Zn1-N16_d	104.3(3)	O2-Zn3-N9	108.0(3)
O5-Zn1-N8	102.7(3)	O2-Zn3-O3_i	116.1(3)
O5-Zn1-N16_d	134.2(3)	O2-Zn3-N6_i	105.3(3)
N8-Zn1-N16_d	108.3(3)	O7_f-Zn4 -O11_h	85.5(3)
O10-Zn2-N2	103.4(4)	O7_f-Zn4-O12_h	119.9(3)
O10-Zn2-N3	106.5(3)	O8_b-Zn4-N14	100.1(3)
O10-Zn2-N12	109.4(3)	O11_h-Zn4-N14	96.5(3)
N2-Zn2-N3	104.5(3)	O7_f-Zn4-O8_b	113.9(3)
N3-Zn2-N12	112.7(3)	O8_b-Zn4-O12_h	97.4(3)
O3_i-Zn3 -N9	96.6(4)	O3_i-Zn3-N6_i	120.1(4)
N6_i-Zn3 -N9	109.9(3)	O7_f-Zn4-N14	103.7(3)
O8_b-Zn4-O11_h	150.3(3)	O12_h -Zn4-N14	120.3(4)
Symmetry code:b =x,-1+y,z; d =1+x,y,z; e =-x,-y,1-z; f =x,1-y,-z; h =1-x,-y,-z; i =1-x,1-y,1-z			

Here, one 1,4-ndc act as a bridging bidentate linker whereas other two 1,4-ndcs connect three Zn atoms through a mono-dentate carboxylate oxygen and *syn-anti/ syn-syn* carboxylate bridging. Both the mono anionic bim linkers in the asymmetric unit act as four connected nodes and both 1,4-ndc and bim link the Zn atoms giving rise to the three dimensional structure (Figure 1b).The topological analysis of the structure with TOPOS software that consider all the Zn centres to be a single node reveals Point 6-nodal 4,5,6-c net with stoichiometry (4-c)3(5-c)2(6-c). The Schläfli symbol for this net is $\{3^245^26^47\}$ $\{3^246^57^2\}\{3^25^26^67^48\}\{456^27^2\}\{45^26^27\}\{5^26^4\}$ which is unprecedented (Figure 1c). The 3D structure has 1D small channels formed by the Zn2 and four imidazole panels of bim along the crystallographic *a*-axis occupied by the water molecules (Figure 2).
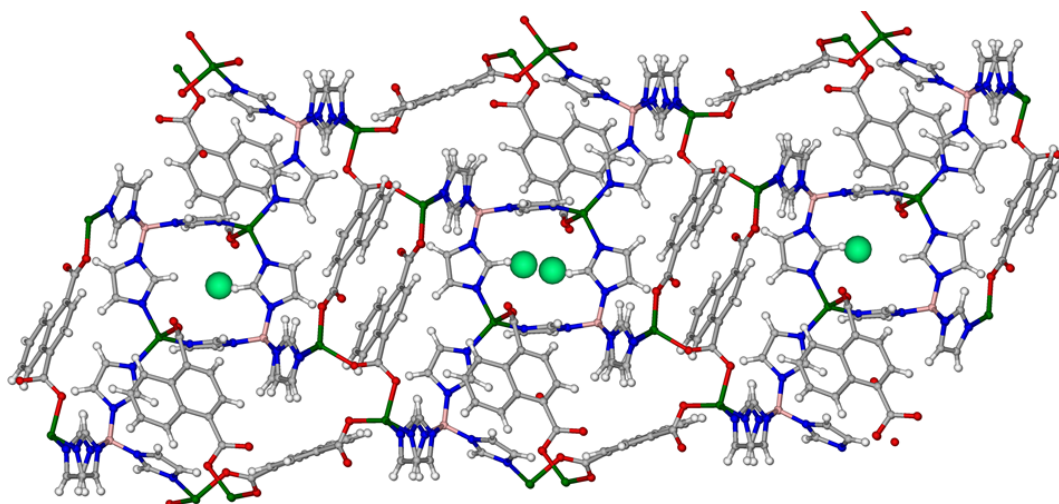
Figure 2 View of the 3D framework of **1** bridged by the bim linkers and 1,4-naphthalene dicarboxy- lates showing small channels occupied by the water molecules.

8.2.4.2 Framework Stability

Thermogravimetric analysis (TGA) of **1** showed a step-wise release of two guest water molecules in the temperature range of 50-125 ^{o}C and the resultant desolvated solid was stable up to ~ 550°C without any further weight loss (Figure 3). Above this temperature, the framework decomposes to an unidentified product.
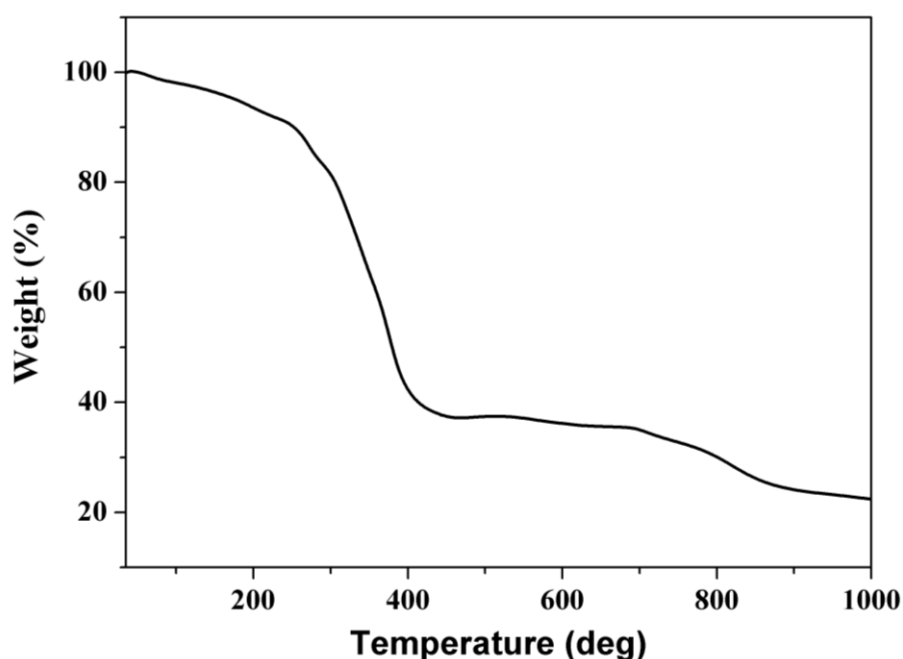
Figure 3 Thermo gravimetric analysis (TGA) of compound **1** in the temperature range of 28-1000 °C with a heating rate of 5 °C/min.

The powder XRD pattern of the desolvated **1** exhibits sharp lines without any shifts in the peak positions and intensities suggesting that the framework is highly rigid and robust (Figure 4)
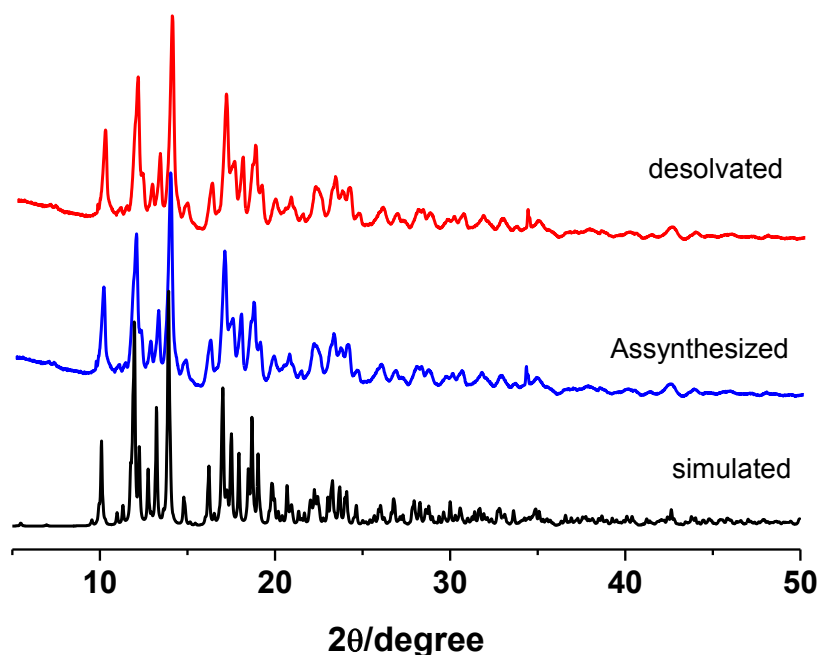
Figure 4 Powder X-ray diffraction patterns (a) simulated of **1,** (b) assynthesized **1,** (c) dehydrated of **1**.

8.2.4.3 Synthesis and Characterization of Boron MOF Derived Borocarbonitride

We have employed {Zn$_4$(1,4-ndc)$_3$(bim)$_2$]·2H$_2$O} (**1**) as the precursor to synthesize a borocarbonitride as depicted in Scheme 1. **1** was pyrolysed at 450°C and the powder X-ray diffraction pattern (PXRD) of the resulting sample shows the diffraction peaks due to hexagonal ZnO (*JCPDS Card No. 79–0208*) (Figure 5). The borocarbonitride was obtained by dissolving the ZnO nanoparticles in HCl solution, followed by washing with a water-ethanol mixture. The sample was characterized by elemental analysis and energy dispersive X-ray analysis (EDAX) (Figure 6). The powder X-ray diffraction (PXRD) pattern showed two broad reflections at 24.3° and 45.6° reflecting the graphitic nature of sample, with a low-angle reflection around 4.8° indicating structural ordering (Figure 7). The XRD pattern suggests the presence of 5 to 6 layers as in few layer graphene. The Raman spectrum shows bands at 1340 (D band) and 1593 cm^{-1} (G band), the latter being characteristics of sp^2 sheet structures. The high

intensity of the D-band suggests the presence of defects (Figure 8). The borocarbonitride remains thermally stable up to 600 °C as shown in TGA (Figure 9).
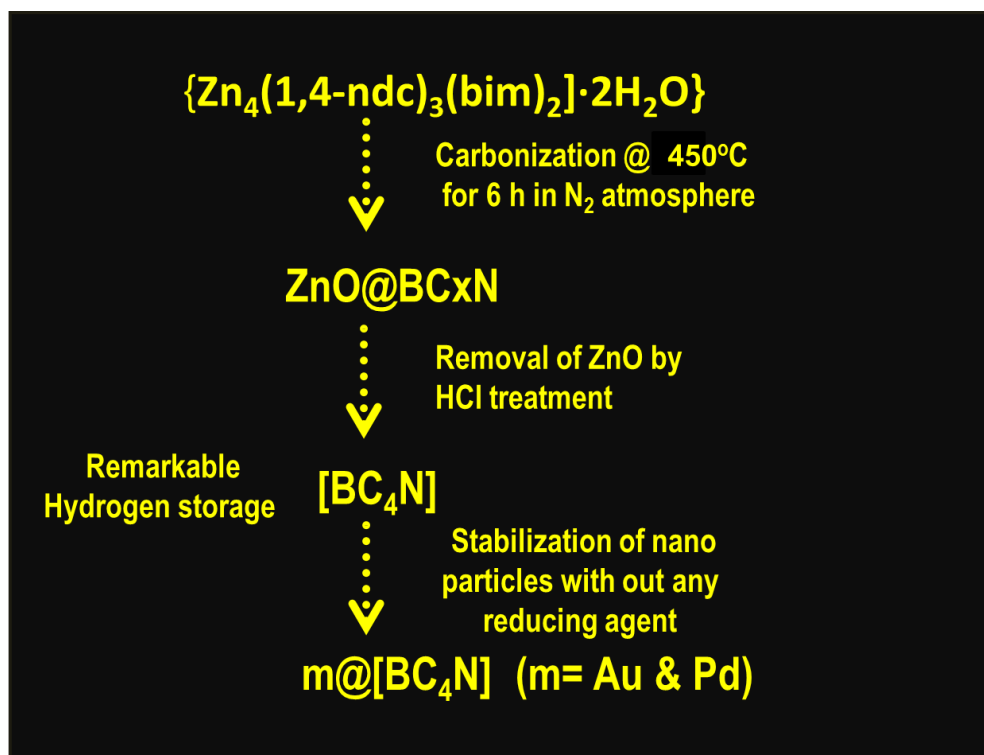
Scheme 1 Flow chart showing detailed synthetic methodology for nanoporous BC$_4$N and in situ stabilization of metal nanoparticles.
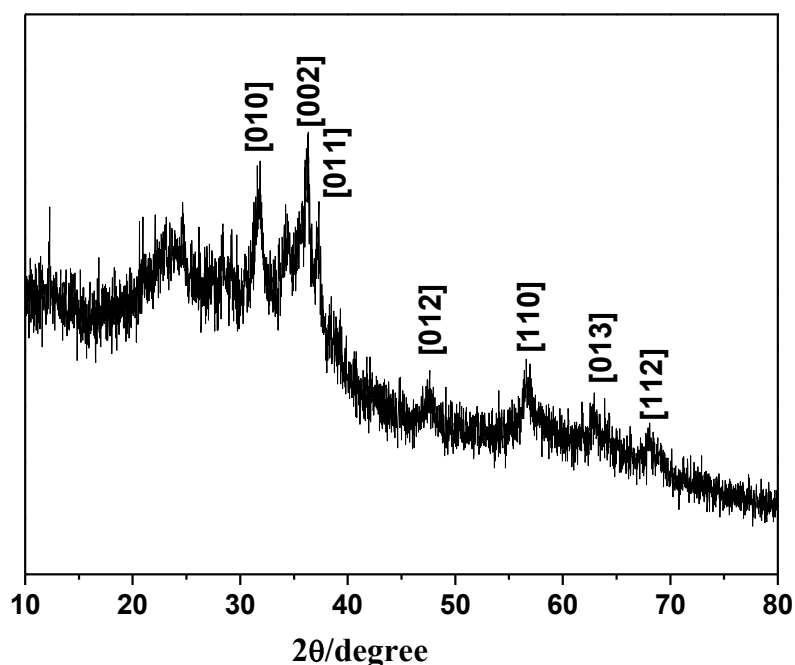
Figure 5 PXRD pattern of the resultant compound after pyrolysis of **1** at 450 °C and before HCl treatment. The sharp peaks have been assigned to ZnO.
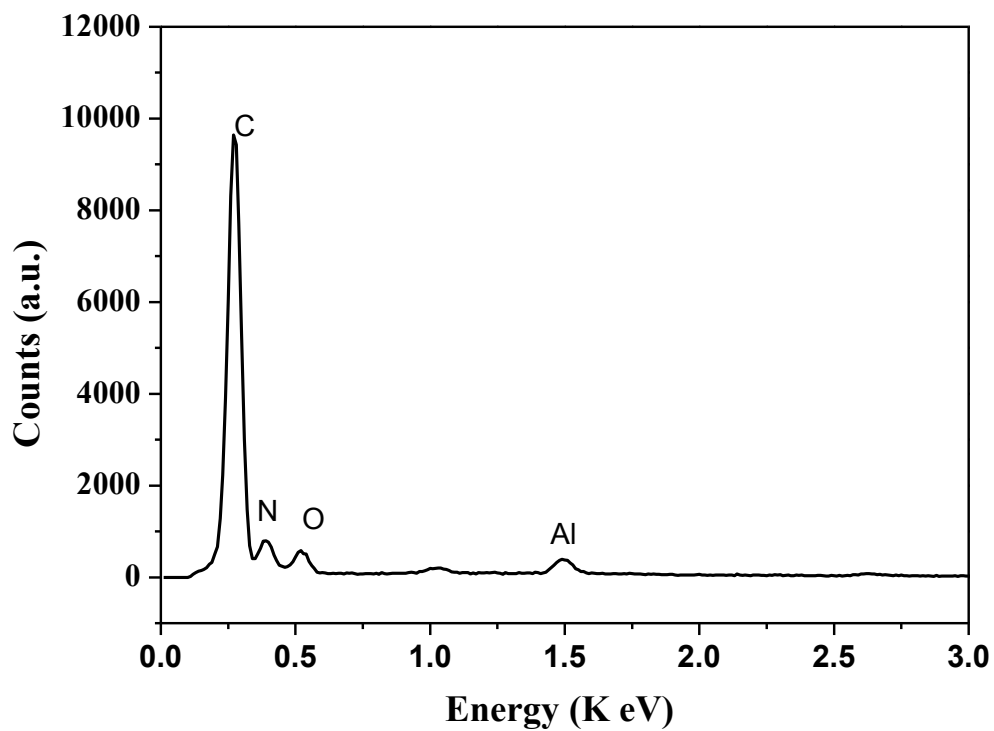
Figure 6 EDAX spectra of the resultant borocarbonitride sample after HCl treatment and washing with water-ethanol mixture.
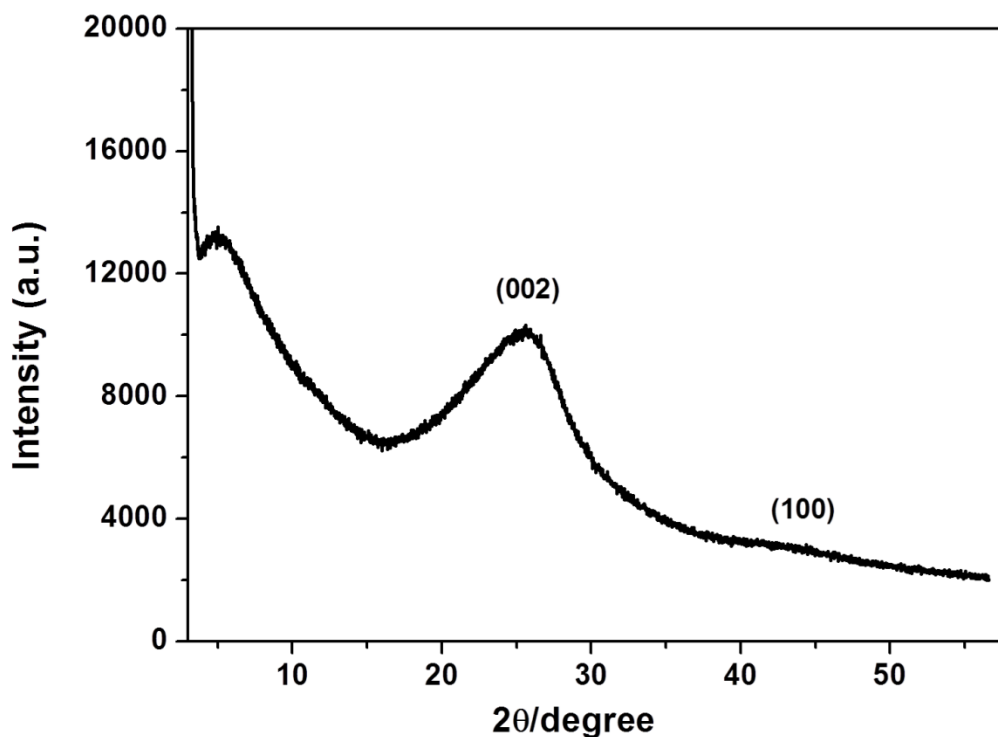
Figure 7 PXRD pattern of the resultant BC_4N sample
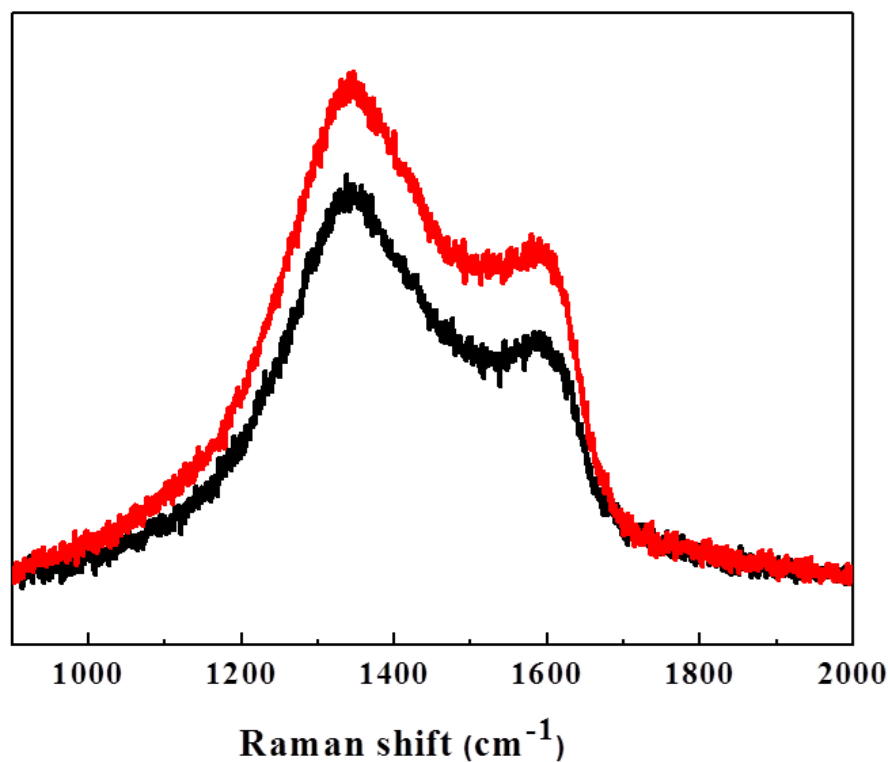
Figure 8 Raman spectrum of the resultant borocarbonitride derived from **1** ; Black curve before treating with HCl and red curve after treating with HCl and washing with water and ethanol.
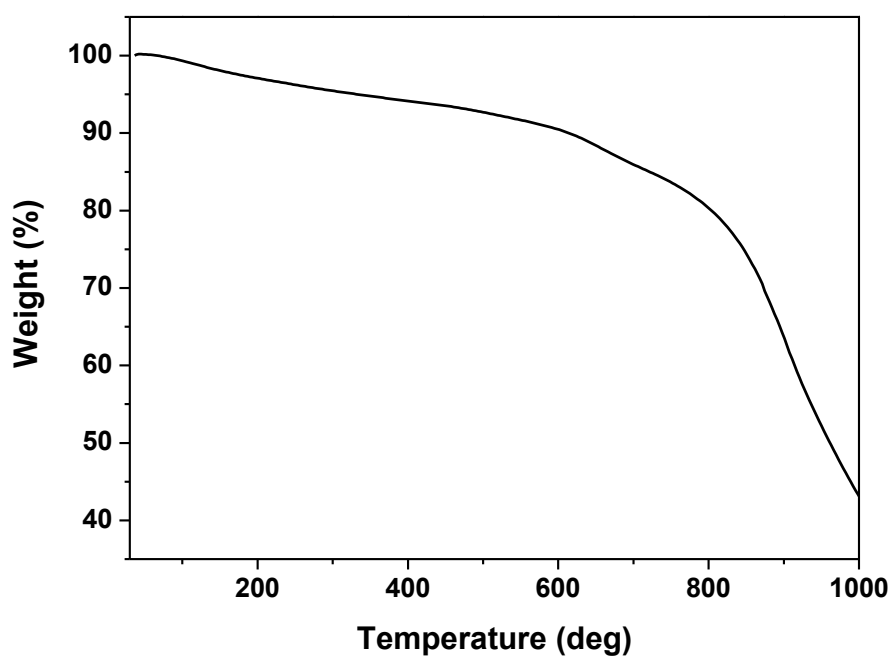
Figure 9 Thermogravimetric analysis of the resultant borocarbonitride.

8.2.4.4 Structure and Nature of Coordination Environment of Borocarbonitride

The FT-IR spectrum exhibits a broad band around 3360-3164 cm^{-1} due to the stretching modes of NH_2 group (Figure 10). The band is a doublet with the peaks at 3360 cm^{-1} and 3160 cm^{-1} is attributed to the asymmetric and symmetric stretching in primary amines. Peaks at 1328 and 774 cm^{-1} correspond to in-plane B-N and out of plane B-N-B vibrations respectively. While the peaks at 1612 cm^{-1} and 2194 cm^{-1} are due to -C=C- and -C=N- stretching respectively.
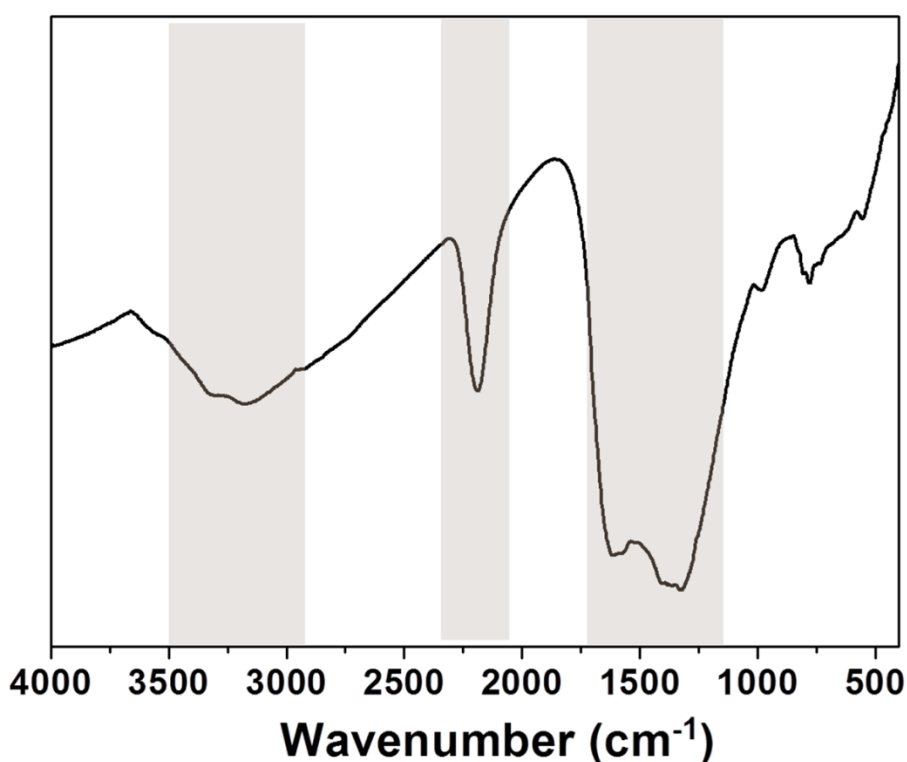
Figure 10 IR spectrum of the BC_4N sample.

Field-emission scanning electron microscope (FE-SEM) images of borocarbonitride reveal a coral-like architecture with numerous branches of reefs (Figures 11 and 12). Transmission electron microscope (TEM) images show the existence of the coral morphology with a hollow interior (Figure 11c). The high resolution TEM image (Figure 11d) suggests the porous nature with a size of 1 to 2 nm. The electron energy loss spectroscopy (EELS) clearly shows the presence of boron, carbon and nitrogen atoms with K features at 193, 285 and 405 eV respectively (Figure 13 left). The peaks appear as doublets showing the sp^2 nature of the atoms (Figure 13 left).
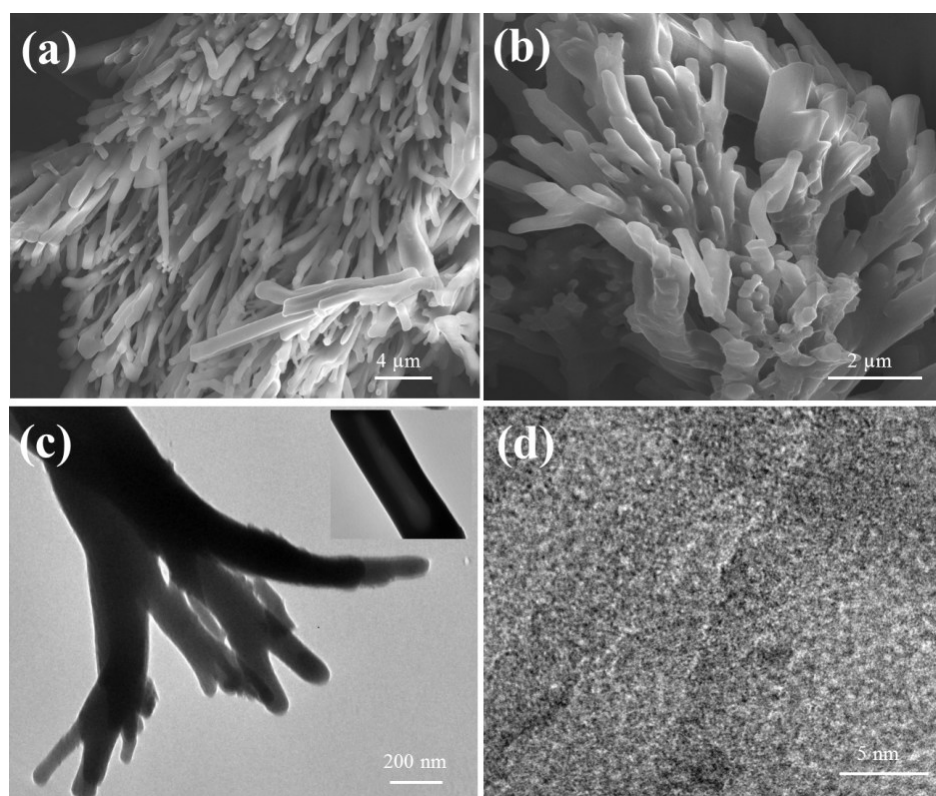
Figure 11 (a-b) FESEM image of nanoporous borocarbonitride showing coral architecture (c) TEM image showing a coral-head with nanoscale reefs. (d) HRTEM image showing the nano porous nature of the sample.
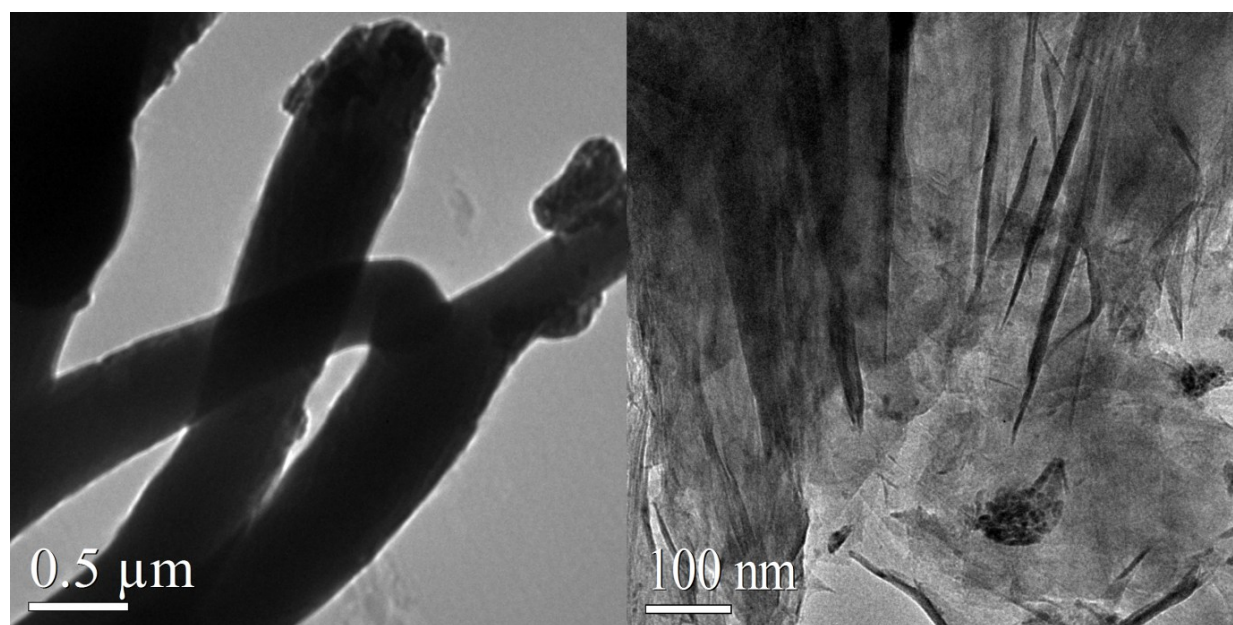
Figure 12 TEM image of nanoporous borocarbonitride showing coral reefs with wrapped paper sheet nature.
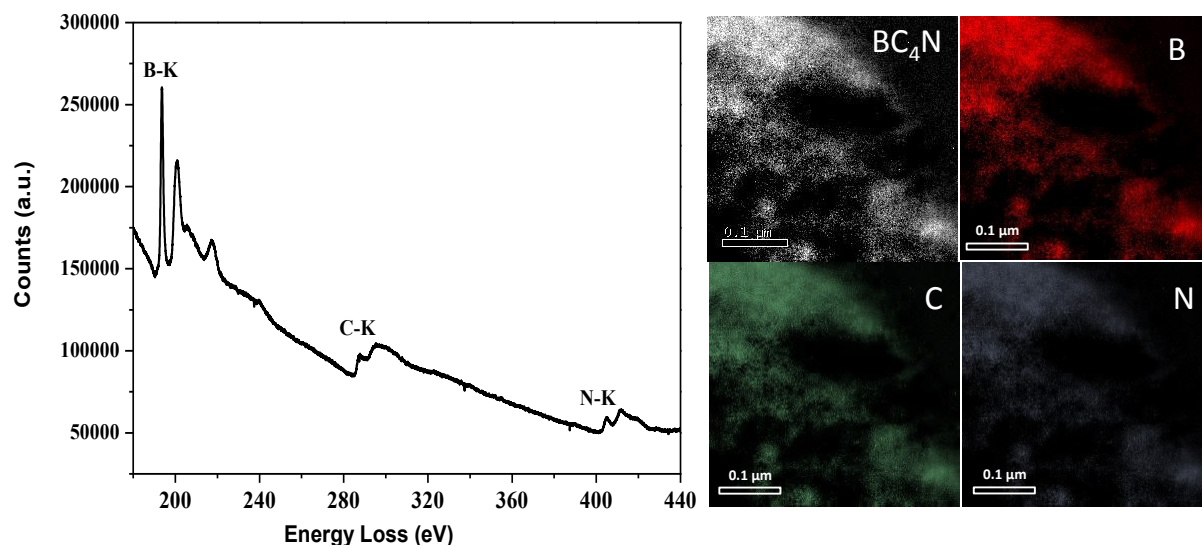
Figure 13 (a) Electron energy loss spectrum and (b) Elemental mapping of borocarbonitride suggesting presence of boron, carbon and nitrogen.
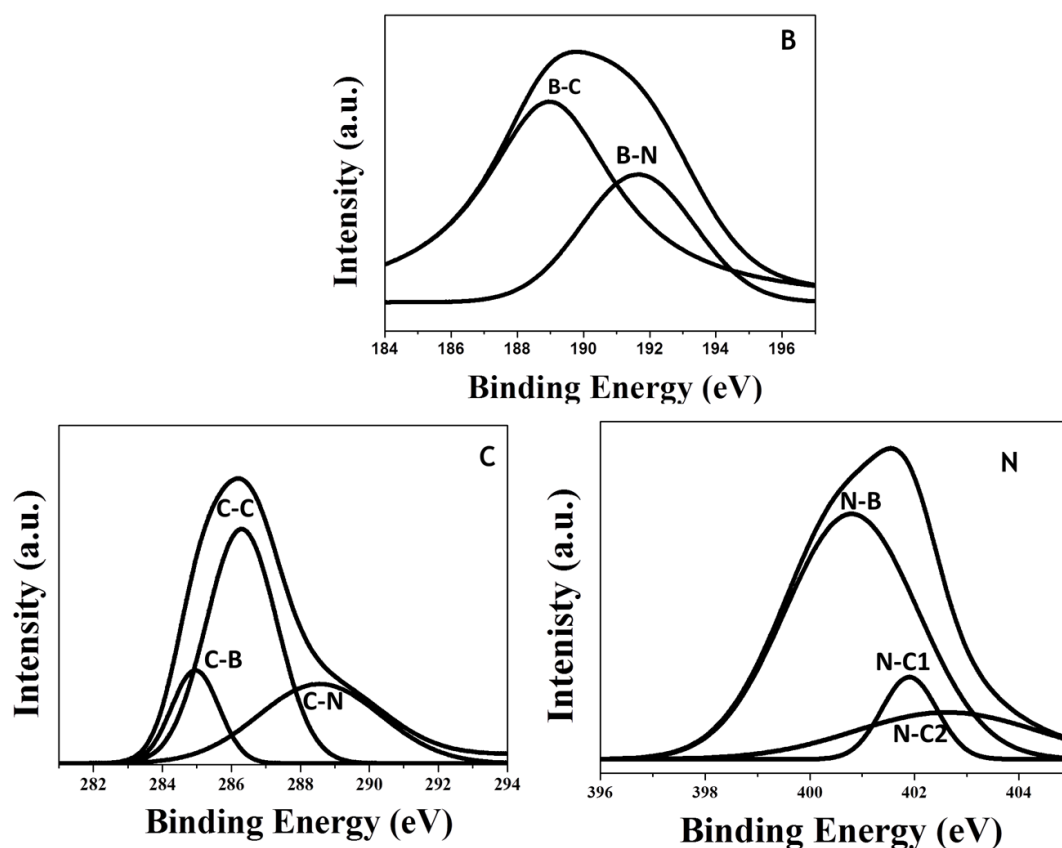
Figure 14 X-ray photo electron spectroscopy (XPS) of the resultant borocarbonitride.

X-ray photoelectron spectroscopy (XPS) measurements show sharp signals for B, C and N atoms (Figure 14). The B 1s signal can be deconvoluted into two peaks at 191.6

and 192.1 eV which are assigned to B-C and B-N respectively. The C 1s signal can be deconvoluted into the three peaks with binding energies 283.1, 285.4 and 289.2 eV which are assigned to C-B, C-C and C-N respectively. The N 1s spectrum shows three peaks centered at 398.4, 401.1 and 402.7 eV which could be attributed to the N-B, pyrolic nitrogen and pyridinic nitrogen atoms. Based on the EELS and XPS results, the composition of borocarbonitride is found to be BC_4N. The HRTEM elemental mapping indicated homogeneous distribution throughout the sample (Figure 13d right).

8.2.4.5 Adsorption Study: CO_2 and H_2 Uptake Characteristics

Figure 15a displays the nitrogen adsorption-desorption isotherms of BC_4N, typical of type-IV isotherms (H1 type broad hysteresis loop), the hysteresis at higher relative pressure ($P/P_0 > 0.4$) indicating capillary condensation of nitrogen within the uniform meso pores in the sample. The estimated textural parameters from adsorption isotherm are compiled in Table 3. The steep uptake of nitrogen at low pressure region (up to P/P_0 ~ 0.4) suggesting the sample contains a high degree of micro pores. The BET and Langmuir surface area of the sample area about 988 m^2/g and 1356 m^2/g respectively with large pore volume of 1.03 cm^3/g. It is worth mentiong that the percentage of micro pore is much higher compared to the other reported boroncarbonitride samples synthesized in different techniques. The N_2 adsorption isotherm reveals the wide pore size distribution centered at 0.9 to 1.5 nm as calculated using Non-Localized Density Functional Theory (NLDFT) method (Figure 15b). The high surface area, large pore volume and heterogeneous surface nature of BC_4N motivated us to study H_2 and CO_2 storage in this BC_4N sample. The sample shows a significant hydrogen uptake of 1.3 wt% (P~1 atm) and 3.26 wt% (40 bar) at 77 K (Figure 15c). The CO_2 storage capacity of the sample is high, the values being 48.6 wt% at 195 K (1 atm) and 31 wt% at 273 K (30 bar) (Figure 15d). The high uptakes of H_2 and CO_2 by this material can be attributed to the heterogenous surface structure with the polar B-C and C-N bonds and $-NH_2$ functional groups, which provide effective interactions with H_2 and CO_2 molecules. It may be noted that BC_4N micro spheres and nanotubes prepared by the reactiion of carbon, boric acid and urea are reported to have surface areas of 428 and 356 m^2/g with CO_2 uptakes of 40 and 23 wt% at 1 atm respectively at 195 K.[7b-c]
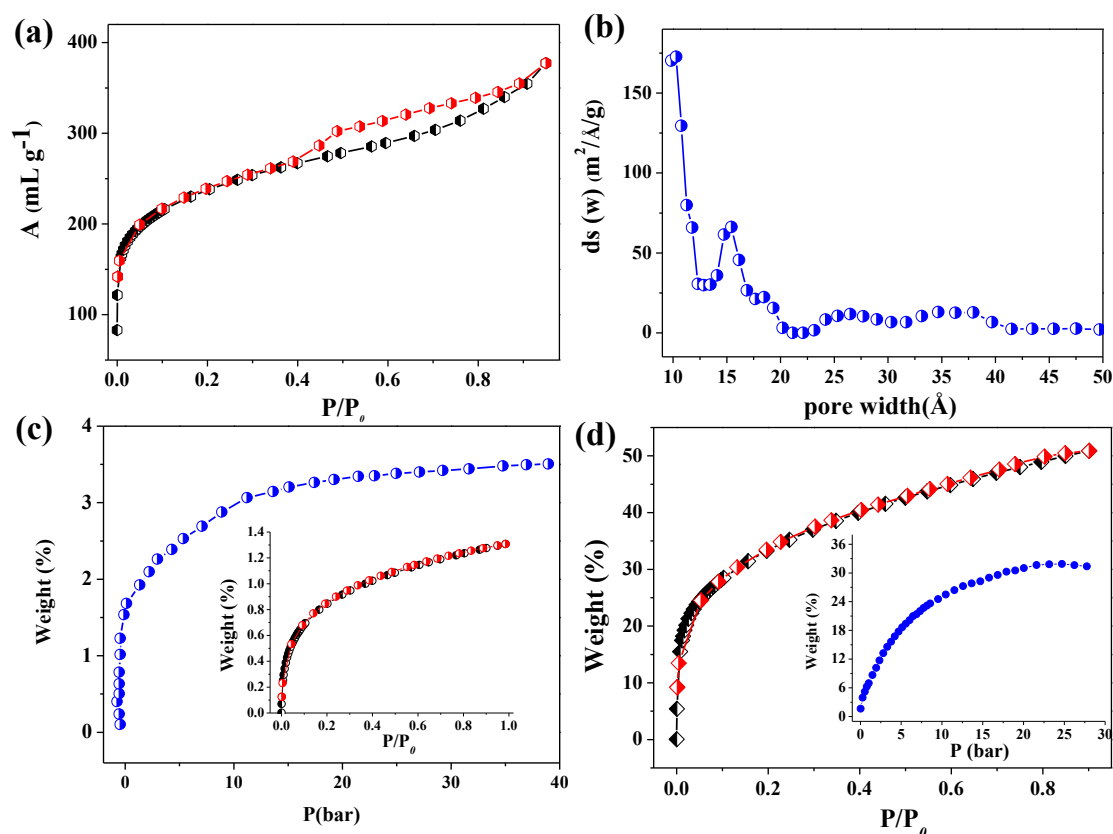
Figure 15 (a) Nitrogen adsorption-desorption isotherm at 77 K; (b) Pore size distribution based on N_2 adsorption profile by the NLDFT method; (c) High pressure hydrogen adsorption isotherm (up to 50 bar) at 77 K (inset showing 1 atm 77 K (d) Carbon dioxide adsorption –desorption isotherm at 195 K and inset showing 298 K 40 bar pressure respectively of nanoporous BC_4N.

8.2.4.6 *In-situ* Stabilization of Au and Pd

We were able to deposit Au and Pd nanoparticles on BC_4N by *in-situ* reduction of the metal salts. The procedure for depositing nanoparticles is described in supporting information. The PXRD patterns exhibit the characteristic reflections of metal nanoparticles. TEM images of the resulting hybrids show, Au@BC_4N and Pd@BC_4N, well separated particles of the size 5-7 nm homogeneously distributed all over the BC_4N sheets (Figure 16). The Au and Pd particles are present in the nano channels of the porous matrix with the heterogeneous surface and anchoring NH_2 groups favouring the binding.
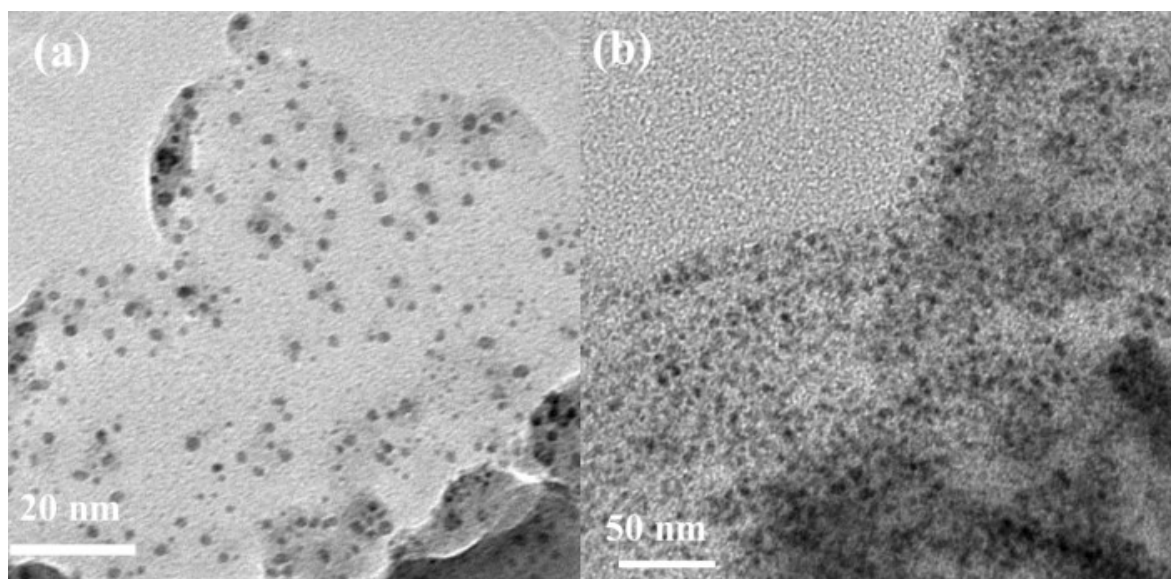
Figure 16 Stabilization of metal nanoparticles on BC_4N: (a) TEM image showing the homogeneous distribution of Au nano particles (size 5-7 nm) over the BC_4N sheets; (b) Similarly Pd nano particles (size 4-7 nm) distribution on the BC_4N surface.

8.2.5 Conclusions

In summary, we have successfully synthesized a three-dimensional boron-based MOF $\{Zn_4(1,4\text{-}ndc)_3(bim)_2]\cdot 2H_2O\}$ from Zn^{II}, tetrakis(1-imidazolyl)borate and 1,4-naphthalene dicarboxylate. We demonstrate that pyrolysis of the MOF produces a nanoporous borocarbonitride with the composition BC_4N. The unusual coral morphology of this material is noteworthy. Furthermore, the borocarbonitride has a large surface area of 988 m^2/g and exhibits high uptake of H_2 and CO_2, compared to the other reported $B_xC_yN_z$ materials. To the best of our knowledge, this is the first report of the synthesis a nanoporous borocarbonitride from a metal-organic framework precursor.

8.2.6 References

1) a) J. Lee, J. Kim, T. Hyeon, *Adv. Mater.* **2006**, *18*, 2073; b) Y. Wang, X. Wang, M. Antonietti, *Angew. Chem. Int. Ed.* **2012**, *51*, 68; c) G. P. Mane, S. N. Talapaneni, C. Anand, S. Varghese, H. Iwai, Q. Ji, K. Ariga, T. Mori, A. Vinu, *Adv. Fun. Mater.* **2012**, *22*, 3596; d) Y. Zhai, Y. Dou, D. Zhao, P. F. Fulvio, R. T. Mayes, S. Dai, *Adv. Mater.* **2011**, *23*, 4828.

2) a) D. Portehault, C. Giordano, C. Gervais, I. Senkovska, S. Kaskel, C. Sanchez, M. Antonietti, *Adv. Fun. Mater.* **2010**, *20*, 1827; b) Y. P. Wu. C. Jiang, R.

Holze, *J. Power Sources* **2002**, *111*, 329; c) P. Wu. S. B. Fang, Y. Y. Jiang *J. Mater. Chem*. **1998**, *8*, 222; d) A. Thomas, A. Fischer, F. Goettmann, M. Antonietti, J. O. Muller, R. Schlogl, J. M. Carlsson, *J. Mater. Chem*. **2008,** *18*, 4893.

3) L.Song, Z. Liu, A. L. M. Reddy, N. T. Narayanan, J. T. Tijerina, J. Peng, G. Gao, J. Lou, R. Vajtai, P. M. Ajayan, *Adv. Mater*. **2012**, *24*, 4878.

4) a) W. L. Wang, X. D. Bai, K. H. Liu, Z. Xu, D. Golberg, Y. Bando, E. G. Wang, *J. Am. Chem. Soc.* **2006,** *128*, 6530; b) D. Golberg, Y. Bando, P. Dorozhikin, Z. C. Dong, Z. C. *MRS Bull.* **2004**, *29*, 38; c) S. H. Jhi, Y. K. Kwon, *Phys. Rev.* **2004**, *69,* 24507; d) J. Pattanayak, T. Kar, S. Scheiner*, J. Phys. Chem. A* **2002**, *77*, 1949.

5) a) R. Sen, B. C. Satishkumar, A. Govindaraj, K. R. Harikumar, G. Raina, J. P. Zhang, A. K. Cheetham, C. N. R. Rao, *Chem. Phys. Lett.* **1998**, *287*, 671; b) R. Ma, Y. Bando, *Sci. Technol. Adv. Mater.* **2003**, *4*, 403; c) R. Ma, D. Golberg, Y. Bando, T. Sasaki, *Nanotechnology of Carbon and Related Materials*, **2004**, *362*, 2161; d) R. Arenala, X. Blaseb, A. Loiseaua, *Adv. Phys.* **2010**, *59*, 101.

6) a) A. Vinu, M. Terrones, D. Golberg, S. Hishita, K. Ariga, T. Mori, *Chem. Mater.* **2005,** *17*, 5887.

7) a) N. Kumar, K. S. Subrahmanyam, P. Chaturbedy, K. Raidongia, A. Govindaraj, K. P. S. S. Hembram, A. K. Mishra, U. V. Waghmare, C. N. R. Rao, *ChemSusChem* **2011**, *4*, 1662; b) K. Raidongia, D. Jagadeesan, M. U. Kahalay, U. V. Waghmare, S. K. Pati, C. N. R. Rao, *J. Mater. Chem*. **2008**, *18*, 83; c) K. Raidongia, K. P. S. S. Hembram, U. V. Waghmare, M. Eswaramoorthy, C. N. R. Rao, *Z. Anorg. Allg. Chem.* **2010**, *636*, 30.

8) a) H. L. Jiang, B. Liu, Y. Q. Lan, K. Kuratani, T. Akita, H. Shioyama, F. Zong, Q. Xu, *J. Am. Chem. Soc.* **2011**, *133*, 11854; b) M. Hu, J. Reboul, S. Furukawa, N. L. Torad, Q. Ji, P. Srinivasu, K. Ariga, S. Kitagawa , Y. Yamauchi, *J. Am. Chem. Soc.* **2012,** *134*, 2864; c) S. J. Yang, T. Kim, J. H. Im, Y. S. Kim, K. Lee, H. Jung, C. R. Park, *Chem. Mater.* **2012**, *24,* 464; d) P. Su, L. Jiang, J. Zhao, J. Yan, C. Li, Q. Yang, 2012. *DOI: 10.1039/C2CC34234K.*

9) a) H. C. Zhou, J. R. Long, O. M. Yaghi, *Chem. Rev.* **2012**, *112*, 673; b) R. J. Kuppler, D. J. Timmons, Q. R. Fang, J.-R. Li, T. A. Makal, M. D. Young, D.

Yuan, D. Zhao, W. Zhuang, H. C. Zhou, *Coord. Chem. Rev.* **2009**, *253*, 3042 ; c) K. Jayaramulu, S. K. Reddy, A. Hazra, S. Balasubramanian, T. K. Maji, *Inorg. Chem.* **2012**, *51*, 7103; d) Y. Cui, Y. Yue, G. Qian, B.Chen, B. *Chem. Rev.* 2012, 112, 1126; e) Y. K. Hwang, D. Y. Hong, J. S. Chang, S. H. Jhung, Y. K. Seo, J. Kim, A. Vimont, M. Daturi, C. Serre, G. Ferey, *Angew. Chem. Int. Ed.* **2008**, *47*, 4144.

10) a) B. H. Hamilton, K. A. Kelly, W. Malasi, C. J. Ziegler, *Inorg. Chem.* **2003**, *42*, 3067; b) J. Zhang, T. Wu, C. Zhou, S. Chen, P. Feng, X. Bu, *Angew. Chem.Int. Ed.* **2009**, *48*, 2542 ; c) S. Zheng, T. Wu, J. Zhang, M. Chow, R. A. Nieto, P. Feng, X. Bu, *Angew. Chem. Int. Ed*. **2010**, *49*, 5362.

11) SMART (V 5.628), SAINT (V 6.45a), XPREP, SHELXTL; Bruker AXS Inc. Madison, Wisconsin, USA, **2004**.

12) G. M. Sheldrick, *Siemens Area Detector Absorption Correction Program*, University of Göttingen, Göttingen, Germany, **1994**.

13) A. Altomare, G. Cascarano, C. Giacovazzo, A. Gualaradi, *J. Appl. Cryst.* **1993**, *26,* 343.

14) G. M. Sheldrick, SHELXL-97, *Program for Crystal Structure Solution and Refinement*; University of Göttingen, Göttingen, Germany, **1997**.

15) A. L. J. Spek, *Appl. Cryst.* **2003**, *36,* 7.

16) L. J. Farrugia, *WinGX - A Windows Program for Crystal Structure Analysis*. *J. Appl. Crystallogr.* **1999**, *32*, 837.

Publications

1. Tunable emission from a porous metal-organic framework by employing an excited-state intramolecular proton transfer responsive ligand.
   K. Jayaramulu, P. Kanoo, S. J. George and T. K. Maji
   Chemical Communications, 2010, 46, 7906-7908.

2. Luminescent microporous metal-organic framework with functional lewis basic sites on the pore surface: specific sensing and removal of metal ions
   K. Jayaramulu, R. P. Narayanan, S. J. George and T. K. Maji,
   Inorganic Chemistry 2012, 51, 10089-10091.

3. Shape assisted fabrication of fluorescent cages of squarate based metal-organic coordination frameworks
   K. Jayaramulu, S. K. Katla, S. J. George, M. Eswaramoorthy and T. K. Maji.
   Chemical Communications 2013, **49**, 3937-3939
   (Highlighted as both Coverage and Hot articles in that issue)

4. Facile Synthesis Multifunctional porous-magneto-luminescent nano tape metal-organic frameworks for highly Selective Sensing For Adenosine Triphosphate (ATP)
   K. Jayaramulu and T.K. Maji.
   (Submitted to Chemical Communications)

5. PH dependent tunable one dimensional nano ribbon coordination polymers
   K. Jayaramulu, K. Ventkatarao, S.J. Geroge, and T.K. Maji
   (Under submission)

6. Conducting nano porous coordination polymers based on NDI with selective adsorption properties.
   K. Jayaramulu, K. V. Rao, S.J. Geroge, and T.K. Maji
   (Under submission)

7. A luminescent mesoporous metal-organic Framework for selective CO_2 uptake, selective dye inclusion and light harvesting properties
   K. Jayaramulu, R. Haldar, K. Ramachadran, I. Swathi and T.K. Maji.
   (Submitted to Chemical Communications)

8. Supramolecular template based hierarchical porous metal-organic framework MMIL-110 (Al]: dye scavenging and efficient scaffold for light harvesting application
   K. Jayaramulu, M.V. Suresh, Symantak Roy and T.K. Maji
   (Submitted to Angewandte Chemie Internarnational Edition)

9. Enzyme Immobilization@MMIL-110(Al) and Catalysis applications

K. Jayaramulu, M.V. Suresh and T.K. Maji
(Submitted)

10. Three-Dimensional Metal-Organic Framework with Highly Polar Pore Surface: H_2 and CO_2 Storage Characteristics.
K. Jayaramulu, S. K. Reddy, S. Balasubramanian and T. K. Maji.
Inorganic Chemistry 2012, 51, 7103-7111.

11. Facile Synthesis of MOF-silica Composites with Tunable Textural Properties with CO_2 Storage and Controlled Drug delivery.
K. Jayaramulu and T.K. Maji
(Submitted)

12. $_pH$ dependent switchable ordered-disordered transformation of ordered hierarchical porous MOC-Clay with remarkable CO_2 and H_2 uptake properties.
K. Jayaramulu, M. Eswaramoorthy and T.K. Maji
(Submitted)

13. Hybrid nanocomposites of ZIF-8 with graphene oxide exhibiting tunable morphology, significant CO2 uptake and other novel properties.
R. Kumar, **K. Jayaramulu**, T.K. Maji and C .N. R. Rao

14. Self-assembly of tetrabromoterephthalic acid with different metal system: Diversity in dimensionalities, structures and gas adsorption.
K. Jayaramulu, R. Haldar and T. K. Maji
Polyhedron, 2013, 52, 553-559.

15. A 3D Bio-MOF of Fe(III): Guest-Responsive Structural Formation, Selective CO_2 Uptake and Controlled Drug Delivery
K. Jayaramulu, B. Saytyanarayana, S. Balasubramanian, S. Kitagawa and T. K. Maji. (Under submission)

16. Honeycomb Porous Framework of Zinc (II): Effective Host for Palladium Nano particles for Efficient Three-Component (A3) Coupling and Selective Gas Storage.
K. Jayaramulu, K. K. R. Datta, M. V. Suresh, G. Kumari, R. Datta, C. Narayana, M Eswaramoorthy and T. K. Maji.
ChemPlusChem 2012, 77, 743-747.
(Hot article in Wiley- Meso Porous materials, 2012)

17. Controllable fabrication and catalytic activity of cuprous oxide nano particles immobilized on the metal-organic framework.
K. Jayaramulu, M.V. Suresh and T.K. Maji
(Submitted to Inorganic Chemistry)

18. Formation and stabilization of metal nano particles (Au, Pt and Au@Pt) by pendant hydroxy groups of porous honeycomb framework**.**
    K. **Jayaramulu**, M.V. Suresh, G. Kumari and T.K. Maji
    (Under Submission)

19. Facile synthesis MOF protected silver nanoparticles for SERS.
    K. Jayaramulu, G. Kumari, Chandrabhas Naryanan and T.K. Maji
    (Under submission)

20. Nanoporous Carbons from MOF with Tunable Porosity Based on Carbonizing Agent: Excellent candidates for Gas Storage and Electrochemical storage.
    K. Jayaramulu, K. K. R. Datta, K. Siva, A. Bhattacharaya, D. Jytosana, M Eswaramoorthy and T. K. Maji.
    (Summited to Journal of Materials Chemistry A)

21. Shape controlled Nitrogen Rich Porous Carbon Material acts Efficient Scaffold for Gold Nanoparticles: Gas storage and Lithium battery application.
    K. Jayaramulu, K. Siva, K. K. R. Datta, M Eswaramoorthy, A. Bhattacharya and
    T. K. Maji.
    (Under submission)

22. Facile synthesis porous C, CN derived from cationic metal-organic framework; **K Jayaramulu**, A. Hazra and T.K. Maji
    (Under submission)

23. A nanoporous borocarbonitride (BC_4N) with novel properties derived from a boron imidazolate based metal-organic framework**.**
    K. Jayaramulu, N. Kumar, A. Hazra, T.K. Maji and C.N.R. Rao
    Chemistry- A European Journal, 2013, 19, 6966-6970.

24. Morphology Controlled Synthesis of Fe_3O_4@C Nanocrystals: Waste Water Treatment and Lithium-ion Battery Applications;
    K. Jayaramulu, K. Siva, A. Bhattacharya, and T. K. Maji
    (Under submission)

25. In-situ stabilization of TiO_2 nano particles encapsulated in to carbon matrix derived from MIL-125 (Ti) and photo catalytic applications
    K. Jayaramulu, U. Maitra, T.K. Maji and C.N.R. Rao
    (Under submission)

26. Sn quantum dots in a porous carbon matrix derived from metal-organic framework as high capacity and high rate capability lithium-ion battery anodes.
    K. Shiva, **K. Jayaramulu**, H.B. Rajendra, T.K. Maji and A. J Bhattacharyya.

(Under Review in ChemSusChem)

27. SnO2@C for high capacity and high rate capability lithium-ion battery anodes.
K. Shiva, **K. Jayaramulu** and A. J Bhattacharyya.
(Submitted)

28. Growth of 2D sheets of a MOF on graphene surfaces to yield composites with novel gas adsorption characteristics.
R. Kumar, **K. Jayaramulu**, T.K. Maji and C .N. R. Rao
(Submitted to Dalton Trans)

29. Raman spectroscopic investigations of temperature dependent gas adsorption on ZIF-8
G. Kumari, **K. Jayaramulu**, T. K. Maji   and C. Narayana.
(Under revision)

30. Guest Responsive conducing coordination polymers
N. Sikdar**, K. Jayaramulu** and T.K.Maji
(Under submission)

31. Supramolecular hydrogels and high-aspect-ratio nanofibers through charge-transfer-induced alternate coassembly.
K. V. Rao, **K. Jayaramulu,** T. K. Maji and S. J. George.
Angewandte Chemie International Edition 2010, 49, 4218-4222

32. Spontaneous self-assembly of designed cyclic dipeptide (Phg-Phg) into two-dimensional nano- and mesosheets
T. Govindaraju, M. Pandeeswar, **K. Jayaramulu**, G. Jaipuria, H. Atreya.
Supramolecular Chemistry 2011, 23, 487-492.

Book Chapter

1. Facile synthesis of porous hetero atom carbon and metal oxide nanostructures derived from metal-organic frameworks: Energy and Environmental applications
 K. Jayaramulu and T. K. Maji
(ERATO Integrated Pores Project)

Dye separation or Dye Scavenging Principle

Several researchers have been trying to use the cloud point technique for the separation of harmful dye molecules and predicting future applications for the recovery of toxic pollutants. However, till the date, metal-organic frameworks (MOFs) are still largely restricted to the microporous regime, despite the negative impact of small pore size on diffusion and mass transfer. Here in, by making use of the merits of the meso pore size, the MOFs are demonstrated to be useful for separation and scavenging for large dye molecules. In chapter 4.1. A luminescent mesoporous framework, $\{[Zn_6(L)_2(H_2O)_6]\cdot 5DMF\}_n$ (**1**) that contains three different cages of different sizes interconnected by several windowsis discussed and it shows size selective dye uptake which is of paramount importance in waste water treatment. The separation of dyes is based on size of dyes and the window dimension of frameworks plays the crucial role. A time dependent UV-vis spectroscopy study shows, the framework **1** selectively adsorbs Acridine Orange (AO) dye ($\sim 1.3 \times 0.65$ Å^2) compared to Rhodamine 6G (Rh6G) (estimated $\sim 1.6 \times 0.9$ Å^2).Chapter 4.2.reports the design and synthesis of nanoscale hierarchical porous metal-organic framework of aluminiumtrimesate (MIL-110) $Al_8(OH)_8\{(OH)_3(H_2O)_3\}[btc]_3\cdot nH_2O$ or MMIL-110c of octahedron morphology where mesopores are interconnected with the inherent micropores of the MOFs. Herein, MMIL-110c exploited for dye scavenging based one meso pore size using various dyes such as Acridine orange (AO), Rhodamine B (RhB) and Methylene blue dye (MB) using UV-visible study.

Erratum

The following corrections were included in the thesis as suggested by referees

1. Page vii, third paragraph, the middle of synthesis and structural should be added " and"

   The sentence has been re written

2. page 9 the first paragraph, metal- organic should be "metal-organic"

   The sentence has been re written

3. Page 13, second paragraph, the second (vi) should be (vii)

   It is modified accordingly

4. Dye separation and Dye scavenger principle has to be included in the thesis.

   We have included principle of dye separation and dye scavenge at the end of thesis.

5. Page 131: Figure 7 should be Figure 8 and Page 134, Figure 11 should be Figure 10.

   It is modified accordingly

6. Title " Structural formation" should be " structural transformation"

   It is modified accordingly

Kolleboyina Jayaramulu

Chemistry and Physics of Materials Unit
Jawaharlal Nehru Centre for Scientific Research Jakkur Bangalore, India-560064
Email (Work): jram@jncasr.ac.in; Personal: jayaram72@gmail.com

Education

Jan 2009- Present	Ph.D
Jawaharlal Nehru Centre for Scientific Research (JNCASR) Jakkur, Bangalore, INDIA.
Thesis Title: "Versatile Applications of Metal-Organic Frameworks (MOFs) and Derived Materials"
Aug 2006- Dec 2008	M.Sc. (Chemical Science)
Aggregate (7.5 out 10 DGPA)
Faculty of Science, Department of Chemistry
Banaras Hindu University (BHU), Varanasi Uttar Pradesh, INDIA.

Research Experience

- Fabrication of functional porous materials into appropriate scales will advance the development of important technologies.
- Tunable emission from microporous MOF based excited state intramolecular proton transfer (ESIPT) responsive linker with selective sensing and removal of metal ions.
- Nanoscale hybrid porous materials mainly, shape assisted fabrication of fluorescent cages with mechanistic inputs, multifunctional (porous, magnetic, luminescent) nano MOF for sensing ATP and conducting porous nano coordination polymer.
- Meso porous MOFs and ordered hierarchical (micro/meso) for gas storage, dye separation light harvesting applications.
- MOF and MOF hybrids of graphene, silica, amino clay materials for gas storage (CO_2, H_2).
- MOF acts template of various metal and metal oxide nano particles (Au, Pd, Pt, Cu_2O, Ru Au@Pt, Au@Pd,) towards SERS, catalysis applications.
- Synthesis of heterodopant porous carbon (CN, BCN) materials into various morphologies from MOF utilized for gas storage, super capacitor and lithium battery applications.
- MOF derived metal oxides (SnO_2, Fe_2O_3, Fe_3O_4, TiO_2) for exploited for lithium battery, water splitting applications.
- Flexible Bio-MOFs for controlled drug delivery applications.

Journal Publications:

1. Tunable emission from a porous metal-organic framework by employing an excited-state intramolecular proton transfer responsive ligand.
   K. Jayaramulu, P. Kanoo, S. J. George, T. K. Maji Chem. Commun. 2010, 46, 7906.
   (Highlighted complete article including TOC in Chem. Rev. 2012, 112, 1126)
2. Supramolecular hydrogels and high-aspect-ratio nanofibers through charge-transfer-induced alternate coassembly.
   K. V. Rao, K. **Jayaramulu,** T. K. Maji , S. J. George. Angew. Chem. Int. Ed. 2010, 49, 4218.
   (Highlighted in Nature India news)
3. Spontaneous self-assembly of designed cyclic dipeptide (Phg-Phg) into two-dimensional nano- and mesosheets T. Govindaraju, M. Pandeeswar, **K. Jayaramulu**, G. Jaipuria, H. Atreya. Supramolecular Chemistry 2011, 23, 487-492.

4. Three-Dimensional Metal-Organic Framework with Highly Polar Pore Surface: H2 and CO_2 Storage Characteristics.
   K. Jayaramulu, S. Reddy, S. Balasubramanian, T. K. Maji. Inorg. Chem. 2012, 51, 7103.

5. Luminescent microporous metal-organic framework with functional lewis basic sites on the pore surface: specific sensing and removal of metal ions
   K. Jayaramulu, R. P. Narayanan, S. J. George ,T. K. Maji, Inorg. Chem. 2012, 51, 10089.

6. Honeycomb Porous Framework of Zinc (II): Effective Host for Palladium Nano particles for Efficient Three-Component (A3) Coupling and Selective Gas Storage.
   K. Jayaramulu, K. K. R. Datta, M. V. Suresh, G. Kumari, R. Datta, C. Narayana, M Eswaramoorthy and T. K. Maji. ChemPlusChem 2012, 77, 743.
   (Hot article in Wiley- Meso Porous materials, 2012)

7. Shape assisted fabrication of fluorescent cages of squarate based metal-organic coordination frameworks **K. Jayaramulu**, S. K. Katla, S. J. George, M. Eswaramoorthy and T. K. Maji. Chem. Commun. 2013, 49, 3937.
   (Highlighted as both Coverage and Hot articles in that issue)

8. A nanoporous borocarbonitride (BC_4N) with novel properties derived from a boron imidazolate based metal-organic framework**.**
   K. Jayaramulu, N. Kumar, T.K. Maji and C.N.R. Rao Chem. Eur. J. 2013, 19, 6966.

9. Self-assembly of tetrabromoterephthalic acid with different metal system: Diversity in dimensionalities, structures and gas adsorption.
   K. Jayaramulu, R. Haldar and T. K. Maji   Polyhedron, 2013, 52, 553.

10. Hybrid nanocomposites of ZIF-8 with graphene oxide exhibiting tunable morphology, significant CO2 uptake and other novel properties.
    R. Kumar, **K. Jayaramulu**, T.K. Maji , C .N. R. Rao Chem. Commun. 2013, 49, 4947.

Submitted:

11. Bifunctional Magnetic and Luminescent Porous Nano Coordination Polymer: Highly Selective Sensing For Adenosine Triphosphate (ATP)
    K. Jayaramulu T.K. Maji (Submitted to Chem. Commun.)

12. A mesoporous metal-organic Framework for selective dye inclusion and light harvesting properties
    K. Jayaramulu, R. Haldar, K. R. Chadran T.K. Maji. (Submitted to Chem. Commun.)

13. Light Harvesting Octahedron Morphology based Ordered Hierarchical Porous Metal-Organic Frameworks.
    K. Jayaramulu, M.V. Suresh, S. Roy and T.K. Maji (Submitted to Angew. Chem. Int. Ed.)

14. Facile Synthesis of MOF-Silica Composites with Tunable Textural Properties with Remarkable CO_2 Storage and Controlled Drug delivery.
    K. Jayaramulu and T.K. Maji(Submitted to Chem. Mater.)

15. $_PH$ dependent switchable ordered-disordered transformation of MOF-Silica with remarkable CO_2 storage**.**
    K. Jayaramulu, M. Eswaramoorthy and T.K. Maji (Submitted to Angew. Chem. Int. Ed.)

16. Controllable fabrication and catalytic activity of cuprous oxide nano particles immobilized on the metal-organic framework.
    K. Jayaramulu, M.V. Suresh and T.K. Maji (Submitted to Inorg. Chem.)

17. Formation and stabilization of metal nano particles (Au, Pt and Au@Pt) by pendant hydroxy groups of porous honeycomb framework**. Jayaramulu**, M.V. Suresh, G. Kumari and T.K. Maji (Under Submission)

18. Facile synthesis MOF protected silver nanoparticles for SERS.
    K. Jayaramulu, G. Kumari and T.K. Maji (Under submission)

19. Nanoporous Carbons from MOF with Tunable Porosity Based on Carbonizing Agent: Excellent candidates for Gas Storage and Electrochemical storage.
    K. Jayaramulu, K. K. R. Datta, K. Siva, A. Bhattacharaya, D. Jytosana, M Eswaramoorthy and T. K. Maji. (Under submission)

20. Shape controlled Nitrogen Rich Porous Carbon Material acts Efficient Scaffold for Gold Nanoparticles: Gas storage and Lithium battery application.
    K. Jayaramulu, K. Siva, K. K. R. Datta, M Eswaramoorthy, A. Bhattacharya and T. K. Maji. (Under submission)

21. Morphology Controlled Synthesis of Fe_3O_4@C Nanocrystals: Waste Water Treatment and Lithium-ion Battery Applications;
    K. Jayaramulu, K. Siva, A. Bhattacharya, and T. K. Maji (Under submission)

22. In-situ stabilization of TiO_2 nano particles encapsulated in to carbon matrix derived from MIL-125 (Ti) and photo catalytic applications
    K. Jayaramulu, U. Maitra, T.K. Maji and C.N.R. Rao (Under submission)

23. PH dependent tunable one dimensional nano ribbon coordination polymers
    K. Jayaramulu, K. Ventkatarao, S.J. Geroge, and T.K. Maji (Under submission)

24. Conducting nano porous coordination polymers based on NDI with selective adsorption properties.
    K. Jayaramulu, K. V. Rao, S.J. Geroge, and T.K. Maji (Under submission)

25. Sn quantum dots in a porous carbon matrix derived from metal-organic framework as high capacity and capability lithium-ion battery anodes.K. Shiva, **K. Jayaramulu**, H.B. Rajendra, T.K. Maji and A. J Bhattacharyya (Submitted to J. Am. Chem. Soc.)

26. Raman spectroscopic investigations of temperature dependent gas adsorption on zif-8.
    G. Kumari, **K. Jayaramulu**, T.K. Maji and C. Narayana (Submitted to J. Phys. Chem. A)

27. Facile synthesis porous C, CN derived from cationic metal-organic framework; **K Jayaramulu**, A. Hazra and T.K. Maj (Under submission)

28. Guest Responsive conducing coordination polymers
    N. Sikdar, **K. Jayaramulu** and T.K.Maji (Under submission)

29. Morphology controlled MOF-Graphene composites with Adsorption properties R. Kumar, **K. Jayaramulu**, T.K. Maji and C .N. R. Rao (Submitted to Dalton Trans)

30. Dynamic guest responsive three dimensional bio-MOF acts efficient controlled drug delivery: Template for both magnetite and hematite nanoparticles.
    K. Jayaramulu, B. Saytyanarayana, S. Balasubramanian, S. Kitagawa and T. K. Maji (Under submission)

Review and Book Chapter:
- Facile synthesis of porous hetero atom carbon and metal oxide nanostructures derived from metal-organic frameworks: Energy and Environmental applications
  K. Jayaramulu and T. K. Maji (ERATO Integrated Pores Project)

Highlights of my work
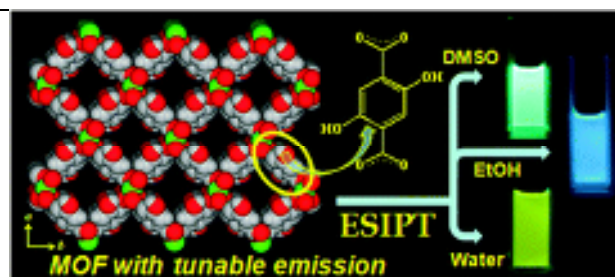
A novel molecular design concept to control the emission of a metal–organic framework, $\{Mg(DHT)(DMF)_2\}_n$, (DHT: 2,5-dihydroxyterephthalate)based on excited state proton transfer (ESIPT) of the organic linker, DHT, is demonstrated. The framework unveils permanent porosity and exhibits ligand-based multicolor emission that can be tuned and well controlled by the solvent molecules in solution as well as in the solid state.
(See. ***Chem. Commun.***, 2010,**46,** 7906-7908, Hight cited article)
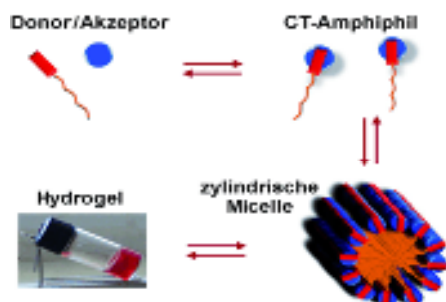
The alternate coassembly of a noncovalent donor–acceptor (D–A) amphiphilic pair in water results in very long nanofibers that form hydrogels (see scheme). Microscopic and single-crystal studies have provided an insight into the hierarchical self-assembly of the charge-transfer (CT) amphiphile, which consists of coronene and a viologen derivative, into cylindrical micelles and gels as the concentration of the D–A pair is increased.(see Angewandte Chemie International Edition 2010, 49, 4218-4222 and highlighted ***nature India)***
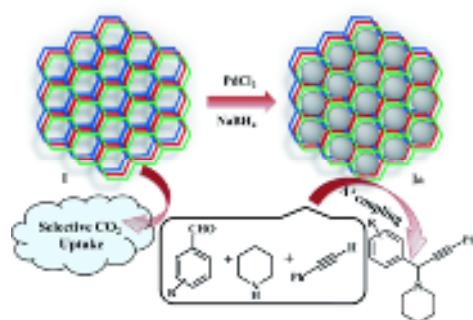
A porous, layered MOF system {[Zn(Himdc)(bipy)]. DMF} (**1**; Himdc=4,5 imidazole dicarboxylate, bipy=4,4'-bipyridine) shows selective gas-storage properties, while the polar nanochannels serve as functional scaffold for the stabilization of highly dispersed Pd nanoparticles. The **Pd@MOF1 a** hybrid is a highly active and recyclable catalyst for the synthesis of propargylamine derivatives through A^3 coupling reactions.

(see, ChemPlusChem 2012, 77, 743-747, it is hot article in meso porous materials in Wiley journals)

Micronic cage structures of squarate based metal–organic coordination frameworks (MOCFs) have been fabricated for the first time by specific anion selective etching of metal squarate cubes. Time and stoichiometry dependent synthesis and the corresponding microscopic studies have provided mechanistic insight into the cage formation. Furthermore, a non-covalent post-synthetic strategy has been adopted to functionalize the micronic cubes or cages with chromophores rendering the resulting hybrids green fluorescent.

(Hot and cover page articles see chem. Commun. 2013,**49**, 3937-3939)

Awards and Recognitions:

- **2013**: Best speaker for oral presentation, entitled as " Varanasi is melting pot of spirituality, Art and culture"
- **2012**: Travel Grant from Department of Science and Technology (DST) for international conference on materials science, Singapore.
- **2011**: Senior Research Fellowship, United Grant Commission (UGC), India.
- **2009:** Junior Research Fellowship, United Grant Commission (UGC), India.
- **2008:** Graduate Aptitude Test in Engineering (GATE) Research Fellowship, India.
- **2008:** Inorganic chemistry topper in M.Sc. Chemical sciences.
- **2006:** Best Student in bachelor of sciences in Andhra Loyola College.
- **2003:** Intermediate (MPC) topper in Andhra Loyola College, Vijayawada.
- **2001:** School topper of A.P.S.R.M. CH. School, Vijayawada, got cash prize from Municipal Corporation of Vijayawada.
- **2000**: Won third place in Chemistry Quiz Competition organized by United Teachers Association, Andhra Pradesh, India.

Personal Information

- Date of birth : 22nd March 1986
- Nationality : Indian
- Languages fluent with : Telugu, English.

References:

Prof. Tapas Kumar Maji Molecular Materials Laboratory International Centre for Materials Science Chemistry and Physics of Materials Unit, New Chemistry Unit Jawaharlal Nehru Centre for Advanced Scientific Research Jakkur, Bangalore, India-560 064 E-mail: tmaji@jncasr.ac.in	**Prof. C. N. R. Rao** CSIR Centre of Excellence in Chemistry and International Centre for Materials Science Chemistry and Physics of Materials Unit, New Chemistry Unit Jawaharlal Nehru Centre for Advanced Scientific Research Jakkur, Bangalore, India-560 064 E-mail: cnrrao@jncasr.ac.in
Prof. Chandrabhas Narayana Chemistry and Physics of Materials Unit Jawaharlal Nehru Centre for Advanced Scientific Research Jakkur, Bangalore, India-560 064 E-mail: cbhas@jncasr.ac.in	**Prof. Balasubramanian Sundaram** Molecular Modelling Laboratory Chemistry and Physics of Materials Unit Jawaharlal Nehru Centre for Advanced Scientific Research Jakkur, Bangalore, India-560 064 E-mail: bala@jncasr.ac.in
Prof. M. Eswaramoorthy Nanomaterials Laboratory Chemistry and Physics of Materials Unit Jawaharlal Nehru Centre for Advanced Scientific Research Jakkur, Bangalore, India-560 064 E-mail: eswar@jncasr.ac.in	**Prof. Subi J George** Supramolecular Laboratory New Chemistry Unit Jawaharlal Nehru Centre for Advanced Scientific Research Jakkur, Bangalore-560 064 India E-mail: george@jncasr.ac.in